UNIVERSITY OF NAPLES, FEDERICO II

PhD Program in: STRUCTURAL, GEOTECHNICAL ENGINEERING AND SEISMIC RISK

XXXII CYCLE

INNOVATIVE SEISMIC RESISTANT STRUCTURAL SYSTEMS FOR TIMBER CONSTRUCTIONS

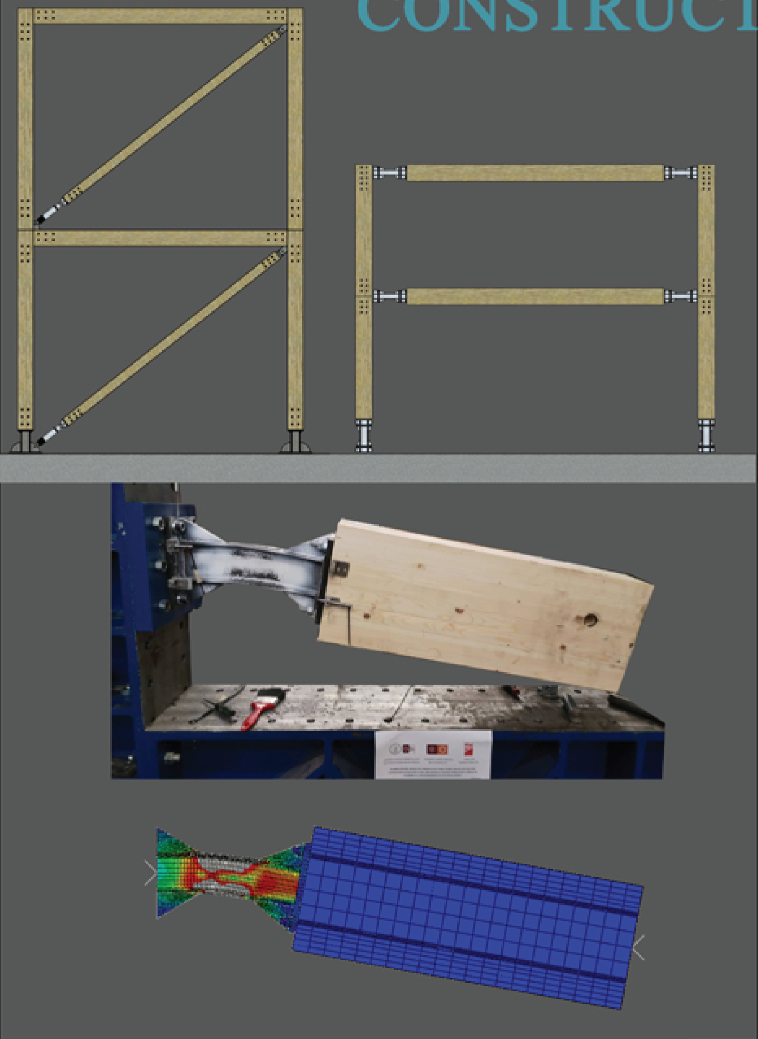

Giacomo Iovane

April 2020

UNIVERSITY OF NAPLES, FEDERICO II

PhD Program in:

STRUCTURAL, GEOTECHNICAL ENGINEERING AND SEISMIC RISK

Coordinator: Prof. L. Rosati

XXXII Cycle

GIACOMO IOVANE

Ph.D. THESIS

INNOVATIVE SEISMIC RESISTANT STRUCTURAL SYSTEMS FOR TIMBER CONSTRUCTIONS

Tutor

PROF. B. FAGGIANO

April 2020

A mio nonno.

Table of Contents

List of Figures

List of Tables

INTRODUCTION

The interest of the scientific community to timber structures in seismic areas is enhanced nowadays, as it is testified by the research activities carrying on worldwide, like in Italy, Portugal, Canada, New Zealand, Japan, devoted to either experimental test campaigns on timber structural systems and nodal assemblages, or numerical modelling and structural capability evaluation (Faggiano and Iovane, 2016).

The acquired knowledge and technology of timber engineering allows to introduce seismic resistant timber multi-story multi-span buildings, with moment resisting frames and concentric or eccentric braced frames, as well as shear wall, concrete wall and concrete core frames. These structural systems are widely used and consolidated in the anti-seismic steel constructions, which have the similarity with timber constructions to be assemblage of members through appropriate joints, even though steel and timber are different materials for origins and mechanical properties. In fact, timber material has an elastic and fragile behaviour up to failure, so that, in order to comply with the current approach to the seismic design of dissipative structures, the common view is that joints should be dissipative through plastic deformations of metallic connectors. This is up to now indicated in the present anti-seismic regulations, such as in Europe the Eurocode 8. However, joints are primary structural elements, with a crucial role in bearing the design loads, therefore the dissipation function should be assumed by ad hoc conceived dissipation devices, as an alternative to connections.

In this perspective the work deals with the seismic design of heavy timber framed structures, specifically equipped with 2 dissipative devices: timber heavy frame structures with *steel link* joints and timber heavy frame structures with *fluid viscous dampers* (FVD).

As regards timber heavy frame structures with steel link joints, capacity design concepts, for seismic moment resisting and bracings heavy timber frames, both not dissipative and dissipative ones, have been recently formulated (Faggiano and Iovane, 2016). Combining timber with a ductile material, like steel, it is possible to realize multi-storey dissipative framed structures, taking advantage of the high strength to weight ratio of wood in lowering seismic design forces (as respect to steel and concrete structures) and, at the same time, by integrating modern timber connection technology into hybrid timber-steel system, brittle wood failure modes can be avoided and the overall seismic performance of timber structures can be improved. The steel devices act as a joint between the timber elements and they are able to develop a significant dissipative capacity. In this context it is possible to take advantage of the knowhow on steel constructions related to the seismic design criteria, according to the approach based on the ductile and dissipation requirements (capacity design approach), for setting up the chapter of the seismic resistant heavy timber structures in the international standards, which are very lacking on this topic, adopting necessary adaptations corresponding to the peculiarities of timber, which should be based on the calibration of the fundamental parameters.

As regards to timber heavy frame structures with fluid viscous dampers (FVD), the principle is to delegate the role of seismic energy dissipation to seismic control devices appropriately designed. FVDs have the aim of dissipating seismic energy, while timber elements and steel connections remain in the elastic field. Literature research and applications demonstrate the use of anti-seismic devices mainly for light-frame timber structures, while on heavy timber frame structures there are still few studies.

In this context, the work aims to define the design criteria for dissipative heavy timber braced and not braced frame structures with ad hoc conceived dissipation devices, steel link joints and FVD devices, through the evaluation of the seismic performance parameters: behaviour factor (q), stiffness, strength, ductile and dissipation capacity. The crucial aspect is the conception of joints. In timber structures engineering this issue is certainly innovative and it has required a significant detailed study aimed at characterizing the mechanical behaviour of the joints in terms of stiffness, strength and ductility.

Specifically, the study is developed in 5 chapters.

In Chapter I “Seismic resistant timber structures”, the state of the art on historical and modern timber structures and design criteria in current regulations (European and Italian standards, CNR-dt 206 r1/2018) are exposed, starting from the main issues for timber structures in seismic areas.

In Chapter II “Conception and design criteria for dissipative seismic resistant heavy timber framed structures”, the main features of the two innovative systems are described. In particular, starting from the most recent researches on the timber frame structures, the concept of the systems (steel links and FVDs) and the design criteria of the structures with the innovative systems are explained. A particular attention is also given to timber joints. Starting from the knowhow on steel constructions related to the Eurocode joints classification, the design criteria and the classification of joints with steel link are proposed.

The Chapter III, “Evaluation of the seismic behaviour of dissipative heavy timber frame structures through numerical analysis”, deals with the application of the systems’ design criteria for dissipative heavy timber structures. In particular, with regard to the system with steel link, 2D single-storey, 2-, 4- and 6-storeys structures equipped with links, in different configurations, where the link is located in the diagonal (CBF) or in the beam (MRF and EBF), are studied, assuming several plan layouts with different number of spans and different values of seismic acceleration. A total of 72 structures are designed and 315 non-linear static analysis are carried out to understand the seismic performance through the behaviour factor q, structural mass, stiffness and strength of the structures. For the FVD system, 2D single-storey structures with dissipative bracing systems, equipped with FVDs, in different configurations, are studied, assuming several rates of possible dampings, with a total of 29 structures, to understand the seismic performance through the structural mass and dissipative capacity of the structures.

The Chapter IV “Beam-to-column joint with steel link: mechanical characterization through numerical analysis and design” deals with beam-to-column timber joints equipped with steel links for dissipative heavy timber seismic resistant MRF structures. The study is inspired by the experimental campaign, consisting of monotonic and cyclic tests on timber beam-to-column assemblages, conducted at the University of Trento. In particular, starting from the numerical simulation of one of the monotonic tests (P10 specimen), the chapter presents a parametrical investigation based on monotonic non-linear numerical analyses of the joint considering the variation of several parameters that can affect the joint behaviour, especially the dissipative capacity and the collapse mode. Based on results, 2 types of joints with two different behaviour are designed through the capacity design procedure, based on the component method application, and monotonic numerical analysis are carried out to check the mechanical behaviour and the accuracy of the design.

In Chapter V “Experimental campaign on timber beam to column joint with steel link”, an experimental campaign, with monotonic and cyclic tests, is carried out on two types of joints, at the Department of Civil Engineering (DECivil) of University of Minho, in Guimaraes (Portugal), during an international Ph.D. research period, in a cooperation with Prof. Jorge Branco, based on the preliminary analytic and numerical design, with the capacity design procedure. The test results are then compared with numerical analysis and analytical design to confirm the design criteria.

At the end, in “Conclusive remarks”, the results of the study are discussed.

Chapter I

1. SEISMIC RESISTANT TIMBER STRUCTURES

1.1 MAIN ISSUES FOR TIMBER STRUCTURES IN SEISMIC AREAS

1.1.1 GENERAL FEATURES

Timber has always been one of the more plentiful natural resources available and consequently is one of the oldest known materials used in constructions. It is a material that is used for a variety of structural forms, such as beams, columns, trusses, girders and is also used in building systems such as piles, deck members, railway foundations and for temporary forms in concrete.

Basically, there are two types of lumber for carpentry: softwoods and hardwoods. The first ones generally come from trees with needle-like leaves (conifers); they are “evergreens”. Hardwoods comprise the broad-leaved trees, mostly deciduous, although there are many broad-leaved trees that are evergreen in certain climates. Generally, the hardwoods are harder and stronger than the softwood. In structural engineering, the term “wood” is usually reserve for small clear elements, free from defects and irregularities on the macro level. Instead, the term “timber” is used to describe elements with structural dimensions, characterized by the presence of macro defects which influence its mechanical behaviour (Grippa, 2009).

Wood is an organic and anisotropic material derived from trees. Its cellular structure is composed of longitudinally arranged fibres which confer to wood a good structural efficiency, represented by a high strength/density ratio, especially in tension. Due to the complex anatomical structure, the strength and stiffness properties of wood in parallel to grain direction are very large in relation to the same ones in transversal orientation. Because timber structural members are cut from trees rather than being formed from a human-made material, they will have some strength-reducing characteristics, defects and biological alterations, such as knots, cross grain, checks, shakes, compression wood, wane and decay. Thus the presence of faults should be considered in the design of structural members. Other factors which affect the mechanical properties of timber are the moisture content, which has a direct effect on both strength and swelling or shrinkage, the creep effect and duration of load. This chapter provides the basic information of the structure and properties of wood and the main features of timber as structural material in constructions, essential in seismic design (Grippa, 2009).

There are many general advantages in using timber for building purposes. It is an environmentally friendly, easily recyclable material. The energy consumption during production is very low compared to that of other building materials. Timber has a low weight in relation to strength, which is advantageous for transport, handling and production. Furthermore, wood has aesthetic qualities, which give great possibilities in architectural design. However, key to the success of the wooden structures is their excellent performance in earthquake.

Timber constructions subjected to earthquake actions provide relevant advantages if compared to traditional materials. Related to its strength, timber has a low mass therefore during earthquake actions the mass excited to oscillations (“seismic mas”) is lower than with other materials, and therefore resulting forces are thus smaller. Furthermore, the large amount of damping derived from friction of contacting surfaces reduces the destructive structural response to the seismic ground shaking. On the basis of these advantages and unlike the fire resistance and the durability due to the biotic attack the seismic performance has never been considered a problem in the determination of the reliability of wood as construction material.

The usage of timber as a construction material dates back to ancient history, with specific techniques differently developed within several countries. In Europe wood has never been used singly as construction material suitable to build earthquake-resistant structures but has always been combined with traditional materials such as brickwork or stone. The usage of wooden structural elements in order to improve the seismic resistance of masonry buildings has been a practice widespread as consequence of disastrous earthquakes that destroyed buildings made with traditional constructive systems. Examples of these constructive systems are the mixed wood-stone building of the Greek islands (Touliatos, 2000), the building system named “Pombalino” developed in Portugal after the earthquake of Lisbon in 1755 (Cóias, 2007; Cóias et al, 2002) and the traditional “himis” in Turkey (Aytun, 1976,), another version of the wood framed walls filled with masonry which survey to the serious earthquake that caused 25000 victims in Izmit in 1999. Moreover, in China and Japan there are excellent samples of seismic-resistant architecture: the century-old monumental temples and pagodas have survived a number of strong ground motions. However, the more common and widespread building systems is the wood-frame constructions which are largely used as residential buildings in USA, Canada, North Europe and Japan. One of the proven features of wood-frame construction is its excellent life safety performance in earthquakes. The results from a scientific research performed in Canada (Karacabeyl et al, 2000) on the behaviour of wood-frame structure after severe earthquakes highlights a very low number of victims compared to the number of buildings involved by the earthquake. These data support the theory that timber buildings are safer than non-timber ones. Despite the previous examples represent the excellence in the earthquake-resistant architecture, experience shows that even a timber structure may suffer significant damage due to an intense seismic event.

The performance of timber buildings under very severe seismic forces was verified following the Loma Prieta and the Northridge (1994) earthquakes in the United States, and the earthquake in Kobe (1995), which affected a wide area of Japan in 1995 and in which such circumstance is clearly emphasized. The former, in particular, highlighted the inadequacies of some timber structures with regard to post-earthquake usability, as a result of significant structural and non-structural damage, especially when buildings were not appropriately designed (Karacabeyli and Popovski, 2003). Some images of earthquake consequences highlight structural problems and damage found to the buildings (Fig. I.1). Many of the structures that were seriously compromised by the earthquakes in Kobe and Northridge were later demolished in the phase of post-seismic operations.

a) b) c) d)

Figure I.1 – a) and b): damage to timber buildings after the Northridge Earthquake; California, 1994 (FEMA 2010; NBCC. 2005); c) and d): damage and collapse of timber buildings after the Kobe Earthquake; (Kitagawa and Hiraishi, 2004; Ceccotti et al, 2007)

These negative examples show that the seismic resistance of the timber buildings is given by a combination of factors and not only by the material lightness. Once defined such seismic resistant factors it is possible to understand the behaviour of the historical timber building and design modern timber structure safety also in seismic zones.

The factors that provide good performance of timber structure in seismic events are: low weight of timber structures, ductility of joints, clear layout of timber houses and good lateral stability of the house as a whole. On the contrary for timber buildings vulnerable parts are: the anchorage of the house, the diaphragm action of floors and the first soft storey which sometimes has been left without sufficient lateral bracing (for example crawl spaces, garages).

It is clear that the cost of repair or reconstruction of buildings after an earthquake can be very high. For some classes of buildings, we need to ensure full or partial use after the earthquake, so that essential services can be maintained. Moreover, today's demand for more sustainable technologies has led to the rediscovery of building techniques and materials that better satisfy this condition. Wood is one of these materials and it is no coincidence that in North America two research projects have been financed, both aiming to mitigate the effect of earthquakes on timber residential buildings (NEESWood Project; Seesl 2006 and CUREE-Caltech Woodframe Project; Curee 2008). So, the new challenge in seismic design is to build structures in which the acceptable level of damage caused by the earthquake is predetermined. This means implementing a reliable design code that relates the building performance, damage and the intensity of ground motion as much as possible (Karacabeyli and Popovski, 2003).

1.1.2 Timber properties

Intrinsic characteristics of wood make it not only suitable but even recommended for use in seismic areas. Anyway, it is also important to consider the weaknesses of this material and design criteria to ensure adequate levels of security as well as an acceptable cost.

As a structural material, wood offers some advantages over other materials in earthquake performance. Wood, generally used for structure, has a density of 500 kg/m^3, about 1/5 of that of the concrete. However, the resistance of wood is similar to the concrete one, with the advantage that wood resist also in tension. The strength/density ratio is quite equal to that of steel; consequently, ground accelerations do not generate as much energy in timber buildings as in other buildings (Tab. I.1).

Table I.1 – Mean features values of traditional construction materials

Mean value	Timber	Steel	Concrete
ρ [kg/m^3]	500	7850	2500
f_k [MPa]	26,5	235	25
E [MPa]	10200	210000	31500

Wood is a building material with good strength capacity compared to the strength/weight ratio of a generic element. The strength characteristics of wood are influenced by its anisotropy and its rheological behaviour (Piazza et al, 2005). The strength and stiffness of a timber construction element vary depending on the defects and the orientation of the applied load compared to the fibre.

The stress-strain curves (σ-ε) of a timber element show a behaviour which is markedly fragile, except for elements compressed perpendicular to the grain (Piazza et al, 2005), as illustrated in Figure I.2. Failure mechanisms due to bending or shear actions are brittle and must therefore be avoided in seismic zones.

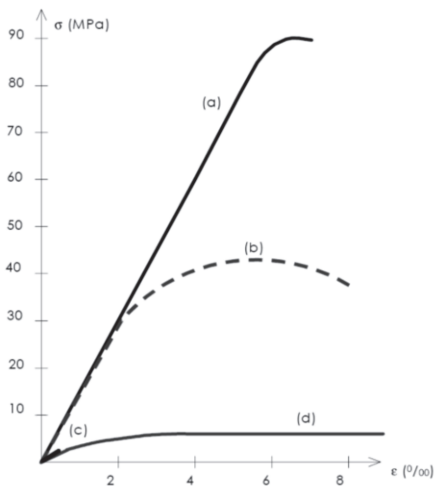

Strength values for clear wood and structural timber

Stress conditions [N/mm^2]	Clear wood	Structural timber
Tension // to grain	80-100	15-40
Tension ⊥ to grain	0,5-0,6	<0,5
Compression // to grain	40-70	20-40
Compression ⊥ to grain	5-10	<5

Figure I.2 – Typical stress-strain curves for clear coniferous wood: (a) tension parallel to the grain, (b) compression parallel to the grain, (c) tension perpendicular to the grain, (d) compression perpendicular to the grain (Piazza et al, 2005).

Under cyclic actions, wood usually performs linearly and elastically. Failures are brittle and these are caused by natural defects in wood, such as knots.

In detail, timber is brittle in tension, especially when the tension is perpendicular to grains. Therefore, perpendicular tension stresses should be avoided. Timber behaves in a ductile manner when loaded under compression, especially compression perpendicular to the grain. This is advantageous in seismic design as, for example, in the traditional carpentry joints used in the pagodas or traditional blockbau houses. However, wood in itself has a low capability for dissipating energy, thus the behaviour of timber structures during seismic events is fully dependent on the behaviour of the joints under cyclic loading. The detailing of joints is thus very important in seismic design (Pozza, 2013).

1.1.3 Joints and connections

Joints represent crucial issue for the seismic resistance of timber structures. There are substantially three different typologies of joints:

- Carpentry joints
- Glued joints
- Mechanical joints

In the first typology the stresses are transferred from one timber element to another one through special work-processing of the elements themselves, such as tenons, tails of swallows, grooves, carvings, etc, without mechanical elements. In glued and mechanical joints, on the other hand, the transfer of stress from one timber element to another one is entrusted to elements in steel, aluminium, carbon fabrics, etc., held together with dry-type systems called connectors (nails, pins, bolts, screws, toothed plates), or epoxy resins.

The carpentry joints (i.e. woodwork joints) are made by means of notches, inlay and grooves on timber elements without using any mechanical connectors. Figure I.3 reports as an example some typical woodwork joints such as mortise and tenon joints, lap joints etc.

These woodwork joints transfer the action by means of perpendicular compression stresses. As states above timber behaves in a ductile manner under perpendicular to grain compression. Furthermore, the friction between the numerous wood-wood contact surfaces confers to these joints a good energy dissipation capacity.

The most significant use of these woodwork joints in timber engineering regards the realization of monumental building such as the Japanese pagodas (Pozza, 2013).

a) b) c)

Figure I.3 – a) and b) example of carpentry joints; c) stress distribution in a carpentry joint.

Glued joints (Fig. I.4) perform linearly and elastically. These do not involve plastic deformations and they do not dissipate energy. For this reason, timber structures with glued joints should be classified as structures that do not dissipate energy and possess no plastic strains. The plasticity and energy dissipation property can be introduced to the connections, if the connections are "semi-rigid" as most mechanical connections used for timber structures are, instead of perfectly rigid joints as, for example, glued joints. Well-designed mechanical connections perform usually in a semi-rigid manner.

Glued joints can be differentiated into 2 types:

- joints with glued steel bars in tension or in shear;
- joints with glued steel plate.

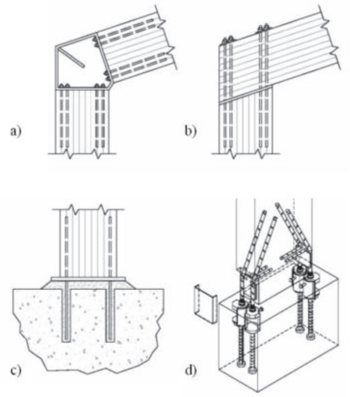

Figure I.4 – Joints with glued steel plate (Andreolli, 2011).

Mechanical joints (Fig. I.5) in timber structures usually perform in a semi-rigid manner and plastic strains may develop, if fastener spacing and end distances match the design rules. The successful performance of mechanical connections is due to high ductility, lack of sensitivity to cyclic loads and their ability to dissipate energy. To ensure the dissipation of energy, it is possible to take advantage of the slenderness of the fastener. The slenderness is defined as the ratio between the timber member thickness and the fastener diameter. Fasteners with high slenderness ratios dissipate more energy since the plastic yield points are, in this case, always formed in the fastener. Fasteners with low slenderness ratios perform more elastically and do not dissipate as much energy. In addition, the wood splitting may be prevented by increasing the member thickness in comparison to the fastener diameter. To avoid an unacceptable strength loss in cyclic loading, three general principles should be followed. Details should be designed so that elements cannot easily pull out, brittle material failures should be avoided, and materials should be used which retain their mechanical properties during cyclic loading. Mechanical joints are largely used in modern timber structure and different typologies of joint can be realized depending on the fasteners employed. As an example, the following Figure I.5 reports the typical fasteners used in mechanical joints (Pozza, 2013).

a) b)

Figure I.5 – Mechanical joints: a) steel connectors; b) toothed plates.

To ensure a ductile response of the structure, the design of the connections should respect the Capacity Design rules (CD rules). The CD rules ensure that the connections are the weakest link between timber elements. The ductility of the system is thus achieved through the proper selection and design of connections (Dolan, 1994). The dissipative capacity of connections, under repeated loadings, is related to the strength of the materials and to the geometric configuration of the joints. Only certain types of connections give the level of ductility and the hysteretic behaviour desired (Piazza et al, 2005).

1.1.4 Building lateral stability

The timber structures are very similar to those in steel which, unlike reinforced concrete structures, are prefabricated. The nodes, in reinforced concrete structures, are rigid, while in timber and steel structures they are configured as hinges. Timber constructions require well designed lateral load resisting systems (LLRS) to transfer forces induced by wind and earthquakes to the foundation of the structure. Such systems include shear walls (panel-type elements with high in-plane stiffness), braced frames (which use pinned beam-column joints with additional inclined members to transfer lateral loads through axial forces), and moment-resisting frames (MRFs) (which transfer loads as applied moments through rigid beam-column connections). In modern construction, lateral load resisting systems are typically comprised of steel or concrete, since their seismic behaviour is well understood; these materials are capable of providing high strength, ductility, and stiffness. The high strength-to-weight ratio of wood gives it inherent benefits for seismic design.

1.2 Structural typologies

1.2.1 General features

The different types of timber structures and how they have evolved over time are described below, starting from the knowledge of the built heritage. Specifically, masonry and timber are materials used since ancient times in construction. Masonry buildings constitute an important percentage of the existing buildings. A drawback on the use of unreinforced masonry is the low resistance to tensile stresses, leading often to an inadequate behaviour under seismic actions. A historical construction solution to improve the mechanical behaviour of ancient masonry adopted in different locations at different times, namely in seismic regions, has been the reinforcement of masonry with timber. Subsequently, the new structural typologies present in the current regulations, their global and local behaviour and construction technologies are described (Vasconcelos et al, 2013).

1.2.2 Historical timber structures

The origin of timber frame structures probably goes back to the Roman Empire, as in archaeological sites half-timbered houses were found and were referred to as Opus Craticium by

Vitruvius (Langenbach, 2009). But timber was used in masonry walls even in previous cultures. According to (Tsakanika-Theohari, 2008; Tampone, 1996; 2001) in the Minoan palaces in Knossos and Crete, timber elements were used to reinforce the masonry. Half-timbered constructions later spread not only throughout Europe, such as Portugal (edifícios pombalinos), Italy (casa baraccata), Germany (fachwerk), Greece, France (colombages or pan de bois), Scandinavia, United Kingdom (half-timber), Spain (entramados) etc., but also in India (dhajidewari) and Turkey (himis) (Langenbach, 2009; Cóias, 2007). In each country, different typologies were used, but the common idea is that the timber frame can resist to tension, contrary to masonry, which resists to compression, thus providing a better resistance to horizontal loads.
Historic buildings with timber structure have developed in highly seismic regions and generally as a result of devastating earthquakes. The more relevant historical earthquake-resistant timber structure are: the mixed wood-stone building of the Lefkas island, Greek (Touliatos, 2000), the Pombalino building system Lisbon, Portugal (Cóias, 2007; Cóias et al, 2002), the Himis building in Turkey (Aytun, 1976) and the Japanese Pagodas (Fujita et al, 2004). Another construction technique largely spread in the past in the European and Middle East areas is the wood-block system (Akan, 2004). Below is reported a brief description of the main characteristics of these building systems.

The Lefkas Island is characterized by high seismic hazard. In 1825 a severe earthquake destroyed all buildings therefore the English authority issued the regulations for seismically safe. Such standards imposed the realization of multi-storey building using a specific constructive system characterized by the 1st storey walls made by stone or masonry which represent the load bearing system of the upper storeys realized within a timber structure. This timber structure was realized by means of frame braced by diagonal elements. Each frame was stiffened by the angular elements located in the corners as depicted in the following Figure I.6 (Touliatos, 2000).

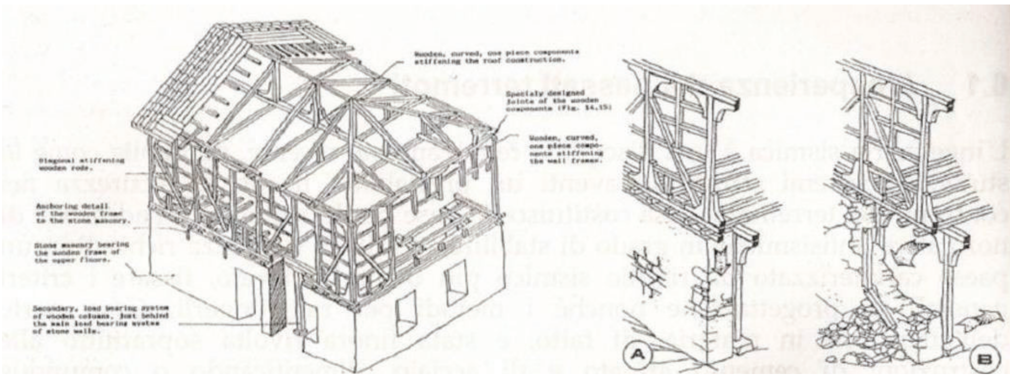

Figure I.6 – View of the seismic-resistant building of Lefkas Island – Greek and the resistant mechanisms under earthquake. In static condition masonry bear vertical load (A) but in case of partial collapse of the wall under earthquake the gravity load is bore by the wooden pillars (B) (Touliatos, 2000).

The particularity of this mixed wood-masonry building is represented by the usage of an additional timber system place in parallel with the walls of the ground floor suitable to bear the vertical loads. Such coupling of timber pillars and masonry wall allows to withstand earthquakes of high intensity that can also cause the partial collapse of the masonry walls but without causing the building collapse. In fact, the timber system in parallel with the masonry bear the vertical load and prevent the collapse of the building as shown in Figure I.6 (A) and (B). The seismic resistance of this constructive system is based on the difference in the deformation capacity under seismic loads of timber and masonry. This coupling ensures high seismic performance although Lefkas Island is highly seismic, and nowadays there are numerous examples of buildings made with this constructive system without damages.

The "Pombalino" system was developed as a result of the earthquake that destroyed the city of Lisbon in 1755. After the earthquake, this building system was chosen as the anti-seismic construction system by an experienced team of engineers appointed by the Marquis of Pompal. This building system consists of a timber frame system made of square fields braced with crosses. The triangles formed of the elements of the frame were filled with masonry. As a result, this building system consists in a timber cage (the "gaiola") filled with masonry which allows the construction of buildings up to 5 floors. The following Figure I.7 reports an example of the Pombalino building (Cóias, 2007; Cóias et al, 2002).

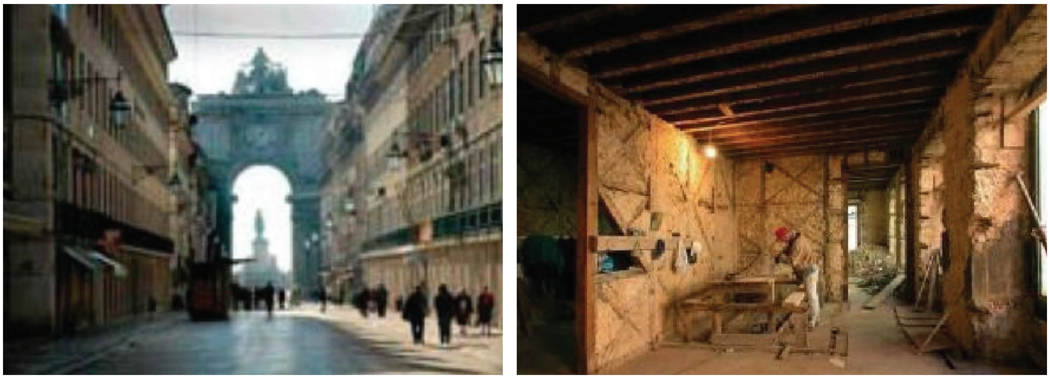

a) b)

Figure I.7 – Lisbon area rebuild with "Pombalino" system: a) after 1755; b) typical "gaiola" wall (Cóias, 2007).

The basic idea of this building system is the usage of timber structural elements in order to improve the seismic resistance of masonry buildings. This building typology is also widespread in non-seismic areas of Europe such as in France, named "Colombage" system (Fig. I.8a), in Germany "Fackwerk" system (Fig. I.8b) and in England "Half-timbered" system. In Germany, fachwerk construction was very popular and several examples of timber frame constructions are present all over the country. Different timber frame styles can be found, characterized by a varying number of storeys and geometry of the timber frame. In Germany, this construction system was introduced in the 7th century and it flourished particularly in the 16th and 17th century. Three main styles can be recognized (Alemannic, Lower Saxonian and Franconian), differentiating mainly in regards of the spacing between the elements, dimensions and disposition of the framing. An example of the German constructions is presented in the lexicon by Otto Lueger (Lueger, 1894).

a) b)

Figure I.8 – a) Example of a “Colombage” building in France (http://www.frenchimmersion.wordpress.com/2012/10/15/house/colombage-house/); b) example of a “Fackwerk” building in Germany (http://www.old-fachwerk-house-in-wolfenbuttel--niedersachsen-germany).

Another example of timber frame construction is the casa baraccata in Italy. After the 1783 earthquake in Calabria, authorities adopted construction methods similar to those imposed some decades before in Lisbon. The same construction technique, with slight changes, was also adopted after the Messina earthquake in 1908. In particular, Vivenzio proposed a 3-storey building with a timber skeleton aiming at reinforcing the external masonry walls, avoiding their premature out-of plane collapse. The timber-framed walls constituted the internal shear walls, presenting a bracing system of S. Andrew’s crosses, similar to what can be found in Lisbon (Copani, 2007). A difference to the Portuguese solution is the continuity of the vertical timber posts from the foundation to the roof, being anchored in the foundation (especially in the buildings built after 1908) (Tobriner et al, 1997; Bianco, 2010).

In Turkey there are several timber and mixed wood-masonry building systems. Similar houses were also found in India and Turkey. Turkey is a prone seismic zone and is frequently subjected to strong earthquakes, meaning that the buildings need to be able to resist seismic actions. Besides, Turkey has an abundance of wood, as well as stone and clay, which promoted the growth of timber frame structures (Vasconcelos et al, 2013).

An extensively treatment about the historical Turkish timber building can be found in (Akan, 2004). The well-known building system used in in Turkey is the traditional “himis” (Aytun, 1976), another version of the timber framed walls filled with masonry which survey to the serious earthquake that caused 25000 victims in Izmit in 1999.

The structural layout of the “himis” building consists of wood bearing structure composed by frame braced by diagonal elements filled-in by masonry or stone. According to the characteristic of regions some variations are observed between structures in different areas as infill material, types of wood, etc. In detail there are three main types of “himis”: sun-dried brick fill, stone fill and brick-fill (Akan, 2004).

The Sun-Dried Brick fill himis system used as filling material sun-dried bricks. It is the most primitive and poor technique used to realize the himis buildings. The following Figure I.9 reports some buildings achieved with this technique.

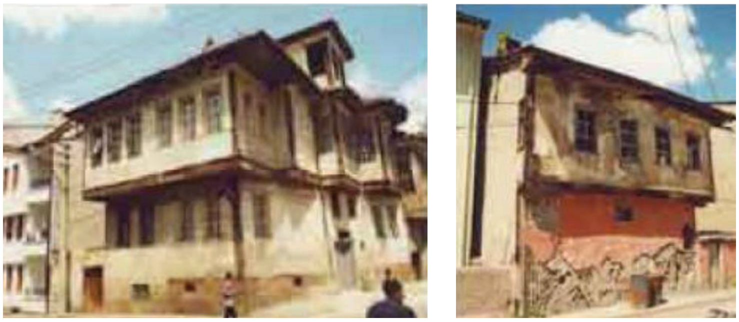

Figure I.9 – Example of Sun-Dried Brick infill himis structures (Akan, 2004).

The Stone fill himis systems are commonly used in areas characterized by coast and forest. In this system, spaces between members of timber frame are filled with stones, which dimensions vary between 10-15 cm. Some examples are shown in Figure I.10.

a) b)

Figure I.10 – Example of Stone fill himis systems (http://www.frenchimmersion.wordpress.com/2012/10/15/house/colombage-house/).

The Brick fill himis system was first use in 16th century. In this method brick is used for infill material and the thickness of the wall was approximately equal to the size of half brick. Filling the bricks into wall can be shaped into horizontal, vertical and crosswise. In Figure I.11 is reported an example of this brick fill himis (Vasconcelos et al, 2013).

a)

b)

Figure I.11 – Example of Brick fill himis system (http://www.frenchimmersion.wordpress.com/2012/10/15/house/colombage-house/).

The proper seismic behaviour of these building typologies is confirmed by numerous comparative studies carried out by Langenbach (Langenbach, 2003).

Traditional timber pagodas in Japan are believed to have high seismic performance. This is because there is no documented record of the destruction of a multi-story timber pagoda during an earthquake, despite their height and low rigidity. The height of timber pagodas ranges from 15 meter to over 50 meters. The structure has a square and symmetrical plan, usually three spans by three spans. The aspect ratio has a tendency to increase and the structure becomes slender for newer pagodas. The structural system of timber pagodas in Japan is composed of the center column and the surrounding multi story frame as shown in Figure I.12. The center column is structurally independent of the surrounding frame structure and is based on the foundation or on top of the beam of the first floor or suspended from the frame. On top of the center column, metal ornamentation called the "sour in" is installed. The columns of the surrounding frame are all based on top of the beam of the lower story and have small aspect ratio.

The seismic performance of timber pagodas has been of interest to seismologists as well as structural engineers, and many analytical studies have been performed and hypotheses proposed. The seismic resistance of traditional timber pagodas has not yet been clarified quantitatively because of the lack of experimental data. However, it seems that the high seismic performance may be due to particular building methodology. The usage of wood-wood joints to realize the structure ensures great flexibility and energy dissipation due to the friction that develops between the carpentry joint surfaces.

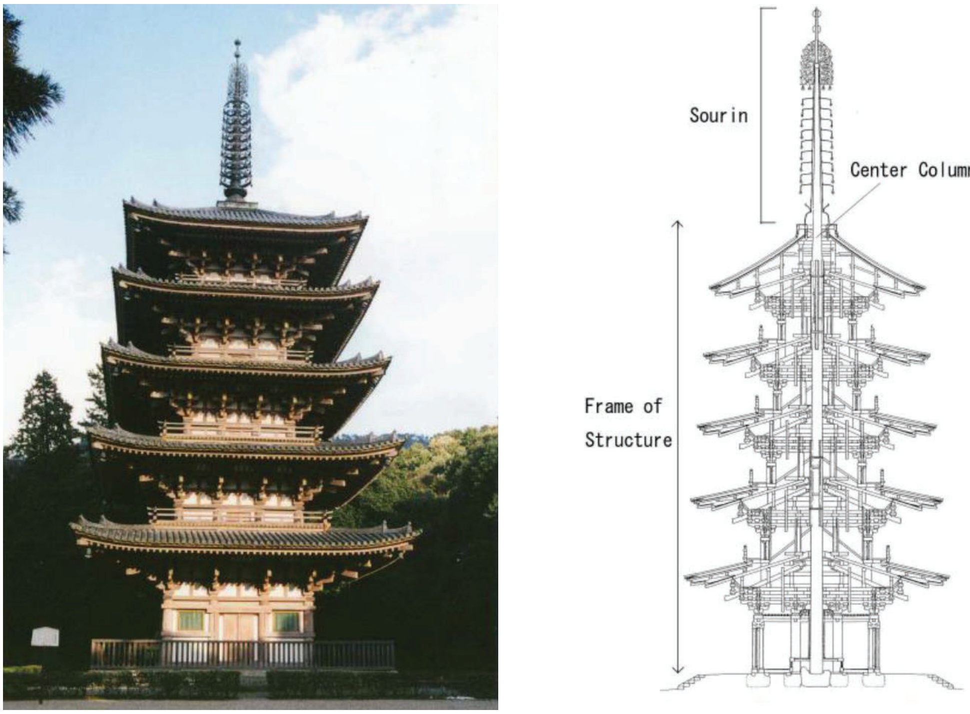

Figure I.12 – Example of the section and picture of Daigo-ij Pagoda (Fujita, 2004).

The wood-block system is a typical constructive technique of the mountain and rural villages of the European and Middle East area characterized by high timber volume. In this construction system the walls are made overlapping round logs that cross in the corner. Two different solutions of corner joints were typically used. In the first solution, a half-lap joint was used while in the second one the wood is removed in both the upper and lower face of the log as depicted in the following Figure I.13.

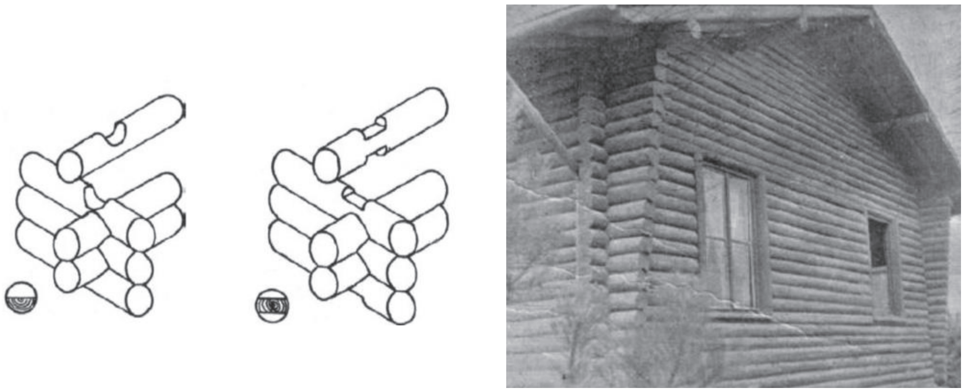

Figure I.13 – Simple wood-block system (Akan, 2004)

The resistance to the horizontal action of this timber system is exclusively due to the friction in the contact surface of the overlapped logs. Such circumstance joined with the vertical load condition perpendicular to the grain imposed the usage of this constructive technique only for small one storey building. Nowadays this building system is steel used in north Europe and alpine area for single storey building named “Log-house” (Vasconcelos et al, 2013).

Among India’s traditional buildings, a half-timbered construction typology can be distinguished in the dhajji-dewari (patchwork quilt wall) system, which is a braced timber frame with masonry infill, frequently used for the upper storeys of buildings (Fig. I.14). Buildings date as back as the XII century (Langenbach, 2009).

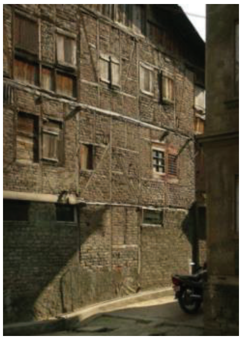

Figure I.14 – India - dhajji-dewari building in Kashmir (Tsakanika, 2008).

Timber frame construction has also been used in South America. In Peru, for example, the quincha presents a one-storey timber frame made of round or square wood (bamboo is often used) and filled with canes covered with earth and gypsum (Gulkan, 2004). This type of construction was for example proposed by Peruvian experts for the reconstruction of Haiti after the severe earthquake of 2010 (Vasconcelos et al, 2013). One of the few buildings which survived the earthquake was actually built with the construction system quincha. The reconstruction proposed is being done with the improved quincha. The posts are grounded in a concrete foundation, the infill consists of canes covered with clay and mud and, once dried, everything is covered with a cement plaster (Vasconcelos et al, 2013).

Based on the analysis carried out on damage state of traditional timber frame buildings located in high prone seismic regions after important seismic events, it has been seen that very reasonable behaviour is exhibited by this structural system in distinct countries with high seismicity (Langebach, 2007). With this respect, it is important to consider that the state of conservation of the traditional buildings can influence its seismic behaviour. After the strong earthquake in 2003 in Lefkada, a high prone seismic region, it was observed that in spite of damages developed in the traditional buildings, they were not so severe than the ones observed in reinforced concrete buildings and no collapse of traditional buildings was recorded. Different authors have pointing out the reasonable earthquake resistance of timber frame buildings, especially with comparison with other structural systems such as masonry or reinforced concrete structures (Fig. I.15), namely during the 1894 Istambul earthquake, 1970 Gediz earthquake and more recent 1999 Marara (Kocaeli) earthquake (Gülhan and Güney, 2000). According to Gülhan and Güney (2000), in Kocaeli-Gölcük, in the Sehitler district, 51% of the buildings are RC buildings (up to 7 storeys), while the rest are traditional (either half-timbered or timber-laced masonry or plain masonry up to three storeys). From these, only 0,5% of the traditional structures presented heavy damages or collapsed against 7,4% of the RC structures, 0,6% of the traditional structures presented moderate damage versus 8,6% of the RC and 10% and 16,5% respectively presented light damages.

a) b) c)

Figure I.15 – Examples of damages in timber frame buildings: a) out-of-plane collapse of masonry infill (Lefkada, Greece, Makarios and Demosthenous, 2006) ; b) comparison of damages to traditional and modern building after the 1999 Duzce earthquake; c) failure of connection in timber frame (1999 Kocaeli earthquake (Gülhan and Güney, 2000).

The earthquakes of India 2001 and El Salvador 1986 are other two examples where the timber-laced masonry buildings and the Bahareque timber frame buildings behaved considerably better than reinforced concrete or unreinforced masonry (Langebach, 2007). The heavy damage and inadequacy of timber frame building under earthquakes, as occurred in Nicaragua 1936, can often be attributed to the poor condition of the connections due to inadequate conservation. More recently, during the earthquake of Haiti in Januray 2010, it was seen that a great number of concrete block and reinforced concrete buildings were heavily damaged, resulting in the loss of a dramatic number of human lifes and in a huge economic impact in the economy (Langebach, 2010). Contrarily, the behaviour of traditional timber frame buildings did not exhibit so much severe damage. Both the braced timber frame and the colombage, with more flexible, energy dissipating systems tended to perform best than the other structural systems (masonry and reinforced concrete) (Langebach, 2010; Vasconcelos et al, 2013).

1.2.3 New timber structures

1.2.3.1 General aspects

In recent times the interest of the scientific community to timber structures in seismic areas is enhanced, as it is testified by the research activities carrying on worldwide, like in Italy, New Zealand, Japan, devoted to either experimental test campaign on structural systems and nodal assemblages, or numerical modelling and structural capability evaluation (Faggiano and Iovane, 2016).

With regards to the seismic resistant structural type, the acquired knowledge and technology on timber engineering allow to introduce for timber multi-storey multi-span buildings the moment resisting frames and concentric or eccentric braced structures, but also shear wall and concrete wall frames and concrete core frames. These structural systems are widely used and consolidated in the steel constructions seismic engineering. Even though steel and timber are different materials for origins and mechanical properties, the similarity between steel and timber structures comes from the assemblage in both cases of members through appropriate joints.

The seismic-resistant timber structures can be divided, therefore, into three categories according to the system used to counteract the seismic actions, as reported in the CNR regulation:

- Heavy timber framed structure;
- Shear wall structure;
- Blockhaus system.

In the field of heavy timber framed structures, similarly to steel seismic resistant structures, it is possible to introduce the distinction among different types of seismic structures, with reference either to the structural system resistant to horizontal actions or, specifically for dissipative structures, to the mode of dissipation of the seismic energy. They are (Fig. I.16):

- Moment Resisting Frame (MRF);
- Frame with bracings (Concentric Bracings - CBF; Eccentric Bracings - EBF);
- Frame with shear walls (SWF);
- Frame with concrete cores or concrete walls (CCF-CWF).

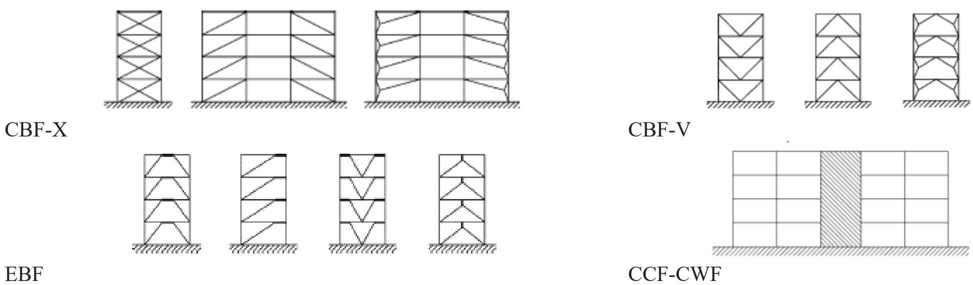

Figure I.16 – Seismic resistant structural types (according to EC8 - Steel Structures: EN 1998-1-1, 2005)

In particular, the timber framed structures can be made of solid or glue-laminated timber. Structural members can have square or rectangular solid cross sections, or box cross sections; columns can also be composed by two vertical elements adjacent each other or connected by battens disposed at constant spaces; lattice members may be realized.

Connections between the elements can be realized by means of metal devices, such as cylindrical shank connectors, or of carpentry glued joints, the latter being deemed as not dissipative. Connections should realize various conditions of constraint depending on the static scheme of the structural type adopted and in dissipative structures they can have the function of dissipative zone. In this case, for an appropriate conception of connections, it is necessary to apply the capacity design between the joint components, so that the ultimate condition corresponding to the plasticization of the connectors, thus guaranteeing high ductility, can be achieved. The dimensional features of the components should be calibrated so that fragile collapse modes are prevented. In case of dissipative structures timber members have to behave as elastic and feature adequate overstrength as respect to dissipative elements.

1.2.3.2 Heavy timber framed structure

Heavy timber moment resisting frames

Moment resisting frames (MRF) are constituted by the assemblage of beams and columns through connections. Members are subjected to bending, predominantly. Beam-to-column connections should be rigid, able to transfer the cyclic forces, including bending, induced by the seism. The column-foundation connection can realize a fix (or semi-rigid connection) or a pin restraint.

Dissipative MRFs could present, as dissipative zones, the connections themselves between the members or the links located at the beam ends (Fig. I.17). The seismic energy dissipation could occur through the plastic deformation of the connections or the links for cycles in bending, forming the so-called plastic hinges.

Figure I.17 – Example of MRF timber structure.

Heavy timber frame with bracings

They are lattice structures that resist the horizontal actions thanks to the diagonal bracings. Members are mainly subjected to axial forces. The connections between the structural elements should realize a pin constraint.

Frames with bracings can be distinguished in frames with concentric bracing (CBF) and frames with eccentric bracings (EBF), depending on the geometry and the dissipative modality, as indicated hereafter.

Concentric Braced Frames

X braces (CBF-X, Fig. I.18a). The diagonal braces can be made of either steel or timber. In case of steel braces, only the diagonal in tension is considered effective for the purpose of resistance, while the diagonal in compression can buckle and, at collapse, it is deemed as not effective; for this reason, at the ultimate limit state, the model of only diagonal in tension active is adopted. In case of timber braces, both the diagonals in tension and compression can be considered and dimensioned, offering a high stiffness to the bracing frame even at the ultimate limit state, therefore the model with both diagonals actives could be adopted.

V Braces (CBF-V, Fig. I.18b). Both diagonals in tension and compression can be considered active. The peculiarity of this configuration is that diagonal braces converge in the beam, thus requiring specific design criteria for the beam itself.

Dissipative CBFs could present as dissipative zones, in case of steel braces, only the diagonal in tension, while, in case of timber braces, the connections between elements or the links placed at the braces ends. The dissipation of the seismic energy could occur through the plastic deformation of either diagonals in tension or connections or links, if diagonals are made of steel or timber, respectively, for cycles of axial forces.

Eccentric Braced Frames

The particular configuration of the diagonal braces (Fig. I.18c) allows to realize structures, which combine the advantages of MRFs, such as freedom of space composition and possibility of wide openings within the façades, and that of CBFs, like the high lateral stiffness.

Dissipative EBFs could present as dissipative zones the links. Such elements are geometrically and mechanically identified in function of the position of the diagonals. Generally, they can be located within the beams, but in case of the inversed chevron braces, they can be vertical elements, which join the diagonals vertex with the middle of the beam. The dissipation of seismic energy could occur through the plastic deformation of the links for cycles of bending or shear or bending and shear.

a) b) c)

Figure I.18 – Example of a a) CBF-X, b) CBF-V and c) EBF timber structures.

Heavy timber frames with shear walls, concrete cores or concrete walls

These structures are composed by two combined structural systems: a beam-column frame, which can be made of both solid and glue-laminated timber, designed only for vertical loads, and a vertical structural system, with stiffening and stabilization functions against horizontal actions.

The bracing role can be fulfilled through several systems, such as for example (Fig. I.19):

- Timber CLT (X-LAM) walls (cross laminated timber);

- Timber-based or gypsum panels;
- Masonry panels;
- Reinforced concrete walls or cores;
- Cold-formed steel structure panels;
- Steel MR or Braced Frames.


a)

b)

Figure I.19 – a) Example of a frame structure with CLT (X-LAM) wall; b) Example of a frame structure with reinforced concrete wall.

1.2.3.3 Shear wall structure

Cross Laminated Timber structure (CLT) or X-LAM

One of the most common main structural systems, especially for multi-storey buildings, is that called CLT or X-LAM (laminated solid wood panels with crossed layers) that presents a variable thickness from 5 to 30 cm and is made by gluing cross-layers of boards of medium thickness of 2 cm. And they can reach lengths up to 16 m and with a height equal to the inter-floor height, prefabricated by cutting with numerical control machines and already complete with openings. Once they arrive at the construction site, they are hoisted with mechanical lifting means and connected to each other and to the foundations: the construction process is very fast, although transport may be more difficult, especially in construction site areas with limited accessibility. A schematic diagram of the functioning of structural shear walls against lateral loads is shown in Figure I.20, where a simple “box-like” building is loaded laterally.

The floor diaphragm is supported at the ends by shear walls, which in turn transfer the load to the foundations. Such structural configurations may be side by side or one on top of the other as in a multi-storey house. In multi-storey houses the lateral loads cumulate to the lower storeys. The structural parts should, of course, be properly attached to each other in order to ensure that an intact path for the lateral forces does exist. This includes the connection between the floors and supporting shear walls and between the shear walls and the foundations.


a)


b)

Figure I.20 – a) Example of a CLT (X-LAM) structure; b) foundation connection of a CLT (X-LAM) structure.

Light-frame or Platform frame structure

Another shear wall structure is the Light-frame system or Platform frame system. It is a system with shear walls made of small frames with structural elements in solid wood or laminated wood stiffened by panels. The frame, made with uprights and currents (Figure I.21), is opposed to the vertical actions while the frame with the panel to the horizontal ones. The panels used in this type of system, for the NTCs in chapter 7.7.2 can be either particle type, with a specific weight exceeding 650 kg/m^2 and a thickness not less than 13 mm, or plywood with a thickness not less than 9 mm. Furthermore, due to the distances imposed for nailing, the minimum base of the element constituting the frame (at least at the joints of the panels) must be 80 mm. Among the particle board panels, those with the best mechanical characteristics are OSB (Oriented Strand Board), made with synthetic resins and with thin veneers (strand). The strands are pressed in 3-4 layers: those of the outer layers are generally oriented longitudinally with respect to the length of the panel, while the strands of the intermediate layers are transverse.


a)


b)

Figure I.21 – a) Example of a light-frame (platform frame) structure; b) a complete shear wall with light-frame system.

1.2.3.4 Blockhaus system

The Blockhaus system (Fig. I.22) foresees that, on the construction site, the solid or lamellar fir wood planks are stacked horizontally on top of each other to form the dividing or structural wall, fixed by grooves and jointing tabs. The corner joint between the walls is generally obtained by means of a visible male-female carpentry knot or dovetail joint and potentially reinforced with metal bars or screws. The connection between wooden walls and the reinforced concrete foundations is obtained using resin-coated metal bars. Blockhaus mainly entrusts resistance to static action (vertical loads and wind) and seismic action almost exclusively to the wood (resistance to horizontal action is guaranteed by the tapping of the crossover and friction between overlaying beams or trunks) and the mechanical connection elements are used to a very limited degree. Significant in Central-Northern Europe and in the Italian sub-Alpine and Alpine areas.


a)


b)

Figure I.22 – a) Example of a blockhaus system structure; b) wall's assemblage detail.

1.3 Codifications

1.3.1 General aspects

The field of timber structures is strongly developed all over the world in the last decade. In fact, thanks to easiness and quickness of construction, transportation, sustainability, energy efficiency and good seismic response they have become a valid alternative with respect to traditional construction materials, such as reinforced concrete, steel, etc. A significant increase of the use of timber-based structures has been recorded not only in North Europe, which represents the typical area devoted to the use of timber systems, but also in the countries of Mediterranean area, like in Italy. In fact, according to Federlegno Arredo (2018), the timber building stock was estimated in Italy as a percentage of 7,0% of the overall market of residential buildings, percentage destined to grow in the coming years.

The technological progress in the case of timber structures is not immediately accompanied by an updating of design standards. In this light, at European level a revision of the Eurocode 8 (chapter 8) (EC8, UNI EN 1998-1, 2005), regarding the seismic design of timber buildings is recently started and it is quite to the conclusion (Follesa et al, 2018). Parallel to this, in Italy, there is the Technical standards for construction (NTC2018) and a review process of the Technical Document DT

206/2007 “Instructions for the design, execution and control of timber structures” is started in 2015 and concluded in 2018.

1.3.2 THE EUROCODE 8 – PART 1 - CHAP. 8: SPECIFIC RULES FOR TIMBER STRUCTURES

According to Eurocode 8 (EC8, UNI EN 1998-1, 2005) it is possible to design two types of timber structures:

- Non-dissipative structures;
- Dissipative structures.

The *non-dissipative* structures are designed so that, under the seismic action, all the structural elements remain in the elastic field, exploiting only their own resistance.

Commonly, *dissipative* structures, instead, are conceived so that a part of the seismic energy can be dissipated through cycles of inelastic deformation of special devices or parts of the structural elements (dissipative zones) specifically identified and introduced in the structural scheme. These elements have to ensure large plastic deformation, before collapse, while the remaining parts of the structural elements have to behave as elastic during the earthquake. The modern philosophy of seismic design at the Ultimate Limit States (SLU) allows reducing the linear elastic spectrum through the so-called behaviour factor q, trusting in the capability of the structure to dissipate the seismic energy.

The non-dissipative structures are designed with a behaviour factor $q=1$.

Among the dissipative structures, the Eurocode 8 provides different levels of seismic energy dissipation capacity as a function of the structural type:

a) Structures with “Low” capacity to dissipate energy (DCL);
b) Structures with “Medium” (DCM) or “High” (DCH) capacity to dissipate energy.

DCL structures (a) are designed as elastic, without any particular requirement for elements and connections, beyond what indicated for aseismic structures in Eurocode 5 (EC5, EN 1995-1-1, 2005). However, accounting for an even small extent of energy dissipation capacity, the behaviour factor q, to be applied to reduce the elastic response spectrum, is greater than 1 and equal to 1,5. Timber members, as well as the connections, are verified on the basis of the design forces, without applying the capacity design, as the hierarchy resistance criterion.

Dissipative structures (b), as a function of the ability to dissipate energy, are classified according to two possible levels, High or Medium, characterized by appropriate values of the behaviour factor (q>1,5). Since timber is a material with predominantly elastic-brittle behaviour up to collapse, only connections can be considered as dissipative, while the timber elements should behave as elastic, therefore designed with an appropriate overstrength as respect to the dissipative elements. In this way the capacity design is applied, with the purpose to achieve plastic deformation concentrated in the dissipative zones, so that at the SLU the desired collapse mechanism can develop.

Definitely, three ductility classes are defined and associated to structural typologies with related behaviour factors in Table 8.1 of EC8, here reported in Figure I.23a. The values given in Table 8.1 are the highest usable for each structural type; they still should be reduced by 20%, if full regularity in elevation is not provided.

The structural cases presented in Table 8.1 could be used as seismic structures, if connections are designed according to specific details. In particular, materials and mechanical devices should be able to perform with an appropriate non-linear cyclic behaviour, being connections assumed as dissipative zones. Glued joints should be considered as non-dissipative. The appropriate dissipative behaviour of connections is assumed to be guaranteed, if they undergo cyclic tests, through a specific procedure, consisting in 3 full cycles, with a static ductility ratio (ratio between the ultimate deformation and the deformation at the elastic limit evaluated in quasi-static cyclic tests) equal to 4 and 6 in case of DCM and DCH structures, respectively, with a maximum resistance reduction equal to 20%.

Nevertheless, it is not always easy to provide experimental tests, therefore such requirements are assumed as satisfied in case the thickness of the timber elements and the diameter of connectors are adequate. If these conditions are not satisfied, but at least a minimum thickness of the connected elements is assured, reduced values of the q factor should be adopted as given in Table 8.2 of the EC8 reported in Figure I.23b.

The carpentry joints, which can be realized also in new constructions, could be used only if they are able to assure an adequate dissipation capacity. Such joints should not develop fragile collapse modes, due for example to shear or tension in perpendicular direction as respect to the grain, and they could be used only on the basis of reliable tests results, demonstrating the post-elastic capabilities.

Table 8.1: Design concept, Structural types and upper limit values of the behaviour factors for the three ductility classes.

Design concept and ductility class	q	Examples of structures
Low capacity to dissipate energy - DCL	1,5	Cantilevers; Beams; Arches with two or three pinned joints; Trusses joined with connectors.
Medium capacity to dissipate energy - DCM	2	Glued wall panels with glued diaphragms, connected with nails and bolts; Trusses with doweled and bolted joints; Mixed structures consisting of timber framing (resisting the horizontal forces) and non-load bearing infill.
	2,5	Hyperstatic portal frames with doweled and bolted joints (see **8.1.3(3)P**).
High capacity to dissipate energy - DCH	3	Nailed wall panels with glued diaphragms, connected with nails and bolts; Trusses with nailed joints.
	4	Hyperstatic portal frames with doweled and bolted joints (see **8.1.3(3)P**).
	5	Nailed wall panels with nailed diaphragms, connected with nails and bolts.

a)

Table 8.2: Structural types and reduced upper limits of behaviour factors

Structural types	Behaviour factor q
Hyperstatic portal frames with doweled and bolted joints	2,5
Nailed wall panels with nailed diaphragms	4,0

b)

Figure I.23 – a) Structural typologies and behaviour factors q for the ductility classes according to Eurocode 8; b) Structural typologies and behaviour factors q reduced according to Eurocode 8.

1.3.3 THE NTC2018 - ITALIAN TECHNICAL CODE FOR CONSTRUCTIONS - CHAP. 7.7: TIMBER STRUCTURES

The NTC 2018, in the chapter on the seismic design of timber constructions, fully refers to EC8, with the only variation related to the ductility classification of the structures. In Table I.2, which presents the English version of the Table 7.7.I of the NTC2018, the ductility classes associated to the structural typologies with the related behaviour factors are defined.

In particular, similar to steel constructions, non-dissipative and dissipative structures, the latter divided in two ductility classes (CD), low CDB and high CDA, are distinguished.

In Table I.2, the behaviour factor is indicated as "q_0", it being the maximum reference value, depending on the structural typology and the ductility class. The *q* factor is calculated as $q=q_0\ K_r$, where *Kr* is the reduction coefficient due to irregularities of the structure, being equal to 1 and 0,8 for regular and irregular structures, respectively. Definitely, due to irregularity the same EC8 20% reduction is applied.

For non-dissipative structures q-factor is equal to 1,5. No capacity design is applied; therefore members and connections are verified on the basis of the design forces, without any overstrength. For CDB and CDA structures, q_0 values range between 2-2,5 and 3-5 respectively.

It is worth noticing that the structural types presented are few and they do not include multi-story structures. Furthermore, the detailed rules for the design are totally inadequate for realizing the connections as dissipative zones and allowing a controlled exploitation of the dissipative capacity as well as the desired collapse modes.

Table I.2 – Structural typologies and behaviour factors q_0 for the ductility classes according to NTC2008.

Class		q_0	Examples of structures
A	Structures with high capacity to dissipate energy	3	Nailed wall panels with glued diaphragms, connected with nails and bolts; trusses with nailed joints
		4	Hyperstatic portal frames with doweled and bolted joints
		5	Nailed wall panels with nailed diaphragms, connected with nails and bolts
B	Structures with low capacity to dissipate energy	2	Glued wall panels with glued diaphragms, connected with nails and bolts; trusses with doweled and bolted joints; mixed structures consisting of timber framing (resisting the horizontal forces) and non-load bearing infill.
		2,5	Hyperstatic portal frames with doweled and bolted joints

1.3.4 THE CNR-DT 206-R1 - INSTRUCTIONS FOR THE DESIGN, EXECUTION AND CONTROL OF TIMBER STRUCTURES - CHAP. 10: DESIGN FOR EARTHQUAKE

The technical document DT 206-R1 - 2018 - "Instructions for the design, execution and control of timber structures" has the purpose to provide a technical support to the operators of the sector, in line with the most advanced knowledge at that time. The world of timber engineering largely use such document, even though the instructions are not mandatory standard rules, so that they became the most common tool in Italy for the structural use of timber, opening the markets and favouring competition and new applications. The document comes from the spontaneous cooperation of an open group of specialists and operators of the sector, based on a wide discussion on the common scientific and technical expertise and knowledge.

In analogy with the other structural systems (i.e. reinforced concrete and steel buildings) the capacity design approach is considered also to design timber structures in seismic prone area (Faggiano and Iovane, 2016; Casagrande et al, 2019). Then, the plastic behaviour of the connection elements, behaviour factors, ductility classes and hierarchy of strength to be used in linear static analyses are described in detail.

Earthquake-resistant timber buildings shall be designed in accordance with one of the following concepts:

a) Low-dissipative structural behaviour;
b) High- or Moderate-dissipative structural behaviour.

In concept a) the design spectrum can be applied with a behaviour factor q not greater than 1,5.

In concept *b)* the value of the behaviour factor is given in Table 1.3 according to the structural type and assigned ductility class (High "A" or Medium "B"). Dissipative zones are generally assumed to be located in mechanical joints, whereas timber members behave elastically.

Structures may be classified in ductility classes A or B without any further specification if the following conditions for the mechanical connections in the dissipative zones are met: brittle failure modes like splitting, shear plug, tear out and tensile fracture of wood in the connection regions are avoided; for timber-to-timber dissipative connections, the failure mode is a ductile failure mode characterized by the formation of two plastic hinges in the metal fastener for DCA, one plastic hinge in the metal fastener for DCB. Some design criteria for structural details characterizing the ductility classes are also given. To ensure yielding of the dissipative zones, all non-dissipative members and connections in DC "A" or DC "B" structures should be designed according to hierarchy resistance criteria. Therefore, the design strength of the brittle components should not be less than the design strength of the ductile parts multiplied by an overstrength factor. The latter should be equal to 1,6 for heavy moment-resisting timber frames and vertical cantilever walls and 1,3 for all other structural types in DCA, and respectively 1,4 and 1,1 in DCB (Tab. I.3).

Horizontal diaphragms should be designed against a design seismic load increased by a factor equal to 1,3 and connections to the seismic resistant vertical structures should be also designed with an overstrength factor equal to 1,3 in DCA and 1,1 in DCB (Calderoni et al, 2019).

Table I.3 – Behaviour factors q_o for buildings (Calderoni et al, 2019)

STRUCTURAL TYPE	DCA	DCB
Light-frame structures	4,0	2,5
Heavy timber moment resisting frames	4,0	2,5
Heavy timber braced frames	-	2,0
X-Lam buildings	3,0	2,0
Blockhaus buildings	-	2,0

Chapter II

2. CONCEPTION AND DESIGN CRITERIA FOR DISSIPATIVE SEISMIC RESISTANT HEAVY TIMBER FRAME STRUCTURES

2.1 INTRODUCTION

Timber material has an elastic and fragile behaviour up to failure, so that, in order to comply with the current approach to the seismic design of dissipative structures, the common view is that joints should be dissipative through plastic deformations of steel connectors. This is up to now indicated in the present anti-seismic regulations, such as in Europe the Eurocode 8. However, joints are primary structural elements, with a crucial role in bearing the design loads. Furthermore, most existing timber structures, generally roof of heritage buildings, large roofs and industrial buildings, are not designed to resist the present earthquake levels and it is not always easy to apply traditional retrofitting techniques and a seismic adaptation could be too expensive compared to the value of the structure.

Therefore, the dissipation function should be assumed by ad hoc conceived dissipation devices, as an alternative to connections, so that the timber members and the steel connections between the structural elements are designed to remain in the elastic field (non-dissipative elements).

In this context, the chapter deals with the application of 2 innovative techniques for the dissipation of seismic energy in timber structures: *steel link* and *fluid viscous damper* (FVD).

In particular, the state of the art of research on the behaviour of seismic resistant heavy timber framed structures and on the application of fluid-viscous devices is discussed. Particular attention is given to the timber-steel connections, which have been examined, analysing the stiffness, the strength and the dissipative capacities, as well as the ductility. Taking advantage of the know-how on steel structures for the connections classification reported within Eurocode 3, a classification of the timber connections is proposed and the main connections present in the state of the art, on which experimental tests have been carried out, are been classified.

In particular, the fields of application and the design criteria, both global and local, of seismic resistant heavy timber framed structures with steel link and FVDs devices are described.

2.2 Heavy timber frame structures with steel Link

2.2.1 State of the art on heavy timber frame structures

Recently, heavy timber structures are becoming attractive as seismic resistant structures (Faggiano and Iovane, 2016). Researches in this field are mainly devoted to the experimental study of connections, structural sub-assemblages and small- and full-scale buildings. Hereafter a brief overview of recent studies is presented, and recent developments and technologies are discussed in detail.

Moment resisting frame

Concerning timber MRF, in 2008, Zonta et al. (2008, Fig. II.1a) presented a methodology for the application of the Displacement Based Design, DBD, to glued laminated timber portal frames to compare the results with those obtained using Eurocode 8. This is an extension to glulam frames of the general methodology developed by Priestley (Priestley, 2000) for concrete and steel structures. The work refers to a specific case study, a warehouse, characterized by single-story structure with 5 portal frames. The comparison with the results of Eurocode 8 shows that the DBD method potentially can overcome some of the simplifications that a Force Based Design (FBD) method necessarily leads to.

In Ishigaki et al. (2008), the way to make hysteresis model of the moment resisting joints from experiment results is proposed. Elements which constitutes moment resisting joint are shown in Figure II.1b. By using the model, it becomes possible to carry out seismic response analysis. The purpose of this research is to conduct response analysis and to investigate seismic response characteristics of the timber structure with moment resisting joint. And it proposes about the way to improve energy dissipation performance of the timber structure based on the analysis results.

In 2010, Kasal et al. (2010, Fig. II.1c) studied the behaviour of a 3-story timber structure (the footprint of 900x900 mm with three-story heights of 660-700-700mm, first to third floor) in which the columns have cross sections of 80x80mm and the beams had cross sections of 40x20mm and with moment connections made with special L-shaped aluminium angles located at the top and the bottom of the beam end, connected to the beam and the column through full thread screws (column 5x70 mm, beam 5x140 mm). Two sets of experiments were conducted: moment connections between beams and columns were tested using quasi-static cyclic loads to establish moment-rotation curves, energy dissipated per cycle, and total cumulative dissipated energy, and a scaled model of the three-story frame was tested on a shake table under various dynamic loads.

Studies by Jorissen and Fragiacomo (2011, Fig. II.1d) in 2011, are focused on the possible application of the capacity design, assuming that members should be over strengthened as respect to connections, evidencing the need for experimental tests on nodal assemblages in order to calibrate the overstrength factors to be applied for timber structures. In particular, they have calculated for multiple doweled connections loaded parallel to the grain based on the results of an extensive experimental programme carried out on timber splice connections with 10,65 and 11,75mm diameter steel dowels grade 4.6. A tentative classification of timber moment connection as respect to stiffness and strength is attempted by Leijten (2011, Fig. II.1e) with reference to both the traditional non-reinforced dowel-type fastener connections and the timber connections reinforced with steel plates. In particular, Leijten reports tests on column–beam connections. Two types of connections have been tested: the traditional timber-to-timber moment connections with tight fitting dowels (8 and 12 dowels) of d=16mm diameter and connections with 600x600mm steel plates of 3 and 5mm thickness with d=16mm diameter injection bolts (6 and 10 bolts) were tested. For all tests, glued laminated members were used 110x600mm for the middle member and 70x600mm for the side members.

In 2012, Smith et al. (2012, Fig. II.1f) studied the seismic performance of an innovative three-dimensional, three-storey post-tensioned timber structure in 2/3rd scale. The inter-storey height of the building is 2m and the frame footprint is 4x3m. The base of the column is fitted with a steel shoe which is epoxied into the base of the column and left free to rock on a base plate (which will be used to represent the building foundations in the case of the test building). Four φ20mm bars of 300mm length will be used for this connection. Shear transfer will be achieved using a φ76mm, 1mm steel tube which extends 15mm from the steel shoe and slots into a cavity in the base plate. Passing through the centre of the beam is a single 26,5mm diameter bar which will be tensioned, and the various dissipater types are attached to the column though the use of M16 bolts which pass through the width of the column and attach to a backing plate. Two methods of passive hysteretic energy dissipation to be added are used: the "yielding steel angle" device and the "plug and play" axial device. Seismic loading during testing will be mono-directional applied along the north-south axis of the building. This technology is an extension of the analytically and experimentally studies carried out by Ricles et al. (2001), Christopoulos et al. (2002) and on the seismic performance of a post-tensioned energy dissipating connection for steel frames and steel moment resisting frames, MRF (Faggiano, 2012) and of an overview of recent developments and on-going research on precast concrete buildings with jointed ductile connections, relying on the use of unbonded post-tensioned tendons with self-centering capabilities given by Pampanin et al. (2005).

In 2014, Kasal et al. (2014, Fig. II.1g) continued their studies on the seismic behaviour of timber structures presented in 2014 the seismic performance of a full-scale single-story timber frame (the footprint of 3000x3000mm with height of 3100mm) in which the columns have cross sections of 220x220mm and the beams had cross sections of 220x340mm and with three-dimensional (3D) rigid connections made with self-tapping screws and hardwood blocks used to support the beams. To connect the beam and the column a timber deck of 4,4x4,4x200mm made of cross laminated timber (CLT) plates was used. The solid plates were attached to the beams via self-tapping screws (120–350mm with diameters ranging from 6,5-12mm.) that went through the hardwood blocks and into the beam at a 45° angle to the beam, while two screws were placed alternating between them at a

45° angle into the column in toe-nail like fashion. Also in this case, two sets of experiments were conducted: 3D moment connections were tested using quasi-static cyclic loads and a full-scaled model single-story timber frame was tested on a shake table under various dynamic loads.

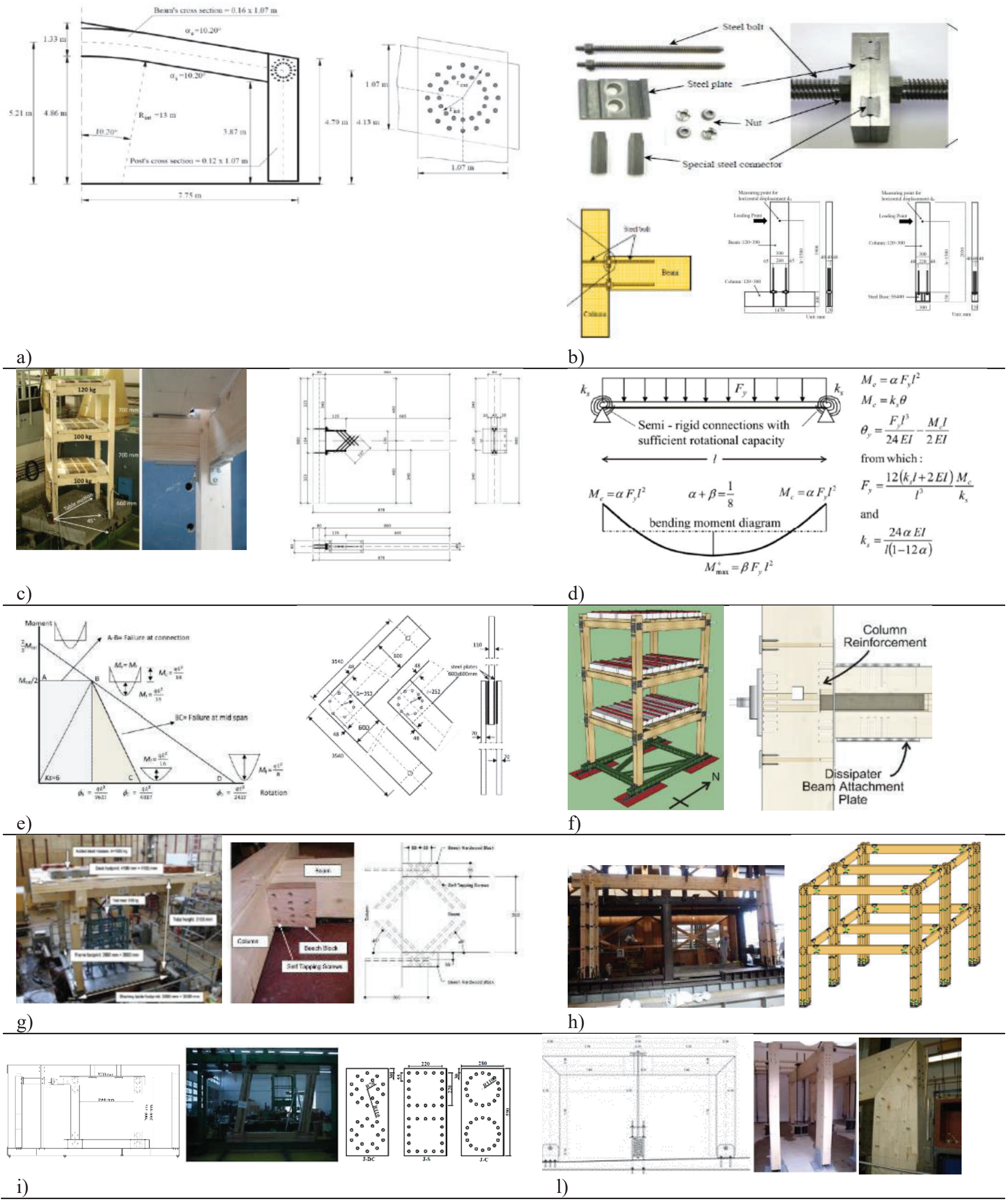

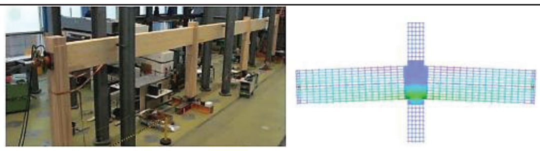

m)

n)

Figure II.24 – Heavy timber moment resisting frames studies: a) Ishigaki et al, 2008; c) Kasal et al, 2010; d) Jorissen and Fragiacomo, 2011; e) Leijten et al, 2011; f) Smith et al. 2012; g) Kasal et al, 2014; h) Kohara et al, 2016; i) Yeh et al, 2016; l) koj et al, 2016; m) Ogrizovic et al, 2016; n) Liu and Xiong, 2018.

In 2016, Kohara (2016, Fig. II.1h) developed a portal frame structure with the combined columns that made with the glued-laminated timbers (GLT) for general large-scale office, store or school with length of 4000 or 6000mm and height of 2880 or 3030mm. The column is combined four glued-laminated timbers with each section of 120x120mm or 150x150mm while the beam has a cross section of 120390 or 450mm and static loading tests were carried out. Yeh et al (2016, Fig. II.1i) studied the behaviour of box type portal moment-resisting frame subjected to a lateral load, with the height of 2600mm and the width of 3000mm and the size of the glulam elements was 135×304mm in cross-section. An aluminium plate was used for the connection between the beam and column members and the fasteners used in the connection were self-tapping screws, which have a length of 125mm and a diameter of 8mm. The protocol of the lateral loads consisted of 7 stages of cyclic application. 1/240, 1/170, 1/120, 1/100, 1/75, 1/50, and 1/30 radian. Three cyclic loadings were applied in each stage, and then a final monotonic load was applied until failure. In Koj et al. (2016, Fig. II.1l) have developed timber connections using self-tapping screws as reinforcing and joining elements. The focus was put on rigid frame corners that achieved high load-bearing capacities for both negative and positive bending moments, for long-term loading. In Ogrizovic et al. (2017, Fig. II.1m), a post-tensioned moment resisting timber frame is analysed. The global structural response was investigated through pushover tests on a full-scale 3-bay frame. In addition, a finite element analysis was performed to verify the behaviour of the column beam joint.

In Liu and Xiong (2018, Fig. II.1n), structural analysis were conducted on a semi-rigid timber portal frame; the formulas were derived in terms of the internal force and the lateral stiffness, and the influence of the semi-rigid connections was discussed. Moreover, experimental tests were performed on three full-scale timber portal frames and five bolted timber connections to study the lateral performance of the frames and the moment resistance of the connections. For consistency, the connections from the portal frames and the connections for bending tests were of the same configuration. Finally, a calculation flowchart of the lateral performance on a semi-rigid frame was presented to verify the derived formulas and to show a framework of the lateral structural design process.

Frame with bracings

With regards to timber braced frames a lower number of studies can be found.

In 2008, Popowski and Karacabeyli (2008, Fig. II.2a) carried out monotonic and cyclic tests on diagonal braces with riveted end connections, with the aim at quantifying the seismic behaviour.

Non-linear analytical models are developed for diagonal brace members as well as for the entire braced frames. Non-linear static and time history dynamic analyses are performed. Some guidelines on the implementation of capacity design procedures for braced timber frames are proposed. Displacement controlled monotonic tension and cyclic tests were conducted on a total of 48 brace specimens with four different wood products, Spruce-Pine (SP) Glulam, Laminated Veneer Lumber (LVL), Parallel Strand Lumber (PSL) and Laminated Strand Lumber (LSL). Based on the results obtained from the cyclic tests on diagonal braces, non-linear models for the braces were developed using the "Florence" model that was incorporated in the DRAIN-2DX computer package for two-dimensional non-linear analysis of building structures. The case study is a three-storey typical industrial building with column height of 2,4m and beam length of 3m. Moreover, some guidelines on the implementation of capacity design procedures for braced timber frames are proposed.

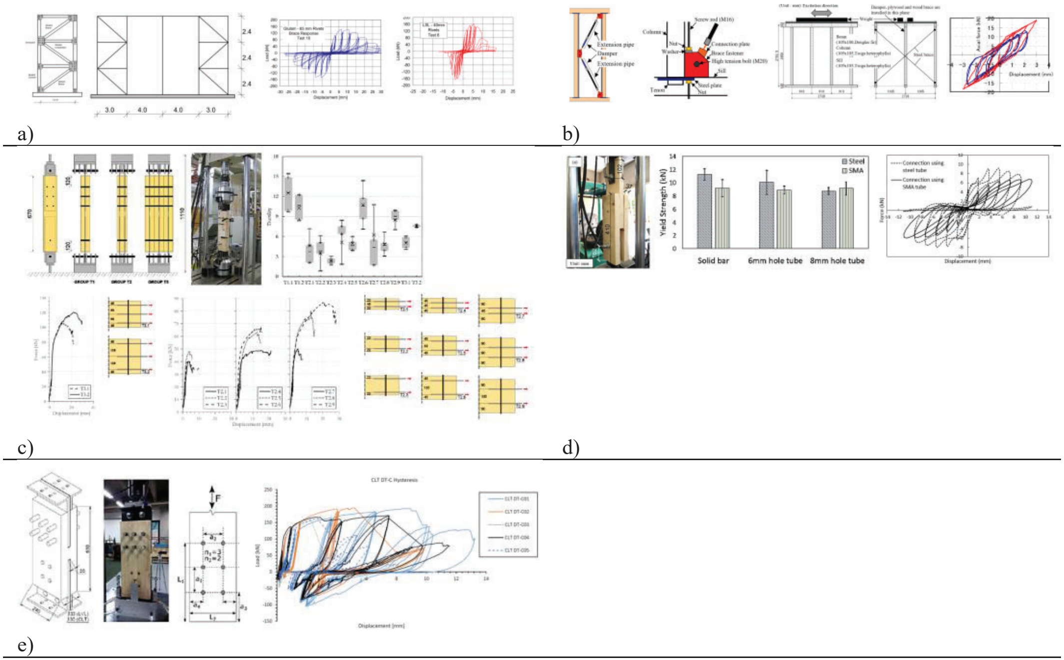

Figure II.25 – Heavy timber frames with bracings studies: a) Popowski and Karacabeyli, 2008; b) Yamaguchi et al, 2012; c) Rossi et al, 2016; d) Huang et al, 2016; e) Ottenhaus et al, 2016.

In 2012, Yamaguchi et al. (2012, Fig. II.2b) carried out both quasi-static loading tests and shaking table tests on a K braced frame equipped with bracing dampers. The size of the frames is 910mm width and 2730mm height. Species and dimensions of the sill and columns of the frames are Tsuga (Hem Fir) and 105x105mm, those of the beam are Douglas Fir and 180x105mm. The K-braded damper or typical shear walls are installed in any spaces between two columns in the frame and the diameter and length of the damper is 48,6 mm and 350 mm. Quasi-static loading tests use a wood frame of two spans with three columns. Shaking table test used three wood frames of three spans with four columns and the K-braced damper or typical shear walls are installed in the centre frame of the three wood frames.

Rossi et al. (2016, Fig. II.2c) studied dowel-type connections with multiple slotted-in steel plates, in order to assess the performance of the timber joints in terms of load-bearing capacity, stiffness and ductility. Design guidance for preventing premature brittle failure of the connection are provided. In fact, the layout of the connection should optimize the ductile behaviour and thus the possible load redistribution among the dowels, so to contribute to the overall robustness of the structure. A novel timber dowel-type connection that provides self-centring effect by super-elastic shape memory alloy (SMA) bar and tubes as dowels is investigated by Huang et al. (2016, Fig. II.2d). Results reveal that tube dowels provides the connection with higher equivalent viscous damping than solid bar, as the tube allows larger deformation and then dissipation of energy. Ottenhaus et al. (2018, Fig. II.2e) present an experimental study on LVL and CLT dowelled connections. Monotonic and quasi-static cyclic tests were performed to the purpose of evaluating ductility and overstrength. Results were compared with strength predictions through literature analytical models for ductile and brittle failure under monotonic loading. A generalized overstrength factor has been defined.

<u>Frame with shear walls and shear wall structures</u>

Finally, timber walls are worth mentioning as lateral load resisting system for structures. In Sarti el al. (2014, Fig. II.3a) quasi-static test on a single wall system and on a column-wall-column coupled system both applying post-tensioned devices is presented. In particular, the prototype case study building is a three-storey building with two suspended floors and a lightweight timber penthouse on third floor. The building has an approximate plan of 32m in the longitudinal direction and 18m in the transverse direction with a floor area of approximately 600m2 per floor.

This technology has been studied by many authors. Small-scale specimens of single wall subassemblies were tested with internal and external dissipaters (Palermo et al, 2006; Smith et al, 2007, Fig. II.3b); moreover, coupled walls with U-shape Flexural Plates (UFPs) dissipaters were tested by Newcombe et al. (2011, Fig. II.3c). The experimental results showed the system can provide high levels of hysteretic damping and excellent re-centering, and virtually no damage is observed in the structural members. Following the extensive research on the Pres-Lam technology supported by the Structural Timber Innovation Company (STIC), few post-tensioned timber buildings were recently constructed in New Zealand. The Nelson and Marlborough Institute of Technology in Nelson was the first post-tensioned timber building constructed worldwide; it is a three storey timber building with coupled walls resisting the horizontal actions (Devereux et al, 2011, Fig. II.3d) which uses UFPs (Skinner et al, 1974) as dissipative source between the walls. Figure 1b shows the Carterton Events Center (Carterton), a single-story building with large timber trusses for carrying the gravity loads and single walls with internal dissipaters resisting the seismic loading (Palermo et al, 2012). The vertical uplift generated by the gap opening at the base of the wall element can cause some displacement incompatibility issues when interacting with the diaphragm system. That vertical displacement can bring to damage in the diaphragm when the connection is not properly designed, thus influencing its capacity (Moroder et al, 2014, Fig. II.3e);

moreover, the interaction of the two systems can increase the vertical load on the wall. The increased axial force amplifies the capacity of the wall system but reduces the energy dissipated of the system since the dissipaters might not be activated. The increased axial load can also cause global instability as well as higher local damage at the compression area.

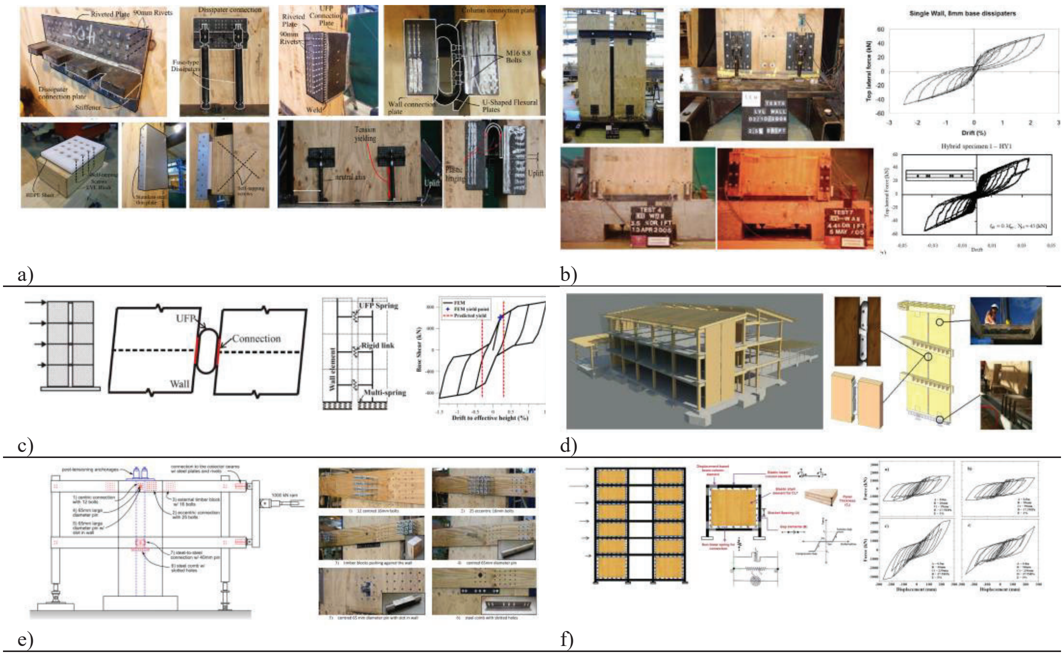

Figure II.26 – Heavy timber frames with shear walls and shear wall structures: a) Sarti et al, 2014; b) Palermo et al, 2006 and Smith et al, 2007; c) Newcombe et al, 2011; d) Devereux et al, 2011; e) Moroder et al, 2014; f) Bezabeh et al, 2016.

To mitigate that issue, an alternative configuration, referred to as Column-Wall-Column (CWC), was proposed and tested. The new solution comprises of a single wall as the main resisting system; boundary columns provide the support to the diaphragm drag beams and are coupled using U-shaped Flexural Plates (UFPs), also providing energy dissipation to the system. A similar precast concrete solution was proposed and tested by (Henry et al, 2012).

Recently Bezabeh et al. (2016, Fig. II.3f) have studied a steel-timber hybrid structure, which consists of a steel moment resisting frame filled in with Cross Laminated Timber (CLT) shear panels. An equivalent viscous damping-ductility law for CLT, based on an extensive parametric analysis is proposed. Static monotonic pushover analysis was carried out for the 243 models. In particular, three levels of bracket spacing were considered (0,4, 0,8 and 1,6m); gap magnitude between steel frame and CLT infill of 20, 50, and 80mm, panel thickness of 99, 169, 239mm, panel strength of 17,5, 25 and 37,5MPa and post stiffness yielding ratio of 1, 3, 5 % were selected.

2.2.2 CONCEPTION OF THE SYSTEM

To the dissipative seismic resistant timber structures design, in order to take advantage of the high strength to weight ratio of wood in lowering seismic design forces (relative to steel and concrete), steps must be taken to overcome the seismic deficiencies inherent of wood that limit the ductility and plastic rotation capacity. Since timber is a material with an elastic-fragile behaviour, in the present anti-seismic regulations, such as in Europe the Eurocode 8 is indicated that the joints could dissipate through the plastic deformations of metallic connectors but the joints are structural elements with an important role in bearing the design loads.

In view of the development of heavy timber seismic resistant structures, in the context of modern seismic design approach based on the mechanical triad of strength, stiffness and ductility, the dissipative capabilities should be delegated to specific devices, considering that timber mechanical behaviour is typically fragile (Faggiano and Iovane, 2016).

By integrating modern timber connection technology into hybrid timber-steel system, brittle wood failure modes can be avoided, and overall seismic performance can be improved.

For example, the Eurocode 8 limits the ductility factor (q_d) to 2,0 for timber moment frames due to the brittle nature of wood under some loading conditions, but steel MRFs classed as "Ductile Moment-Resisting Frames" are assigned a ductility factor of 4,0, greatly reducing seismic design forces imparted on the frame.

By developing systems which are primarily wood-based with steel yielding components, designers can take advantage of the low weight of wood as well as the high ductility factor associated with steel MRFs (but also of frames with bracings) to greatly lower the design base shear on the frame and the structural mass. This results in smaller structural elements and lower foundation forces and allows for cost savings that can potentially offset the higher cost of wood as compared to steel or concrete.

Due to susceptibility of timber moment-resisting connections to brittle failure modes, some recent research has focused on the development of hybrid timber-steel, instead of relying on an all-timber structure and, although most experimental research are done on small-scale specimens, findings of studies show good potential for improving the hysteretic behaviour of timber systems.

Humbert et al. (2014, Fig. II.4a) experimented on various configurations of timber column base connections using embedded steel knife plates that were bolted to the foundation and connected to the timber using steel dowels. Komatsu et al. (2014, Fig. II.4b) used a newly developed moment connection formed by U-shaped brackets that were attached to the beam and column and bolted together using slotted steel plates. Similar research was presented using inclined lag screw bolts in (Nakatani et al, 2012, Fig. II.4c) in which a beam-column bending connection is analysed using a steel link placed at the end of the beam. The connection is made using special screws called "Lag Screw Bolt". Two types of connection have been tested: both the connection between the column with a single beam (Test L) and that between the column with two beams (Test X) varying, for both cases, the arrangement of the screws LSB inside the column. In 2016, Schick and Seim (2016, Fig. II.4d) proposed to provide braced timber structure with ductile behaviour through steel hollow section shear links that connects the diagonals to the beam and the column base to a steel profile fixed to the concrete foundation.

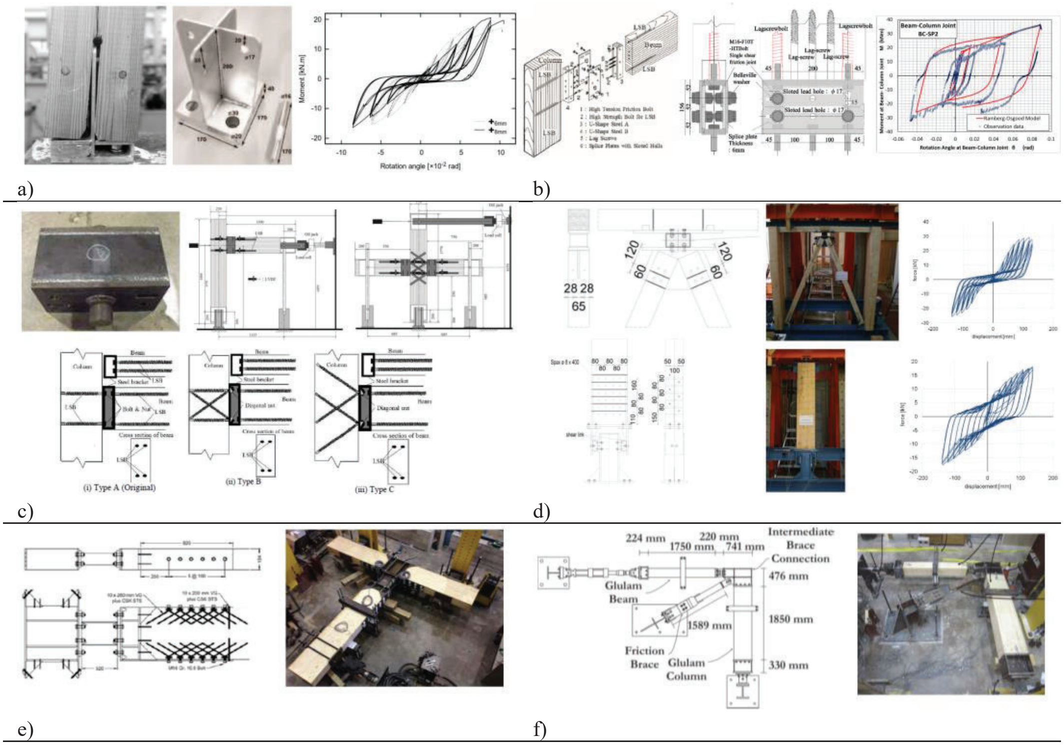

Figure II.27 – Heavy timber-steel hybrid frames studies: a) Humbert et al, 2014; b) Komatsu et al, 2014; c) Nakatani et al, 2012; d) Schick and Seim, 2016; e) Gohlich et al, 2015; f) Gohlich et al, 2016.

Research into hybrid timber-steel connections beyond that of typical dowel fasteners with steel plates is fairly limited; for this reason, a method of providing both high strength and high ductility by using steel special devices has been developed: *steel links*.

These steel devices, which act as a joint between the timber elements, are able to develop a significant dissipative capacity if designed with adequate strength, stiffness and in order to avoid the relative sliding between the elements.

In this context, it is possible to take advantage of the knowhow on steel constructions related to the seismic design criteria, according to the approach based on the ductile and dissipation requirements (capacity design procedure), adopting necessary adaptations corresponding to the peculiarities of timber, which should be based on the calibration of the fundamental parameters.

The objective of capacity design is to confirm a structure undergoes controlled ductile behaviour in order to avoid collapse in a design-level earthquake. This involves designing the structure to allow ductile failure at key predictable locations within the structure and to prevent other failure types occurring near these locations or elsewhere in the structure. In particular, it is a design process in which it is decided which elements within a structural system will be permitted to yield (ductile components) and which elements will remain elastic (brittle components). Once ductile and brittle systems are decided upon, design proceeds according to the following guidelines:

- *Ductile components* are designed with sufficient deformation capacity such that they may satisfy displacement-based demand-capacity ratio.
- *Brittle components* are designed to achieve sufficient strength levels such that they may satisfy strength-based demand-capacity ratio.

In other words, in a structure that contains both brittle and ductile elements, capacity design is a method to provide the structure with an overall ductile characteristic.

To highlight the simple concept of capacity design philosophy, the chain shown in Figure II.5 will be considered.

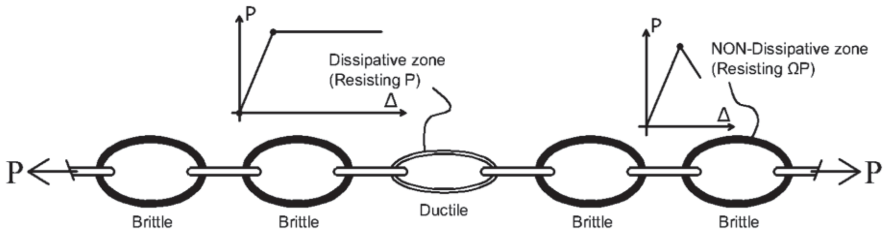

Figure II.28 – Principle of capacity design by (Paulay and Priestley, 1992).

The chain consists of links made of brittle and ductile materials. Each of these links will fail when elongated. Holding the last link at either end of the chain a force "P" is apply. Since the same force "P" is being transferred through all the links, the force in each link is the same i.e. "P". As more and more force is applied, eventually the chain will break when the weakest link in it breaks. If the ductile link is the weak one (i.e. its capacity to take loads is less), then the chain will show large final elongation. Instead, if the brittle link is the weak one, then the chain will fail suddenly and show small final elongation. Therefore, to have such a ductile chain, we have to make the ductile link to be the weakest link.

Steel links located at the ends of the beams (MRF), in the bracing (CBF) or in the link (EBF) are very promising solutions (Faggiano et al, 2016, 2018), aimed to allow the plastic hinge should be form in the steel links in order to achieve a ductile behaviour and to develop a significant dissipative capacity while the timber members and the connections between the structural elements should be designed with an adequate over-strength, stiffness and to remain in elastic field.

In particular, the design criteria used within this work aim at harmonizing the hierarchy requirements among the strengths of "macro-components" (e.g. the connection, the timber beam, the timber column and the steel link) and connection link-timber "sub-components" (e.g. end-plate, bolts and stiffeners, etc.), as well (Fig. II.6). Each macro-component and sub-component are individually designed according to specific assumptions and then simply capacity design criteria are applied, in order to obtain different design objectives, in function of the dissipative and ductile capacity to reach. Therefore, to design the heavy timber frame structure with steel link, the capacity design approach is applied at 2 levels: for "macro-components", to design the hierarchy of resistance between the structural elements; for "sub-components", to design the hierarchy of resistance between the elements constituting the connection between the link and the timber structural elements.

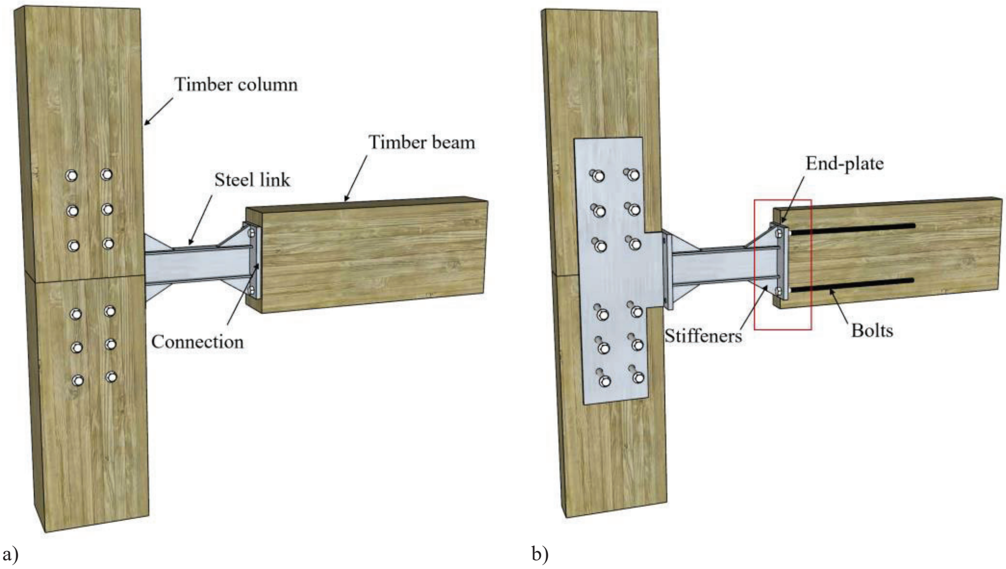

Figure II.29 – Principle of capacity design. Identification of a) macro-components and b) connection sub-components.

Recently Montuori and Savarese (2018) have applied the steel reduced beam sections, commonly proposed for steel MR frames (Faggiano et al, 2003; Montuori, 2014), to timber beams. Tomasi (2008) and Andreolli (2011) focus on a beam-column timber joint equipped with steel links for dissipative heavy timber seismic resistant MRF under monotonic and cyclic tests. Gilbert and Gohlich (2015, Fig. II.4e) have proposed two innovative modern hybrid timber structures: steel-timber buckling restrained braced frame (BRBF) and steel-timber ductile moment frame (DMRF) equipped with steel links (Gohlich et al, 2018). In 2016, Gohlich (Gohlich et al, 2016, Fig. II.4f) develops a new moment-resistant connection using a steel link connected to the beam through self-tapping screws.

The crucial aspect is the conception of joints. In timber structures engineering this issue is certainly innovative, it requiring a significant detailed study aimed at characterizing the mechanical behaviour of connections in terms of stiffness, strength and ductility. In particular the seismic design parameters are to be calibrated and the dissipative zones to be characterized, being the connections themselves or specific dissipative devices.

2.2.3 DESIGN CRITERIA FOR HEAVY TIMBER FRAME STRUCTURES WITH STEEL LINK

2.2.3.1 *GENERAL ASPECTS*

Being an innovative structural system, for which there are no design criteria, for the seismic resistant dissipative heavy timber framed structures with steel link joint design criteria definition, the know-out of the steel structures has been exploited. In particular, according to EC8, the seismic design of steel structures is based on the concept of dissipative structures, where specific zones of the structures should be able to develop plastic deformation in order to dissipate the seismic energy. On the contrary, the non-dissipative parts should be elastically under seismic action in order to avoid brittle collapse. The hierarchy of the resistances is the fundamental principle allowing this performance by detailing non-dissipative zones to resist the full plastic strength of the related dissipative members. According to design procedure developed within the work, the plastic hinge should be form in the steel links in order to achieve a ductile behaviour and to develop a significant dissipative capacity while the timber members and the connection should be designed with an adequate over-strength, stiffness and in order to be in elastic field.

Specifically, below, the design criteria for "macro-components" are presented, for heavy timber framed structures, i.e. moment resisting frames (MRF), frames with concentric braces (CBF), frames with eccentric braces (EBF) and frames with shear walls, concrete cores or concrete walls.

2.2.3.2 *HEAVY TIMBER MOMENT RESISTING FRAMES*

MRFs should be designed so that the plastic hinges form in the steel links placed at the beams ends and at the base of the columns, in order to achieve a ductile behaviour.

Dissipative elements (links) should be designed and satisfy the following conditions, in order to achieve a pure bending behaviour:

$$\left(\frac{M_{Ed}}{M_{pl,Rd}}\right)_j \leq 1; \quad \left(\frac{N_{Ed}}{N_{pl,Rd}}\right)_j \leq 0{,}15;$$

$$\left(\frac{V_{Ed,G} + V_{Ed,M}}{V_{pl,Rd}}\right)_j \leq 0{,}50$$

where j denotes the j-th dissipative element; M_{Ed}, N_{Ed} are the design values of bending moment and axial force, respectively; $V_{Ed,G}$ is the design shear due to the non-seismic actions; $V_{Ed,M}$ is the design shear corresponding to the formation of plastic hinges in the dissipative elements; $M_{pl,Rd}$, $N_{pl,Rd}$ and $V_{pl,Rd}$ are the design plastic resistances, in bending, tension and shear.

For non-dissipative elements, such as timber beams and columns, the capacity design criterion should be satisfied as it follows:

$$N_{Ed} = N_{Ed,G} + (\gamma'_{Rd} \cdot \gamma_{RD} \cdot \Omega \; N_{Ed,E})$$

$$M_{Ed} = M_{Ed,G} + (\gamma'_{Rd} \cdot \gamma_{RD} \cdot \Omega \ \ M_{Ed,E})$$

$$V_{Ed} = V_{Ed,G} + (\gamma'_{Rd} \cdot \gamma_{RD} \cdot \Omega \cdot V_{Ed,E})$$

where N_{Ed}, M_{Ed}, V_{Ed} are the design values of axial force, bending moment and shear; $N_{Ed,G}$, $M_{Ed,G}$, $V_{Ed,G}$ are the design values of axial force, bending moment and shear due to the non-seismic actions; $N_{Ed,E}$, $M_{Ed,E}$, $V_{Ed,E}$ are the design values of axial force, bending moment and shear due to seismic actions; γ_{Rd} is the overstrength factor of the material, which the dissipative element is made of (the links are made of steel); γ'_{Rd} is the overstrength factor, accounting for the peculiarities of both the dissipative element and the overall structural systems, where they are applied, it should be properly calibrated; Ω is the coefficient of structural overstrength, equal to the minimum value among $\Omega_i = M_{pl,Rd,i}/M_{Ed,i}$ calculated for all the dissipative elements (links), being $M_{Ed,i}$ the design bending moment of the i-th dissipative element in seismic conditions and $M_{pl,Rd,i}$ the corresponding design plastic resistance.

The rotational equilibrium at the beam-to column node should also be satisfied, in the condition of plastic deformation of the dissipative elements placed in the beams converging in the node, according to the hierarchy resistance criterion, along with columns should remain in the elastic range:

$$\Sigma M_{pl,Rd,i} \geq \gamma_{RD} \cdot \Sigma M_{pl,Rd,j}$$

where $M_{pl,Rd,i}$ is the design plastic resistance in bending of the i-th timber column converging in the node, calculated for the axial force in the column due to the seismic combinations of actions; $M_{pl,Rd,j}$ is the design plastic resistance of the j-th dissipative element; γ_{RD} is a overstrength factor (for steel structures it is equal to 1,3).

Finally, the connections between the links and the timber members should be designed for having adequate overstrength, in order to avoid plastic deformation of components. In particular, the bending moment resistance of the connection, $M_{j,Rd}$, should satisfy the following relationship:

$$M_{j,Rd} \geq \gamma'_{RD} \cdot \gamma_{RD} \cdot M_{pl,Rd,j}$$

2.2.3.3 Heavy timber frames with concentric braces

Dissipative CBFs with steel braces present, as dissipative elements, the diagonals in tension, while in dissipative CBFs with timber braces the dissipative zones are concentrated in the steel link at the end of the bracing. The diagonals or links in tension are designed under the axial force of the seismic action and the seismic energy dissipation occurs through the yielding of the diagonals/link in tension for cycles of axial forces.

The design rules related to steel structures with concentric bracings given in the section 7.5.5 of NTC 2008 and section 6.7 of EC8 could be applied.

In particular, for steel dissipative diagonals, the following conditions should be satisfied for ensuring adequate cyclic behaviour:

- Diagonals should belong to the first or second ductility class;
- In case of tubular or box-shaped diagonal, the local slenderness should not exceed the following values, respectively: diameter/thickness, $d/t \leq 36$, and width/thickness ≤ 18;
- The adimensional slenderness of the diagonals should be limited, in order both to ensure a stable cyclic behaviour and to obtain a global stability in plastic range:
-

$1{,}3 \leq \bar{\lambda} \leq 2$ for X bracing

$\bar{\lambda} \leq 2$ for V bracing;

- the coefficient of structural overstrength, $\Omega_i = N_{pl,Rd,i}/N_{Ed,i}$, calculated for all bracing elements, should differ no more than 25% between the maximum and the minimum values, in order to ensure a homogeneous dissipative behaviour of the diagonals along the structure;
- In the elements in tension particular attention should be paid to the weakened zones where bolted connections are located; there, the standard codes require the following check:
-

$$\frac{A_{res}}{A} \geq 1{,}1 \frac{\gamma_{M2}}{\gamma_{M0}} \cdot \frac{f_{yk}}{f_{tk}}$$

- where A is the gross area and A_{res} is the resistant area, such as the net area at the holes alignment integrated by a possible strengthening area; γ_{M0} and γ_{M2} are partial factors equal to 1,05 and 1,25, respectively.

For timber diagonals with steel links, the dissipative elements (links) are designed under the axial force of the seismic action, and without presenting instability.

For non-dissipative elements, such as timber beams and columns, the hierarchy resistance criterion should be satisfied as it follows:

$$N_{Ed} = N_{Ed,G} + (\gamma'_{Rd} \cdot \gamma_{Rd} \cdot \Omega \; N_{Ed,E})$$

where the terms assume the same meaning as in §4.3.1. In particular the coefficient of structural overstrength Ω is equal to the minimum value among $\Omega_i = N_{pl,Rd,i}/N_{Ed,i}$ calculated for all dissipative elements, being $N_{Ed,i}$ the design axial force of the i-th diagonal in seismic conditions and $N_{pl,Rd,i}$ the corresponding design plastic resistance.

In case of V steel bracing the following design features should be considered:

- The diagonal in compression should be considered active, so, at the ultimate limit state, it should be designed to resist seismic actions as respect to buckling;
- At the ultimate limit states, the beams should resist on one side against non-seismic actions disregarding the support given by diagonals, on the other side against the unbalanced vertical forces that develop in case of seism, in case the diagonals in tension yields and at the same time the diagonal in compression buckle. This effect can be taken into account by assuming an axial force equal to $N_{pl,Rd}$ in the diagonal in tension and to $\gamma_{pb} \cdot N_{pl,Rd}$ in the diagonal in compression, being γ_{pb} a factor that allows to estimate the residual strength after buckling.

For timber diagonals with steel links, the same design criteria of the X bracing structures is applied.

Finally, the connections should be designed, in order to have adequate overstrength. In particular, the axial force of the connection, $N_{j,Rd}$, should satisfy the following relationship:

$$N_{j,\,Rd} \geq \gamma'_{Rd} \cdot \gamma_{Rd} \cdot N_{pl,Rd,j}$$

2.2.3.4 *Heavy timber frames with eccentric braces*

Dissipative EBFs present, as dissipative zones, the steel links in corresponding of the timber beam. The seismic energy dissipation occurs through the plastic deformation of the links for cycles of bending or shear or bending and shear.

The design rules related to steel structures with eccentric bracings given in the section 7.5.6 of NTC 2008 and section 6.8 of EC8 could be applied.

The design of the dissipative elements, the links, should reflect the dissipative behaviour that they can exhibit. In this regard, links are distinguished in 3 categories depending on the length:

Short links: the dissipation occurs in shear;

$$e \leq 0{,}8\,(1+\alpha)\frac{M_{1,Rd}}{V_{1,Rd}}$$

Intermediate links: the dissipation occurs in bending, combined with shear;

$$0{,}8\,(1+\alpha)\frac{M_{1,Rd}}{V_{1,Rd}} < e < 1{,}5\,(1+\alpha)\frac{M_{1,Rd}}{V_{1,Rd}}$$

Long links: the dissipation occurs in bending.

$$e \geq 1{,}5\,(1+\alpha)\frac{M_{1,Rd}}{V_{1,Rd}}$$

where α is the ratio between the minimum and the maximum bending moments at the link ends; $M_{l,Rd}$, and $V_{l,Rd}$ are the design bending and shear resistances of the link, respectively. In case the link is made with double-T profiles, they are defined, in absence of axial force, by the following relationships:

$$M_{1,Rd} = f_y \cdot b \cdot t_f\,(h - t_f)$$

$$V_{1,Rd} = \frac{f_y}{\sqrt{3}} \cdot t_w\,(h - t_f)$$

When the design axial force N_{Ed} in the link exceeds 15% of the plastic resistance in tension, $N_{pl,Rd}$, the reduction of the plastic shear and bending resistances of the link, $V_{l,Rd}$ and $M_{l,Rd}$, should be appropriately considered.

The link plastic rotation θ_p in the ultimate conditions should be limited as it follows:

Short links: $\theta_p \leq 0{,}08$rad
Long links: $\theta_p \leq 0{,}02$rad

For the intermediate links the plastic rotation should be determined by interpolation. Both the ultimate bending, M_u, and shear, V_u, resistances of the link should be obtained considering further influencing aspects, like strain hardening, randomness of the yield strength, presence of the reinforced concrete slab on the link. They should be calculated as it follows:

- Short links: $\begin{cases} M_u = 0{,}75\ e\ V_{1,Rd} \\ V_u = 1{,}5\ V_{1,Rd} \end{cases}$

- Long links: $\begin{cases} M_u = 1{,}5 \cdot M_{1,Rd} \\ V_u = 2\ \frac{M_{1,Rd}}{e} \end{cases}$

For intermediate links the ultimate strength should be determined by interpolation.

The coefficients of structural overstrength Ω_i, calculated for all links, should differ no more than 25% between the maximum and the minimum vales, in order to ensure a homogeneous dissipative behaviour of the links along the structure. They should be calculated as it follows:

- Short links: $\Omega_i = 1{,}5 \cdot M_{l,Rd,i} / M_{Ed,i}$
- Long links: $\Omega_i = 1{,}5 \cdot V_{l,Rd,i} / V_{Ed,i}$

where $M_{Ed,i}$ e $V_{Ed,i}$ are the design values of bending moment and shear obtained by the seismic combination.

For non-dissipative elements, such as beams, columns and diagonals, the hierarchy resistance criterion should be applied as it follows:

$$N_{Ed} = N_{Ed,G} + (\gamma'_{Rd} \cdot \gamma_{Rd} \cdot \Omega \cdot N_{Ed,E})$$

$$M_{Ed} = M_{Ed,G} + (\gamma'_{Rd} \cdot \gamma_{Rd} \cdot \Omega \cdot M_{Ed,E})$$

$$V_{Ed} = V_{Ed,G} + (\gamma'_{Rd} \cdot \gamma_{Rd} \cdot \Omega \cdot V_{Ed,E})$$

where the terms assume the same meaning as in §2.2.3.2.

The connections between the links and the timber members should be designed with an adequate overstrength, for avoiding the plastic deformation of the components. In particular, depending on the category of the link, the following relationships should be satisfied:

$$N_{j,Rd} \geq \gamma'_{Rd} \cdot \gamma_{Rd} \cdot N_{pl,Rd,j}$$

$$M_{j,Rd} \geq \gamma'_{Rd} \cdot \gamma_{Rd} \cdot M_{pl,Rd,j}$$

$$V_{j,Rd} \geq \gamma'_{Rd} \cdot \gamma_{Rd} \cdot V_{pl,Rd,j}$$

2.2.3.5 Heavy timber frames with shear walls, concrete cores or concrete walls

These structures are composed by two combined structural systems. The beam-column frame, designed only for vertical loads, can be made of both solid and glue-laminated timber. The connections between the timber members can be realized by metal connectors, designed to provide a pin constraint, ensuring the transfer of forces between the members.

The vertical structural systems, with stiffening and stabilization functions against horizontal actions, should be designed on the basis of the structural type and the material adopted.

For dissipative structures, the timber beam-column frame, resisting vertical loads only, and the connections with the seismic-resistant structure should be designed with an appropriate overstrength as respect to the bracing dissipative system.

2.3 Heavy timber frame structures with FVD devices

2.3.1 State of the art on seismic protection systems for timber structures

In the last three decades anti-seismic devices, in particular those implementing the passive control of structural response through seismic isolation and energy dissipation, have undergone great development, finding many applications in both new and existing structures. With regards to the application of seismic devices for the consolidation of existing buildings, huge literature is available in the case of steel and reinforced concrete buildings, generally dealing with experimental studies on connections, structural sub-assemblages and small- and full-scale buildings. In particular, for steel framed structures studies are vastly developing (Fiorino et al, 2013; Latour et al, 2018; Della Corte et al, 2012; Faella et al, 2000; Lemonis, and Gantes, 2009).

However, this issue is achieving a great importance also in the field of timber constructions (Dietsch and Winter, 2018; Gaspari et al, 2018; Masse et al, 2018; Faggiano et al, 2019). Particularly for seismic resisting timber structures several solutions are proposed ranging from timber walls with friction dampers (Filiatrault, 1990) or viscoelastic dampers (Dinehart and Shenton,1998; Dinehart et al, 1999) or hysteretic rod (Higgins, 2001) or seismic isolation system with high-friction sliding system (Jampole et al, 2017); light frames with braces equipped with dampers (Yamaguchi et al, 2012) or elastomeric and flat sliding bearings (Reed and Kircher,1986; Zayas and Low, 1997) or base isolation systems (Sakamoto et al, 1990; Pall and Pall, 1991); moment resisting frames (Kasal et al, 2014), also equipped with Post Tensioned Energy Dissipated (PTED) devices (Di Cesare et al, 2017) or with frictional beam-to-column connection (Polocoser et al, 2018); bracing frames with slip friction joints (Yousef-beik et al, 2018).

With specific regards to the application of fluid viscous dampers, once more the upgrading of existing steel and reinforced concrete buildings is concerned, considering the addition of FVD braces in the structural frames (Losanno et al, 2015; Alotta et al, 2016; Ras et al, 2016; Abhilash et al, 2017; Dong et al, 2018), while the first study on the application of FVD within timber frame structures was carried out by Symans et al. (2001; 2002), on light frame structures (Dolan, 1989) and, on heavy timber framed structures, an extensive experimental campaign was carried out by Pampanin et al, (2006).

Literature research and applications, therefore, demonstrate the use of anti-seismic devices mainly for light-frame timber structures. The state of the art reveals that elastomeric bearings, sliding bearings, friction dampers, viscoelastic dampers, hysteretic dampers, and fluid viscous dampers have been considered for implementation within the framing of wood buildings. Although there are a number of impediments to the widespread implementation of such advanced seismic protection systems, the reviewed literature clearly demonstrates that advanced seismic protection systems offer promise for enabling light-framed wood structures to resist major earthquakes with minimal damage.

Reed and Kircher (1986) discuss a seismic retrofit study on a five-story timber light-frame building using two different isolation system configurations: one with elastomeric bearings and the other with flat sliding bearings. For both isolation system configurations, a horizontal steel truss system was designed to stiffen the first floor so as to achieve rigid diaphragm action immediately above the isolation level.

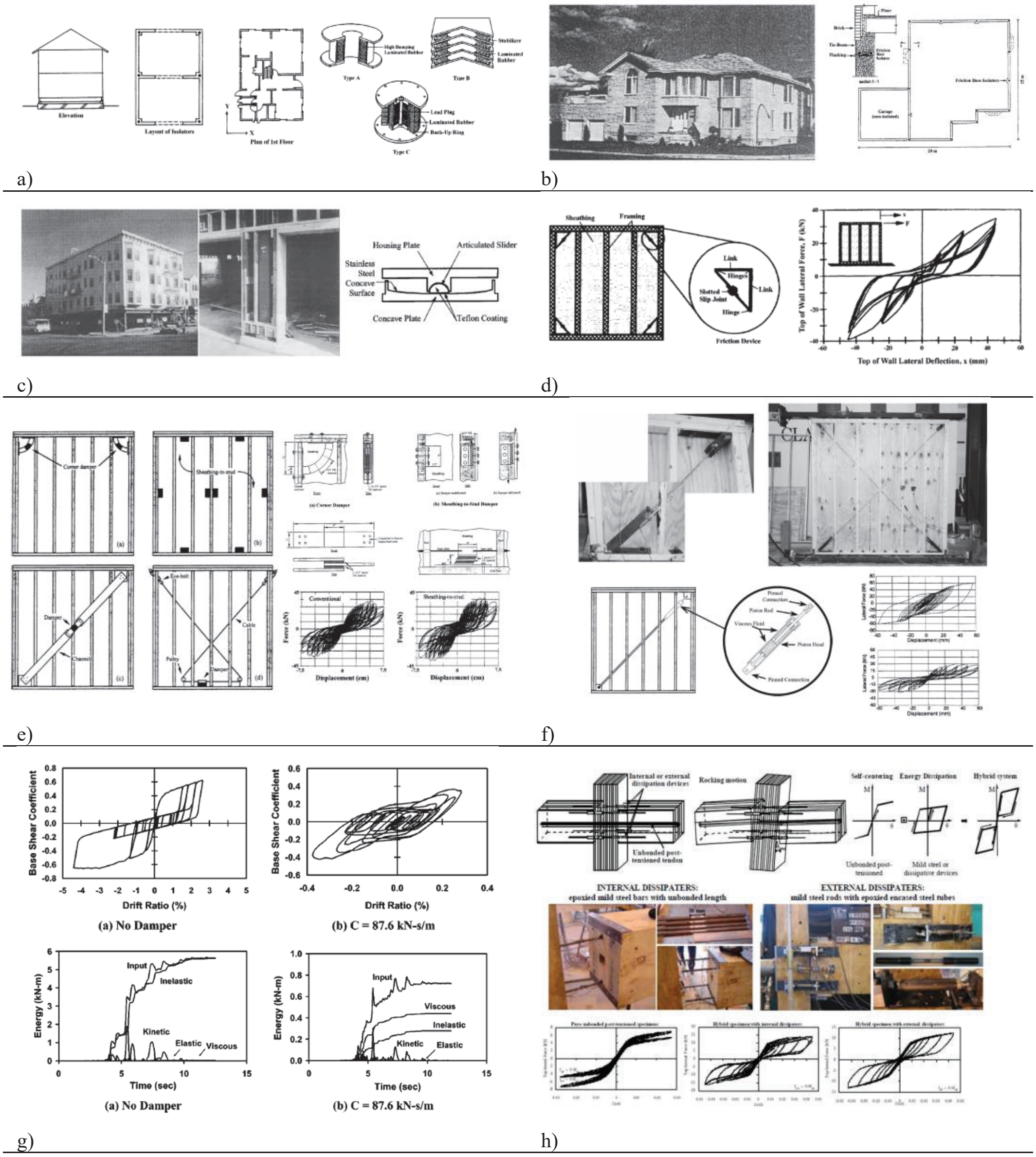

Figure II.30 – Timber structures with seismic protection systems studies: a) Sakamoto et al, 1990; b) Pall and Pall 1991; c) Zayas and Low, 1997; d) Filiatrault, 1990; e) Dinehart et al, 1999; f) Higgins, 2001; g) Symans et al, 2002; h) Pampanin et al, 2006.

In addition, a vertical truss system was designed to transfer loads between the isolation system and the wood-framed superstructure. They produced peak base shear response reductions ranging from 74% to 98%. Thus, the isolation systems appear to be very effective in terms of limiting the force transferred into the wood-framed superstructure.

Sakamoto et al. (1990, Fig. II.7a) present an experimental and analytical study of a two-story light-framed wood building supported on a base isolation system, at the University of Tokyo, which consists of six laminated elastomeric bearings located along the perimeter of the foundation. Three different types of bearings were used in the experimental testing; namely, high damping rubber bearings, multi-stage rubber bearings, and lead-rubber bearings. The peak ground acceleration at the building site was 0,108g. The effectiveness of the isolation system is demonstrated by the reduction of acceleration (approximately 70%) transmitted from the ground level to the first floor.

In 1988, a base isolation system was implemented within a two-story light-framed wood house in Montreal, Canada by Pall and Pall (1991, Fig. II.7b). The house has two stories above grade and a basement below grade. The basement walls are reinforced concrete and the superstructure consists of light-framed wood construction with brick veneer. The isolation bearings used in this application are flat sliding bearings. A total of 15 bearings were installed along the perimeter of the basement wall. The results of the analyses show that the acceleration at the top of the structure is reduced by about 42% for the design peak ground acceleration of 0,18g.

The implementation of sliding bearings in a four-story wood-framed apartment building in San Francisco, California, is discussed by Zayas and Low (1997, Fig. II.7c). The building was severely damaged during the 1989 Loma Prieta earthquake and was retrofitted using sliding friction pendulum system (FPS) bearings. The four-story structure has a garage at the first story with apartments in the top three stories. The damage to the first story during the Loma Prieta earthquake was so severe that the entire first-story wood framing was replaced with a steel moment-resisting frame. The sliding bearings were installed under the base plates of each column of the steel frame. The effect of the isolation system is to reduce the peak interstory drift by about 95%.

The seismic response of friction-damped timber shear walls has been studied by Filiatrault (1990, Fig. II.7d). The cyclic lateral force-displacement relation for conventional light framed shear walls exhibits both a progressive loss of stiffness and pinching of the hysteresis loops. Such behaviour is a direct result of damage to the shear wall. Note that, due to the pinching of the hysteresis loops, the shear wall must experience large deformations in order to dissipate the seismic input energy. Filiatrault proposed the concept of installing supplemental energy dissipation elements at the four corners of a shear wall. The elements are friction dampers that absorb a significant portion of the seismic input energy, reducing the amount of energy that needs to be dissipated by the framing via inelastic behaviour. The friction dampers consist of a slotted slip joint that dissipates energy via friction as the two sides of the joint slide with respect to each other. Sliding motion of the slip joint is induced by deformation of the four corners of the shear wall. Thus, the wood framing of the shear wall must deform to activate the friction dampers. However, since the friction dampers absorb a portion of the seismic energy input, the energy dissipation demand on the framing will be reduced. The friction dampers improve the seismic performance by reducing the peak force and displacement at the top of the wall and essentially eliminating the pinching of the hysteresis loops and, at the end of the earthquake, approximately 60% of the input energy is dissipated by the friction dampers.

The dynamic behaviour of light-framed wood shear walls with viscoelastic damperswas experimentally evaluated by Dinehart and Shenton (1998) and Dinehart et al. (1999, Fig. II.7e). The experimental tests were conducted on shear walls framed with two 11,9mm thick plywood sheets were used as sheathing panels. Four different damper configurations were investigated. In each configuration, the viscoelastic damper dissipates energy via shearing action of a viscoelastic rubber-like material. The shearing action is induced by relative motion between the two ends of the damper at their points of attachment to the shear wall. Thus, the shear wall must deform for the viscoelastic dampers to dissipate energy. In addition to the corner damper configuration where the dampers are located in the top corners, a separate configuration with the dampers located in the bottom corners was investigated.

the viscoelastic dampers provide a stable source of energy dissipation during cyclic motion of the shear wall. A stable source of energy dissipation is particularly important in terms of the ability of a wood-framed structure to resist strong earthquake aftershocks.

The application of a hysteretic damper to a wood-framed shear wall is investigated by Higgins (2001, Fig. II.7f). The hysteretic damper consists of a diagonal brace with a fixed anchorage at the top corner of the wall and a sliding anchorage at the opposite corner. In compression, the diagonal rod is allowed to slip through the sliding anchorage, eliminating the possibility of buckling. In tension, the diagonal rod is gripped by the sliding anchorage.

Experimental tests were performed in which a wood-framed shear wall was outfitted with two of the dampers; one along each diagonal. The dampers were effective in reducing the strength and stiffness degradation of the wall and increasing the energy dissipation capacity. In addition, the characteristic pinching behaviour of wood-framed shear walls is virtually absent for the wall with the damper.

The seismic response of a wood-framed shear wall with fluid viscous dampers is presented in a numerical study by the Symans et al. (2002, Fig. II.7g). A wall model was developed based on a series of walls that were experimentally tested by Dolan (1989). The weight at the top of the wall was such that the wall represented a single wall in the first story of a three-story apartment building. A nonlinear finite element model of the shear wall was developed and utilized to perform the numerical simulations. The inelastic behaviour of the wall was accounted for via nonlinear sheathing connections. Fluid viscous dampers were oriented within the shear wall framing and consists of a cylinder filled with a low-viscosity fluid. As the damper is cycled, the fluid passes through small orifices at high speeds, resulting in the development of heat energy that is transferred to the environment via convection and conduction. The wall was outfitted with a damper having a viscous damping coefficient of 87,6 kN-s/cm, resulting in an increase in the fundamental mode-damping ratio from an assumed value of 2% (under elastic conditions) for the wall without a damper to a value of approximately 20%. The results demonstrate a significant reduction in energy dissipation demand on the wall (reduction of approximately 95% compared to no damper case) while the viscous energy dissipated by the fluid damper represents a large portion of the final seismic input energy (approximately 57%). Thus, the fluid damper has effectively provided for a transfer of energy dissipation demand from the wall to the damper.

More recent studies, instead, concern the use of FVD for timber frame structures. Pampanin et al. (2006, Fig. II.7h) describe an extensive experimental program at the University of Canterbury, for the development of new structural systems and connections for multilayer laminated wood (LVL) buildings in seismic areas. the structural solution adopted is particularly efficient as it combines the self-centering capacities of post-tensioned cables and the dissipation of energy provided by additional devices. Consequently, the behaviour is characterized by a particular "flag-shaped" hysteresis loop.

2.3.2 Conception of the system

The implicit performance level ascribed to structures designed according to seismic building code procedures corresponds to minimum life-safety criteria. Current thinking, however, is shifting away from this narrow point-of-view toward a seismic design philosophy in which multiple performance levels are considered. To achieve high performance levels for strong earthquakes generally requires the use of an innovative seismic protection system.

Structural passive control systems have been developed with a design philosophy different than that of the traditional seismic design method. These control systems primarily include seismic isolation systems and energy dissipation systems. A variety of energy dissipation systems have been developed in the past two decades, such as friction dampers, metallic dampers, viscos-elastic dampers and viscous dampers that have seen a steadily increasing number of applications in large steel and concrete buildings over the past decade. A structure installed with these dampers does not rely on plastic hinging to dissipate the seismic energy. On the contrary, the dissipation of energy is concentrated on some added dampers so that the damage of the main structure is reduced, and the functions of the structure can then be possibly preserved.

The research discussed herein seeks, particularly, to study the behaviour of innovative seismic protection systems applicated to existing and new timber frame structures by investigating the suitability of a supplemental energy dissipation system. Specifically, the suitability of fluid dampers, which dissipate energy via orificing of a fluid, has been explored. A unique feature of the fluid dampers that have been studied is that they are capable of providing a very high-energy dissipation density (i.e., the energy dissipated is very large in comparison to the physical size of the damper). Thus, it is likely that the dampers could be conveniently located within the walls of a timber framed structure or within the diagonals of a timber frame with bracings with the aim of dissipating seismic energy, while timber elements and steel connections remain in the elastic field.

In line with this, a first proposal of design criteria for dissipative heavy timber framed structures with FVD devices has been recently formulated by Faggiano et al, (2019). In particular, in order to preserve the connections, to the FVDs is delegated the dissipative function while e structural timber members and the connections are designed to remain in elastic field.

2.3.3 Main features of fluid viscous damper for seismic structures

Anti-seismic devices are defined by the relevant European standard as devices that are provided in structures with the aim of modifying their response to the seismic action. Such modification can be done by isolating the structure, by dissipating energy. The seismic isolation and energy dissipation, often combined, have come of age in the last 30 years as an alternative to conventional seismic design methods.

The approach of seismic energy dissipation is made clear by considering the following time-dependent conservation of energy relationship (Uang and Bertero, 1988):

$$E(t) = E_k(t) + E_s(t) + E_h(t) + E_d(t)$$

where

- E is the absolute energy input from the earthquake motion;
- E_k is the absolute kinetic energy;
- E_s is the elastic (recoverable) strain energy of the structure;
- E_h is the irrecoverable energy dissipated by the structural system through inelastic or other forms of action (viscous and hysteretic);
- E_d is the energy dissipated by the supplemental damping system;
- t represents time.

The right hand side is basically the energy capacity or supply of the structure and the left hand side is the energy demand by the earthquake ground motion on the structure: the absolute input energy, E, represents the work done by the total base shear force at the foundation on the ground displacement and thus accounts for the effect of the inertia forces on the structure.

For a structure to survive the earthquake, the energy supply must be larger than the energy demand. In conventional seismic design, the energy supply relies mostly on the hysteretic energy term, E_h, which results from the inelastic deformations of the structure. For a structure with viscous dampers, the energy dissipation capacity of the system will increase due to the addition of E_d, and the system will normally be designed to allow for an early engagement of the viscous dampers in dissipating the input energy prior to the inelastic deformation of the primary structure. In other words, the primary frame will be better protected, and the performance of the structure subjected to a ground motion can be improved.

Fluid viscous dampers were initially used in the military and aerospace industry. They were designed for use in structural engineering in the late of 1980s and early of 1990s. FVD typically consist of a piston head with orifices contained in a cylinder filled with a highly viscous fluid, usually a compound of silicone or a similar type of oil. Energy is dissipated in the damper by fluid orifice when the piston head moves through the fluid (Soong and Constantinou, 1994; Whittaker and Constantinou, 2000). The fluid in the cylinder is nearly incompressible, and when the damper is subjected to a compressive force, the fluid volume inside the cylinder is decreased as a result of the piston rod area movement. A decrease in volume results in a restoring force. This undesirable force is prevented by using an accumulator. An accumulator works by collecting the volume of fluid that is displaced by the piston rod and storing it in the makeup area. As the rod retreats, a vacuum that has been created will draw the fluid out. A damper with an accumulator is illustrated in Figure II.8 (Seleemah and Constantinou, 1997).

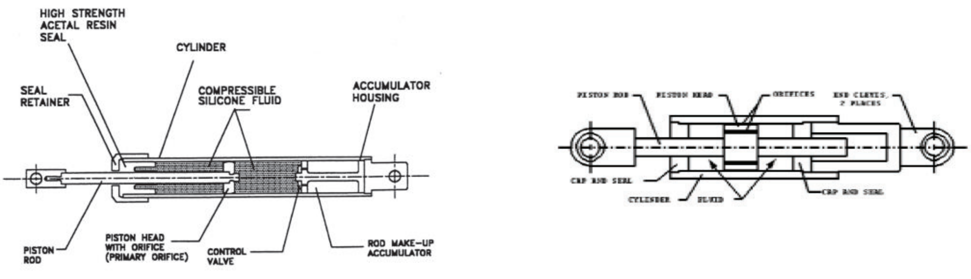

a) b)

Figure II.31 – Longitudinal cross section of a Fluid Damper: a) Damper with an accumulator (Seleemah and Constantinou, 1997); b) Damper with a run-through rod (Hwang, 2002).

A suitable mathematical model to describe the behaviour of linear and non-linear fluid viscous dampers is given by the following force - velocity relationship:

$$F_D(t) = C \cdot \mathring{u}_d^{\alpha} \cdot (t)$$

where F_D is the damper force, C is the damping constant, $\mathring{u}_d$ is the relative velocity between the two ends of the damper, and α is the exponent between 0 and 1. The damper with $\alpha=1$ is called a linear viscous damper in which the damper force is proportional to the relative velocity. The dampers with α larger than 1 have not been seen often in practical applications. The damper with α smaller than 1 is called a nonlinear viscous damper which is effective in minimizing high velocity shocks. Figure II.9a shows the force-velocity relationships of the three different types of viscous dampers. This Figure demonstrates the efficiency of nonlinear dampers in minimizing high velocity shocks. For a small relative velocity, the damper with a α value less than 1 can give a larger damping force than the other two types of dampers.

For seismic applications, the α exponent generally has a value ranging between about 0,15 to 1,0. Figure 1b shows the force-velocity relationship for the three different types of viscous dampers, demonstrating that for a relatively small speed, dampers with a value of $\alpha<1$ can provide a greater damping force than the other two types. For a fixed value of displacement, force and amplitude, the dissipated energy for each cycle by a non-linear fluid damper is larger than the one by the linear case and monotonically increases as the exponent of the velocity decreases (Fig. II.9b). For a fixed value of motion frequency and displacement amplitude $u_{d,0}$, for dissipating the same amount of energy per cycle, the damping coefficient of the nonlinear damper, C_{NL}, must be greater than that of the linear damper, C_L (Hwang, 2002).

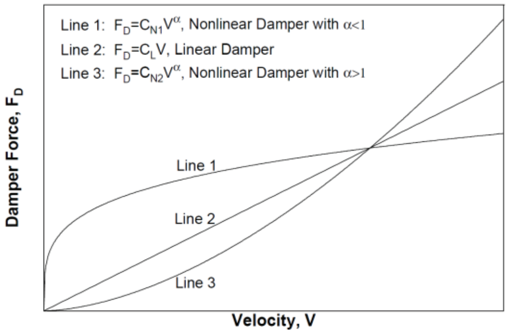

a)

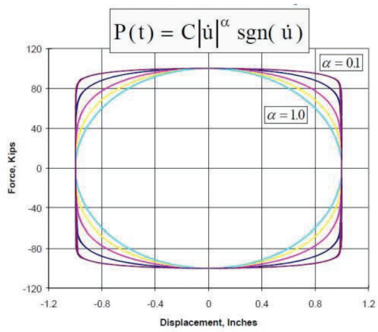

b)

Figure II.32 – a) Force-Velocity (F_D-V) relationships of non-linear and linear viscous dampers; b) Force-displacement relationships for three different types of viscous dampers (Hwang 2002).

The Figure II.10-(a) shows the hysteresis loop of a pure linear viscous behaviour. The loop is a perfect ellipse under this circumstance. The absence of storage stiffness makes the natural frequency of a structure incorporated with the damper remain the same. This advantage will simplify the design procedure for a structure with supplemental viscous devices. However, if the damper develops restoring force, the loop will be changed from Figure II.10-a to Figure II.10-b. In other words, it turns from a viscous behaviour to a viscoelastic behaviour (Hwang, 2002).

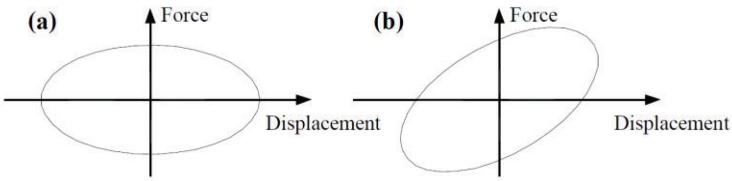

Figure II.33 – Hysteresis loops of dampers with pure viscous and viscoelastic behaviour (Hwang 2002).

2.3.4 Design criteria criteria for heavy timber frame structures with FVDs

Considering a single degree of freedom system equipped with a linear viscous damper under an imposed sinusoidal displacement time history:

$$u = u_0 \cdot \sin \cdot \omega \cdot t$$

where u is the displacement of the system and the damper; u_0 is amplitude of the displacement; and the ω is the excitation frequency. The measured force response is:

$$P = P_0 \cdot \sin(\omega \cdot t + \delta)$$

where P is the force response of the system; P_0 is amplitude of the force; and the δ is the phase angle. The energy dissipated by the damper, W_D, is:

$$W_D = \oint F_D \cdot du$$

where F_D is the damper force which equals to $C\dot{u}$; C is the damping coefficient of the damper; and $\dot{u}$ is the velocity of the system and the damper. Therefore,

$$W_D = \oint C\dot{u} \cdot du = \int_0^{2\pi/w} C \cdot \dot{u}^2\, dt = C \cdot u_0^2 \cdot \omega^2 \int_0^{2\pi} \cos^2 \omega \cdot t \cdot d(\omega t) = \pi \cdot C \cdot u^2{}_0 \cdot \omega$$

Recognizing that the damping ratio contributed by the damper can be expressed as $\xi_d = C/C_{cr}$, it is obtained:

$$W_D = \pi \cdot C \cdot \dot{u}_0 \cdot \omega = \pi \cdot \xi_d \cdot K_{u_0^2} \frac{\omega}{\omega_0} = 2 \cdot \pi \cdot \xi_a \cdot W_s \frac{\omega}{\omega_0}$$

where C_{cr}, K, m, ω_0 and W_s are respectively the critical damping coefficient, stiffness, mass, nature frequency and elastic strain energy of the system. The damping ratio attributed to the damper can then be expressed as:

$$\xi_d = \frac{W_D}{2 \cdot \pi \cdot W_s} \frac{\omega_0}{\omega}$$

W_d and W_s are illustrated in Figure II.11. Under earthquake excitations, ω is essentially equal to ω_0, and the previously equation is reduced to:

$$\xi_d = \frac{W_D}{2 \cdot \pi \cdot W_s}$$

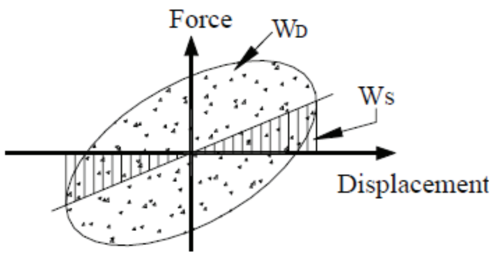

Figure II.34 – Definition of energy dissipated W_D in a cycle of harmonic motion and maximum strain energy W_s of a SDOF system with viscous damping devices (Hwang 2002).

In particular, the damping ratio attributed to the damper can be defined also as:

$$\xi_d = \frac{C}{C_{cr}} = \frac{C}{2 \cdot \omega \cdot m}$$

Considering a MDOF system (Fig. II.12), the total effective damping ratio of the system, ξ_{eff}, can be expressed as:

$$\xi_{eff} = \xi_0 + \xi_d$$

where ξ_0 is the inherent damping ratio of the MDOF system without dampers, and ξ_d is the viscous damping ratio attributed to added dampers. Extended from the concept of a SDOF system, the equation shown below is used by FEMA273 to represent ξ_d.

$$\xi_d = \frac{\Sigma W_j}{2 \cdot \pi \cdot W_k}$$

where $\sum W_j$ is the sum of the energy dissipated by the j-th damper of the system in one cycle; and K W is the elastic strain energy of the frame. W_k is equal to $\sum F_i \Delta_i$ where F_i is the story shear and Δ_i is the story drift of the i-th floor.

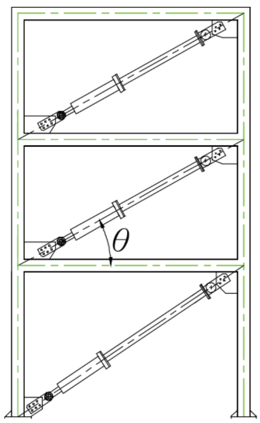

Figure II.35 – A MDOF model of a structure with viscous dampers (Hwang 2002).

The structure with FVDs is designed under a static horizontal force evaluated reducing the design response spectrum through a damping coefficient equal to ξ_{eff}. In particular, the structural timber members are designed to remain in elastic field, with a damping capacity ξ_0, while to the FVDs is delegated the dissipative function, with damping capacity ξ_d. By keeping the ξ_0 coefficient constant, as ξ_{eff} increases, the dissipative capacity of the FVD increases (ξ_d).

2.4 Design of joints

2.4.1 Recurrent types

Although timber has many inherent benefits with regards to seismic design, use of timber frame structures, and specially the MRFs is still primarily limited to low rise structures. Timber is quite effective in single storey portal frames, and bays can span up to 40 metres in length (Buchanan and Fairweather, 1993). For this reason, timber structures with MRFs and frames with bracings, respect to wall frames and platform frames are typically used in commercial buildings that require large open spaces (Buchanan and Fairweather, 1993). Due to the orthotropic nature of wood and the presence of defects, wood tends to fail in a brittle manner, even in bending (unlike concrete or steel). Consequently, designers rely upon the connections between timber elements to provide the necessary ductility and energy dissipation required to withstand severe ground motions (Andreolli et al, 2011). The difficulty designers face, especially regarding timber MRFs, is detailing connections to achieve both high strength, as well as high ductility.

Designers may overcome the aforementioned design issues using either traditional dowel type connections or modern connections using adhesives, CFRP, and advanced fasteners. If the connection is properly detailed, incorporating steel components to provide the necessary ductility to protect brittle components, high strength and ductility may be achieved. To date, only a moderate amount of ductility has been achieved for timber moment-resisting connections. Most traditional moment connections utilize dowel type fasteners, such as bolts, steel dowels, or nails. Design of these fasteners in both Europe and North America are based on the works of Johansen (1949) and is dependent on both the embedment strength of timber and the resistance of dowels in bending. Other connection types include timber rivets and glued-in rods. Examples of moment connections using the aforementioned Buchanan and Fairweather (1993) have provided a detailed summary of traditional timber moment-resisting connections that are available to designers. One of the most popular connections for portal frames consists of steel dowels driven through timber beams and columns in a circular configuration. High aesthetic quality and ease of construction make this an attractive option; however these connections generally cannot develop the full strength of the connecting members, and can often lead to splitting failure. Bouchair et al. (2007) experimented on reinforced and unreinforced connections with this configuration. The unreinforced connection exhibited brittle failure while the connection reinforced with glued-on wood side panels accommodated large plastic rotations with a capacity nearly twice that of the unreinforced alternative. The connections were designed according to European standards and Bouchair et al. (2007) presented design methods. Nailed moment connections generally connect beams to columns using steel or plywood side plates as shown in Figure II.13b. Application is usually limited to deep slender sections, but tests show potential for good hysteretic behaviour (Buchanan and Fairweather, 1993). Riveted connections are very similar to nailed connections; often using steel side plates. Timber rivets tend to be stiffer than nails, and the oblong shape prevents damage to the wood fibres during installation. Popovski and Karacabeyli (2004) have shown that well-detailed riveted moment connections can fail in a ductile manner by means of rivet yielding, and can sustain large plastic deformations without abrupt failure. Glued-in threaded steel rods have been gaining popularity since the early 1990's (Tlustochowicz et al, 2011). As the name implies, threaded rods are inserted into a hole in the timber section and held in place using high-strength epoxy. Figure II.13c shows one of many possible configurations for glued-in rod moment connections. Use of this connection type requires high quality control and assembly is usually completed in a shop, prior to delivery on site. Benefits include good fire performance, high aesthetic quality, and limited induced splitting stresses. Tlustochowicz et al. (2011) presents design recommendations for glued-in rods. Bolted connections with embedded steel plates similar to that shown in Figure II.13d are among the most common used in timber frames. They are typically designed to transfer shear forces due to gravity loading. Since the moment capacity is commonly overlooked by designers, in the event of a severe ground motion, unforeseen applied moments usually lead to abrupt splitting failure of the timber elements (Lam et al, 2010).

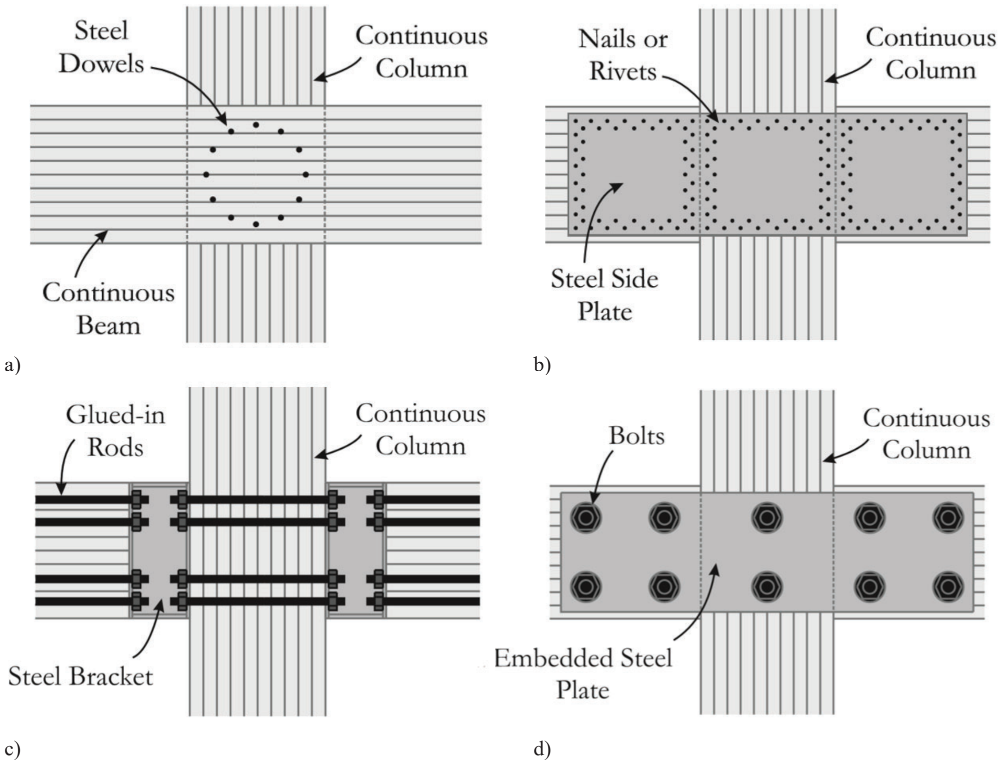

Figure II.36 – Traditional timber moment-resisting connections: a) circular dowels; b) nails or rivets; c) glued-in rods; d) bolts with embedded plate (Gohlich, 2015).

Lam et al. (2010) showed that while standard bolted connections exhibit poor hysteretic behaviour, using self-tapping screws as reinforcement can increase capacity by over 70%, and delay brittle failure modes. In order to develop enough moment capacity for use in multi-storey structures, connections with many fasteners are necessary since there is often an inherent group effect associated with large connections.

Jorissen (1999) studied the effects of the number of fasteners in a group using bolted wood-wood tension connections. It was determined that fastener spacing within a row had the most considerable effect; the most balanced distribution came when fastener spacing is at a maximum. Furthermore, Jorissen found that load distribution among fasteners was nearly uniform at the time of failure because deformations in the bolts carrying higher loads allowed for stress redistribution within the group. A design method was developed for determining the effect of the number of fasteners within a group (Jorissen, 1999). Zarnani and Quenneville (2014, Fig. II.13a) experimented with timber rivets to develop a design approach for the group effect of fasteners based on the relative stiffness of each plane of resistance in the connection. In order to overcome the limited ductility and rotation capacity exhibited by traditional timber moment-resisting connections, it is necessary to improve upon or develop new methods of forming rigid beam-column joints in timber frames. The traditional bolted moment-resisting timber connection tested by Lam et al. (2010) achieved a ductility of only 2,76, significantly lower than that achievable by steel moment-resisting connections. Tests by Bouchair et al. (2007) on a typical dowel-type moment-resisting connections exhibited a ductility of only 2,1. Furthermore, both systems achieve little energy dissipation due to the early onset of brittle failure modes. In order to take advantage of the high strength to weight ratio of wood in lowering seismic design forces (relative to steel and concrete), steps must be taken to overcome the seismic deficiencies inherent of wood that limit the ductility and plastic rotation capacity. Over the years, numerous experimental tests have been carried out on the connections in order to verify their ductility using cylindrical shank metal connectors. In Zarnani et al. (2016, Fig. II.14a), an innovative Resilient Slip Friction (RSF) joint (patent filed) is introduced. Design procedures are developed for capacity prediction of different possible configuration of the joint. The outer cap plates and the centre slotted plates are grooved and clamped together by use of high strength bolts. When the imposed force to the joint overcomes the frictional resistance between the surfaces, the centre slotted plates start to slide and energy will be dissipated through cycles of sliding. The specific shape of the plates grooves along with the use of Belleville washers (also known as coned-disc springs) and high strength bolts provide the desirable self-centring characteristic for this slip-friction joint. In order to experimentally investigate the hysteretic behaviour of the RSF joint, a symmetric RSF joint with the grooves angle of 30 degrees was fabricated and tested under quasi-static loading. Cap plates were manufactured with mild steel grade 300 and slotted centre plates with basally grade 400 for achieving a more uniform frictional behaviour between sliding surfaces. The test results demonstrate the capacity of the joint to dissipate earthquake energy, as well as the self-centring capability allowing to minimize both the local damage and the overall residual drift of the structure after a severe event. The joint could be also instrumented, so that it can be used as a reliable connection system for structural health monitoring purposes. Gonzalez (2016, Fig. II.14b) carried out a test campaign on twelve specimens of beam-to-column connection, with different geometric characteristics of the joint itself and the bolt patterns, wood species and type of bolts, aiming at determining the structural behaviour and static ductility factor. Members are made of glulam timber. The beam segment was loaded at the free end to induce a moment in the connection; the ends of the column segment were simply supported. As a result, the ductility factors achieved by the test specimens ranged from 2,0 to 2,7 in average.

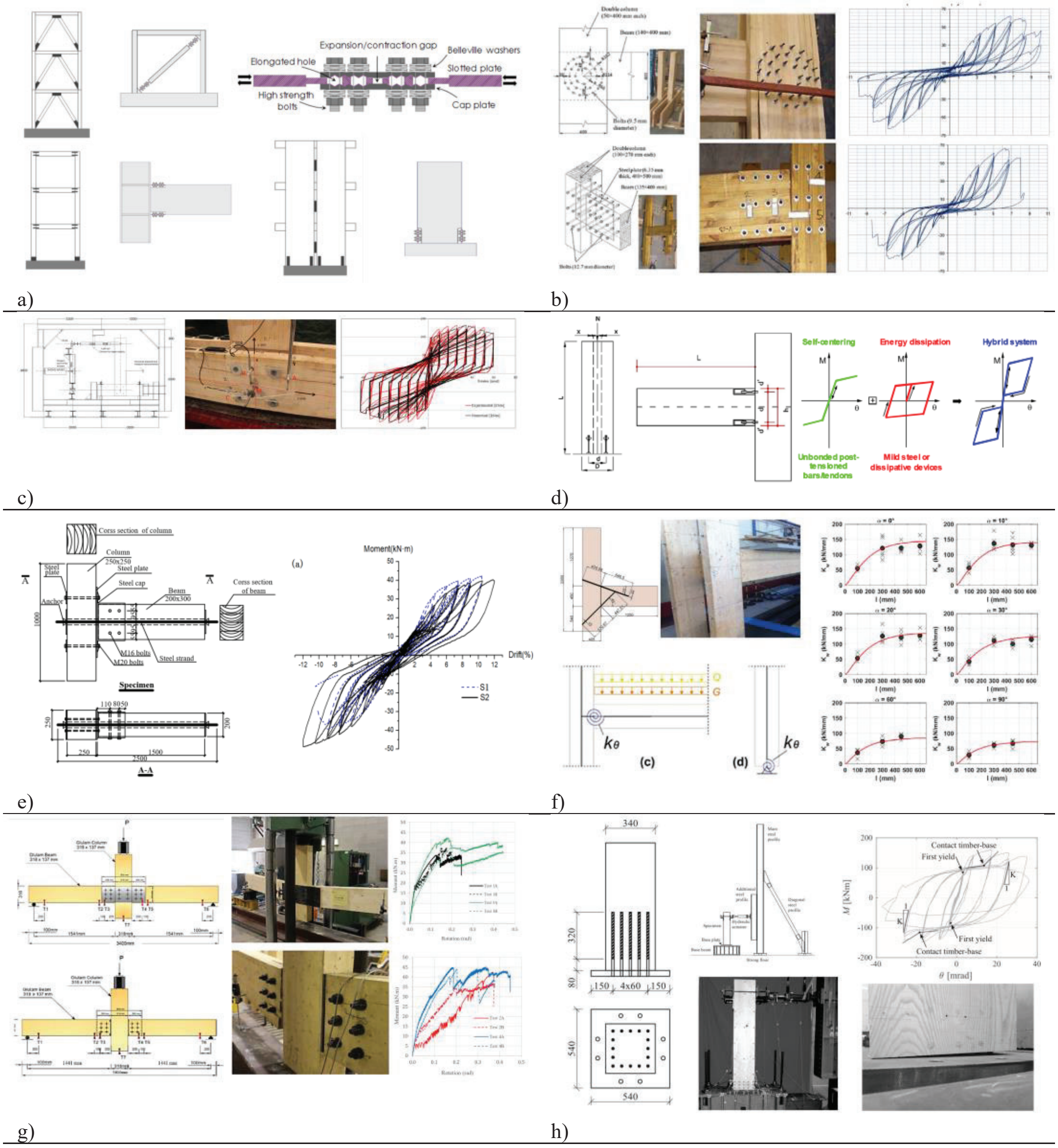

Figure II.37 – Beam to column connections studies: a) Zarnani et al, 2016; b) Gonzalez et al, 2016; c) Bakel et al, 2016; d) Pampanin et al, 2016; e) Wang et al, 2016; f) Malo et al, 2016); g) Salem, 2016; Salem and Petrycki, 2016; h) Ogrizovic et al, 2017.

In Bakel et al. (2016, Fig. II.14c), some cyclic experimental tests on beam-column timber joints with expanded tube fasteners are analysed. The connections are reinforced with Densified Veneer

Wood. A good energy dissipative capacity is observed for each joint tested, making them particularly suited for use in earthquake-zone. Hence, a numerical model for the cyclic behaviour of these joints is presented and validated against the experimental data. In Pampanin et al. (2016, Fig. II.14d) post tensioned energy dissipating connections for timber structural systems are proposed. The research activity, including extensive experimental and numerical investigations on subassemblies, is carried out at the University of Canterbury, New Zealand. Study systems all exhibited almost complete re-centering capabilities and significant energy dissipation without any structural damage. Numerical models were developed and calibrated upon the experimental results to suggest values of relevant parameters for design applications. Also Wang et al. (2016, Fig. II.14e) have analysed the seismic performance of a post-tensioned (PT) energy dissipating beam-to column joint for glulam heavy timber structure. The connection incorporates post-tensioned high-strength strand to provide self-centering capacity along with a special steel cap, which is attached to the timber beam, both to provide energy dissipation and to prevent the end bearing failure of wood. Malo et al. (2016, Fig. II.14f) studied a moment resisting connection with inclined threaded rods installed in predrilled holes. Laboratory tests were carried out. The behaviour was also interpreted through analytical formulations, aimed at defining the relevant stiffness requirements. Salem (2016) and Salem and Petrycki (2016), in Figure II.14g, carried out static tests on eight full-size glulam beam-column assemblies equipped with moment-resisting connections. The effect of bolt's end distance and number of bolt rows were investigated. The number of bolt rows from two to three significantly affect the connection moment capacity.

In Ogrizovic et al. (2017, Fig. II.14h) a moment-rotation behaviour of a semi-rigid connection with glued-in rods was investigated in a series of quasi-static cyclic tests. A moment resisting connection was established between timber columns and steel base plates. Three different timber products, including hardwood and softwood species, and two different rod diameters were used. The columns were subjected to shear force and bending, to simulate the loading conditions of a column in a frame under lateral loads. The tests were performed with increasing rotation demand on the column until the failure. The connections provided high moment capacity and rotational stiffness. All of the tested specimens demonstrated ductile response, while the connections with hardwood performed especially well.

2.4.2 Joint classification

The performance of timber structures is greatly influenced by the capacity of their connections. In this part of the chapter, a new classification procedure for timber beam-to-column connections in timber frame structures is proposed. At present, there is not a method, both in the national and in international standards, that allows to recognize the real connection behaviour for stiffness and strength. In particular, it is not possible to affirm which type of connection is *pinned*, *semi-rigid* or *rigid*. For this reason, and to encourage the realization of framed and braced multi-storey multi-span timber structures, a method based on the initial rotation stiffness is proposed.

Although materials are different, it is possible to apply the same criteria used for the classification of steel connections, well described in EC3, conveniently modified to considerate the timber characteristics. Therefore, with reference to the experimental studies available in the scientific literature on the many beam-to-column connections, this classification has been applied. The results show that the most type of connections are into pinned joint area while only a few belong to semi-rigid joint family.

It is commonly stated that "*a structure is a constructed assembly of joints separated by members*" (McLain, 1998) and in timber engineering the joint is generally the critical factor in the structural design. In the joint the strength of the connectors will normally dictate the strength of the structure; their stiffness will greatly influence its overall behaviour and members sizes will generally be determined by the numbers and physical characteristics of the connector rather than by the strength requirements of the member material. Moreover, the transfer of internal forces, caused by external action, at other members will be via a joint.

When all the different parts in the joint are sufficiently stiff, (i.e. ideally infinitely stiff), the joint is *rigid*, and there is no difference between the respective rotations at the end of the members connected at this joint (Fig. II.15a).

Should the joint be without any stiffness, then the beam will behave just as simply supported whatever the behaviour of the other connected member(s) (Fig. II.15b). This is a *pinned joint*. For intermediate cases (non-zero and non-infinite stiffness), the transmitted moment will result in a difference between the absolute rotations of the two connected members (Fig. II.15c). The joint is *semi-rigid* in these cases.

a) b) c)

Figure II.38 – Classification of joints according rotation stiffness: a) rigid joint; b) pinned joint; c) semi-rigid joint (Jaspart, 2000).

The main parameters defining the mechanical behaviour of a joint are moment resistance ($M_{j,Rd}$), stiffness ($S_{j,ini}$ or S_j) and rotation capacity (φ_{Cd}). These parameters are obtained from the moment–rotation curve, typically represented in Figure II.16a. Characterising the behaviour of the joint through moment-rotation curves, the bending moment is evaluated in the contact section between the column flange and the beam end plate. The rotation of the joint is described as the variation of the angle between the tangent to the beam axis and the tangent to the column axis, after deformation (Fig. II.16b,c). In general, the rotation of a joint has two components: rotation due to the deformation of the components situated in the connection zone (connection rotation φ_M) and rotation due to the horizontal column web deformation due to the shear force (shear panel rotation φ_V).

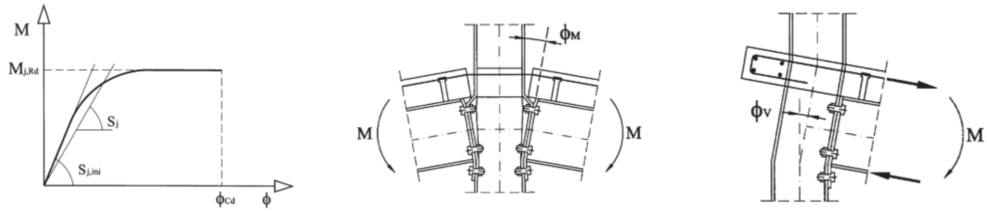

a) b) c)

Figure II.39 – a) Typical moment–rotation curve of a joint; b) Connection rotation φ_M; c) Shear panel rotation φ_V.

In accordance with EC3-1-8 (EN 1993-1-8, 2005), joints are classified in terms of stiffness and moment resistance. In line with the joint classification by stiffness, a joint may be classified as *rigid*, nominally *pinned* or *semi-rigid* according to its rotational stiffness, by comparing its initial rotational stiffness $S_{j,ini}$ with the classification boundaries that can be expressed in terms of a non-dimensional stiffness parameter:

$$\bar{k} = \frac{S_{j,ini} \cdot L_b}{E \cdot I_b}$$

where $S_{j,ini}$ is the initial joint rotation stiffness corresponding to a bending moment that does not exceed $\frac{2}{3} M_{j,Rd}$ ($M_{j,Rd}$ is the design moment resistance of the joint), L_b is the span of the supported beam, E is the elastic modulus of structural steel and I_b is the second moment of area of the supported beam section. A joint can be classified as:

Zone 1: rigid if $\bar{k} \geq k_b$
Zone 2: semi-rigid if $0,5 < \bar{k} < k_b$
Zone 3: pinned if $\bar{k} \leq 0,5$

where k_b is a factor that depends on the frame type. For braced frames where the bracing system reduces the horizontal displacement by at least 80% k_b admits a value of 8. For all others frames k_b can be taken as 25, provided that the ratio of the relative rigidity $k_b = I_b/L_b$ of all the beams at the top of the storey to the relative rigidity $K_c = I_c/L_c$ of all the columns of the same storey is greater than or equal to 0,1, i.e. $K_b/K_c \geq 0,1$. If the ratio is less than 0,1, the joint should be classified as semi-rigid irrespective of the non-dimensional stiffness parameter value.

Regarding the joint classification by strength, a joint may be classified as full-strength, nominally pinned or partial strength by comparing its design moment resistance $M_{j,Rd}$ with the design moment resistances of the members that it connects. The design resistance of a full strength joint should be not less than that of the connected members, whilst a nominally pinned joint should be capable of transmitting the internal force without developing significant moments which might adversely affect the members or the structure as a whole. On the other hand, a joint which does not meet the criteria for either a full-strength joint or a nominally pinned joint should be classified as a partial-strength joint. The joint classification according to the moment resistance can be also expressed in terms of a non-dimensional moment resistance parameter:

$$\overline{\mathrm{m}} = \frac{\mathrm{M_{j,Rd}}}{\mathrm{M_{pl,Rd}}}$$

$$\overline{\varphi} = \varphi\,\frac{\mathrm{E}\cdot\mathrm{I_b}}{\mathrm{L_b}\cdot\mathrm{M_{pl,Rd}}}$$

where $M_{pl,Rd}$ is the design plastic moment resistance of the connected member. For joints located at the top storey $M_{pl,Rd}$ is the smallest of the design plastic moment resistances of the connected beam and column, while for joints at lower storeys $M_{pl,Rd}$ should be taken as the smallest of the beam design plastic moment resistance and twice the column design plastic moment resistance. In this way, joints can be categorized as (Fig. II.17):

Pinned	if $\overline{\mathrm{m}} \leq 0{,}25$
Full-strength	if $\overline{\mathrm{m}} \geq 1$
Partial-strength	if $0{,}25 < \overline{\mathrm{m}} < 1$

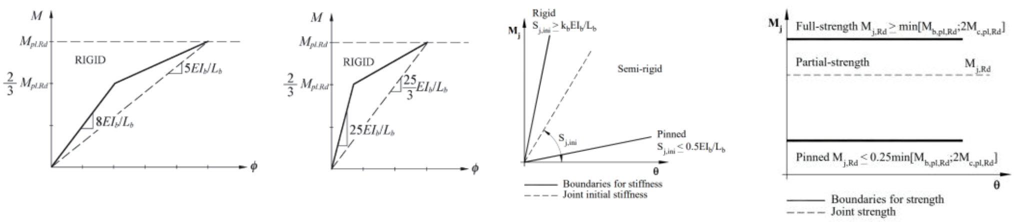

a) b) c) d)

Figure II.40 – The Eurocode 3 classification boundaries for rigid joints: a) joints in braced frame and b) joints in unbraced frame; c) stiffness and d) strength classification boundaries.

It is possible to apply the same criteria used for the classification of steel connections, conveniently modified to considerate the timber characteristics. In particular, since timber material has an elastic-fragile behaviour, the elastic-moment resistance, $M_{el,Rd}$, is used. in terms of a non-dimensional stiffness and moment resistance parameters:

$$\overline{\mathrm{k}} = \frac{\mathrm{S_{j,ini}}\cdot\mathrm{L_b}}{\mathrm{E}\cdot\mathrm{I_b}}$$

$$\overline{\mathrm{m}} = \frac{\mathrm{M_{j,Rd}}}{\mathrm{M_{el,Rd}}}$$

$$\overline{\varphi} = \varphi \frac{E \cdot I_b}{L_b \cdot M_{el,Rd}}$$

2.4.3 APPLICATIONS TO TYPICAL JOINT CONFIGURATION

With reference to the experimental studies available in the scientific literature on the many beam-to-column connections, this method has been applied on some joints (Tab. II.1).

Table II.4 – Scientific literature timber beam-to-column connections classification

Connection	Non-dimensional classification	Connection description
Salem, 2016: Experimental testing of steel-wood-steel glulam frame bolted connections (World Conference Timber Engineering 2016)		
	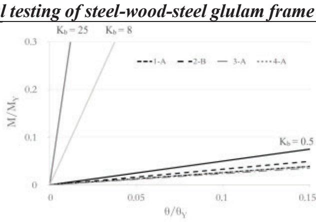	An experimental study to evaluate how end distance and number of bolt rows influence the strength and stiffness of beam-to-column connection is conduced. Glulam beams are connected to their supporting glulam column using two large 12,7 mm-thick plates of 300W grade steel and four different configurations are assembled.
Salem et al, 2016: Experimental testing of wood-steel-wood glulam moment resisting bolted connections (World Conference Timber Engineering 2016)		
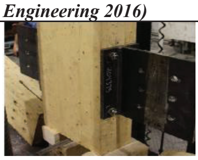	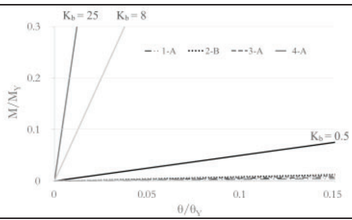	An experimental study, aimed to investigate the structural behaviour of wood-steel-wood glulam frame moment-resisting connections that were subjected to static bending, is conduced. Each frame test assembly was consisted of two glulam beams simply supported at their far ends and were connected to an inversely loaded glulam column in the centre using two steel T-stub connectors.
Wang et al, 2016: Investigation into the hysteretic performance of self-centering timber beam-to-column joints (World Conference Timber Engineering 2016)		
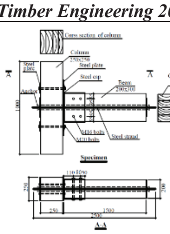	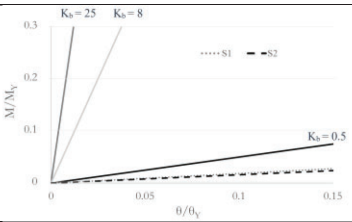	An experimental study on the seismic performance of a post-tensioned (PT) energy dissipating beam-to-column joint for glulam heavy timber structure is conduces. The experiment analyses the post-tension force effects on the dissipative energy and failure mode, testing two specimen S_1 and S_2, with a post-tension force of 40kN and 60kN respectively.

Minjuan et al, 2014: Comparison of glulam post-to-beam connections reinforced by two different dowel-type fasteners (Construction and Building Materials)

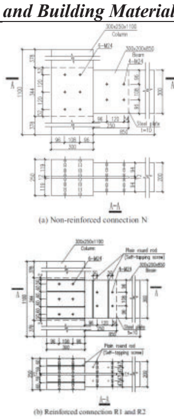

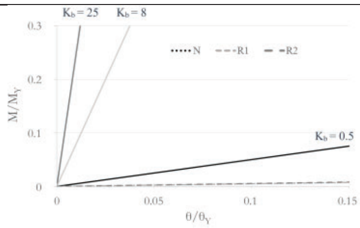

An experimental study on how the resistance of a beam-column connection is achieved by using a rectangular plate and bolts when reinforced with the use of bars (R1) or self-tapping screws (R2) arranged orthogonal to the grains is conduced. Configuration N corresponds to the non-reinforced case.

Minjuan et al, 2016: Experimental investigation on lateral performance of pre-stressed tube bolted connection with high initial stiffness (Advances in Structural Engineering)

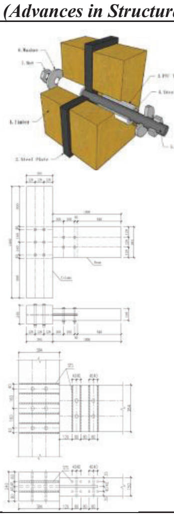

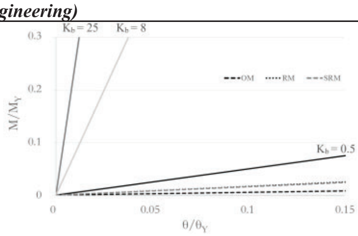

An experimental study on a semi-rigid pre-stressed tube bolted connection (PTBC) is conducted in order to improve the initial stiffness of bolted connections in timber constructions. This connection consists of timber members, steel plate, tubes, high-strength bolts, washers, and nuts. The tube has two layers that are bonded together, its inner layer made of steel and its outer layer made of polyvinyl chloride (PVC). The experiments consisted of monotonic tests and reversed cyclic tests. The test results of OBCs (series O) were used as baseline data, PTBCs were considered to be reinforced connections (series R), and PTBCs reinforced with STSs were set as series SR.

Wang et al, 2015: Rotational Behaviour of Bolted Beam-to-Column Connections with Locally Cross-Laminated Glulam (Journal of Structural Engineering)

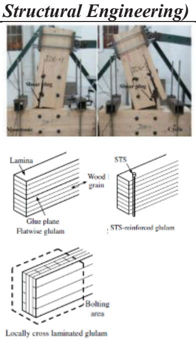

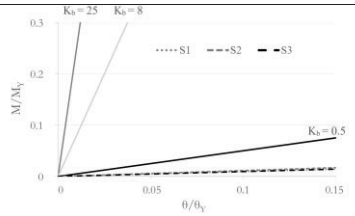

An experimental study on the rotational behaviour of bolted beam-to-column glulam connections reinforced using locally cross-laminated glulam members is conduced. Three specimen groups were tested using monotonic loading, with the first group, S_1, made with glulam timber, the second group, S_2, made with glulam timber and reinforced by STSs, and the third group, S_3, made with locally cross-laminated glulam timber

Kasal et al, 2010: Shake table test of a three-story spatial timber frame with moment connection (World Conference Timber Engineering 2010)

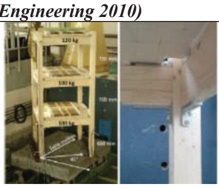

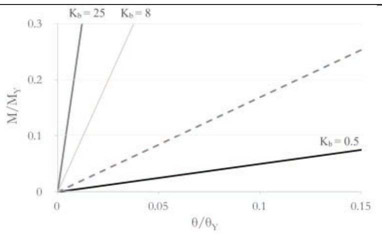

An experimental study on the connections made with special L-shaped aluminium angles located at the top and the bottom of the beam end, connected to the beam and the column through selft-tapping screws (STS) in conduced.

Kasal et al, 2014: Heavy laminates timber frames with rigid three-dimensional beam-to-column connections (Journal of Performance of Constructed facilities)

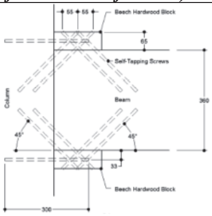

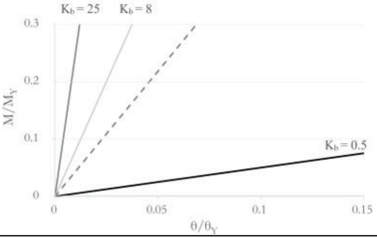

An experimental study on the seismic performance of a timber frame with three-dimentional (3D) with rigid moment connections in conduced. The connection is made with self-tapping screws and hardwood blocks were used to support the beams, The frame was designed to resist high seismic excitations with the goal of controlling the drift.

Polastri, 2015: Caratterizzazione del comportamento di giunti semirigidi per strutture lignee in zona sismica (PhD thesis)

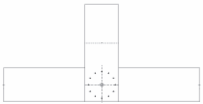

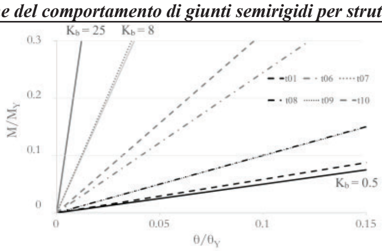

An experimental study on beam-to-column connections realized in different ways, to analyze in terms of strength and stiffness, is conduced: T01 specimen a single concentric circle, drift pin Ø16; T06 specimen a single concentric circle, glued bars Ø14; T07 glued joint; T08 specimen two concentric circles, drift pin Ø12; T09 specimen two concentric circles, drift pin Ø14; T10 specimen two concentric circles, glued bars Ø12.

Gohlich et al, 2016: Development of a heavy timber moment-resisting frame with ductile steel links (World Conference Timber Engineering 2016)

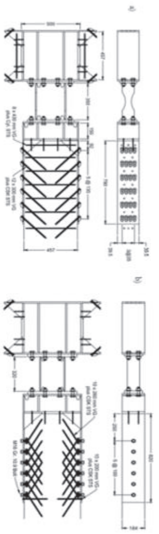

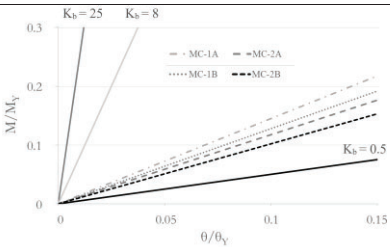

An experimental study on a hybrid timber steel moment-resisting connection in conduced, that incorporates specially detailed replaceable steel yielding link elements fastened to timber beams and columns using self-tapping screws (STS). For this study, the steel-to timber connection was made using two configurations of self-tapping screws and were considered two link types to promote ductile yielding away from the brittle weld metal. For a total of four configurations: Dog-bone W250x28 with STS installed at a 45-degree angle to the grain (MC-1A); Dog-bone W250x28 using ZD-plate to connections, that utilize STS installed at a 30-degree angle (MC1B); - W 200x25 with STS installed at a 45-degree angle to the grain (MC-2A); W 200x25 using ZD-plate to connections, that utilises STS installed at a 30-degree angle (MC2B).

Nakatani et al, 2012: Development of cross embedded joint using lagscrewbolt (World Conference Timber Engineering 2012)

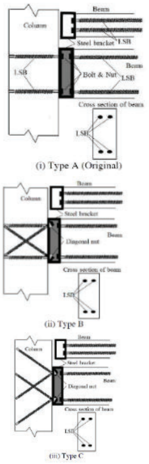

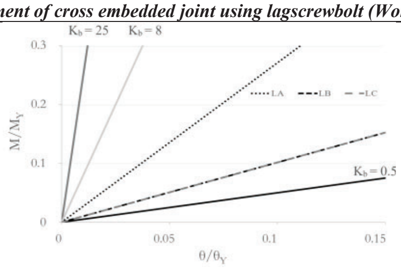

An experimental study on connections using a steel bracket, connected to the column by lagscrewbolts (LSB), some of which were embedded at different skew angles is conduced. LSB has a screw thread on the outside surface and a female thread inside the shank head. In particular, the behaviour of three different type of connections is studied.

2.4.4 Component method

Usually, the joints in the design of steel-framed and timber-frame structures are assumed as either fully rigid or ideally pinned. The first assumption considers the stiff joint, where the associated small rotations under the transmitted beam end moments have negligible effect on the distribution of internal forces and moments within the structure. On the other hand, ideally pinned joint does not transmit bending moments between the connected members but it can develop significant rotations.

However, it is widely recognized that these two extremes cannot accurately represent the actual joint behaviour, which in most cases can be described as semi-rigid, where considerable joint rotations can be developed under transmitted beam end moments.

Plenty of analytical models for the evaluation of the mechanical properties of structural joints (rotational stiffness, moment resistance, rotation capacity) are available in the literature for different types of joint configurations and connection types. But progressively one of these models, because of the advantages it offers in comparison to the others, slowly became the reference and is now considered as such by most of the researchers. In particular, it has been followed in Eurocode 3 Revised Annex J on “Joints in Building Frames”. It is known as the *component method*.

Component model of connections builds up on standard procedures of evaluation of internal forces in connections and their checking. Zoetemeijer et al (1985) was the first who equipped this model with prediction of stiffness and deformation capacity. The elastic stiffness was improved in the work of Steenhuis et al (1994). Basic description of components behaviour in major structural steel connections was used by Jaspart (2001) for beam to column connections and by Wald for column bases (Wald et al, 2008). The model was generalised by De Silva (2008). Method implemented in the current European structural standard for steel and composite connections (EC3 and EC4) can be applied in majority of software for structural steel used in Europe.

Roughly speaking the component method may be presented as the application of the well-known finite element method to the calculation of structural joints.

The mechanical behaviour of steel joints in terms of strength, stiffness and rotation capacity is a complex phenomena. To determine this complex behaviour, the joint can be decomposed into different parts, the so-called components. A component forms an identity in a joint and may include more than just a bolt or steel plate. For instance, in beam-to-column joints, an end plate in bending forms a component, but this component can include an extended part and transfer loads through several bolt rows and a variety of welds.

The mechanical behaviour of these components is studied separately. When all components of a joint have been characterised in terms of strength, stiffness and deformation capacity, the mechanical behaviour of a joint can be determined by assembling the individual contributions of the components with help of mechanical models. The originality, therefore, of the component method is to consider any joint as a set of "individual basic components".

The joint basic components associated with these connection types are presented in Figure II.18 and identified in Figure II.19. Besides this, Figure II.19 presents the mechanical model associated with each connection type.

EC3-1-8 (2005) Identification	*Basic Component*	*Adopted Notation*
1	*Column web panel in shear*	*cws*
2	*Column web in transverse compression*	*cwc*
3	*Column web in transverse tension*	*cwt*
4	*Column flange in bending*	*cfb*
5	*Endplate in bending*	*epb*
6	*Flange/web cleat in bending:*	
	- top angle in bending	*ta*
	- web angles in bending	*wa*
7	*Beam flange and web in compression*	*bfwc*
8	*Beam web in tension*	*bwt*
9	*Plate in tension or compression*	
	- top angle leg in tension	*tat*
	- web angle leg in tension	*wat*
	- seat angle in compression	*sac*
10	*Bolts in tension*	*bt*
11	*Bolts in shear*	*bs*
12	*Bolts in bearing*	*bb*
13	*Welds*	*wel*
	Plate in bearing:	
	- top angle leg in bearing	*tab*
	- seat angle leg in bearing	*sab*
	- beam flanges in bearing	*bfb*
	- beam web in bearing	*bwb*
	- web angle leg in bearing	*wab*

Figure II.41 – Joint basic components (Eurocode 3).

According to the component method, the design moment resistance $M_{j,Rd}$ of any joint may be derived from the distribution of internal forces within the joint and the resistances of its basic components to these forces. In addition, the flexibilities of the basic components, each one represented by an elastic stiffness coefficient k_i that has units of length (normalised relative to the elastic modulus of structural steel), can be combined to determine the joint rotational stiffness S_j.

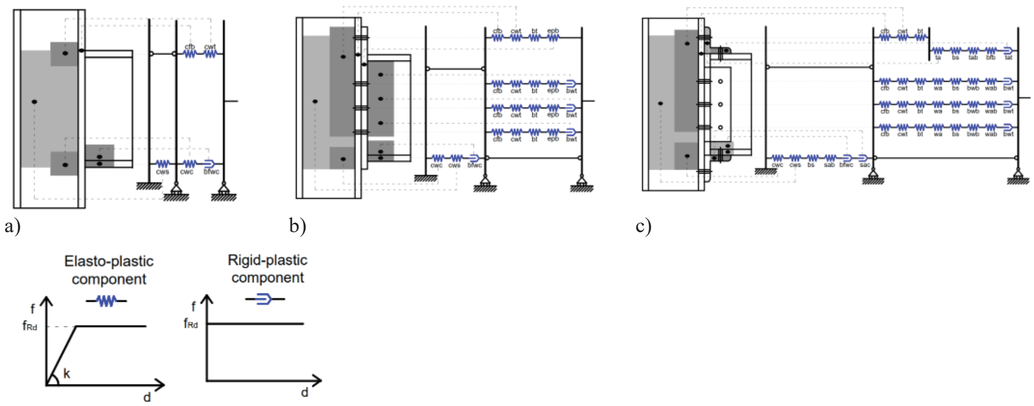

Fig **Figure II.42** – Joints and their associated mechanical models: a) welded connections; b) endplate connections; c) angle flange cleat connections (Del Savio, 2009).

The application of the component method requires the following steps:

1. Identification of the active components for the studied joint;
2. Evaluation of the mechanical characteristics of each individual basic component (specific characteristics - initial stiffness, design strength, ... - or the whole deformability curve);
3. “Assembly” of the components in view of the evaluation of the mechanical characteristics of the whole joint (specific characteristics - initial stiffness, design resistance, ... - or the whole deformability M-qi moment-rotation curve).

These three steps are schematically illustrated in Figure II.20 in the particular and simple case of a beam- to-column steel joint with a welded connection.

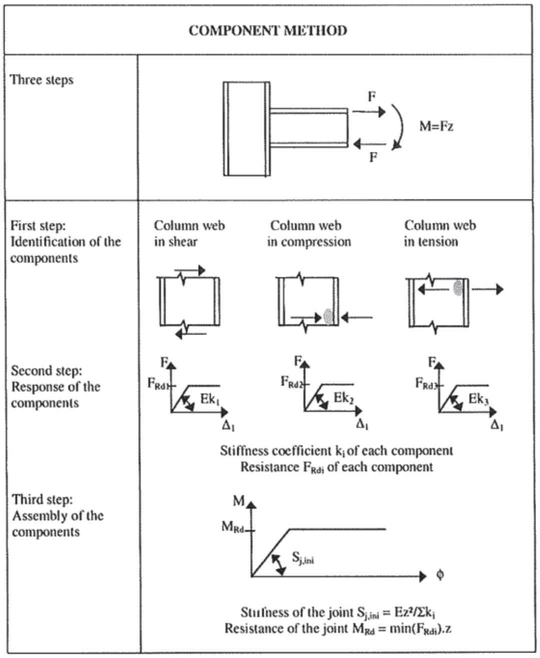

Figure II.43 – Application of the component method to a welded steel joint (simplified bi-linear component and joint deformability curves) (EC3).

As specified here above, the parallelism with the finite element method is obvious. To "component" and "joint" may then be substituted the words "finite element" and "structure".

A key aspect to the component method relates to the characterisation of the force–deformation curves for each individual extensional spring. Following (Jaspart, 1998), the various components relevant for steel joints are classified in three main groups: (a) components with high ductility, (b) components with limited ductility; and (c) components with brittle failure. Common to all is the identification of four properties, namely elastic stiffness (K^e), post-limit stiffness (K^{pl}), limit load (F^y), yield displacement (Δ^y) and limit displacement (Δ^f), as seen in Figure II.21.

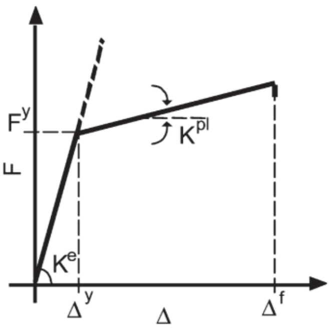

Figure II.44 – Bi-linear characterisation of component behaviour (Da Silva and Coelho, 2001).

Components with high ductility present a force–deformation curve that changes from an initial linear elastic mode into a second carrying mode, which allows increasing deformation with increasing force (Kuhlmann et al, 1998). The deformation capacity of the component is nearly unlimited, not imposing any bounds on the overall rotation ability of the joint, and is typically illustrated in Figure II.22a or, as a bi-linear approximation, in Figure II.22b. Components falling into this classification include: (i) column web panel in shear, (ii, iii) beam and web in tension, (iv) end-plate in bending, and (v) column flange in bending, the latter two being usually evaluated using a simple substitute model, the T-stub (Zoetemeijer, 1974).

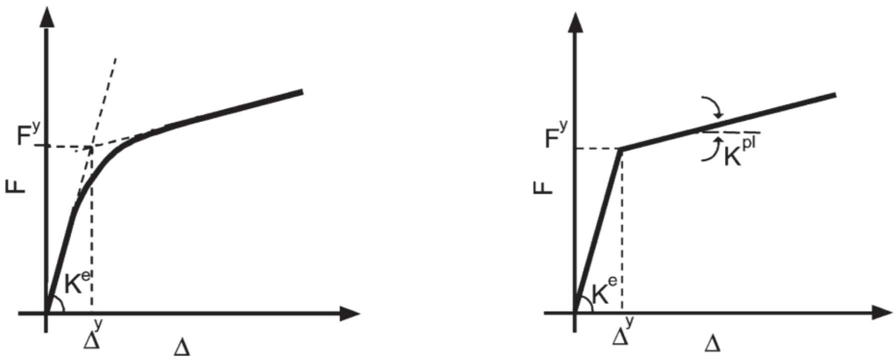

a) b)

Figure II.45 – Components with high ductility: a) actual behaviour; b) bi-linear approximation (Da Silva and Coelho, 2001).

Components with limited ductility are characterised by a force–deformation curve exhibiting a limit point and a subsequent softening response, as shown in Figure II.23a or, as a bi-linear approximation, in Figure II.123b, and comprise: (vi) column web in compression and (vii) beam flange/web in compression.

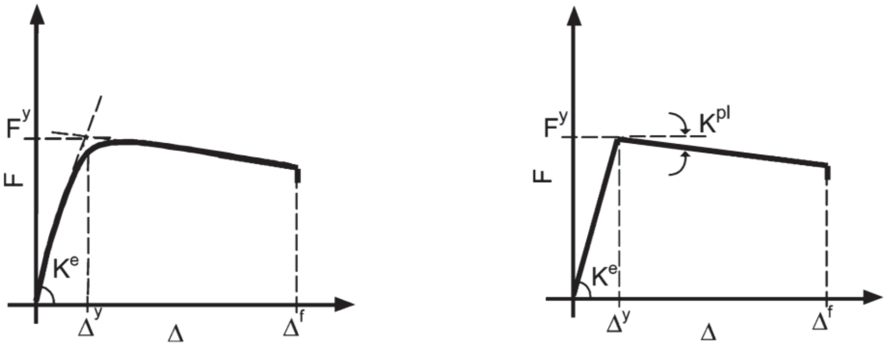

a) b)
Figure II.46 – Components with limited ductility: a) actual behaviour; b) bi-linear approximation (Da Silva and Coelho, 2001).

Components with brittle failure behave linearly until collapse, with very little deformation before failure, as shown in Figure II.24a or, as a linear approximation, in Figure II.24b, typical examples being: (viii) bolts in tension, (ix) bolts in shear, and (x) welds.

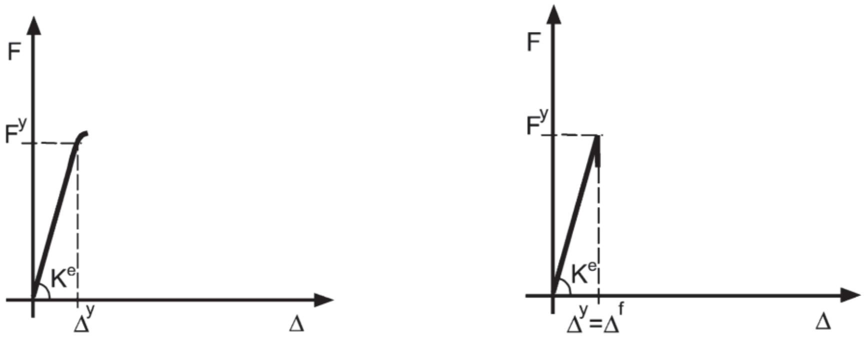

a) b)
Figure II.47 – Components with brittle failure: a) actual behaviour; b) linear approximation (Da Silva and Coelho, 2001).

The design properties (resistance and initial stiffness) of the various components can be found in Part 1.8 of EC3 and are summarised in Figure II.25, little or no guidance currently being available for the remaining properties (De Silva and Coelho, 2001).

Component behaviour	Strength	Initial Stiffness
Components with high ductility		
Column web panel in shear	$V_{wp,Rd} = \frac{0.9 f_{y,wc} A_{vc}}{\sqrt{3}\gamma_{M0}}$	$K_1 = E\frac{0.38 A_{vc}}{\beta z}$
End-plate in bending	Equivalent T-stub model [Part 1.8 — EC3, 6.2.6.5]	$K_5 = E\frac{0.85 l_{eff} t_p{}^3}{m^3}$
Column flange in bending	Equivalent T-stub model [Part 1.8 — EC3, 6.2.6.4]	$K_3 = E\frac{0.7 b_{eff,t,wc} t_{wc}}{d_c}$
Beam web in tension	$F_{t,wb,Rd} = \frac{b_{eff,t,wb} t_{wb} f_{y,wb}}{\gamma_{M0}}$	$K_8 = \infty$
Components with limited ductility		
Column web in tension	$F_{t,wc,Rd} = \frac{\omega b_{eff,t,wc} t_{wc} f_{y,wc}}{\gamma_{M0}}$	$K_4 = E\frac{0.85 l_{eff} t_{fc}{}^3}{m^3}$
Column web in compression	$F_{c,wc,Rd} = \frac{\omega b_{eff,c,wc} t_{wc} f_{y,wc}}{\gamma_{M0}}$ but $F_{c,wc,Rd} \leq \frac{\omega \rho b_{eff,c,wc} t_{wc} f_{y,wc}}{\gamma_{M1}}$	$K_2 = E\frac{0.7 b_{eff,c,wc} t_{wc}}{d_c}$
Beam-flange/web in compression	$F_{c,fb,Rd} = \frac{M_{c,Rd}}{z}$	$K_7 = \infty$
Components with brittle failure		
Bolts in tension	$F_{t,Rd} = \frac{0.9 f_{ub} A_s}{\gamma_{Mb}}$	$K_{10} = E\frac{1.6 A_s}{L_b}$
Bolts in shear	Varying according to bolt grade	$K_{11} = E\frac{16 n_b d^2 f_{ub}}{E d_{M16}}$
Welds	$F_{w,Rd} = a\frac{f_u/\sqrt{3}}{\beta_w \gamma_{Mw}}$	$K_{19} = \infty$

Figure II.48 – Design values for the response of components (Part 1.8- EC3, 2000).

2.4.5 Ductile design

In case of large seismic events the design of structures must be able to accurately approximate the response of the structure beyond the elastic range. As a consequence, a mechanism must be supplied within some elements of the structural system so to accommodate the large displacement demand imposed by earthquake ground motions.

In everyday applications, structural elements, such as walls, beams, braces and to a lesser extent columns and connections, are designed to undergo local deformations well beyond the elastic limit of the material without significant loss of capacity. Provisions of such large deformation capacity, known as "ductility", are a fundamental tenet of seismic design.

In most cases, good seismic design practice has incorporated an approach that would provide for the "ductility" to occur in the members rather than the connections. This is especially the case for the steel frame structures, were the basic material has long been considered the most ductile of all materials used for building construction (Tamboli, 1993).

Another design philosophy encourages the contributions to the displacement ductility demand of connections through absorption of substantial energy quantities, as for the timber structures. Connections between members, in particular, are the regions where the material is exposed to higher deformations demands. The designer then has to ensure that they undergo large inelastic deformations.

According to EN 1993-1-8, for example, the joints may be classified based on their rotational stiffness, by comparing its initial rotational stiffness with the bending stiffness of the connected members.

A joint may be classified as rigid/fully restrained (FR), nominally pinned/simple or semi-rigid/partially restrained (PR) according to its rotational stiffness, by comparing its initial rotational stiffness. A nominally pinned joint shall be capable of transmitting the internal forces, without developing significant moments which might adversely affect the members or the structure as a whole.

A connection can be also be classified in terms of strength as either a full-strength, nominally pinned or partial-strength. The design resistance of a full-strength joint shall be not less than that of the connected members, while a partial-strength connection can only develop a portion of it. A nominally pinned joint shall be capable of transmitting the internal forces, without developing significant moments which might adversely affect the members or the structure as a whole.

Proper system selection is a critical element in successful seismic design. Various systems, such as fully and partially restrained moment-resisting frames, concentrically braced frames and eccentrically braced frames, are addressed in the EN 1998-1 and AISC 341-05 seismic provisions. These provisions have specific requirements for the different structural system that address connection design (Tab. II.2).

Table II.5 – Type of joint model (EN 1998-1; AISC 341-05).

Method of global analysis	**Classification of joint**		
Elastic	Nominally pinned	Rigid	Semi-rigid
Rigid–Plastic	Nominally pinned	Full-strength	Partial-strength
Elastic–Plastic	Nominally pinned	Rigid and full-strength	Semi-rigid and partial-strength, Semi-rigid and full-strength, Rigid and partial-strength
Type of joint model	Simple	Continuous	Semi-continuous

Connection design depends very much on the designer's decision regarding the method by which the structure is analysed. Eurocode 3 gives four approaches for the design of a structure in which the behaviour of the connection is fundamental. These design methods are defined as simple design, semi-continuous design, continuous design and experimental verification. Elastic, plastic and elastic–plastic methods of global analysis can be used with any of the first three approaches, and Table II.4 shows how the joint classification, the type of framing and the method of global analysis are related (EC3).

In order to properly incorporate these elements into seismic design a much greater level of attention needs to be paid than for standard connection design or for moment connections to be subjected only to typical static loads. Besides typical strength requirements, such connections should take into account factors like:

- Toughness of joining elements in the connections, including any weldments;
- High level of understanding of the distribution of stresses and strains throughout the connection;
- Elimination of stress concentrations;
- Detailed consideration of the flow of forces and the expected path of yielding in the connection;
- Good understanding of the properties of the materials being joined at the connection, the need for heightened quality control in fabrication erection, and inspection of the connection.

Considering these difficulties of the dissipative connections design for timber structures, in this work, to perform the seismic resistant ductile timber frame structures with timber-steel link design, is used the “capacity design” procedure per “macro-components” and “sub-components”, starting from the design criteria of ductile steel structures. Specifically, the dissipation is delegated at the link, while the connections and the timber structural elements should be designed to remain in the elastic filed. In the chapter 2.2.3, is presented the capacity design procedure for “macro-components” to design the structural elements of the structure: steel link, timber beam and timber column. To really ensure the formation of the plastic hinge in the link, preserving the connections, it is necessary to know both global (structural elements) and local (components of the connection) behaviour. It is necessary, therefore, to apply capacity design also for “sub-components”. For this reason, a classification of the timber-steel link joint is proposed.

According to this design procedure, the timber-steel link joint is considered as made of four macro-components (i.e. the connection, the timber beam, the timber column and the steel link, Fig. II.26); each macro-component is individually designed according to specific assumptions and then simply capacity design criteria are applied, in order to obtain different design objectives, defined by comparing the resistance of the connection (i.e. of its sub-components) with the bending capacity of the link, such as: (i) Full strength connection; (ii) Equal strengths connection; (iii) Partial strength connection.

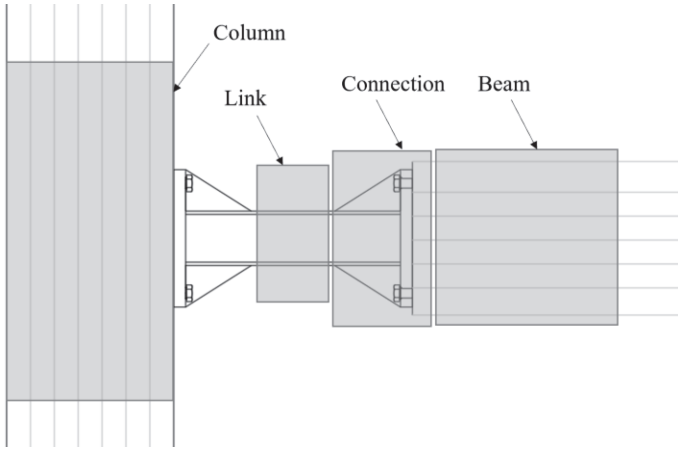

Figure II.49 – Timber-steel link joint. Identification of the joint macro-components.

The following design objectives can be adopted for the connection (Tab. II.3):

- Full-strength connection: the connection is designed to be stronger than the link, such that yielding occur in it.
  In this case, 2 levels of timber-steel link joint ductility are introduced with design concepts and range of reference values of over-strength components:

  Low Ductility Joint (LDJ): the joint is designed so that the yielding occur in the link and the connection is the first over-resistant macro-component respect to the link (with the recommended "strong column-weak beam" mechanism of the EC8.);
  High Ductility Joint (HDJ): the joint is designed so that the yielding occur in the link and the connection is not the first over-resistant macro-component respect to the link.

- Equal-strength connection: the connection is designed to have a strength close to the link. Theoretically yielding should occur in both macro-components (link and connection);
- Partial-strength connection: the connection is designed to develop plastic deformations with its sub-components (end-plate, bolts, stiffeners, etc.) and the other macro-components (link, beam and column) have an over-strength respect to the connection.

It should be also noted that both EC3 and EC8 do not consider the case of equal strength joint, which is proposed within the project Equaljoint Plus (Landolfo et al, 2018) as an intermediate performance level. According to the current Eurocode classification, an equal strength connection falls on the category of partial strength.

Table II.6 – Classification of timber-steel link joint for macro-components.

Collapse hierarchy	Full-strength		Equal-strength	Partial-strength
	High Ductility Joint (HDJ)	**Low Ductility Joint (LDJ)**		
Yielding-component	Link	Link	Link/Connection	Connection
2° macro-component	Connection	Beam	Beam	Link
3° macro-component	Beam	Connection	Column	Beam
4° macro-component	Column	Column	/	Column

If the connection is made up of several sub-components, some of which may develop fragile collapse modes, such as pull-out or failure of the timber adjacent to the glue-line, for the *Full-strength* and *Equal-strength* connection typologies, an addition classification design of the connection can be introduced, based on its sub-components (Tab. II.4):

- Ductile connection: the ductile collapse modes of the connection sub-components occur before the fragile ones (end-plate, stiffeners, bolts, etc.);
- Fragile connection: the fragile collapse modes of the connection sub-components occur before the ductile ones (pull-out, failure of the timber adjacent to the glue-line, etc).

Table II.7 – Classification of timber-steel link joint for sub-components.

Collapse hierarchy	Ductile Connection (DC)	Fragile Connection (FC)
1° Sub-component	Ductile collapse modes	Fragile collapse modes
2° Sub-component	Fragile collapse modes	Ductile collapse modes

So, according to the aim developed within the work, to have a performant timber-steel link joint, with the highest dissipating capacity, stiffness and strength, the plastic hinge should be form in the steel links (*Full-strength* connection), while the timber beam, the column and the connection (macro-component) should be designed with an adequate over-strength, in which the connection is the first macro-component over-resistant respect to the link (*High Ductility Joint* - HDJ) characterized by its fragile sub-components over-resistant respect to its ductile sub-components (*Ductile connection*)

Chapter III

3. EVALUATION OF THE SEISMIC BEHAVIOUR OF DISSIPATIVE HEAVY TIMBER FRAME STRUCTURES THROUGH NUMERICAL ANALYSIS

3.1 SEISMIC RESISTANT HEAVY TIMBER FRAME STRUCTURES WITH STEEL LINK

3.1.1 METHODOLOGY OF ANALYSIS

The chapter deals with the application of steel links for the development of seismic resistant dissipative timber frames, characterized by assemblage of beams and columns: steel links have the aim of dissipating seismic energy, while timber elements and steel connections remain in the elastic field, applying the capacity design approach. Specifically, 2D single-storey, 2-storey, 4-storey and 6-storey structures equipped with links, in different configurations, where the link is positioned in the diagonal (CBF) or in the beam (MRF and EBF) are studied, assuming several plan layout with a different number of spans and a different value of seismic acceleration, and designing the structural sizes through linear dynamic analysis. Therefore, non-linear static analysis are performed with the aim of evaluating the global behaviour, the collapse hierarchy and the behaviour factor for each structural type, using the structural calculation program SAP2000 (v18).

Six structural schemes are designed by varying the number of floors, the plan layout and the seismic acceleration with a total of 72 structures, and 315 non-lineal static analysis are carried out. The study is aimed at proving the suitability and the efficiency of the system.

3.1.2 Study cases

3.1.2.1 Design parameters

A numerical parametric study is carried out on 6 2D structural types.

The plan layout considered are:

- 1A (1 span in transversal direction y);
- 2A (2 spans in transversal direction y);
- 3A (3 spans in transversal direction y).

In addition, four structural elevation schemes are considered:

- 1S (1-storey);
- 2S (2-storeys);
- 4S (4-storeys);
- 6S (6-storeys).

In particular, 7 seismic-resistant frames are analysed:

- MRF-SLV (moment resisting frame, designed only for SLV);
- MRF-SLD (moment resisting frame, designed also for SLD);
- CBF V π (frame with concentric braces V, with the timber beam interrupted by the steel link);
- CBF V Λ (frame with concentric braces V, with continuous timber beam);
- CBF X (frame with concentric braces X);
- CBF X D (frame with concentric braces X, with the only diagonal in tension);
- EBF (Fame with eccentric braces).

Each structural type is designed as:

- Dissipative structure with behaviour factor $q=1$, without links (only for 1S);
- Dissipative structure with behaviour factor $q=1$, applying the capacity design approach and the design criteria adopted by steel (only for 1S);
- Dissipative structure in low ductility class with behaviour factor and design criteria adopted by steel (q_d), applying the capacity design approach.

Structures are designed according to the technical standards Eurocode 5 and Eurocode 8, through linear dynamic analysis and non-linear static analysis, considering the seismic zones of the OPCM 3274 (20/03/2003) assumed for the sake of simplicity:

- 1Z (seismic zone 1: 0,35g);
- 2Z (seismic zone 2: 0,25g);
- 3Z (seismic zone 3: 0,15g).

The parametric analysis carried out for the structural systems are shown in Table III.1.

Table III.8 – Parametric analysis: study cases parameters.

Storeys		**1S**		**2S**	**4S**	**6S**
Spans	1A	2A	3A		2A	
Seismic Zones		1Z-2Z-3Z			1Z-2Z-3Z	
Behaviour factor		1; q_d			q_d	
Schemes	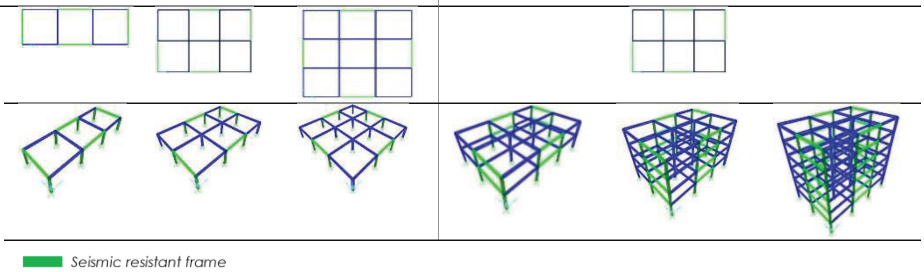					

3.1.2.2 *Geometrical and material features*

The 1-span scheme (1A) is 3 m high with a rectangular plan layout 6x18m wide, 6m in the longitudinal direction y. The floor is oriented along the transverse direction supported by secondary beams in the longitudinal direction (Fig. III.1). The 2-spans scheme (2A) has a rectangular plan layout 12x18m wide, while the 3-spans scheme (3A) has a rectangular plan layout 18x18m wide. Each structure has 4 seismic-resistant frames for storey, 2 for each direction.

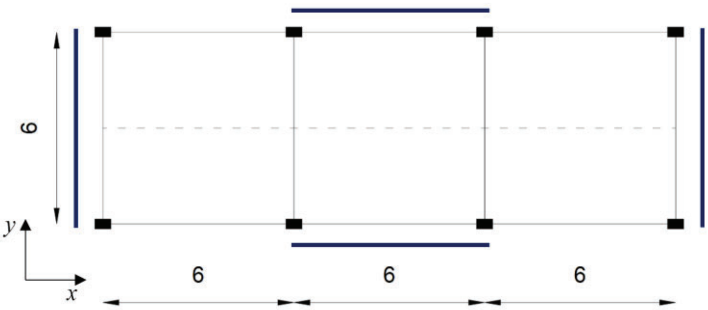

Figure III.50 – Plan layout (1A).

Each single seismic-resistant frame is characterized by a column height of 3 m and a beam length of 6m. MRF is characterized by steel links at the ends of the beams and at the base of the columns of the first storey (2 links for beam and 1 link for column); CBF X, CBD X D, CBF V Λ and CBF V π are characterized by the presence of steel links at the ends of the diagonals (2 links for diagonal), while EBF is characterized by the steel link at the beam (Fig. III.2). Specifically, the CBF V Λ has a continuous timber beam and 1 steel plate to which the 2 diagonal links are welded, while CBF V π has a steel link, to which the 2 diagonal links are welded, with a discontinuous timber beam.

In particular, the link length, for MRF, CBF X, CBD X D, CBF V Λ and CBF V π, is 500mm, while for EBF is 1000mm.

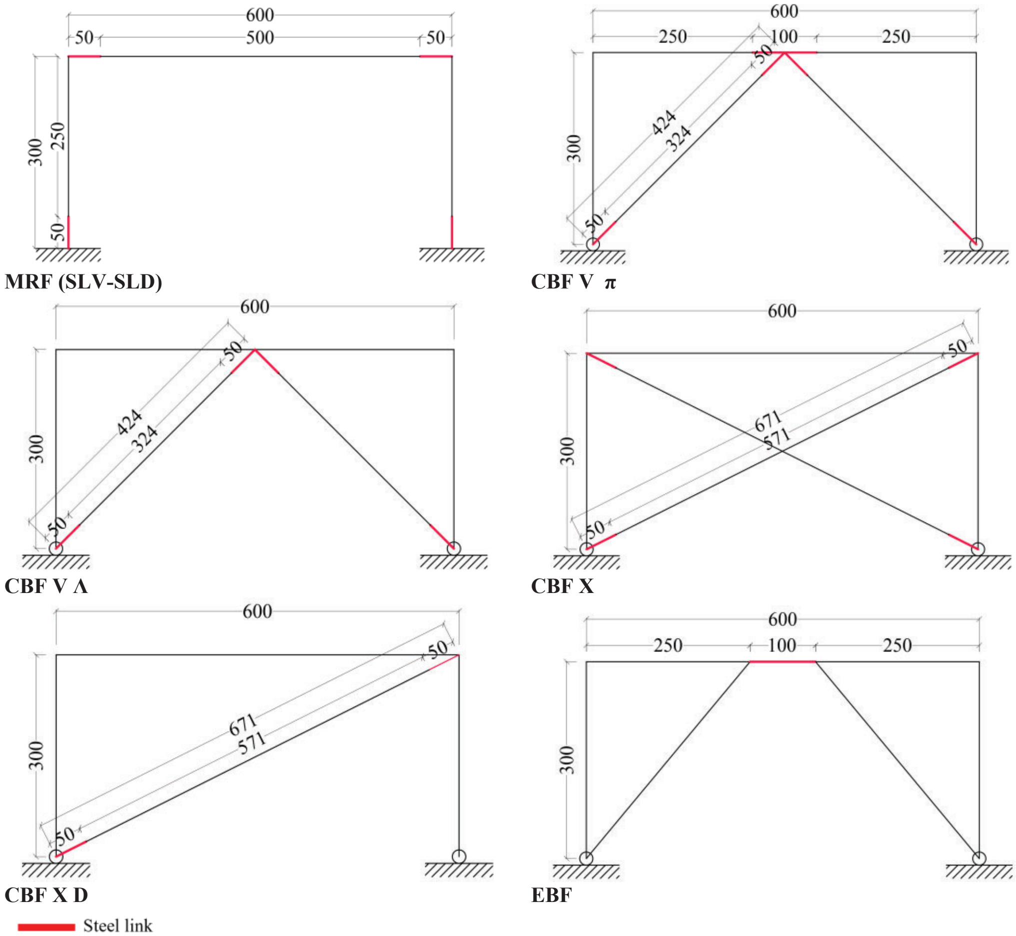

Figure III.51 – Structures' geometric features (1S) [m].

All the structural schemes considered for the analysis are indicated in the Figure III.3.

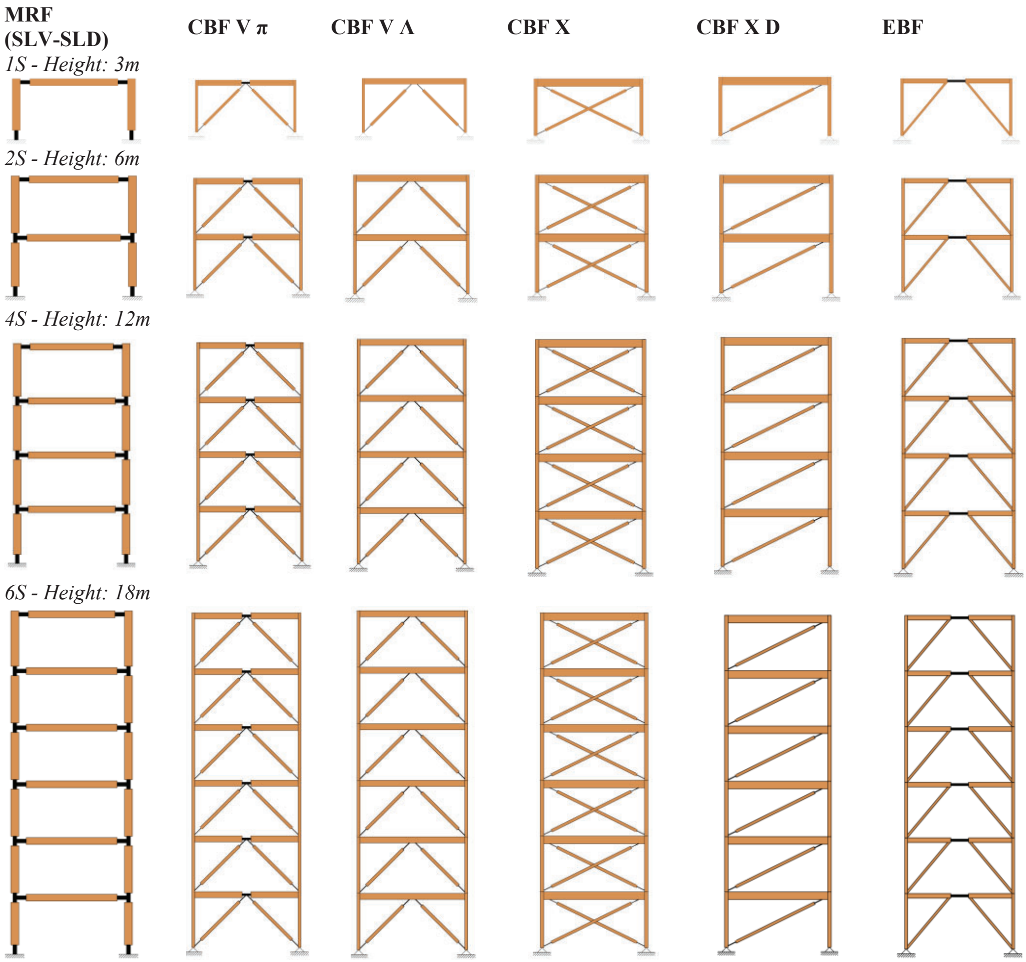

Figure III.52 – Structural schemes (1S-2S-4S-6S).

Structural members are made of glulam GL28h timber grade while the links and the connection between the structural members are in S235 steel grade (Tab. III.2).

Table III 9 – Material characteristics: timber and steel.

Timber: GL28h				**Steel: S235**	
$f_{m,g,k}$ [MPa]	28	$E_{0,g,mean}$ [MPa]	12600	$f_{y,k}$ [MPa]	235
$f_{t,0,g,k}$ [MPa]	19,5	$E_{0,05}$ [MPa]	10200	$f_{t,k}$ [MPa]	360
$f_{t,90,g,k}$ [MPa]	0,45	$E_{90,g,mean}$ [MPa]	420	E [MPa]	210000
$f_{c,0,g,k}$ [MPa]	26,5	$G_{g,mean}$ [MPa]	780		
$f_{c,90,g,k}$ [MPa]	3,0	$E_{0,g,mean}$ [MPa]	12600		
$f_{v,g,k}$ [MPa]	3,2	$E_{0,05}$ [MPa]	10200		

The value of the safety coefficients of the materials (k_{mod}, k_{def}, Υ_{m},) for timber and timber-based structural products are indicated below (Tab. III.3).

Table III.10 – Safety coefficients.

Service class	Load-duration class	K_{mod}	K_{def}	Υ_{m}
2	Medium-term	0,8	1	1,45
	Instantaneous (seismic condition)	1		

3.1.3 Loads analysis

3.1.3.1 Vertical loads

The floor consists of timber planks with a thin concrete screed and tiles (Tab. III.4). The only variable load (Q) that is considered is the operating load that, for residential build, is relating to category A.

Table III.11 – Characteristic loads.

Load	
G_{K1}	0,22 kN/m^2
G_{K2}	1,30 kN/m^2
Q	2,00 kN/m^2

The longitudinal seismic resistant frames (longitudinal direction x) are distinguished from the transversal ones (transversal direction y) due to the different loading conditions: on the longitudinal frames there is a distributed load while on the transversal frames there is a force due to the secondary beam (Fig. III.4).

On each longitudinal frame there is the following distributed load:

$$q = 7{,}85\mathrm{kN/m}$$

On each transversal frame there is the following force:

$$F = 47{,}82\mathrm{kN}$$

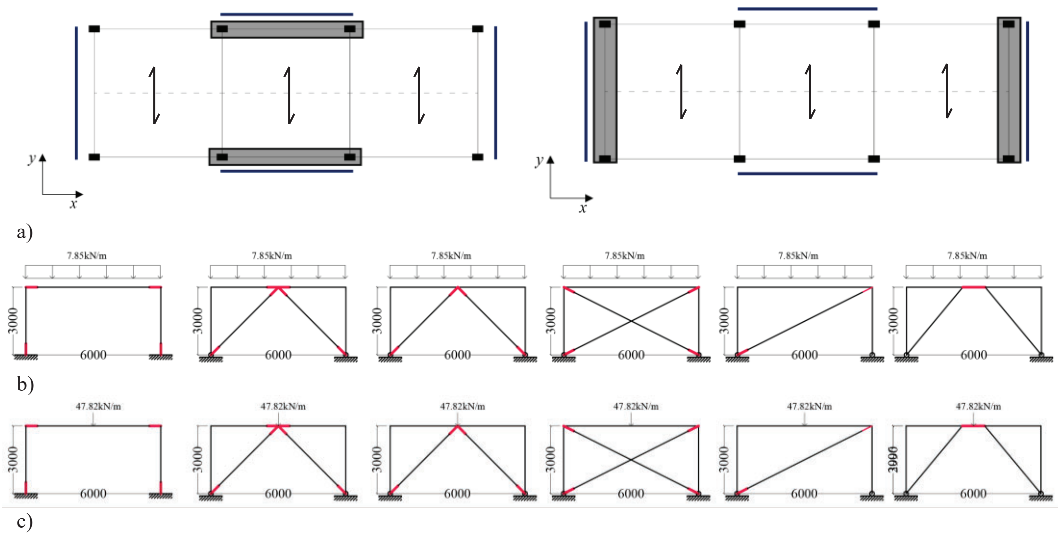

Figure III.53 – a) Seismic resistant structures position; b) longitudinal direction y; c) transversal direction x [mm].

3.1.3.2 Seismic loads

For the buildings with seismic response primarily dominated by the fundamental vibration mode (low- to mid-rise buildings), the equivalent lateral force analysis procedure can also be applied. In this procedure, the seismic loading is idealized as an equivalent static force pattern applied to a linear elastic structural model. Considering the expected ductility of structure and the over-strength, the combined force demands are reduced by a response modification factor (usually denoted by q) to get the inelastic seismic force demands. In various structural design codes and performance-based seismic evaluation guidelines, this equivalent lateral force analysis is referred to as the linear static procedure (LSP).

In this study, this type of analysis is used to determine the structural sections of the investigated structures and linear dynamic analysis to check the results. In order to assess the structures' response under seismic actions with different acceleration intensity, the seismic zones defined in the OPCM 3274 of 03/20/2003 are considered. The OPCM divided the Italian territory into 4 seismic zones, distinguished by a different value of the parameter a_g (maximum horizontal acceleration on category A soil). The values of a_g to be adopted are in Table III.5:

Table III.12 – The values of a_g for the seismic zones (OPCM 3274)

Seismic zone	a_g
1	0,35g
2	0,25g
3	0,15g
4	0,05g

In particular, in the seismic zone 4 the design of the dissipative structures is avoided because of there are too modest acceleration values. The OPCM 3274 is used only for the response spectra (elastic and design) definition, while the seismic action definition and the structural design refer to the currently standards: NTC 2018, Eurocode 5 and Eurocode 8.

For the seismic design, the following limit states are considered:

- Limit state for the safeguard of human life or Ultimate state (SLU): after an earthquake, the construction is affected by failures and collapses of non-structural components and apparatuses and significant damage to structural components that result in a significant reduction of stiffness and resistance against horizontal actions. The construction retains significant stiffness and resistance against vertical actions and retains, as a whole, a significant safety margin against collapse from horizontal seismic actions;
- Limit state of prompt use or Damage (SLD): after an earthquake, the entire structure, including structural elements, non structural elements, and apparatuses relevant to its functionality, has damage that does not compromise its stiffness and resistance against vertical and horizontal actions. The structure is ready to be used but the apparatuses might be subject to malfunctioning.

The elastic response spectrum in terms of acceleration is expressed by a spectral form referred to a conventional 5% damping multiplied by the value of the maximum acceleration a_g on the horizontal rigid reference site. The elastic response spectrum of the horizontal component proposed by the OPCM 3274 is defined by the following expressions (Fig. III.5):

$$0 \leq T < T_B \qquad S_e(T) = a_g \cdot S \cdot \left[1 + \frac{T}{T_B} \cdot (\eta \cdot 2{,}5 - 1)\right]$$

$$T_B \leq T < T_C \qquad S_e(T) = a_g \cdot S \cdot \eta \cdot 2{,}5$$

$$T_C \leq T < T_D \qquad S_e(T) = a_g \cdot S \cdot \eta \cdot 2{,}5 \cdot \left(\frac{T_C}{T}\right)$$

$$T_D \leq T \qquad S_e(T) = a_g \cdot S \cdot \eta \cdot 2{,}5 \cdot \left(\frac{T_C \cdot T_D}{T^2}\right)$$

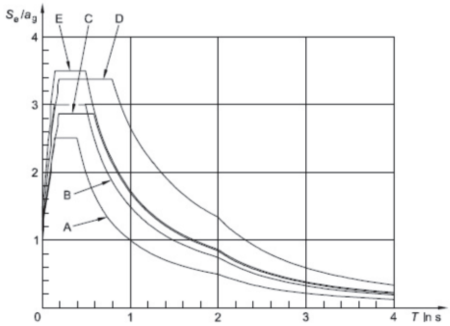

Figure III.54 – The EC8 response spectrum (Eurocode 8).

In which T and S_e are respectively: period of vibration and horizontal spectral acceleration. The values of T_B, T_C, T_D and S for the categories of foundation soil are shown in the following Table extracted from the OPCM 3274 (Tab. III.6).

Table III.13 – The values of T_B, T_C, T_D and S for the soil categories (OPCM 3274)

Soil category	**S**	**T_B**	**T_C**	**T_D**
A	1,0	0,15	0,40	2,0
B, C, E	1,25	0,15	0,50	2,0
D	1,35	0,20	0,80	2,0

A "category B" soil has been hypothesized.

The value of the behaviour factor q depends on the structural type, the hyperstaticity degree and the design criteria adopted, and takes into account the non-linearity of the material. It can be calculated using the following expression:

$$q = q_0 \cdot K_R$$

- q_0 is the maximum value of the behaviour factor that depends on the expected ductility level, on the structural type and on the α_u/α_1 ratio.
- K_R is a reductive factor that depends on the regularity characteristics of the building.

For non-dissipative structures a behaviour factor $q=1$ is assumed, consequently the design spectrum coincides with the elastic one (Tab. III.7f).

For dissipative structures, as already reported in chapter I, there is no a standard defining the design of a timber structure with dissipative steel links, consequently for the implementation of capacity design, the standard for steel structures is used (see EC3: §§1.3.1-1.3.2). This assumption is motivated by the fact that the dissipative elements are made of steel and, therefore, a dissipative capacity similar to that of a steel structures is expected. In fact, the same behaviour factors proposed by the NTC 2018 for steel structures are used.

The timber dissipative structures have been designed only in low ductility class (CDB), since, in this condition, there are higher seismic actions. For the low ductility class the values of the behaviour factor defined in § 7.5.2.2 of the NTC 2018 are assumed (Tab. III.7). By reducing the spectral coordinate of the acceleration in the elastic response spectrum with the *q* factor, the design spectrum is obtained using the following expressions:

$$0 \le T < T_B \qquad S_e(T) = a_g \cdot S \cdot \left[1 + \frac{T}{T_B} \cdot \left(\frac{1}{q} \cdot 2{,}5 - 1\right)\right]$$

$$T_B \le T < T_C \qquad S_e(T) = a_g \cdot S \cdot \frac{1}{q} \cdot 2{,}5$$

$$T_C \le T < T_D \qquad S_e(T) = a_g \cdot S \cdot \frac{1}{q} \cdot 2{,}5 \cdot \left(\frac{T_C}{T}\right)$$

$$T_D \le T \qquad S_e(T) = a_g \cdot S \cdot \frac{1}{q} \cdot 2{,}5 \cdot \left(\frac{T_C \cdot T_D}{T^2}\right)$$

The response spectrum for the dissipative structures is reported in the Table III.7.

Table III.14 – Behaviour factor q_d and design response spectra for SLU of each seismic zone (1,2,3,4): a) MRF dissipative structures (q=4); b) CBF V dissipative structures (q=2); c) CBF X dissipative structures (q=4); d) EBF dissipative structures (q=4); e) for non-dissipative structures (q=1); f) design response spectra for SLD. Sd_1= 1 seismic zone; Sd_2= 2 seismic zone; Sd_3= 3 seismic zone; Sd_4= 4 seismic zone.

Structural type	q_d (CDB) – Eurocode 8 (Steel part)
MRF-SLD	4
MRF-SLV	4
CBF V π	2
CBF V Λ	2
CBF X	4
CBF X D	4
EBF	4

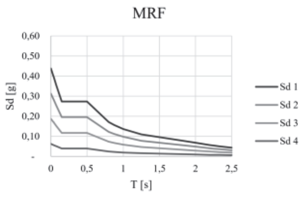

a)

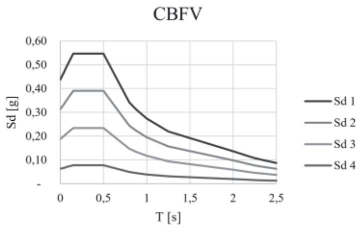

b)

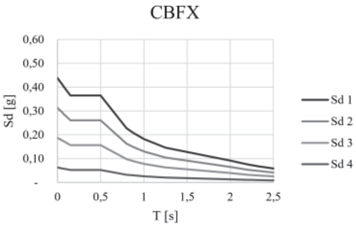

c)

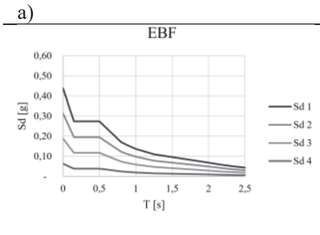

d)

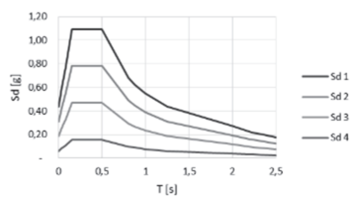

e)

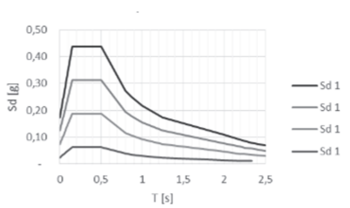

f)

An approximate evaluation of the vibration period of the structure can be made by the following formula.

$$T = C_1 \cdot H^{0.75}$$

For the single-storey (1S) structures is less than T_B, while for the 6-storey (6S) structures, the period is higher than T_B but less than T_C.

$$T = C_1 \cdot H^{0.75} = 0{,}05 \cdot (3)^{0.75} = 0{,}11s$$
$$T = C_1 \cdot H^{0.75} = 0{,}05 \cdot (18)^{0.75} = 0{,}44s$$

The elastic static seismic analysis is carried out by evaluating the elastic force acting on the deck, calculated with the following formula:

$$F_i = \frac{F_h \cdot z_i \cdot W_i}{\Sigma_j \cdot z_j \cdot w_j}$$

- $F_h = S_d(T_1) w \frac{\lambda}{g}$
- F_i is the force to be applied to the i-th mass;
- W_i and W_j are the weights, respectively, of the mass i and of the mass j;
- z and z_j are the distance from the foundation plane of the masses i and j;
- $S_d(T_1)$ is the ordinate of the design response spectrum;
- W is the total weight of the construction;
- λ is a coefficient equal to 0,85 if the construction has at least three horizontal sections and if $T_1<2TC$, equal to 1,0 in all other cases;
- g is the gravity acceleration.

To evaluate the seismic mass, it is necessary to calculate the masses associated with gravitational loads, combined according to the following seismic combination defined in the NTC 2018:

$$W = G_{1k} + G_{2k} + \sum_j \psi_{2j} \cdot Q_{kj}$$

- G_{1k} takes into account the weight of the planks, beams, columns and bracings;
- G_{2k} takes into account the weight of the screed and flooring;
- ψ_{2j} is the combination coefficient of the variable load Q_{kj} which takes into account the probability that all loads $\psi_{2j} x Q_{kj}$ are present on the entire structure at the time of the earthquake.

3.1.3.3 Loads combinations

The loads combinations considered are indicated in § 2.5.3. of the NTC'08 and are shown below. For the gravitational loads:

Ultimate State limit

$$q_{SLU} = \gamma_{G1} \cdot G_1 + \gamma_{G2} \cdot G_2 + \gamma_{Q1} \cdot Q_{k1} + \gamma_{Q2} \cdot \Psi_{02} \cdot Q_{k2} + \gamma_{Q3} \cdot \Psi_{03} \cdot Q_{k3} + \cdots$$

$$q_{SLU} = 1{,}3 \cdot 0{,}22 + 1{,}5 \cdot 1{,}3 + 1{,}5 \cdot 2{,}0 = 5{,}24\ \mathrm{kN/m^2}$$

For SLE, rare and semi-permanent combinations are considered for deformability checks:

Rare combination

$$q_{rara} = G_1 + G_2 + Q_{k1} + \Psi_{02} \cdot Q_{k2} + \Psi_{03} \cdot Q_{k3} + \cdots$$

$$q_{rara} = 0{,}22 + 1{,}30 + 2{,}00 = 3{,}52\mathrm{kN/m^2}$$

Semi-permanent combination

$$q_{semi-perm.} = G_1 + G_2 + \Psi_{21} \cdot Q_{k1} + \Psi_{22} \cdot Q_{k2} + \cdots$$

$$q_{semi-perm.} = 0{,}22 + 1{,}30 = 1{,}52\ \mathrm{kN/m^2}$$

The seismic combinations considered are indicated in § 2.5.3. of the NTC 2018 and are shown below.

$$q_{SLV} = E + G_1 + G_2 + \Psi_{21} \cdot Q_{k1} + \Psi_{22} \cdot Q_{k2} + \cdots$$

3.1.4 Structural design

The linear-static analysis and, after, the linear-dynamic analysis are carried out and for the seismic design of the structural members the capacity design approach presented in chapter 2.2.3 is applied. Specifically, to perform the seismic resistant ductile timber frame structures with steel link design, is used the capacity design procedure for "macro-components" between the steel link, the timber beam and the timber column. In this context, the connection between the steel links and the timber beam has not been designed, which will be discussed in chapter 4, but it is assumed to be "rigid". In particular, to have a performant joint, a *Full-strength connection* should be assumed, to be stronger than the steel link, such that yielding occur in the link, and a *High Ductility Joint* (HDJ) should be designed, so that the yielding occur in the link and the connection is the first macro-component to be over-resistant respect to the link, with a *Ductile Connection*, so that the sub-components with a fragile collapse modes present an over-strength respect to those with a ductile collapse modes.

For MRF and EBF structures HE and IPE steel profiles while for CBF (V π, V Λ, X and X D) box-shaped section profiles are used for the steel links, that are designed under the highest seismic combination according to the formulas present in the EC3. For the timber elements design, the formulas present in the EC5 are used. The outputs of the analysis are presented in terms of structural sections, mass and vibration period (evaluated through modal analysis). In particular, for the 1-storey

(1S) structures the analysis results are presented for 1A, 2A, and 3A plan layout, while for 2-storey (2S), 4-storey (4S) and 6-storey (6S) structures the analysis results are presented for only 2A plan layout. All the structures are designed under seismic acceleration, a_g, for seismic zones 1Z, 2Z and 3Z. 1S structures are designed both with $q=1$ and with q_d (behaviour factor of steel structures), while 2S, 3S, 4S and 6S structures are designed only with q_d. Moreover, for each structure, the value of the coefficient Ω used for the design of the non-dissipative elements is shown. In particular, Ω coefficient indicated is the smallest coefficient between that of the link in the column (Ω_c) and the link in the timber beam (Ω_b): $\Omega = \Omega_{min} = (\Omega_c; \Omega_b)$.

- <u>MRF structures</u>

Dissipative steel link (in beams and base-columns):

$$\left(\frac{M_{Ed}}{M_{pl,Rd}}\right)_j \leq 1; \quad \left(\frac{N_{Ed}}{N_{pl,Rd}}\right)_j \leq 0{,}15; \quad \left(\frac{V_{Ed,G}+V_{Ed,M}}{V_{pl,Rd}}\right)_j \leq 0{,}50$$

Non-dissipative elements (timber beams and columns):

$$N_{Ed} = N_{Ed,G} + (\gamma'_{Rd} \cdot \gamma_{Rd} \cdot \Omega \cdot N_{Ed,E})$$
$$M_{Ed} = M_{Ed,G} + (\gamma'_{Rd} \cdot \gamma_{Rd} \cdot \Omega \cdot M_{Ed,E})$$
$$V_{Ed} = V_{Ed,G} + (\gamma'_{Rd} \cdot \gamma_{Rd} \cdot \Omega \cdot V_{Ed,E})$$
$$\Omega_i = \frac{M_{pl,Rd,i}}{M_{Ed,i}}$$

- <u>CBF (V and X) structures</u>

Dissipative steel link (in diagonals):

$$\left(\frac{N_{Ed}}{N_{pl,Rd}}\right)_j \leq 1$$

Non-dissipative elements (timber beams, column and diagonals):

$$N_{Ed} = N_{Ed,G} + (\gamma'_{Rd} \cdot \gamma_{Rd} \cdot \Omega \cdot N_{Ed,E})$$
$$M_{Ed} = M_{Ed,G} + (\gamma'_{Rd} \cdot \gamma_{Rd} \cdot \Omega \cdot M_{Ed,E})$$
$$V_{Ed} = V_{Ed,G} + (\gamma'_{Rd} \cdot \gamma_{Rd} \cdot \Omega \cdot V_{Ed,E})$$
$$\Omega_i = \frac{M_{pl,Rd,i}}{M_{Ed,i}}$$

- <u>EBF structures</u>

Dissipative steel link (long link):

$$e \geq 1{,}5(1+\alpha)\frac{M_{1,Rd}}{V_{1,Rd}}$$
$$\theta_p \leq 0{,}02\text{rad}$$

$$\begin{cases} M_u = 1{,}5 M_{1,Rd} \\ V_u = 2\dfrac{M_{1,Rd}}{e} \end{cases}$$

Non-dissipative elements (timber beams, column and diagonals):

$$N_{Ed} = N_{Ed,G} + (\gamma'_{Rd} \cdot \gamma_{Rd} \cdot \Omega \cdot N_{Ed,E})$$

$$M_{Ed} = M_{Ed,G} + (\gamma'_{Rd} \cdot \gamma_{Rd} \cdot \Omega \cdot M_{Ed,E})$$

$$V_{Ed} = V_{Ed,G} + (\gamma'_{Rd} \cdot \gamma_{Rd} \cdot \Omega \cdot V_{Ed,E})$$

$$\Omega_i = 1{,}5\,\frac{M_{pl,Rd,i}}{M_{Ed,i}}$$

As an example, below the outputs for all structural schemes, 1S, 1Z and 1A are presented (Tab. III.8). The structural design results of the other study cases are shown in Annex A.3.1.4.

- 1S - 1A scheme

Table III.15 – Output results for timber structures – seismic zone 1: 1Z (1S-1A).

Type	q	Elements size						F_d [kN]	m [ton]	T* [s]	Ω
		Beam		Column		Diagonal					
		Timber	Link	Timber	Link	Timber	Link				
MRF	1	200x300	IPE200	340x400	HE160M	-	-	132,64	13,30	0,33	1,04
SLD	4	200x300	IPE200	320x380	HE140M	-	-	44,33	13,19	0,38	2,35
MRF	1	200x300	IPE200	320x380	HE140M	-	-	44,33	13,19	0,38	2,35
SLV	4	160x240	IPE240	260x280	HE100M	-	-	44,33	12,98	0,63	1,04
CBF	1	200x320	HE180A	260x280	-	160x160	40x40x4	130,19	12,95	0,09	1,44
V π	2	160x240	HE120B	140x140	-	140x140	30x30x2,5	72,40	12,78	0,11	1,15
CBF	1	200x320	-	260x280	-	160x160	40x40x4	130,19	12,95	0,09	1,44
V Λ	2	160x240	-	220x240	-	140x140	30x30x2,5	72,40	12,77	0,11	1,15
CBF	1	180x280	-	260x280	-	200x200	40x40x3	31,88	13,05	0,07	1,58
X	4	140x220	-	220x240	-	150x150	20x20x2	4,07	12,81	0,13	1,44
CBF	1	180x260	-	280x300	-	210x210	50x50x4	131,88	12,97	0,10	1,05
X D	4	140x240	-	220x240	-	160x160	25x25x3	44,07	12,76	0,16	1,09
EBF	1	240x340	IPE180	300x320	-	170x170	-	130,16	13,00	0,14	1,69
	4	120x180	IPE120	200x220	-	130x130	-	43,50	12,67	0,33	1,75

** evaluated through modal analysis*

3.1.5 Seismic performance evaluation

3.1.5.1 Methodology of the analysis

The nonlinear counterpart of the LSP is referred to as the nonlinear static procedure (NSP) (i.e. a nonlinear structural model subjected to a static lateral loading). The most essential component of all existing nonlinear static procedures (NSPs) is the monotonic pushover analysis procedure (POA). In fact, these two terms (i.e. the pushover analysis procedure and the NSP) are also sometimes used interchangeably in literature. It is the key to evaluate the quasi-static lateral inelastic response of structures. The basic principle of pushover analysis is to subject the floors of an inelastic structural model of building (after loaded with gravity loads) to an incrementally increasing lateral force pattern representing a simplified distribution of earthquake induced forces. Subsequently, the strength and stiffness properties of every structural component are updated after each load increment to account for the reduced resistance of yielding components. This process is continued until the structure becomes unstable or until a predetermined target displacement is reached.

The primary objective is to obtain the estimates of the global lateral strength, global displacement ductility and the failure mechanism of a structure under lateral forces induced by the earthquake ground motion. The pushover (or capacity) curves for the structure at a global level are generated by applying this procedure to the detailed structural models directly incorporating the anticipated nonlinearity of its components. These pushover curves are then idealized as simplified relationships and the expected maximum seismic deformation and other response quantities can then be determined using any established NSP. Compared to the linear static analysis procedures, the primary advantage of the NSPs is their ability to account for the redistribution of internal forces as the structural components experience nonlinearity under incremental lateral forces. This allows a clear understanding of variations in structural response and the achievement of various limit states as the structure enters in inelastic range.

Various NSPs are based on the idea that the detailed nonlinear structural models of buildings can be idealized as the equivalent single-degree-of-freedom (SDF) systems. The actual pushover curves of a full structure can be idealized to represent a nonlinear force-deformation relationship. This relationship is assigned to an equivalent SDF system which is then expected to represent the detailed nonlinear structural model. In other words, an equivalent SDF is “mapped” to the actual global behaviour of the detailed structural model. This concept is illustrated in Figure III.6 where an approximated form of a capacity (pushover) curve is used as the governing force-displacement relationship of an equivalent SDF system.

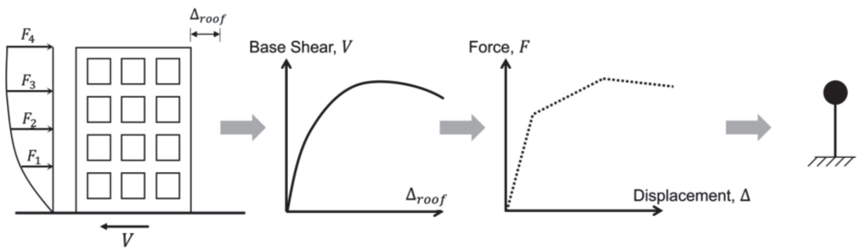

Figure III.55 –The basic conversion of a detailed structural model in to an equivalent SDF system: the pushover analysis using a monotonically-increasing lateral load vector; pushover (capacity) curve; the idealized force-displacement (F-Δ) relationship; an equivalent single-degree-of-freedom (SDOF) system (Najam, 2018).

The POA has no strict theoretical base. It is mainly based on the assumption that the response of the structure is controlled by the first mode of vibration and mode shape, or by the first few modes of vibration, and that this shape remains constant throughout the elastic and inelastic response of the structure. This provides the basis for transforming a dynamic problem to a static problem which is theoretically flawed. Furthermore, the response of a MDOF structure is related to the response of an equivalent SDOF system, ESDOF.

The POA methods that are used can be divided into three general groups: the Conventional POA methods, the Adaptive POA methods, and the Energy-Based POA methods. Some other pushover procedures exist in the literature. The Conventional POA methods are the following (Najam, 2018):

- Capacity Spectrum Method (CSM);
- Improved Capacity Spectrum Method (ICSM);
- N2 method;
- Displacement Coefficient Method (DCM);
- Modal Pushover Analysis (MPA).
-

The CSM and N2 methods differ in the use of appropriate inelastic spectra to calculate the ESDOF maximum displacement, the ICSM method is a modification of the CSM procedure, and resembles the N2 method in the use of inelastic spectra while the Adaptive POA methods are more recent sophisticated variations of the Conventional POAs.

The POA in EC8 follows the approach developed by Prof. Fajfar of the University of Ljubljana, Slovenia (Fajfar 1999, 2004), as an alternative to the CSM method. The basic idea of the N2 method stems from the Q-model developed by Saiidi et al. (1981) which in turn is based on the work of Gulkan et al. (1974). The main difference of the method with respect to the CSM method is the type of demand spectra used for the estimation of the target displacement.

The employment of the non-linear static procedure involves four distinct phases as described below and illustrated following:

1. <u>Structural model</u>: define the mathematical model with the non-linear force deformation relationships for the various components/elements;
2. <u>Load pattern and structure capacity</u>: define a suitable lateral load pattern and use the same pattern to define the capacity of the structure;
3. <u>Performance evaluation</u>: define the seismic demand in the form of an elastic response spectrum and evaluate the performance of the building.

3.1.5.2 Structural model

The non-linear force deformation relationships for the components/elements should define the non-linear behaviour, i.e. initial stiffness, yield point, post yielding stiffness, ultimate resistance and, if required, the behaviour beyond the ultimate resistance of the section.

Structural analyses are performed by means of the FEM software SAP2000. Timber and steel members are modelled as beam elements with lumped plasticity in the links, columns are continuous along the total height and the behaviour model of the plastic hinge assumed for the study is shown in Figure III.7.

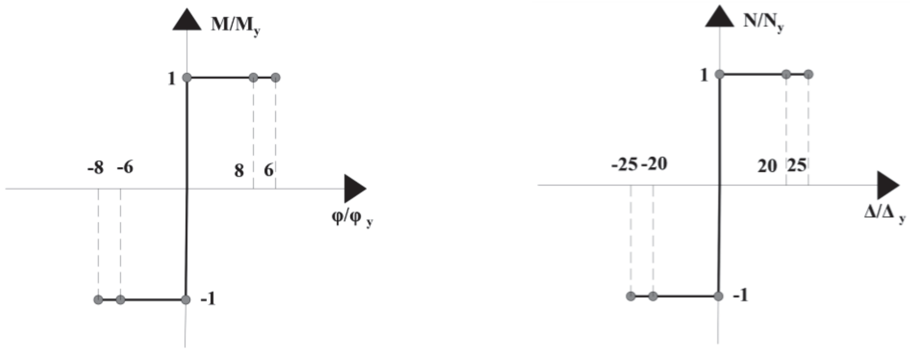

a) b)
Figure III.56 –The link material behaviour: assumed model for a) MRF, EBF and b) CBF structures.

In particular, in MRF structures the link in beams and columns is subjected to combined bending and compression, in CBF structures the link in the diagonals is subjected to compression and tension while in EBF structures the link in the timber beams is subjected to bending (long link). For all types of links, for simplicity, a model of the perfect plasticity elastic material is considered, with values based on FEMA 356 and on studies conducted by Professor Mazzolani (Mazzolani and Ballio, 1979).

3.1.5.3 LOAD PATTERN AND STRUCTURE CAPACITY

For an adequate performance evaluation, the proper selection of the load pattern is imperative. These patterns should bound approximately the likely distribution of inertia forces in a design earthquake, thus requiring to incorporate, in some cases, higher mode effects into the selected lateral load pattern. An invariant load pattern assumes that: the inertia forces will be almost constant throughout the earthquake and; the maximum deformations obtained with this constant load pattern will be close to that expected to occur during the design earthquake. These two assumptions are very close to the reality when the structural response is mainly influenced by the first mode and has only a single load yielding mechanism. As no single load distribution can identify the variation of the local demands expected in a design earthquake, the use of at least two load patterns is recommended.

The POA in EC8 and FEMA-356 requires development of a pushover curve by first applying gravity loads followed by monotonically increasing lateral forces with a specified height-wise distribution. At least two force distributions must be considered.

The first is to be selected from among the following:

- Fundamental (or first) mode distribution;
- Equivalent Lateral Force (ELF) distribution;
- SRSS distribution.

The second distribution is either the “Uniform” distribution or an adaptive distribution; the first is a “uniform” pattern with lateral forces that a proportional to masses and the second pattern, varies with change in deflected shape of the structure as it yields. EC 8 gives two vertical distributions of lateral forces:

- The uniform load pattern with lateral forces that a proportional to masses. It leads to conservative values of demands in lower stories, compared to the upper values, and emphasizes the importance of story shear forces compared with overturning moments;
- A modal pattern, proportional to lateral forces consisting with the lateral force distribution determined in elastic analysis. It can account for elastic higher mode effects, makes a good choice for the second load pattern.

A non-linear static analysis is then carried out to give a Base Shear – Roof Displacement Curve, the Capacity Curve. The non-linear force-displacement (i.e., Base shear V_b vs roof top displacement, Δ_{rt}) curve of the MDOF system, obtained from a POA, is converted to that of its equivalent SDOF system using the following equations.

$$F^* = \frac{V_b}{\Gamma}$$

$$d^* = \frac{\Delta_{rt}}{\Gamma}$$

where:

$$\Gamma = \frac{\sum_{i=1}^{N} m_i \cdot \phi_i}{\sum_{i=1}^{N} m_i \cdot \phi_i^2}$$

For each point on the converted pushover curve, the yield points (F_y* and d_y*) are determined by equivalent bilinear representation (idealized elasto-perfectly plastic) on equivalent Pushover curve (F^*-d^*), by the following equation, where E_m* = Area beneath the pushover curve up to the point under consideration (the actual deformation energy up to the formation of the plastic mechanism) and d^* is the displacement of the control point at the yield force corresponding formation of plastic mechanism.

$$d_y^* = \frac{F_y{}^*}{k^*} = 2\left(d^* - \frac{E_m^*}{F_y^*}\right)$$

$$F_y{}^* = \frac{F_{bu}}{\Gamma}$$

where F_{bu} is the maximum resistance of the building and k^* is the secant stiffness of the equivalent system obtained from energy equivalence (Fig. III.8).

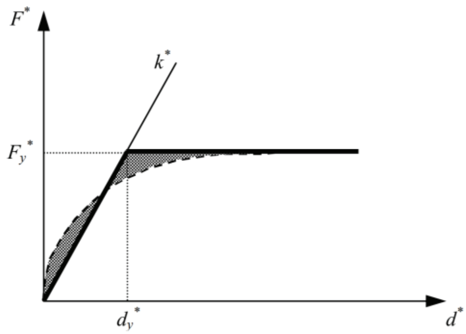

Figure III.57 – Bi-linear approximation of the capacity curve.

The time period of the idealized SDOF system is:

$$T^* = 2\pi\sqrt[2]{\frac{m^* \cdot d_y^*}{F_y^*}}$$

$$m^* = \sum_{i=1}^{N} m_i \cdot \phi_i$$

is the mass of an equivalent SDOF system (m_i is the mass in the i-th floor, and Φ_i is the normalized mode shape value in such a way that $\Phi_n=1$, where n is control node).

In this study, the bilinearization of the pushover curves is performed with the "A method" proposed by the NTC 2018 [§C7.3.4.2]. The elastic stretch is defined by intersecting the capacity curve at the point having $F=0,6Fbu^*$. The plasticization force F_y* is defined by imposing the equality between the subtended areas of the bilinear curve and the capacity curve for the maximum displacement d_u* corresponding to a reduction in resistance $\leq 0,15F_{bu}$* (Fig. III.9).

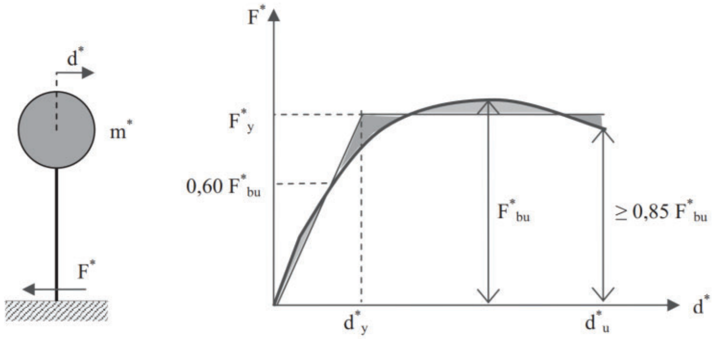

Figure III.58 – Equivalent bi-linear representation (NTC2018).

3.1.5.4 Performance evaluation

In this procedure, the seismic demand is represented by the elastic response spectrum with a damping inherent of the structure under consideration, valuated in the chapter 3.1.3.2.

Finally, the target displacement is determined by comparing capacity spectrum and design spectrum (or demand spectrum). The comparison is conveniently carried out on the Acceleration Displacement Response Spectrum (ADRS), as shown in Figure III.10.

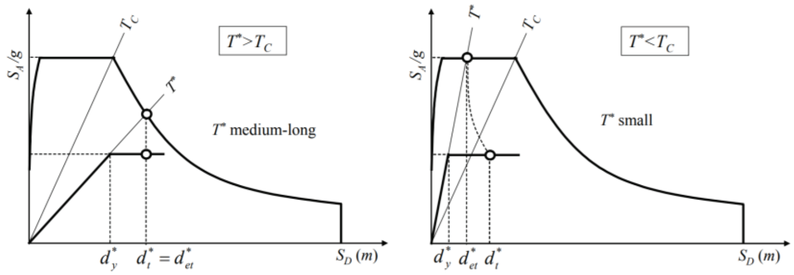

Figure III.59 – Transformation of pushover curve into SDOF response.

The comparison between the two spectra is not immediate, because the design spectrum is linear elastic. EC8 follows a simplified approach in order to compare the two spectra. For long periods, EC8 assumes equal max displacements for linear and elastic-perfectly-plastic (EPP) oscillators. For short periods, EC8 assumes equal energy between the two oscillators. In conclusion, the target displacement d_t* of the equivalent nonlinear SDOF system is:

a) $T^* < T_C$ (short periods)

a.1) The response remains linear elastic:

$$\frac{F_y^*}{m^*} \geq S_e(T^*)$$
$$d_t^* = d_{et}^*$$

a.2) The response enters the nonlinear plateau:

$$\frac{F_y^*}{m^*} < S_e(T^*)$$
$$d_t^* = \frac{d_{et}^*}{q_u}\left(1 + (q_u - 1)\frac{T_C}{T^*}\right) \geq d_{et}^*$$

where

$$q_u = \frac{S_e(T^*)}{F_y^*} m^*$$

b) $T^* \geq T_C$ (medium and long periods)

$$d_t^* = de_t^* = S_{De}(T^*) = S_e(T^*)\left(\frac{T^*}{2\pi}\right)^2$$

The target displacement correspond to the MDOF system corresponds to the control node is given by:

$$d_t = \Gamma \cdot d_t^*$$

3.1.5.5 BEHAVIOUR FACTOR EVALUATION

The behaviour factor q is a coefficient which allows to perform an elastic seismic analysis of the structure, taking into account the inelastic behaviour capabilities. It is a measure of the structural ductility and depends on the type of seismic resistant system. The q factor is used as a reduction coefficient of the elastic spectrum, which characterizes the elastic response at the earthquake site, thus obtaining a design inelastic spectrum. In this way it is possible to perform a seismic structural analysis in elastic field, with reduced seismic actions as respect to those corresponding to the elastic response under the site earthquake, accepting at the ultimate limit state a degree of permanent damage due to inelastic deformation associated to seismic input energy dissipation. Therefore, the q factor represents the ratio between the resistance that the structure has to possess to remain in elastic range, Fe, and the design resistance under earthquake, F_h. The latter is generally slightly lower than the actual structure resistance corresponding to the occurrence of the first nonlinear event in the structural system, F_1, because of the intrinsic design overstrength (Fig. III.11).

With this premises, also the definition of the behaviour factor q is an open issue.

The q factor assumed in the study is determined, coherently with the previous definitions, according to the following equation (Uang, 1991):

$$q = \frac{F_e}{F_h} = q_\Omega \cdot q_\mu = \left(\frac{F_1}{F_h} \cdot \frac{F_u}{F_1}\right) \cdot \frac{d_u}{d_y} = \frac{F_u}{F_h} \cdot \frac{d_u}{d_y}$$

where q_Ω and q_μ are the behaviour factor contributions related to overstrength and ductility, respectively; F_1 is the base shear at the first non-linear event, F_h is the design base shear, F_u is the maximum base shear value on the pushover curve, d_y is the displacement corresponding to the conventional elastic limit and d_u is the ultimate displacement.

The q_Ω factor takes into account the structure overstrength, through the ratio F_1/F_h, and the plastic redistribution capacity through the ratio F_u/F_1. In particular the q_μ factor represents the structure ductility, it being given by the ratio d_u/d_y (for $T^*>T_C$, where T^* is the fundamental period of the equivalent SDOF system and T_C is the limit period between the constant acceleration region and constant velocity region of the design spectrum).

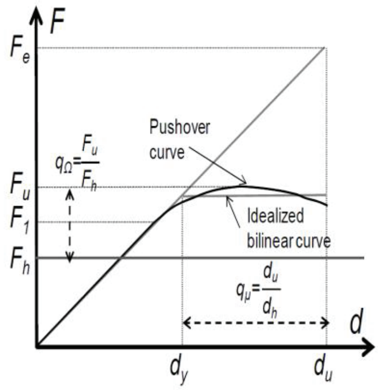

Figure III.60 – Evaluation of the behaviour factor *q* (Uang, 1991).

The application of previously equation for the definition of the *q* factor requires another assumption to be made, it being related to the selection of the ultimate condition, which d_u corresponds to. In particular, q_Ω and q_μ are assumed equal to:

$$q_\mu = \sqrt{2 \times \mu - 1} \qquad T^* < T_c$$

$$q_\mu = \frac{d_u}{d_y} \qquad T^* > T_c$$

In this work, the behaviour factor is calculated according to three different conditions for the ultimate displacement d_u, corresponding at the achievement of the inter-storey drift equal to 2,5% (for MRF), 1,5% (for CBF and EBF) and 5% (for MRF), 2% (for CBF and EBF), as provided by FEMA 356 for steel structures, respectively, at Collapse Prevention limit and at Life Safety limit state, and at the Collapse Mechanism, with the labile mechanism and the achievement of the plastic hinge ultimate rotational capacity (Tab. III.9).

Table III.16 – Inter-storey drift limits by FEMA 356.

Structural type	Life Safety	Collapse Prevention	Collapse Mechanism
MRF	2,5%	5%	Plastic hinge ultimate rotational capacity
CBF / EBF	1,5%	2%	

3.1.5.6 Output

The seismic performance of MRF-SLV, MRF-SLD, CBF V π, CBF V Λ, CBF X, CBF X D and EBF is analysed and the outputs are the following (from Tab. III.10 to Tab. III.19).

For **MRF-SLV** and **MRF-SLD**:

- 1S

1) For 1A, 2A and 3A, the comparison between the push-over curves (V-δ/h diagram), with the indication of the two reference ultimate displacements d_u (2,5% and 5%), with q=1 and q=4, for 1Z, 2Z and 3Z.
2) For 1A, 2A and 3A, the comparison between the push-over curves, with q=1, for 1Z, 2Z and 3Z, and between strength, stiffness and behaviour factor q (with its contributions related to overstrength, q_Ω, and ductility, q_μ), evaluated for the two reference ultimate displacements d_u (2,5% and 5%).
3) For 1A, 2A and 3A, the comparison between the push-over curves (V-δ/h diagram), with q=4, for 1Z, 2Z and 3Z, and between strength, stiffness and behaviour factor q (with its contributions related to overstrength, q_Ω, and ductility, q_μ), evaluated for the two reference ultimate displacements d_u (2,5% and 5%).
4) For 1A, 2A and 3A, the comparison between the push-over curves (V-δ/h diagram) of MRF-SLV and MRF-SLD, with the indication of the two reference ultimate displacements d_u (2,5% and 5%), with q=1 and q=4, for 1Z, 2Z and 3Z.

- 2S

For 2A, the comparison between the push-over curves (V-Δ diagram) of 2S and 1S elevation schemes, with q=4, for 1Z, 2Z and 3Z, and between strength, stiffness and behaviour factor q (with its contributions related to overstrength, q_Ω, and ductility, q_μ), evaluated for the two reference ultimate displacements d_u (2,5% and 5%).

- 4S

For 2A, the comparison between the push-over curves (V-Δ diagram) of 4S and 1S elevation schemes, with q=4, for 1Z, 2Z and 3Z, and between strength, stiffness and behaviour factor q (with its contributions related to overstrength, q_Ω, and ductility, q_μ), evaluated for the two reference ultimate displacements d_u (2,5% and 5%).

- 6S

For 2A, the comparison between the push-over curves (V-Δ diagram) of 6S and 1S elevation schemes, with q=4, for 1Z, 2Z and 3Z, and between strength, stiffness and behaviour factor q (with its contributions related to overstrength, q_Ω, and ductility, q_μ), evaluated for the two reference ultimate displacements d_u (2,5% and 5%).

For **CBF V π** and **CBF V Λ**:

- 1S

1) For 1A, 2A and 3A, the comparison between the push-over curves (V-δ/h diagram), with q=1, for 1Z, 2Z and 3Z, and between strength, stiffness and behaviour factor q (with its contributions related to overstrength, q_Ω, and ductility, q_μ), evaluated for the two reference ultimate displacements d_u (1,5% and 2%).
2) For 1A, 2A and 3A, the comparison between the push-over curves (V-δ/h diagram), with q=2, for 1Z, 2Z and 3Z, and between strength, stiffness and behaviour factor q (with its contributions related to overstrength, q_Ω, and ductility, q_μ), evaluated for the two reference ultimate displacements d_u (1,5% and 2%).

- 2S

For 2A, the comparison between the push-over curves (V-Δ diagram) of 2S and 1S elevation schemes, with q=2, for 1Z, 2Z and 3Z, and between strength, stiffness and behaviour factor q (with its contributions related to overstrength, q_Ω, and ductility, q_μ), evaluated for the two reference ultimate displacements d_u (1,5% and 2%).

- 4S

For 2A, the comparison between the push-over curves (V-Δ diagram) of 4S and 1S elevation schemes, with q=2, for 1Z, 2Z and 3Z, and between strength, stiffness and behaviour factor q (with its contributions related to overstrength, q_Ω, and ductility, q_μ), evaluated for the two reference ultimate displacements d_u (1,5% and 2%).

- 6S

For 2A, the comparison between the push-over curves (V-Δ diagram) of 6S and 1S elevation schemes, with q=2, for 1Z, 2Z and 3Z, and between strength, stiffness and behaviour factor q (with its contributions related to overstrength, q_Ω, and ductility, q_μ), evaluated for the two reference ultimate displacements d_u (1,5% and 2%).

For **CBF X**, **CBF X D** and **EBF**:

- 1S

1) For 1A, 2A and 3A, the comparison between the push-over curves (V-δ/h diagram), with q=1, for 1Z, 2Z and 3Z, and between strength, stiffness and behaviour factor q (with its contributions related to overstrength, q_Ω, and ductility, q_μ), evaluated for the two reference ultimate displacements d_u (1,5% and 2%).
2) For 1A, 2A and 3A, the comparison between the push-over curves (V-δ/h diagram), with q=4, for 1Z, 2Z and 3Z, and between strength, stiffness and behaviour factor q (with its contributions related to overstrength, q_Ω, and ductility, q_μ), evaluated for the two reference ultimate displacements d_u (1,5% and 2%).

- 2S

For 2A, the comparison between the push-over curves (V-Δ diagram) of 2S and 1S elevation schemes, with q=4, for 1Z, 2Z and 3Z, and between strength, stiffness and behaviour factor q (with its contributions related to overstrength, q_Ω, and ductility, q_μ), evaluated for the two reference ultimate displacements d_u (1,5% and 2%).

- 4S

For 2A, the comparison between the push-over curves (V-Δ diagram) of 4S and 1S elevation schemes, with q=4, for 1Z, 2Z and 3Z, and between strength, stiffness and behaviour factor q (with its contributions related to overstrength, q_{Ω}, and ductility, q_{μ}), evaluated for the two reference ultimate displacements d_u (1,5% and 2%).

- 6S

For 2A, the comparison between the push-over curves (V-Δ diagram) of 6S and 1S elevation schemes, with q=4, for 1Z, 2Z and 3Z, and between strength, stiffness and behaviour factor q (with its contributions related to overstrength, q_{Ω}, and ductility, q_{μ}), evaluated for the two reference ultimate displacements d_u (1,5% and 2%).

As an example, below the outputs for MRF-SLV and MRF-SLD, 1S, 2S, 4S and 6S, for 1Z, 2Z, 3Z and 1A, 2A, 3A, are presented. The seismic performance results of the other structural types are shown in Annex A.3.1.5.6.

Table III.17 – Analysis results: 1S, MRF-SLD with $q=1$ and $q_d=4$: a) 1A; 1Z, 2Z, 3Z; b) 2A; 1Z, 2Z, 3Z; c) 3A; 1Z, 2Z, 3Z.

Pushover curve

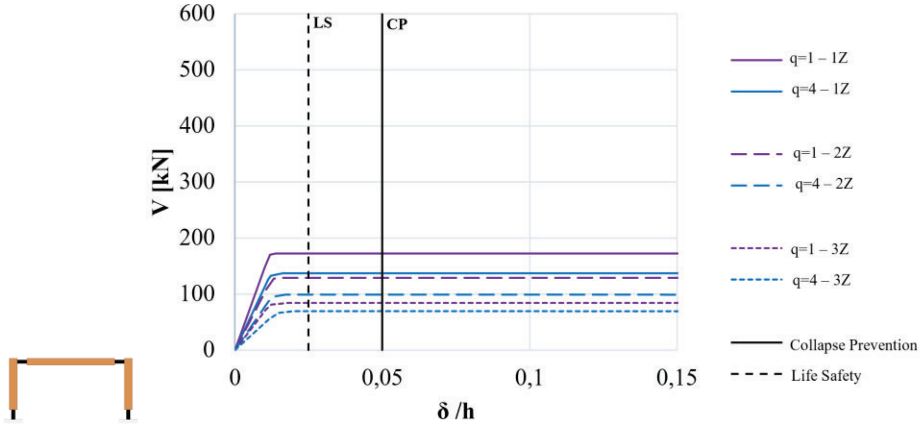

a)

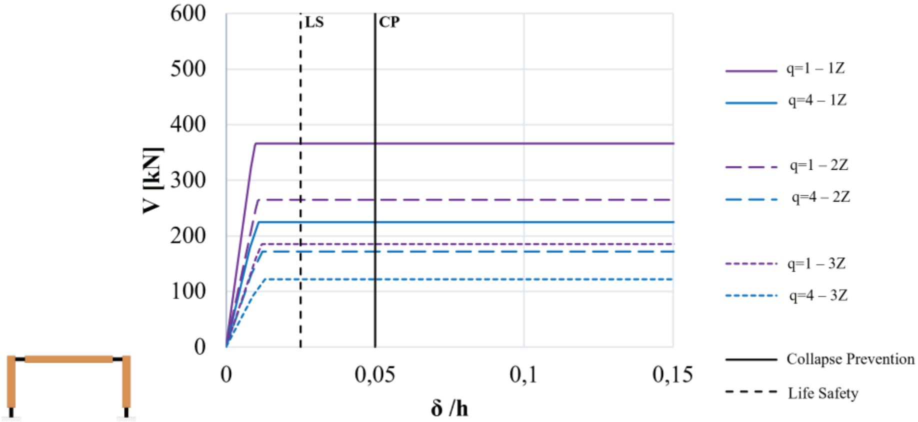

b)

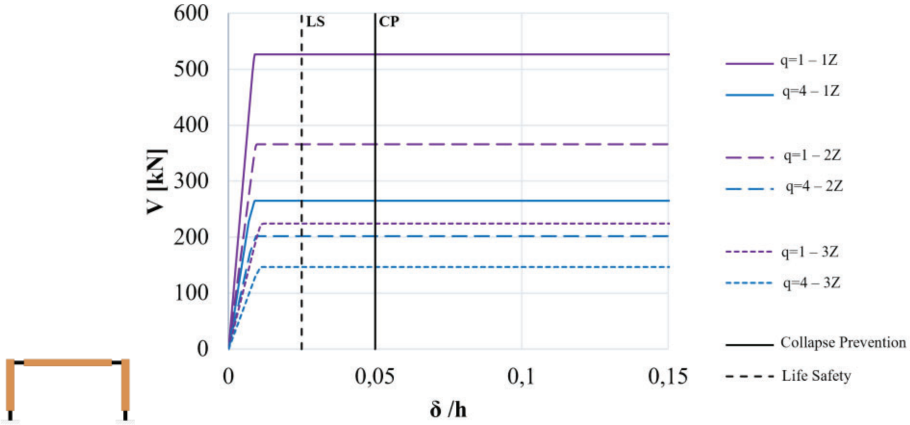

c)

Table III.18 – Analysis results: 1S, MRF-SLD with $q=1$; 1A, 2A, 3A; 1Z, 2Z, 3Z.

Pushover curve

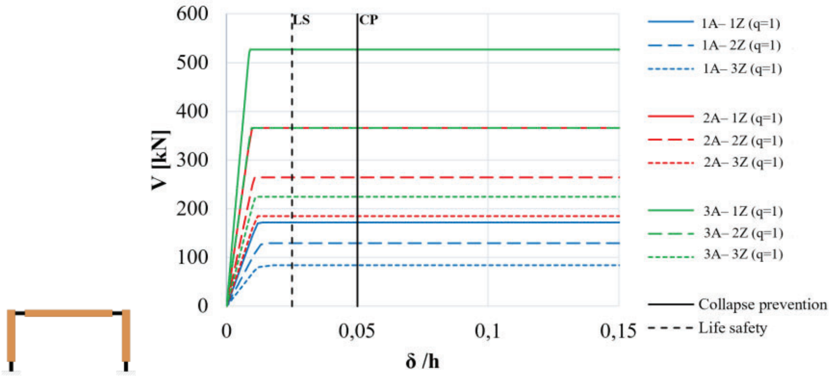

Strength [kN]

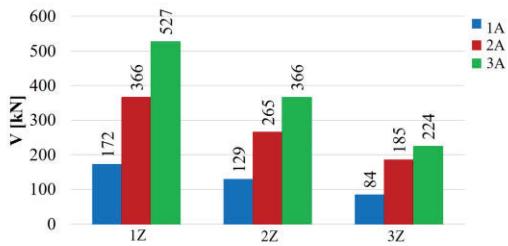

Stiffness [kN/cm]

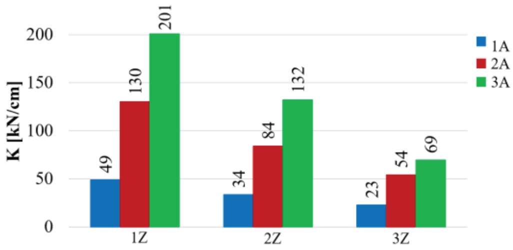

q_Ω **(behaviour factor - overstrength)**

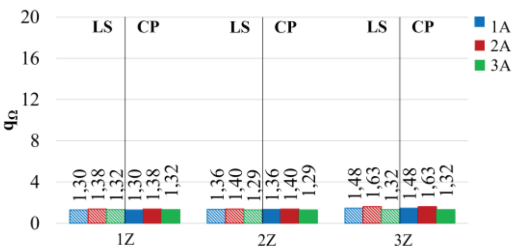

q_μ **(behaviour factor - ductility)**

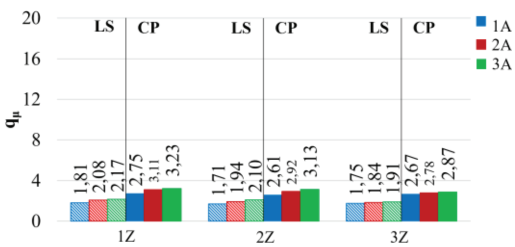

q **(behaviour factor)**

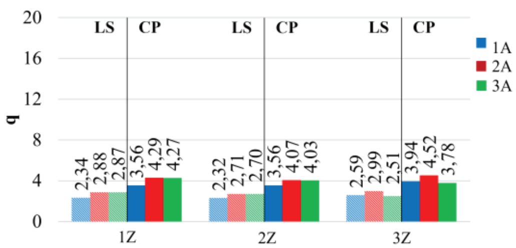

Table III.19 – Analysis results: 1S, MRF-SLD with q_d=4; 1A, 2A, 3A; 1Z, 2Z, 3Z.

Pushover curve

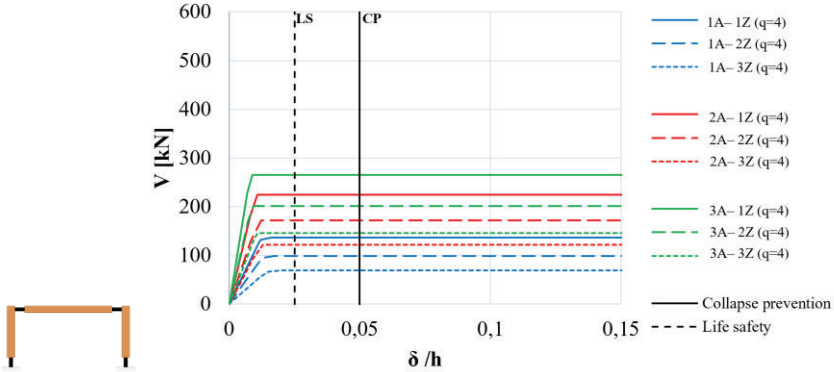

Strength [kN]

Stiffness [kN/cm]

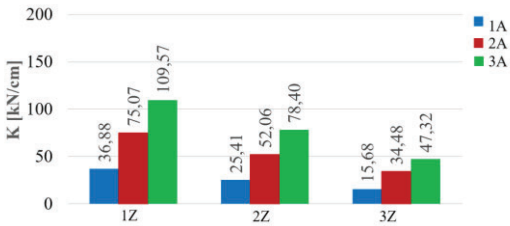

q_Ω **(behaviour factor - overstrength)**

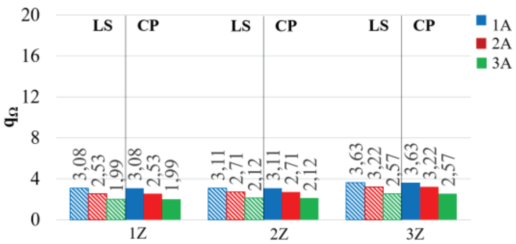

q_μ **(behaviour factor - ductility)**

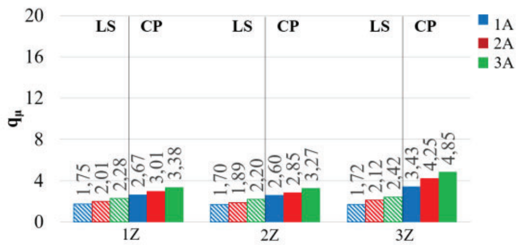

q **(behaviour factor)**

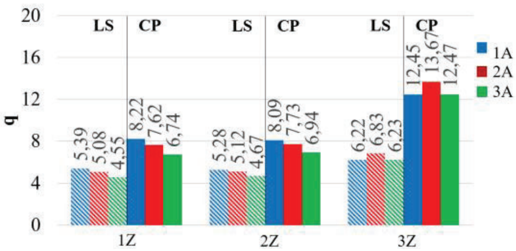

Table III.20 – Analysis results: 1S, MRF-SLV vs MRF-SLD with q_d=4: a) 1A; b) 2A; c) 3A.

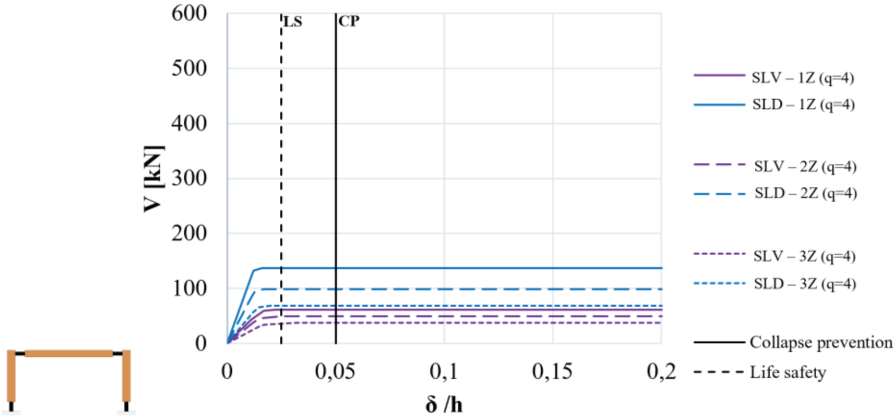

a)

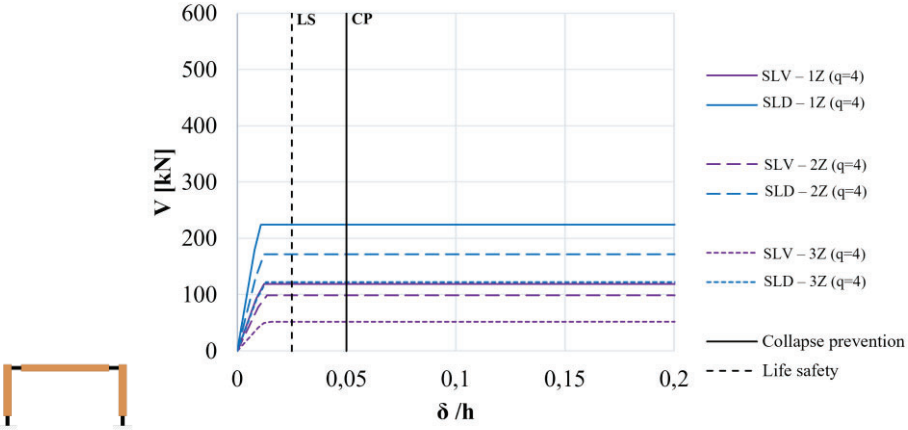

b)

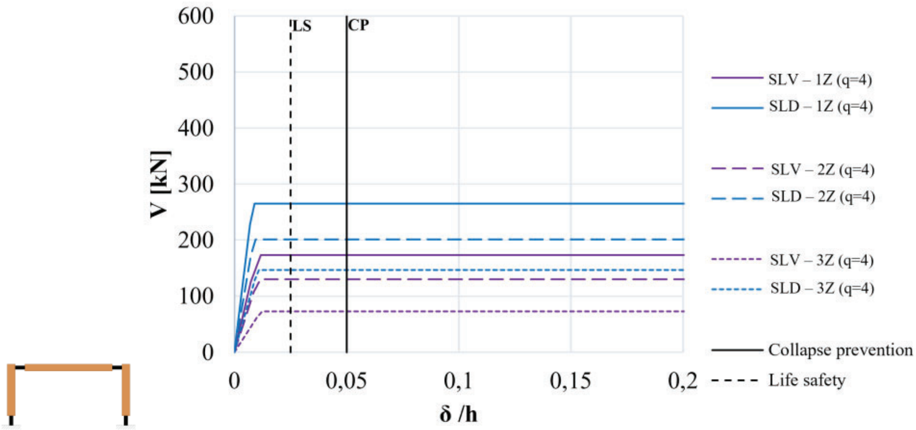

c)

Table III.21 – Analysis results: 2S vs 1S, MRF-SLD with $q_d=4$: 2A; 1Z, 2Z, 3Z.

Pushover curve

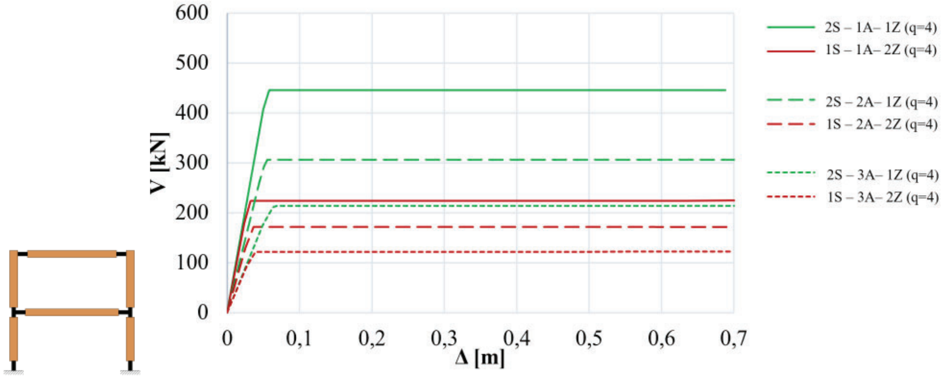

Strength [kN]

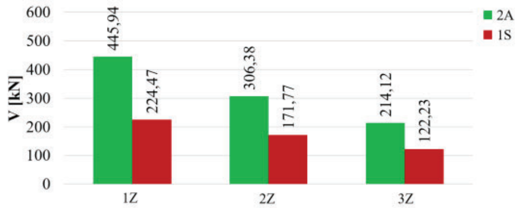

Stiffness [kN/cm]

***q_Ω* (behaviour factor - overstrength)**

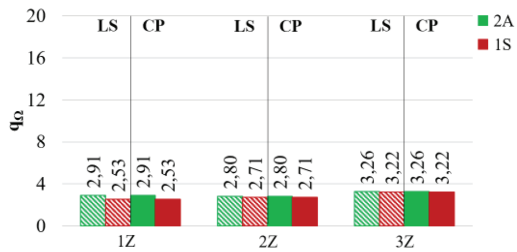

***q_μ* (behaviour factor - ductility)**

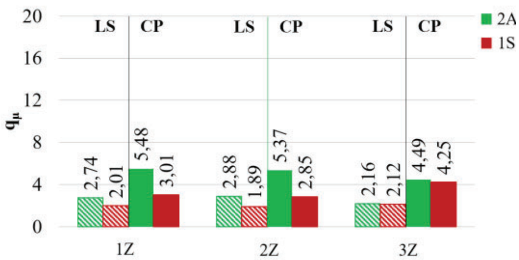

***q* (behaviour factor)**

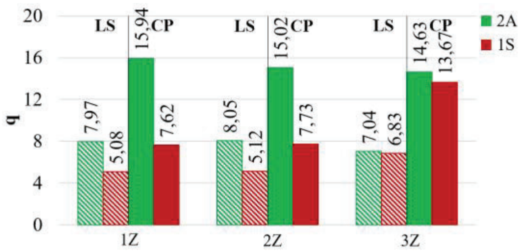

Table III.22 – Analysis results: 2S vs 1S, MRF-SLV with q_d=4: 2A; 1Z, 2Z, 3Z.

Pushover curve

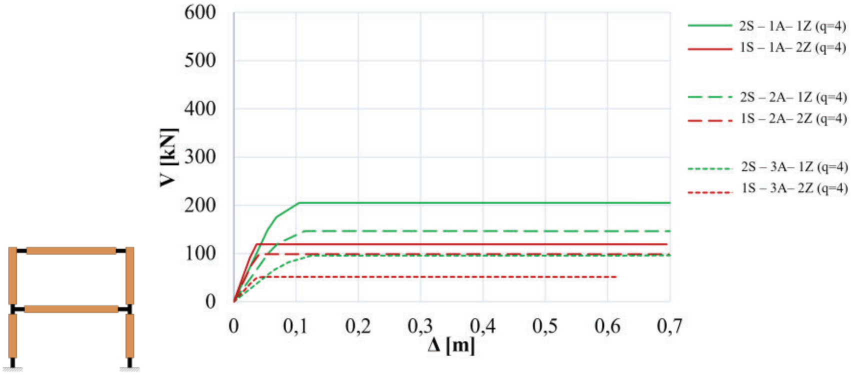

Strength [kN]

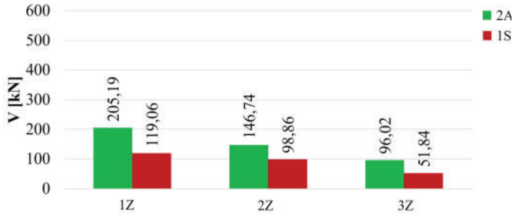

Stiffness [kN/cm]

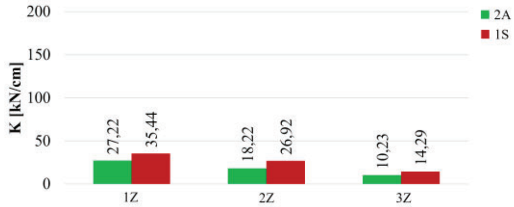

***q*$_\Omega$ (behaviour factor - overstrength)**

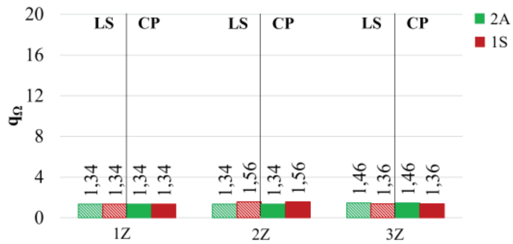

***q*$_\mu$ (behaviour factor - ductility)**

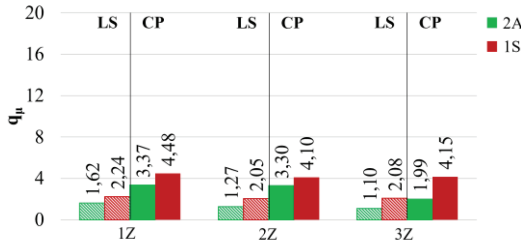

***q* (behaviour factor)**

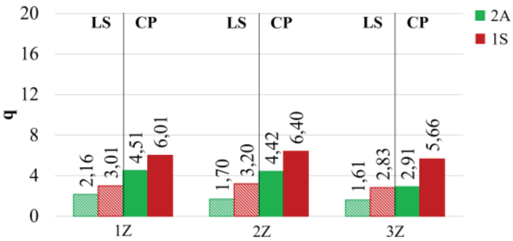

Table III.23 – Analysis results: 4S vs 1S, MRF-SLD with q_d=*4*: 2A; 1Z, 2Z, 3Z.

Pushover curve

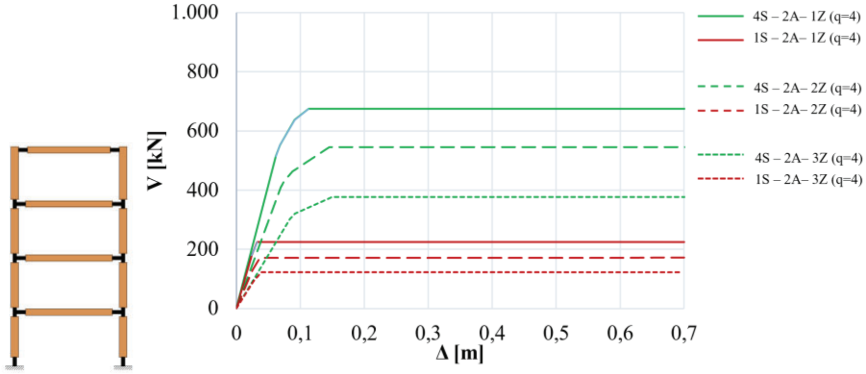

Strength [kN]

Stiffness [kN/cm]

q_Ω **(behaviour factor - overstrength)**

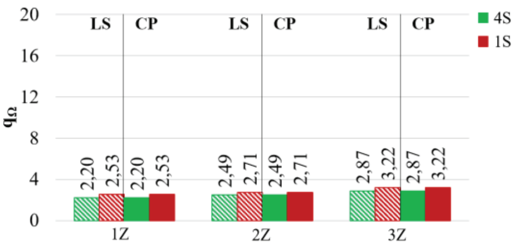

q_μ **(behaviour factor - ductility)**

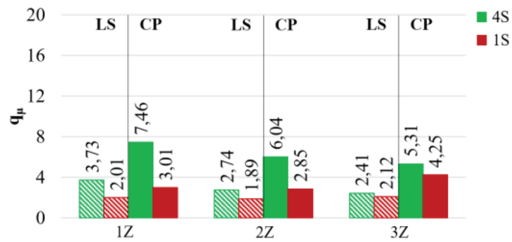

q **(behaviour factor)**

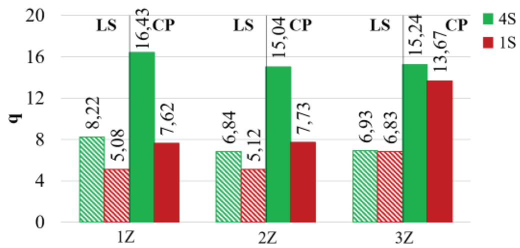

Table III.24 – Analysis results: 4S vs 1S, MRF-SLV with $q_d=4$: 2A; 1Z, 2Z, 3Z.

Pushover curve

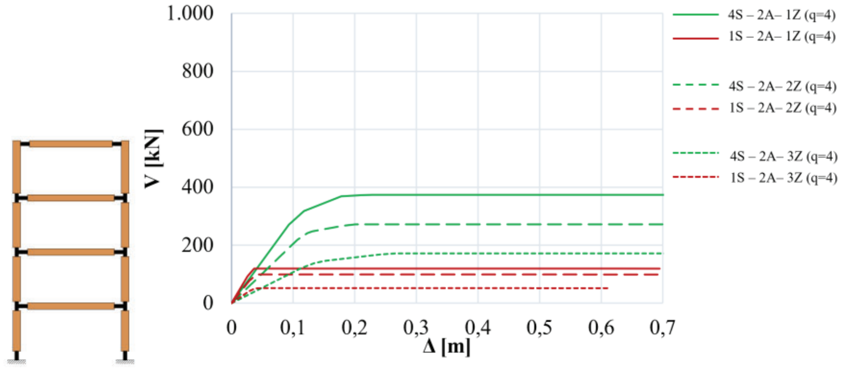

Strength [kN]

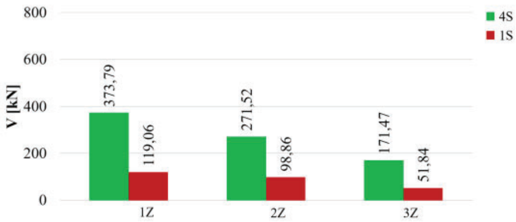

Stiffness [kN/cm]

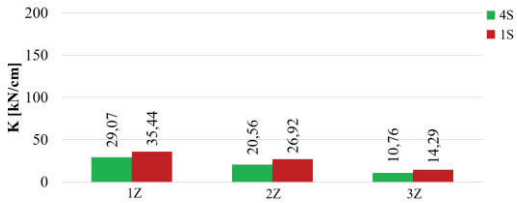

***q*$_\Omega$ (behaviour factor - overstrength)**

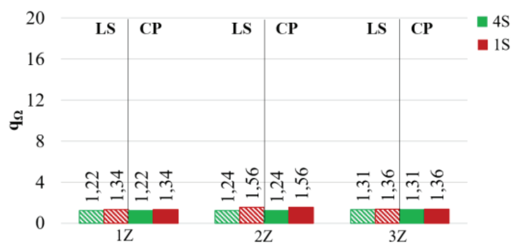

***q*$_\mu$ (behaviour factor - ductility)**

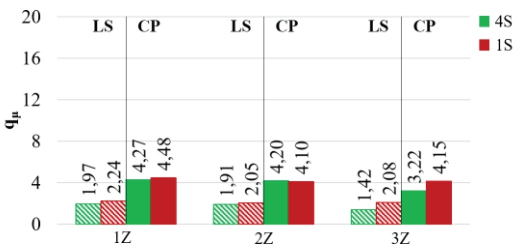

***q* (behaviour factor)**

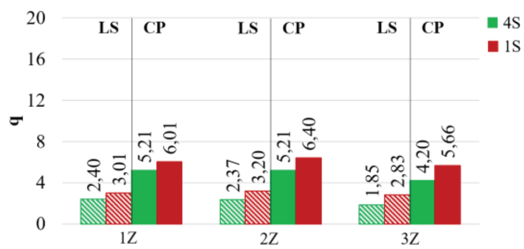

Table III.25 – Analysis results: 6S vs 1S, MRF-SLD with $q_d=4$: 2A; 1Z, 2Z, 3Z.

Pushover curve

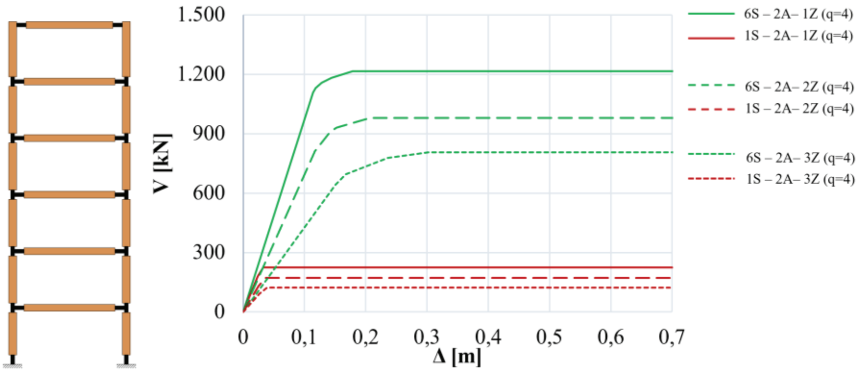

Strength [kN]

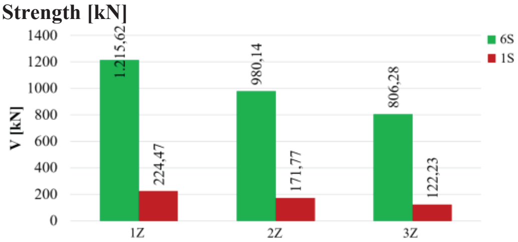

Stiffness [kN/cm]

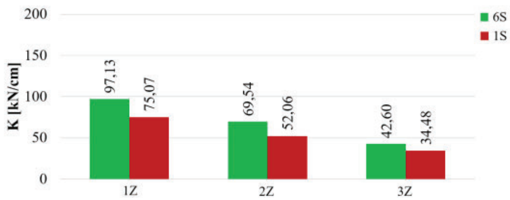

q_Ω (behaviour factor - overstrength)

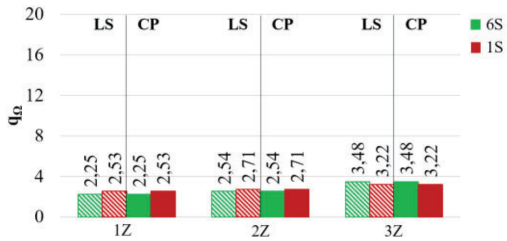

q_μ (behaviour factor - ductility)

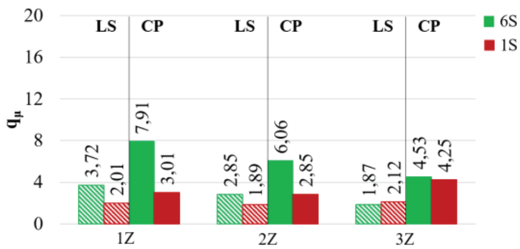

***q* (behaviour factor)**

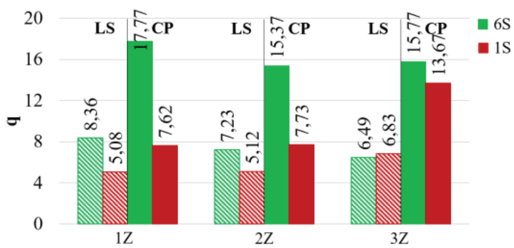

Table III.26 – Analysis results: 6S vs 1S, MRF-SLV with q_d=4: 2A; 1Z, 2Z, 3Z.

Pushover curve

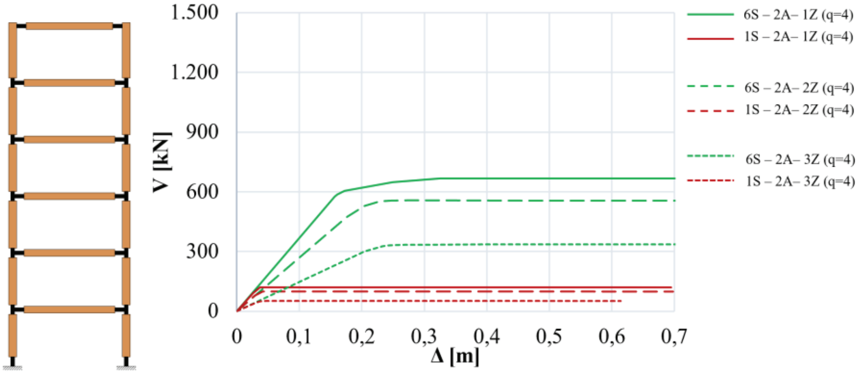

Strength [kN]

Stiffness [kN/cm]

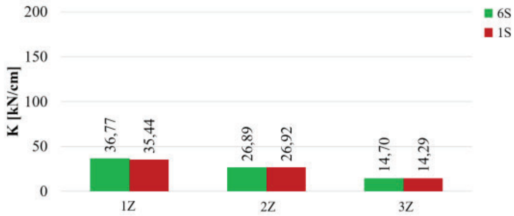

***q_Ω* (behaviour factor - overstrength)**

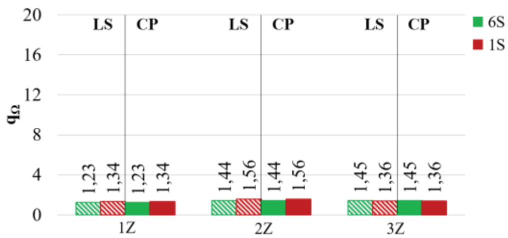

***q_μ* (behaviour factor - ductility)**

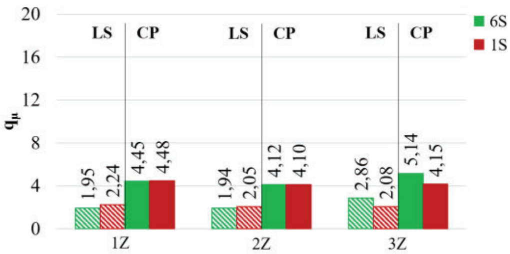

***q* (behaviour factor)**

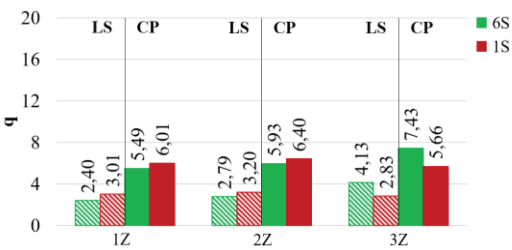

3.1.6 Analysis of results

The comparisons of the analyses results are presented, for all the structural typologies, only for the plan layout 2A in the seismic zone 1Z, that in the unfavourable condition. Furthermore, from the analysis of all the structural typologies, the same trend of the variation of the structural mass, vibration period, strength, stiffness and behaviour factor from 1Z to 3Z and from 1A to 3A was observed (1S, 2S, 4S, 6S: 2A only for 1Z): Structural mass, Vibration period (T), Strength of structure, Stiffness of structure and Behaviour factor q (with its contributions related to overstrength, q_{Ω}, and ductility, q_{μ}).

Structural mass

First of all, the effect of the different extent of dissipation is quantified through the mass of the designed structures, and the results, by varying the number of storeys from 1S to 6S, for MRF-SLV, MRF-SLD, CBF V π, CBF V Λ, CBF X, CBF X D and EBF, are presented.

In particular, in Figure III.12 the comparison between the Non-Dissipative (M_{ND}) structures and Dissipative (M_D) structures are reported for, respectively, 1S, 2S, 4S and 6S, with 2A plan layout, while in Figure III.13 a summery with the comparison between all the structural typologies for 1S, 2S, 4S and 6S for 2A plan layout is indicated.

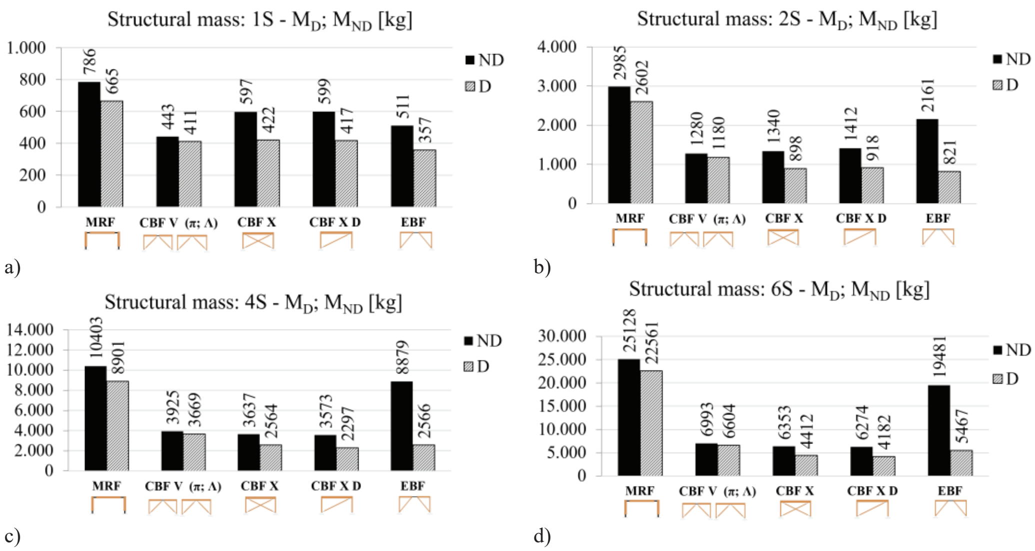

Figure III.61 – Comparison between the structural mass of dissipative (M_D) and non-dissipative (M_{ND}) structures for 2A, 1Z: a) 1S; b) 2S; c) 4S; d) 6S.

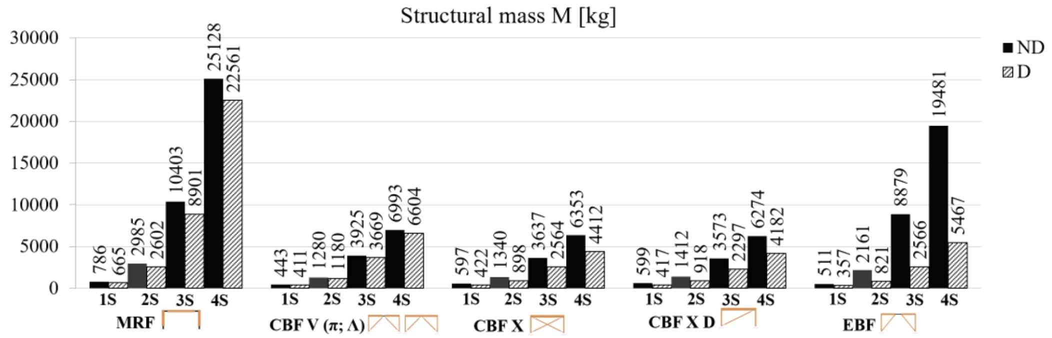

Figure III.62 – Summary results of the comparison between the structural mass of dissipative (M_D) and non-dissipative (M_{ND}) structures for 2A, 1Z: a) 1S; b) 2S; c) 4S; d) 6S.

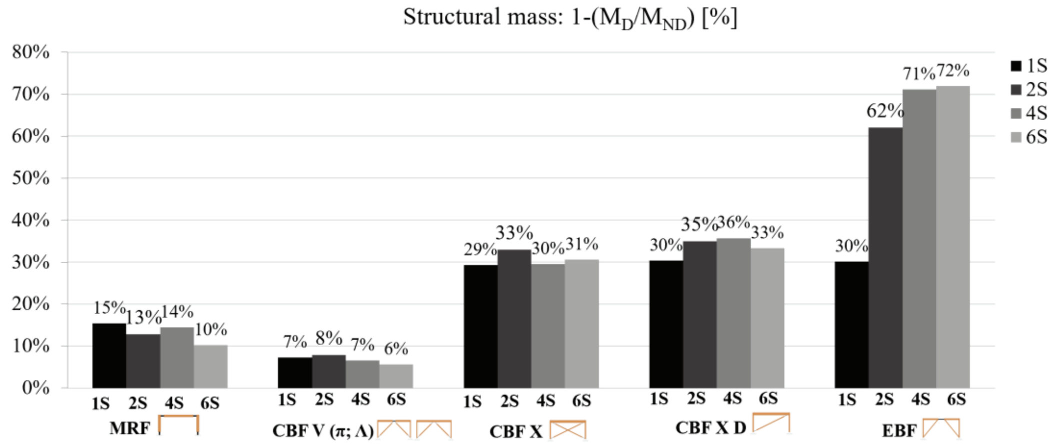

Figure III.63 – DCR_M [1-(M_D/M_{ND})] for the structural mass of dissipative (M_D) structures respect to non-dissipative (M_{ND}) structures for 2A, 1Z: a) 1S; b) 2S; c) 3S; d) 4S.

In the Figure III.14, the $\Delta M_{D\text{-}ND}$ [$\Delta M_{D\text{-}ND}$ = 1-(M_D/M_{ND})] is provided for the same structural cases.

It is possible to note that as far as the storeys number increases from 1S to 6S, for MRF_D a reduction of the structural mass as respect to MRF_{ND} is achieved from 15% [$\Delta M_{D/ND\text{-}MRF\text{-}1S}$] to 10% [$\Delta M_{D/ND\text{-}MRF\text{-}6S}$], for CBF V_D as respect to CBF V_{ND} from 7% [$\Delta M_{D/ND\text{-}CBF\ V\text{-}1S}$] to 6% [$\Delta M_{D/ND\text{-}CBF\ V\text{-}6S}$], for CBF X_D as respect to CBF X_{ND} from 29% [$\Delta M_{D/ND\text{-}CBF\ X\text{-}1S}$] to 31% [$\Delta M_{D/ND\text{-}CBF\ X\text{-}6S}$], for CBF X D_D as respect to CBF X D_{ND} from 30% [$\Delta M_{D/ND\text{-}CBF\ X\ D\text{-}1S}$] to 33% [$\Delta M_{D/ND\text{-}CBF\ X\ D\text{-}6S}$] and for EBF_D as respect to EBF_{ND} from 30% [$\Delta M_{D/ND\text{-}EBF\text{-}1S}$] to 72% [$\Delta M_{D/ND\text{-}EBF\text{-}6S}$].

Moreover, by varying the structural typology from MRF to EBF, there is a progressive mass reduction of the dissipative structures as respect to the non-dissipative structures, which ranging, for 1S from 15% [$\Delta M_{D/ND\text{-}MRF\text{-}1S}$] to 30% [$\Delta M_{D/ND\text{-}EBF\text{-}1S}$], for 2S from 13% [$\Delta M_{D/ND\text{-}MRF\text{-}2S}$] to 62% [$\Delta M_{D/ND\text{-}EBF\text{-}2S}$], for 4S from 14% [$\Delta M_{D/ND\text{-}MRF\text{-}4S}$] to 71% [$\Delta M_{D/ND\text{-}EBF\text{-}4S}$], for 6S from 10% [$\Delta M_{D/ND\text{-}MRF\text{-}6S}$] to 72% [$\Delta M_{D/ND\text{-}EBF\text{-}6S}$].

It is apparent that CBF V is the least efficient system among the three types analysed, following by MRF configuration. This is evidently, for CBF V, due to the lower value of the behaviour factor (q=2) which induces a less seismic force reduction compared to the other structural cases (q=4). The MRF configuration, however, has a modest reduction of the structural mass since the dimensions of the structural elements cross-sections derive from the SLD seismic verification of structure horizontal displacement.

Conversely, the best performance is offered by the structural configuration EBF, following by CBF X and, on an equal footing, by CBF X D. The EBF configuration has a considerable reduction of the structural mass since, in the non-dissipative structure, the dimensions of the timber beam cross-section derive from the high shear force produced by the diagonals which, in the dissipative structure, is absorbed by the steel link with a less section dimensions. So that, applying the capacity design procedure, the timber beam cross-section, evaluated to be over-resistant respect to the steel link, has less dimension respect to that of the timber beam in non-dissipative structures.

In particular, from 1S to 6S, for MRF, the ratio between the structural mass of dissipative structure and the structural mass of non-dissipative structure presents an increase of t 33% [$\Delta M_{D/ND-MRF-6S/1S}$], since it is very deformable against horizontal actions, and the cross section of the structural elements has been increased to contain the P-δ effects. In CBF V, CBF X and CBF X D, from 1S to 6S, the ratio between the structural mass of dissipative structure and the structural mass of no-dissipative structure is almost constant and equal to, respectively, 14% [$\Delta M_{D/ND-CBF\ V-6S/1S}$], 6% [$\Delta M_{D/ND-CBF\ X-6S/1S}$] and 10% [$\Delta M_{D/ND-CBF\ X\ D-6S/1S}$].

Vibration period

In the Table III.20, Table III.21 and Figure III.15, the vibration periods of the dissipative structures are presented. In particular, the vibration periods obtained through the modal analysis shows the same value of the vibration period obtained by the inclination of the elastic field of the push-over curve.

Table III.27 – Summary of results of the vibration period *T* [s] of the structural typologies for 1S, 2S, 4S and 6S.

Storey	Vibration Period T [s]					
	EC8	MRF	CBF V	CBF X	CBF X D	EBF
1S	0,11	0,46	0,13	0,13	0,22	0,29
2S	0,19	0,64	0,19	0,23	0,31	0,40
4S	0,32	0,91	0,38	0,43	0,59	0,64
6S	0,44	1,03	0,60	0,71	0,88	0,83

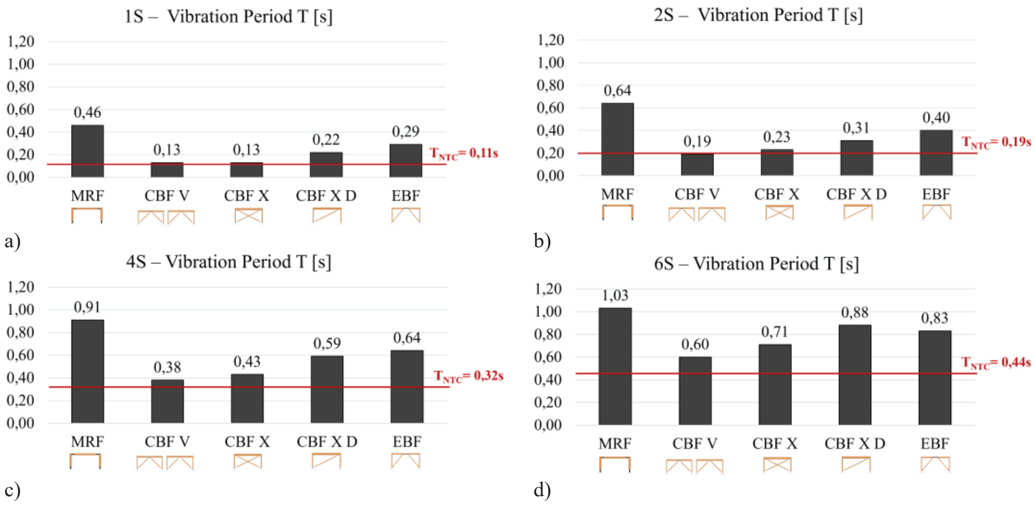

Figure III.64 – Vibration period *T* [s] of the structural typologies for 2A, 1Z: a) 1S; b) 2S; c) 4S; d) 6S respect to the standard formula ($T_{NTC2018}$= $CH^{3/4}$).

In particular, the MRF, which has the lowest lateral stiffness among all configurations, shows the highest vibration period ($T_{MRF\text{-}1S}$ = 0,46s; $T_{MRF\text{-}2S}$ = 0,64s; $T_{MRF\text{-}4S}$ = 0,91s; $T_{MRF\text{-}6S}$ = 1,03s;), while the CBF, in which the braces allow a higher lateral stiffness, presents the lower vibration period. Specially, the CBF V has a vibration period equal to $T_{CBF\ V\text{-}1S}$ = 0,13s for 1S, $T_{CBF\ V\text{-}2S}$ = 0,19s for 2S, $T_{CBF\ V\text{-}4S}$ = 0,38s for 4S and $T_{CBF\ V\text{-}6S}$ = 0,60s for 6S, the CBF X has a vibration period equal to $T_{CBF\ X\text{-}1S}$ = 0,13s for 1S, $T_{CBF\ X\text{-}2S}$ = 0,23s for 2S, $T_{CBF\ X\text{-}4S}$ = 0,43s for 4S and $T_{CBF\ X\text{-}6S}$ = 0,71s for 6S, and the CBF X D has a vibration period equal to $T_{CBF\ X\ D\text{-}1S}$ = 0,22s for 1S, $T_{CBF\ X\ D\text{-}2S}$ = 0,31s for 2S, $T_{CBF\ X\ D\text{-}4S}$ = 0,59s for 4S and $T_{CBF\ X\ D\text{-}6S}$ = 0,88s for 6S.

Obviously the EBF is the structural typology interposed between the two extreme configuration cases and shows a vibration period equal to $T_{EBF\text{-}1S}$ = 0,29s for 1S, $T_{EBF\text{-}2S}$ = 0,40s for 2S, $T_{EBF\text{-}4S}$ = 0,64s for 4S and $T_{EBF\text{-}6S}$ = 0,83s for 6S. This testifies how the formula for the vibration period evaluation ($T_1 = C\ H^{0,75}$) is not appropriate for MRF and EBF.

Conversely, for the CBF, the vibration period value is similar to that of the approximate formula.

Table III.28 – Summary of results of the vibration period T [s] of the structural typologies for 2A, 1Z: a) 1S; b) 2S; c) 4S; d) 6S respect to the standard formula ($T_{NTC2018}$= $CH^{3/4}$) and structural members cross section.

		Vibration Period T [s]					
Storey	**$CH^{3}/_{4}$**	**MRF**	**CBF V π**	**CBF V Λ**	**CBF X**	**CBF X D**	**EBF**
1S	0,11	0,46 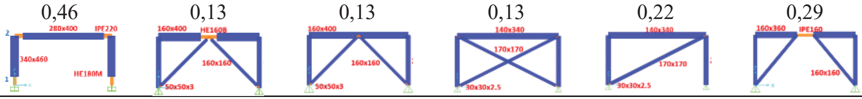	0,13	0,13	0,13	0,22	0,29
2S	0,19	0,64 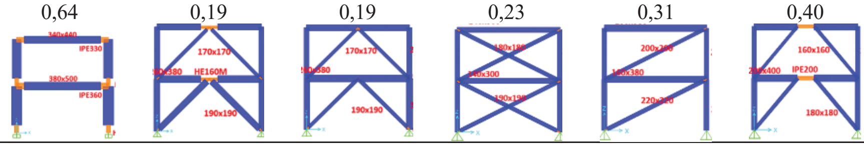	0,19	0,19	0,23	0,31	0,40
4S	0,32	0,91 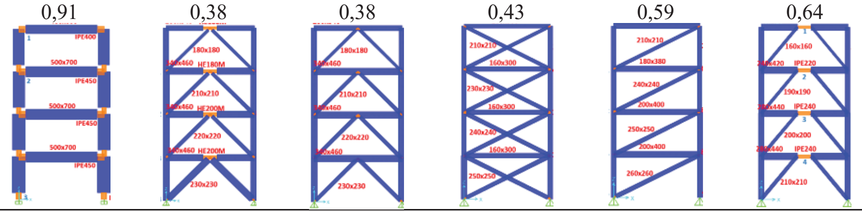	0,38	0,38	0,43	0,59	0,64
6S	0,44	1,03 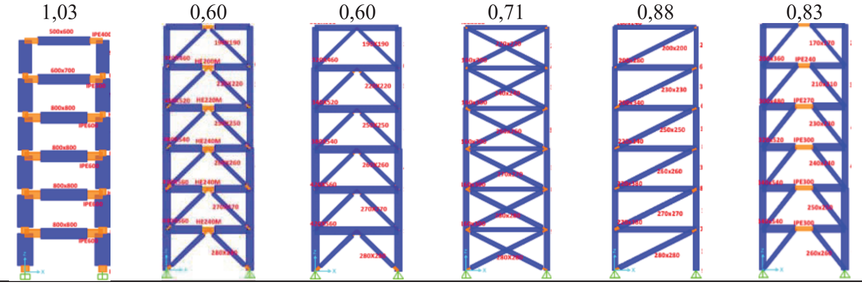	0,60	0,60	0,71	0,88	0,83

Strength and Stiffness

Below, the comparison between the push-over curves for MRF-SLV, MRF-SLD, CBF V π, CBF V Λ, CBF X, CBF X D and EBF is presented and the results, in terms of strength and stiffness, are analysed.

<u>MRF-SLV and MRF-SLD</u>

The MRF-SLD shows a greater lateral stiffness as respect to the MRF-SLV, since the MRF-SLD presents higher dimensions of the link sections, in the beam and at the base of the column, derived from the SLD seismic verification of structure horizontal displacement, as respect to MRF-SLV. In the same time, the MRF-SLD has a higher strength as respect to MRF-SLV, since the strength of the structure depends on the plastic strength of the link.

Therefore, the increase of the stiffness and strength of the MRF-SLD as respect to the MRF-SLV is motivated by the higher dimensions of the steel links section (Fig. III.16).

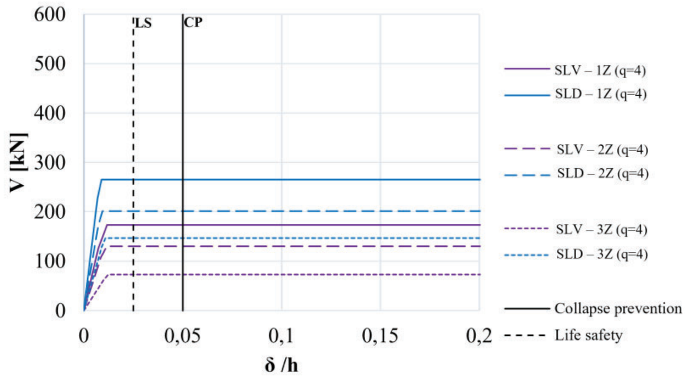

Figure III.65 – Pushover curves: 1S, MRF-SLD and MRF-SLV with $q=1$ and $q_d=4$ for 2A; 1Z.

<u>CBF V Λ and CBF V π</u>

The CBF V frames have been designed according to two different technological solutions: the CBF V Λ has a continuous timber beam and 1 steel plate to which the 2 diagonal links are welded, while CBF V π has a steel link, to which the 2 diagonal links are welded, in a discontinuous timber beam.

The strength of the structures depends on the plastic strength of the link and the stiffness is significantly influenced by the dimension of the diagonal link sections.

It is observed that, for the same seismic zone, the CBF V Λ and the CBF V π have almost the same strength and lateral stiffness, due the same dimension of the link sections.

The only difference between the CBFV Λ and CBFV π is the formation of the second plastic hinge which, in the CBFV π, occurs for greater deformations (Fig. III.17).

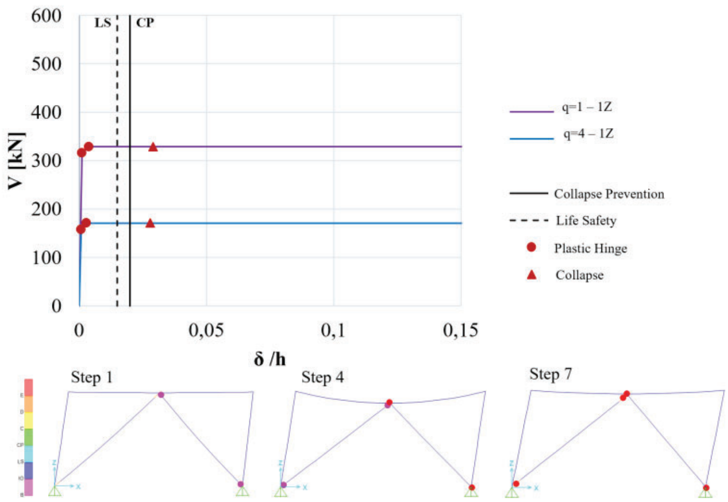

a)

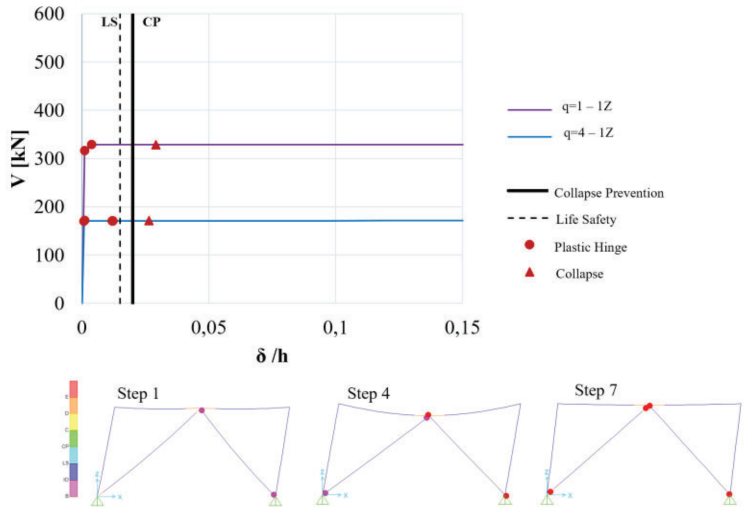

b)

Figure III.66 – Pushover curves for q_d=*1* and q_d=*4*, 1S; 2A; 1Z: a) CBFV Λ and b) CBFV π.

<u>CBF X and CBF X D</u>

The CBF X frames have been designed according to two different technological solutions: the CBF X has 2 diagonals (with 2 links for diagonal) and CBF X D has only 1 diagonal (with 2 links). Specifically, the CBF X D presents the same behaviour of a buckling restrained braces (BRB) system, in which the timber diagonal has a compressive and tensile strength.

The CBF X D has a less lateral stiffness, since when the links of the diagonal catch the complete rotation capacity of the plastic hinge, the structure reaches the collapse, while in the CBF X, the seismic force is shared between the other 2 links, ensuring further strength and stiffness to the structure.

EBF

The EBF shows no design variations except those relating to the different seismic areas and the ductility classes.

With the increase of the storey, the strength increases almost proportionally, but the stiffness decreases having increasingly the slender structures.

Below, the comparison between the push-over curves for MRF-SLV, MRF-SLD, CBF V π, CBF V Λ, CBF X, CBF X D and EBF, for 1S, 2S, 4S and 6S, with the behaviour factor q=4 (MRF, CBF X, CBF X D and EBF) and q=2 (CBF V π and CBF V Λ), for 2A and 1Z, is presented.

In particular, it is possible define a classification of the structural configuration in terms of strength and stiffness. The MRF shows the higher strength almost all the structural configurations, following by the CBF V and CBF X. It is apparent that CBF X D is the least efficient system among the types analysed, while the EBF shows an intermediate strength. It should be noted that the MRF-SLV has a lower strength than CBF V which, consequently, should be theoretically the structural type with the best behaviour, but the increase of the section dimensions in MRF-SLD involves an increase in strength. Up to 2 storey (1S and 2S) the MRF is the most resistant structure but, from 4 storey onwards (4S and 6S), the CBF V becomes the most resistant scheme due its behaviour factor q=2 respect to that of the other structures (q=4).

The CBF V has a higher stiffness, following by CBF X, due the presence of 2 diagonal braces. Specially, the CBF V presents a bigger stiffness than the CBF X due the presents of the steel link in the discontinuous timber beam, The CBF X D shows an intermediate stiffness between the CBF X and the EBF, while the MRF is the least efficient system. It is also observed that, with the seismic zone variation, the braced frames retain the same stiffness, while for the MRF, the stiffness decreases as the number of storey increases, as evidence of how stiffness is a very influential parameter for their seismic design (Fig. III.18).

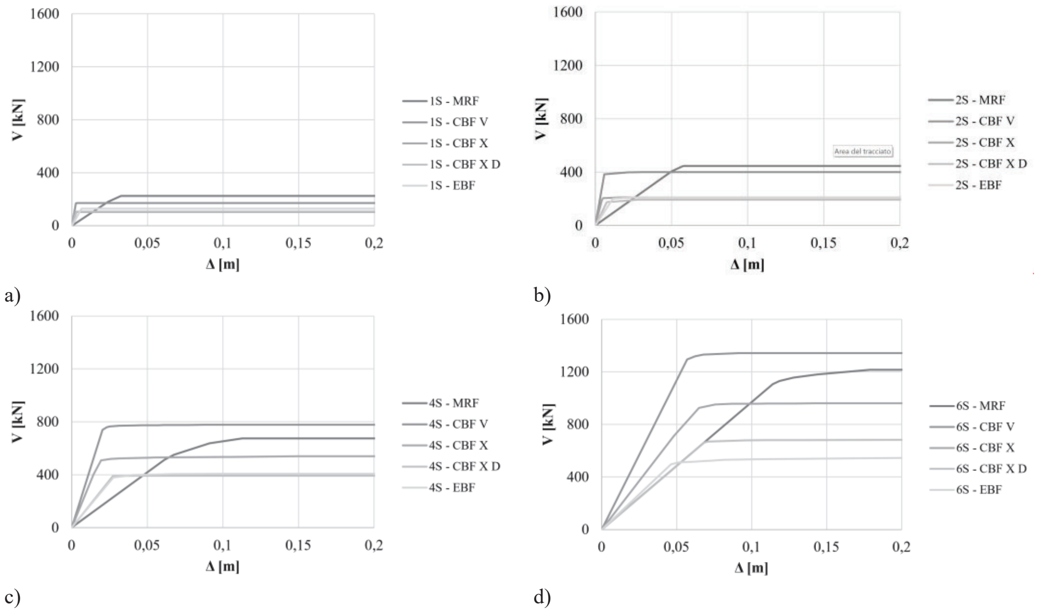

Figure III.67 – Pushover curves for q_d=4 (MRF, CBF X, CBF X D and EBF) and q_d=2 (CBF V Λ and CBFV π); 2A; 1Z: a) 1S; b) 2S; c) 4S and d) 6S.

It is also possible to do a comparison between the same structural schemes in steel construction material (Tab. III.22), for which the MRF structure has a higher strength, due the dimension of steel elements (specially of the column ones), following by the EBF, which presents an intermediate strength between the MRF and the CBF structures. The CBF X has, finally, a bigger strength than the CBF V.

The CBF X is the structural scheme with the highest stiffness, following by the CBF V and the EBF is the intermediate case between CBF and MRF, which is the least efficient system.

The strength classification of the examined cases is totally different from that of the steel structures because the timber diagonals of the braced structures are not subject to the buckling and, therefore, ensure a greater contribution to the structural strength. In terms of stiffness, on the other hand, the cases examined reflect the same behaviour as the steel structures.

Table III.29 – Comparison between timber and steel structural types in terms of strength and stiffness.

Strength		Stiffness	
Timber structures	**Steel structure**	**Timber structures**	**Steel structure**
MRF	MRF	CBF V	CBF X
CBF V	EBF	CBF X	CBF V
CBF X	CBF X	CBF X D	EBF
EBF	CBF V	EBF	MRF
CBF X D		MRF	

Behaviour factor q

In the Figure III.19, behaviour factor, q, with its contributions related to overstrength, q_{Ω}, and ductility, q_{μ} is presented and calculated according to three different conditions for the ultimate displacement d_u, corresponding at the achievement of the inter-storey drift equal to 2,5% (for MRF), 1,5% (for CBF and EBF) and 5% (for MRF), 2% (for CBF and EBF), as provided by FEMA 356 for steel structures, respectively, at Collapse Prevention limit and at Life Safety limit state, and at the Collapse Mechanism, with the labile mechanism and the achievement of the plastic hinge ultimate rotational capacity.

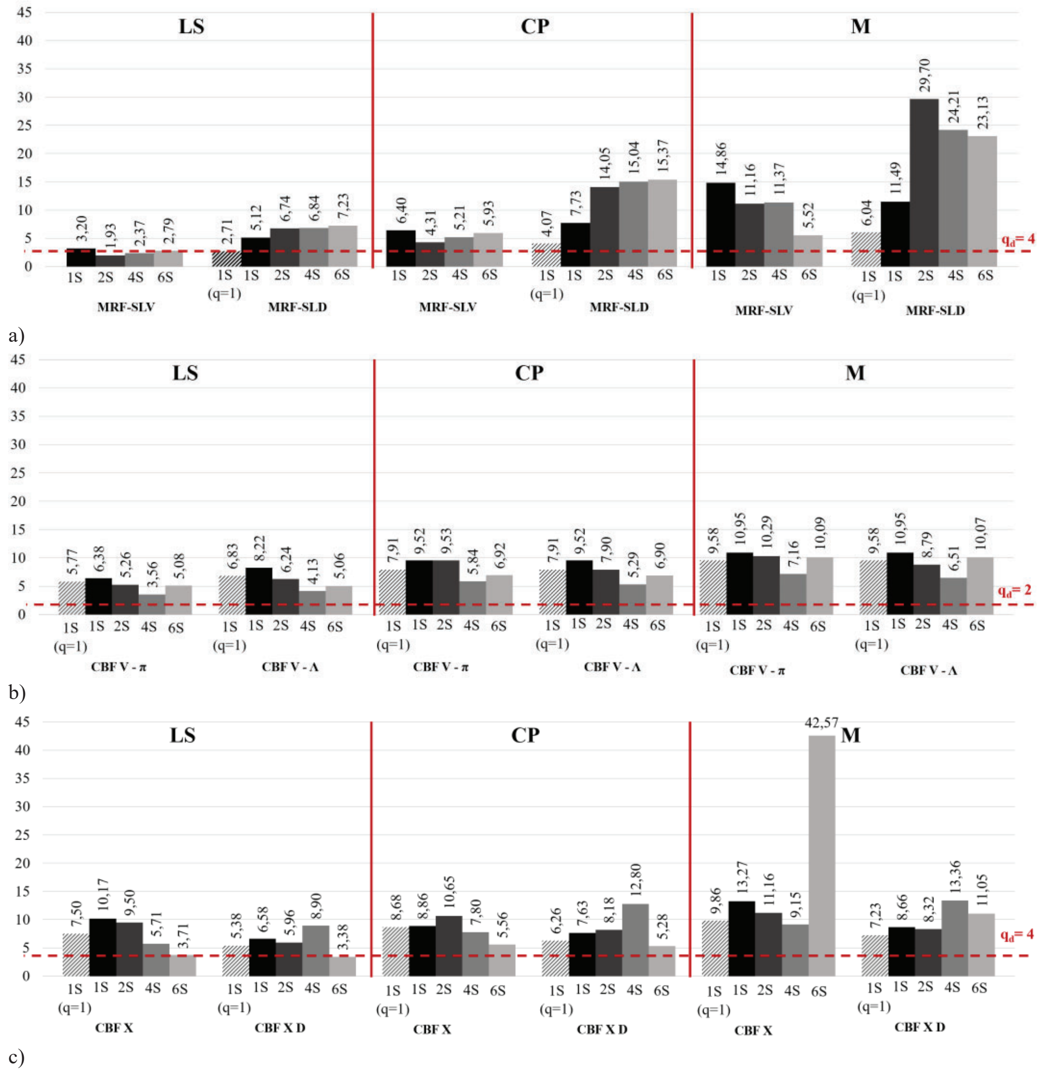

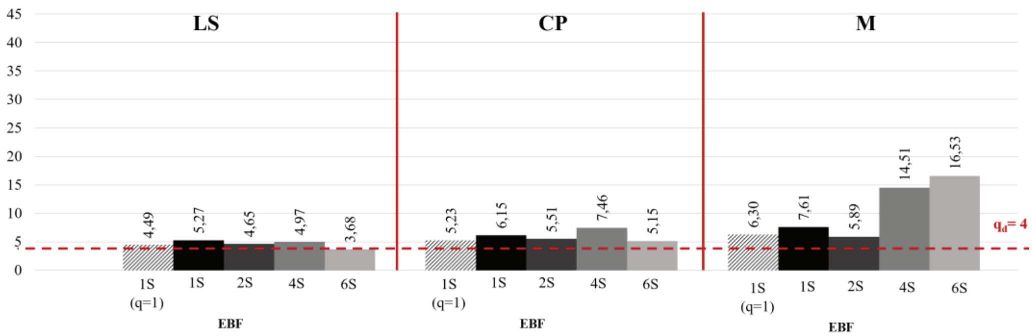

d)

Figure III.68 – Behaviour factor, *q*, evaluated for the inter-storey drift 2,5% (for MRF) and 1,5% (for CBF and EBF) at *Collapse Prevention limit state*; 5% (for MRF) and 2% (for CBF and EBF) at *Life Safety limit state*; at the *Collapse Mechanism* for 1S, 2S, 4S, 6S; 2A; 1Z: a) MRF-SLD and MRF-SLV with *q=1* and *q=4*; b) CBF V Λ and CBFV π with *q=1* and *q=2*; c) CBF X, CBF X D and d) EBF with *q=1* and *q=4*.

At Life Safety Limit State (LS), the MRF has a behaviour factor $q_{LS\text{-}MRF}$=5, the EBF $q_{LS\text{-}EBF}$=4, the CBF V π $q_{LS\text{-}CBF\ V\ \pi}$=4 and CBF V Λ $q_{LS\text{-}CBF\ V\ \Lambda}$=4, CBF X $q_{LS\text{-}CBF\ X}$=5 and CBF X D $q_{LS\text{-}CBF\ X\ D}$=4, evaluated as average between 1S, 2S, 4S, and 6S.

At Collapse Prevention Limit State (CP), the MRF has a behaviour factor $q_{CP\text{-}MRF}$=7, the EBF $q_{CP\text{-}EBF}$=5, the CBF V π $q_{CP\text{-}CBF\ V\ \pi}$=5 and CBF V Λ $q_{CP\text{-}CBF\ V\ \Lambda}$=5, CBF X $q_{CP\text{-}CBF\ X}$=7 and CBF X D $q_{CP\text{-}CBF\ X\ D}$=6, evaluated as average between 1S, 2S, 4S, and 6S.

At Collapse Mechanism (M), the MRF has a behaviour factor $q_{M\text{-}MRF}$=11, the EBF $q_{M\text{-}EBF}$=5, the CBF V π $q_{M\text{-}CBF\ V\ \pi}$=7 and CBF V Λ $q_{M\text{-}CBF\ V\ \Lambda}$=6, CBF X $q_{M\text{-}CBF\ X}$=9 and CBF X D $q_{M\text{-}CBF\ X\ D}$=7, evaluated as average between 1S, 2S, 4S, and 6S.

In particular, at Life Safety Limit State, the CBF X D and the EBF have the same value of the design q_d-factor, while the MRF, the CBF V and the CBF X have a higher value.

For the CBF V and CBF X, this is mainly due to the absence of buckling problem in the diagonal braces, which obviously increases the structural stiffness that has a directly influence on the ductility factor q_μ. The behaviour factor, q_d, used during the design, refers to the braced steel frames which present buckling problems with a less lateral stiffness of the structures. For the MRF, the MRF-SLD case presents a bigger q_{LS}-factor respect to the design one, q_d, due the high lateral deformation of the timber-steel system, while the MRF-SLV has a q_{LS}-factor very close to q_d.

Another important parameter that influences the q-factor is the vibration period, *T*. The factor q_μ, which represents the structural ductility, is assumed equal to:

$$q_\mu = \sqrt{2 \times \mu - 1} \qquad T_1 < T_c$$

$$q_\mu = \frac{d_u}{d_y} \qquad T_1 > T_c$$

where T_c is the limit vibration period between the constant acceleration and constant speed regions in the design response spectrum. If $T_1 < T_c$, the “Principle of Areas Equality” is applied while, if $T_1 > T_c$, the “Principle of Displacement Equality” is applied. From the first principle to the second one, there is an increase of ductility and of the q-factor, as it is possible to observe for the MRF ductility evaluation, from 2S to 6S.

At Collapse Prevention Limit State, the MRF, when $T_1 < T_c$, has q_M=7 while, when $T_1 > T_c$, the q-factor double, reaching q_M=14.

The same observation is possible to apply at the Collapse Mechanism (M). In particular, for MRF q_M-factor is double as respect to q_{CP}-factor evaluated at Collapse Prevention Limit State. For CBF V, CBF X and EBF there are minimal variations respect to Collapse when $T_1 < T_c$, while when $T_1 > T_c$, for 6S, a considerable increase of q_M-factor can be observed due the q_μ-factor.

Table III.30 – Behaviour factor q: summary of results.

	q_d (CDB)	q_{LS}	q_{CP}	q_M
MRF	4	5	7	11
CBF V π	2	4	5	7
CBF V Λ	2	4	5	6
CBF X	4	5	7	9
CBF X D	4	4	6	7
EBF	4	4	5	5

In the Table III.23 the q-factor for all the structural typologies is presented: design q-factor q_d, Life Safety Limit State q-factor q_{LS}, Collapse Prevention q-factor q_{CP} and Collapse Mechanism q-factor q_M. In particular, to evaluate the effective behaviour factor for the structures, the q_{LS} is considered and, for all the structures, side of safety, it possible to use a q-factor q_d=4.

Analysing the numerical results, the following observations can be drawn. First of all, the steel links play a key role in the structural strength since it is significantly influenced by their plastic strength. The influence of the dissipative joints, regarding the global stiffness, varies according to the structural type. In general, for braced frames (especially for the CBFs) the presence of links does not determine any variation of the stiffness, while, for MRF, the increase of the steel links section dimensions for the SLD verification, mostly that of the column-link, produces a stiffness and strength variation. The analysis is started from the one-storey structures and 1A, 2A and 3A plan layout is studied to understand if the q-factor, q_d, of the steel structure could be apply also for the hybrid-structures timber-steel. Ascertained this phase, the multi-storey structures are analysed 2S, 4S and 6S, for which there was a proportional variation of the strength and the stiffness, with the low variation of q-factor. Regarding the vibration period of the structures, as the number of storeys and the plan layout change, only the CBF showed values similar to the design vibration period, therefore the standard approximate formula is not very efficient for hybrid-structures timber-steel.

With regards to the structural mass variation of the dissipative structure as respect to the non-dissipative ones, for EBF, CBF X and CBF X D there is a consistent reduction of the mass with a maximum value equal to 72%, while, for the MRF, there is not a so high advantage, due the SLD verification.

3.1.7 STRUCTURAL DETAILS

In this chapter, 3D-models of the different structural types, created with GOOGLE SKETCHUP, are proposed. The different details of the hypothesis of connections are shown for each one (from Figure III.20 to Figure III.23).

Below, the structural details of MRF structure are presented. In particular, in Figure III.20a there is the global 3D-model for 2S of the MRF structure; in the Figures III.20b,c,d there is the assemblage between the timber members and the steel link with glued bars. The column-beam node is characterized by an assemblage between 2 steel links: column-link (that is a dissipative element only at the base of column) and beam-link (dissipative element). The connection between the column and beam links is designed by bolts. In particular, how it is possible to note, the connection is designed to be removed after earthquake.

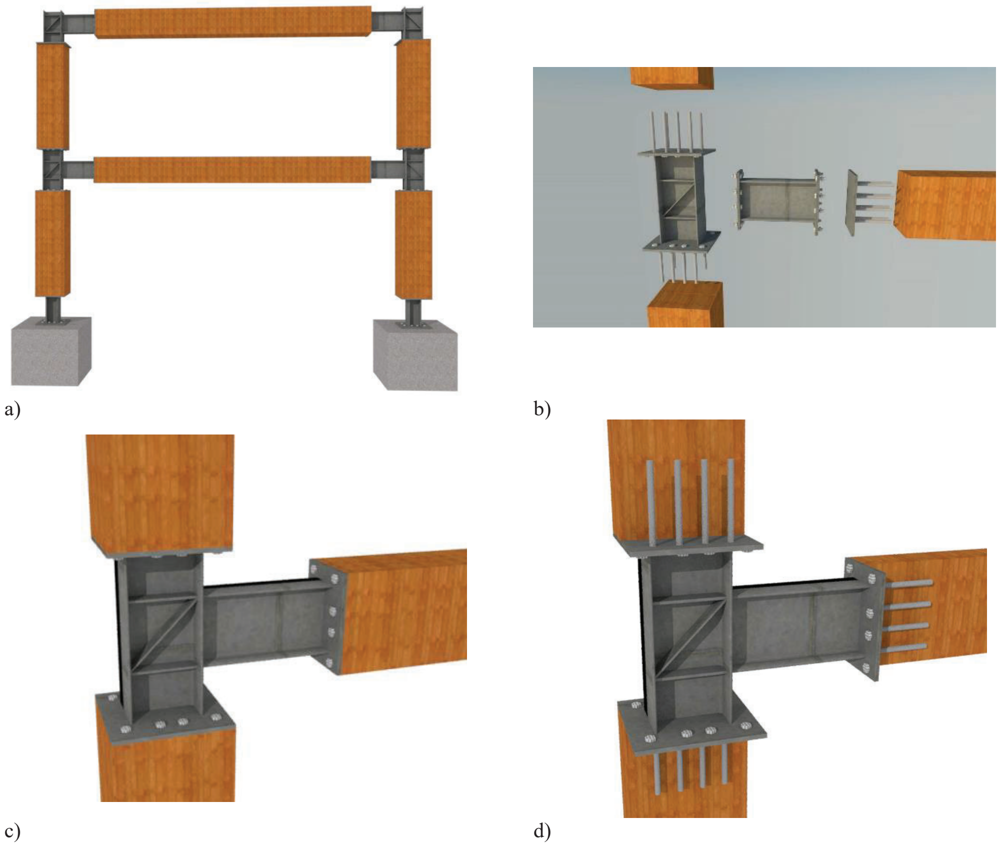

Figure III.69 – Example of MRF structure 2S: a) global 3D-model; b), c) and d) assemblage between the timber beam, columns and the steel link with glued bars.

Below, the structural details of CBF V π and CBF V Λ structures are presented. In particular, in Figure III.21a and Figure III.21b there is the global 3D-model for 2S of, respectively, CBF V π and CBF V Λ structures; in the Figures III.21c and Figure III.21d there is the assemblage between the timber members and the steel link for both the technological. In particular, CBF V π (Fig. III.21c) has a steel link, to which the 2 diagonal links are welded, with a discontinuous timber beam. The horizontal steel (non-dissipative) link is connected to the timber beam through glued bars, while the dissipative links are connected to the timber diagonals through an internal plate with bolts.

The CBF V Λ (Fig. III.21d), however, has a continuous timber beam and 1 steel plate, to which the 2 diagonal links are welded, that is connected to the beam through vertical bolts.

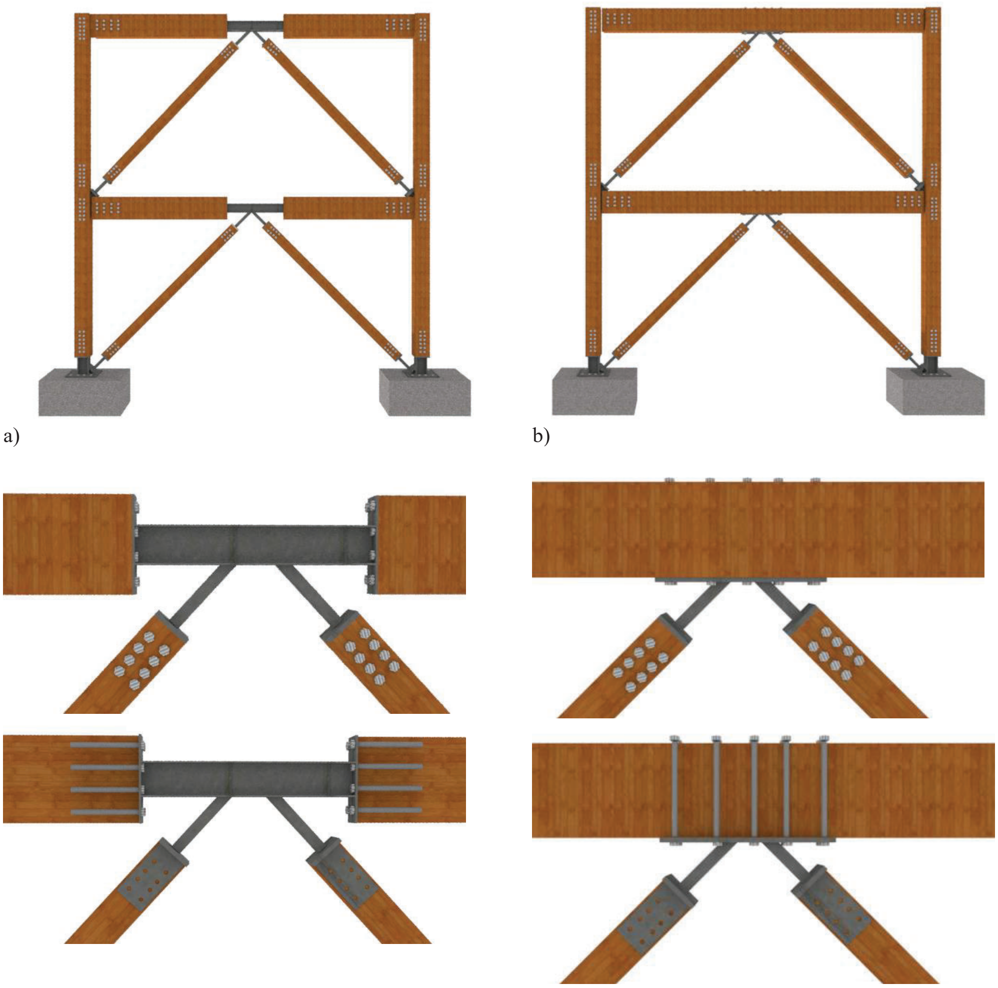

a) b) c) d)

Figure III.70 – Example of CBF V Λ and CBFV π structure 2S: a) CBFV π and b) CBFV Λ global 3D-models; c) CBFV π assemblage between the timber beams, diagonals and the steel link with glued bars; d) CBFV Λ assemblage between the timber beam, diagonals and the steel link with glued bars.

In the Figure III.22a is presented the detail assemblage of the CBF V π link with the timber structure. In particular, the connection is designed to be removed after earthquake. In Figure III.22b is indicated the connection between the dissipative link and the column with the foundation, in the Figure III.22c,d is presented the connection between the dissipative link, the beam and the column.

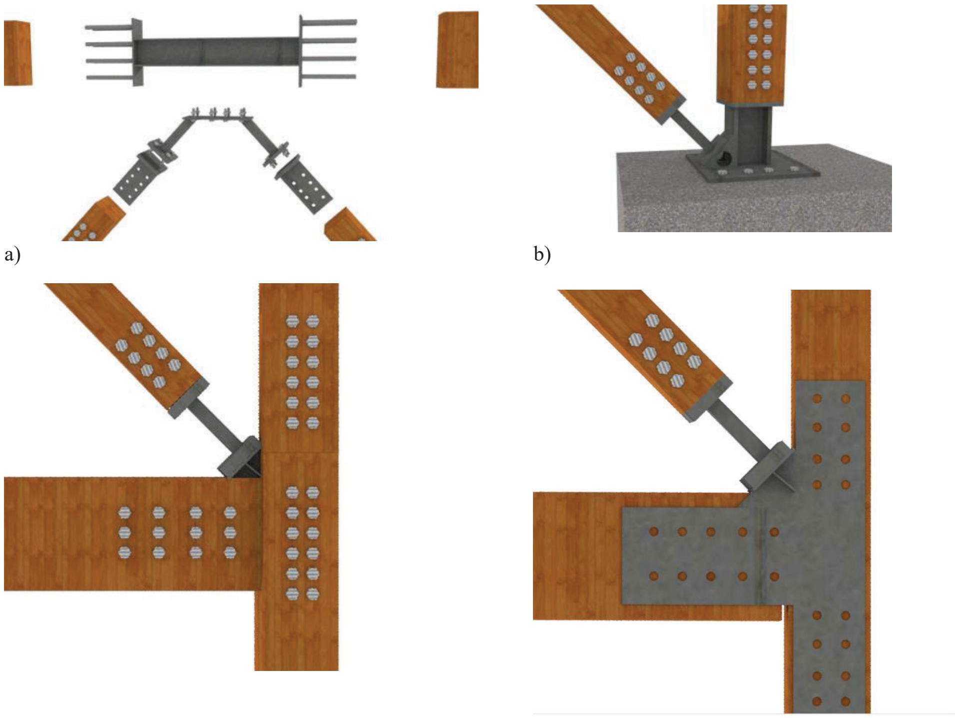

a) b) c) d)

Figure III.71 – Example of CBFV π structure 2S: a) assemblage between the timber beam, diagonals and the steel link with glued bars; b), c) and d) assemblage between the timber beam, diagonals and column.

Below, the structural details of CBF X D and EBF structures are presented. In particular, in Figure III.23a and Figure III.23b there is the global 3D-model for 2S of, respectively, CBF X D and EBF structures; in the Figures III.23c and Figure III.43d there is the assemblage between the timber members and the steel link for EBF. In particular, the EBF has a link that is connected, through bolts, to 2 internal steel plates in the timber beam with horizontal bots.

The timber diagonals are connected to the structure through an internal steel plate with horizontal bolts.

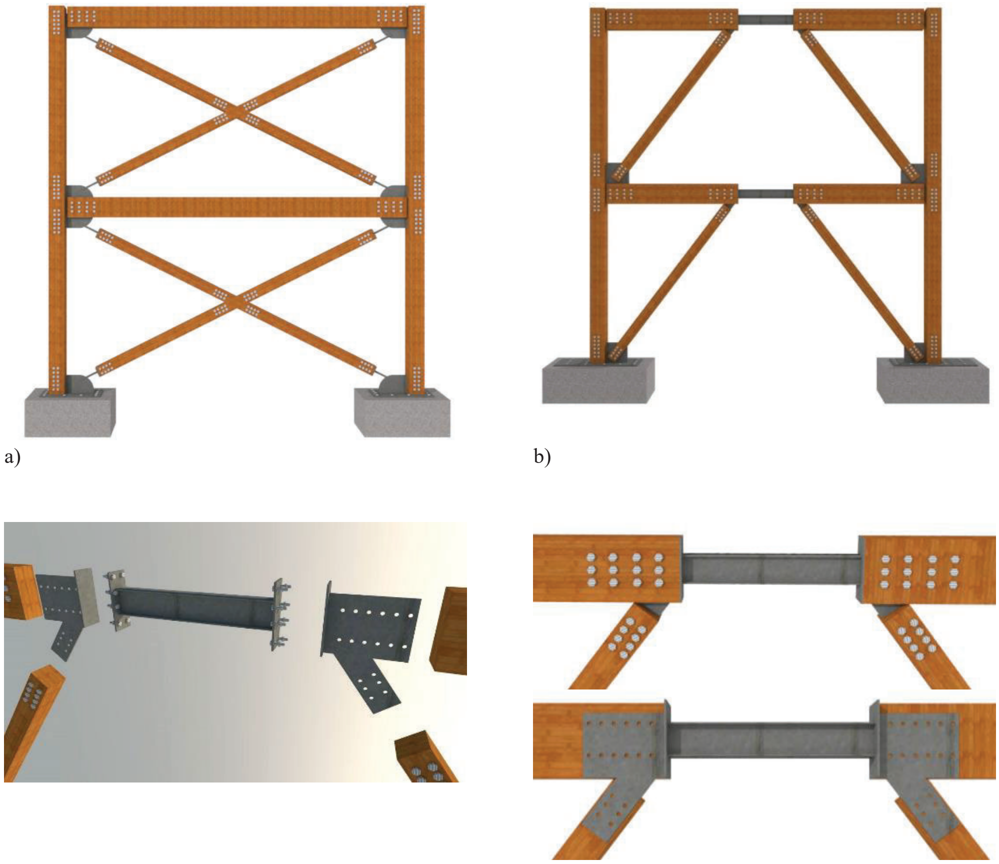

a) b) c) d)

Figure III.72 – Example of CBF X and EBF structure 2S: a) CBF X and b) EBF global 3D-models; c) and d) EBF assemblage between the timber beam, diagonals and the long steel link with glued bars.

3.2 Seismic resistant heavy timber frame structures with FVD devices

3.2.1 Methodology of analysis

The chapter deals with the application of fluid viscous dampers (FVD) for the development of seismic resistant timber frames, characterized by assemblage of beams and columns: FVDs have the aim of dissipating seismic energy, while timber elements and steel connections remain in the elastic field. Specifically, 2D single-storey structures with dissipative bracing systems, equipped with FVDs, in different configurations, are studied, assuming several rates of possible dampings, designing the structural sizes through linear dynamic analysis. Therefore, nonlinear dynamic time history analyses are performed considering a group of 7 accelerograms compatible with the design elastic response spectrum, using the structural calculation program SAP2000 (v18).

Eleven structural schemes are designed by varying the ξ_{eff} coefficient with a total of 29 structures, and 203 non-lineal dynamic analysis are carried out. The study is aimed at proving the suitability and the efficiency of the system.

3.2.2 Study cases

3.2.2.1 Design parameters

A numerical parametric study is carried out on 11 2D single-storey frame types.

The plan layout considered for all the structural schemes is:

- 1A (1 span in transversal direction x).

The structural elevation scheme considered is:

- 1S (1-storey);

Dissipative seismic-resistant timber frame types, with dissipative bracing systems, equipped with FVDs, differing for the position of the seismic devices are considered:

- MRF (moment resisting frame, without FVDs);
- MRF-D (with only one diagonal);
- MRF-H_iL_j (i,j= 1,2,3. H_i and L_j define the location at the column and at the beam, and then the inclination, of the dissipative brace).

Structures are designed according to the technical standards Eurocode 5 and Eurocode 8 (EC5, EC8), through linear and non-linear dynamic analysis, considering the seismic zone of the OPCM 3274 (20/03/2003) assumed for the sake of simplicity:

- 1Z (seismic zone 1: 0,35g).

The structures equipped with FVDs are designed by varying the equivalent viscous damping coefficient ξ_{eff}:

- 5% (MRF);
- 20% (MRF-H_1L_2; MRF-H_1L_3; MRF-H_2L_1; MRF-H_2L_2; MRF-H_2L_3; MRF-H_3L_1; MRF-H_3L_2)
- 10, 15, 20, 25, 30, 40, 50% (MRF-D; MRF-H_1L_1; MRF-H_3L_3).

The parametric analysis carried out for the structural systems are shown in Table III.24.

Table III.31 – Parametric analysis: types of seismic-resistant frames.

	MRF	**MRF D**	**MRF H_1L_1**	**MRF H_1L_2**	**MRF H_1L_3**	**MRF H_2L_1**	**MRF H_2L_2**	**MRF H_2L_3**	**MRF H_3L_1**	**MRF H_3L_2**	**MRF H_3L_3**
ξ_{eff} [%]	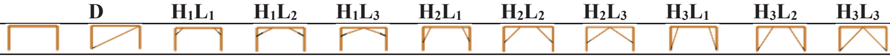										
	5	10,15,20,25,30, 40,50					20				10,15,20,25, 30,40,50

3.1.2.2 Geometrical and material features

The 1-span scheme (1A) is 3 m high with a rectangular plan layout 6x18m wide, 6m in the longitudinal direction y. The floor is oriented along the transverse direction supported by secondary beams in the longitudinal direction (Fig. III.24). Each structure has 4 seismic-resistant frames for storey, 2 for each direction.

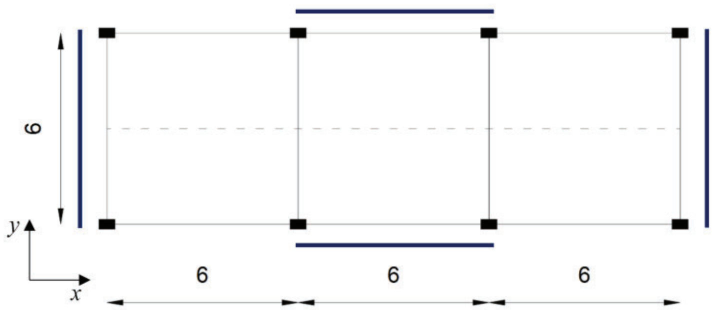

Figure III.73 – Plan layout [m].

Each single seismic-resistant frame is characterized by a column height of 3 m and a beam length of 6 m. MRF doesn't have FVDs, MRF-D is characterized by one FVD at the end of the diagonal (base column-diagonal) while MRF-H_iL_j are characterized by two FVDs, one for each brace. All the structural schemes considered for the analysis are indicated in the Figure III.25.

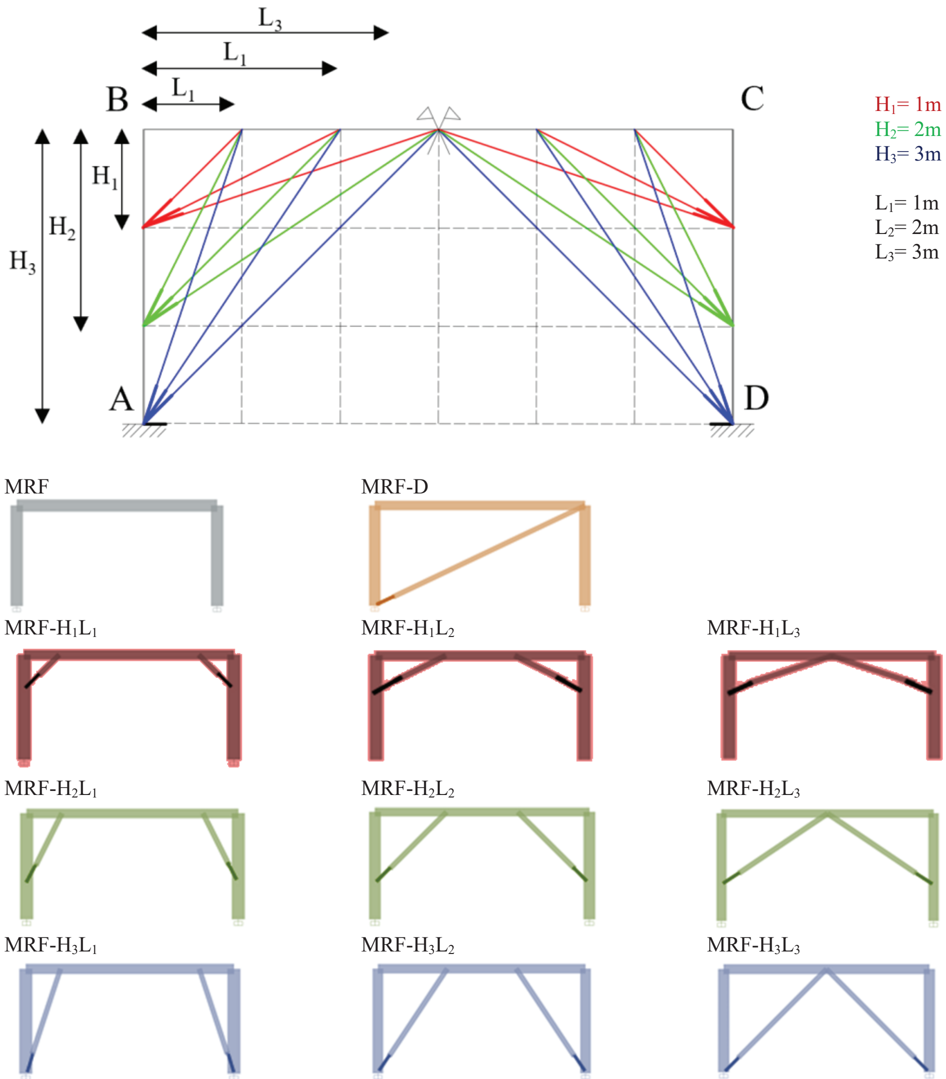

Figure III.74 – Types of seismic-resistant frames [m].

Structural members are made of glulam timber GL28h grade while the joints are in S235 steel grade (Tab. III.25).

Table III.32 – Material characteristics: timber and steel.

Timber: GL28h				**Steel: S235**	
$f_{m,g,k}$ [MPa]	28	$E_{0,g,mean}$ [MPa]	12600	$f_{y,k}$ [MPa]	235
$f_{t,0,g,k}$ [MPa]	19,5	$E_{0,05}$ [MPa]	10200	$f_{t,k}$ [MPa]	360
$f_{t,90,g,k}$ [MPa]	0,45	$E_{90,g,mean}$ [MPa]	420	E [MPa]	210000
$f_{c,0,g,k}$ [MPa]	26,5	$G_{g,mean}$ [MPa]	780		
$f_{c,90,g,k}$ [MPa]	3,0	$E_{0,g,mean}$ [MPa]	12600		
$f_{v,g,k}$ [MPa]	3,2	$E_{0,05}$ [MPa]	10200		

The value of the safety coefficients of the materials (k_{mod}, k_{def}, Υ_m,) for timber and timber-based structural products are indicated below (Tab. III.26).

Table III.33 – Safety coefficients

Service class	**Load-duration class**	K_{mod}	K_{def}	Υ_m
2	Medium-term	0,8	1	1,45
	Instantaneous (seismic condition)	1		

3.2.3 Loads analysis

3.2.3.1 Vertical loads

The floor consists of timber planks with a thin concrete screed and tiles (Tab. III.27). The only variable load (Q) that is considered is the operating load that, for residential build, is relating to category A.

Table III.34 – Characteristic loads.

Load	
G_{K1}	0,22 kN/m^2
G_{K2}	1,30 kN/m^2
Q	2,00 kN/m^2

The longitudinal seismic resistant frames (longitudinal direction x) are distinguished from the transversal ones (transversal direction y) due to the different loading conditions: on the longitudinal frames there is a distributed load while on the transversal frames there is a force due to the secondary beam (Fig. III.26).

On each longitudinal frame there is the following distributed load:

$$q = 7{,}85 \mathrm{kN/m}$$

On each transversal frame there is the following force:

$$F = 42{,}82 \mathrm{kN}$$

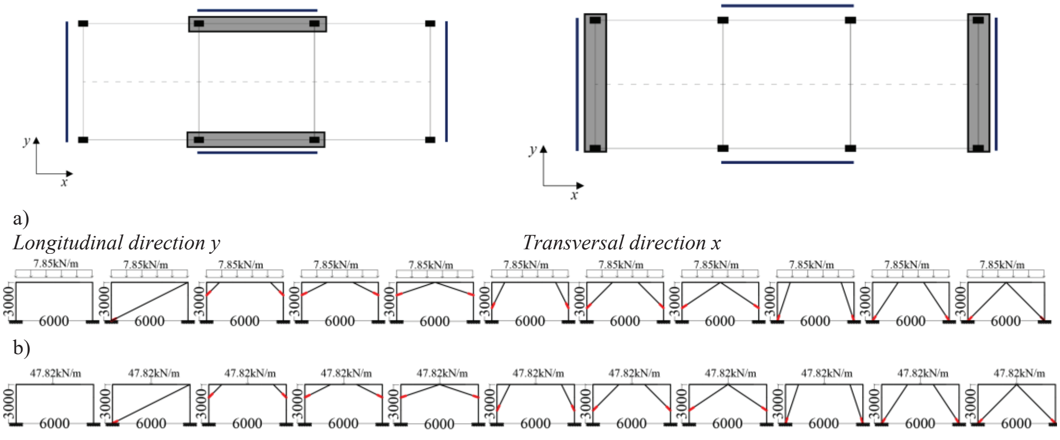

Figure III.75 – a) Seismic resistant structures position; b) longitudinal direction y; c) transversal direction x [mm].

3.1.3.2 Seismic loads

For the structural members sizes design a linear dynamic analysis is used. In order to assess the structures' response under seismic actions, the 1 seismic zone (1Z) defined in the OPCM 3274 of 03/20/2003 is considered with a value of a_g= 0,35g.

The OPCM 3274 is used only for the response spectra (elastic) definition, while the seismic action evaluation and the structural design refer to the currently standards: NTC 2018, Eurocode 5 and Eurocode 8.

For the seismic design, the following limit states are considered: limit state for the safeguard of human life or Ultimate state (SLU); limit state of prompt use or Damage state (SLD).

For simulating the inelastic dissipative capacity of the structures due to the presence of the FVDs, a reduction of the elastic forces is considered for MRF-D, MRF-H_1L_1 and MRF-H_3L_3 structures by varying the equivalent viscous damping coefficient ξ_{eff} from 10% to 50%, while for the other structural typologies MRF-H_iL_j a damping coefficient ξ=*20%,* being in the range 5-28% of conventional values according to current standards (EC8), obtaining the corresponding acceleration and displacement response spectrum. Of course, the damping coefficient for MRF without dissipative devices is assumed equal to 5%.

A "category B" soil has been hypothesized, in which S=1,25, T_B=0,15 T_C=0,50 T_D=2.

The elastic response spectrum for the structures is reported in the Figure III.27a,b respectively for SLU and SLD.

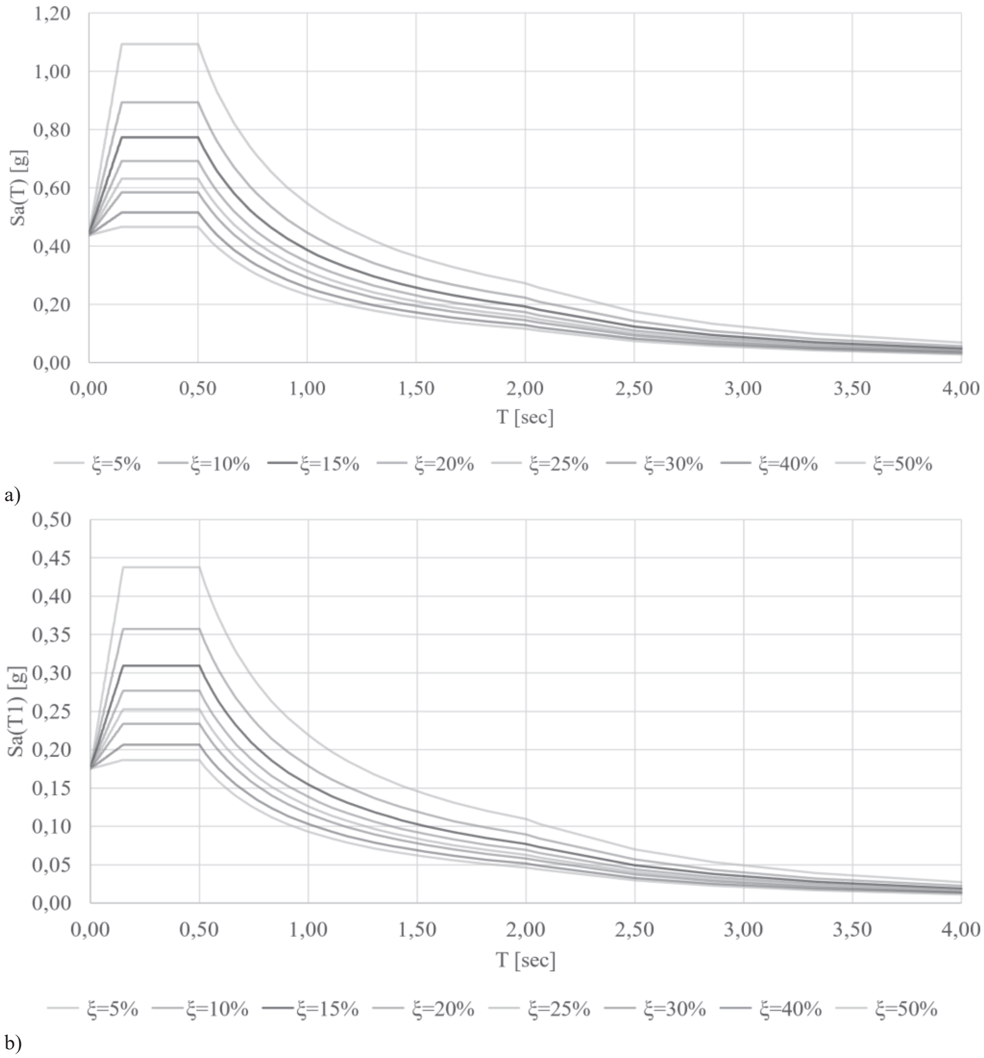

Figure III.76 – Design response spectra in terms of accelerations for the 1 seismic zone by varying ξ coefficient, for a) SLU and b) SLD.

An approximate evaluation of the vibration period of the structure can be made by the following formula.

$$T = C_1 \cdot H^{0,75}$$

$$T = 0,05 \cdot (3)^{0.75} = 0,11s$$

To evaluate the seismic mass, it is necessary to calculate the masses associated with gravitational loads, combined according to the following seismic combination defined in the NTC 2018:

$$W = G_{1k} + G_{2k} + \sum_j \psi_{2j} \cdot Q_{kj}$$

- G_{1k} takes into account the weight of the planks, beams, columns and bracings;
- G_{2k} takes into account the weight of the screed and flooring;
- ψ_{2j} is the combination coefficient of the variable load Q_{kj} which takes into account the probability that all loads $\psi_{2j} x Q_{kj}$ are present on the entire structure at the time of the earthquake.

3.1.3.3 LOADS COMBINATIONS

The loads combinations considered are indicated in § 2.5.3. of the NTC'08 and are shown below. For the gravitational loads:

Ultimate State limit

$$q_{SLU} = \gamma_{G1} \cdot G_1 + \gamma_{G2} \cdot G_2 + \gamma_{Q1} \cdot Q_{k1} + \gamma_{Q2} \cdot \Psi_{02} \cdot Q_{k2} + \gamma_{Q3} \cdot \Psi_{03} \cdot Q_{k3} + \cdots$$
$$q_{SLU} = 1{,}3 \cdot 0{,}22 + 1{,}5 \cdot 1{,}3 + 1{,}5 \cdot 2{,}0 = 5{,}24\ \mathrm{kN/m^2}$$

For SLE, rare and semi-permanent combinations are considered for deformability checks:

Rare combination

$$q_{rara} = G_1 + G_2 + Q_{k1} + \Psi_{02} \cdot Q_{k2} + \Psi_{03} \cdot Q_{k3} + \cdots$$
$$q_{rara} = 0{,}22 + 1{,}30 + 2{,}00 = 3{,}52\mathrm{kN/m^2}$$

Semi-permanent combination

$$q_{semi-perm.} = G_1 + G_2 + \Psi_{21} \cdot Q_{k1} + \Psi_{22} Q \cdot_{k2} + \cdots$$
$$q_{semi-perm.} = 0{,}22 + 1{,}30 = 1{,}52\ \mathrm{kN/m^2}$$

The seismic combination considered are indicated in § 2.5.3. of the NTC 2018 and are shown below.

$$q_{SLU,seismic} = E + G_1 + G_2 + \Psi_{21} \cdot Q_{k1} + \Psi_{22} \cdot Q_{k2} + \cdots$$

3.2.4 STRUCTURAL DESIGN

The linear-dynamic analysis is carried out to the member sizes design, using the structural calculation program SAP2000. For timber elements verification, the formulas present in the EC5 are used while the steel joints are designed using the formulas present in the EC3. The outputs of the analysis are presented in terms of structural sections and damping constant C (Tab. III.28), that is evaluated based on the equivalent viscous damping coefficient ξ_{eff} required to the system (structure + FVDs), using the following formula:

$$C = \xi_d \cdot 2 \cdot \omega \cdot m$$
$$\xi_d = \xi_{eff} - \xi_0$$

Where:

- ω is the natural frequency of the structure;
- m is the structural mass;
- ξ_d is the damping ratio of the FVD device;
- ξ_{eff} is the total effective damping ratio of the system (structure + FVDs), varying from 10% to 50%;
- ξ_0 is the inherent damping ratio of the structure, equal to 5.

Table III.35 – Structural sizes and *C* coefficients for MRF structures by varying the damping coefficient ξ [cm]

ξ_{eff} [%]		**MRF** 	**MRF D** 	**MRF H_1L_1** 	**MRF H_1L_2** 	**MRF H_1L_3** 	**MRF H_2L_1** 	**MRF H_2L_2** 	**MRF H_2L_3** 	**MRF H_3L_1** 	**MRF H_3L_2** 	**MRF H_3L_3** 
5	**B**	24x36	/	/	/	/	/	/	/	/	/	/
	C	36x38	/	/	/	/	/	/	/	/	/	/
	D	14x14	/	/	/	/	/	/	/	/	/	/
	C	/	/	/	/	/	/	/	/	/	/	/
10	**B**	/	20x28	22x32	/	/	/	/	/	/	/	22x28
	C	/	32x34	36x36	/	/	/	/	/	/	/	32x36
	D	/	14x14	14x14	/	/	/	/	/	/	/	14x14
	C	/	*23*	*14*	/	/	/	/	/	/	/	*12*
15	**B**	/	20x26	20x30	/	/	/	/	/	/	/	20x26
	C	/	28x28	34x36	/	/	/	/	/	/	/	30x32
	D	/	14x14	14x14	/	/	/	/	/	/	/	14x14
	C	/	*37*	*25*	/	/	/	/	/	/	/	*20*
20	**B**	/	16x24	22x24	22x24	20x24	22x24	22x24	20x24	22x26	22x26	20x26
	C	/	24x24	36x38	34x36	34x34	36x36	34x32	30x32	34x36	30x32	26x28
	D	/	14x14	14x14	14x14	14x14	14x14	14x14	14x14	14x14	14x14	14x14
	C	/	*42*	*36*	*36*	*34*	*39*	*32*	*25*	*41*	*31*	*24*
25	**B**	/	16x20	20x26	/	/	/	/	/	/	/	12x22
	C	/	22x22	32x34	/	/	/	/	/	/	/	26x26
	D	/	14x14	14x14	/	/	/	/	/	/	/	14x14
	C	/	*41*	*44*	/	/	/	/	/	/	/	*30*
30	**B**	/	14x20	20x26	/	/	/	/	/	/	/	16x20
	C	/	20x20	30x34	/	/	/	/	/	/	/	24x24
	D	/	14x14	14x14	/	/	/	/	/	/	/	14x14
	C	/	*50*	*51*	/	/	/	/	/	/	/	*32*
40	**B**	/	12x20	20x26	/	/	/	/	/	/	/	14x20
	C	/	18x18	30x30	/	/	/	/	/	/	/	20x20
	D	/	14x14	14x14	/	/	/	/	/	/	/	14x14
	C	/	*59*	*69*	/	/	/	/	/	/	/	*34*
50	**B**	/	12x20	18x26	/	/	/	/	/	/	/	12x20
	C	/	16x16	28x30	/	/	/	/	/	/	/	18x18
	D	/	14x14	/	/	/	/	/	/	/	/	14x14
	C	/	*65*	*90*	/	/	/	/	/	/	/	*37*

B: beam; C: column; D: diagonal; *C*: damper constant of FVD

In the Table III.29 is presented the structural mass for each structure.

Table III.36 – Structural mass [kg].

ξ [%]	MRF	MRF-D	MRF-H_1L_1	MRF-H_1L_2	MRF-H_1L_3	MRF-H_2L_1	MRF-H_2L_2	MRF-H_2L_3	MRF-H_3L_1	MRF-H_3L_2	MRF-H_3L_3
5	676	/	/	/	/	/	/	/	/	/	/
10	/	459	498	/	/	/	/	/	/	/	503
15	/	375	492	/	/	/	/	/	/	/	432
20	/	290	489	467	453	485	427	383	481	418	375
25	/	252	396	/	/	/	/	/	/	/	299
30	/	221	379	/	/	/	/	/	/	/	289
40	/	193	349	/	/	/	/	/	/	/	235
50	/	176	322	/	/	/	/	/	/	/	207

3.2.5 SEISMIC PERFORMANCE EVALUATION

3.2.5.1 METHODOLOGY OF THE ANALYSIS

Non-linear analysis (Fast Nonlinear Analysis) on the structures is carried out using the structural calculation program SAP2000. 7 earthquake accelerograms compatible with the design response spectrum assumed are selected through REXEL (Iervolino et al, 2010). They are reported in Table III.30 and Figure III.28. A total of 203 analyses on 29 structures are carried out.

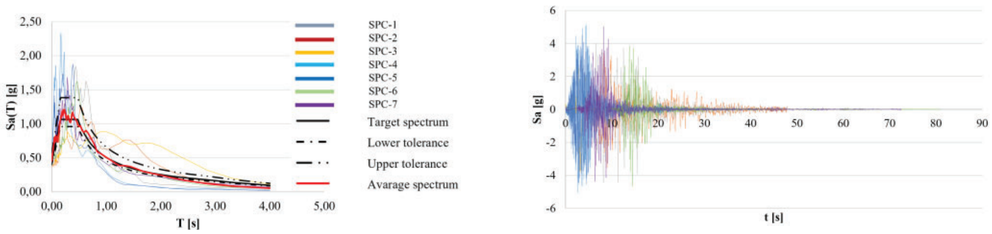

a) b)

Figure III.77 – REXEL (OPCM 3274, ag=0,35g): 7 response spectrum and b) earthquake accelerograms compatible with the design response spectrum.

Table III.37 – Earthquakes accelerograms selected

Accelerograms	Earthquake ID	Station ID	Earthquake	Mw	Epicentral Distance [km]	PGA_X [m/s^2]	PGA_Y [m/s^2]
ACC-1	1635	ST2484	South Iceland	6,5	7	0,61	0,50
ACC-2	1635	ST2482	South Iceland	6,5	15	0,20	0,47
ACC-3	93	ST62	Montenegro	6,5	25	0,45	0,30
ACC-4	286	ST60	Umbria Marche	6	11	0,51	0,45
ACC-5	286	ST60	Umbria Marche	6	11	0,51	0,45
ACC-6	93	ST67	Montenegro	6,9	16	0,37	0,36
ACC-7	250	ST205	Erzincan	6,9	13	0,38	0,50
	mean			6,4	14	0,43	0,43

The more complicated problem associated with large displacements, which cause large strains in all members of the structure, requires a tremendous amount of computational effort and computer time to obtain a solution. However, certain types of large strains, such as those in rubber base isolators and gap elements, can be treated as a lumped nonlinear element using the Fast Nonlinear Analysis (FNA) method. Fast Nonlinear Analysis (FNA) is a modal analysis method useful for the static or dynamic evaluation of linear or nonlinear structural systems. Because of its computationally efficient formulation, FNA is well-suited for time-history analysis, and often recommended over direct-integration applications. During dynamic-nonlinear FNA application, analytical models should:

- Be primarily linear-elastic;
- Have a limited number of predefined nonlinear members;
- Lump nonlinear behaviour within link objects.
-

In addition to nonlinear material force-deformation relationships, these link objects may simulate concentrated damping devices, isolators, and other energy-dissipating technologies.

The FNA (Fast Nonlinear Analysis, Ibrahimbegovic and Wilson, 1989; Wilson, 1993) method is a simple approach in which the fundamental equations of mechanic (equilibrium, force-deformation and compatibility) are satisfied. The *exact* force equilibrium of the computer model of a structure at time *t* is expressed by the following matrix equation:

$$\mathbf{M}\ddot{\mathbf{u}}(t) + \mathbf{C}\dot{\mathbf{u}}(t) + \mathbf{K}\mathbf{u}(t) + \mathbf{R}_{NL}(t) = \mathbf{R}(t)$$

where $\boldsymbol{M}$, $\boldsymbol{C}$ and $\boldsymbol{K}$ are the mass, proportional damping and stiffness matrices, respectively. The size of these three-square matrices is equal to the total number of unknown node point displacements. The elastic stiffness matrix $\boldsymbol{K}$ neglects the stiffness of the nonlinear elements. The time-dependent vectors $\ddot{\boldsymbol{u}}(t)$, $\dot{\boldsymbol{u}}(t)$, $\boldsymbol{u}(t)$ and $\boldsymbol{R}(t)$ are the node point acceleration, velocity, displacement and external applied load, respectively. And $\boldsymbol{R}_{NL}(t)$ is the global node force vector from the sum of the forces in the nonlinear elements and is computed by iteration at each point in time.

The first step in the solution of previously equation is to calculate a set of *N* orthogonal Load Dependent Ritz vectors, Φ, which satisfy the following equations:

$$\Phi^T\mathbf{M}\boldsymbol{\Phi} = \mathbf{II}$$
$$\Phi^T\mathbf{K}_L\boldsymbol{\Phi} = \Omega^2$$

where I is a unit matrix and Ω^2 is a diagonal matrix in which the diagonal terms are defined as ω^2_n. The response of the system can now be expressed in terms of those vectors by introducing the following matrix transformations:

$$\mathbf{u}(t) = \boldsymbol{\Phi}\mathbf{Y}(t) \qquad \dot{\mathbf{u}}(t) = \boldsymbol{\Phi}\dot{\mathbf{Y}}(t) \qquad \ddot{\mathbf{u}}(t) = \boldsymbol{\Phi}\ddot{\mathbf{Y}}(t)$$

If the computer model is unstable without the nonlinear elements, one can add "effective elastic elements" (at the location of the nonlinear elements) of arbitrary stiffness. The exact equilibrium equations can be written as:

$$\mathbf{M}\ddot{\mathbf{u}}(\mathrm{t}) + \mathbf{C}\dot{\mathbf{u}}(\mathrm{t}) + (\mathbf{K} + \mathbf{K_e})\mathbf{u}(\mathrm{t}) = \mathbf{R}(\mathrm{t}) - \mathbf{R}_{\mathrm{NL}}(\mathrm{t}) + \mathbf{K_e}\mathbf{u}(\mathrm{t})$$

The substitution of those equations into principal equation and the multiplication of both sides of the equation by Φ^T yield a set of N uncoupled equations expressed by the following matrix equation:

$$\mathbf{I}\ddot{\mathbf{Y}}(\mathrm{t}) + \mathbf{\Lambda}\dot{\mathbf{Y}}(\mathrm{t}) + \mathbf{\Omega}\mathbf{Y}(\mathrm{t}) = \mathbf{F}(\mathrm{t})$$

in which the linear and nonlinear modal forces are given by:

$$\mathbf{F}(\mathrm{t}) = \Phi^{\mathrm{T}}\overline{\mathbf{R}}(\mathrm{t}) = \Phi^{\mathrm{T}}\mathbf{R}(\mathrm{t}) - \Phi^{\mathrm{T}}\mathbf{R}_{\mathrm{NL}}(\mathrm{t}) + \Phi^{\mathrm{T}}\mathbf{K_e}\mathbf{u}(\mathrm{t})$$

The assumption that the damping matrix can be diagonalized is consistent with the classical normal mode superposition method in which damping values are assigned, in terms of percent of critical damping, at the modal level. The diagonal terms of the Λ matrix are $2\xi_n\omega_n$ in which ξ_n is the damping ratio for mode n. It should be noted that the forces associated with concentrated dampers at any location in the structure can be included as part of the nonlinear force vector.

Also, if the number of LDR vectors used is equal to the total number of degrees of freedom N_d, equation is *exact* at time t. Therefore, if very small-time steps are used and iteration is used within each time step, the method converges to the exact solution. The use of LDR vectors significantly reduces the number of modes required.

Because $\boldsymbol{u}(t)=\Phi\boldsymbol{Y}(t)$, the deformations in the nonlinear elements can be expressed directly in terms of the modal coordinate as:

$$\mathbf{d}(\mathrm{t})=\mathbf{BY}(\mathrm{t})$$

where the *element deformation - modal coordinate* transformation matrix is defined by:

$$\mathbf{B}= \mathbf{b}\mathbf{\Phi}$$

It is very important to note that the L by N $\boldsymbol{B}$ matrix is not a function of time and is relatively small in size; also, it needs to be calculated only once before integration of the modal equations.

At any time, given the deformations and history of behaviour in the nonlinear elements, the forces in the nonlinear elements $\boldsymbol{f}(t)$ can be evaluated from the basic nonlinear properties and deformation history of the element. From the basic principle of virtual work, the nonlinear modal forces are then calculated from:

$$\mathbf{F}_{\mathrm{NL}}(\mathrm{t}) = \mathbf{B}^{\mathrm{T}}\mathbf{f}(\mathrm{t})$$

The effective elastic forces can also be rewritten as:

$$\mathbf{F}_{\mathrm{e}}(\mathrm{t}) = \Phi^{\mathrm{T}}\mathbf{K}_{\mathbf{e}}\mathbf{u}(\mathrm{t}) = \Phi^{\mathrm{T}}\mathbf{b}^{\mathrm{T}}\mathbf{k}_{\mathbf{e}}\mathbf{b}\mathbf{u}(\mathrm{t}) = \mathbf{B}^{\mathrm{T}}\mathbf{k}_{\mathrm{e}}\mathbf{b}(\mathrm{t})$$

where $\boldsymbol{k}_e$ is the effective linear stiffness matrix in the local nonlinear element reference system.

3.2.5.2 *FLUID-VISCOUS DAMPER DEVICES FEATURES*

For a relatively small speed, the FVDs with a value of $\alpha<1$ can provide a greater damping force than the other two types and the dissipated energy per cycle by a fluid non-linear dissipator is larger than the linear case and increases monotonically as the velocity exponent decreases. For a given displacement frequency and displacement amplitude $u_{d,0}$, to dissipate the same amount of energy per cycle, the damping coefficient of the non-linear damper, C_{NL}, must be greater than that of the linear damper, C_L. An example of a possible constitutive relationship for a linear (Fig. III.29a) and non-linear (Fig. III.29b) FVD with the SAP2000 calculation program with sinusoidal force (2Hz, +/- 100 mm) with imprinted displacement is shown. For the design of the FVD, a non-linear fluid-viscous damper with $\alpha=0,15$ is considered, which is a recommended value corresponding to a commonly used viscous fluid.

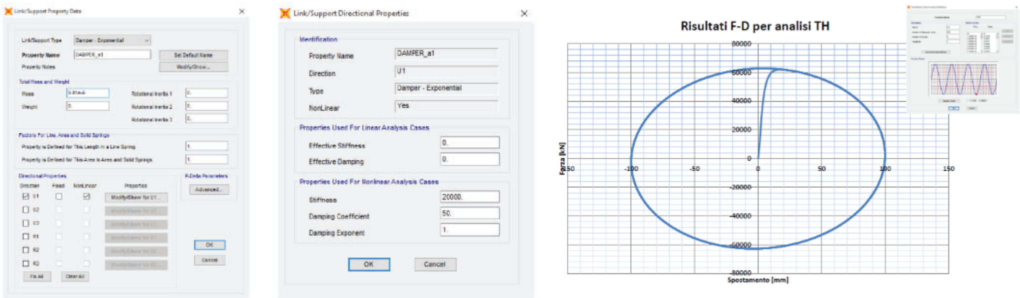

a)

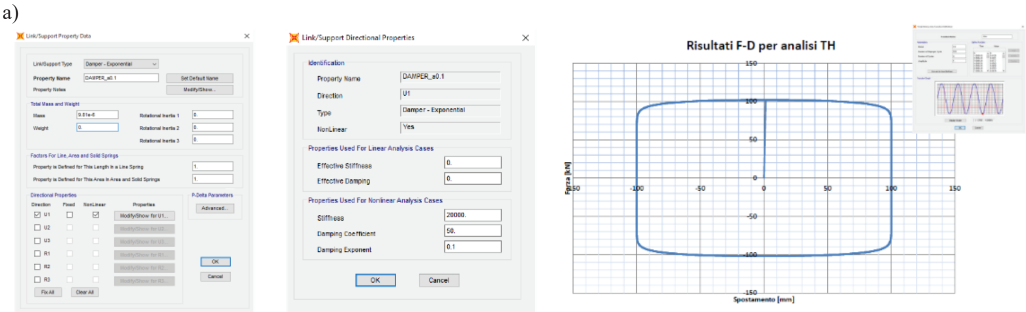

b)

Figure III.78 – Input e output of a a) non-linear and b) linear FVD by SAP200, force-displacement curve of FVD.

The viscous fluid device used has a length of 520 mm, a diameter of 100 mm and it is provided at one end with a perforated plate (with a diameter hole of 21 mm) connected to the steel connection by means of a bolt (diameter 22 mm) to the steel joint at the timber beams and columns, and at the other end with a circular steel endplate (diameter 200 mm) bolted to the corresponding equal size plate at the timber braces by means of bolts (diameter 8 mm) (Fig. III.30).

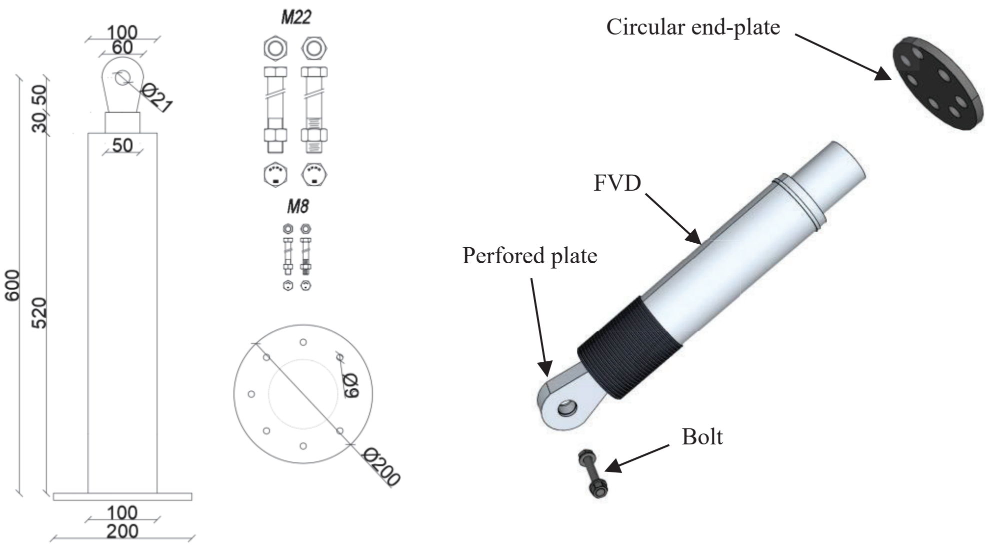

a) b)
Figure III.79 – FVD device: a) structural sizes; b) FVD features.

The heatsinks used, produced by Fip Industriale (S.P.A.), are classified, according to EN 15129: 2009, as "type 4" and "type 6" (Fig. III.31), in which "1" and "2" indicate the material used for anchoring the FVD to the structure and "β" represents the slope of the FVD. In particular, the type 4 one is used for the MRF-H_1L_1 design, while the type 6 is used for the other structural schemes design.

a) b)
Figure III.80 – FVD device according to EN 15129: 2009: a) type 4; b) type 6.

3.2.5.3 NON LINEAR DYNAMIC ANALYSIS

Results of the non-linear dynamic analyses are provided in terms of variation with time (t) of lateral displacements (s-t curve), structure velocities (v-t curve) and accelerations (a-t curve), bending moment-rotation relationships at the beam to column joints (M_B-ϕ_B, M_C-ϕ_C curves), force-displacement relationship of the fluid-viscous devices (F_{FVD}-s_{FVD} curve).

The energy balance of the structures (E(t)-t curve) is also examined, it being expressed considering that the seismic input energy absorbed by the structure, E_i, is spent in the following contributions: E_e, the elastic deformation energy; E_k, the kinetic energy; E_v, the viscous energy.

From a mathematical point of view, starting from the classic equation of motion for an S-DOF, one can write (Uang and Bertero, 1988):

$$m\ddot{u}(t) + c\dot{u}(t) + ku(t) + h\big(u, \dot{u}(t)\big) = -M\ddot{u}_g(t)$$

Which can be integrated between *0* and *t* by obtaining:

$$\int_0^t m\ddot{u}(t)dt + \int_0^t c\dot{u}(t)dt + \int_0^t ku(t)dt + \int_0^t h\big(u, \dot{u}(t)\big)dt = \int_0^t -M\ddot{u}_g(t)dt$$

And expressing the individual contributions from the energy point of view, we write more clearly:

$$E_i(t) = E_k(t) + E_v(t) + E_e(t)$$

Where:
$E_i(t)$ seismic input energy absorbed by the structure;
$E_k(t)$ kinetic energy;
$E_v(t)$ viscous energy (FVD);
$E_e(t)$ elastic deformation energy;

Moreover, the maximum value of displacement (s_{max}), velocity (v_{max}) and acceleration (a_{max}) of the structures are presented, as well as the structural mass (M).

The DCR_{FVD} [%], as the ratio between viscous energy and seismic input energy [$E_{v,max}/E_{i,max}$], the $\Delta DCR_{FVD,\xi}$ [%], as the ratio between FVD efficiency with a damper coefficient ξ_{eff} *=10%* and ξ_{eff} *=50%* for each structure [$DCR_{FVD,i,\xi10}$/ $DCR_{FVD,i,\xi50}$], the ΔM_{MRF} [%], as the ratio between the structural mass for each structural type and the MRF structure [M_i/M_{MRF}] and the ΔM_ξ [%], as the ratio between the structural mass for each structural type with a damper coefficient ξ_{eff} *=10%* and ξ_{eff} *=50%* [$M_{i,\xi50}$/ $M_{i,\xi10}$] are calculated.

A synthetic performance parameter that takes into account at the same time the mass reduction and the dissipative capacity of the structure due to the application of the FVD can be defined as the $SP_{FVD,i}$ [$DCR_i x \Delta M_i$]. As far as the $SP_{FVD,i}$ is larger the structural performance is better, so that based on $SP_{FVD,i}$ it is possible to identify the most unfavourable and favourable cases.

Specially, among the 7 accelerograms, the structural behaviour is evaluated through non-linear dynamic analysis, with which the s-t, v-t, a-t and E-t curves are presented for the most favourable

(ACC-2) and the most unfavourable accelerogram (ACC-1), while the other outputs are presented only for ACC-1.

Below, for all structural typologies, results are for each damping coefficient ξ_{eff}.

3.2.5.4 *Outputs*

The seismic performance of MRF-D, MRF-H_1L_1 and MRF-H_3L_3 is analysed and the results, by varying the viscous damper coefficient ξ_{eff} from 10% to 50% are presented. In particular, in Tab III.31, Tab III.34 and Tab III.37 the *s* [m]-*t* [s], *v* [m/s]-*t* [s] and *a* [m/s^2]-*t* [s] curves are reported for, respectively, MRF-D, MRF-H_1L_1 and MRF-H_3L_3, while in Tab. III.32, Tab III.35 and Tab III.38 the M_B [kNm]-θ_B [rad], E(t)-t [s] and F_{FVD} [kN]-s_{FVD} [mm] curves are indicated, respectively, MRF-D, MRF-H_1L_1 and MRF-H_3L_3.

Table III.38 – Main outputs for MRF-D: the s [m]-t [s], v [m/s]-t [s] and a [m/s^2]-t [s] curves, ACC-1, ACC-2.

ξ_{eff} [%]	s [m]-t [s]	v [m/s]-t [s]	a [m/s^2]-t [s] 
10	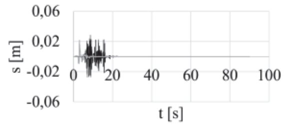	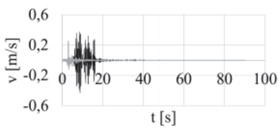	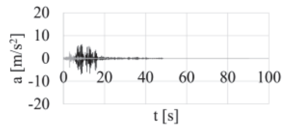
15	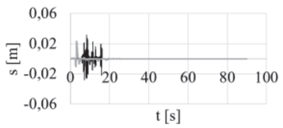	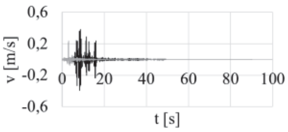	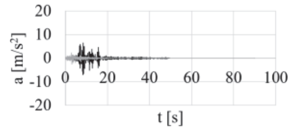
20	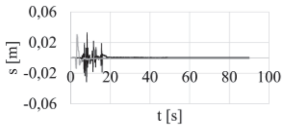	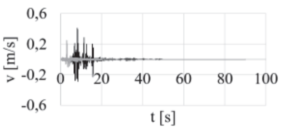	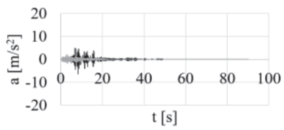
25	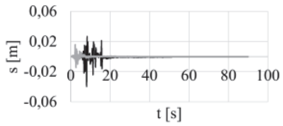	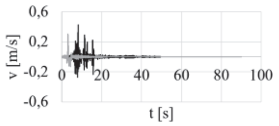	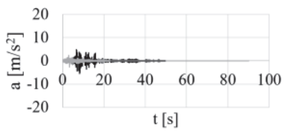
30	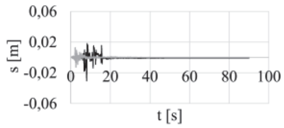	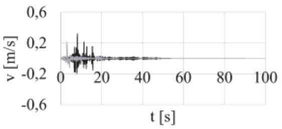	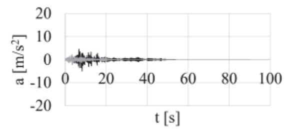
40	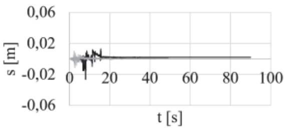	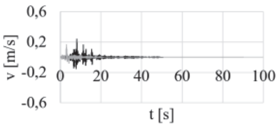	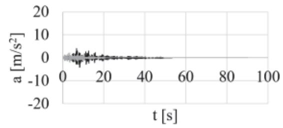
50	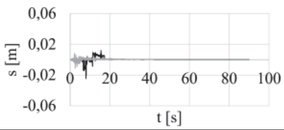	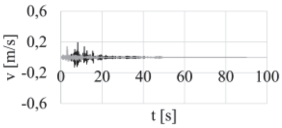	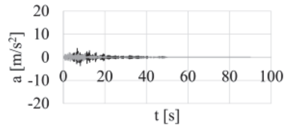

Table III.39 – Main outputs for MRF-H_1L_1: M_B [kNm]-θ_B [rad], E(t)-t [s] and F_{FVD} [kN]-s_{FVD} [mm] curves, ACC-1, ACC-2.

ξ_{eff} [%]	M_B [kNm]-θ_B [rad]	E(t)-t [s]	F_{FVD} [kN]-s_{FVD} [mm] 
10	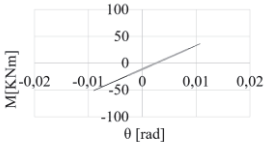	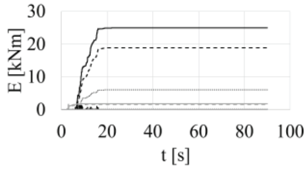	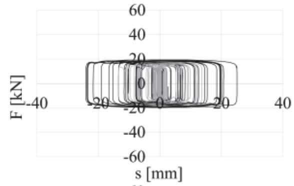
15	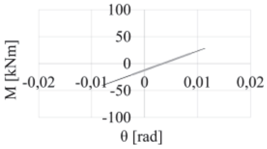	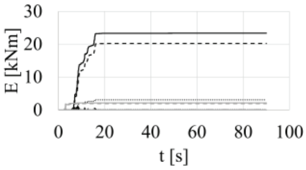	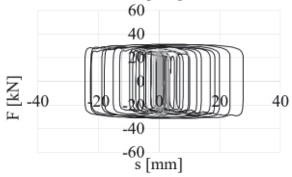
20	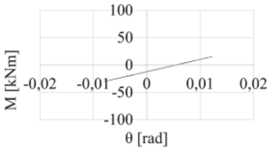	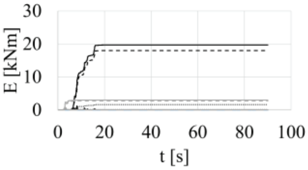	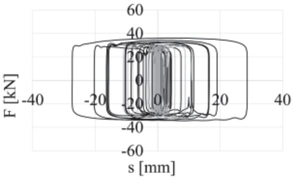
25	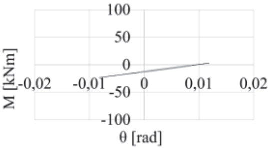	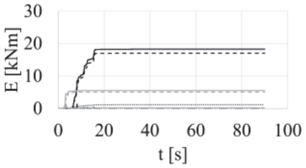	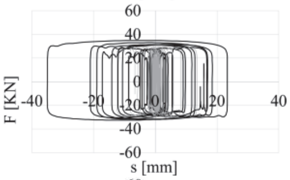
30	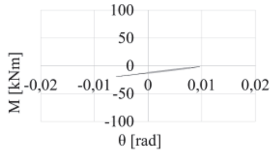	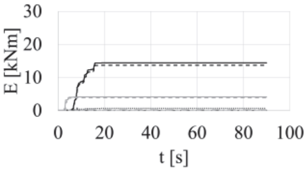	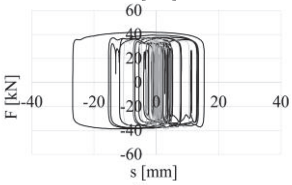
40	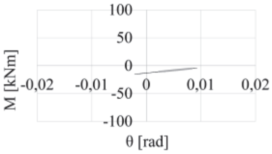	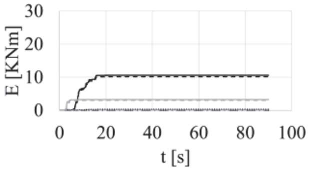	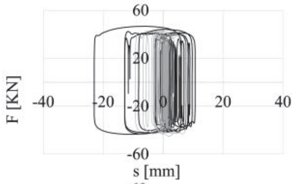
50	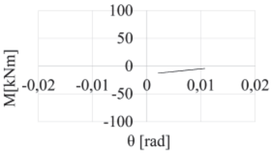	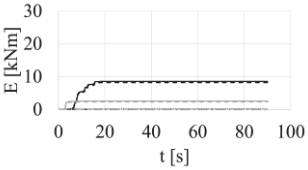	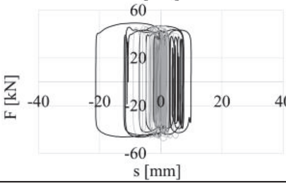

A summary of the results, referred to the mean of the accelerograms outputs, is reported in the Table III.33.

Table III.40 – MRF-D: summery of the analysis results for ACC-1.

ξ_{eff} [%]	s_{max} [mm]	v_{max} [m/s]	a_{max} [m/s^2]	DCR_{FVD} [%]	F_{FVD} [kN]	s_{FVD} [mm]
10	0,035	0,34	6,87	78	18,94	22,79
15	0,032	0,27	5,23	88	29,60	22,62
20	0,028	0,26	4,61	91	33,60	22,44
25	0,024	0,24	4,57	93	33,85	22,18
30	0,021	0,23	4,32	93	39,54	21,93
40	0,020	0,20	4,11	94	44,73	21,34
50	0,019	0,19	4,00	93	47,95	21,02

Table III.41 – Main outputs for MRF-H_1L_1: the s [m]-t [s], v [m/s]-t [s] and a [m/s^2]-t [s] curves, ACC-1, ACC-2.

ξ_{eff} [%]	s [m]-t [s]	v [m/s]-t [s]	a [m/s^2]-t [s]

10

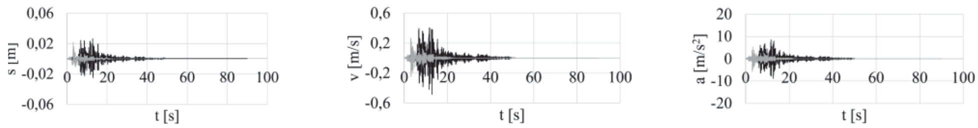

15

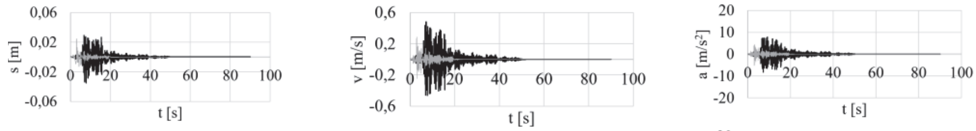

20

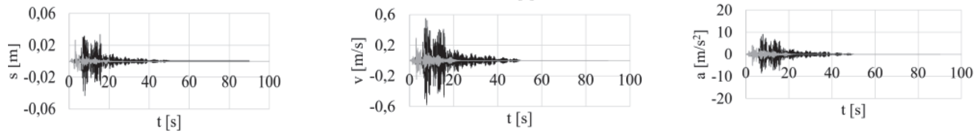

25

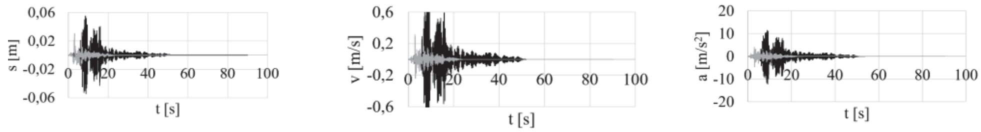

30

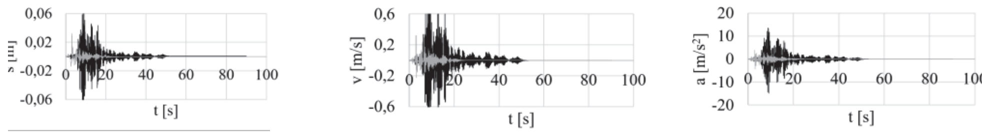

40

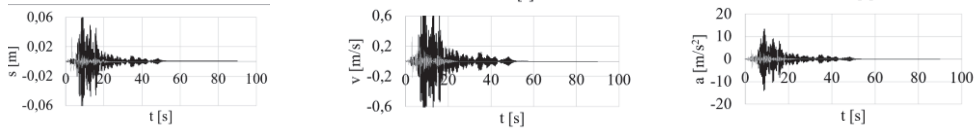

50

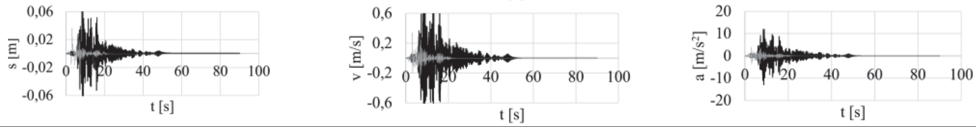

Table III.42 – Main outputs for MRF-H_1L_1: M_B [kNm]-θ_B [rad], E(t)-t [s] and F_{FVD} [kN]-s_{FVD} [mm] outputs curves: ACC-1, ACC-2.

ξ_{eff} [%] | **M_B [kNm]-θ_B [rad]** | **E(t)-t [s]** | **F_{FVD} [kN]-s_{FVD} [mm]**

10

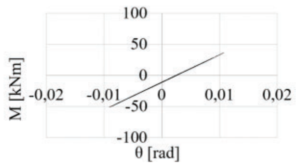

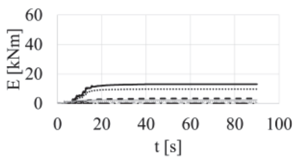

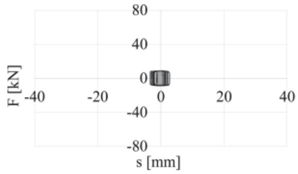

15

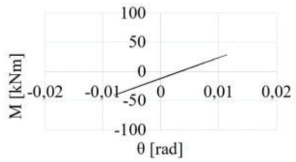

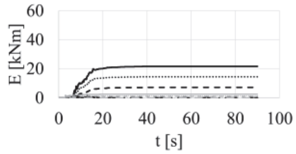

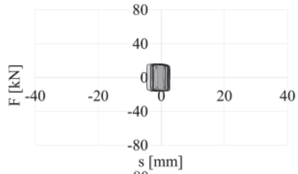

20

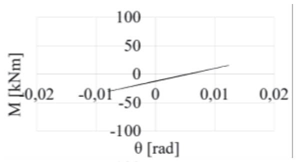

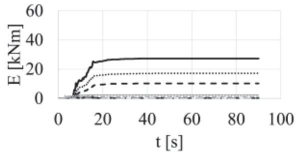

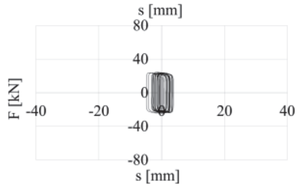

25

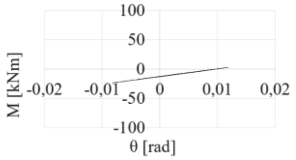

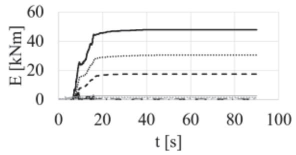

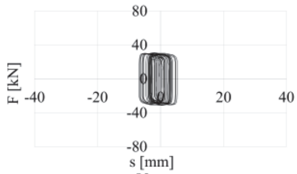

30

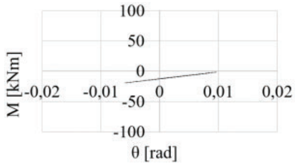

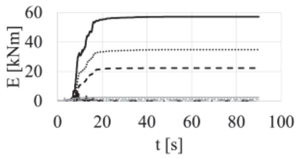

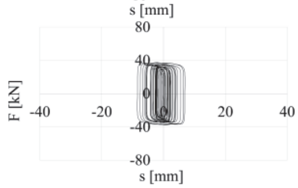

40

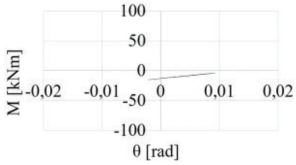

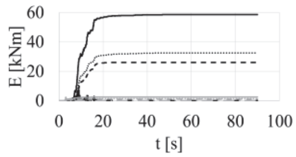

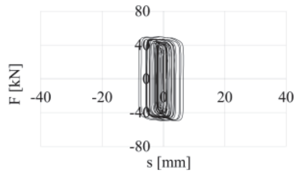

50

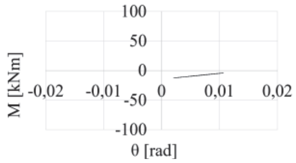

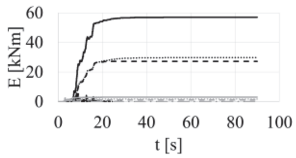

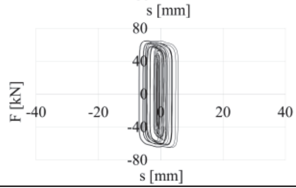

A summary of the results, referred to the mean of the accelerograms outputs, is reported in the Table III.36.

Table III.43 – MRF-H_1L_1: summery of the analysis results for ACC-1.

ξ_{eff} [%]	s_{max} [mm]	v_{max} [m/s]	a_{max} [m/s^2]	DCR_{FVD} [%]	F_{FVD} [kN]	s_{FVD} [mm]
10	0,021	0,45	8,91	20	9,02	25,50
15	0,024	0,49	9,05	30	16,55	28,92
20	0,028	0,50	9,18	35	23,71	31,75
25	0,059	0,56	9,37	38	29,21	37,57
30	0,061	0,57	9,63	41	34,29	39,73
40	0,061	0,57	9,76	45	45,71	40,32
50	0,063	0,59	10,32	46	59,35	42,08

Table III.44 – Main outputs for MRF-H_3L_3: the s [m]-t [s], v [m/s]-t [s] and a [m/s^2]-t [s] outputs curves: ACC-1, ACC-2.

ξ_{eff} [%]	**s [m]-t [s]**	**v [m/s]-t [s]**	**a [m/s^2]-t [s]**
10	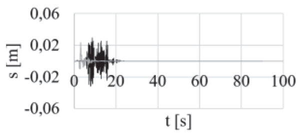	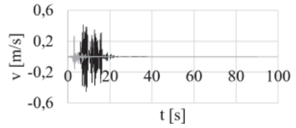	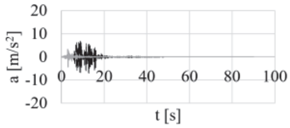
15	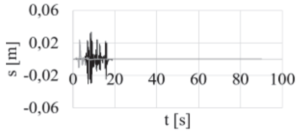	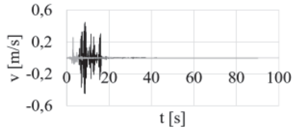	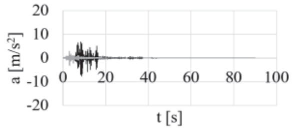
20	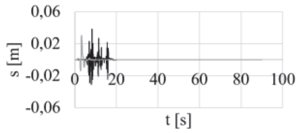	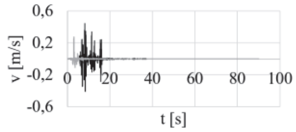	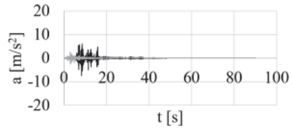
25	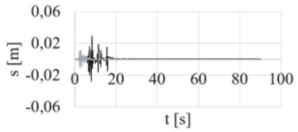	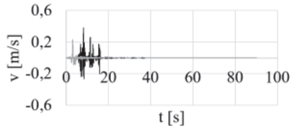	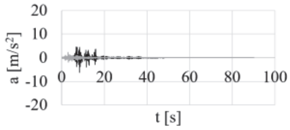
30	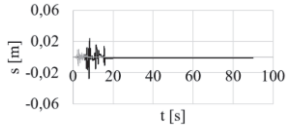	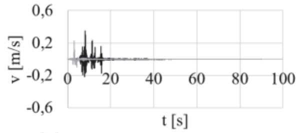	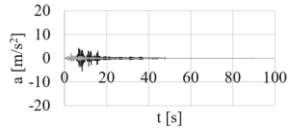
40	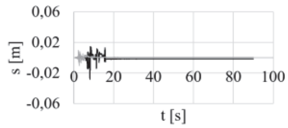	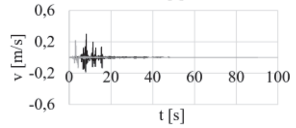	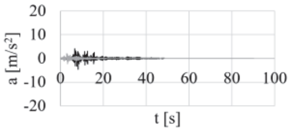
50	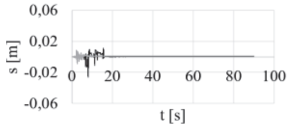	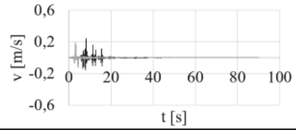	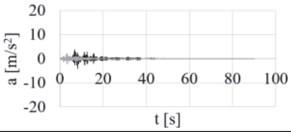

Table III.45 – Main outputs for MRF-H_3L_3: M_B [kNm]-θ_B [rad], E(t)-t [s] and F_{FVD} [kN]-s_{FVD} [mm] outputs curves, ACC-1, ACC-2.

ξ_{eff} [%]	M_B [kNm]-θ_B [rad]	E(t)-t [s]	F_{FVD} [kN]-s_{FVD} [mm] 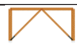
10	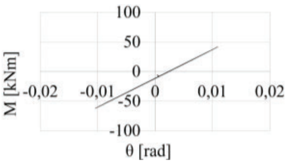	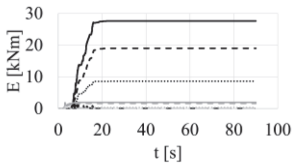	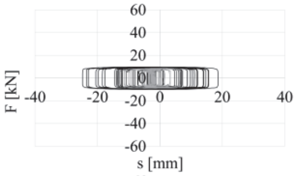
15	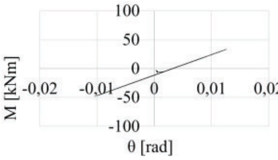	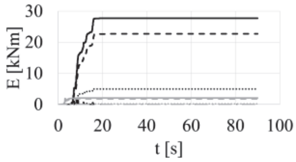	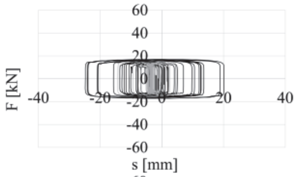
20	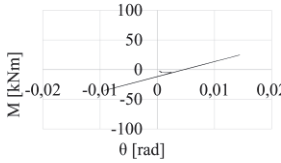	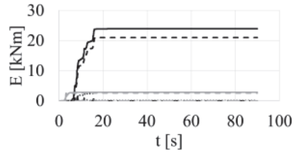	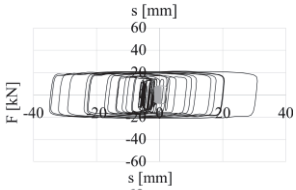
25	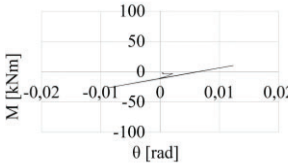	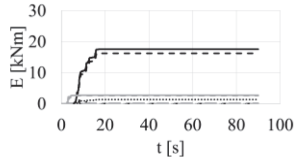	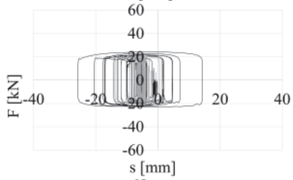
30	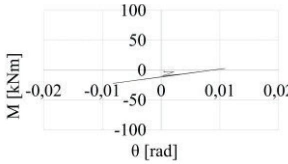	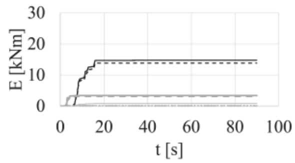	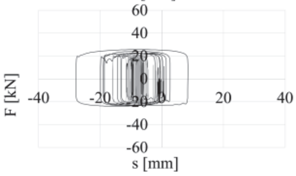
40	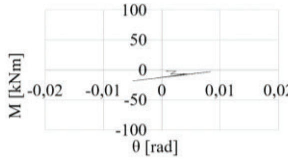	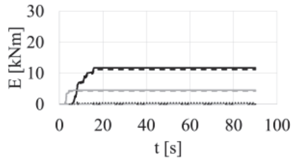	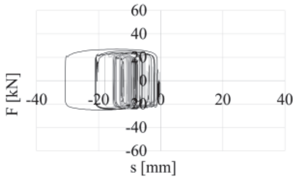
50	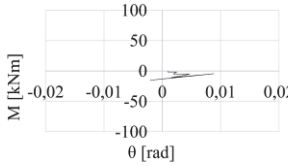	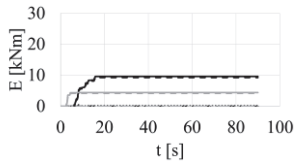	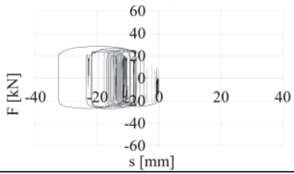

A summary of the results, referred to the mean of the accelerograms outputs, is reported in the Table III.39.

Table III.46 – MRF-H_3L_3: summery of the analysis results for ACC-1.

ξ_{eff} [%]	s_{max} [mm]	v_{max} [m/s]	a_{max} [m/s^2]	DCR_{FVD} [%]	F_{FVD} [kN]	s_{FVD} [mm]
10	0,037	0,38	7,41	72	9,66	24,88
15	0,033	0,31	5,79	85	16,09	24,82
20	0,029	0,29	4,94	90	21,93	23,19
25	0,026	0,24	4,15	93	22,46	20,14
30	0,023	0,23	4,03	94	23,89	19,20
40	0,022	0,21	3,90	95	25,38	18,97
50	0,021	0,18	3,72	95	27,12	16,92

A summary of the results, for MRF-D, MRF-H_1L_1 and MRF-H_3L_3, reported in the Table III.40.

Table III.47 – MRF: D, H_1L_1, H_3L_3: summery of the analysis results for ACC-1.

	s_{max} [mm]			v_{max} [m/s]			a_{max} [m/s^2]			DCR_{FVD} [%]			F_{FVD} [kN]			s_{FVD} [mm]		
ξ_{eff} [%]	D	H_1L_1	H_3L_3	D	H_1L_1	H_3L_3	D	H_1L_1	H_3L_3	D	H_1L_1	H_3L_3	D	H_1L_1	H_3L_3	D	H_1L_1	H_3L_3
10	0,035	0,021	0,037	0,34	0,45	0,38	6,87	8,91	7,41	78	20	72	18,94	9,02	9,66	18,94	9,02	9,66
15	0,032	0,024	0,033	0,27	0,49	0,31	5,23	9,05	5,79	88	30	85	29,60	16,55	16,09	29,60	16,55	16,09
20	0,028	0,028	0,029	0,26	0,50	0,29	4,61	9,18	4,94	91	35	90	33,60	23,71	21,93	33,60	23,71	21,93
25	0,024	0,059	0,026	0,24	0,56	0,24	4,57	9,37	4,15	93	38	93	33,85	29,21	22,46	33,85	29,21	22,46
30	0,021	0,061	0,023	0,23	0,57	0,23	4,32	9,63	4,03	93	41	94	39,54	34,29	23,89	39,54	34,29	23,89
40	0,020	0,061	0,022	0,20	0,57	0,21	4,11	9,76	3,90	94	45	95	44,73	45,71	25,38	44,73	45,71	25,38
50	0,019	0,063	0,021	0,19	0,59	0,18	4,00	10,32	3,72	93	46	95	47,95	59,35	27,12	47,95	59,35	27,12

The analysis results of the intermeddle structural schemes (MRF-H_iL_j) are presented, with a damper coefficient 20%. In particular, in the Tab. III.41 the *s* [m]-*t* [s], *v* [m/s]-*t* [s] and *a* [m/s^2]-*t* [s] curves are reported while in Tab. III.42 the M_B [kNm]-θ_B [rad], E(t)-t [s] and F_{FVD} [kN]-s_{FVD} [mm] curves are indicated.

Table III.48 – Main outputs for MRF-H_iL_i: the s [m]-t [s], v [m/s]-t [s] and a [m/s^2]-t [s] outputs curves, with ξ=20%, ACC-1, ACC-2.

ξ_{eff} [20%]	**s [m]-t [s]**	**v [m/s]-t [s]**	**a [m/s^2]-t [s]**
MRF H_1L_1 	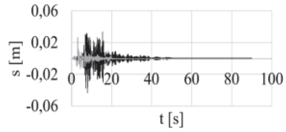	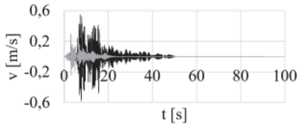	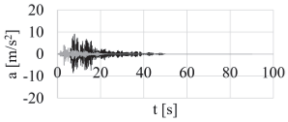
MRF H_1L_2 	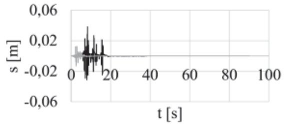	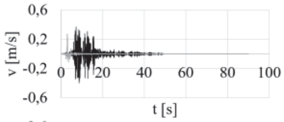	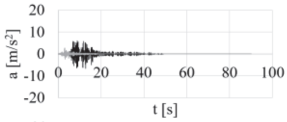
MRF H_1L_3 	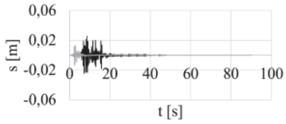	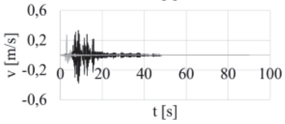	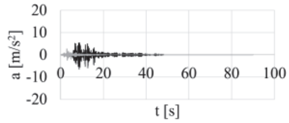
MRF H_2L_1 	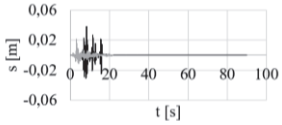	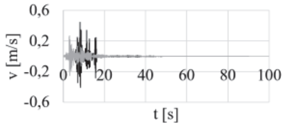	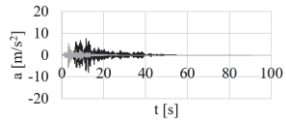
MRF H_2L_2 	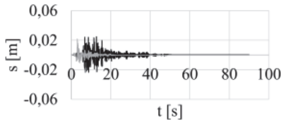	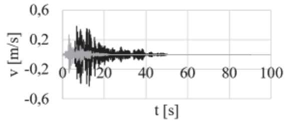	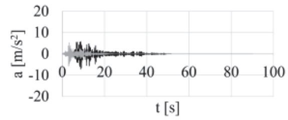
MRF H_2L_3 	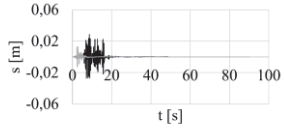	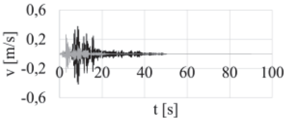	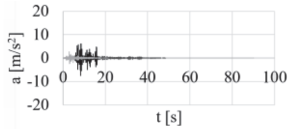
MRF H_3L_1 	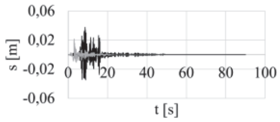	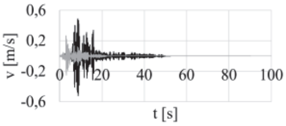	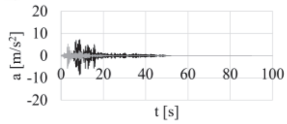
MRF H_3L_2 	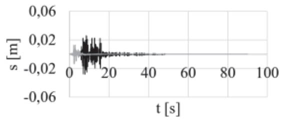	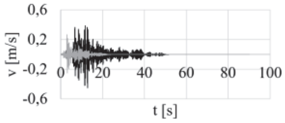	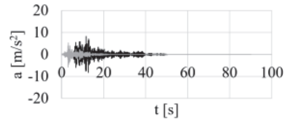
MRF H_3L_3 	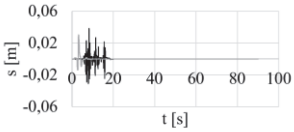	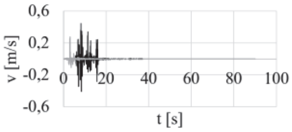	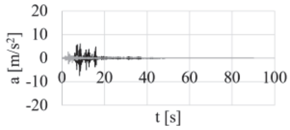

Table III.49 – Main outputs for MRF-H_iL_i: the s [m]-t [s], v [m/s]-t [s] and a [m/s^2]-t [s] outputs curves, with ξ=20%, AcCC-1, ACC-2.

ξ_{eff} [20%]	M_B [kNm]-θ_B [rad]	E(t)-t [s]	F_{FVD} [kN]-s_{FVD} [mm]
MRF H_1L_1 	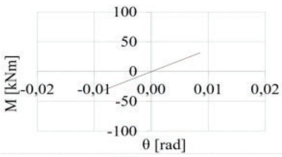	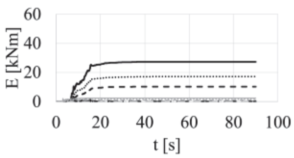	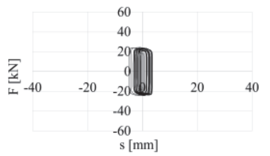
MRF H_1L_2 	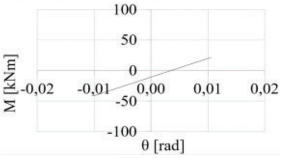	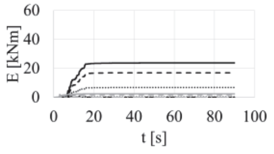	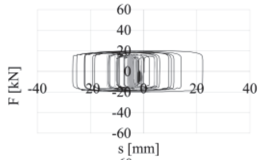
MRF H_1L_3 	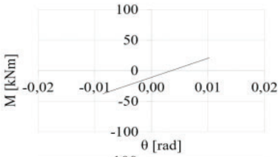	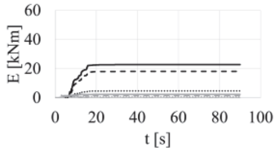	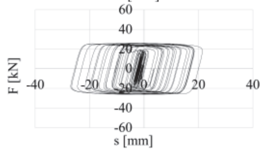
MRF H_2L_1 	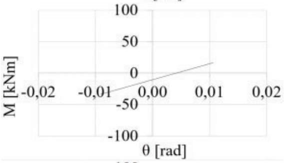	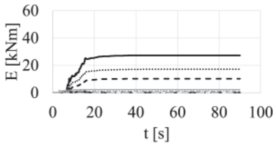	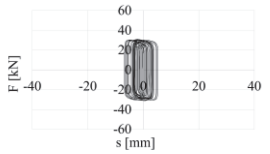
MRF H_2L_2 	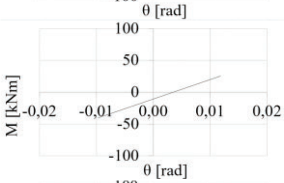	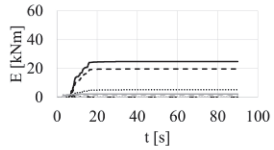	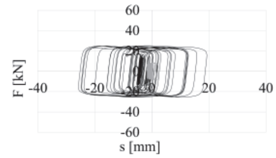
MRF H_2L_3 	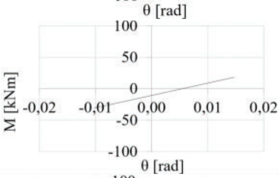	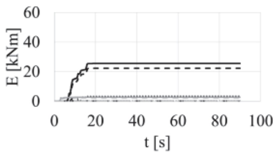	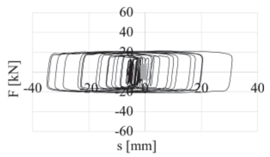
MRF H_3L_1 	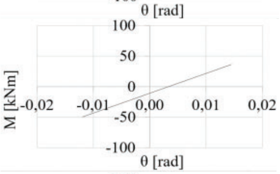	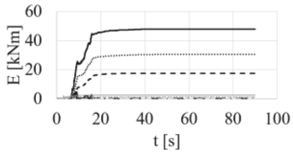	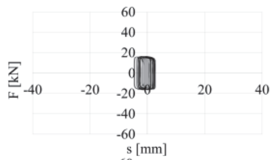
MRF H_3L_2 	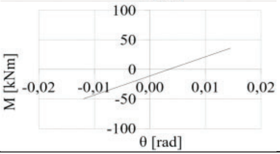	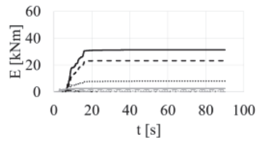	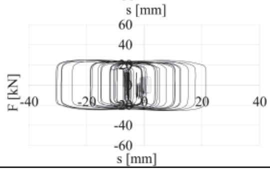

MRF H_3L_3 	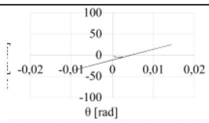	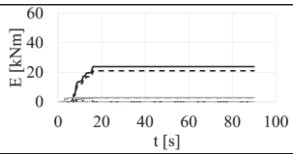	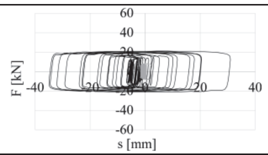

A summary of the results, referred to the mean of the accelerograms outputs, is reported in the Tab. III.43.

Table III.50 – MRF-H_iL_j: summery of the analysis results, with ξ=20% for ACC-1.

ξ_{eff} [20%]		s_{max} [mm]	v_{max} [m/s]	a_{max} [m/s^2]	DCR_{FVD} [%]	F_{FVD} [kN]	M [kg]
MRF H_1L_1		31,75	0,50	9,18	35	23,71	489
MRF H_1L_2		27,82	0,41	6,59	69	26,01	467
MRF H_1L_3		25,69	0,38	6,49	78	26,19	453
MRF H_2L_1		30,26	0,45	8,21	38	27,67	485
MRF H_2L_2		26,90	0,38	6,42	77	25,54	427
MRF H_2L_3		23,46	0,31	5,21	89	21,17	383
MRF H_3L_1		29,98	0,43	7,96	26	18,74	481
MRF H_3L_2		26,02	0,36	5,89	73	25,06	418
MRF H_3L_3		23,19	0,29	4,94	90	21,93	375

3.2.6 Analysis of Results

First of all, the effect of the different extent of damping is quantified through the mass of the designed structures. In Figure III.32 and Table III.44 the cases MRF, MRF-D, MRF-H_1L_1, MRF-H_3L_3, with damping coefficient ξ from 5% to 50%, are presented. In Figure III.33, Figure III.34 and Table III.45 and Table III.46, the other study cases MRF-H_iL_j are referred to, for *ξ=20%.* In the same figures the DCR_{FVD} is provided for the same structural cases.

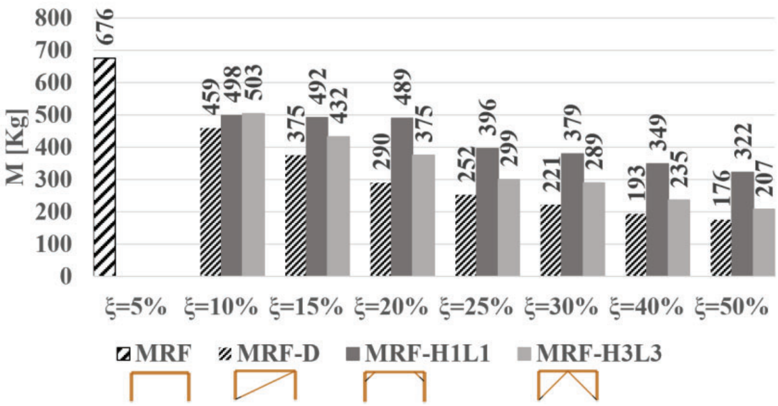

a)

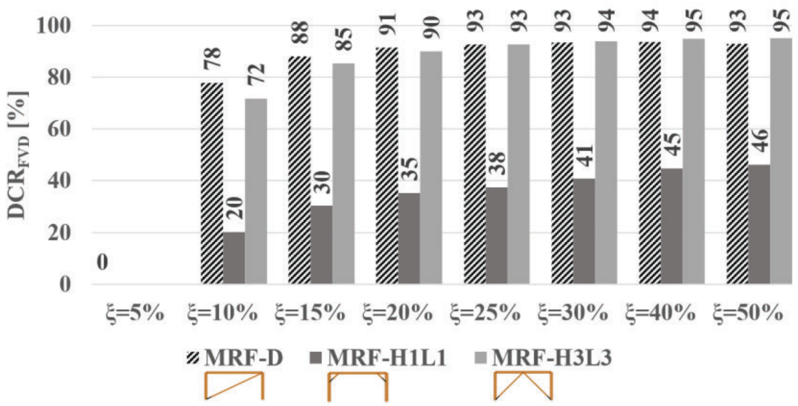

b)

Figure III.81 – a) Mass and b) DCR_{FVD}: MRF - ξ=5% and MRF-D, MRF-H_1L_1, MRF-H_3L_3 - ξ=10% to ξ=50%.

Table III.51 – ΔM_{MRF}, ΔM_ξ and $\Delta DCR_{FVD,\xi}$ for MRF-D, MRF-H_1L_1, MRF-H_3L_3 structures, for ACC-1.

Structural type	ΔM_{MRF} **ξ=10%**	ΔM_{MRF} **ξ=50%**	ΔM_ξ	$\Delta DCR_{FVD,\xi}$	Pros &cons	Performance
MRF-D	32%	74%	61%	16%	Favourable FVD position	- High stiffness - High DCR_{FVD} - High mass reduction $MRF_{,\xi)}$)
MRF-H_1L_1	27%	52%	35%	57%	Unfavourable FVD position Shear forces on columns	- Low stiffness - Low DCR_{FVD} - Low mass reduction ($MRF_{,\xi)}$
MRF-H_3L_3	26%	69%	59%	24%	Favourable FVD position	- High stiffness - High DCR_{FVD} - High mass reduction $MRF_{,\xi)}$)

It is possible to note that as far as *ξ* increases from 10% to 50% a considerable reduction of the structural mass as respect to MRF is achieved [ΔM_{MRF}=1-(M_i/M_{MRF}), Table III.45], it ranging from

26% [$\Delta M_{MRF\text{-}H3L3,\xi10}$] to 74% [$\Delta M_{MRF\text{-}D,\xi50}$]. The effect of the damping coefficient ξ is also noticeable, the mass reduction ΔM_{ξ} [$\Delta M_{\xi}=1\text{-}(M_{i,\xi}/M_{MRF})$] being in the range of 35% (MRF-H_1L_1) to 59% (MRF-H_3L_3), the dissipated energy capacity of the fluid-viscous device [DCR_{FVD}] increases as well $\Delta DCR_{FVD,\xi}$ [$\Delta DCR_{FVD,\xi}=1\text{-}(DCR_{FVD,i,\xi10}/DCR_{FVD,i,\xi50})$] being in the range of 16% (MRF-D) to 57% (MRF-H_1L_1), where *i* is the structural type.

It is apparent that MRF-H_1L_1 is the least efficient system among the three types analysed. This is due evidently to the less favourable position of the devices, which induces on one side a modest exploitation of the fluid-viscous dampers, whose best performance is related to a axial displacement larger than 10mm, on the other side significant shear forces on the columns, which leads to an increase of the mass. Conversely the best performance is offered by the structural configuration MRF-D, following by MRF-H_3L_3.

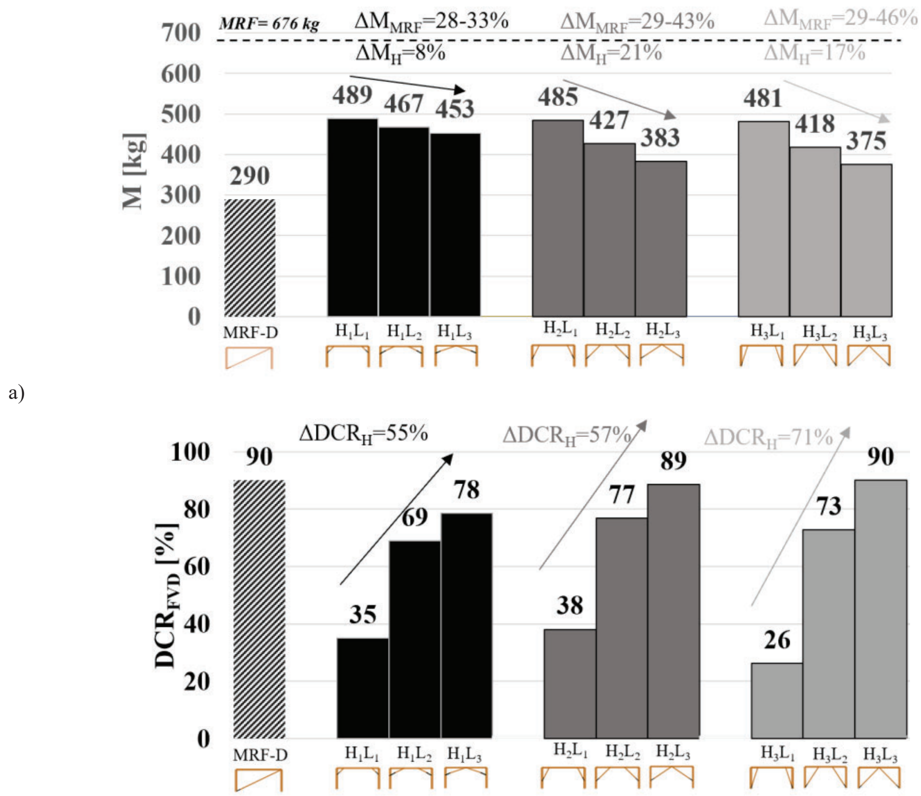

Figure III.82 – a) Mass and b) DCR_{FVD}: MRF-H_iL_j - ξ=20% for the same H_i.

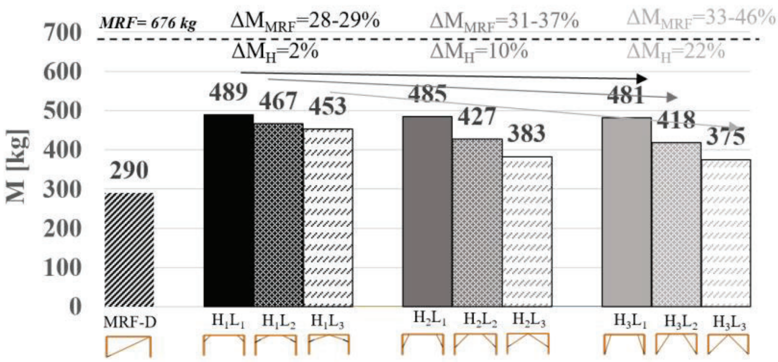

a)

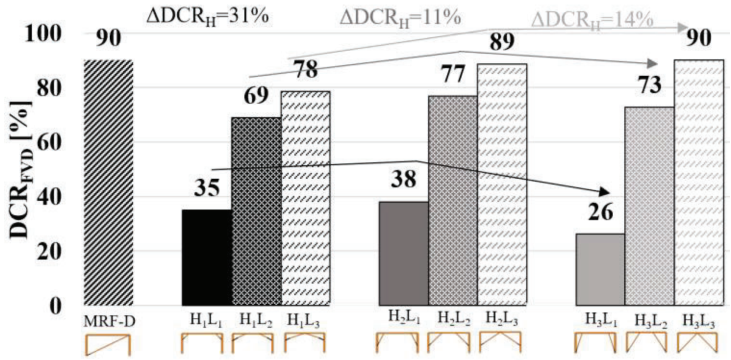

b)

Figure III.83 – a) Mass and b) DCR_{FVD}: MRF-H_iL_j - ξ=20% for the same L_j.

Table III.52 – Performance parameters for ξ=20%. For ACC-1.

	MRFD	H_1			H_2			H_3		
		L_1	L_2	L_3	L_1	L_2	L_3	L_1	L_2	L_3
ΔM_L (%)			8			21			22	
ΔDCR_L(%)			55			57			71	
ΔM_{MRF} (%)	57	28	31	33	29	37	43	29	38	46
DCR_{FVD}(%)	90	35	69	78	38	77	89	26	73	90
SP_{FVD}	0,52	0,1	0,21	0,26	0,11	0,28	0,38	0,08	0,28	0,41

Table III.53 – Performance parameters for ξ=20%, for ACC-1.

	H_1	H_2	H_3		L_1	L_2	L_3
$\Delta M_{MRF,L}$	15	33	37	**$\Delta M_{MRF,H}$**	3	18	28
$\Delta DCR_{FVD,L}$	55	57	71	**$\Delta DCR_{FVD,H}$**	32	10	13
$\Delta SP_{FVD,L}$	62	71	80	**$\Delta SP_{FVD,H}$**	27	25	37

From Figure III.33, Figure III.34 and Table III.45 it is also possible to outline the following observations.

As respect to MRF, a considerable reduction of the structural mass is achieved (ΔM_{MRF}), it ranging in all from 28% ($\Delta M_{MRF,H1L1}$) to 46% ($\Delta M_{MRF,H3L3}$), in particular 28-33%, 29-43%, 29-46%

for H_1, H_2, H_3 cases with variable L_i, as well as 28-29%, 31-38%, 33-46% for L_1, L_2, L_3 cases with variable H_i, respectively. Moreover, for the same H, with the increase of the length L, there is a progressive mass reduction, it ranging from 15% ($\Delta M_{MRF,L,H1}$) to 37% ($\Delta M_{MRF,L,H3}$). Also for the same L, with the increase of the height H, there is a progressive mass reduction, it ranging from 3% ($\Delta M_{MRF,H,L1}$) to 28% ($\Delta M_{MRF,H,L3}$).

With regards to the dissipative capacity, for the same H, DCR_{FVD} increases with the increment of length L, $\Delta DCR_{FVD,L}$ being 55%, 57%, 71% for H_1, H_2, H_3 cases; besides for the same L, $\Delta DCR_{FVD,H}$ is 32%, 10%, 13%, for L_1, L_2, L_3 cases, the worst and best cases being H_3L_1 and H_3L_3 respectively.

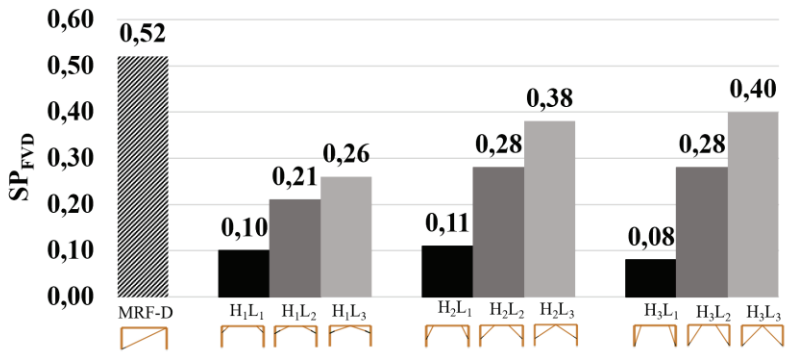

Figure III.84 – SP_{FVD} with ξ=20%.

A synthetic performance parameter that takes into account at the same time the mass re-duction and the dissipative capacity of the structure due to the application of the FVD can be defined as the $SP_{FVD,i}=DCR_i x\Delta M_i$ (Fig. III.35). As far as the $SP_{FVD,i}$ is larger the structural performance is better, so that based on $SP_{FVD,i}$ it is possible to identify the most unfavourable and favourable cases.

In particular, for the same H, SP_{FVD} increases with the increment of length L, $\Delta SP_{FVD,L}$ [$\Delta SP_{FVD,L} = 1-(\Delta SP_{FVD,i,L,min}/\Delta SP_{FVD,L,max})$] being 62%, 71%, 80% for H_1, H_2, H_3 cases; besides for the same L, $\Delta SP_{FVD,H}$ [$\Delta SP_{FVD,H} = 1-(\Delta SP_{FVD,i,H,min}/\Delta SP_{FVD,H,max})$] is 27%, 25%, 37%, for L_1, L_2, L_3 cases, for L_1 it being a decrement. The worst and best cases are H_3L_1 and H_3L_3 respectively.

In conclusion, it can be argued that, in the case with a damping coefficient *ξ=20%*, it being in the range 5-28% of conventional values according to current standards (EC8), the most efficient structure in terms of seismic energy dissipation and therefore mass reduction, is the MRF-D structural type. This typology presents a mass reduction up to 57% compared to the not dissipative configuration (MRF) with a percentage of dissipated seismic energy equal to 91%, the performance parameter SP_{FVD} assumes the maximum value equal to 0,52. The MRF-H_3L_3 structural type shows a slightly inferior performance as respect to the previous case, with a mass reduction of 45% compared to the MRF and 90% of dissipated seismic energy, with $SP_{FVD}=0{,}40$, but it allows a greater freedom of the architectonic-front space of the structural frame, albeit still limited. Moreover, if the damping coefficient increases, these two typologies have a similar performance. The worst performing cases are MRF-L_1, being the FVD position the less efficient, although, it allows large openings of the structural frame.

Outputs will be further discussed with reference to every seismic input considered and as average among all of them. However, in any case, the main advantage acquired by all structural types is that they are designed to remain in the elastic field, under the seismic action, while dissipation of seismic energy is guaranteed by the FVD devices. This lets the structure to be recentred after the earthquake, without any damage or plastic deformations to the structural elements, leading to a huge reduction in maintenance costs.

3.2.7 Structural details

The connections between the structural elements consist of bolted joints and they are designed to guarantee the following two types of constraints:

a) hinge constraint, used for the connection FVD device-foundation node and FVD device-beam-column node;

b) rigid constraint, used for the connection between the timber structural elements and timber diagonal-device FVD.

The types of joints designed and the assembly between the structural parts are shown from the Figure III.36 to Figure III.39. In particular, the most favourable and efficient cases are reported: MRF-D.

Checks on the connections are carried out in accordance with the UNI EN 1995-1-1 and NTC18 standards:

- Spacing and distances from edges and ends for bolts;
- Compression inclined to the grain;
- Johansen's theory;
- Cutting the bolts;
- Removing the plate;
- Plate flexural instability.

As an example, the MRF-D structural scheme with the assembly between the structural parts are shown in the Figure III.36. The other structural types are shown in Annex C.3.2.7.

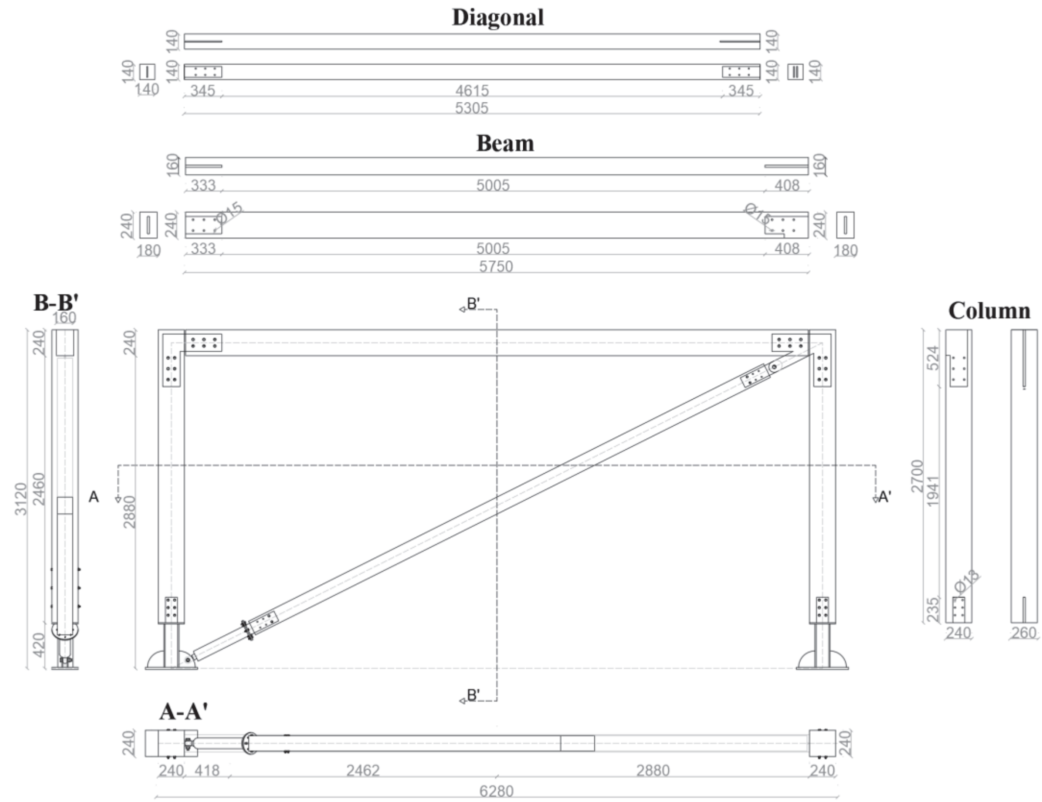
Diagonal
140
345
4615
345
5305
Beam
160
333
5005
408
240
180
Ø15
5750
B-B'
Column
A
A'
B'
3120
2460
420
2880
524
2700
1941
235
Ø18
260
A-A'
418
2462
2880
6280

a)

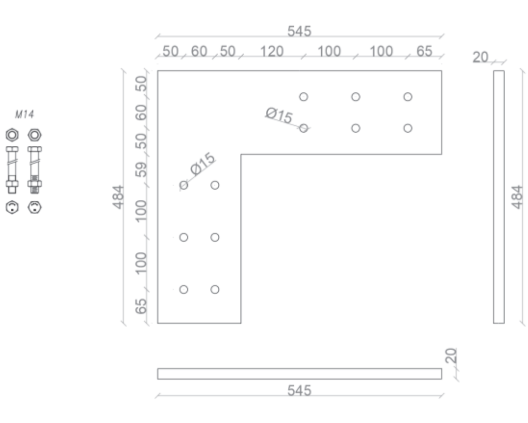
M14
545
50
60
120
100
65
20
484
59
Ø15

b)

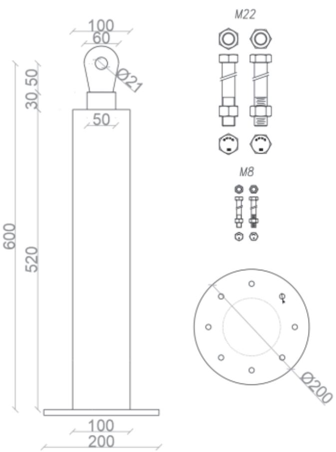
100
60
Ø21
30
50
600
520
M22
M8
Ø200
200

c)

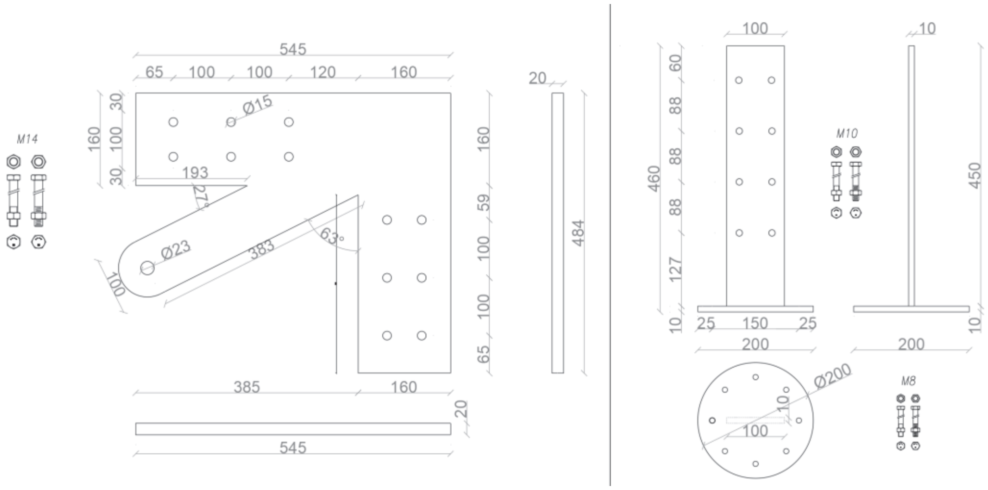

d)

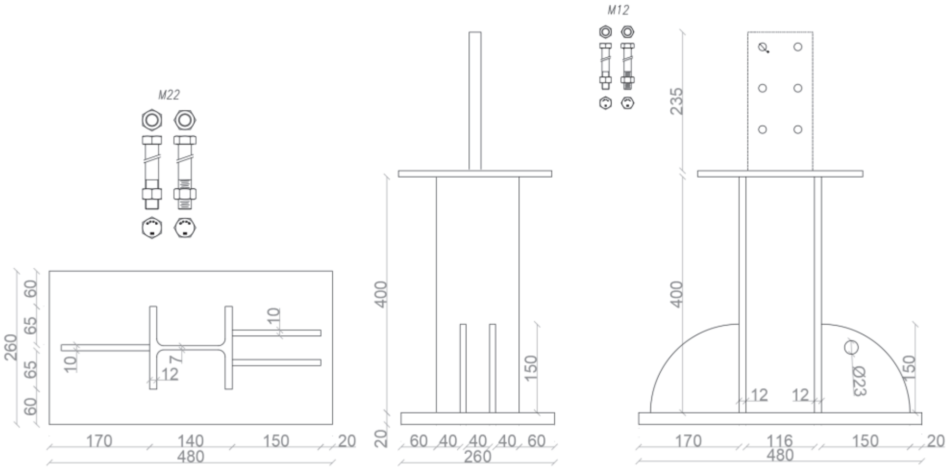

e)

Figure III.85 – MRF-D: a) Structural scheme; b) Beam-column node; c) FVD device; d) Beam-diagonal-column and FVD-diagonal nodes; e) Column-HE140-FVD-fondation node [mm].

Chapter IV

4. BEAM-TO-COLUMN JOINT WITH STEEL LINK: MECHANICAL CHARACTERIZATION THROUGH NUMERICAL ANALYSIS AND DESIGN

4.1 INTRODUCTION

In the previous chapter, the global behavior of heavy timber frame structures with steel link, in which dissipative capabilities is delegated to steel link, was presented and, with reference to Moment Resisting Frames (MRF), steel links located at the beam ends are very promising solutions. In this regard, this chapter deals with a beam-to-column joint equipped with steel links for dissipative timber seismic resistant MRF. The study is inspired by the experimental campaign, consisting of monotonic and cyclic tests on timber beam-to column assemblages with steel link, conducted at the University of Trento (Tomasi et al, 2008; Andreolli et al, 2011) on 8 specimens with variable end-plate (between the link and the timber beam) thickness (t_f = 6, 8, 10, 15, 20 mm). In particular, starting from the reference *P10* specimen, with 10 mm end-plate thickness, the numerical monotonic analysis is simulated (P10 joint) and the FE model is calibrated through the structural calculation program ABAQUS. Therefore, a parametrical investigation based on the monotonic non-linear numerical analyses of the *P10* specimen is carried out, considering the variation of several parameters and features that can affect the joint behaviour, especially the dissipative capacity and the collapse hierarchy. Hence, keeping the same link as the *P10* specimen and taking into account the results of the parametric analysis, the optimization of the system was achieved designing the joint through the capacity design procedure, with the application of the component method, for "macro-components" and "sub-components", aimed to allow the plastic hinge formation in the steel links, while the timber member and the connection are designed to remain elastic, with adequate overstrength (*Full-strength* connection): HE100AA joint. In particular, two types of joint have been analytically designed: *Full-strength* connection with *Low Ductile Joint* and *Full-strength* connection with *High Ductile Joint* and *Fragile Connection*)

Finally, monotonic numerical analysis is carried out on the optimized systems to check the mechanical behaviour and the accuracy of the analytical design.

4.2 NUMERICAL SIMULATION OF THE REFERENCE P-10 TEST

4.2.1 REFERENCE EXPERIMENTAL P-10 TEST

Among the beam-to-column timber joint equipped with steel link for heavy timber MRF tested at the University of Trento (Tomasi et al, 2008; Andreolli et al, 2011), the test named *P10* is selected for the numerical study, it being characterized by 10 mm end plate thickness (Fig. IV.1).

The specimen is made by a laminated timber beams (GL24h), with a 120x230 mm rectangular cross section and 2500 mm long, equipped at one end with a steel link, HE120B profile 250 mm long (steel grade S235) with two welded end-plates (120x230 mm, steel grade S235), with 10 mm and 20 mm thickness. The link is connected at one side to the timber beam by means of 4 glued threaded bars (M16, 6.8, 540 mm long).

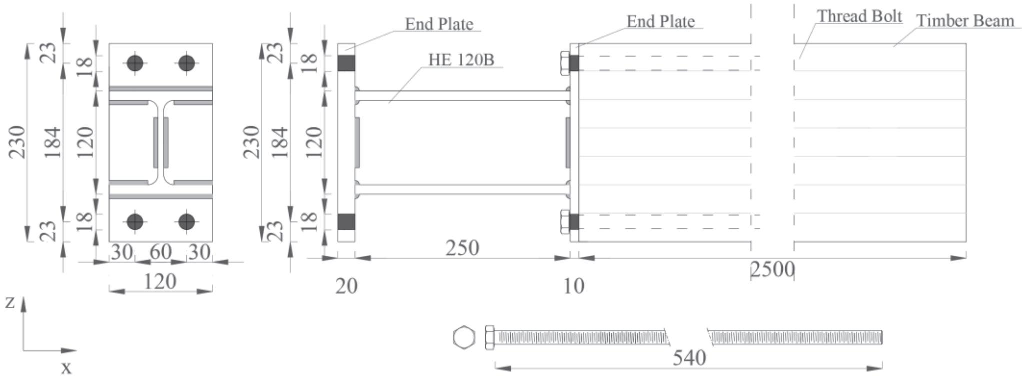

Figure IV.86 – The *P10* specimen: geometrical features [mm].

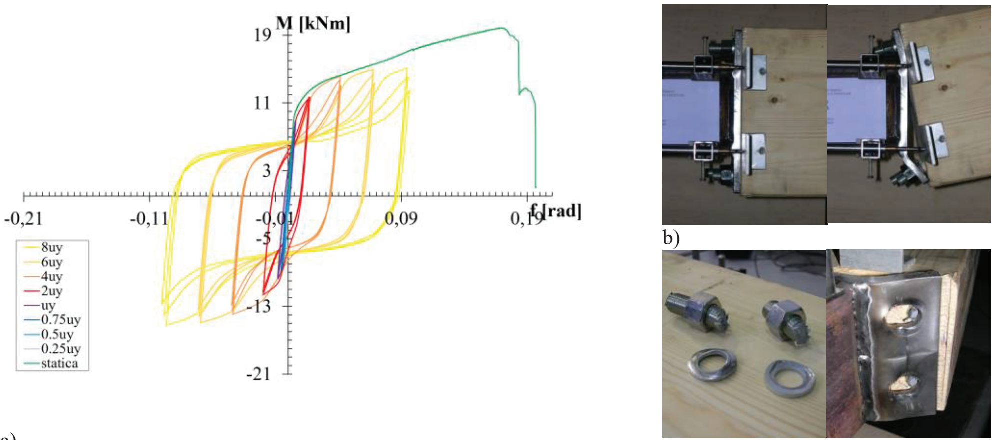

a) b) c)

Figure IV.87 – The *P10* specimen: results of monotonic test a) M_{RD}= 19,85kNm; f= 0,19rad; b) Collapse mode 2; c) Failure modes: combined tensile-bending inelastic deformation of steel bars; bending inelastic deformation of steel plate.

In the monotonic and cyclic tests, the loading was applied under displacement control at a constant rate of 0,2 mm/sec so that failure was achieved in about 30 minutes, according to the European standard EN 12512 (CEN, 2005) and the tests response is given in Fig. IV.2. The collapse mode is characterized by the bending inelastic deformation of the steel end-plate and the combined tensile-bending inelastic deformation of the steel bars (collapse mode 2, Tab. IV.1).

Table IV.54 – Comparison between theoretical model and experimental results in terms of: failure modes for T-stub in tension, strength values and rotation capacity of the joint.

Specimen	**End-plate steel**			**Failure mode of T- stub in tension**		**Moment resistance [kNm]**		**Rotation capacity [rad]**	
	ε_u %	f_y [MPa]	f_u [MPa]	Th.	Exp.	Theoretical	Experimental*	Theoretical	Experimental**
P10	45,9	256,1	374,0	2	2	15,80	19,85	0,13	0,18

**maximum value; ** displacement at failure*

4.2.2 FE MODEL

The FE model of the reference *P10* specimen is set up through the structural calculation software, ABAQUS. Geometrical features, materials and boundary conditions are assumed according to the experimental test (Tab. IV.2) and the *P10* model consists of one end-plate, one timber beam, one link and four thread bolts (Fig. IV.3).

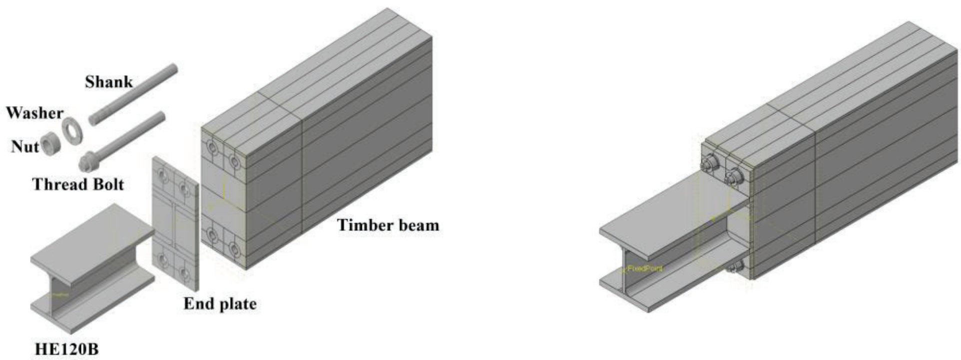

a) b)

Figure IV.88 – The *P10* specimen FE model: a) elements part; b) assembly.

As regard the materials, the timber is modelled with an elastic behaviour, while for the end-plate, the bolts and the link an isotropic hardening model is adopted with material relationships non-linear in the solid elements and tri-linear in the beam elements, with specific values derived by laboratory tests before the experimental campaign. Although for monotonic loading models elasto-plastic approach is sufficient, the model is prepared also to deal with cyclic loading cases. The component parts are modelled through Solid Elements (C3D8RH: 8 nodes, 1 integration point, 3 degrees of freedom per node, Hourglassing problems - zero strain in integration point in bending problems) and the mesh size is different for every component part (Tab. IV.2). C3D8RH is a 8-node linear brick element but with reduced integration (normally using a scheme one order less than the full scheme to integrate the element's internal forces and stiffness with only 1 Gauss point), hourglass control using the artificial stiffness method given in Flanagan and Belytschko (1981).

Table IV.55 – P10 specimen: structural features.

Element		**Timber beam**	**Thread Bolt**		**End plate**	**HE120B**
		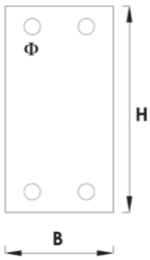			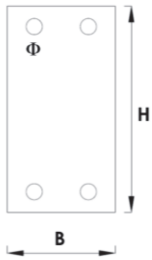	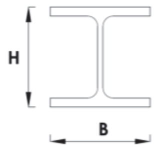
Geometry [mm]		θ= 18 H= 230 B= 120 L= 2500	θ= 16 L= 540 Nut, Washer	Shank	θ= 18 H= 230 B=120 s= 20	L= 250 B= 120 H= 120
Material		**GL24h**	**6.8**		**S235**	
Density [N/mm^3]		3,80x e^{-6}	7,85 x e-5			
Elasticity [MPa]		E_{90}=390 E_0=11600	210000			
Plasticity [MPa]	σ_{el}	24	544	374,4	256	235
	σ_u	/	608	468	374	360
	ε_{el}		0	0	0	0
	ε_u	/	0,138	0,138	0,459	0,261
Model		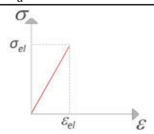			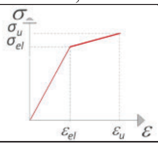	
Mesh		**Solid element**				
		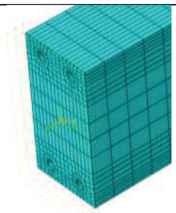	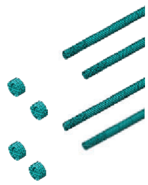			

The element chosen has also hybrid formulation, normally used for fully incompressible material behaviour or, as in this case, if severe plastic deformation is expected, because the rate of total deformation becomes incompressible as the plastic deformation starts to dominate the response. The mesh was automatically generated. To ensure a regular mesh distribution it is necessary to impose some pre-defined conditions. The parts are composed by plane surfaces where a regular distribution of the mesh is usually generated. The major problem are the perturbations in the plane surfaces by the bolt's holes or in the intersections with non-orthogonal surfaces. In those cases, the problem should be divided in such a way that a regular mesh is allowed. Partitions is a tool available in ABAQUS that allows setting some mesh boundaries without actually break the part. In addition to the created partitions, it is also required to define, in some cases, a more refine mesh in some particular zones of the mesh, for example in the edge of the bolt's holes. In those cases, the seed option available in ABAQUS, can be used, the automatic generation of the mesh will try to create the additional number of elements required around the bolts holes, without refining the rest of the mesh of the end-plate (Tab. IV.3).

Table IV.56 – P10 specimen: interaction between the model parts.

	Shank-Washer	**Shank-Plate**	**Washer-Nut**	**Plate-Washer**	**Plate-Beam**
Surface to Surface Contact		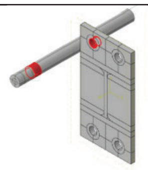	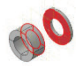	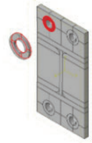	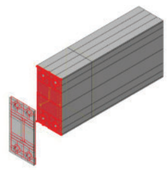
Master surface	Shank	Shank	Washer	Plate	Plate
Slave surface	Washer	Plate	Nut	Washer	Beam
Friction coefficient	0,4				0,3
Pressure - Overclosure			Hard contact		
	Shank-Nut	**Shank-Beam**		**Profile-Plate**	
Tie Contact		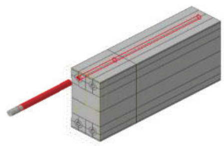		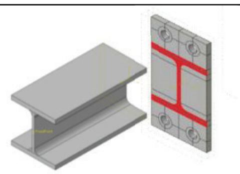	
Master surface	Shank	Shank		Link	
Slave surface	Nut	Beam		Plate	

The various parts of the model interact with each other by continuity links, defining contact properties, called interactions in ABAQUS. The interactions between the shank and the washer, the shank and the end-plate, the washer and the nut, the end-plate and the washer, the end-plate and the beam is a "Surface to Surface Contact", imposed by the general contact algorithm, which uses "hard contact" formulation, using the penalty method to approximate the hard pressure-overclosure behaviour that acts in the normal direction to resist penetration, with a friction coefficient equal to 0,4 for the steel material and 0,3 for the timber material. While the interaction between the link and the end-plate, the shank and the beam, and the link and the end-plate is a "Tie Constraints", schematizing the glue (shank-beam) and the welding (shank-nut and link-end plate).

As for the boundary conditions, the model is fixed at the link free end (FP: fixed point), while at the beam free end a Reference Point (RF), to apply the displacement load, is defined. The selection of interactions is also relevant for the choice of the analysis procedure.

At first, a static analysis was carried out, with greatly reduced computational-time. However, this proved to be inadequate for the case study due to the strong bolt deformations and the distances between the interactions that alter the result, never reaching the last imposed displacement value. Thus, a dynamic implicit analysis is performed.

4.2.3 MONOTONIC NON LINEAR ANALYSIS

To simulate the *P10* monotonic test, the implicit dynamic analysis is performed applying a load history in displacement control bases, i.e., a displacement is imposed in the end of the cantilever formed by the beam, with increment of 20 mm up to collapse, until 380 mm, to respect the speed test of 0,2 mm/s.

ABAQUS divides the problem history into steps. A step is any convenient phase of the history and, in its simplest form, a step can be just a static analysis, a load change from a magnitude to another, an initial pre-stress operation of a part of the structure or the change of a boundary condition in the model. In this particular case, the solution of the problem is obtained in 2 steps. The first step is used to formulate the boundary conditions and prepare the contact interactions defined previously. In the second step the implicit dynamic analysis begins, changing the boundary conditions on the tip of the cantilever by imposing a displacement in the boundary condition parallel to the link web (z-direction). This type of analysis is characterized by an application of the quasi-static load, subdivided into 100-time intervals, and capable of considering also the effects of inertia. The analysis is defined by higher computational-time but allows to obtain an optimal solution to non-linear problems.

In this section, a detailed analysis of the model is performed both for the global and components behavior. The numerical results are compared with the experimental test results described in chapter 4.2.1.

The outputs are provided in terms of the maximum values of stresses (σ), DCR_{el} ($DCR_{el}=\sigma/\sigma_{el}$), DCR_{ul} ($DCR_{ul}=\sigma/\sigma_{ul}$), over-strength respect to the elastic stress, OS_{el} ($OS_{el}= DCR_{link,el}/DCR_{component,el}$), and the ultimate stress, OS_{ul} ($OS_{ul}= DCR_{link,ul}/DCR_{component,ul}$), for each component of the model (link, end-plate, threaded bolts and timber beam), the resistant bending moment (M), valuated in the plasticization point, and rotation (θ), valuated respect to the plasticization point, in in x-z plane, the force (F) and the displacement (u) in z-direction, valuated in the RP point, for the global model. Outputs are detected at specific increments (In.) and times (t.), corresponding to the yield of the first joint component (P_Y) and to the achievement of the ultimate stress (P_C), corresponding to the collapse of the model and the end of the numerical analysis. Moreover, the F-u and the M-θ curves are shown. A special attention is also given to the collapse mode and hierarchy, in terms of the global behaviour and of the single component behaviour, to evaluate the accuracy of model.

Figure IV.4 compares the experimental and numerical F-u and the M-θ curves and the collapse mode. The numerical M-θ and F-u curves obtained are perfectly superimposed on the experimental ones (Fig. IV.4a) and the plastic mechanism (collapse mode 2: bending inelastic deformation of the steel end-plate and the combined tensile-bending inelastic deformation of the steel bars) are also catched (Fig. IV.4b).

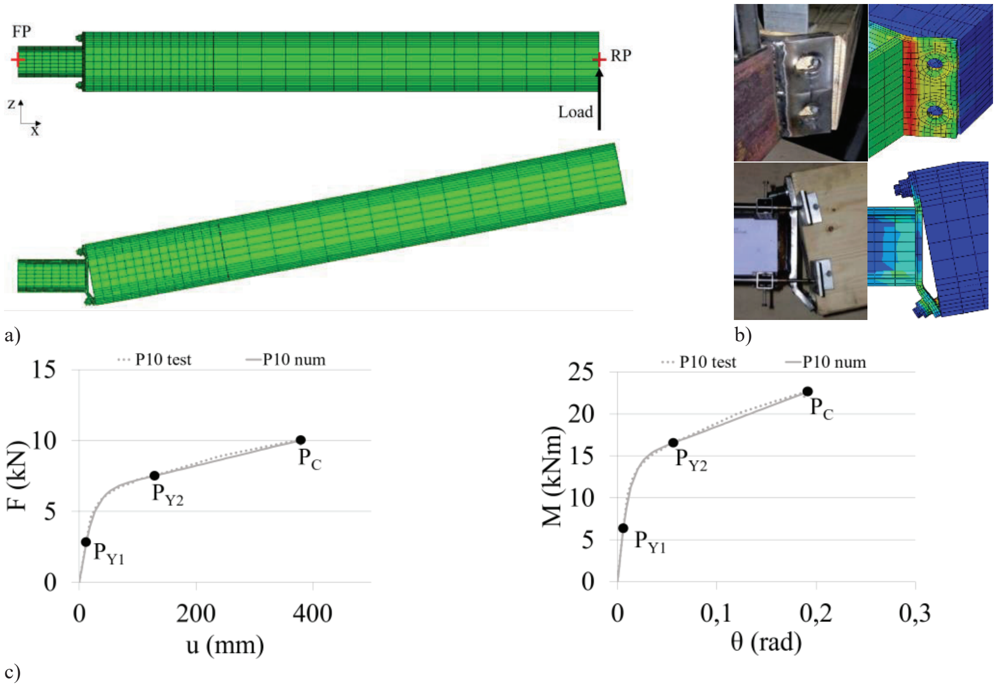

Figure IV.89 – P10 specimen: a) set-up of the monotonic numerical analysis (FP: fixed point, RP: reference point in which the load is applied) and deformed model; b) collapse mode; c) numerical F-u and M-θ curves.

4.2.4 Analysis of results

Analysing the numerical results, the following observations can be drawn. With regards to the state of stress, examining the P_{Y1} instant [In. 33; t. 3,37], the end-plate reaches the yielding stress (256MPa) while the link (116Mpa), the bolts (298MPa) and the timber beam (2,8MPa) are still in the elastic field; at the P_{Y2} instant [In. 47; t. 33,34], the link (235MPa) and the bolts (544MPa) reach the yielding stress while the end-plate (315MPa) and the timber beam are in the elastic field (8MPa); the P_C instant [In. 78; t. 100] corresponds to the collapse of the model, with a combined tensile-bending inelastic deformation of the bolts (608MPa) and bending inelastic deformation of steel plate (374MPa) while the timber beam is still in the elastic field and the steel link presents a small plastic deformations (300MPa) (Tab. IV.4).

Table IV.57 – P10 specimen: yield of the end-plate (P_{Y1}), yield of the link (P_{Y2}) and collapse (P_C) stress value σ, bending moment *M*, rotation *θ*, force *F* and vertical displacement *u*.

Point	σ [MPa]				M	θ	F	u
	HE120B	End Plate	Thread Bolt	Timber beam	[kNm]	[rad]	[kN]	[mm]
P_{Y1}	116	256	298	2,8	6,9	0,011	4,9	19
P_{Y2}	235	315	544	8,0	17	0,057	7,5	133
P_C	300	374	608	18,8	22,45	0,19	10	380

Stress distribution

(P_{Y1}) [In. 33; t. 3,37]	(P_{Y2}) [In. 47; t. 33,34]	(P_C) [In. 78; t. 100]
End-plate: 256 MPa	Link: 235 MPa Bolts: 544 MPa	Bolts: 608 MPa End-plate: 374 MPa

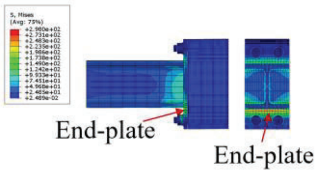

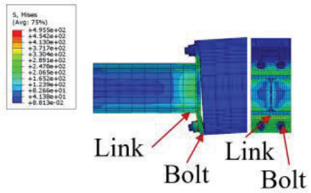

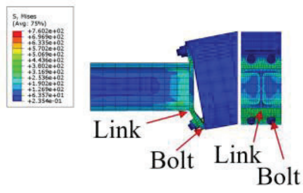

In Table IV.5 are depicted the stress values (σ), the DCR_{el} and the DCR_{ul}, for each connection element, in the P_{Y1}, P_{Y2} and P_C instants. Moreover, the first element that reaches the elastic strength (σ_{el}) and the ultimate strength (σ_u) is highlighted.

Table IV.58 – P10 specimen: yield of the end-plate (P_{Y1}), yield of the link (P_{Y2}) and collapse (P_C) stress value σ, DCR_{el} (σ/σ_{el}) and DCR_{ul} (σ/σ_u).

Point	Link			End Plate			Thread Bolt			Timber beam	
	σ	DCR		σ	DCR		σ	DCR		σ	DCR
	[MPa]	el	ul	MPa	el	ul	[MPa]	el	ul	[MPa]	el
P_{Y1}	116	49%	32%	256	100%	68%	298	55%	49%	2,8	12%
P_{Y2}	235	100%	65%	315	123%	84%	544	100%	89%	8,0	33%
P_C	300	128%	83%	374	146%	100%	608	112%	100%	18,8	78%

It is possible to observe that, at the instant P_{Y1}, the first element to reach the yield is the end-plate, with a DCR_{ul}= 68%. The second joint component most stressed is the bolts, with a DCR_{el}= 55% and DCR_{ul}= 49%; the link is the third joint marco-component with a DCR_{el} = 49% and DCR_{ul}= 32% respect to the yielding end-plate; at the last, the timber beams presents a DCR_{el}= 12%.

At the instant P_{Y2}, the link and the bolts reach the yield, with respectively a DCR_{ul}= 65% and DCR_{ul}= 89%; the end-plate is in the plastic field with a DCR_{el}= 123% and a DCR_{ul}= 84%; the timber beam presents a DCR_{el}= 33%.

At the instant P_C, corresponding to the collapse of the end-plate and the bolts, the link presents a DCR_{el}= 128% and a DCR_{ul}= 83% while the timber beam has a DCR_{el}= 78% (Fig. IV.5).

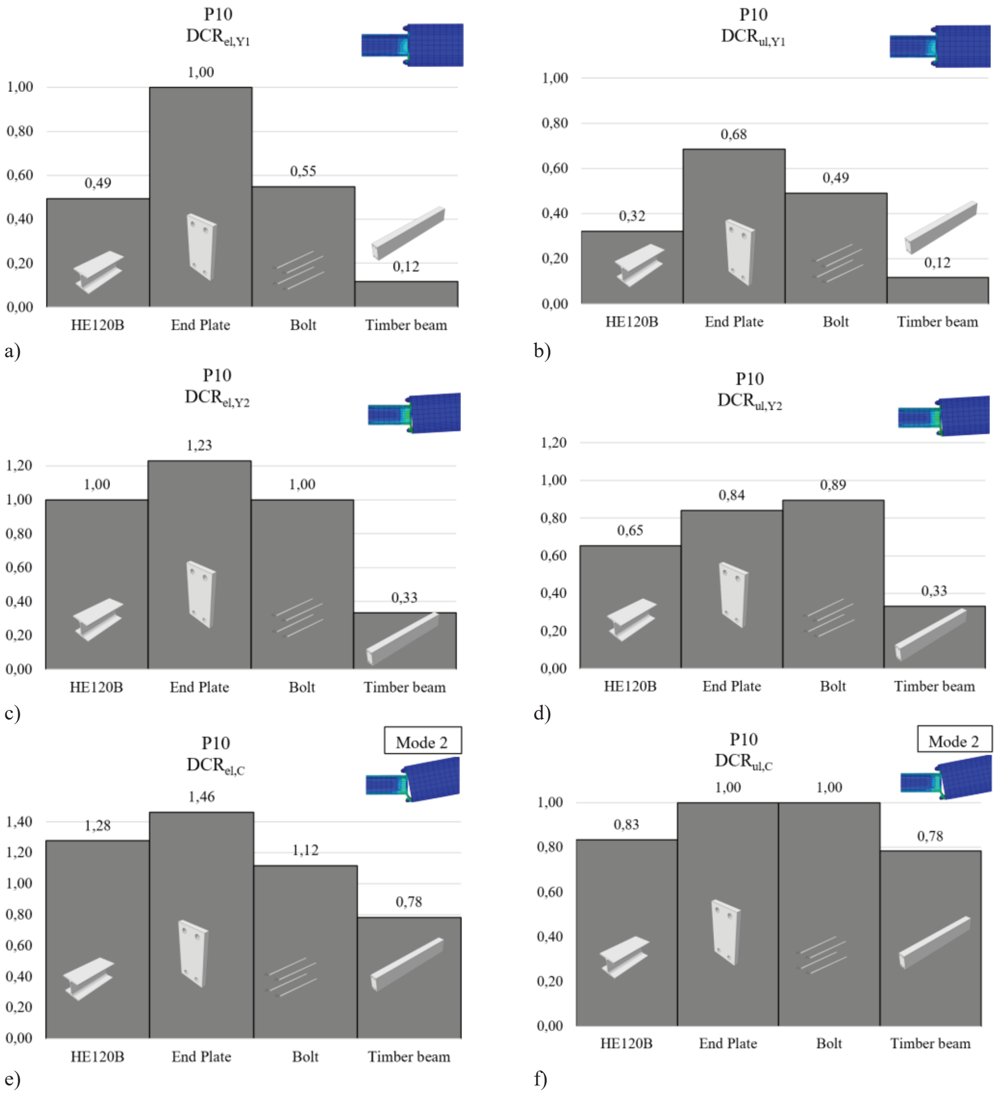

Figure IV.90 – P10 specimen: DCR_{el} [$DCR_{el}=\sigma/\sigma_{el}$] and DCR_{ul} [$DCR_{ul}=\sigma/\sigma_{ul}$] evaluated in P_{Y1}, P_{Y2} and P_C points.

At the end of P_{Y2} and P_C points coinciding, respectively, with the yielding of the link and the joint collapse, the end-plate and the bolts are sub-resistant respect to the link. In particular, At P_{Y2}, the end-plate shows an overstrength coefficient of OS_{el}= 0,81 and OS_{ul}= 0,78, and the bolts of OS_{el}= 1 and OS_{ul}= 0,89, respectively at their elastic limit and ultimate strength. At P_C, the end-plate shows an overstrength coefficient of OS_{el}= 0,47 and OS_{ul}= 0,83, and the bolts of OS_{el}= 0,66 and OS_{ul}= 0,83, respectively at their elastic limit and ultimate strength (Fig. IV.6 and Tab. IV.6).

Table IV.59 – P10 specimen: yield of the link (P_{Y2}) and collapse (P_C) stress value σ, OS_{el} (σ/σ_{el}) and OS_{ul} (σ/σ_u).

Point	Link	End Plate			Thread Bolt			Timber beam		
	σ [MPa]	σ [MPa]	Over-strength		σ [MPa]	Over-strength		σ [MPa]	Over-strength	
			el	ul		el	ul		el	ul
Y_2	235	315	0,81	0,78	544	1	0,89	8,0	3	2
C	300	374	0,47	0,83	608	0,66	0,83	18,8	2,8	1,1

The collapse hierarchy of the elements connection, therefore, is: 1) end-plate/thread bolts, 2) link, 3) timber beam.

In particular, based on the joint classification proposed in the chapter 2.4.2, by the numerical analysis it is possible to classify the joint as a *Partial-strength connection (PS)*, that is designed to develop plastic deformations of connection sub-components (end-plate and bolts) while the other macro-components (link and beam) have an over-strength respect to the connection.

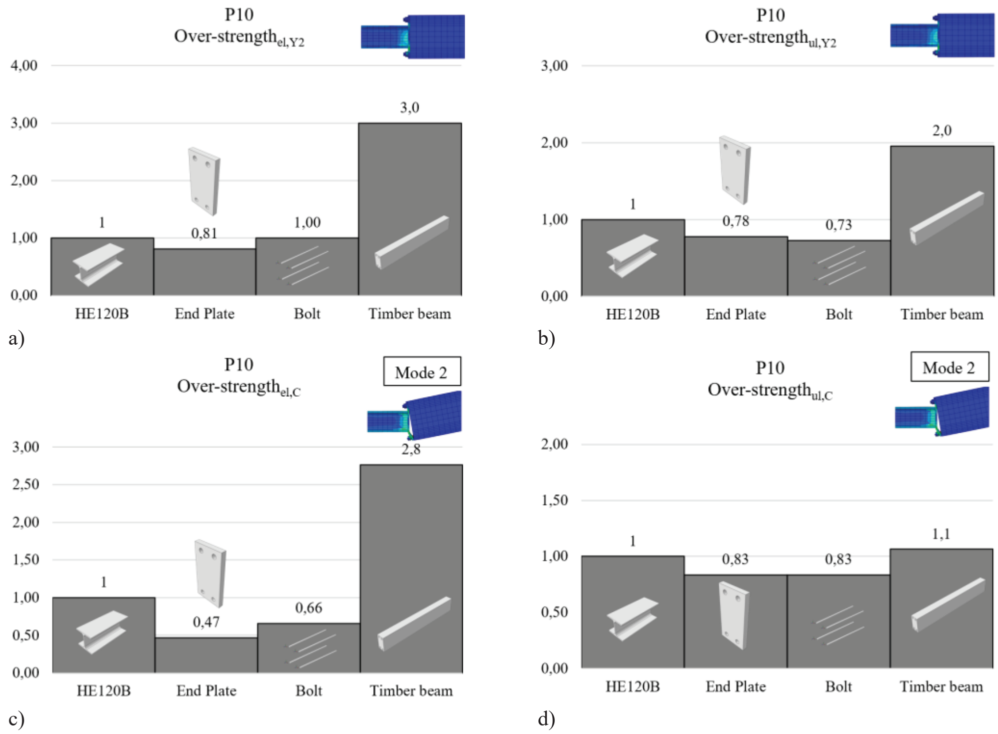

Figure IV.91 – P10 specimen: OS_{el} (σ/σ_{el}) and OS_{ul} (σ/σ_u) evaluated in P_{Y2} and P_C points.

Figure IV.7 shows the deformed configuration, respect to the unformulated configuration, in the 3 points: P_{Y1}, P_{Y2} and P_C. In particular, in P_{Y1}, the vertical displacement is 19 mm, in P_{Y2} is 13 3mm and at the collapse is 380 mm.

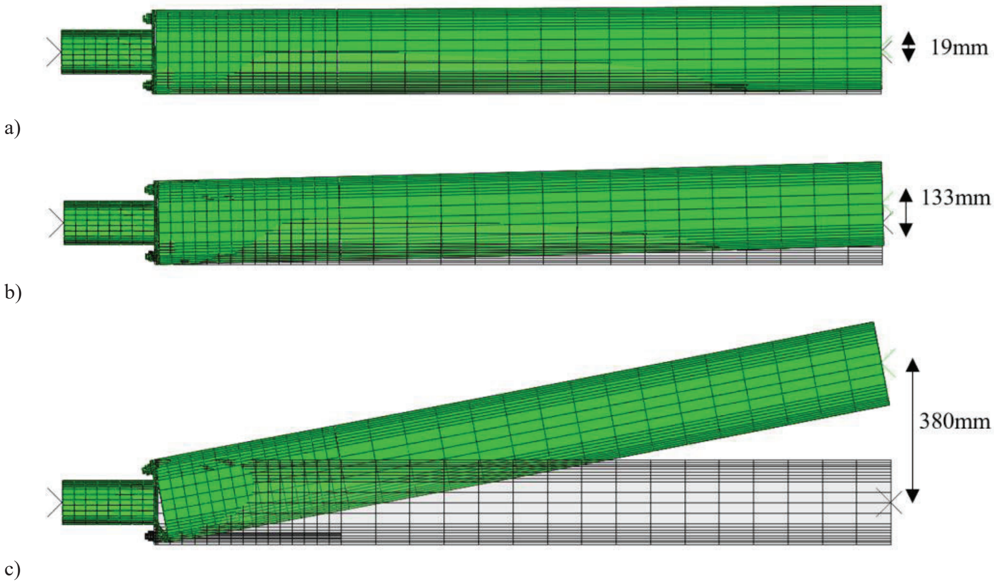

Figure IV.92 – P10 specimen: vertical deformed configuration in a) P_{Y1}, b) P_{Y2} and c) P_C points.

Figure IV.8 shows the AC YIELD diagram, which presents the evolution of the yield through the normal stress distribution (σ). In particular, at the P_{Y1}, the first fiber that catches the yield is in correspondence with the end-plate (Fig. IV.8a,b), while the other elements of the connection (link and bolts) and the timber beam are still in the elastic field. At the P_{Y2} (Fig. IV.8c,d), the link and the bolts reach the yield while the timber beam is still in the elastic field. At the P_C (Fig. IV.8e,f), the ultimate stress (f_{uk}= 360MPa) is reached in the end-plate and the bolts, without an extension of the plastic hinge in the link.

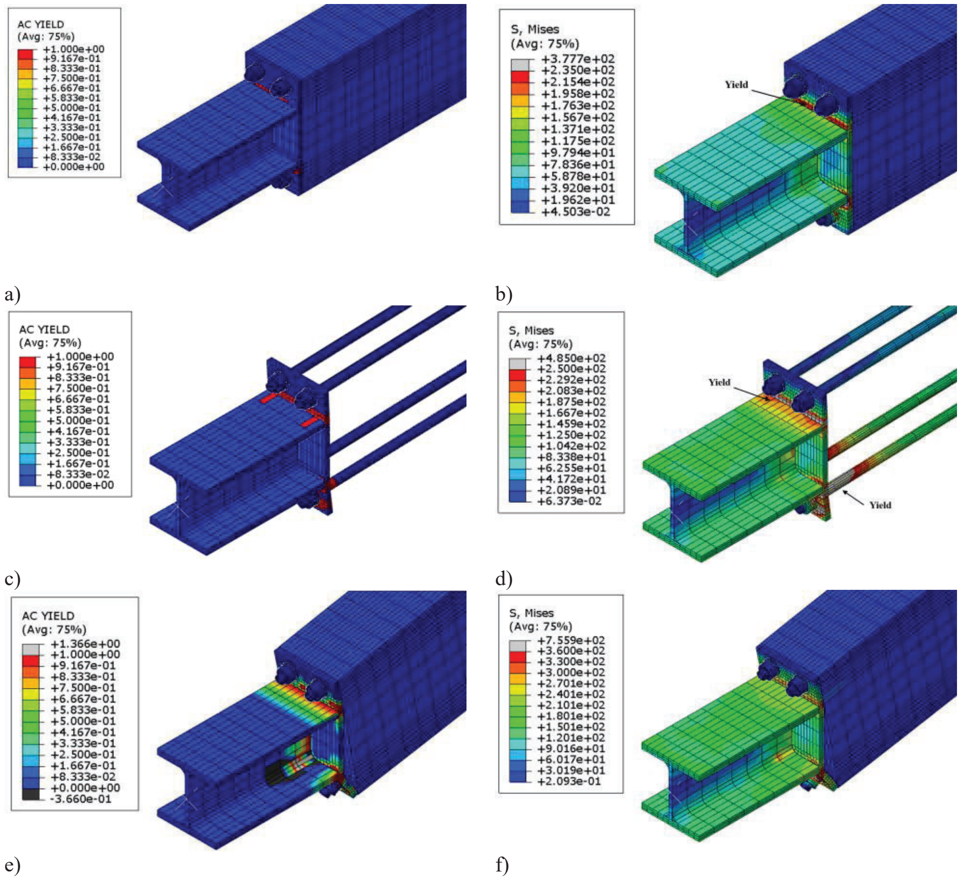

Figure IV.93 – P10 specimen: yielding and stress distribution of the elements in a), b) P_{Y1}, c), d) P_{Y2} and e), f) P_C points.

At the collapse, the following observations can be drawn. The collapse is achieved according to the collapse mode 2 (Fig. IV.9), with small plastic deformation of the end-plate and bolts.

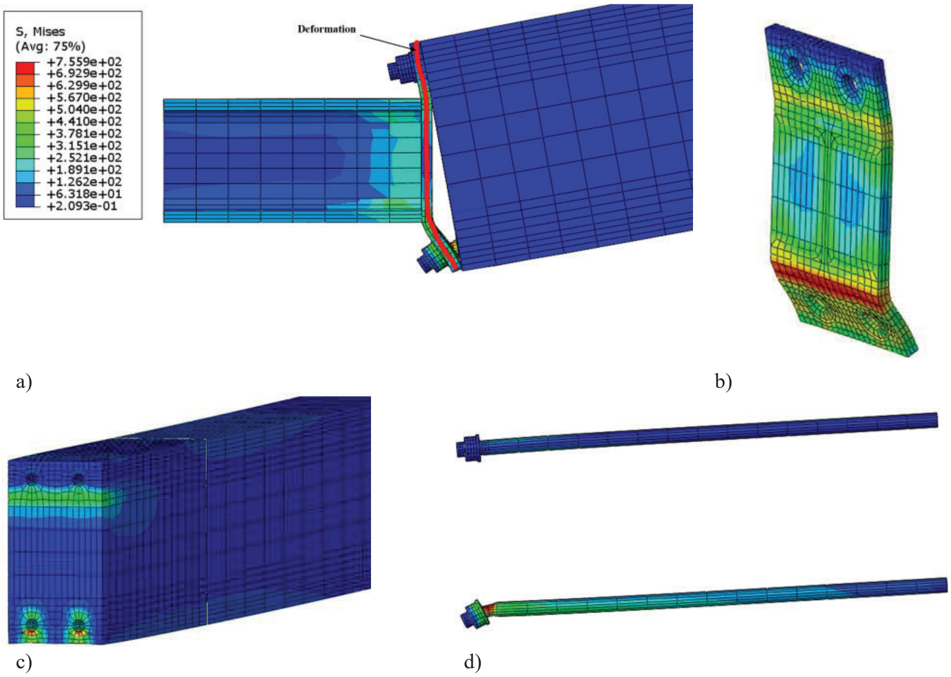

Figure IV.94 – P10 specimen: stress distribution in a) link, b) end-plate, c) timber beam and d) bolts, in P_C point.

4.2.5 Analysis of the mechanical behaviour through the components method

A design model is so put forward and validated, based on the so-called component method, with the:

- "identification" of the basic joint components;
- "mechanical characterisation" (strength, stiffness and deformation capacity) of each component;
- "assembly" of the components and computation of the global joint parameters.

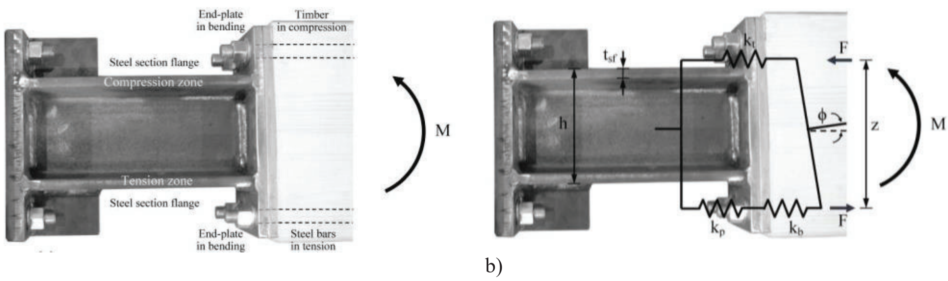

Figure IV.95 – a) Joint components; b) Model for the internal force distribution and related stiffness (Andreolli, 2011).

The "component method" (Jaspart, 2000, EN 1993-1-8, 2005) considers the joint as an "assembly" of components and it enables evaluation of the strength and stiffness of the joint, on the basis of the response parameters of each component. The procedure proposed in Beg et al. (Beg et al, 2004) can be adopted to appraise the rotational ductility.

The joint behaviour is approximated by a simplified trilinear moment-rotation curve. In particular, for the structural analysis, the joint can be represented by a rotational spring (Fig. IV.10), whose behaviour is described by the relation between the applied moment $M_{j,Ed}$ and the corresponding rotation ϕ_{Ed} of the connected structural elements (Fig. IV.11a).

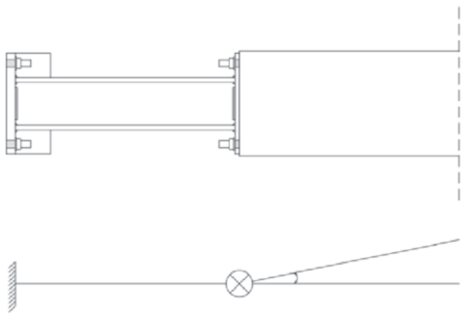

a)

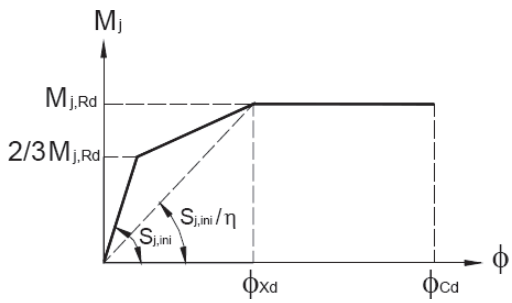

b)

Figure IV.96 – a) Modelling of the joint using rotational springs; b) Tri-linear moment-rotation relationship.

According to the Eurocode EN 1993-1-8 (CEN, 2005), the mechanical properties that characterize the moment-rotation curve are:

- moment resistance $M_{j,Rd}$;
- initial rotational stiffness $S_{j,ini}$;
- rotation capacity ϕ_{Cd}.

The relation between the bending moment $M_{j,Ed}$, applied to the joint, and the corresponding rotation ϕ_{Ed} is illustrated in Figure IV.11b:

- for values of $M_{j,Ed}$ lower than (2/3)$M_{j,Rd}$ an elastic-linear trend is assumed, characterized by a rotational rigidity equal to $S_{j,ini}$;
- for values of $M_{j,Ed}$ comprised between (2/3)$M_{j,Rd}$ and $M_{j,Rd}$, a reduced stiffness is assumed, equal to $S_{j,ini}$ /η;
- for values of $M_{j,Ed}$ equal to $M_{j,Rd}$, with values of ϕ_{Cd} greater than ϕ_{Xd}, a perfectly plastic-linear behaviour is assumed, neglecting the hardening of the material.

Joint moment resistance

The distribution of the internal actions, in the examined joint, is represented in Figure IV.12: the bolts are in tension, while the compression is schematized by the stress-block model.

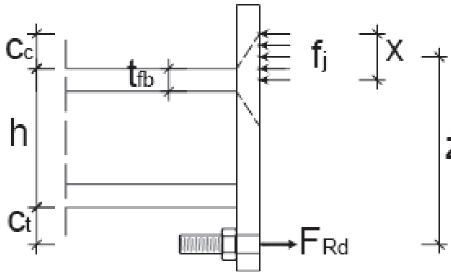

Figure IV.97 – Model for the resistant moment evaluation.

The design moment resistance, $M_{j,Rd}$, can be determined according to:

$$M_{j,Rd} = F_{Rd} \cdot z$$

where z is the lever arm of the internal couple and F_{Rd} is the resistance of the weakest component of the joint, that is the smallest value among:

- the resistance of the equivalent T-stub in tension $F_{t,T\text{-}stub,Rd}$;
- the resistance of the equivalent T-stub in compression $F_{c,T\text{-}stub,Rd}$;
- the resistance of the steel section flange in compression $F_{sf,Rd}$;
- the resistance of the glued-in steel bars in tension and shear $F_{t,bar,Rd}$.

From balance to translation, it is possible to derive x:

$$x \cdot f_j \cdot l_{eff} = F_{Rd,min}$$

$$x = \frac{F_{Ed,min}}{f_j \cdot l_{eff}}$$

The distance, z, can be evaluated as:

$$z = C_t + h + C_c - \frac{x}{2}$$

where is it:
$F_{Rd,min}$ is the strength of the weakest component;
f_j is the resistance of the timber in compression in the direction parallel to the fibers;
l_{eff} is the effective width of the equivalent T-stub element in compression.

<u>Equivalent T-stub in tension</u>

The resistance and the failure mode of the extended end-plate in bending and the bars in tension (Fig. IV.13a - lower part of the connection), are modelled through an equivalent T element (T-Stub), according to EN 1993-1-8 (CEN, 2005). In particular, for the ultimate rotation and the failure mode, the T-stub strength is calculated using Eurocode 3 formulae, where the nominal yield stress f_y is replaced by the ultimate strength f_u measured by tensile tests on specimens from the same steel plate utilized for the experimental campaign, to take into account the phenomena of hardening.

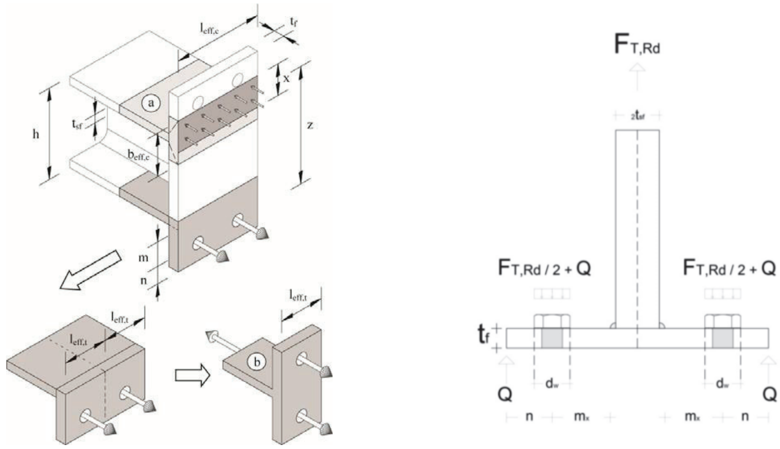

a) b)

Figure IV.98 – a) Modelling of a flange using the equivalent T-stub element (a) in compression and (b) in traction according to EN 1993-1-8; b) Geometrical features of the T-stub element in tension.

For the T-stub in tensile, the possible failure modes are (CEN, 2005; ECCS, 1999, Fig. IV.14):

- Mode 1: complete yielding of the flange;
- Mode 2a: failure of the bars after yielding of the flange in presence of prying forces;
- Mode 2b: yield of the flange without prying forces;
- Mode 3: bar failure.

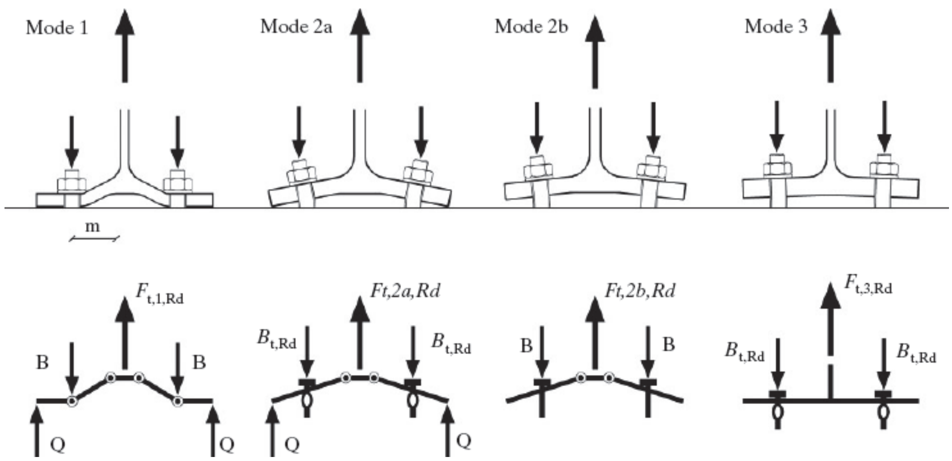

Figure IV.99 – Failure modes and ultimate displacements in a T-stub in tension according to ECCS, 1999 and Beg et al, 2004. Mode 1: complete yielding of the flange; Mode 2a: bar failure and yielding of the flange in presence of prying forces; Mode 2b: yield of the flange without prying forces; Mode 3: bars failure.

Depending on the presence of prying forces, different formulas are used (Tab. IV.7).

Table IV.60 – Resistance of T-stub in tension strength formula.

Collapse mode	**Presence of prying forces**	
Mode 1	**Method 1**	**Method 2**
Without reinforcement plates	$F_{T,1,Rd} = \frac{4M_{pl,1Rd}}{m}$	$F_{T,1,Rd} = \frac{(8n - 2e_w)M_{pl,1,Rd}}{2mn - e_w(m+n)}$
With reinforcement plates	$F_{T,1,Rd} = \frac{4M_{pl,1,Rd} + 2M_{bp,Rd}}{m}$	$F_{T,1,Rd} = \frac{(8n - 2e_w)M_{pl,1,Rd} + 4nM_{bp,Rd}}{2mn - e_w(m+n)}$
Mode 2	$F_{T,2,Rd} = \frac{2M_{pl,1,Rd} + n\Sigma F_{t,Rd}}{m+n}$	
Mode 3	$F_{T,3,Rd} = \Sigma F_{T,Rd}$	
	Without prying forces	
Mode 1 (Mode 1-2)		
Without reinforcement plates	$F_{T1-2,Rd} = \frac{2M_{pl,1,Rd}}{m+n}$	
With reinforcement plates		
Mode 2		
Mode 3	$F_{T,3,Rd} = \Sigma F_{T,Rd}$	

where:

$$M_{pl,1,Rd} = 0{,}25 \cdot \Sigma l_{eff,1} \cdot t^2{}_f \cdot \frac{f_y}{\gamma_{m0}}$$

$$M_{pl,2,Rd} = 0{,}25 \cdot \Sigma l_{eff,2} \cdot t^2{}_f \cdot \frac{f_y}{\gamma_{m0}}$$

$$M_{bp,Rd} = 0{,}25 \cdot \Sigma l_{eff,1} \cdot t^2{}_f \cdot \frac{f_{y,bp}}{\gamma_{m0}}$$

To check the presence of prying forces it is necessary to evaluate the length of the lengthening bolt (effective length), L_b, equal to the tightening zone (thickness of the flange, t_f, and washer, S_r), plus half the sum of the height of the head of the bolt S_T and of the nut S_D, and compare it with the limit length L_b^*.

If $L_b < L_b^*$, then there is development of prying force;
If $L_b \geq L_b^*$, then there is no development of prying force.

In particular, according to the EC3, L_b is evaluated as:

$$L_b = t_f + S_r + S_D$$

and L_b^* is evaluated as:

$$L_b^* = \frac{8{,}8 \cdot m_x^3 \cdot A_{res} \cdot n_{fb}}{\Sigma l_{eff} \cdot t_f^3}$$

where:
l_{eff}: Effective length of the equivalent T-stub element (Tab. IV.8), function of the position, number and model of bolt in tension;

Table IV.61 – Evaluation of the effective length of the equivalent T-stub element, l_{eff}.

	Bolt-row considered individually	
Bolt-row location	**Circular patterns** $l_{eff,cp}$	**Non-circular patterns** $l_{eff,nc}$
Bolt-row outside tension flange of beam	Smallest of: $2\pi m_x$ $\pi m_x + w$ $\pi m_x + 2n$	Smallest of: $4m_x + 1{,}25n$ $e + 2m_x + 0{,}625n$ $0{,}5w + 2m_x + 0{,}625n$
Mode 1	$l_{eff} = l_{eff,nc}$ if $l_{eff,nc} \leq l_{eff,cp}$	
Mode 2	$l_{eff,2} = l_{eff,nc}$	

n_{fb}: number of bolt-rows;
A_{res}: resistance area of the bolt.

The design should account for the presence of the “timber components” (wood in compression, glued-in steel bars) and of the stiffeners that are not dealt with by the European standard for steel structures (CEN, 2005a). Starting from the discussion proposed by the EC3, regarding the anchor bolts drowned in concrete, and implementing it with Volkersen’s considerations for simple overlap joints (Volkersen, 1938), the following parameters are defined (Tomasi et al, 2008) to evaluate L_b (Fig. IV.15 and Fig. IV.16):

$$L_b = \alpha \cdot \varphi + t_f + S_r + S_D$$

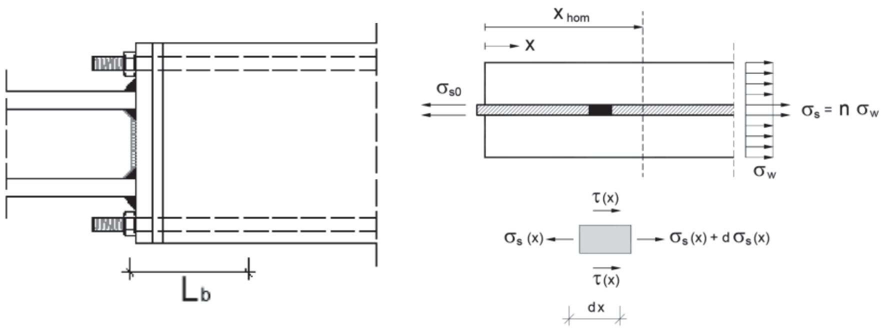

a) b)
Figure IV.100 – a) Effective length of the lengthening bolt, L_b; b) axial-symmetrical joint with glued bar (Andreolli et al, 2011).

$$\alpha = \frac{1}{(1+\psi)\omega \cdot \varphi}$$

with:

$$\psi = \frac{E_s \cdot A_s}{E_{0,d} \cdot A_w}$$

$$\Gamma = \frac{G_{0,d} \cdot \pi \cdot \varphi}{E_s \cdot A_s \cdot t_{glue}}$$

$$\omega^2 = \Gamma\,(1 + \Psi)$$

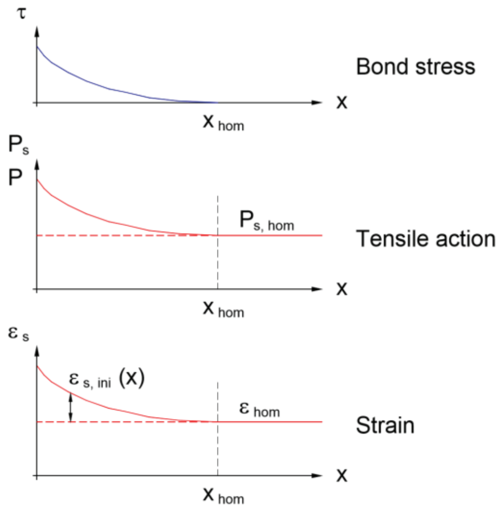

Figure IV.101 – Distribution of shear stresses, axial action and deformation in the steel bar (Andreolli et al, 2011).

where:

$E_{0,d}$: Elastic modulus of wood parallel to the direction of the fibers;

A_w: $36\varphi^2$;

$G_{0,d}$: Shear modulus of wood parallel to the direction of the fibers;

t_{glue}: Glue thickness;

φ: Diameter of the bolt;

S_r: Thickness of the washer;

t_p: Thickness of the end-plate;

S_d: Thickness of the nut.

<u>Equivalent T-stub in compression</u>

The resistance of the basic component 'timber and steel end-plate in bending' under compression, can be modelled through an equivalent T-stub in compression, in accordance with recommendations in EN 1993-1-8 (CEN, 2005) for the case of steel column base joints. If a steel plate is glued on the end cross-section of the timber element against which the end-plate is bearing, such a component can be neglected; in fact the glued-in steel plate has a higher stiffness compared to the wood in compression at the interface and therefore the compression force is spread over a larger area with negligible stresses (Fig. IV.17).

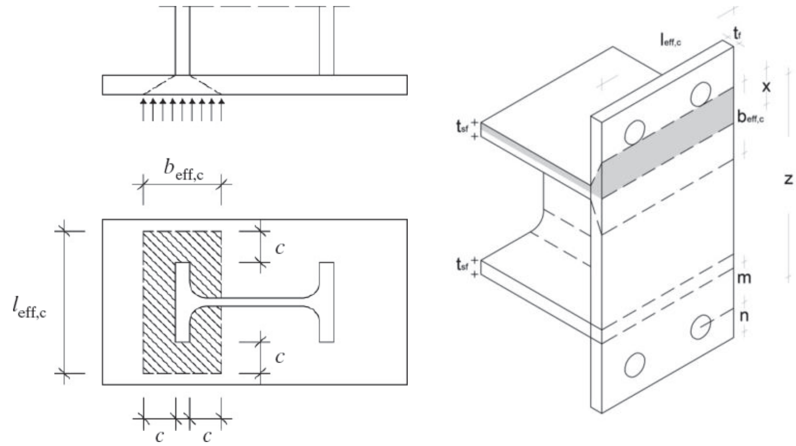

a) b)

Figure IV.102 – a) Flange modelling as an equivalent T-stub element in compression according to EN 1993-1-8 and b) 3D representation.

The resistance of the equivalent T-stub in compression ca be evaluated as:

$$F_{C,Rd} = f_j \cdot b_{eff} \cdot l_{eff}$$

where:

f_j: Compression resistance parallel to wood fibers, $f_{c,0,g,d}$;
b_{eff}: Effective height of the T-Stub;
l_{eff}: Effective width of the T-Stub.

It is assumed that the compression stresses are uniformly distributed over a rectangular area b_{eff} l_{eff} (Fig. IV.17b), with the width of the contact area c. This parameter is defined by referring to the bending verification of the cantilever part of the end-plate. In particular, it ie evaluated by equating the bending resistant moment, M_{Rd}, per unit of length, with the bending soliciting moment, M_{Ed}, per unit of length.

$$M_{Rd} = \frac{1}{\gamma_{M0}} \frac{t_f^2 + f_y}{6} = \frac{f_j \,.\, c^2}{2} = M_{ed}$$

and c is equal to:

$$c = t_f \sqrt{\frac{f_y}{3 \cdot f_j \cdot \gamma_{M0}}}$$

Steel section flange in compression

The plastic resistance of the steel section flange in compression can be determined according to EN 1993-1-8 (CEN, 2005) by the following expression:

$$F_{sf,Rd} = \frac{M_{c,Rd}}{h \ \cdot t_{sf}}$$

where:

$M_{c,Rd}$: Bending resistance moment of the cross-section;
h: Height of the steel profile;
t_{sf}: Thickness of the profile wing.

The plastic resistance of the steel section flange in compression can be determined according to EN 1993-1-8 (CEN, 2005) by the following expression:

Glued-in steel bars in tension

As regard the bolts, to evaluate the length of the glued bars, is used the method presented in an Informative Annex of Eurocode 5: Part 2, that presents four criteria for consideration in joints employing steel rods:

- Rod failure through yielding;
- Failure of the adhesive by debonding from steel or wood;
- Failure of the timber adjacent to the glue-line;
- Failure of the timber member (e.g. pull-out of a whole timber plug with several glued-in rods).

The yield failure of rods is identified as the preferred design mode. The yielding of the steel is a ductile failure mode, reserving capacity to transmit loads even after failure, albeit at excessive deformation levels. To date it has generally been considered that the requirements of adhesives in these cases are to achieve good adhesion to the timber, attain sufficient shear strength to maintain integrity across the adhesive layer and to provide anchorage to the rod through combined adhesion and mechanical interlock.

The strength of the joint (R_{ax}) has be the minimum between the plastic strength of the steel bars and the pull-out strength of the glued bars (Tab. IV.9).

$$R_{ax} = \min\left(f_{y,d} \cdot A_{res};\ \pi \cdot d_{eq} \cdot l_{ad} \cdot f_{k1,d}\right)$$

where:

$f_{y,d}$= yielding strength of the bars;
A_{res} = strength area of the bars;

d_{eq} = equivalent diameter of the bars;
l_{ad} = glue length;
$f_{k1,d}$= glue strength.

Table IV.62 – Glue strength depending to the glue length.

$l_{ad} \leq 250$ mm	250 mm < $l_{ad} \leq 500$ mm	500 mm < $l_{ad} \leq 1000$ mm
4	$5{,}25 - 0{,}005\ l_{ad}$	$3{,}5 - 0{,}0015\ l_{ad}$

In the case of steel bars glued parallel to the grain direction, the tensile strength of the timber element at the end of the bar has also be checked, assuming for the resistant section an area equal to $36d^2$ for each bar.

- **Joint rotational stiffness**

The initial rotational stiffness $S_{j,ini}$ should be determined according to EN 1993-1- 8 (CEN, 2005) by the following expression:

$$S_{j,ini} = \frac{E_s \cdot z^2}{\Sigma \frac{1}{k_i}}$$

where E_s is the elastic modulus of steel and k_i is the stiffness coefficient for i[th] basic component in Figure IV.18:
k_p: is the stiffness coefficient for the steel end-plate in bending under tension;
k_b: is the stiffness coefficient for the steel bars in tension;
k_t: is the stiffness coefficient for timber in compression.

The other basic components give negligible contribution to the rotational stiffness of the joint.

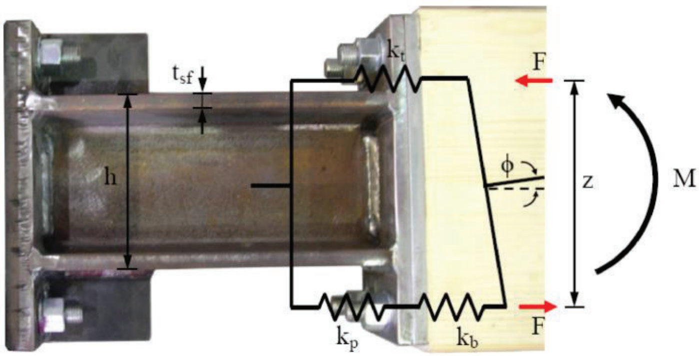

Figure IV.103 – Model for the joint stiffness evaluation (Andreolli et al, 2011).

Stiffness coefficient k_p - steel end-plate in bending under tension

The stiffness coefficient k_p can be determined according to the relationships provided in EN 1993-1-8 (CEN, 2005):

With prying forces:

$$k_p = \frac{0{,}85 \cdot l_{eff,t} \cdot t_f^3}{m^3}$$

Without prying forces:

$$k_p = \frac{0{,}425 \cdot l_{eff,t} \cdot t_f^3}{m^3}$$

where:

$l_{eff,t}$: Effective length of the equivalent T-stub flange in tension;
t_f: Thickness of the equivalent T-stub flange in tension;
m: Geometrical parameter of the equivalent T-stub flange in tension.

Stiffness coefficient k_b - two steel bars in tension in a row

The stiffness coefficient k_b can be determined according to the relationships provided in EN 1993-1-8 (CEN, 2005):

With prying forces:

$$k_b = \frac{1{,}6\ A_s}{L_b}$$

Without prying forces:

$$k_b = \frac{2\ A_s}{L_b}$$

where:

A_s: is the effective bar area;
L_b: is the steel bar elongation length.

The stiffness coefficient k_t can be determined according to the following relationship:

$$k_t = \frac{E_{0,w}\sqrt{b_{eff,c} \cdot l_{eff,c}}}{\beta \cdot E_s}$$

where:

$E_{0,w}$: The wood elastic modulus parallel to the grain;
$b_{eff,c}$: Effective dimensions of the equivalent T-stub flange in compression
$l_{eff,c}$: Effective dimensions of the equivalent T-stub flange in compression;

β: A coefficient that can be assumed equal to 4 (Tomasi et al, 2008).

Joint rotation capacity

The rotation capacity of the joint depends on the deformation capacity of the weakest component, while the other components should be taken into account with their deformation at the stress level corresponding to the ultimate strength. The failure mode of the joint examined is associated with the resistance of the T- stub in tension, while the contribution of elements in compression is negligible, thus, in order to evaluate the rotation capacity ϕ_{Cd}, the joint is modelled according to Figure IV.19 and the following expression may be used:

$$\varphi_{CD} = \frac{\delta_{u,t,T-stub,i}}{d_i}$$

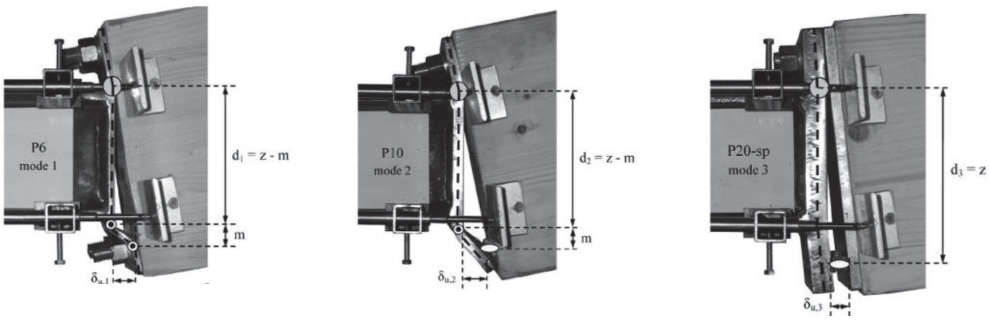

a) b) c)

Figure IV.104 – Model for the joint rotation evaluation (Andreolli et al, 2011).

where:

$\delta_{u,t,T\text{-}stub,i}$: the ultimate displacement of the T-stub in tension;

d_i: assumed as shown in Figure IV.19, depending both on the failure modes.

The T-stub deformation capacity can be evaluated in accordance with the following analytical expressions (Beg and al, 2004) for the three collapse modes (Fig. IV.19).

Mode 1 (complete yielding of the flange):

$$\delta_{u,t,T\text{-}stub,1} = 2 \cdot \varepsilon_u \cdot m$$

where:

ε_u: the ultimate strain of the steel end-plate;

m: a geometrical parameter.

Mode 2 (bar failure and yielding of the flange):

$$\delta_{u,t,T\text{-stub},2} = \varepsilon_{ub} \cdot L_b \left(1 + \frac{m}{n}\right)$$

where:
ε_{ub}: the ultimate strain of the steel bars;
n: a geometrical parameter.
Mode 3 (bars failure, Fig. IV.20):

$$\delta_{u,t,T\text{-stub},3} = \varepsilon_u \cdot L_b$$

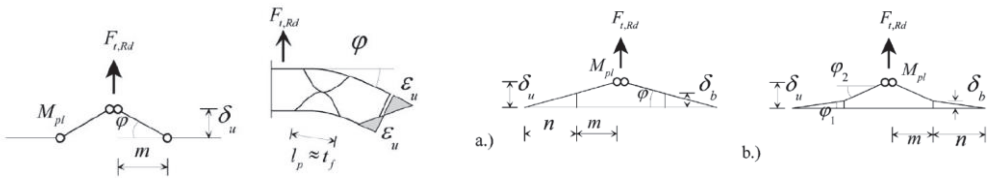

a) b)
Figure IV.105 – a) Ultimate strain for mode 1; b) ultimate strain for (a) mode 2a and (b) mode 2b (Beg and al, 2004).

The bending resistance moment, the ultimate rotation and the failure mode evaluated by the component method and compared with the parameters obtained from the experimental test are reported below. It is possible to observe how the values are cathed (Tab. IV.10).

Table IV.63 – Analysis of results: comparison between the test and the component method parameters.

Failure mode of the T-stub in tension		**Bending resistance moment [kNm]**		**Ultimate rotation [rad]**	
Test	Component method	Test	Component method	Test	Component method
2	2	19,85	16,76	0,18	0,18

4.3 Parametric analysis

4.3.1 Definition of the parameters

Starting to the structural features of the *P10* specimen, it is intended in this section to perform a sensitivity analysis of the timber-steel link to several parameters that can affect the joints behaviour, the collapse hierarchy and, in particular, with the aim to study, to understand what is the parameters combination that caches plastic hinge formation in the steel link. For this reason, the model is modified according to the following key parameters that have the potential to influence the joint response. A numerical parametric study is carried out on 26 timber-steel link joint types, differing by these main parameters: bolts grade, end-plate grade, end-plate thickness, timber grade, the presence of stiffeners.

From the observation of the *P10* test and numerical results, the bolts grade has been changed in order to avoid their premature collapse (6.8, 8.8, 10.9), the end-plate grade has been changed in order to avoid excessive deformation (S275, S355, S450), the end-plate thickness, t_f, has been changed (from 10 mm to 20 mm) in order to increase its strength and bending stiffness. Finally, the connections with different timber grade (GL28h, GL36h) and with two steel stiffeners (55x55x15 mm, steel grade S275) arranged parallel to the link web is also studied. These parameters have been studied separately and in combination, using the same link profile of the *P10* specimen (Tab. IV.11). The parametric study is carried out with the same set-up as the monotonic analysis on the *P10* specimen, using the structural calculation program ABAQUS.

For each numerical model, the outputs are detected at specific increments (In.) and times (t.), corresponding to the yield of the first connection element (P_Y) and to the collapse of the connection (P_C). In particular, for each component of the model (link, end-plate, bolts, timber beam and stiffeners), the output are provided in terms of the maximum values of stresses (σ), DCR_{el} ($DCR_{el}=\sigma/\sigma_{el}$) and DCR_{ul} ($DCR_{ul}=\sigma/\sigma_{ul}$) to study the collapse hierarchy of the connection elements, while the stress distribution at the connection collapse (P_C), the maximum reaction bending moment (M_{max}) and rotation (θ_{max}) in x-z plane, the maximum strength (F_{max}) and the displacement (u_{max}) in z-direction (in the RP point), and the ductility (μ) are evaluated to study the strength and the global stiffness ($S_{j,ini,g}$) of the models. Moreover, for each model, the F-u and M-θ curves are drawn while the non-dimensional curve (M/M_{el}-θ/θ_{el}) is shown to evaluate the local stiffness ($S_{j,ini,l}$), catching the relative rotation between the end-plate and the timber beam, and to classify the models connection with the "joint classification for timber structure procedure" (JCT) reported in the chapter 2.4.2.

Table IV.64 – Numerical parametric analysis: parameters and cases study.

Model	HE120B (L)	End Plate (P)		Thread Bolt (B)	Timber beam (T)	Stiffeners (S)
	Size	Grade	t_f [mm]	Grade	Grade	Size [mm]
B_6.8	HE120B	235	10	6,8	24	-
B_8.8	HE120B	235	10	8,8	24	-
B_10.9	HE120B	235	10	10,9	24	-
B_6.8 - P_275	HE120B	275	10	6,8	24	-
B_6.8 - P_355	HE120B	355	10	6,8	24	-
B_6.8 - P_450	HE120B	450	10	6,8	24	-
B_8.8 - P_275	HE120B	275	10	8,8	24	-
B_8.8 - P_355	HE120B	355	10	8,8	24	-
B_8.8 - P_450	HE120B	450	10	8,8	24	-
B_10.9 - P_275	HE120B	275	10	10,9	24	-
B_10.9 - P_355	HE120B	355	10	10,9	24	-
B_10.9 - P_450	HE120B	450	10	10,9	24	-
T_28	HE120B	235	10	6,8	28	-
T_36	HE120B	235	10	6,8	36	-
P_20	HE120B	235	20	6,8	24	-
P_20 - B_10.9	HE120B	235	20	10,9	24	-
S	HE120B	275	10	6,8	24	55x55x15
S - B_10.9	HE120B	275	10	10,9	24	55x55x15
S - P_20	HE120B	275	20	6,8	24	55x55x15
S - P_20 - B_10.9	HE120B	275	20	10,9	24	55x55x15

At the end, all the numerical results of the joints are compared to the *P10* numerical results in terms of maximum strength DCR_F ($DCR_F = F_{max}/F_{max,P10}$), maximum bending resistant moment DCR_M ($DCR_M = M_{max}/M_{max,P10}$), maximum displacement DCR_u ($DCR_u = u_{max}/u_{max,P10}$), maximum rotation DCR_θ ($DCR_\theta = \theta_{max}/\theta_{max,P10}$), global stiffness $DCR_{S,g}$ ($DCR_{S,g} = S_{j,ini,g}/S_{j,ini,g,P10}$), local stiffness $DCR_{S,l}$ ($DCR_{S,l} = S_{j,ini,l}/S_{j,ini,l,P10}$) and ductility DCR_μ ($DCR_\mu = \mu/\mu_{P10}$).

4.3.2 Outputs

In the Table IV.12 is depicted a summary of the numerical results, with information about the first "sub-component" that catches the yield, the collapse hierarchy, the non-dimensional values of the maximum force ($DCR_F=F_{max}/F_{max,P10}$), bending resistant moment ($DCR_M=M_{max}/M_{max,P10}$), displacement ($DCR_u=u_{max}/u_{max,P10}$) and rotation ($DCR_\theta=\theta_{max}/\theta_{max,P10}$) compared to the *P10* specimen.

Table IV.65 – Numerical parametric analysis results: first yield element, collapse hierarchy, DCR_F, DCR_u, DCR_M, DCR_θ.

Model	First yield component	Collapse hierarchy					DCR_F	DCR_u	DCR_M	DCR_θ
		1°	2°	3°	4°	5°				
B_6.8	End-plate	B	P	L	T	-	0,87	0,52	0,88	0,52
B_8.8	End-plate	P	B	L	T	-	0,96	0,55	0,97	0,57
B_10.9	End-plate	P	B	L	T	-	1,00	0,52	1,00	0,57
B_6.8 - P_275	End-plate/Bolts	B	P	L	T	-	0,87	0,64	0,86	0,68
B_6.8 - P_355	End-plate	B	P	L	T	-	0,92	0,63	0,92	0,63
B_6.8 - P_450	Bolts	B	P	L	T	-	1,03	0,49	0,96	0,47
B_8.8 - P_275	End-plate	B	P	L	T	-	1,06	0,75	1,06	0,78
B_8.8 - P_355	End-plate	B	P	L	T	-	1,10	0,56	1,11	0,57
B_8.8 - P_450	Link/Bolts	B	P	L	T	-	1,17	0,46	1,18	0,47
B_10.9 - P_275	End-plate	P	B	L	T	-	1,23	0,91	1,23	0,94
B_10.9 - P_355	End-plate	B	P	L	T	-	1,35	0,89	1,35	0,89
B_10.9 - P_450	Link	B	P	L	T	-	1,38	0,76	1,39	0,78
T_28	End-plate/Bolts	B	P	L	T	-	0,87	0,64	0,86	0,68
T_36	End-plate/Bolts	B	P	L	T	-	0,87	0,64	0,86	0,68
P_20	End-plate	B	P	L	T	-	1,55	0,55	1,57	0,57
P_20 - B_10.9	End-plate	B	P	L	T	-	1,91	1,00	1,92	0,94
S	End-plate	B	P	L	S	T	1,38	0,57	1,39	0,57
S - B_10.9	End-plate	B	P	L	S	T	1,77	0,37	1,65	0,36
S - P_20	Link/Bolts/Stiffeners	B	L	S	P	T	1,93	0,93	1,94	0,89
S - P_20 - B_10.9	Link	B	L	S	P	T	1,95	0,95	1,97	0,91

In Table IV.13 is depicted the response of the joints in terms of the stress distribution at the collapse point (P_C), the first connection component that catches the yield (P_Y), the M-θ and F-u curves with the yielding connections component points (in green colour) and the collapse hierarchy with the DCR_{ul} and the plastic mechanism type for each study case.

Table IV.66 – Numerical parametric analysis results: first yield element, collapse mode [DCR_{ul} %], collapse mode and hierarchy, F-u and M-θ curves, F_{max}, U_{max}, M_{max}, θ_{max}.

First yield component (P_Y)	Collapse mode (P_C)	DCR$_{ul}$ [%]	F$_{max}$ [kN] (F-u)	u$_{max}$ [mm] (F-u)	M$_{max}$ [kNm] (M-θ)	θ$_{max}$ [rad] (M-θ)
B_6.8						
End-plate	Mode 2	B P (97) L (78) T (67)	8,82	200	19,89	0,10
B_8.8						
End-plate	Mode 1	P B (92) L (81) T (71)	9,7	209	21,88	0,11
B_10.9						
End-plate	Mode 1	P B (81) L (74) T (71)	10,07	201	22,73	0,11
B_6.8 - P_275						
End-plate/ Bolts	Mode 2	B P (83) L (79) T (71)	8,67	246	19,53	0,13
B_6.8 - P_355						
End-plate	Mode 2	B P (79) L (75) T (71)	9,31	243	20,9	0,12

B_6.8:

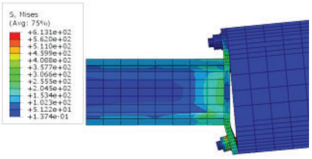
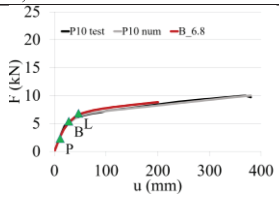

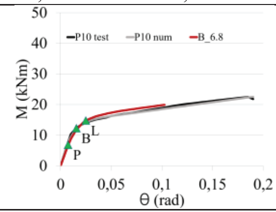

B_8.8:

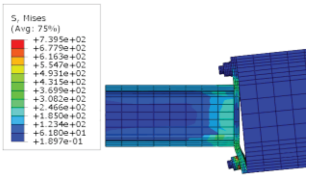
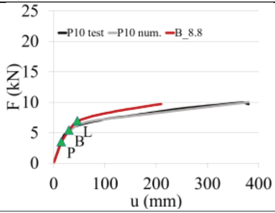

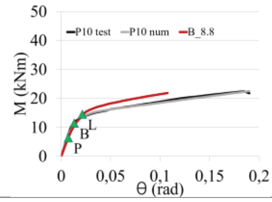

B_10.9:

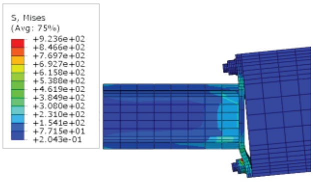
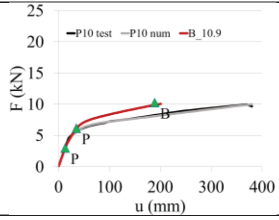

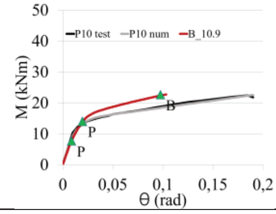

B_6.8 - P_275:

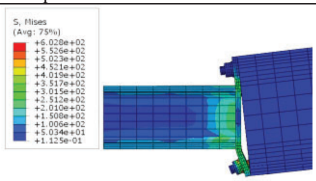
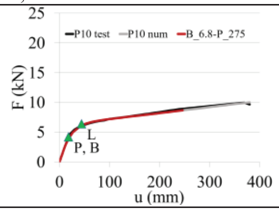

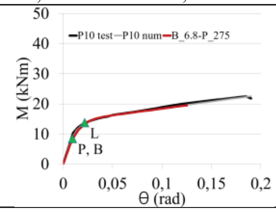

B_6.8 - P_355:

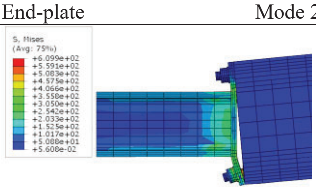
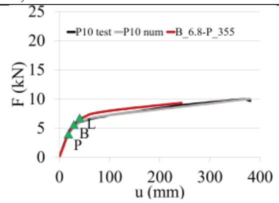

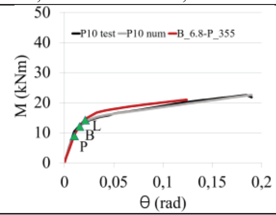

Table IV.67 – Numerical parametric analysis results: first yield element, collapse mode [DCR_{ul} %], collapse mode and hierarchy, F-u and M-θ curves, F_{max}, U_{max}, M_{max}, θ_{max}.

First yield component (P_Y)	Collapse mode (P_C) DCR$_u$ [%]	F-u: F_{max} [kN]	F-u: u_{max} [mm]	M-θ: M_{max} [kNm]	M-θ: θ_{max} [rad]
B_6.8 - P_450					
Bolts	Mode 2	9,59	189	21,63	0,09

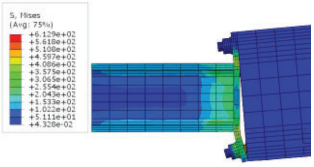

B
P (87)
L (83)
T (71)

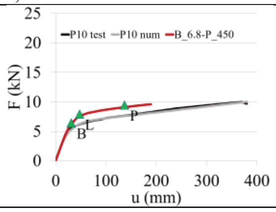

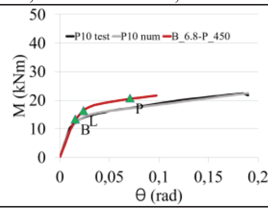

First yield component (P_Y)	Collapse mode (P_C) DCR$_u$ [%]	F-u: F_{max} [kN]	F-u: u_{max} [mm]	M-θ: M_{max} [kNm]	M-θ: θ_{max} [rad]
B_8.8 - P_275					
End-plate	Mode 2	10,69	288	24,02	0,15

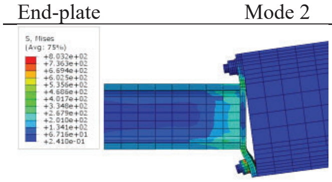

B
P (92)
L (82)
T (71)

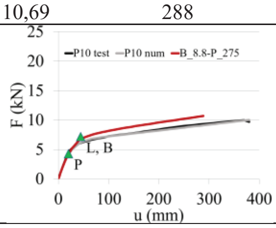

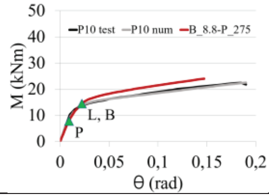

First yield component (P_Y)	Collapse mode (P_C) DCR$_u$ [%]	F-u: F_{max} [kN]	F-u: u_{max} [mm]	M-θ: M_{max} [kNm]	M-θ: θ_{max} [rad]
B_8.8 - P_355					
End-plate	Mode 2	11,15	216	25,13	0,11

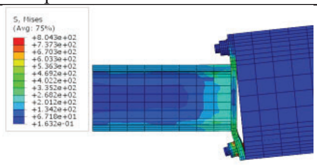

B
P (90)
L (85)
T (71)

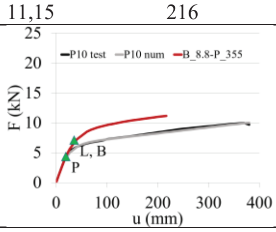

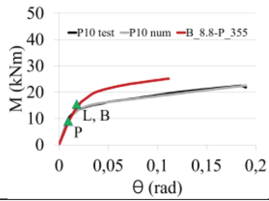

First yield component (P_Y)	Collapse mode (P_C) DCR$_u$ [%]	F-u: F_{max} [kN]	F-u: u_{max} [mm]	M-θ: M_{max} [kNm]	M-θ: θ_{max} [rad]
B_8.8 - P_450					
Link/ Bolts	Mode 2	11,83	178	26,68	0,09

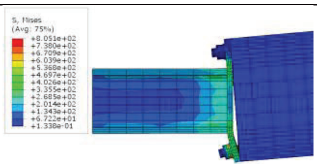

B
P
L (89)
T (71)

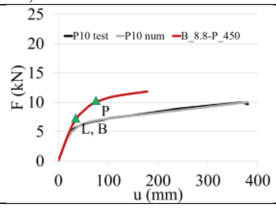

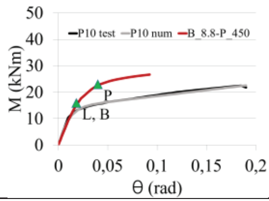

First yield component (P_Y)	Collapse mode (P_C) DCR$_u$ [%]	F-u: F_{max} [kN]	F-u: u_{max} [mm]	M-θ: M_{max} [kNm]	M-θ: θ_{max} [rad]
B_10.9 - P_275					
End-plate	Mode 1	12,47	347	27,81	0,18

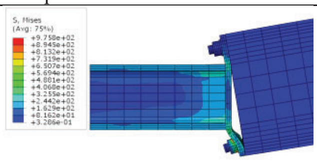

P
B (98)
L (89)
T (71)

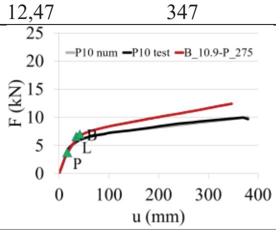

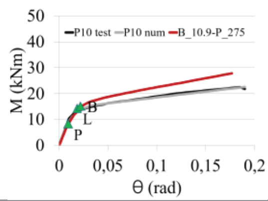

Table IV.68 – Numerical parametric analysis results: first yield element, collapse mode [DCR_{ul} %], collapse mode and hierarchy, F-u and M-θ curves, F_{max}, U_{max}, M_{max}, θ_{max}.

First yield component (P_Y)	Collapse mode (P_C) DCR$_u$ [%]	F-u: F_{max} [kN]	F-u: u_{max} [mm]	M-θ: M_{max} [kNm]	M-θ: θ_{max} [rad]
B_10.9 - P_355					
End-plate	Mode 2	13,62	339	30,52	0,17
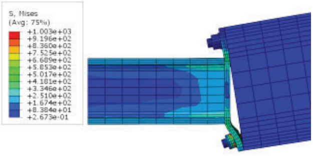	B P (97) L (85) T (71)	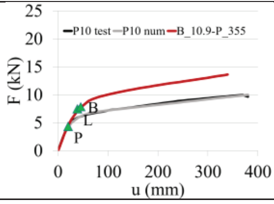		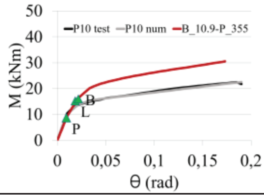	
B_10.9 - P_450					
Link	Mode 2	13,98	289	31,39	0,15
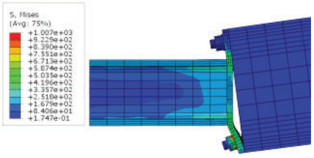	B P (94) L (84) T (71)	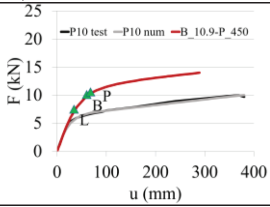		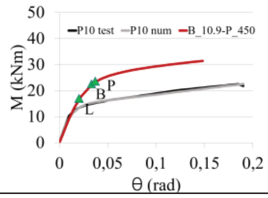	
T_28					
End-plate/ Bolts	Mode 2	8,67	246	19,53	0,13
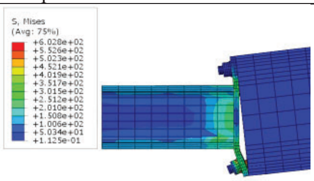	B P (83) L (79) T (71)	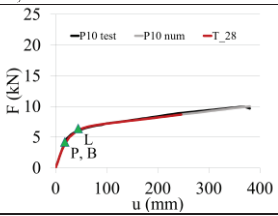		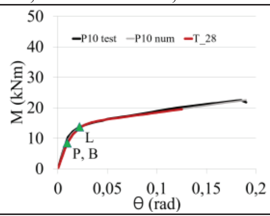	
T_36					
End-plate/ Bolts	Mode 2	8,69	246	19,56	0,13
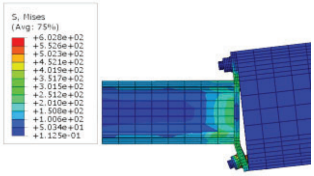	B P (82) L (78) T (71)	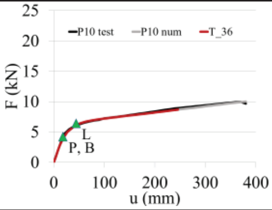		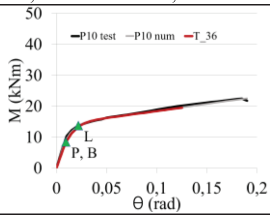	
P_20					
End-plate	Mode 2	15,67	209	35,38	0,11
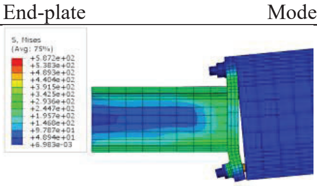	B P (87) L (85) T (71)	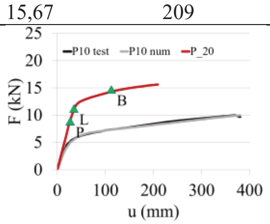		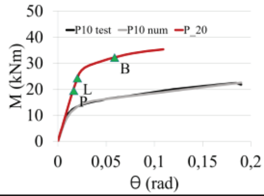	

Table IV.69 – Numerical parametric analysis results: first yield element, collapse mode [DCR_{ul} %], collapse mode and hierarchy, F-u and M-θ curves, F_{max}, U_{max}, M_{max}, θ_{max}.

		F-u		M-θ	
First yield component (P_Y)	**Collapse mode (P_C) DCR_u [%]**	**F_{max} [kN]**	**u_{max} [mm]**	**M_{max} [kNm]**	**θ_{max} [rad]**
P_20 - B_10.9					
End-plate	Mode 2	19,33	380	43,29	0,18
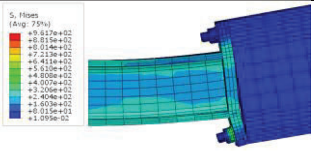	B P (92) L (78) T (78)	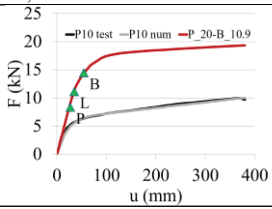		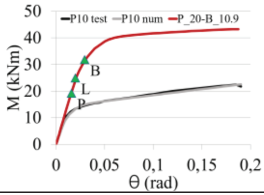	
S					
End-plate	Mode 2	13,94	218	31,40	0,11
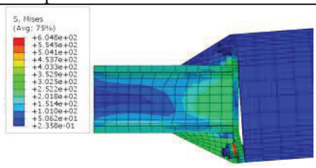	B P (82) L (79) S (66) T (78)	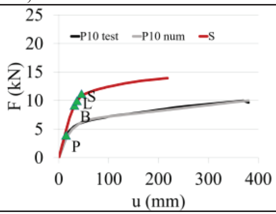		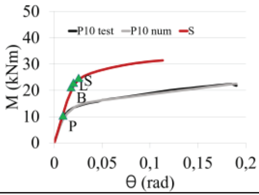	
S - B_10.9					
End-plate	Mode 2	16,49	142	37,23	0,07
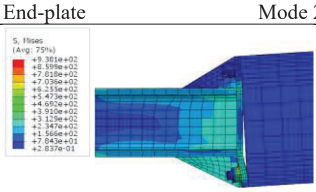	B P (86) L (82) S (67) T (78)	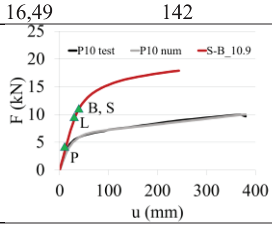		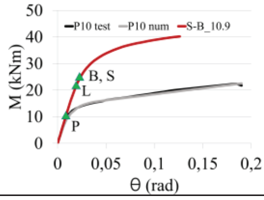	
S - P_20					
Link/Bolts/Stiffeners	Mode 2	19,49	356	43,71	0,17
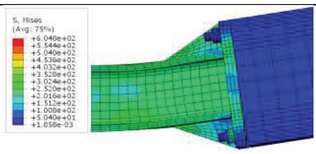	B L (76) S (67) P (65) T (78)	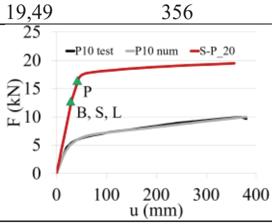		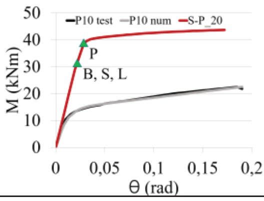	
S - P_20 - B_10.9					
Link	Mode 2	20,01	362	45,62	0,19
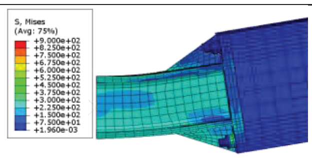	B L (83) S (75) P (72) T (78)	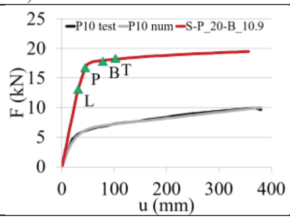		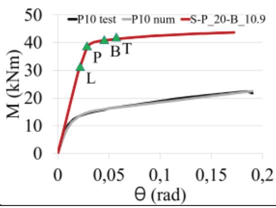	

In Table IV.14 are depicted the stress values (σ), the DCR_{el} and the DCR_{ul}, for each connection element, in the P_Y and P_C instants. Moreover, the first element that reaches the elastic strength (σ_{el}) and the ultimate strength (σ_u) is highlighted.

Table IV.70 – Parametric analysis results: yield (P_Y) and collapse (P_C) stress σ, DCR_{el} (σ/σ_{el}) and DCR_{ul} (σ/σ_u).

	Link			End Plate			Thread Bolt			Timber beam		Stiffeners		
	σ	DCR		σ	DCR		σ	DCR		σ	DCR	σ	DCR	
	[MPa]	el	ul	[MPa]	el	ul	[MPa]	el	ul	[MPa]	el	[MPa]	el	ul
B_6.8														
P_Y	97	41%	27%	235	100%	65%	238	50%	40%	11	46%	-	-	-
P_C	282	120%	78%	348	148%	97%	600	125%	100%	16	67%	-	-	-
B_8.8														
P_Y	107	46%	30%	235	100%	65%	266	41%	33%	12	50%	-	-	-
P_C	292	124%	81%	360	153%	100%	739	114%	92%	17	71%	-	-	-
B_10.9														
P_Y	97	41%	27%	235	100%	65%	238	26%	24%	12	50%	-	-	-
P_C	292	124%	124%	360	153%	100%	922	102%	92%	17	71%	-	-	-
B_6.8 - P_275														
P_Y	223	95%	62%	275	100%	64%	480	100%	80%	12	50%	-	-	-
P_C	284	121%	79%	356	129%	83%	600	125%	100%	17	71%	-	-	-
B_6.8 - P_355														
P_Y	144	61%	40%	355	100%	70%	362	75%	60%	12	50%	-	-	-
P_C	286	122%	75%	385	108%	79%	600	125%	100%	17	71%	-	-	-
B_6.8 - P_450														
P_Y	208	89%	58%	440	98%	80%	480	100%	80%	12	50%	-	-	-
P_C	300	128%	83%	478	106%	87%	600	125%	100%	17	71%	-	-	-
B_8.8 - P_275														
P_Y	137	58%	38%	275	100%	64%	372	58%	47%	12	50%	-	-	-
P_C	295	126%	82%	394	143%	92%	800	125%	100%	17	71%	-	-	-
B_8.8 - P_355														
P_Y	144	61%	40%	355	100%	70%	362	57%	45%	12	50%	-	-	-
P_C	323	137%	85%	435	123%	90%	800	125%	100%	17	71%	-	-	-
B_8.8 - P_450														
P_Y	235	100%	65%	443	98%	81%	640	100%	80%	12	50%	-	-	-
P_C	320	136%	89%	550	122%	100%	800	125%	100%	17	71%	-	-	-
B_10.9 - P_275														
P_Y	137	58%	38%	275	100%	64%	372	41%	37%	12	50%	-	-	-
P_C	322	137%	89%	430	156%	100%	976	108%	98%	17	71%	-	-	-
B_10.9 - P_355														
P_Y	144	61%	40%	355	100%	70%	362	40%	36%	12	50%	-	-	-
P_C	307	131%	85%	493	139%	97%	1000	111%	100%	17	71%	-	-	-
B_10.9 - P_450														
P_Y	235	100%	65%	443	98%	81%	894	99%	89%	12	50%	-	-	-
P_C	305	130%	85%	515	114%	94%	1000	111%	100%	17	71%	-	-	-
P_20														
P_Y	200	85%	56%	235	100%	65%	350	73%	58%	12	50%	-	-	-
P_C	306	130%	85%	314	134%	87%	600	125%	100%	17	71%	-	-	-
P_20 – B_10.9														
P_Y	191	81%	53%	235	100%	65%	456	51%	46%	12	50%	-	-	-
P_C	280	119%	78%	332	141%	92%	1000	110%	100%	17	71%	-	-	-
S														
P_Y	117	50%	33%	275	100%	64%	299	62%	50%	12	50%	122	44%	28%
P_C	283	120%	79%	353	128%	82%	600	125%	100%	17	71%	284	103%	66%
S – B_10.9														
P_Y	121	51%	34%	275	100%	64%	310	34%	31%	12	50%	126	46%	29%
P_C	294	125%	82%	371	135%	86%	1000	111%	100%	17	71%	290	105%	67%
S – P_20														
P_Y	235	100%	65%	229	83%	53%	480	100%	80%	12	50%	275	100%	64%
P_C	272	116%	76%	280	102%	65%	600	125%	100%	17	71%	290	105%	67%
S - P_20 - B_10.9														
P_Y	235	100%	65%	229	83%	53%	480	100%	80%	12	50%	275	100%	64%
P_C	272	116%	76%	280	102%	65%	600	125%	100%	17	71%	290	105%	67%

4.3.3 Analysis of results

The numerical results are analysed comparing the models with the *P10* specimen in terms of maximum strength ($DCR_F=F_{max}/F_{max,P10}$), global ($DCR_{S,g}=S_{j,ini,g}/S_{j,ini,g,P10}$) and local stiffness ($DCR_{S,l}=S_{j,ini,l}/S_{j,ini,l,P10}$), ductility ($DCR_\mu=\mu/\mu_{P10}$) and collapse mode.

<u>(i) Maximum strength (F_{max})</u>

In terms of the maximum strength (F_{max}) of the joints, compared to the *P10* specimen, the results revealed that there is no apparent influence of the steel grade bolt variation B_i (i=6.8, 8.8, 10.9), the end-plate steel grade variation with the bolt grade 6.8 B_6.8-P_i (i=275, 355, 450) and of the beam timber grade variation T_i (i=28, 36) for the joints behaviour (Fig. IV.21).

Only some small differences can be observed in the combinate bolt stell grade 8.8 with the end-plate steel grade variation models B_8.8-P_i (i=275, 355, 450), more notorious in the B_8.8-P_450 one, with a DCR_F=1,17.

This is also noticed in the combinate bolt steel grade 10.9 with the end-plate steel grade variation models B_10.9-P_i (i=275, 355, 450), in which the B_10.9-P_450 one presents a DCR_F=1,38.

The models with the end-plate thickness (P_20, P_20-B_10.9) and the stiffeners (S, S-B_10.9, S-P_20, S-P_20-B_10.9) present a more significant influent for the joint strength. In particular, the P_20 model, that presents the only variation of the thickness parameter, shows a greater DCR_F (1,55) than the other parameters. Compared to P_20, the combinate end-plate thickness 20 mm with the bolt steel grade 10.9 (P_20-B_10.9) presents a DCR_F=1,91 that, with the stiffeners' presence rises to DCR_F=1,93. the most favourable model is S-P_20-B_10.9, which shows a DCR_F=1,95 (Fig. IV.21 and Fig. IV.22).

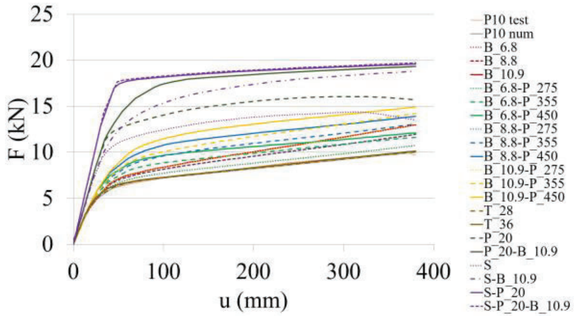

Figure IV.106 – Parametric analysis results: F-u curve.

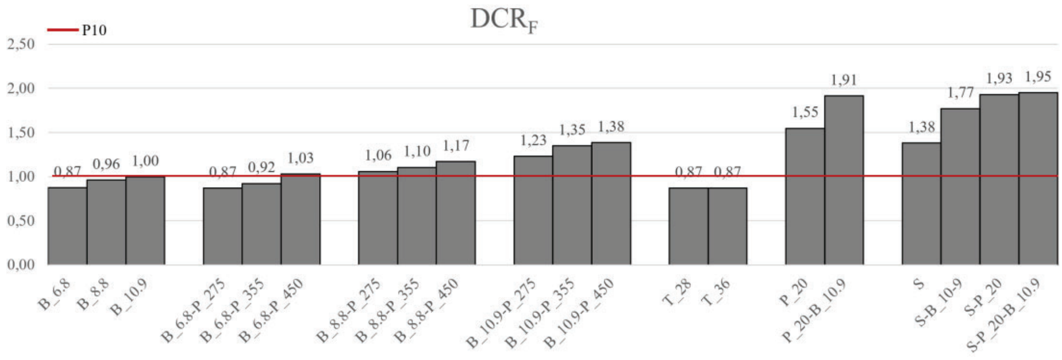

Figure IV.107 – Parametric analysis results: $DCR_F = F_{max}/F_{max,P10}$.

(ii) Global stiffness ($S_{j,ini,g}$)

In terms of the initial global stiffness of the joints ($S_{j,ini,g}$), compared to the *P10* specimen, the results revealed that the models do not present a significative variation of the stiffness, except for the model with an end-plate thickness variation (20 mm), for the model with the stiffeners, S, and for the model with combinate stiffeners and bolt steel grade 10.9, for which some differences can be observed: $DCR_{S,g}$=1,33 for P_20, $DCR_{S,g}$=1,34 for P_20-B_10.9, $DCR_{S,g}$=1,29 for S and $DCR_{S,g}$=1,29 for S-B_10,9.

The models with the combinate stiffeners with 20 mm thickness end-plate (S-P_20) and the combinate stiffeners with 20 mm thickness end-plate and bolt steel grade 10.9 (S-P_20-B_10.9) are more influent for the joint global stiffness, with, respectively, a $DCR_{S,g}$=1,58 and $DCR_{S,g}$=1,59 (Fig. IV.23).

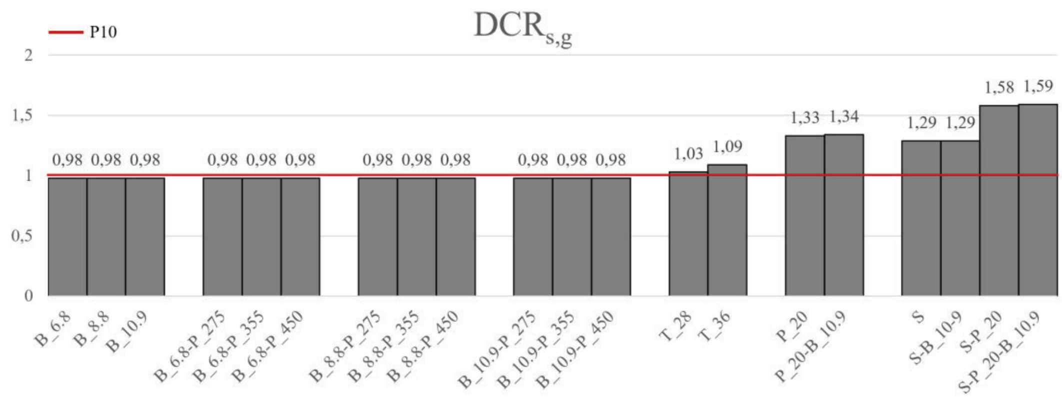

Figure IV.108 – Parametric analysis results: $DCR_{s,g} = S_{j,ini,g}/S_{j,ini,g,P10}$.

(iii) Joint classification ($S_{j,ini,l}$)

In terms of the joint classification, to perform an analytical comparison of the results, the joint classification for timber structure procedure (JCT) reported in the chapter 2.4.2 is applied to the numerical results to assess the joints strength (M_{el}) and stiffness ($S_{j,ini,l}$). The comparison between the numerical responses reveals an apparent difficulty of the models to reach the higher initial stiffness values (Rigid joints) obtained in the JCT procedure. In particular, as it is possible to see in the Figure IV.24, all the models reside in the semi-rigid field: the B_i (i=275, 355, 450), B_j-P_i (j=6.8, 8.8, 10.9; i=275, 355, 450) and T_i (i=28, 36) models present the same initial stiffness of the *P10* specimen; the P_20, P_20-B_10.9, S and S-B_10.9 show a stiffness increment, with a $DCR_{S,l}$=2,43, $DCR_{S,l}$=2,45 and $DCR_{S,l}$=2,20 respectively; the most significant differences occurred in joints S-P_20 and S-P_20-B_10.9, which are in the upper part of the semi-rigid joints field, very closed to the rigid-limit, with the same $DCR_{S,l}$=9,92 (Fig. IV.25).

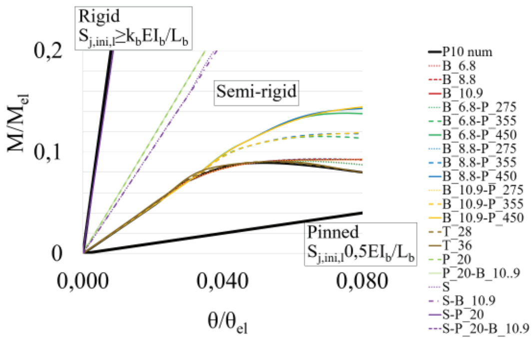

Figure IV.109 – Parametric analysis results: non-dimensional curve (M/M_{el} - θ/θ_{el}).

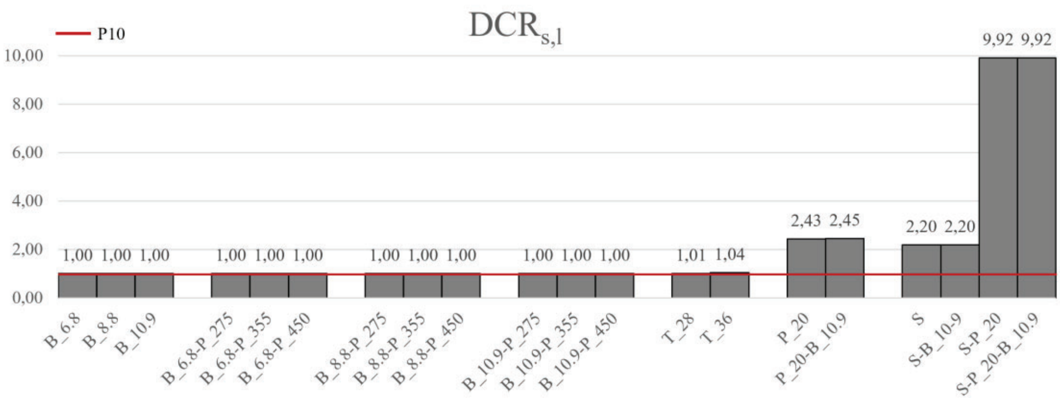

Figure IV.110 – Parametric analysis results: $DCR_{s,l}$= $S_{j,ini,l}/S_{j,ini,l,P10}$.

(iii) Ductility (μ)

In terms of the joint ductility, an inspection to the results revealed that all the models have a lower ductility than the *P10* specimen one. In particular, the combinate bolt steel grade 8.8 with the end-plate grade S275 (B_8.8-P_275) and the combinate stiffeners with 20 mm thickness end-plate (S-P_20) models present, respectively, a DCR_{μ}=0,14 and DCR_{μ}=0,15, while the more ductile model is the combinate stiffeners with bolt grade 10.9 (S-B_10.9) with a DCR_{μ}=0,76.

In the B_6.8-P_450 model the yield is catched by the bolts and in the B_8.8-P_450 and S-P_20-B_10.9 models by the link, while in the remaining models the yield is catched by the end plate. In the models where the link is the first connection element to yield, it presents a small plastic deformation compared to the end-plate and offers to the connection a little ductility (Fig. IV.26). In all the connection models, in fact, most of the ductility is guaranteed by the end plate, as can be seen from numerical results.

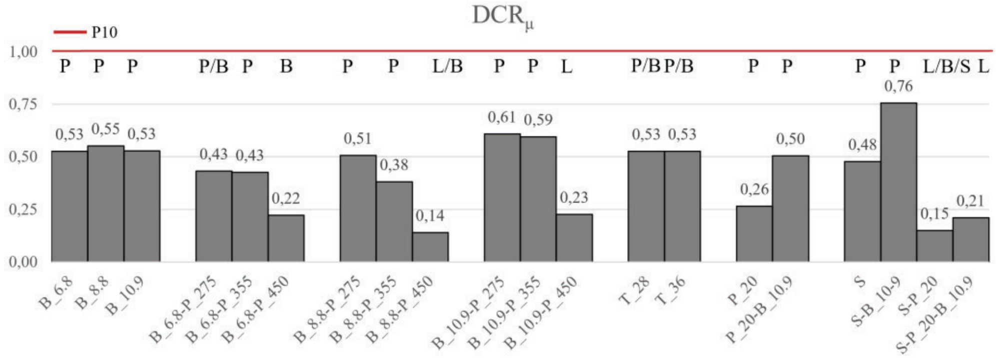

Figure IV.111 – Parametric analysis results: $DCR_{\mu} = \mu/\mu_{P10}$.

(iiii) Collapse hierarchy

In terms of the collapse hierarchy, analysing the models with bolt steel grade variation, an inspection to the results revealed that the bold steel grade 6.8 model (B_6.8) is governed by the end-plate in bending, which corresponds to a collapse mode 2, i.e. bolts failure with yielding of the end-plate. In the case of the B_8.8 and B_10.9 connections, the collapse mode is the type 1 due to the increase of the bolts grade (Fig. IV.27).

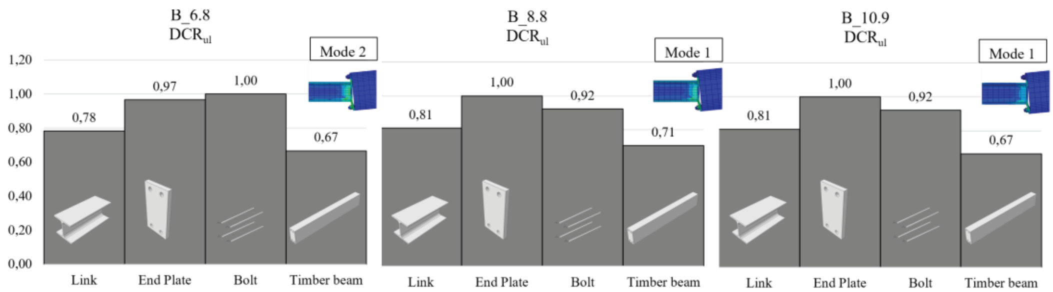

Figure IV.112 – Parametric analysis results: DCR_{ul} (B_i; i=6.8, 8.8, 10.9).

Analysing the combinate bolt steel grade 6.8 and 8.8 with end-plate steel grade variation, the results show that the steel grade increase does not influence the collapse mode. The B_6.8-P_i and B_8.8-P_i (i=275, 355, 450) models exhibit a collapse mode 2 while in the combinate bolt stell grade

10.9 with end-plate steel grade variation, there are two different collapse modes. In particular, the B_10.9-P_355 and the B_10.9-P_450 models present a collapse mode 2 while the B_10.9-P_275 one corresponds to a collapse mode 1, with the complete end-plate yielding, due to the influence of the high bolts steel grade (Fig. IV.28).

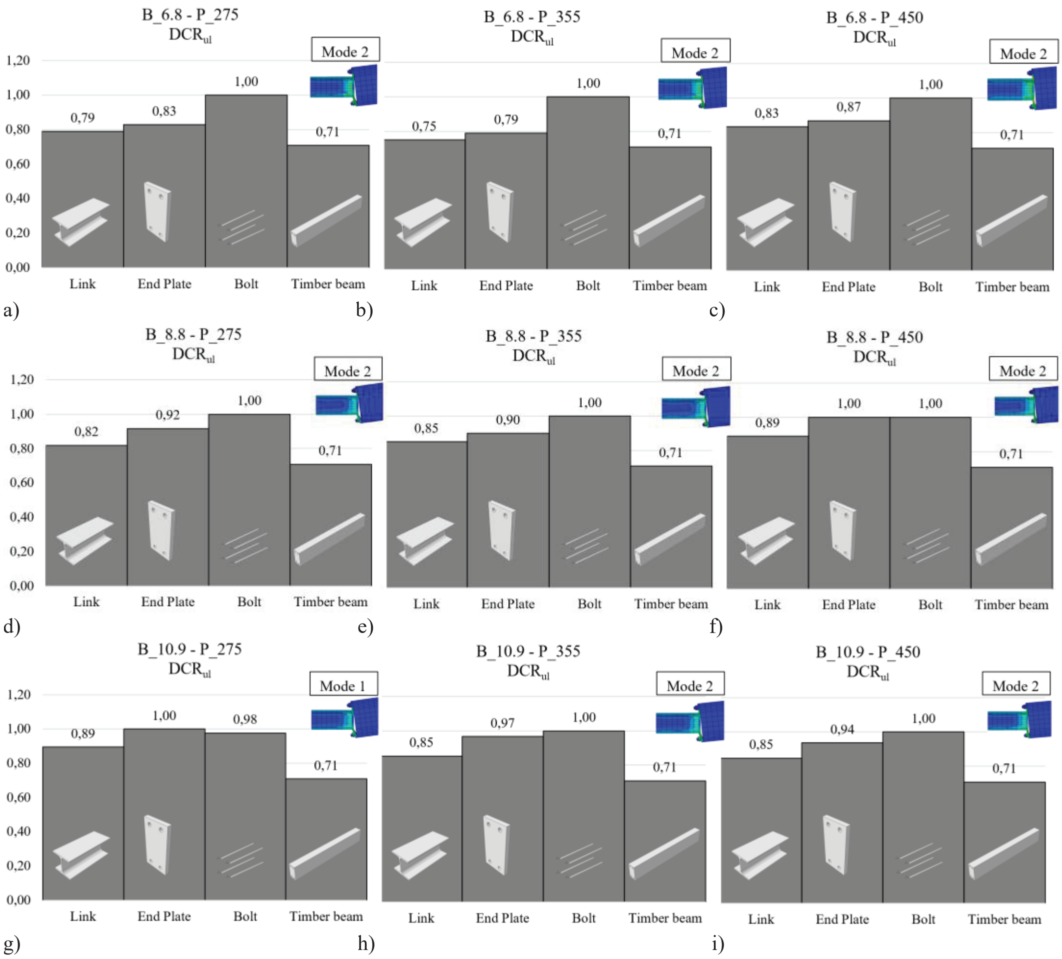

Figure IV.113 – Parametric analysis results: DCR_{ul}: a), b) and c) B_6.8-P_i; i=275, 355, 450; d), e) and f) B_8.8-P_i; i=275, 355, 450; g), h), and i) B_10.9-P_i; i=275, 355, 450.

Below, the remaining cases are presented, with the variation of the beam timber grade (T_28, T_36) the variation of the end-plate thickness (P_20, P_20-B_10.9) and the presence of stiffeners (S, S-B_10.9, S-P-20, S-P_20_B_10.9). All these cases present the same collapse mode 2, with different performance rates (Fig. IV.29).

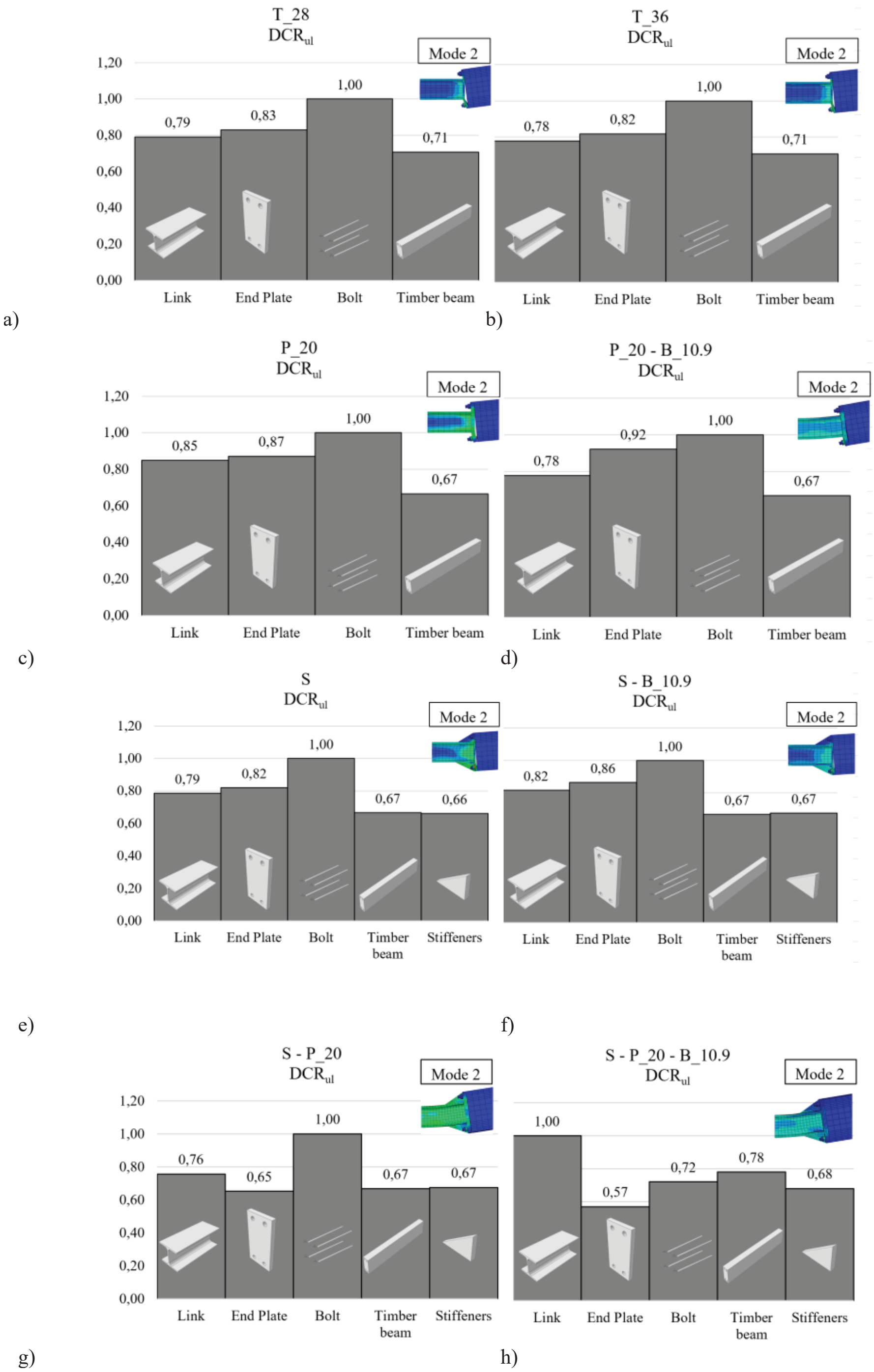

Figure IV.114 – Parametric analysis results: a) and b) T_i; i=28, 36; c) and d) P_20, P_20-B_10.9; e), f), g) and h) S, S-B_10.9, S-P_20, S-P_20-B_10.9.

Comparing the numerical results of the models, with the bolt steel grade increase, in terms of global and local stiffness there is not a significative improvement respect to the *P10* specimen while, in terms of maximum strength, using bolts steel grade 8.8 and 10.9, the end-plate is the first connection sub-component that catches the collapse, changing the collapse mode (Mode 1).

About the end-plate steel grade variation, in terms of maximum strength, using a steel grade S275, with bolts grade 6.8, there is a small increase compared to the other cases while the collapse mode is the same (Mode 2) and in terms of stiffness, global and local, however, there is not a significative improvement. It is possible to see the same behaviour in the B_8.8-P_i (i=S275, S355, S450), with obviously higher percentage of exploitation.

With bolts steel grade 10.9, using S275 steel grade (B_10.9-P_275), the end-plate is the first connection sub-component to catch the collapse (Mode 1) while increasing the steel grade (S355 and S450), it is possible to see collapse mode 2, with the collapse of the bolts and the end-plate. Observing the results, it is clear that, in some cases, it is better to change only one parameter, like the bolts steel grade or the end-plate steel grade, to improve the behaviour: among the models in which there are more than one parameter variation, only the B_10.9-P_275 model presents a collapse mode variation, increasing the maximum strength of the joint respect to the other models with two parameters variation, in which, however, the strength and the stiffness increase is very low.

The beam timber grade variation does not involve improvement, except a minimum increase in terms of stiffness.

On the other hand, with the end-plate thickness increase (20 mm), there is an improvement in terms of maximum strength and stiffness, but it is not possible to exploit the total connection ductility and strength due to the bolts premature collapse. The combinate bolts grade 10.9 with 20 mm end-plate thickness (P_20-B_10.9) model increases the link plastic deformation, reducing the relative rotation between the end-plate and the timber beam, with a high stiffness, as it is possible to see in the Figure IV.30.

At the end, in the model with the stiffeners (S-P_20-B_10.9), it is possible to see the plastic hinge formation in the steel link, with a greater rotational capacity, maximum strength and stiffness, compared to the other cases.

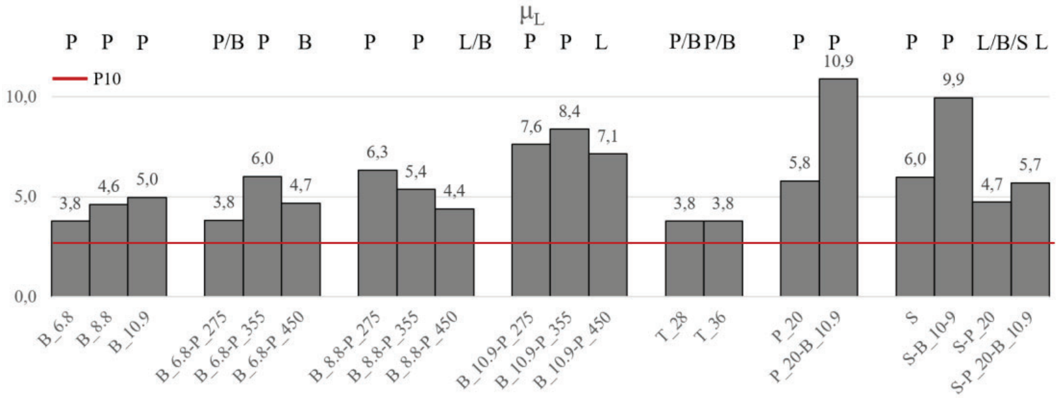

Figure IV.115 – Parametric analysis results: link ductility μ_L.

4.4 CAPACITY DESIGN OF THE JOINTS

4.4.1 FULL-STRENGTH CONNECTION WITH LOW DUCTILE JOINT

It is evident that, from the parametric analysis results obtained, the FE models are capable of representing different types of behaviour governed by the bolts and the end-plate collapse. In particular, analysing the study results, the following observations can be drawn:

(i) The combinate end-plate thickness 20 mm with the bolts grade 10.9 allows the collapse mode 1, avoiding the preventive collapse of the bolts (type 3 or 2);

(ii) The use of the stiffeners allows the plastic hinge formation in the steel link, with a greater exploitation of its rotational capacity, and, in the same time, a high joint stiffness $S_{j,ini,l}$, ensuring a rigid continuity constraint between the timber beam and the steel link.

Extended end-plate connections with haunches are usually used in steel moment resisting frames when it is desired that plastic hinges occur exclusively in the connected beams. Adding a haunch at the lower part of the beam increases the lever arms of bolts, which allows easier fulfilment of the overstrength requirements for non-dissipative connections in EN 1998. At the same time, it leads to larger stiffness of the connection. Zoetemeijer, 1981 (in Bijlaard et al, 1989) investigated haunches with and without flanges as a mean of increasing connections stiffness and proposed a design method. Jaspart (1997) and Maquoi and Chabrolin (1998) analysed in detail the beam-to-column joints with haunches, proposing design rules compatible with the component method in EN 1993-1-8.

After the 1994 Northridge earthquake, which caused widespread damage to welded connections in steel moment-resisting frames, haunches received a lot of attention as a means of repairing damaged connections or strengthening existing and new steel constructions. (Lee and Uang, 1997; NIST 1998; Gross et al, 1999; Yu et al, 2000). Yu et al, (2000) have shown that the haunch alters the moment distribution of the beam and that majority of the beam shear is transferred to the column through the haunch flange rather than through beam and haunch web. In the case of end-plate bolted composite connections, haunches located at the bottom side of the beam flanges are very convenient for constructional point of view. Gross et al, (1999) proposed to adopt a haunch depth equal to 0,33 times the beam depth, with an angle of the haunch equal to 30° to limit the haunch web slenderness. This assumption was based on the Whitmore theory of the propagation of internal stress in elastic system of about 30° slope. However, increasing the slope can be convenient because it allows reducing the size of the haunch as well as the design forces on the connection. Experimental tests carried out by Lachal et al, (2006) showed that haunched bolted joints can improve significantly the cyclic performances as respect to unstiffened end-plate joints. They observed that the rotation capacity can exceed 35mrad without low cycle fatigue rupture in the welds connecting beam flanges on the endplates. In addition, this type of joint guarantees a significant increase of rotational stiffness, moment resistance and rotation capacity were observed in comparison with similar beam-to-column composite joints without haunches.

It is clear, however, that, in the S-P_20-B_10.9 model, the end-plate and the bolts don't have an adequate over-strength compared to the steel link which is, for this reason, unable to catch the ultimate strength, due to the end-plate and bolts preventive collapse. Despite the results, this parametric analysis is very important to understand the joint behaviour and for an its correct design.

To perform a timber-steel link joint design, the "capacity design" procedure for macro-components between the steel link and the timber beam, presented in chapters 2.2 and 2.4, is apply.

In particular, a *Full-strength (FS) connection* (so that the yielding occurs in the link) with a *Low Ductility timber-steel link Joint (LDJ)* (so that the connection is not the first macro-component over-resistant respect to the link) is designed.

In order to obtain a timber-steel link connection similar to the *P10* specimen, both in terms of strength and stiffness, the capacity design approach is applied preserving the dimensions of the timber beam and designing the steel link with an "under-resistance" compared to the beam (macro-component).

The bending resistant moment of the timber beam is:

$$M_{Rd,T} = \frac{f_{m,k} \cdot k_{mod}}{\gamma_m} W = 22{,}34 \text{ kNm}$$

where:

$f_{m,k}$= bending strength, that for GL24h= 24 N/mm^2

k_{mod}= is a partial factor for taking into account the effects on the material of duration of load and moisture content= 1,10

γ_m = partial factor for material for glulam timber= 1,25

W = strength module=1,1E+06 mm^3

Appling the capacity design approach, the timber bending resistant moment, compared that of the steel link, should be:

$$M_{Rd,T} \geq \gamma_{rd} \cdot \Omega \cdot 1{,}1 \cdot M_{Rd,L}$$

The maximum bending resistant moment of the link is:

$$M_{Rd,L,max} = \frac{M_{Rd,T}}{\gamma_{rd} \cdot \Omega \cdot 1{,}1} = 14{,}11 \text{ kNm}$$

where:

γ_{rd}= 1,2 (S235 steel grade);

Ω= 1,2 (80% strength reduction is assumed)

The strain hardening factor γ_{rd} is assumed differently by EN1993:1-8 and EN1998-1. In particular, EN1993:1-8 recommends to consider an overstrength ratio equal to 1,2 for full strength joints, while EN1998-1 contradictorily assumes a value equal to 1,1. Several empirical equations are available in literature to estimate the flexural overstrength γ_{rd} developed by steel beams. Based on the main findings obtained by Mazzolani and Piluso (1992), D'Aniello et al (2012), Güneyisi et al. (2013, 2014) it can be argued that γ_{rd} factor ranges within 1,1-1,2 for European profiles commonly used for beams (i.e. IPE or HE), thus larger than the value recommended by EC8, but in line with AISC358-10 that assumes the following overstrength factor:

$$\gamma_{rd} = \frac{f_y + f_u}{2 f_y} \leq 1{,}2$$

Therefore, in the current procedure γ_{rd} is conservatively assumed equal to 1,20, based also on the characteristic yield and ultimate strength of European mild carbon steel grades.

The maximum plastic strength module ($W_{pl,max}$) of the steel link (S235) section needed to satisfy the capacity design procedure is:

$$W_{pl,max} = M_{Rd,L} \cdot \frac{\gamma_m}{f_{y,k}} = 63{,}03\ \text{mm}^3$$

where:

$\gamma_m = 1{,}05$;

$f_{yk} = 235$ MPa (S235)

The selected steel profile is HE100AA, with a plastic strength module:

$$W_{el,L} = 51{,}98\ \text{mm}^3$$

$$W_{pl,L} = 58{,}36\ \text{mm}^3$$

The bending resistant moment of the link is:

$$M_{Rd,el,L} = W_{el,L} \cdot \frac{f_{yk}}{\gamma_{m0}} = 12{,}22\ \text{kNm}$$

$$M_{Rd,pl,L} = W_{pl,L} \cdot \frac{f_{yk}}{\gamma_{m0}} = 13{,}71\ \text{kNm}$$

The Ω coefficient is:

$$\Omega_{el} = \frac{M_{Rd,T}}{M_{Rd,el,L,max} \cdot \gamma_{rd} \cdot 1{,}1} = 1{,}39$$

$$\Omega_{pl} = \frac{M_{Rd,T}}{M_{Rd,pl,L,max} \cdot \gamma_{rd} \cdot 1{,}1} = 1{,}23$$

The timber-steel link joint, HE100AA joint (LDJ), in the Figure IV.31, is made by a laminated timber beams (GL24h), with a 120x230 mm rectangular cross section and 2500 mm long, equipped at one end with a steel link, HE100AA profile 360 mm long (steel grade S235) with two welded end-plates (120x230 mm, steel grade S275), with 20 mm thickness and four stiffeners (110x70 mm and 20 mm thickness, steel grade S275). The link is connected at one side to the timber beam by means of 4 glued threaded bars (M16, 10.9, 540 mm long).

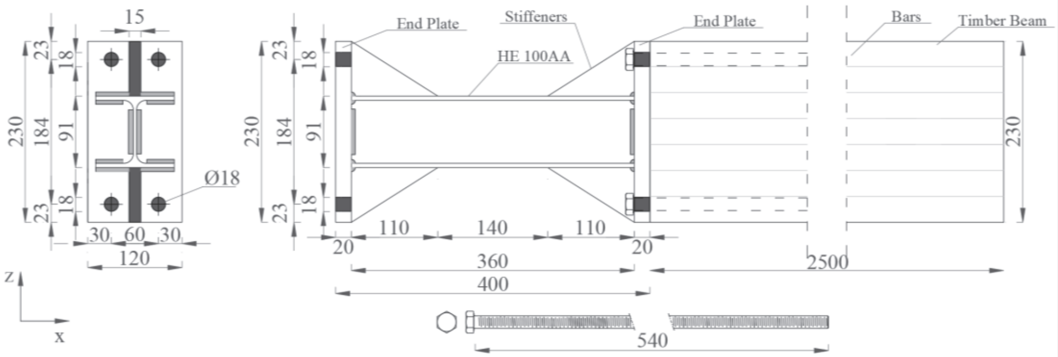

Figure IV.116 – HE100AA joint [FS-LDJ]: geometrical features [mm].

4.4.2 Full-Strength connection with High Ductile Joint

To perform a timber-steel link joint design, the capacity design procedure for "macro-components", between the steel link and the timber beam, and for "sub-components" of the connection, between end-plate, bolts and stiffener, presented in chapter 2.2 and 2.4, is used. In particular, a *Full-strength (FS) connection* (so that the yielding occurs in the link) with a *High Ductility timber-steel link Joint (HDJ)* (so that the connection is the first macro-component over-resistant respect to the link) is designed.

According to design procedure developed within the project, the joint analysed is considered made of 3 macro-components (link, timber beam and connection) and 3 sub-components (end-plate, bolts and stiffeners) (Fig. IV.32); each sub and macro-component is individually designed according to specific assumptions and, then, simply capacity design criteria are applied, using the component method, in order to obtain different design objectives.

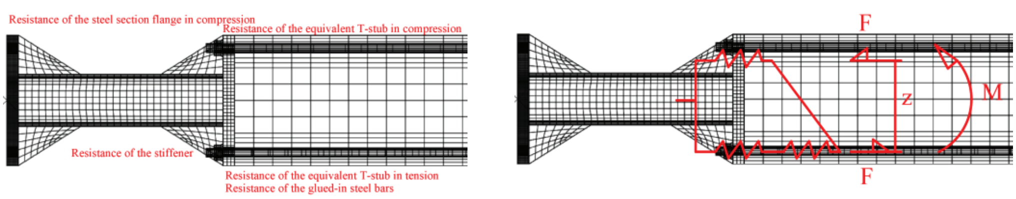

a) b)

Figure IV.117 – a) Joint components; b) model for the internal force distribution and related stiffness.

Joint moment resistance

The distribution of the internal actions, in the examined joint, is represented in Figure IV.33: the bolts are in tension, while the compression is schematized by the stress-block model.

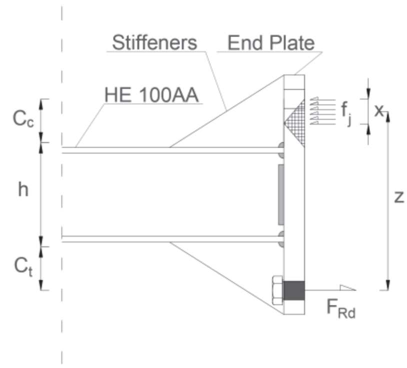

Figure IV.118 – Model for the resistant moment evaluation.

The design moment resistance, $M_{j,Rd}$, can be determined according to:

$$M_{j,Rd} = F_{Rd} \cdot z$$

where z is the lever arm of the internal couple and F_{Rd} is the resistance of the weakest component of the joint, that is the smallest value among:

- the resistance of the glued-in steel bars $F_{ax,Rd}$
- the resistance of the equivalent T-stub in tension $F_{t,T\text{-}stub,Rd}$;
- the resistance of the equivalent T-stub in compression $F_{c,T\text{-}stub,Rd}$;
- the resistance of the steel section flange in compression $F_{sf,Rd}$;
- the resistance of the stiffener $F_{t,s,Rd}$.

Glued-in steel bars

To evaluate the length of the glued bars, is used the method presented in an Informative Annex of Eurocode 5: Part 2, that presents four criteria for consideration in joints employing steel rods:

- Rod failure through yielding;
- Failure of the adhesive by debonding from steel or wood;
- Failure of the timber adjacent to the glue-line;
- Failure of the timber member (e.g. pull-out of a whole timber plug with several glued-in rods).

The strength of the joint (R_{ax}) has be the minimum between the plastic strength of the steel bars and the pull-out strength of the glued bars.

$$F_{ax,Rd} = \min\,(f_{y,d} \cdot A_{res};\ \pi \cdot d_{eq} \cdot l_{ad} \cdot f_{k1,d};\ f_{t,0,d} \cdot A_{eff})$$

where:

$f_{y,d}$= yielding strength of the bars = 900 MPa;
A_{res} = strength area of the bars = 157 mm;
d_{eq} = equivalent diameter of the bars = 16 mm;
l_{ad} = glue length = 540 mm;
$f_{k1,d}$= glue strength

- *Rod failure through yielding*:

$$F_{ax,Rd,1} = f_{y,d} \cdot A_{res} = \left(\frac{900}{1,25}\right) 157 = 113\ \text{kN}$$

- *Failure of the adhesive by debonding from steel or wood* (Fig. IV.33, Tab. IV.15):

$$F_{ax,Rd,2} = \pi \cdot d_{eq} \cdot l_{ad} \cdot f_{k1,d} = \pi \cdot 16 \cdot 540 \cdot 2,69 = 73\ \text{kN}$$

where: l_{ad}= 540 mm

Table IV.71 – Glue strength depending to the glue length

$l_{ad} \leq 250$ mm	250 mm < $l_{ad} \leq 500$ mm	500 mm < $l_{ad} \leq 1000$ mm
4	5,25 – 0,005 l_{ad}	3,5 – 0,0015 l_{ad}

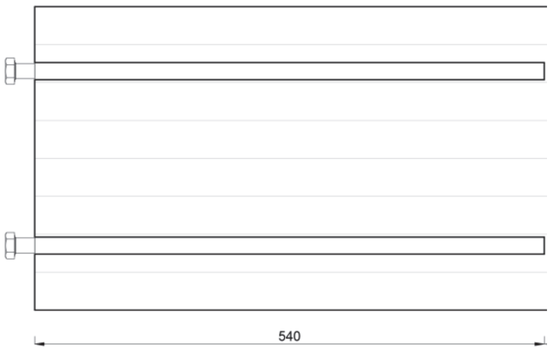

Figure IV.119 – Length of the bars.

- *Failure of the timber member (e.g. pull-out of a whole timber plug with several glued-in rods)*:

This kind of failure can be avoided by respecting the minimum distances according the standards.

As regard the minimum distance from the edge and minimum spaces between the bars, in the study case, the glued bolts are subject to tensile and shear forces in the same time, and should be analyse two cases: (1) bars glued parallel to the grain direction under tensile actions and (2) bars glued parallel to the grain direction under shear action. For the tensile actions, to safeguard against the development of peeling and splitting stresses and the consequent collapse mode, minimum values of wheelbase between the glued bars and distance from the edge have been set (Tab. IV.16a). For the shear actions, the minimum distance from the edge and minimum spaces between the glued bars are illustrated in the Tab. IV.16b.

Table IV.72 – The minimum distance from the edge and minimum spaces between the glued bars a) in tension and b) under shear actions.

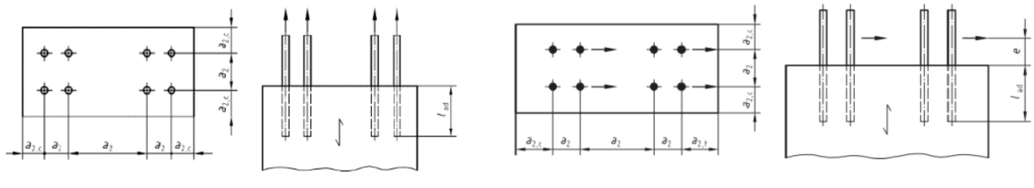

a) b)

a_2= 5d; $a_{2,c}$= 2,5d; $a_{2,t}$= 4d

The minimum length of the bars, l_{min}, is evaluated as:

$$l_{min}= \max (0{,}5d^2; 10d) = \max (128 \text{ mm}; 160 \text{ mm}) = 160 \text{ mm}$$

where *d* is the diameter of the bolt.

Using steel bars with 10.9 steel grade and φ16 of diameter, the minimum distances and length are:

- a_2= 80 mm;
- $a_{2,c}$= 40 mm;
- $a_{2,t}$= 64 mm;
- l_{min}= 160 mm.

In order to respect the minimum distances between the bolts for the timber element, the cross-section size of the beam is 140x320 mm (Fig. IV.35).

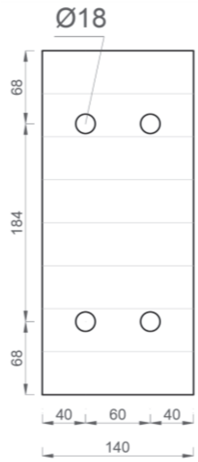

Figure IV.120 – Timber beam cross section [mm].

- *Failure of the timber adjacent to the glue-line*:

$$F_{ax,Rd,3}= f_{t,0,d} \cdot A_{eff}= 16,5 \cdot 6720= 110,88 \text{ kN}$$

In the case of steel bars glued parallel to the grain direction, the tensile strength of the timber element at the end of the bar has also be checked, assuming for the resistant section an area equal to $36d^2$ for each bar (Fig. IV.36).

In this case, the effective resistant area for each bar is equal to:

$$A_{eff}= 96 \cdot 70= 6720 \text{ mm}^2$$

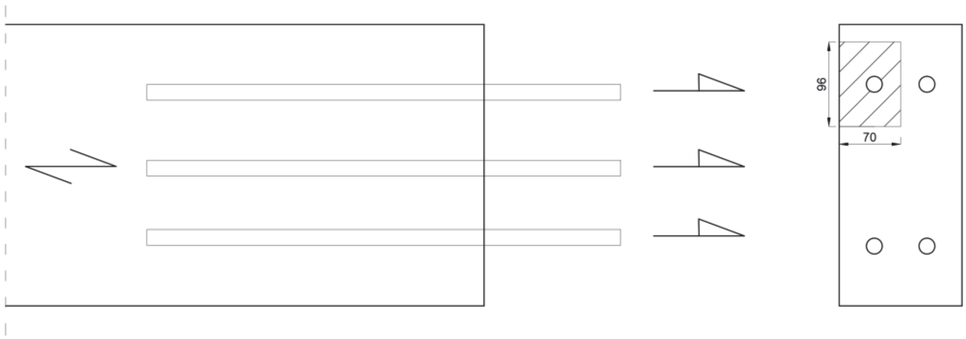

Figure IV.121 – Resistant area for each bar for the timber beam [mm].

The effective number of resistant bars is evaluated as:

$$n_{eff}= n^{0,9}= 2^{0,9}= 1,87$$

and the weakest resistant mechanism of the joint ($F_{ax,rd}$) is the "failure of the adhesive by debonding from steel or wood":

$$F_{ax,Rd} = \min\,(211{,}31\text{ kN};\ 136{,}51\text{ kN};\ 207{,}57\text{ kN}) = 136{,}51\text{ kN}$$

Equivalent T-stub in tension

For the T-stub in tension, the modelling according to EN 1993-1-8 is shown in the Figure IV.37 and the possible failure modes are (CEN, 2005; ECCS, 1999):

- Mode 1: complete yielding of the flange;
- Mode 2a: failure of the bars after yielding of the flange in presence of prying forces;
- Mode 2b: yield of the flange without prying forces;
- Mode 3: bar failure.

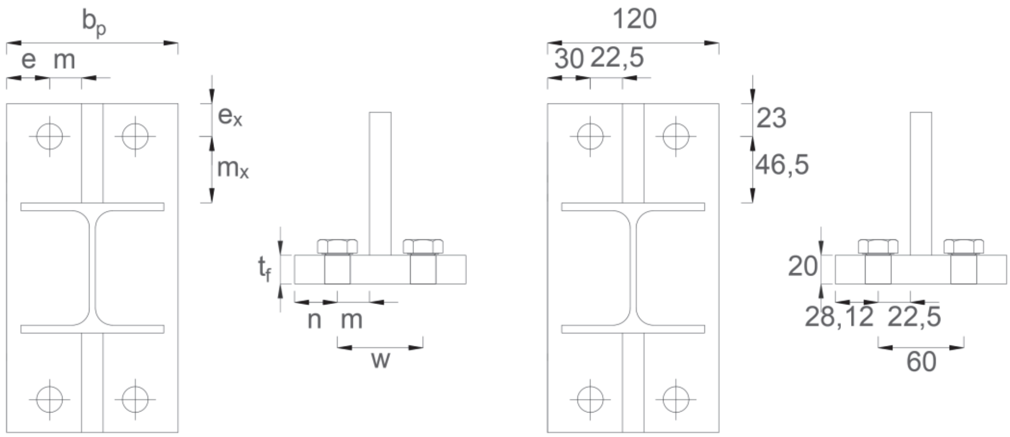

Figure IV.122 – Modelling of a flange using the equivalent T-stub element in tension according to EN 1993-1-8.

To check the presence of prying forces it is necessary to evaluate the length of the lengthening bolt (effective length), L_b, and the limit length, L_b^*.

If $L_b < L_b^*$, then there is development of prying force;
If $L_b \geq L_b^*$, then there is no development of prying force.

To evaluate L_b the following parameters are defined (Volkersen, 1938):

$$\alpha = \frac{1}{(1+\psi)\omega \cdot \varphi} = 0{,}862$$

with:

$$\psi = \frac{E_s \cdot A_s}{E_{0,d} \cdot A_w} = 0{,}421$$

$$\Gamma = \frac{G_{0,d} \cdot \pi \cdot \varphi}{E_s \cdot A_s \cdot t_{glue}} = 0{,}0018$$

$$\omega^2 = \Gamma\,(1 + \Psi) = 0{,}051$$

where:
$E_{0,d}$: Elastic modulus of wood parallel to the direction of the fibers = 11600 MPa;
A_w: $36\varphi^2 = 6748\ mm^2$;
$G_{0,d}$: Shear modulus of wood parallel to the direction of the fibers = 2400 MPa;
t_{glue}: Glue thickness = 2 mm;
φ: Diameter of the bolt = 16 mm;
S_r: Thickness of the washer = 2 mm;
t_p: Thickness of the end-plate = 20 mm;
S_d: Thickness of the nut = 8 mm.

$$L_b = \alpha \cdot \varphi + t_f + S_r + S_D = 43{,}8\ mm$$

and L_b^* is evaluated as:

$$L_b^* = \frac{8{,}8 \cdot m_x^3\ A_{res} \cdot n_{fb}}{\Sigma l_{eff} \cdot t_f^3} = 20{,}87\ mm$$

where:
n_{fb}: number of bolt-rows= 1;
A_{res}: resistance area of the bolt= 157 mm^2;
t_f: Thickness of the enad-plate= 20 mm;
l_{eff}: Effective length of the equivalent T-stub element, function of the position, number and model of bolt in tension:

$$l_{eff} = l_{eff,2} = \min\left[\alpha m - (2m + 0{,}625e) + e_x;\ 2m + 0{,}625e + e_x;\ 4m + 1{,}25e\right] = 94{,}25\ mm$$

$L_b \geq L_b^*$, then there is no development of prying force, and failure mode (Fig. IV.38), $F_{t,T\text{-}stub,Rd}$, is evaluated as:

$$F_{t,T\text{-}stub,Rd} = \min\left(F_{t,T\text{-}stub,Rd,1\text{-}2};\ F_{t,T\text{-}stub,Rd,3}\right) = 219{,}42\ kN$$

where:
$F_{t,T\text{-}stub,Rd,1\text{-}2}$: Mode 1-2
$F_{t,T\text{-}stub,Rd,3}$: Mode 3

$$F_{t,T-stub,Rd,1-2} = \frac{2 \cdot M_{pl,1,Rd}}{m+n} = 219{,}42\ \text{kN}$$

$$F_{t,T-stub,Rd,3} = \Sigma F_{T,Rd} = 282{,}6\ \text{kN}$$

where:

$$M_{pl,1,Rd} = 0{,}25 \cdot \Sigma l_{eff,1} \cdot t^2{}_f \cdot \frac{f_y}{\Upsilon_{m0}} = 2{,}46\ \text{kNm}$$

$l_{eff,1}$= min [2πm; πm + 2e_x; αm – (2m + 0,625e) + e_x; 2m + 0,625e + e_x; 4m + 1,25e]= 94,25 mm

where:
n= min (e; 1,25 m)= (30; 28,125)= 28,125 mm
e= 30 mm
e_x= 23 mm
m= 22,5 mm
m_x= 46,5 mm

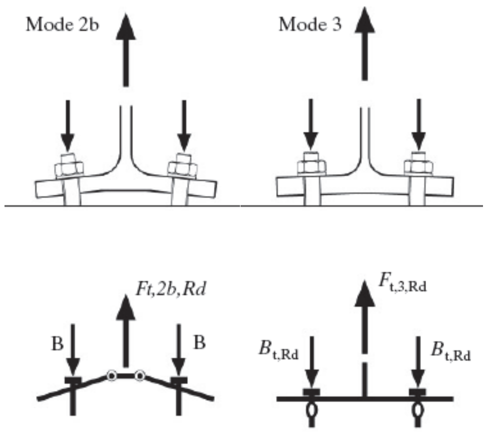

Figure IV.123 – Failure modes and ultimate displacements in a T-stub in tension according to ECCS, 1999 and Beg et al, 2004. Mode 1-2: yield of the flange without prying forces; Mode 3: bars failure.

<u>Equivalent T-stub in compression</u>

EN 1993-1-8 (2005) gives rules for design of joints reinforced with haunches by providing additional criteria for the "beam flange and web in compression" component (Fig. 1V.39). The design compression resistance of the combined beam/haunch flange and web is given by EN 1993-1-8, by dividing the design moment resistance of the beam cross-section at the location of the connection, $M_{c,Rd}$, to the distance between flange centrelines. For a haunched beam $M_{c,Rd}$ may be calculated neglecting the intermediate flange. Also, the design resistance of beam web in compression should be determined, similar to the rules given for the component "column web in transverse compression". Moreover, the following detailing rules apply:

- The steel grade of the haunch should match that of the member;
- The flange size and the web thickness of the haunch should not be less than that of the member;
- The angle of the haunch flange to the flange of the member should not be greater than 45°.

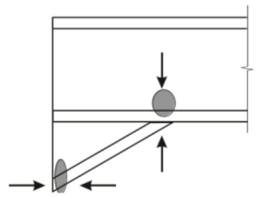

Figure IV.124 – "Haunched beam" component in EN 1993-1-8 (Landolfo et al, 2018).

The SCI/BCSA publication P398 (2013) explains more in detail the design approach in EN 1993-1-8 for connections with haunches, giving also more guidance on the design of welds. Bolted extended end plate beam to column connections with haunches for seismic applications were investigated experimentally within the EQUALJOINJTS (Landolfo et al, 2018) project (Stratan et al, 2017). All tested specimens showed a stable hysteretic response, with plastic deformations concentrated in the beam next to the haunch, qualifying for seismic applications according to ANSI/AISC 358-10/16 criteria. Previous numerical simulations (Maris et al, 2015 and Stratan et al, 2016) have shown that presence of haunches affect some of the design assumptions in EN 1993-1-8. For example, under hogging moment, the centre of compression shifts above the haunch flange. On the other hand, only the bolts close to the tension flange of the beam are active in tension.

Within current EN 1993: 1-8, theoretical strength and stiffness of extended end-plate connections is predicted on the basis of yield line t-stub theory. However, no specific provision is provided for accounting the influence of the rib stiffeners on the Extended stiffened (ES) end-plate bolted joints moment-rotation capacity.

Another key aspect is related to the position of the compression centre: for end-plate joints covered by EN 1993-1-8 provisions, the compression centre is located in the middle of thickness of beam flange. However, experimental and numerical results on bolted ES joints carried out by Abidelah et al. (2012) showed that the compression centre is generally shifted below the position assumed by EC3, and approximately located at the centroid of the "T" section made of the rib stiffener and the beam flange. It is clear that the position of centre of compression varies with the joint rotation demand due to the formation of plastic modes with different engagement of each joint component. However, tests on welded joints carried out by Lee et al. (2005) showed that up to interstorey drift ratios equal to 5% the strut model for rib is effective with centre of compression shifted at 0,6 times the rib height (Fig. IV.40).

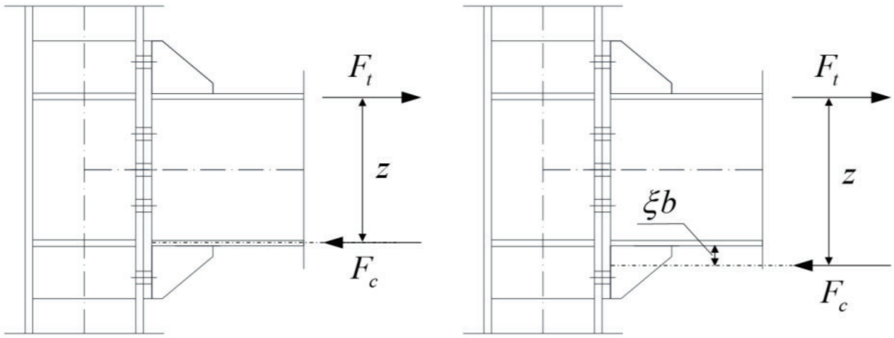

a) b)
Figure IV.125 – Centre of compression and lever arm: a) EC3:1-8 for end-plate connections; b) shifted position due to strut mechanism into the rib stiffener (Landolfo et al, 2018).

D'Aniello et al. (2017) deeply investigate and critically discuss the design criteria and related requirements for bolted extended stiffened end-plate beam-to-column joints currently codified in EN 1993, on the basis of a parametric study based on finite element analyses. In addition, D'Aniello et al. (2017) develop a capacity design procedure in the framework of components method, specifically accounting for the presence of ribs and able to control the joint response for different performance levels. In particular, according to the proposed design procedure and based on both experimental and numerical results from literature (Lee, 2002; Lee et al, 2005; Abidelah et al, 2012) and achieved within the project condition (Maris et al, 2015, Stratan et al, 2016, D'Aniello et al, 2017; Tartaglia and D'Aniello, 2017, Tartaglia et al, 2018), the location of compression centre is assumed as follows (Fig. IV.41):

- In the middle of thickness of beam flange for unstiffened endplate joints;
- At the centroid of the section made by the beam flange and the rib stiffeners, for the stiffened endplate joints;
- At 0,5 the haunch height h_h, in case of haunched joints.

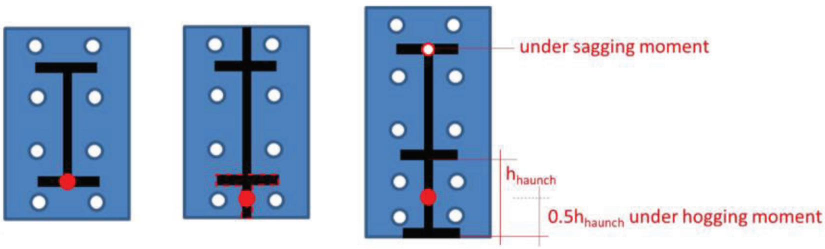

a) b) c)
Figure IV.126 – Location of compression centre for different joint types: a) unstiffened end-plate; b) stiffened end-plate; c) haunched connections (Landolfo et al, 2018).

The resistance of the basic component "timber and steel end-plate in bending" under compression, can be modelled through an equivalent T-stub in compression (Fig. IV.42b), in accordance with recommendations in EN 1993-1-8 (CEN, 2005) for the case of steel column base joints modified taking into account the wood in compression and the location of compression centre for stiffened end-plate.

At first, the compression centre is shown in Figure IV.42a.

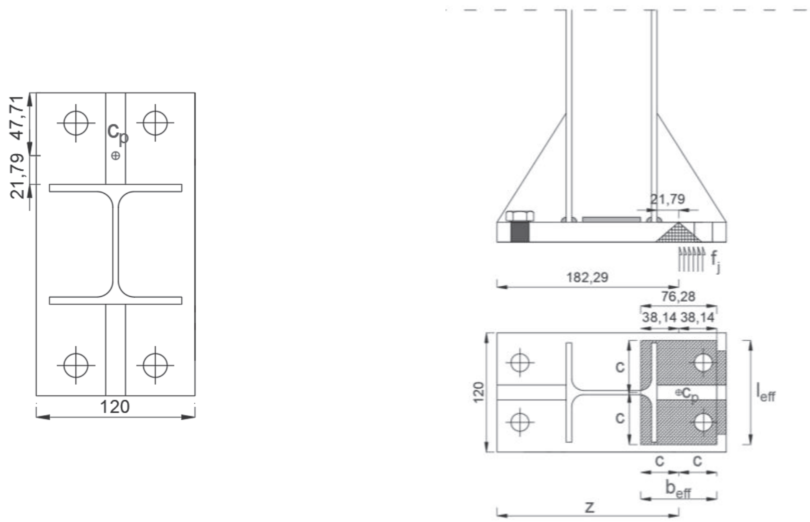

a) b)

Figure IV.127 – a) Compression centre; b) flange modelling as an equivalent T-stub element in compression according to EN 1993-1-8 [mm].

The resistance of the equivalent T-stub in compression ca be evaluated as:

$$F_{c,T\text{-}stub,Rd} = f_j \cdot b_{eff} \cdot l_{eff} = 219{,}71 \text{ kN}$$

where:

f_j: Compression resistance parallel to wood fibers, $f_{c,0,g,d} = 24$ MPa;

b_{eff}: Effective height of the T-Stub = 76,28 mm;

l_{eff}: Effective width of the T-Stub = 120 mm.

It is assumed that the compression stresses are uniformly distributed over a rectangular area b_{eff} l_{eff} (Fig. IV.42b), with the width of the contact area *c*. This parameter is defined by referring to the bending verification of the cantilever part of the end-plate. In particular, it is evaluated by equating the bending resistant moment, M_{Rd}, per unit of length, with the bending soliciting moment, M_{Ed}, per unit of length.

$$M_{Rd}=\frac{1}{\gamma_{M0}}\frac{t_f^2+f_y}{6}=\frac{f_j\cdot c^2}{2}=M_{ed}$$

and c is equal to:

$$c=t_f\sqrt{\frac{f_y}{3\cdot f_j\cdot\gamma_{M0}}}=38{,}12\text{ mm}$$

Steel section flange in compression

The numerical and experimental results on welded joints with rib stiffeners (Lee, 2002; Abidelah et al, 2012; Lee et al, 2015) highlights that bending is mainly transferred from beam-to-column by a truss mechanism rather than the classical beam theory, where the rib behaves as an inclined strut as shown in Figure IV.43.

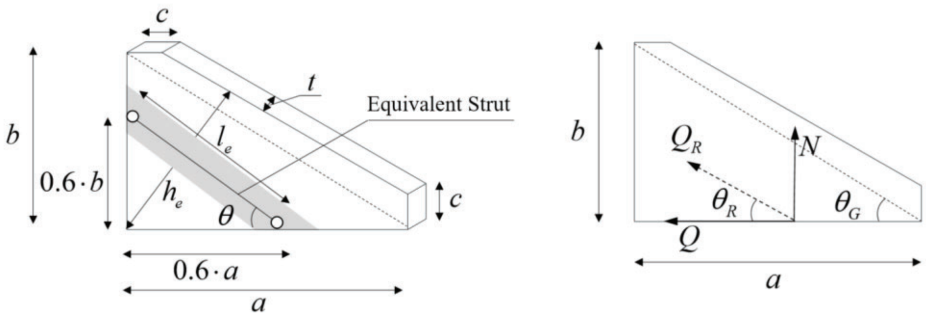

Figure IV.128 – Geometry of rib stiffener (a) and forces developing at beam/column-to-rib interface according to Lee, 2002 (Landolfo et al, 2018).

At current stage, the presence of the rib stiffener is not properly addressed by EC3. With this regard, analytical and semi-empirical formulations given by literature and validated by numerical simulations are assumed within the developed design procedure and described hereinafter. The design strength and stiffness of rib are assumed on the basis of the equivalent truss model provided by Lee (2002), which defines the equivalent strut area of the rib, A_e, as follows:

$$A_e=\eta\cdot h_e\cdot t$$

where η is the equivalent strut area factor and it is equal to 1,5; t is the rib thickness; h_e is the width perpendicular to the strut line and it is defined as:

$$h_e=\frac{a\cdot b-c^2}{\sqrt{(a-c)^2+(b-c)^2}}$$

Being *a*, *b* and *c* the dimensions of rib plate. Based on the available experimental and analytical database (Lee, 2002; Lee et al, 2005; Abidelah et al, 2012; Tartaglia et al, 2016; D'Aniello et al, 2017) the slope θ of the rib can be assumed within the range 30°-40°. The lower limit of 30° is prescribed by AISC 35810, while the upper limit of 40° is assumed in the present study in order to minimize the design bending moment acting on the connection. The design forces acting on the rib stiffeners at the beam/column-to-rib interface should be evaluated as follows:

$$N=\left(\frac{b}{a}\right)Q$$

$$Q=\frac{\dfrac{a\cdot d_0\left(0{,}21a+0{,}51L'\right)}{L_0}}{\dfrac{1}{\eta}\dfrac{0{,}6\sqrt{a^2+b^2}\sqrt{(a-c)^2+(b-c)^2}}{(a\cdot b-c^2)t}+\dfrac{(0{,}81b+0{,}3d_b)(a\cdot d_b)}{l_b}}V_{B,Ed}$$

where d_b and I_b are the depth and second moment of area of the beam, respectively. $V_{B,Ed}$ is the design shear force. The rib stiffener influences the shape of T-Stub mechanisms, which also depend on the number of bolt rows due to possible occurrence of group effect. Two configurations with either one or two bolt rows placed above the beam flange are addressed. In the first case, the effective length is assumed as that for the stiffened column flange. In the second case, due to the group effect the effective length is computed as given by the Green Book P398. Finally, the presence of rib stiffeners also influences the beam web in compression capacity. The compression forces acting on beam web component can be more rationally obtained as follows:

$$F_{c,fb,Rd}=\frac{M_{j,Ed}}{z}=\frac{M_{c,Rd}}{d_b+\xi\cdot b-0{,}5t_{fb}}=451{,}89\text{ kN}$$

where ξ_b is the position of the compression centre as shown in Figure IV.40b.
In particular:

$$M_{c,Rd}=\frac{w_{pl,z}\cdot f_{yk}}{\gamma_{M0}}=49{,}73\text{ kN}$$

where:
ξ_b= 21,79 mm;
d_b= 91 mm;
b= 69,5 mm;
$t_{f,b}$= 5,5 mm;
$W_{pl,z}$= 58000 mm^3;
f_{yk}= 235 MPa.

<u>Design moment resistance</u>

From balance to translation, it is possible to derive *x*:

$$x \cdot f_j \cdot l_{eff} = F_{Rd,min}$$

$$x = \frac{F_{Ed,min}}{f_j \cdot l_{eff}} = 0{,}047 \text{ mm}$$

The distance, *z*, can be evaluated as:

$$z = C_t + h + C_c - \frac{x}{2} = 197{,}42 \text{ mm}$$

The design moment resistance, $M_{j,Rd}$, can be evaluated as:

$$M_{j,Rd} = F_{Rd,\,min} \cdot z = 136{,}51 \cdot 0{,}19742 = 26{,}95 \text{ kNm}$$

where *z* is the lever arm of the internal couple and F_{Rd} is the resistance of the weakest component of the joint.

The bending resistant moment of the new timber beam is:

$$M_{Rd,T} = \frac{f_{m,k} \cdot k_{mod}}{\gamma_m} W = 50{,}46 \text{ kNm}$$

where:

$f_{m,k}$= bending strength, that for GL24h = 24 N/mm^2

k_{mod}= is a partial factor for taking into account the effects on the material of duration of load and moisture content = 1,10

γ_m = partial factor for material for glulam timber = 1,25

W = strength module = 2,38E+06 mm^3

The selected steel profile is HE100AA, with a plastic strength module:

$$W_{el,L} = 51{,}98 \text{ mm}^3$$

$$W_{pl,L} = 58{,}36 \text{ mm}^3$$

The bending resistant moment of the link is:

$$M_{Rd,el,L} = W_{el,L} \cdot \frac{f_{yk}}{\gamma_{m0}} = 12{,}22\ \text{kNm}$$
$$M_{Rd,pl,L} = W_{pl,L} \cdot \frac{f_{yk}}{\gamma_{m0}} = 13{,}71\ \text{kNm}$$

where:
γ_{m0}= 1,05;
f_{yk} = 235 MPa (S235)

The Ω coefficient is:

$$\Omega_{el} = \frac{M_{Rd,T}}{M_{Rd,el,L,max} \cdot \gamma_{rd} \cdot 1{,}1} = 3{,}13$$
$$\Omega_{pl} = \frac{M_{Rd,T}}{M_{Rd,pl,L,max} \cdot \gamma_{rd} \cdot 1{,}1} = 2{,}79$$

The analytical results of the model are shown in Table IV.17.

- The resistance of the glued-in steel bars: $F_{ax,Rd}$
  Rod failure through yielding: $F_{ax,Rd,1}$ =226,08 kN
  Failure of the adhesive by debonding from steel or wood: $F_{ax,Rd,2}$ = 73 kN
  Failure of the timber adjacent to the glue-line: $F_{ax,Rd,3}$ = 110,88 kN
- The resistance of the equivalent T-stub in tension $F_{t,T\text{-}stub,Rd,1\text{-}2}$ = 219,42 kN
- The resistance of the equivalent T-stub in tension $F_{t,T\text{-}stub,Rd,3}$ = 282,6 kN
- The resistance of the equivalent T-stub in compression $F_{c,T\text{-}stub,Rd}$ = 219,71 kN
- The resistance of the steel section flange in compression $F_{sf,Rd}$ = 451,89 kN
- The resistance of the stiffener $F_{t,s,Rd}$ = 70,32 kN

Table IV.73 – Summary of analytical results: HE100AA joint [FS-HDJ-FC].

	Collapse hierarchy	Analytical evaluation			
		$F_{i,Rd}$ [kN]	M_{rd} [kNm]	Over-strength$_{,ana}$ [%]	$\Omega_{,ana}$ [%]
1)	Link	/	12,22	/	/
2)	Stiffners	70,32	23,88	1,14	0,86
3)	Pull-out	136,51	26,95	2,21	1,67
4)	Timber tensile break	207,57	40,98	3,35	2,59
5)	End-plate/Bolts (mode 1-2)	219,42	43,32	3,55	2,69
6)	End-plate (flange compression)	219,71	43,38	3,55	2,69
7)	Timber beam bending	/	50,46	4,13	3,13
8)	Bolts (mode 3)	282,6	55,79	4,57	3,46

From the analytical results observation, a *Full-strength connection (FS)* with a *High Ductility timber-steel link Joint (HDJ)* and *Fragile connection (FC)* is designed, so that the yielding occur in the link and the timber beam has an over-strength respect to the connection (only the bolts have an over-strength respect to the timber beam since they have an important function in bearing the loads), that is not the first macro-component over-resistant respect to the link. In particular, the connection is made up of glued bars (sub-component), for which the "Pull-out" and the "Tensile timber breaking" are fragile collapse modes, that occur before the ductile collapse modes of the connection ("T-stub in tension" and "T-stub in compression").

The timber-steel link joint (HE100AA Link), in Figure IV.44, is made by a laminated timber beams (GL24h), with a 140x320 mm rectangular cross section and 2500 mm long, equipped at one end with a steel link, HE100AA profile 360 mm long (steel grade S235) with two welded end-plates (120x230 mm, steel grade S275), with 20 mm thickness and four stiffeners (110x70 mm and 20 mm thickness, steel grade S275). The link is connected at one side to the timber beam by means of 4 glued threaded bars (M16, 10.9, 540 mm long).

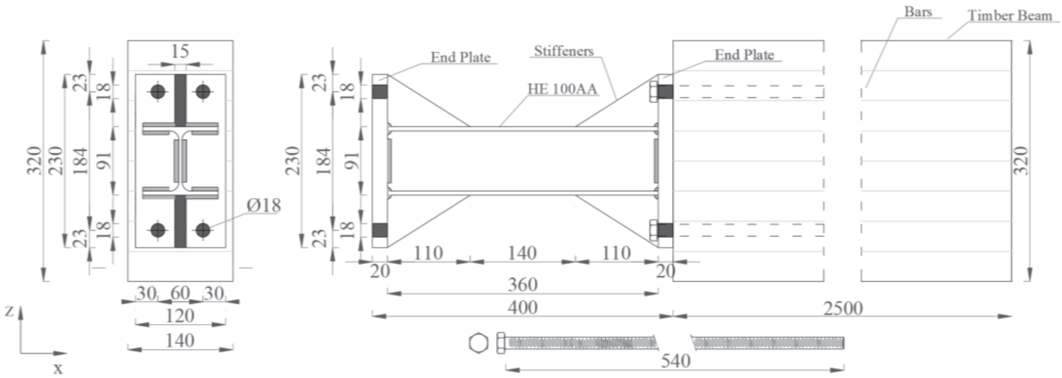

Figure IV.129 – HE100AA joint [FS-HDJ-FC]: geometrical features [mm].

4.5 Numerical analysis of the ductile joints

4.5.1 Full-Strength connection with Low Ductile Joint

The numerical analysis of the HE100AA joint, in the *Full-Strength* connection with *Low Ductile Joint* configuration (LDJ) model, is carried out with the same set-up of the monotonic analysis on the *P10* specimen, using the structural calculation program ABAQUS. Geometrical features and materials are illustrated in the following table (Tab. IV.18).

The outputs are provided in terms of the maximum values of stresses (σ), DCR_{el} ($DCR_{el}=\sigma/\sigma_{el}$) and DCR_{ul} ($DCR_{ul}=\sigma/\sigma_{ul}$), for each component of the model (link, end-plate, threaded bolts, timber beam and stiffeners), the resistant bending moment (M) and rotation (θ) in in x-z plane, the force (F) and the displacement (u) in z-direction, valuated in the RP point, for the global model. Outputs are detected at specific increments (In.) and times (t.), corresponding to the yielding of the steel link

(P_Y), the complete plasticization of the link cross-section (P_P) and the ultimate strength of the link (P_C), defined by the collapse of the model and the end of the numerical analysis. Moreover, the F-u and the M-θ curves are shown. A special attention is also given to the collapse hierarchy, in terms of the global behaviour and of the single component, to evaluate the accuracy of model and the over-strength of each component (macro- and sub-component) respect to the yielding one ($OS_{el}= DCR_{el\text{-}link}/DCR_{el\text{-}component}$; $OS_{ul}= DCR_{ul\text{-}link}/DCR_{ul\text{-}component}$), both for analytical and numerical evaluation.

Table IV.74 – HE100AA joint [FS-LDJ]: structural features.

	Timber beam	Thread Bolt	End plate	Stiffeners	HE100AA
Element	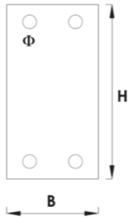		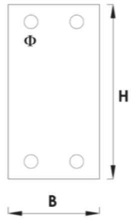	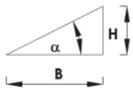	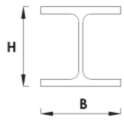
Geometry [mm]	θ= 18 H= 230 B= 120 L= 2500	θ= 16 L= 540 Nut, Washer / Shank	θ= 18 H= 230 B=120 S= 20	H= 70 B=110 S= 15	L= 360 B= 100 H= 91
Material	**GL24h**	**10.9**	**S275**		**S235**
Density [N/mm³]	3,80x e-6	7,85 x e-5			
Elasticity [MPa]	E_{90}=390 E_0=11600	210000			
Plasticity [MPa]	σ_{el} 24	900	275		235
	σ_u /	1000	430		360
	ε_{el}	0	0		0
	ε_u /	0,178	0,376		0,261
Model	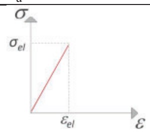		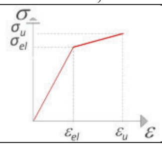		
Mesh	**Solid element**				
	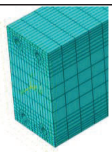	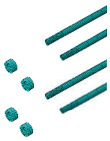			

Figure IV.35 (a) and (b) compares the experimental (*P10* specimen) and numerical (HE100AA joint - LDJ) F-u and the M-θ curves and the collapse mode.

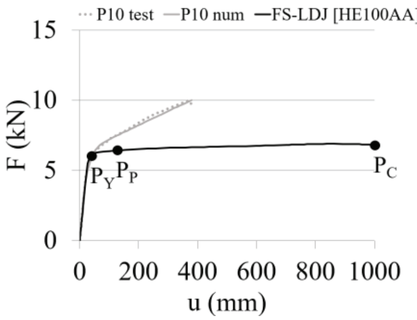

a)

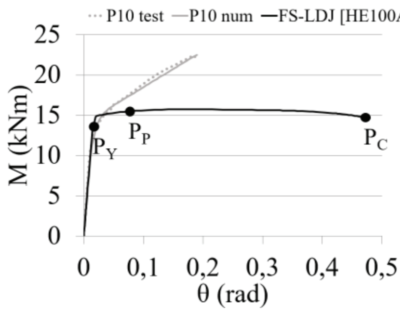

b)

Figure IV.130 – HE100AA joint [FS-LDJ]: numerical (a) F-u and (b) M-θ curves.

Analysing the numerical results, the following observations can be drawn. With regards to the state of stress, examining the P_Y instant, the link reaches the yielding stress (235 MPa) while the end-plate (131 MPa), the bolts (291 MPa), the beam (13 MPa) and the stiffeners (249 MPa) are still in the elastic field; at the P_P instant, the cross-section of the link reaches the complete yielding, with a maximum value equal to 252 MPa, while the end-plate (141 MPa), the bolts (319 MPa), the beam (15 MPa) and the stiffeners (276 MPa) are in the elastic field; at the P_C instant, corresponding to the collapse of the model with the catching of the ultimate stress by the link (360 MPa), the stiffeners (290 MPa) reach the yield while the end-plate (167 MPa), the bolts (322 MPa) and the beam (15 MPa) are still in elastic field (Tab. IV.19).

Table IV.75 – HE100AA joint [FS-LDJ]: yield (P_Y), plastic (P_P) and collapse (P_C) stress value σ, bending moment *M*, rotation *θ*, force *F* and vertical displacement *u*.

Point	σ [MPa]					M	θ	F	u
	HE100AA	End Plate	Thread Bolt	Timber beam	Stiffeners	[kNm]	[rad]	[kN]	[mm]
P_Y	235	131	293	13	249	13,87	0,01	5,92	25,46
P_P	251	141	319	15	276	14,7	0,06	6,48	157,09
P_C	360	167	322	15	290	14,9	0,47	6,84	1000

Stress distribution

(P_Y) [In. 49; t. 1.975]

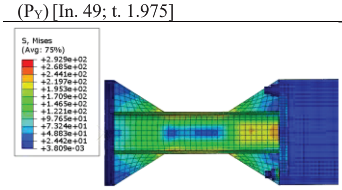

(P_P) [In. 59; t. 12.01]

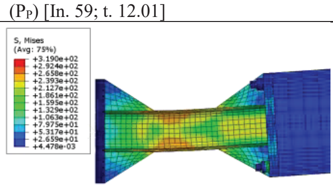

(P_C) [In. 109; t. 100]

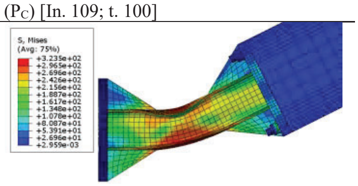

In Table IV.20 are depicted the stress values (σ), the DCR_{el} and the DCR_{ul}, for each connection element, in the P_Y, P_P and P_C instants. Moreover, the first element that reaches the elastic strength (σ_{el}) and the ultimate strength (σ_u) is highlighted.

Table IV.76 – HE100AA joint [FS-LDJ]: yield (P_Y), plastic (P_P) and collapse (P_C) stress σ, DCR_{el} (σ/σ_{el}) and DCR_{ul} (σ/σ_u).

	Link			**End Plate**			**Thread Bolt**			**Timber beam**		**Stiffeners**		
	σ	**DCR**		**σ**	**DCR**		**σ**	**DCR**		**σ**	**DCR**	**σ**	**DCR**	
	[MPa]	**el**	**ul**	**[MPa]**	**el**	**ul**	**[MPa]**	**el**	**ul**	**[MPa]**	**el**	**[MPa]**	**el**	**ul**
P_Y	235	100%	65%	131	48%	30%	293	33%	29%	13	54%	249	91%	58%
P_P	247	107%	69%	141	51%	33%	319	35%	32%	15	63%	276	100%	64%
P_C	360	153%	100%	167	61%	39%	322	36%	33%	15	63%	290	105%	67%

It is possible to observe that, at the instant P_Y, the first element to reach the yield is the link, with a DCR_{ul}= 65%. The second joint component most stressed is the stiffener, with a DCR_{el}= 91% and DCR_{ul}= 58%, the timber beam is the third joint component with a DCR_{el}= 54% respect to the yielding link and, at the last, the end-plate presents a DCR_{el}= 48% and DCR_{ul}= 30% and the bolts a DCR_{el}= 33% and DCR_{ul}= 29%.

At the instant P_P, there is the complete hinge plasticization of the link and the stiffeners reach the yield, with respectively a DCR_{ul}= 69% and DCR_{ul}= 64%, while the end-plate (DCR_{el}= 51% and a DCR_{ul}= 33%), the bolts (DCR_{el}= 35% and a DCR_{ul}= 32%) and the timber beam (DCR_{el}= 63%) are in the elastic field.

At the instant P_C, corresponding to the collapse of the joint with the link's failure, the stiffeners present a DCR_{el}= 105% and a DCR_{ul}= 67%, while the end-plate (DCR_{el}= 61% and a DCR_{ul}= 39%), the bolts (DCR_{el}= 36% and a DCR_{ul}= 33%) and the timber beam (DCR_{el}= 63%) are in the elastic field (Fig. IV.46c,d).

At the end of P_Y, coinciding with the yielding of the link, the end-plate (OS_{el}= 2,10), the stiffeners (OS_{el}= 1,10), the bolts (OS_{el}= 3,07) and the timber beam (OS_{el}= 1,80) have an over-strength (OS_{el}). In particular, they show an overstrength coefficient (OS_{el}) indicated in the Table IV.21 and Figure IV.46a,b.

The collapse hierarchy of the elements connection, therefore, is: 1) Link; 2) Stiffeners; 3) Timber beam; 4) End-plate; 5) Bolts.

Table IV.77 – HE100AA joint [FS-LDJ]: analytical evaluation vs numerical analysis of over-strength (OS) and Ω.

	Collapse hierarchy	**Analytical evaluation**		**Numerical analysis**	
		$OS_{el,ana}$ [%]	**$\Omega_{,ana}$ [%]**	**$OS_{el,num}$ [%]**	**$\Omega_{,num}$ [%]**
1)	**Link**	/	/	/	/
2)	**Stiffneers**	/	/	1,10	0,84
3)	**Timber Beam bending**	1,83	1,39	1,8	1,40
4)	**End-plate**	/	/	2,10	1,59
5)	**Bolts**	/	/	3,07	2,33

From the numerical results observation, a *Full-strength connection* with a *Low Ductility timber-steel link Joint (LDJ)* is designed, so that the yielding occur in the link and the connection has an over-strength respect to the timber beam.

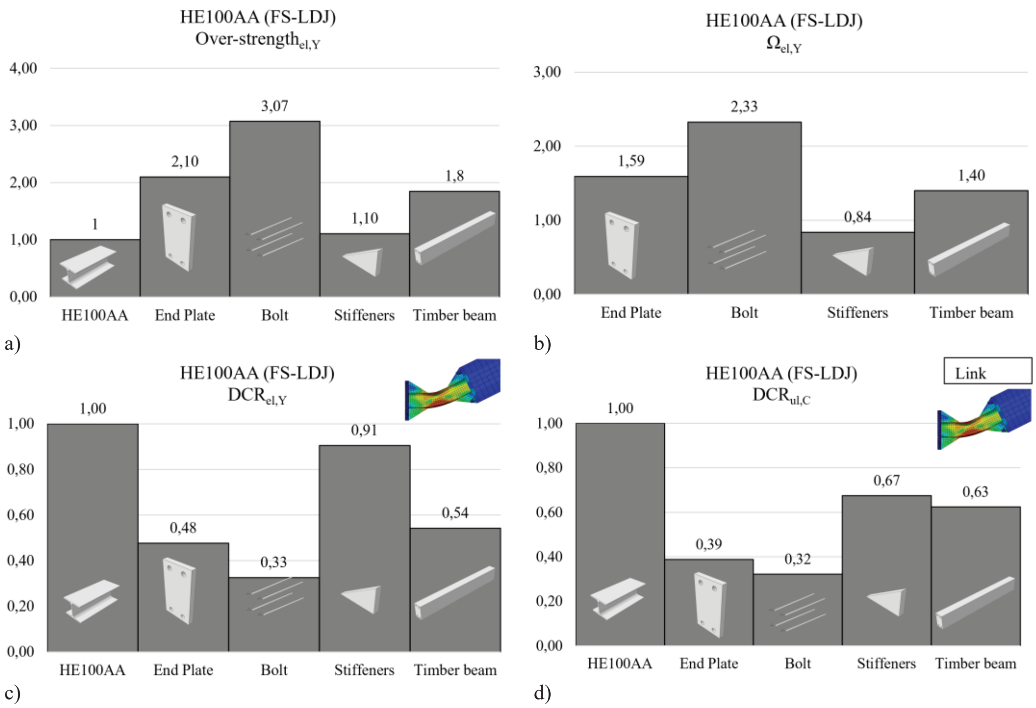

Figure IV.131 – HE100AA joint [FS-LDJ]: DCR$_{el}$ [DCR$_{el}$=σ/σ_{el}], DCR$_{ul}$ [DCR$_{ul}$=σ/σ_{ul}], OS$_{el}$ (σ/σ_{el}) and Ω evaluated for P_Y and P_C points.

Figure IV.47 shows the deformed configuration, respect to the unformulated configuration, in the 3 points: yielding, complete plasticization of the plastic hinge and collapse. In particular, in Y-point, the vertical displacement is 25,46 mm, in P-point in 157,09 mm and at the collapse is 1000 mm.

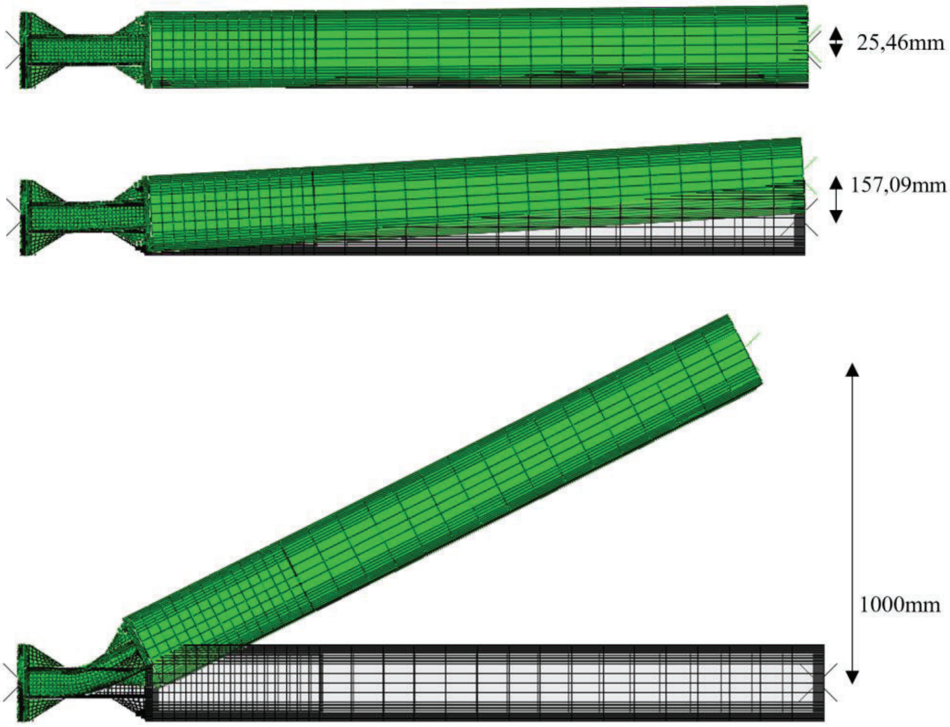

a)

b)

c)

Figure IV.132 – HE100AA joint [FS-LDJ]: vertical deformed configuration in a) P_Y, b) P_P and c) P_C points.

Figure IV.48 shows the AC YIELD diagram, which shows the evolution of the link yield and the extension of the plastic hinge through the normal stress distribution (σ). In particular, at the Y point, the first fiber that catches the yield is in correspondence with the stiffener (Fig. IV.48a,b), while the other elements of the connection (end-plate, bolts and stiffeners) and the timber beam are in the elastic field. At the P point (Fig. IV.48c,d), when the yield has reached the full height of the cross section of the link (Hp= 100 mm), the yield extension is equal to the distance between the stiffeners (Lp= 140 mm). At the collapse, the following observations can be drawn. The capacity design procedure allowed the complete development of the plastic hinge (Lp= 140 mm) and the collapse for reaching the ultimate stress value in the link (f_{uk}= 360MPa) (Fig. IV.48e,f and Fig. IV.49a).

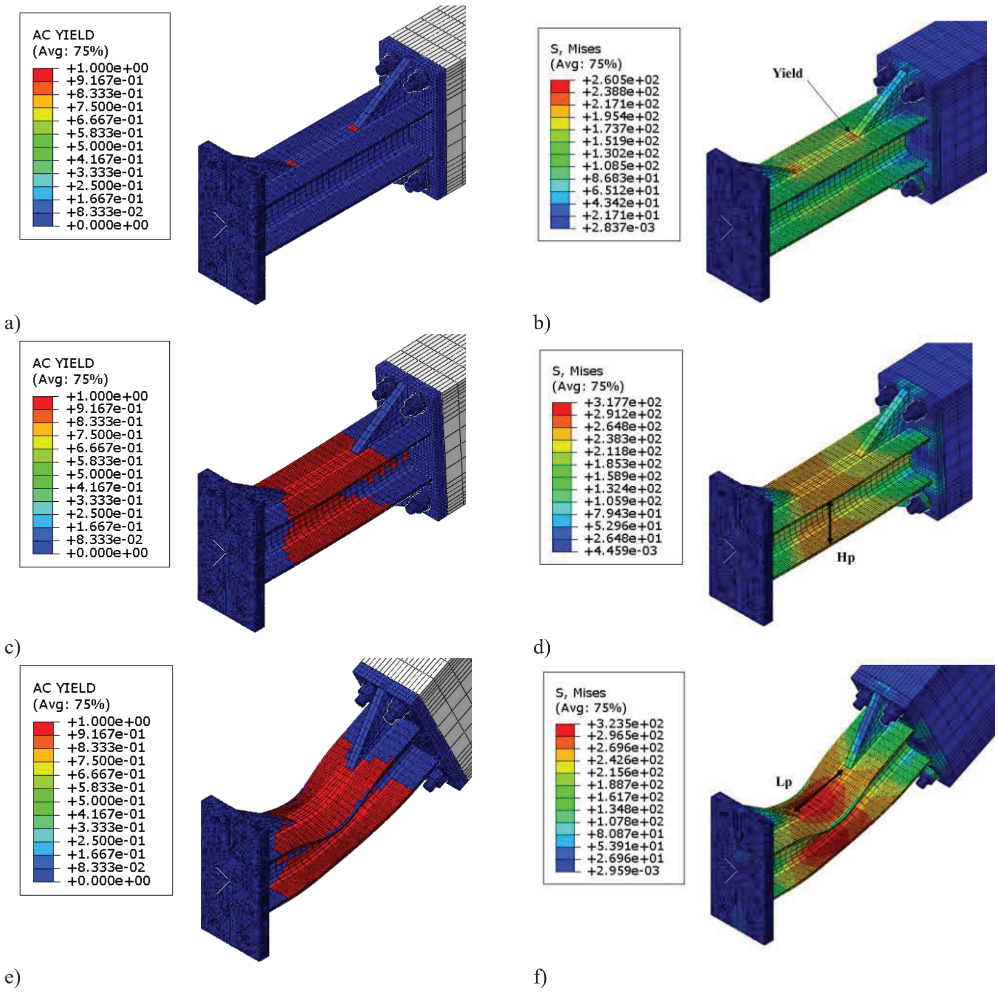

Figure IV.133 – HE100AA joint [FS-LDJ]: yielding and stress distribution of the elements in a), b) P_Y, c), d) P_P and e), f) P_C points. *Hp*: height of the plastic hinge; *Lp*: length of the plastic hinge.

The sub-components constituting the joint are shown in Figure IV.49, in the ultimate condition, with the stress distribution.

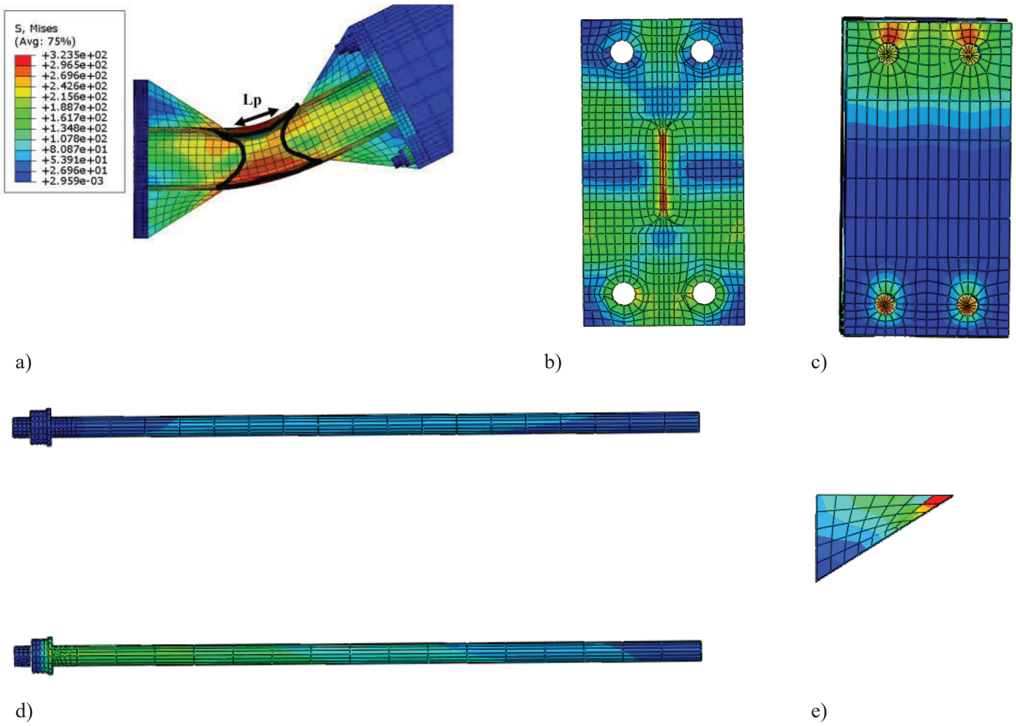

Figure IV.134 – HE100AA joint [FS-LDJ]: stress distribution in a) link, b) end-plate, c) timber beam and d) bolts, in P_C point.

4.5.2 Full-Strength connection with High Ductile Joint

The numerical analysis of the HE100AA joint (HDJ), in the *Full-Strength* connection with *High Ductile Joint* and *Fragile Connection* configuration model, is carried out with the same set-up of the monotonic analysis on the *P10* specimen, using the structural calculation program ABAQUS. Geometrical features and materials are illustrated in the following table (Tab. IV.22).

Table IV.78 – HE100AA joint [FS-HDJ-FC]: structural features.

		Timber beam	**Thread Bolt**	**End plate**	**Stiffeners**	**HE100AA**
Element		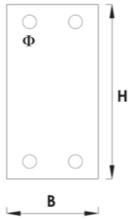		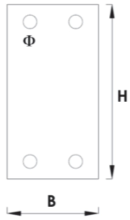	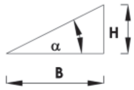	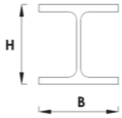
Geometry [mm]		θ= 18 H= 320 B= 140 L= 2500	θ= 16 L= 540 Nut, Washer / Shank	θ= 18 H= 230 B=120 S= 20	H= 70 B=110 S= 15	L= 360 B= 100 H= 91
Material		**GL24h**	**10.9**	**S275**		**S235**
Density [N/mm^3]		3,80x e^{-6}	7,85 x e-5			
Elasticity [MPa]		E_{90}=390 E_0=11600	210000			
Plasticity [MPa]	σ_{el}	24	900	275		235
	σ_u	/	1000	430		360
	ε_{el}		0	0		0
	ε_u	/	0,178	0,376		0,261
Model		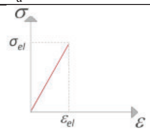		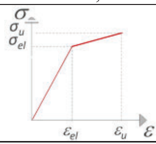		
Mesh		**Solid element**				
		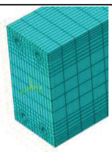	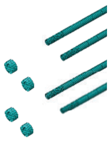			

The outputs are provided in terms of the maximum values of stresses (σ), DCR_{el} ($DCR_{el}=\sigma/\sigma_{el}$) and DCR_{ul} ($DCR_{ul}=\sigma/\sigma_{ul}$), for each component of the model (link, end-plate, threaded bolts, timber beam and stiffeners), the resistant bending moment (M) and rotation (θ) in in x-z plane, the force (F) and the displacement (u) in z-direction, valuated in the RP point, for the global model. Outputs are detected at specific increments (In.) and times (t.), corresponding to the yielding of the steel link (P_Y), the complete plasticization of the link cross-section (P_P) and the ultimate strength of the link (P_C), defined by the collapse of the model and the end of the numerical analysis. Moreover, the F-u and the M-θ curves are shown. A special attention is also given to the collapse hierarchy, in terms of the global behaviour and of the single component (macro- and sub-component), to evaluate the accuracy of model and the over-strength of each component respect to the yielding one ($OS_{el}= DCR_{el\text{-}link}/DCR_{el\text{-}component}$; $OS_{ul}= DCR_{ul\text{-}link}/DCR_{ul\text{-}component}$), both for analytical and numerical evaluation.

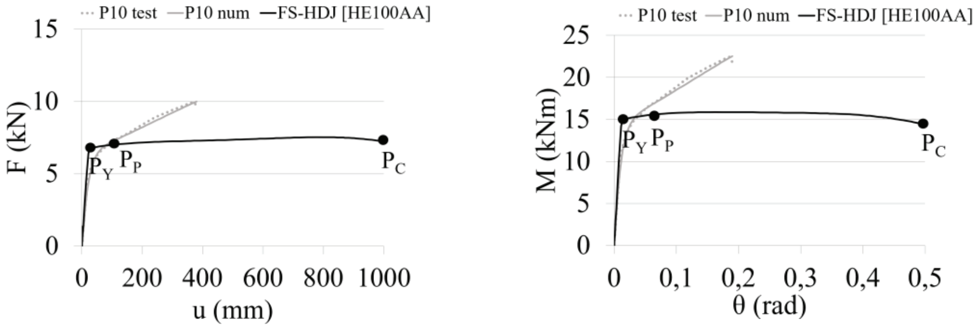

a) b)

Figure IV.135 – HE100AA joint [FS-HDJ-FC]: numerical (a) F-u and (b) M-θ curves.

Figure IV.50a,b compares the experimental (*P10* specimen) and numerical (HE100AA Link - HDJ) F-u and the M-θ curves and the collapse mode.

Analysing the numerical results, the following observations can be drawn. With regards to the state of stress, examining the *Y* instant, the link reaches the yielding stress (235 MPa) while the end-plate (139 MPa), the bolts (228 MPa), the beam (7,9 MPa) and the stiffeners (275 MPa) are still in the elastic field; at the *P* instant, the cross-section of the link reaches the complete yielding, with a maximum value equal to 258 MPa, while the end-plate (146 MPa), the bolts (242 MPa), the beam 8,6 MPa) and the stiffeners (275 MPa) are in the elastic field; at the *C* instant, corresponding to the collapse of the model with the catching of the ultimate stress by the link (360 MPa), the stiffeners (311 MPa) reach the yield while the end-plate (217 MPa), the bolts (247 MPa) and the beam (8,9 MPa) are still in elastic field (Tab. IV.23).

Table IV.79 – HE100AA joint [FS-HDJ-FC]: yield (P_Y), plastic (P_P) and collapse (P_C) stress value σ, bending moment *M*, rotation *θ*, force *F* and vertical displacement *u*.

Point	σ [MPa]					M	θ	F	u
	HE100AA	End Plate	Thread Bolt	Timber beam	Stiffeners	[kNm]	[rad]	[kN]	[mm]
P_Y	235	138	222	7,3	261	14,11	0,011	6,4	21,57
P_P	258	145	245	8,2	276	15,21	0,06	7,0	137,2
P_C	360	217	247	8,3	311	15,61	0,50	7,23	1000
Stress distribution									
(P_Y) [In. 33; t. 2.157]			(P_P) [In. 42; t. 13.71]			(P_C) [In. 98; t. 100]			
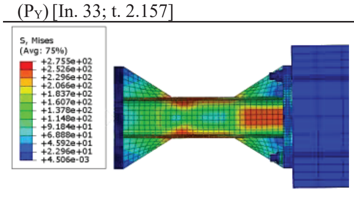			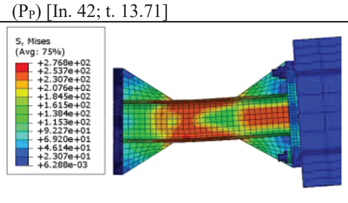			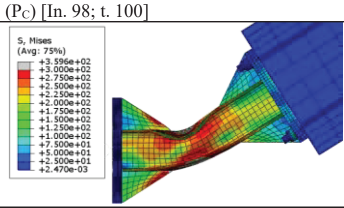			

In Table IV.24 are depicted the stress values (σ), the DCR_{el} and the DCR_{ul}, for each connection element, in the P_Y, P_P and P_C instants. Moreover, the first element that reaches the elastic strength (σ_{el}) and the ultimate strength (σ_u) is highlighted.

Table IV.80 – HE100AA joint [FS-HDJ-FC]: yield (P_Y), plastic (P_P) and collapse (P_C) stress σ, DCR_{el} (σ/σ_{el}) and DCR_{ul} (σ/σ_u).

	Link			End Plate			Thread Bolt			Timber beam		Stiffeners		
	σ	DCR		σ	DCR		σ	DCR		σ	DCR	σ	DCR	
	[MPa]	el	ul	[MPa]	el	ul	[MPa]	el	ul	[MPa]	el	[MPa]	el	ul
P_Y	235	100%	65%	138	50%	32%	222	25%	22%	7,3	30%	261	95%	61%
P_P	247	107%	70%	145	53%	34%	245	27%	25%	8,2	34%	276	100%	64%
P_C	360	153%	100%	217	79%	50%	247	27%	25%	8,3	35%	311	113%	72%

It is possible to observe that, at the instant P_Y, the first element to reach the yield is the link, with a DCR_{ul}= 65%. The second joint component most stressed is the stiffener, with a DCR_{el}= 95% and DCR_{ul}= 61%; the timber beam is the third joint component with a DCR_{el}= 30% respect to the yielding link; at the last, the end-plate presents a DCR_{el}= 50% and DCR_{ul}= 32% and the bolts a DCR_{el}= 25% and DCR_{ul}= 22%.

At the instant P_P, there is the complete hinge plasticization of the link and the stiffeners reach the yield, with respectively a DCR_{ul}= 70% and DCR_{ul}= 64%; the end-plate (DCR_{el}= 53% and a DCR_{ul}= 34%), the bolts (DCR_{el}= 27% and a DCR_{ul}= 25%) and the timber beam (DCR_{el}= 34%) are in the elastic field.

At the instant P_C, corresponding to the collapse of the joint with the link's failure, the end-plate (DCR_{el}= 70% and a DCR_{ul}= 50%), the stiffeners (DCR_{ul}= 72%), the bolts (DCR_{el}= 27% and a DCR_{ul}= 25%) and the timber beam (DCR_{el}= 35%) are in the elastic field (Fig. IV.51c,d).

At the end of P_Y, coinciding with the yielding of the link, the end-plate (OS_{el}= 1,99), the stiffeners (OS_{el}= 1,05), the bolts (OS_{el}= 4,05) and the timber beam (OS_{el}= 3,3) are over-resistant. In particular, they show an overstrength coefficient (OS_{el}) indicated in the Table IV.25 and Figure IV.51a,b.

Table IV.81 – HE100AA joint [FS-HDJ-FC]: analytical evaluation vs numerical analysis of over-strength (OS) and Ω.

Collapse hierarchy		Analytical evaluation		Numerical evaluation	
		$OS_{el,ana}$ [%]	$\Omega_{,ana}$ [%]	$OS_{el,num}$ [%]	$\Omega_{,num}$ [%]
1)	**Link**	/	/	/	/
2)	**Stiffners**	1,14	0,86	1,05	0,8
3)	**Pull-out**	2,21	1,67	/	/
4)	**Timber tensile break**	3,35	2,59	/	/
5)	**End-plate/Bolts (mode 1-2)**	3,55	2,69	1,99	1,51
6)	**End-plate (flange compression)**				
7)	**Timber beam bending**	4,13	3,13	3,3	2,49
8)	**Bolts (mode 3)**	4,57	3,46	4,05	3,07

The collapse hierarchy of the elements connection, therefore, is: 1) Link; 2) Stiffeners; 3) Timber beam; 4) End-plate; 5) Bolts.

In particular, the numerical analysis has confirmed a *Full-strength connection* with a *High Ductility timber-steel link Joint (HDJ)* and *Fragile connection*.

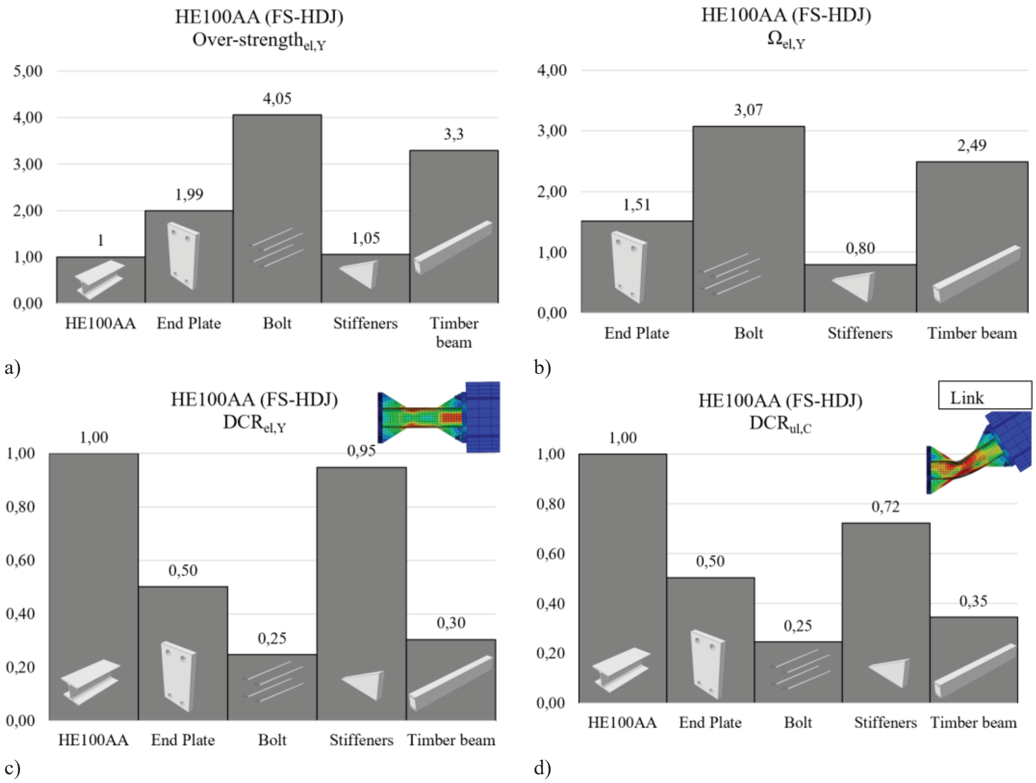

Figure IV.136 – HE100AA joint [FS-HDJ-FC]: DCR$_{el}$ [DCR$_{el}$=σ/σ_{el}], DCR$_{ul}$ [DCR$_{ul}$=σ/σ_{ul}], OS$_{el}$ (σ/σ_{el}) and Ω evaluated for P_Y and P_C points.

Figure IV.52 shows the deformed configuration, respect to the unformulated configuration, in the 3 points: yielding, complete plasticization of the plastic hinge and collapse. The achievement of a displacement of 1000 mm to the collapse manifests a high ductility of the system.

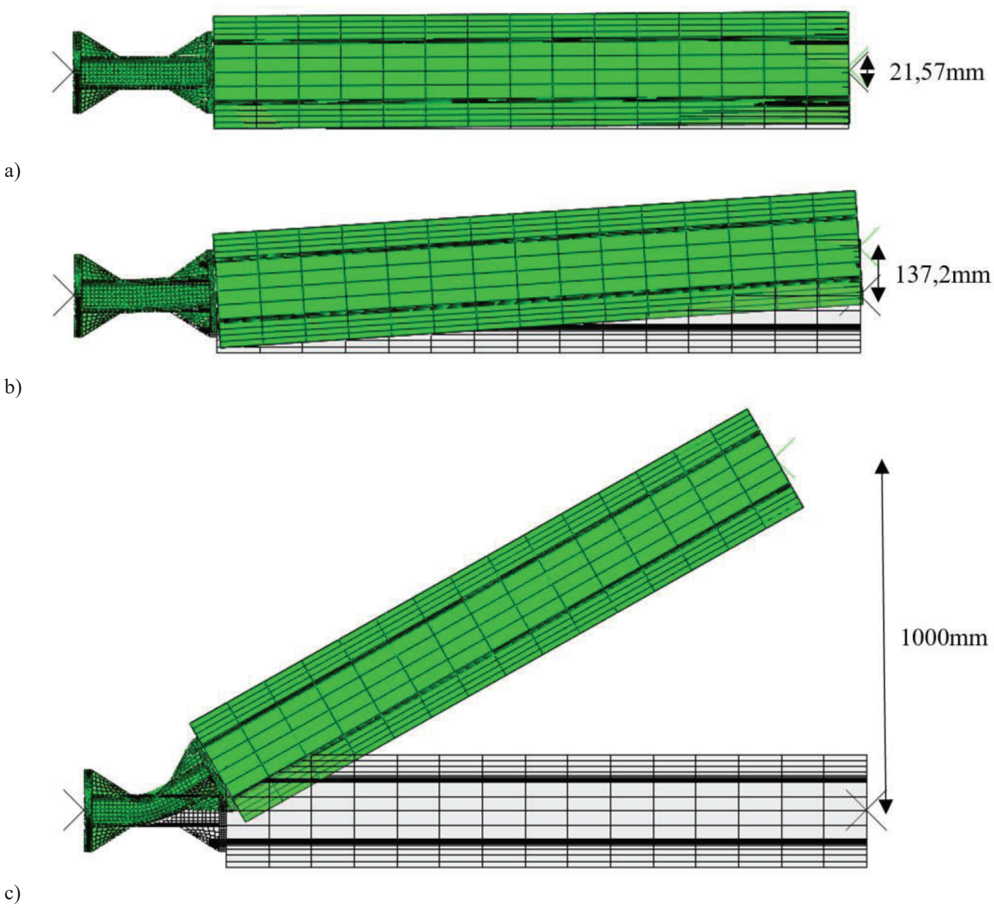

Figure IV.137 – HE100AA joint [FS-HDJ-FC]: vertical deformed configuration in a) P_Y, b) P_P and c) P_C points.

Figure IV.53 shows the AC YIELD diagram, which shows the evolution of the link yield and the extension of the plastic hinge through the normal stress distribution (σ). In particular, at the Y point, the first fiber that catches the yield is in correspondence with the stiffener (Fig. IV.53a,b), while the other elements of the connection (end-plate, bolts and stiffeners) and the timber beam are in the elastic field. At the P point (Fig. IV.53c,d), when the yield has reached the full height of the cross section of the link (Hp= 100 mm), the yield extension is equal to the distance between the stiffeners (Lp= 140 mm).

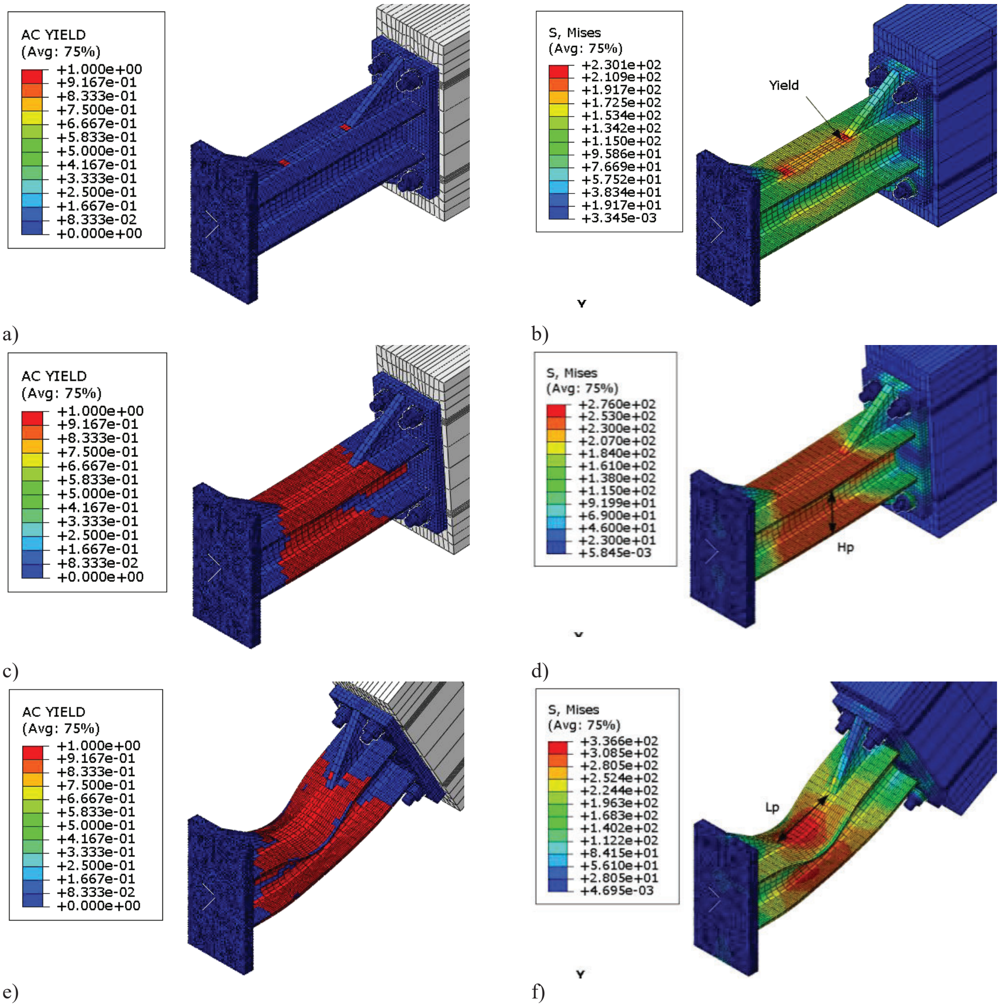

Figure IV.138 – HE100AA joint [FS-HDJ-FC]: yielding and stress distribution of the elements in a), b) P_Y, c), d) P_P and e), f) P_C points. *Hp*: height of the plastic hinge; *Lp*: length of the plastic hinge.

At the collapse, the following observations can be drawn. The capacity design procedure allowed the complete development of the plastic hinge (Lp= 140 mm) and the collapse for reaching the ultimate stress value in the link (f_{uk}= 360MPa) (Fig. IV.53e,f and Fig. IV.54a). As can be seen from Figure IV.54b, the presence of the stiffener in compression has led to the variation of the position of the centre of pressure between the upper end of the end-plate and the upper wing of the link.

The timber beam shows a rather uniform stress distribution, except for the areas around the holes and in correspondence with the compressed part, with low stress values (Fig. IV.54c). Observing the stress distribution in the glued-bars in the timber beam, it is possible to notice that after about 250 mm from the nut there is a reduction of the stress values of 200% (from 247MPa to

12MPa). This length is, however, necessary to ensure an over-strength respect to the bending resistance of the link (Fig. IV.54d). The stiffeners show a very variable stress distribution with a maximum value of 311MPa at the tip (Fig. IV.54e).

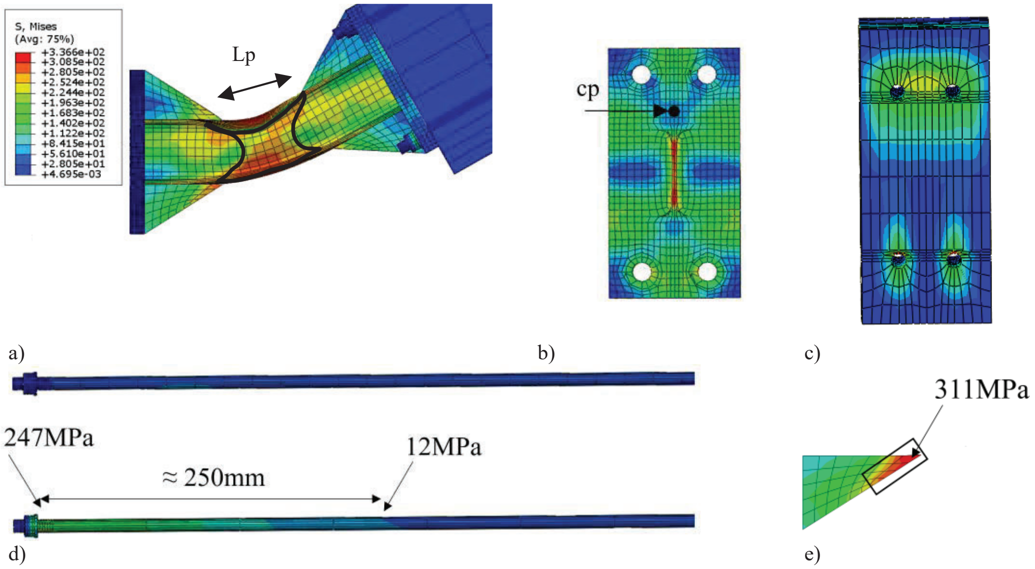

Figure IV.139 – HE100AA joint [FS-HDJ-FC]: stress distribution in a) link, b) end-plate, c) timber beam and d) bolts, in P_C point.

4.4 COMPARISON OF RESULTS

From the comparison of the results of the analytical design and the numerical analysis, for both types of joints, the proposed design criteria could be considered valid. In particular, the numerical analysis confirms the collapse hierarchy defined by the analytical design with the capacity design for "macro-components" and "sub-components", as it possible to see in the Table IV.26, Table IV.27. In the Figure IV.55 is presented the comparison between the two types of HE100AA-joints (FS-LDJ; FS-HDJ-FC) in terms of numerical F-u and M-θ curves.

Table IV.82 – Analytical evaluation FU-LDJ [HE100AA]

Point	F [kN]		u [mm]		M [kNm]		θ [rad]	
	Ana.	**Num.**	**Ana.**	**Num.**	**Ana.**	**Num.**	**Ana.**	**Num.**
P_Y	5,54	5,92	/	25,46	12,22	13,87	/	0,01
P_P	6,12	6,48	/	157,09	13,71	14,71	/	0,06
P_C	6,20	6,84	/	1000	13,86	14,97	/	0,47

Table IV.83 – Analytical evaluation FU-HDJ [HE100AA]

Point	F [kN]		u [mm]		M [kNm]		θ [rad]	
	Ana.	Num.	Ana.	Num.	Ana.	Num.	Ana.	Num.
P_Y	5,54	6,4	/	21,57	12,22	14,11	/	0,01
P_P	6,12	7,0	/	137,2	13,71	15,21	/	0,06
P_C	6,20	7,23	/	1000	13,86	15,61	/	0,50

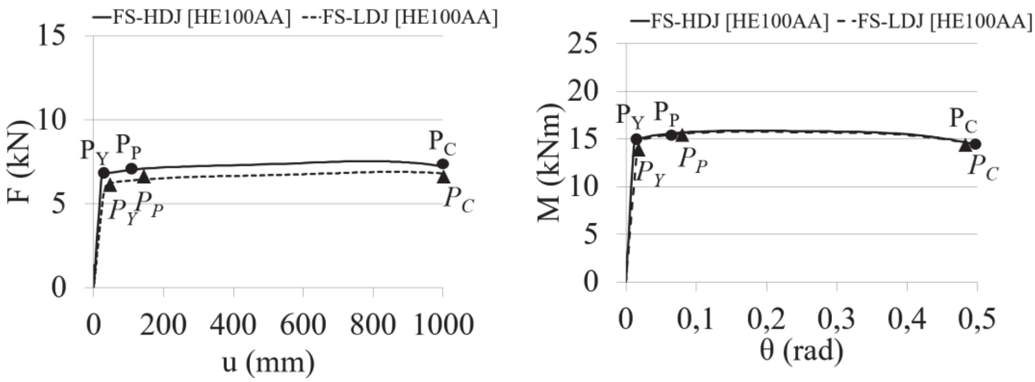

a) b)

Figure IV.140 – a) FS-LDJ [HE100AA] and b) FS-HDJ [HE100AA]: numerical (a) F-u and (b) M-θ curves.

For the FS-LDJ joint, the collapse hierarchy of the elements connection is: 11) Link; 2) Stiffeners; 3) Timber beam; 4) End-plate; 5) Bolts (Tab. IV.28). In particular, the numerical analysis has confirmed a *Full-strength connection* with a *Low Ductility timber-steel link Joint (LDJ)*, so that the yielding occur in the link and the connection is not the first macro-component over-resistant respect to the link.

For the FS-HDJ, the collapse hierarchy of the elements connection, therefore, is: 1) Link; 2) Stiffeners; 3) Timber beam; 4) End-plate; 5) Bolts (Tab. IV.28).

In particular, the numerical analysis has confirmed a *Full-strength connection* with a *High Ductility timber-steel link Joint (HDJ)* and *Fragile connection*, so that the yielding occur in the link and the connection is the first macro-component over-resistant respect to the link.

Therefore, the collapse hierarchy derived from the numerical analyses respects that deriving from the analytical design.

Table IV.84 – Comparison between FS-LDJ [HE100AA] and FS-HDJ [HE100AA] in terms of collapse hierarchy; stress distribution in P_Y, P_P and P_C points.

Collapse hierarchy

FS-Low Ductile Joint [HE100AA]

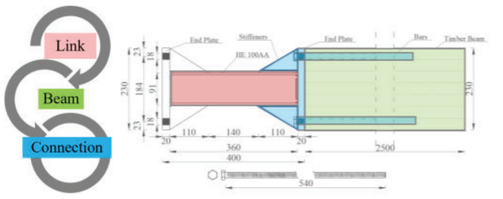

FS-High Ductile Joint [HE100AA]

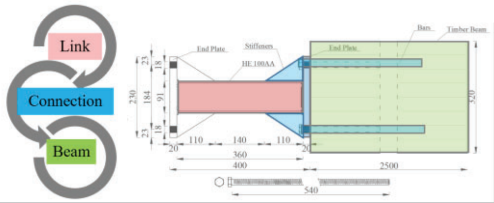

Stress distribution

P_Y

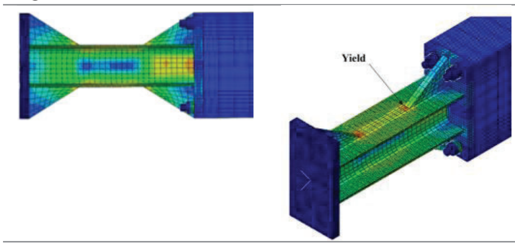

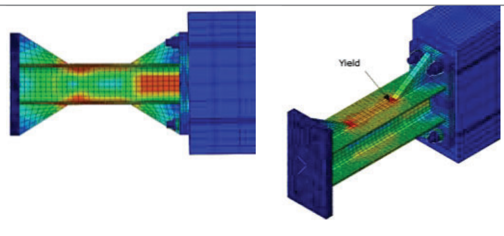

P_P

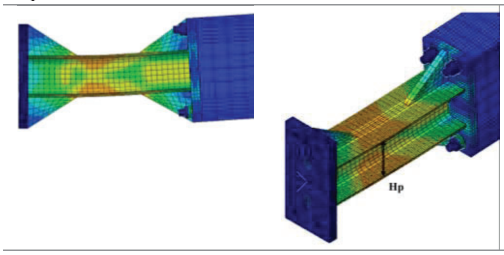

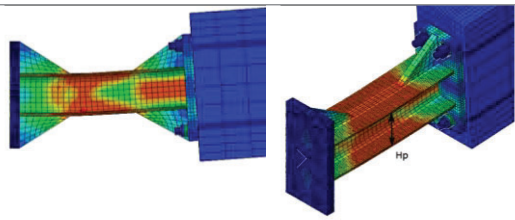

P_C

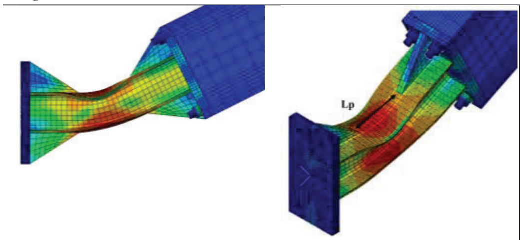

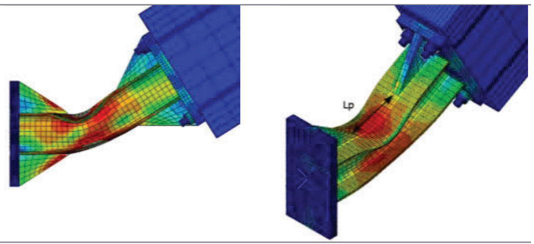

Chapter V

5. EXPERIMENTAL CAMPAIGN ON TIMBER BEAM TO COLUMN JOINT WITH STEEL LINK

5.1 INTRODUCTION

In this chapter, starting from the design criteria presented in chapter 2.2 and 2.4, 2 types of joints are analytically and numerically designed, applying the capacity design procedure for "macro-components" and for connection "sub-components":

- *Full-strength connection* (so that the connection is stronger than the link, such that yielding occur in it) with a *High Ductility timber-steel link Joint (LDJ)* (so that the connection is the first macro-component over-resistant respect to the link) and *Fragile connection* (so that the fragile collapse modes occur before the ductile collapse modes of the connection);
- *Full-strength connection* (so that the connection is stronger than the link, such that yielding occur in it) with a *High Ductility timber-steel link Joint (HDJ)* (so that the connection is the first macro-component over-resistant respect to the link) and *Ductile connection* (so that the ductile collapse modes occur before the fragile collapse modes of the connection).

In particular, starting from the primary design, 8 full-scale timber-steel link joint specimens are tested under monotonic and cyclic loading at the Department of Civil Engineering (DECivil) laboratory of the Minho University, in Guimaraes (Portugal), during an international Ph.D. research period, in a cooperation with Prof. Jorge Branco: 4 specimens FS-HDJ-FC (2 monotonic and 2 cyclic tests) and 4 specimens FS-HDJ-DC (2 monotonic and 2 cyclic tests) are made.

The objective of each test was to evaluate the overall ductility and energy dissipated by the joint, as well as to verify that expected strength and deformation levels could be reached without excessive strength degradation in the link or brittle failure of the timber beam or glued bars connections when designed according to existing timber design standards and approvals, as well as the accuracy of the design criteria and numerical models.

In this work, only 5 specimens results of 8 tested are presented: 1 specimen for the preliminary test to understand the global and local behaviour of the joint under monotonic loading; 1 monotonic and 1 cyclic test, for each joint typology, are discussed and the results are compared with the analytical and numerical design.

5.2 Preliminary design

5.2.1 General features

For both the joint typologies, the length of the bars and the timber beam cross section are the same geometrical features presented in the chapter 4.4.2. but the length of the beam is different. In particular, to carry out the tests, the beam must have a maximum length of 850 mm, derived from the laboratory test machine dimensions limit.

The geometry of the timber beam is presented in the Figure V.1 and the bending resistant moment of the timber beam is:

$$M_{Rd,T} = \frac{f_{m,k} \cdot k_{mod}}{\gamma_m} W = 50{,}46 \text{ kNm}$$

where:

$f_{m,k}$= bending strength, that for GL24h = 24 N/mm^2

k_{mod}= is a partial factor for taking into account the effects on the material of duration of load and moisture content = 1,10

γ_m = partial factor for material for glulam timber = 1,25

W = strength module = 2,38E+06 mm^3

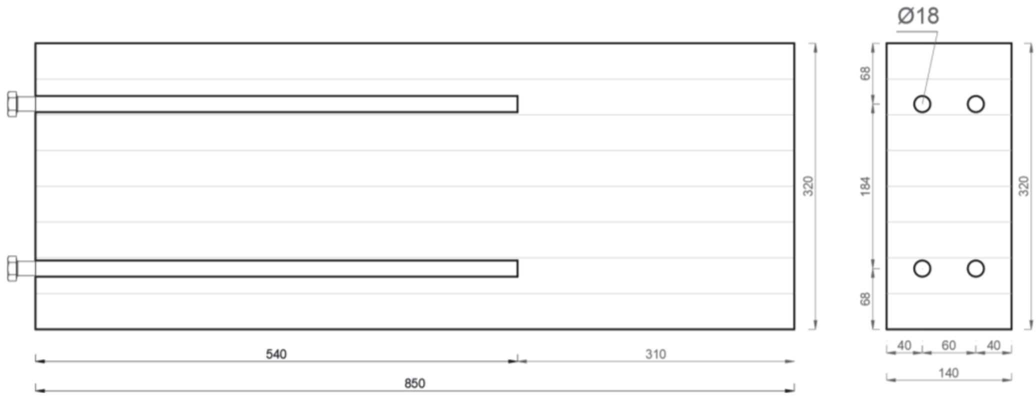

Figure V.141 – Timber beam: geometrical features [mm].

Starting from the common timber beam dimensions, below the 2 types of joint are designed: FS-HDJ-FC and FS-HDJ-DC.

5.2.2 FS - HDJ WITH FRAGILE CONNECTION (FC)

The capacity design approach is applied designing the steel link with an "under-resistance" compared to the timber beam (macro-component).

The selected steel profile is HE100A, with a plastic strength module:

$$W_{el,L} = 72{,}76\ mm^3$$

$$W_{pl,L} = 83{,}01\ mm^3$$

The bending resistant moment of the link is:

$$M_{Rd,el,L} = W_{el,L} \cdot \frac{f_{yk}}{\gamma_{m0}} = 25{,}83\ kNm$$
$$M_{Rd,pl,L} = W_{pl,L} \cdot \frac{f_{yk}}{\gamma_{m0}} = 29{,}47\ kNm$$

where:

γ_{m0}= 1,05;

f_{yk} = 355 MPa (S355)

The *Ω* coefficient is:

$$\Omega_{el} = \frac{M_{Rd,T}}{M_{Rd,el,L,max} \cdot \gamma_{rd} \cdot 1{,}1} = 1{,}48$$
$$\Omega_{pl} = \frac{M_{Rd,T}}{M_{Rd,pl,L,max} \cdot \gamma_{rd} \cdot 1{,}1} = 1{,}30$$

Below, the capacity design approach is applied for connections "sub-components".

The distribution of the internal actions, in the examined joint, is represented in Figure V.2 and the design moment resistance, $M_{j,Rd}$, can be determined according to:

$$M_{j,Rd} = F_{Rd} \cdot z$$

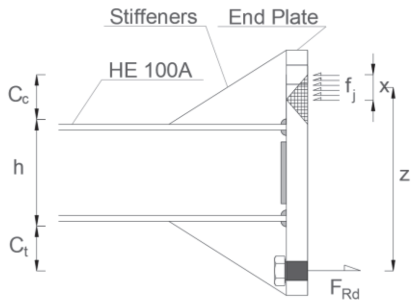

Figure V.142 – Model for the resistant moment evaluation.

where z is the lever arm of the internal couple and F_{Rd} is the resistance of the weakest component of the joint, that is the smallest value among:

- the resistance of the glued-in steel bars $F_{ax,Rd}$
- the resistance of the equivalent T-stub in tension $F_{t,T\text{-}stub,Rd}$;
- the resistance of the equivalent T-stub in compression $F_{c,T\text{-}stub,Rd}$;
- the resistance of the steel section flange in compression $F_{sf,Rd}$;
- the resistance of the stiffener $F_{t,s,Rd}$.

<u>Equivalent T-stub in tension</u>

For the T-stub in tension, the modelling according to EN 1993-1-8 is shown in the Figure V.3 and the possible failure modes are (CEN, 2005; ECCS, 1999):

- Mode 1: complete yielding of the flange;
- Mode 2a: failure of the bars after yielding of the flange in presence of prying forces;
- Mode 2b: yield of the flange without prying forces;
- Mode 3: bar failure.

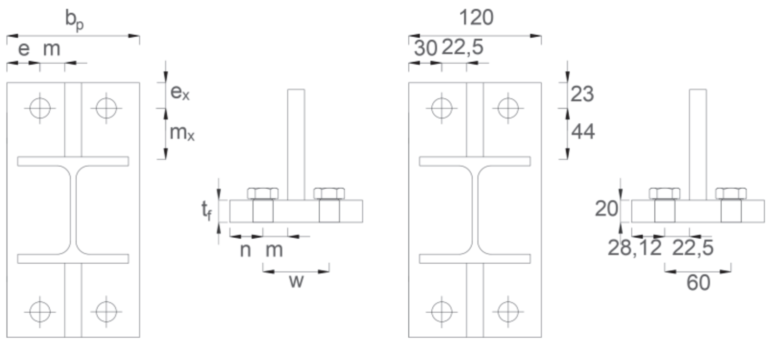

Figure V.143 – Modelling of a flange using the equivalent T-stub element in tension according to EN 1993-1-8.

To check the presence of prying forces it is necessary to evaluate the length of the lengthening bolt (effective length), L_b, and the limit length, L_b^*.

If $L_b < L_b^*$, then there is development of prying force;
If $L_b \geq L_b^*$, then there is no development of prying force.

To evaluate L_b the following parameters are defined (Volkersen, 1938):

$$\alpha = \frac{1}{(1+\psi)\omega \cdot \varphi} = 0{,}862$$

with:

$$\psi = \frac{E_s \cdot A_s}{E_{0,d} \cdot A_w} = 0{,}421$$

$$\Gamma = \frac{G_{0,d} \cdot \pi \cdot \varphi}{E_s \cdot A_s \cdot t_{glue}} = 0{,}0018$$

$$\omega^2 = \Gamma\ (1 + \Psi) = 0{,}051$$

where:
$E_{0,d}$: Elastic modulus of wood parallel to the direction of the fibers = 11600 MPa;
A_w: $36\varphi^2 = 6748$ mm^2;
$G_{0,d}$: Shear modulus of wood parallel to the direction of the fibers = 2400 MPa;
t_{glue}: Glue thickness = 2 mm;
φ: Diameter of the bol t= 16 mm;
S_r: Thickness of the washer = 2 mm;
t_p: Thickness of the end-plate = 20 mm;
S_d: Thickness of the nut = 8 mm.

$$L_b = \alpha \cdot \varphi + t_f + S_r + S_D = 43{,}8 \text{ mm}$$

and L_b^* is evaluated as:

$$L_b^* = \frac{8{,}8 \cdot m_x^3\ A_{res} \cdot n_{fb}}{\Sigma l_{eff} \cdot t_f^3} = 20{,}87 \text{ mm}$$

where:
n_{fb}: number of bolt-rows = 1;
A_{res}: resistance area of the bolt = 157 mm^2;
t_f: Thickness of the enad-plate = 20 mm;

l_{eff}: Effective length of the equivalent T-stub element, function of the position, number and model of bolt in tension:

$$l_{eff}= l_{eff,2}= \min [\alpha m – (2m + 0{,}625e) + e_x; 2m + 0{,}625e + e_x; 4m + 1{,}25e]= 94{,}25 \text{ mm}$$

$L_b \geq L_b^*$, then there is no development of prying force, and failure mode (Fig. V.4), $F_{t,T\text{-}stub,Rd}$, is evaluated as:

$$F_{t,T\text{-}stub,Rd}= \min (F_{t,T\text{-}stub,Rd,1\text{-}2}; F_{t,T\text{-}stub,Rd,3}) = 219{,}42\text{kN}$$

where:

$F_{t,T\text{-}stub,Rd,1\text{-}2}$: Mode 1-2

$F_{t,T\text{-}stub,Rd,3}$: Mode 3

$$F_{t,T-stub,Rd,1-2} = \frac{2 \cdot M_{pl,1,Rd}}{m+n} = 219{,}42\text{kN}$$

$$F_{t,T-stub,Rd,3} = \Sigma F_{T,Rd} = 282{,}6\text{kN}$$

where:

$$M_{pl,1,Rd} = 0{,}25 \cdot \Sigma l_{eff,1} \cdot t^2{}_f \cdot \frac{f_y}{\Upsilon_{m0}} = 2{,}46\text{kNm}$$

$l_{eff,1}= \min [2\pi m; \pi m + 2e_x; \alpha m – (2m + 0{,}625e) + e_x; 2m + 0{,}625e + e_x; 4m + 1{,}25e]= 94{,}25$ mm

where:

n= min (e; 1,25m)= (30; 28,125)= 28,125 mm

e= 30 mm

e_x= 23 mm

m= 22,5 mm

m_x= 44 mm

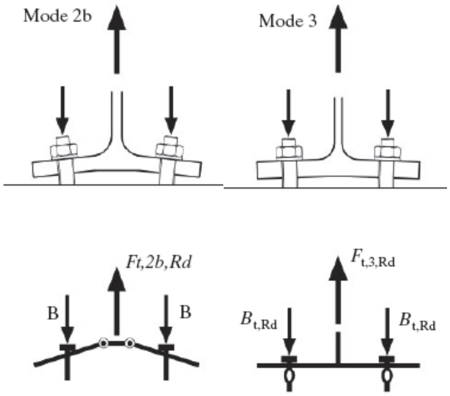

Figure V.144 – Failure modes and ultimate displacements in a T-stub in tension according to ECCS, 1999 and Beg et al, 2004. Mode 1-2: yield of the flange without prying forces; Mode 3: bars failure.

Equivalent T-stub in compression

The resistance of the basic component "timber and steel end-plate in bending" under compression, can be modelled through an equivalent T-stub in compression (Fig. V.5b), in accordance with recommendations in EN 1993-1-8 (CEN, 2005) for the case of steel column base joints modified taking into account the wood in compression and the location of compression centre for stiffened end-plate.

At first, the compression centre is shown in Figure V.5a.

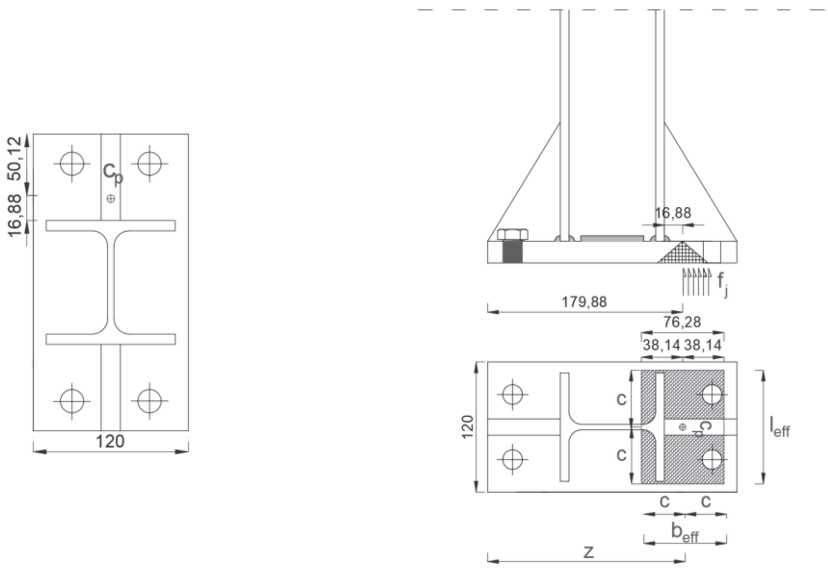

a) b)

Figure V.145 – a) Compression centre; b) Flange modelling as an equivalent T-stub element in compression according to EN 1993-1-8 [mm].

The resistance of the equivalent T-stub in compression ca be evaluated as:

$$F_{c,T\text{-}stub,Rd} = f_j \cdot b_{eff} \cdot l_{eff} = 219{,}71\text{kN}$$

where:
f_j: Compression resistance parallel to wood fibers, $f_{c,0,g,d}$= 24 MPa;
b_{eff}: Effective height of the T-Stub = 76,28 mm;
l_{eff}: Effective width of the T-Stub = 120 mm.

It is assumed that the compression stresses are uniformly distributed over a rectangular area b_{eff} l_{eff} (Fig. V.5b), with the width of the contact area *c*. This parameter is defined by referring to the bending verification of the cantilever part of the end-plate. In particular, it is evaluated by equating the bending resistant moment, M_{Rd}, per unit of length, with the bending soliciting moment, M_{Ed}, per unit of length.

$$M_{Rd} = \frac{1}{\gamma_{M0}} \frac{t_f^2 + f_y}{6} = \frac{f_j \cdot c^2}{2} = M_{ed}$$

and *c* is equal to:

$$c = t_f \sqrt{\frac{f_y}{3 \cdot f_j \cdot \gamma_{M0}}} = 38{,}14 \text{ mm}$$

Steel section flange in compression

The rib stiffener influences the shape of T-Stub mechanisms, which also depend on the number of bolt rows due to possible occurrence of group effect. The compression forces acting on beam web component can be more rationally obtained as follows:

$$F_{c,fb,Rd} = \frac{M_{j,Ed}}{z} = \frac{M_{c,Rd}}{d_b + \xi \cdot b - 0{,}5 t_{fb}} = 579{,}95 \text{ kN}$$

where ξ_b is the position of the compression centre as shown in Figure IV.40b, indicated in the chapter IV.

In particular:

$$M_{c,Rd} = \frac{w_{pl,z} \cdot f_{yk}}{\gamma_{M0}} = 60{,}97 \text{ kN}$$

where:
ξ_b= 16,88 mm;
d_b= 91 mm;
b= 67 mm;
$t_{f,b}$= 8 mm;

$W_{pl,z}$= 83010 mm^3;
f_{yk}= 355 MPa.

Design moment resistance
From balance to translation, it is possible to derive *x*:

$$x \cdot f_j \cdot l_{eff} = F_{Rd,min}$$

$$x = \frac{F_{Ed,min}}{f_j \cdot l_{eff}} = 0{,}047 \text{ mm}$$

The distance, *z*, can be evaluated as:

$$z = C_t + h + C_c - \frac{x}{2} = 190{,}01 \text{ mm}$$

The design moment resistance, $M_{j,Rd}$, can be evaluated as:

$$M_{j,Rd} = F_{Rd,\,min} \cdot z = 136{,}51 \cdot 0{,}19001 = 25{,}94 \text{ kNm}$$

where *z* is the lever arm of the internal couple and F_{Rd} is the resistance of the weakest component of the joint.

The analytical results of the model are shown in Table V.1.

- The resistance of the glued-in steel bars: $F_{ax,Rd}$
  Rod failure through yielding: $F_{ax,Rd,1}$ =211,31kN
  Failure of the adhesive by debonding from steel or wood: $F_{ax,Rd,2}$ = 136,51kN
  Failure of the timber adjacent to the glue-line: $F_{ax,Rd,3}$ = 207,57kN
- The resistance of the equivalent T-stub in tension $F_{t,T\text{-}stub,Rd,1\text{-}2}$ = 219,42kN
- The resistance of the equivalent T-stub in tension $F_{t,T\text{-}stub,Rd,3}$ = 282,6kN
- The resistance of the equivalent T-stub in compression $F_{c,T\text{-}stub,Rd}$ = 219,71kN
- The resistance of the steel section flange in compression $F_{sf,Rd}$ = 579,94kN
- The resistance of the stiffener $F_{t,s,Rd}$ = 183,07kN

Table V.85 – Summary of analytical results: HE100A joint [FS-HDJ-FC].

	Collapse hierarchy	Analytical evaluation			
		$F_{i,Rd}$ [kN]	**M_{rd} [kNm]**	**Over-strength$_{,ana}$ [%]**	**$\Omega_{,ana}$ [%]**
1)	**Link**	/	25,83	/	/
2)	**Pull-out**	136,51	25,94	1,00	0,76
3)	**Stiffners**	183,07	37,78	1,35	1,02
4)	**Timber tensile break**	207,57	39,44	1,53	1,16
5)	**End-plate/Bolts (mode 1-2)**	219,42	41,69	1,61	1,22
6)	**End-plate (flange compression)**	219,71	41,75	1,62	1,22
7)	**Timber beam bending**	/	50,46	1,95	1,48
8)	**Bolts (mode 3)**	282,6	53,69	2,08	1,57

From the analytical results observation, the timber-steel link joint designed (HE100A) is a *Full-strength connection* with a *High Ductility timber-steel link Joint (HDJ)* and *Fragile connection*, since the “Pull-out” and the “Tensile timber breaking”, that are fragile collapse modes, occur before the ductile collapse modes of the connection, i.e. “T-stub in tension” and “T-stub in compression”.

The timber-steel link joint (HE100A Link), in Figure IV.6, is made by a laminated timber beams (GL24h), with a 140x320 mm rectangular cross section and 850 mm long, equipped at one end with a steel link, HE100A profile 360 mm long (steel grade S355) with two welded end-plates (120x230 mm, steel grade S275), with 20 mm thickness and four stiffeners (110x70 mm and 20 mm thickness, steel grade S275). The link is connected at one side to the timber beam by means of 4 glued threaded bars (M16, 10.9, 540 mm long).

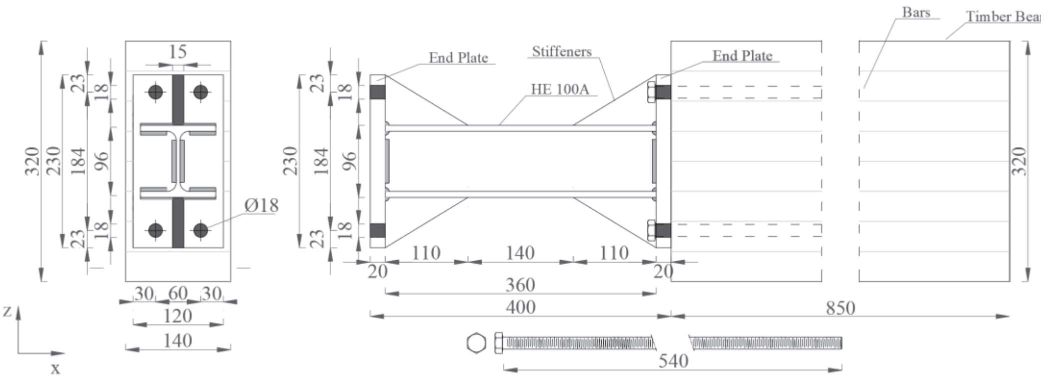

Figure V.146 – HE100A joint [FS-HDJ-FC]: geometrical features [mm].

5.2.3 FS - HDJ WITH DUCTILE CONNECTION (DC)

The capacity design approach is applied designing the steel link with an “under-resistance” compared to the timber beam (macro-component).

The selected steel profile is IPE100, with a plastic strength module:

$$W_{el,L} = 34{,}20 \text{ mm}^3$$

$$W_{pl,L} = 39,41 \text{ mm}^3$$

The bending resistant moment of the link is:

$$M_{Rd,el,L} = W_{el,L} \cdot \frac{f_{yk}}{\gamma_{m0}} = 12,14 \text{ kNm}$$
$$M_{Rd,pl,L} = W_{pl,L} \cdot \frac{f_{yk}}{\gamma_{m0}} = 13,99 \text{ kNm}$$

where:
γ_{m0}= 1,05;
f_{yk} = 355 MPa (S355)

The Ω coefficient is:

$$\Omega_{el} = \frac{M_{Rd,T}}{M_{Rd,el,L,max} \cdot \gamma_{rd} \cdot 1,1} = 3,15$$
$$\Omega_{pl} = \frac{M_{Rd,T}}{M_{Rd,pl,L,max} \cdot \gamma_{rd} \cdot 1,1} = 2,73$$

Below, the capacity design approach is applied for connections sub-components.

The distribution of the internal actions, in the examined joint, is represented in Figure IV.7 and the design moment resistance, $M_{j,Rd}$, can be determined according to:

$$M_{j,Rd} = F_{Rd} \cdot z$$

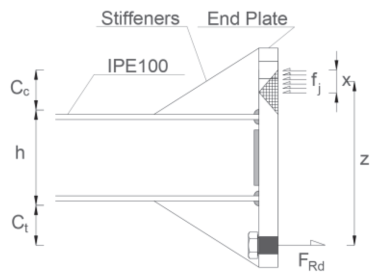

Figure V.147 – Model for the resistant moment evaluation.

where z is the lever arm of the internal couple and F_{Rd} is the resistance of the weakest component of the joint, that is the smallest value among:

- the resistance of the glued-in steel bars $F_{ax,Rd}$
- the resistance of the equivalent T-stub in tension $F_{t,T\text{-}stub,Rd}$;
- the resistance of the equivalent T-stub in compression $F_{c,T\text{-}stub,Rd}$;

- the resistance of the steel section flange in compression $F_{sf,Rd}$;
- the resistance of the stiffener $F_{t,s,Rd}$.

Equivalent T-stub in tension

For the T-stub in tension, the modelling according to EN 1993-1-8 is shown in the Figure IV.8 and the possible failure modes are (CEN, 2005; ECCS, 1999):

- Mode 1: complete yielding of the flange;
- Mode 2a: failure of the bars after yielding of the flange in presence of prying forces;
- Mode 2b: yield of the flange without prying forces;
- Mode 3: bar failure.

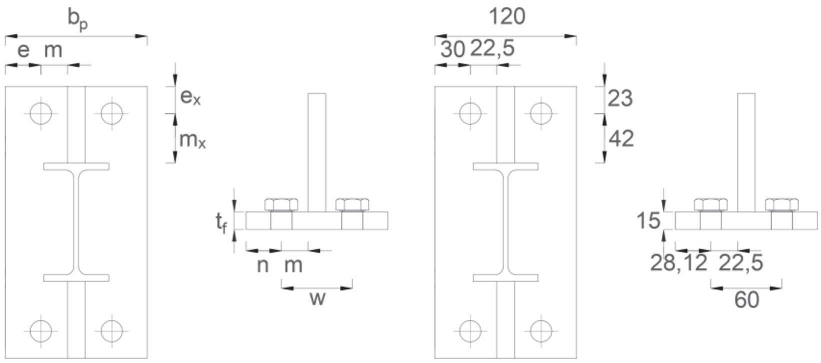

Figure V.148 – Modelling of a flange using the equivalent T-stub element in tension according to EN 1993-1-8.

To check the presence of prying forces it is necessary to evaluate the length of the lengthening bolt (effective length), L_b, and the limit length, L_b^*.

If $L_b < L_b^*$, then there is development of prying force;
If $L_b \geq L_b^*$, then there is no development of prying force.

To evaluate L_b the following parameters are defined (Volkersen, 1938):

$$\alpha = \frac{1}{(1+\psi)\omega \cdot \varphi} = 0{,}862$$

with:

$$\psi = \frac{E_s \cdot A_s}{E_{0,d} \cdot A_w} = 0{,}421$$

$$\Gamma = \frac{G_{0,d} \cdot \pi \cdot \varphi}{E_s \cdot A_s \cdot t_{glue}} = 0{,}0018$$

$$\omega^2 = \Gamma\,(1 + \Psi) = 0{,}051$$

where:
$E_{0,d}$: Elastic modulus of wood parallel to the direction of the fibers = 11600 MPa;
A_w: $36\varphi^2 = 6748\ mm^2$;
$G_{0,d}$: Shear modulus of wood parallel to the direction of the fibers = 2400 MPa;
t_{glue}: Glue thickness = 2 mm;
φ: Diameter of the bolt = 16 mm;
S_r: Thickness of the washer = 2 mm;
t_p: Thickness of the end-plate = 15 mm;
S_d: Thickness of the nut = 8 mm.

$$L_b = \alpha \cdot \varphi + t_f + S_r + S_D = 38{,}79\ mm$$

and L_b^* is evaluated as:

$$L_b^* = \frac{8{,}8 \cdot m_x^3\ A_{res} \cdot n_{fb}}{\Sigma l_{eff} \cdot t_f^3} = 49{,}47\ mm$$

where:
n_{fb}: number of bolt-rows = 1;
A_{res}: resistance area of the bolt = 157 mm^2;
t_f: Thickness of the enad-plate = 15 mm;
l_{eff}: Effective length of the equivalent T-stub element, function of the position, number and model of bolt in tension:

$$l_{eff} = l_{eff,2} = \min\,[\alpha m - (2m + 0{,}625e) + e_x;\ 2m + 0{,}625e + e_x;\ 4m + 1{,}25e] = 94{,}25\ mm$$

$L_b < L_b^*$, then there is the development of prying force, and failure mode (Fig. IV.9), $F_{t,T\text{-}stub,Rd}$, is evaluated as:

$$F_{t,T\text{-}stub,Rd} = \min\,(F_{t,T\text{-}stub,Rd,1};\ F_{t,T\text{-}stub,Rd,2};\ F_{t,T\text{-}stub,Rd,3}) = 132{,}24\ kN$$

where:
$F_{t,T\text{-}stub,Rd,1}$: Mode 1
$F_{t,T\text{-}stub,Rd,2}$: Mode 2
$F_{t,T\text{-}stub,Rd,3}$: Mode 3

$$F_{t,T-stub,Rd,1} = \frac{4 \cdot M_{pl,1,Rd}}{m} = 132{,}24\ \text{kN}$$
$$F_{t,T-stub,Rd,2} = \frac{2M_{pl,1,Rd} + n\Sigma F_{t,Rd}}{m+n} = 176{,}09\ \text{kN}$$
$$F_{t,T-stub,Rd,3} = \Sigma F_{T,Rd} = 226{,}08\ \text{kN}$$

where:

$$M_{pl,1,Rd} = 0{,}25 \cdot \Sigma l_{eff,1} \cdot t^2{}_f \ \frac{f_y}{\Upsilon_{m0}} = 1{,}27\ \text{kNm}$$

$l_{eff,1}$= min [2πm; πm + 2e_x; αm – (2m + 0,625e) + e_x; 2m + 0,625e + e_x; 4m + 1,25e]= 86,75 mm

where:
n= min (e; 1,25m)= (30; 28,125)= 28,125 mm
e= 30 mm
e_x= 23 mm
m= 22,5 mm
m_x= 42 mm

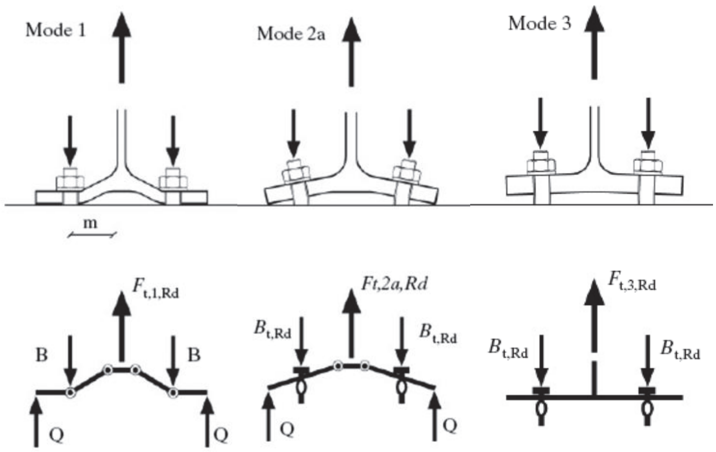

Figure V.149 – Failure modes and ultimate displacements in a T-stub in tension according to ECCS, 1999 and Beg et al, 2004. Mode 1: complete yielding of the flange; Mode 2a: bar failure and yielding of the flange in presence of prying forces; Mode 3: bars failure.

Equivalent T-stub in compression

The resistance of the basic component "timber and steel end-plate in bending" under compression, can be modelled through an equivalent T-stub in compression (Fig. IV.10b), in accordance with recommendations in EN 1993-1-8 (CEN, 2005) for the case of steel column base joints modified taking into account the wood in compression and the location of compression centre for stiffened end-plate.

At first, the compression centre is shown in Figure IV.10a.

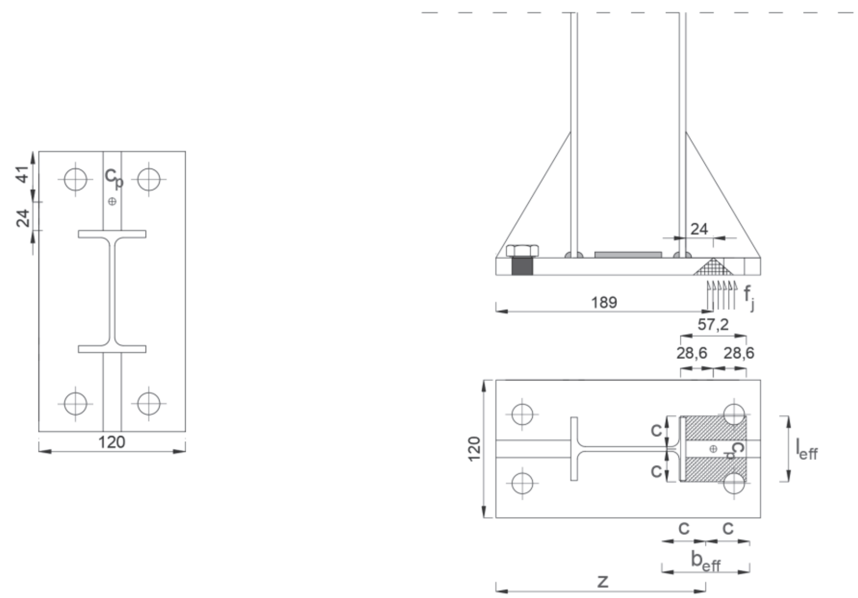

a) b)
Figure V.150 – a) Compression centre; b) Flange modelling as an equivalent T-stub element in compression according to EN 1993-1-8 [mm].

The resistance of the equivalent T-stub in compression ca be evaluated as:

$$F_{c,T\text{-}stub,Rd} = f_j \cdot b_{eff} \cdot l_{eff} = 164{,}78 \text{ kN}$$

where:

f_j: Compression resistance parallel to wood fibers, $f_{c,0,g,d}$= 24 MPa;
b_{eff}: Effective height of the T-Stub = 57,21 mm;
l_{eff}: Effective width of the T-Stub = 120 mm.

It is assumed that the compression stresses are uniformly distributed over a rectangular area b_{eff} l_{eff} (Fig. IV.10b), with the width of the contact area *c*. This parameter is defined by referring to the bending verification of the cantilever part of the end-plate. In particular, it is evaluated by equating the bending resistant moment, M_{Rd}, per unit of length, with the bending soliciting moment, M_{Ed}, per unit of length.

$$M_{Rd} = \frac{1}{\gamma_{M0}} \frac{t_f^2 + f_y}{6} = \frac{f_j \cdot c^2}{2} = M_{ed}$$

and *c* is equal to:

$$c = t_f \sqrt{\frac{f_y}{3 \cdot f_j \cdot \gamma_{M0}}} = 28{,}60 \text{ mm}$$

<u>Steel section flange in compression</u>

The rib stiffener influences the shape of T-Stub mechanisms, which also depend on the number of bolt rows due to possible occurrence of group effect. The compression forces acting on beam web component can be more rationally obtained as follows:

$$F_{c,fb,Rd} = \frac{M_{j,Ed}}{z} = \frac{M_{c,Rd}}{d_b + \xi \cdot b - 0{,}5 t_{fb}} = 511{,}45 \text{ kN}$$

where ξ_b is the position of the compression centre as shown in Figure IV.40b, indicated in the chapter IV.

In particular:

$$M_{c,Rd} = \frac{w_{pl,z} \cdot f_{yk}}{\gamma_{M0}} = 61{,}96 \text{ kN}$$

where:
ξ_b= 24 mm;
d_b= 100 mm;
b= 65 mm;
$t_{f,b}$= 5,7 mm;
$W_{pl,z}$= 39410 mm^3;
f_{yk}= 355 MPa.

<u>Design moment resistance</u>

From balance to translation, it is possible to derive *x*:

$$x \cdot f_j \cdot l_{eff} = F_{Rd,min}$$

$$x = \frac{F_{Ed,min}}{f_j \cdot l_{eff}} = 0{,}047 \text{ mm}$$

The distance, *z*, can be evaluated as:

$$z = C_t + h + C_c - \frac{x}{2} = 194{,}58 \text{ mm}$$

The design moment resistance, $M_{j,Rd}$, can be evaluated as:

$$M_{j,Rd} = F_{Rd,\,min} \cdot z = 132{,}23 \cdot 0{,}19458 = 25{,}73 \text{ kNm}$$

where z is the lever arm of the internal couple and F_{Rd} is the resistance of the weakest component of the joint.

The analytical results of the model are shown in Table V.2.

- The resistance of the glued-in steel bars: $F_{ax,Rd}$
  Rod failure through yielding: $F_{ax,Rd,1}$ =211,31 kN
  Failure of the adhesive by debonding from steel or wood: $F_{ax,Rd,2}$ = 136,51 kN
  Failure of the timber adjacent to the glue-line: $F_{ax,Rd,3}$ = 207,57 kN
- The resistance of the equivalent T-stub in tension $F_{t,T\text{-}stub,Rd,1}$ = 132,23 kN
- The resistance of the equivalent T-stub in tension $F_{t,T\text{-}stub,Rd,2}$ = 176,09 kN
- The resistance of the equivalent T-stub in tension $F_{t,T\text{-}stub,Rd,3}$ = 226,08 kN
- The resistance of the equivalent T-stub in compression $F_{c,T\text{-}stub,Rd}$ = 164,78 kN
- The resistance of the steel section flange in compression $F_{sf,Rd}$ = 511,45 kN
- The resistance of the stiffener $F_{t,s,Rd}$ = 89,12 kN

Table V.86 – Summary of analytical results: IPE100 joint [FS-HDJ-DC].

	Collapse hierarchy	Analytical evaluation			
		$F_{i,Rd}$ [kN]	**M_{rd} [kNm]**	**Over-strength$_{,ana}$ [%]**	**$\Omega_{,ana}$ [%]**
1)	**Link**	/	12,14	/	/
2)	**Stiffners**	89,12	17,34	1,43	1,08
3)	**End-plate yielding (mode 1)**	132,23	25,73	2,12	1,61
4)	**Pull-out**	136,51	26,56	2,19	1,66
5)	**End-plate (flange compression)**	164,78	32,07	2,64	2,01
6)	**End-plate/Bolts (mode 2)**	176,09	34,26	2,82	2,14
7)	**Timber tensile break**	207,57	40,39	3,33	2,52
8)	**Bolts (mode 3)**	226,08	43,99	3,62	2,75
9)	**Timber beam bending**	/	50,46	4,16	3,15

From the analytical results observation, the timber-steel link joint designed (HE100A) is a *Full-strength connection* with a *High Ductility timber-steel link Joint (HDJ)* and *Ductile connection*, since the “Pull-out” and the “Tensile timber breaking”, that are fragile collapse modes, occur after the ductile collapse modes of the connection, i.e. “T-stub tensile – mode 1”.

The timber-steel link joint (IPE100 Link), in Figure IV.11, is made by a laminated timber beams (GL24h), with a 140x320 mm rectangular cross section and 850 mm long, equipped at one end with a steel link, IPE100A profile 360 mm long (steel grade S355) with two welded end-plates (120x230 mm, steel grade S275), with 15 mm thickness and four stiffeners (110x70 mm and 20 mm thickness, steel grade S275). The link is connected at one side to the timber beam by means of 4 glued threaded bars (M16, 10.9, 540 mm long).

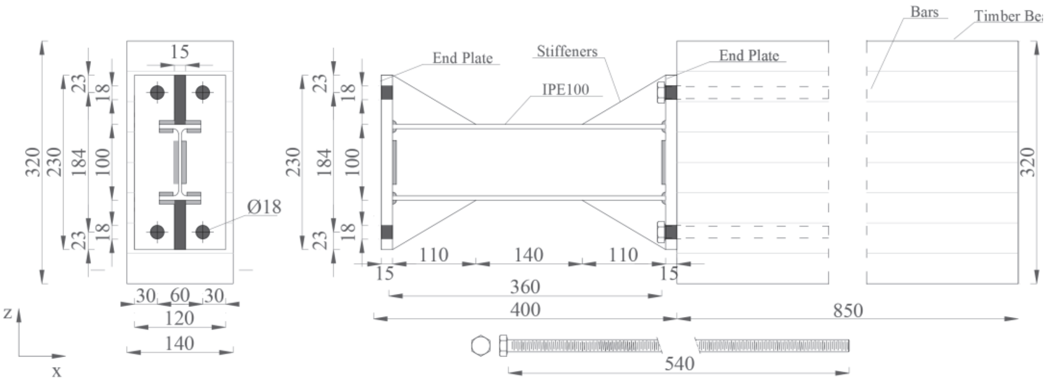

Figure V.151 – IPE100 joint [FS-HDJ-DC]: geometrical features [mm].

5.3 Preliminary numerical analysis

5.3.1 FS - HDJ with Fragile connection (FC)

The numerical analysis of the HE100A Link (FU-HDJ-FC) model is carried out with the same set-up of the monotonic analysis on the *P10* specimen, using the structural calculation program ABAQUS. Geometrical features and materials are illustrated in the following table (Tab. V.3).

Table V.87 – HE100A joint [FS-HDJ-FC]: structural features.

		Timber beam	Thread Bolt	End plate	Stiffeners	HE100A
Element		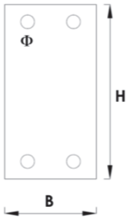		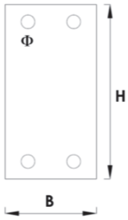	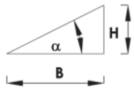	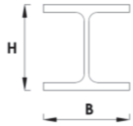
Geometry [mm]		θ= 18 H= 320 B= 140 L= 850	θ= 16 L= 540 Nut, Washer / Shank	θ= 18 H= 230 B=120 S= 20	H= 70 B=110 S= 15	L= 360 B= 100 H= 96
Material		**GL24h**	**10.9**	**S275**		**S355**
Density [N/mm³]		3,80x e-6	7,85 x e-5			
Elasticity [MPa]		E_{90}=390 E_0=11600	210000			
Plasticity [MPa]	σ_{el}	24	900	275		355
	σ_u	/	1000	430		510
	ε_{el}		0	0		0
	ε_u	/	0,178	0,376		0,261
Model		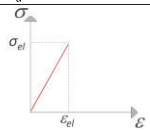		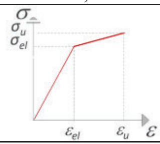		
Mesh		**Solid element**				
		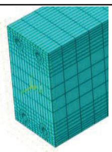	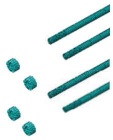		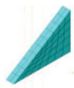	

The outputs are provided in terms of the maximum values of stresses (σ), DCR_{el} ($DCR_{el}=\sigma/\sigma_{el}$) and DCR_{ul} ($DCR_{ul}=\sigma/\sigma_{ul}$), for each component of the model (link, end-plate, threaded bolts, timber beam and stiffeners), the resistant bending moment (M), valuated in the "plastic hinge point" (PH), corresponding to the plastic hinge position in the link, and rotation (θ) in in x-z plane, valuated in the "load application point" (RP), the force (F) and the displacement (u) in z-direction, valuated in the “fixed point” (RF), corresponding to the fixed end-plate, for the global model. Outputs are detected at specific increments (In.) and times (t.), corresponding to the yielding of the steel link (P_Y), the complete plasticization of the link cross-section (P_P), the ultimate strength of the link (P_C), defined by the collapse of the model and the end of the numerical analysis, and the displacement value equal to 200 mm (P_{200}), corresponding to the maximum value of the vertical displacement reached by the transducer of the laboratory machine. Moreover, the F-u and the M-θ curves are shown. A special attention is also given to the collapse mode and hierarchy, in terms of the global behaviour and of the single component behaviour, to evaluate the accuracy of the numerical model respect to the analytical one, and the over-strength, *OS*, of each component respect to the yielding one (OS_{el}= $DCR_{el\text{-}link}/DCR_{el\text{-}component}$; OS_{ul}= $DCR_{ul\text{-}link}/DCR_{ul\text{-}component}$).

In the Figure V.12a,b presents the numerical F-u and the M-θ curves.

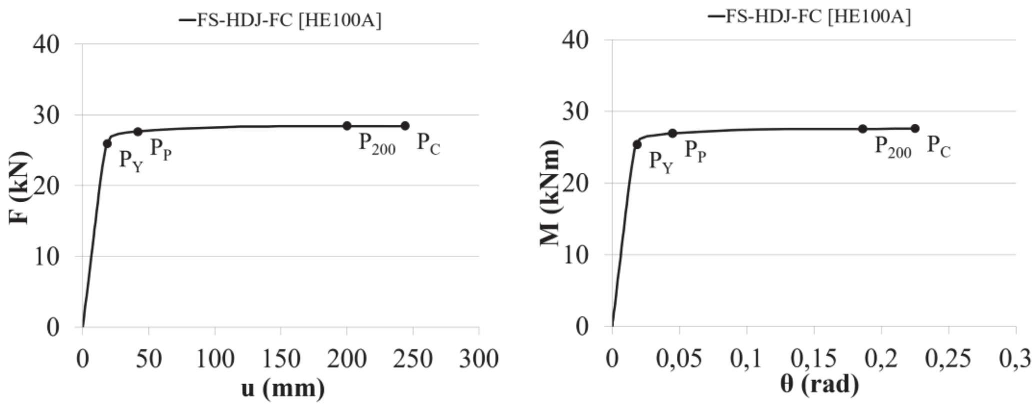

a) b)

Figure V.152 – HE100A joint [FS-HDJ-FC]: numerical (a) F-u and (b) M-θ curves.

In Table V.4 and Tab. V.5 are depicted the stress values (σ), the DCR_{el} and the DCR_{ul}, for each connection component, in the P_Y, P_P, P_{200} and P_C instants. Moreover, the first element that reaches the elastic strength (σ_{el}) and the ultimate strength (σ_u) is gree-highlighted.

Table V.88 – HE100A joint [FS-HDJ-FC]: yield (P_Y), plastic (P_P), 200mm (P_{200}) and collapse (P_C) stress value σ, bending moment *M*, rotation *θ*, force *F* and vertical displacement *u*.

Point	σ [MPa]					M	θ	F	u
	HE100A	End Plate	Thread Bolt	Timber beam	Stiffeners	[kNm]	[rad]	[kN]	[mm]
P_Y	355	192	401	11	251	24,73	0,016	25,5	17,42
P_P	364	223	482	11,1	277	26,85	0,041	27,68	44,58
P_{200}	424	248	528	11,5	294	27,52	0,187	28,40	200
P_C	438	260	537	11,9	299	28,41	0,215	29,35	242

Stress distribution

(P_Y) [In. 40; t. 1,74]

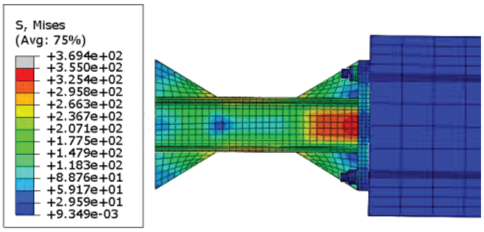

(P_P) [In. 46; t. 4,45]

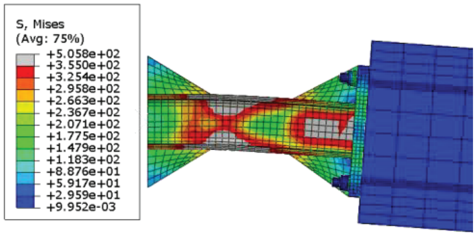

(P_{200}) [In. 56; t. 20,36]

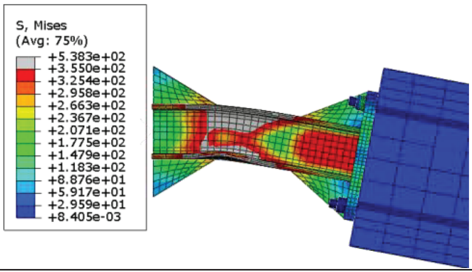

(P_C) [In. 62; t. 25,92]

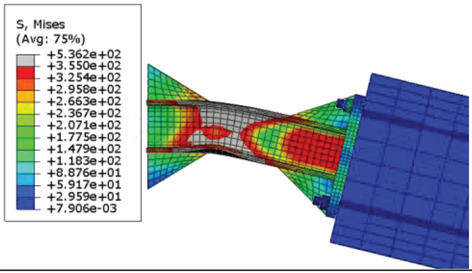

Table V.89 – HE100A joint [FS-HDJ-FC]: yield (P_Y), plastic (P_P), 200mm (P_{200}) and collapse (P_C) stress σ, DCR_{el} (σ/σ_{el}) and DCR_{ul} (σ/σ_u).

	Link			End Plate			Thread Bolt			Timber beam		Stiffeners		
	σ	DCR		σ	DCR		σ	DCR		σ	DCR	σ	DCR	
	MPa	el	ul	MPa	el	ul	MPa	el	ul	MPa	el	MPa	el	ul
P_Y	355	100%	70%	192	79%	45%	401	45%	40%	11	46%	251	91%	58%
P_P	364	103%	71%	223	81%	52%	482	54%	48%	11,1	46%	277	101%	64%
P_{200}	424	119%	83%	248	90%	58%	528	59%	53%	11,5	48%	294	107%	68%
P_C	438	123%	96%	260	95%	60%	537	60%	54%	11,9	50%	299	109%	70%

Analysing the numerical results, the following observations can be drawn. At the instant P_Y, the first element to reach the yield is the link, with a DCR_{ul}= 70%. The second joint component most stressed is the stiffener, with a DCR_{el}= 91% and DCR_{ul}= 58%; the end-plate is the third joint component with a DCR_{el}= 70% respect to the yielding link and a DCR_{ul}= 45%; the bolts have a DCR_{el}= 45% and DCR_{ul}= 40% at the last, the timber beam with a DCR_{el}= 46%.

At the instant P_P, there is the complete hinge plasticization of the link with a DCR_{el}= 103% and a DCR_{ul}= 71%, and the stiffeners reach the yield, with a DCR_{el}= 101% and DCR_{ul}= 64%, while the end-plate (DCR_{el}= 81% and a DCR_{ul}= 52%) and the bolts (DCR_{el}= 54% and a DCR_{ul}= 48%) are in the elastic field and the timber beam presents a DCR_{el}= 46%.

At the instant P_{200}, corresponding to the maximum value of the vertical displacement reached by the transducer, the link presents a DCR_{el}= 119% and a DCR_{ul}= 83%, the stiffeners have a DCR_{el}= 107% and a DCR_{ul}= 68%, while the end-plate (DCR_{el}= 90% and a DCR_{ul}= 58%) and the bolts (DCR_{el}= 59% and a DCR_{ul}= 53%) are in the elastic field and the timber beam has a DCR_{el}= 48%.

At the instant P_C, corresponding to the collapse of the joint with the link's failure (DCR_{el}= 123% and a DCR_{ul}= 86%), the stiffeners have a DCR_{el}= 109% and a DCR_{ul}= 70%) while the end-plate (DCR_{el}= 95% and a DCR_{ul}= 60%) and the bolts (DCR_{el}= 60% and a DCR_{ul}= 54%) are in the elastic field, and the timber beam presents a DCR_{el}= 50%) (Fig. V.13 and Fig. V.14). In particular, the joint has reached the collapse due to the buckling of the link web.

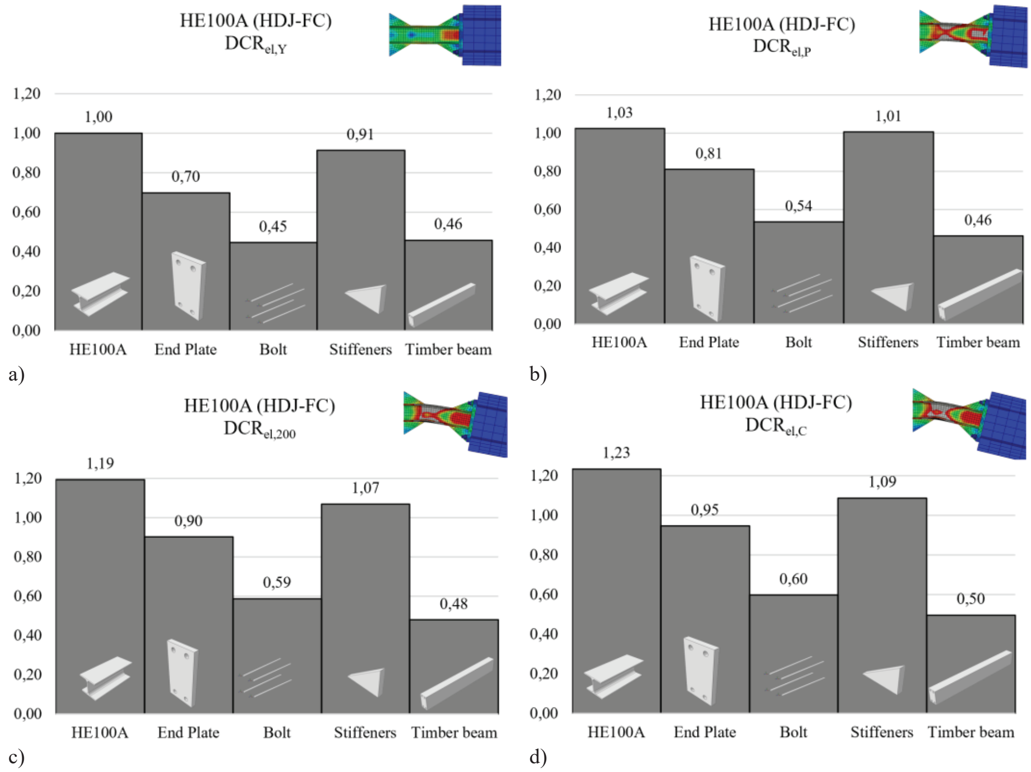

Figure V.153 – HE100A joint [FS-HDJ-FC]: DCR_{el} in a) yield (P_Y), b) plastic (P_P), c) 200mm (P_{200}) and d) collapse (P_C) points.

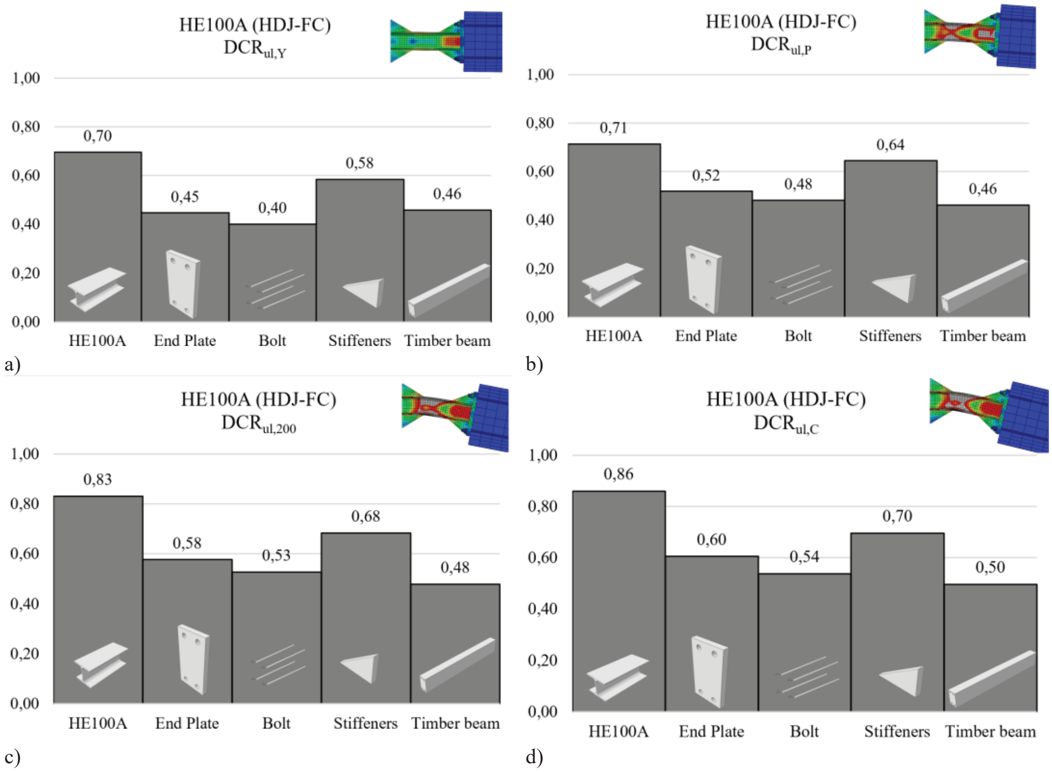

Figure V.154 – HE100A joint [FS-HDJ-FC]: DCR$_{ul}$ in a) yield (P_Y), b) plastic (P_P), c) 200mm (P_{200}) and d) collapse (P_C) points.

At the end of P_Y, coinciding with the yielding of the link, the stiffeners (OS_{el}= 1,10), the end-plate (OS_{el}= 1,43), the bolts (OS_{el}= 2,24) and the timber beam (OS_{el}= 2,18) are over-resistant respect to the steel link, and the overstrength coefficient, OS_{el}, is indicated in the Table V.6 and Figure V.15a.

The $\Omega_{,el}$ coefficient, at the instant P_Y, is presented in the Table V.6 and in the Figure V.15b. In particular, the stiffeners have a $\Omega_{,el}$= 0,83, the end-plate a $\Omega_{,el}$= 1,09, the bolts a $\Omega_{,el}$= 1,70 and the timber beam a $\Omega_{,el}$= 1,65.

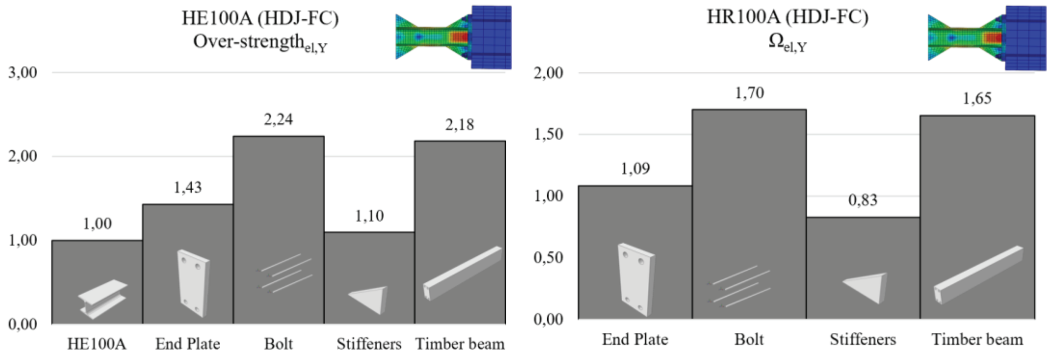

a) b)

Figure V.155 – HE100A joint [FS-HDJ-FC]: a) over-strength (OS_{el}) and b) Ω-coefficient valuated in P_Y.

The collapse hierarchy of the elements connection, therefore, is: 1) Link; 2) Stiffeners; 3) End-plate; 4) Timber beam; 5) Bolts.

In particular, the numerical analysis has confirmed the analytical design criteria and the type of joint is a *Full-strength connection (FS)* with a *High Ductility timber-steel link Joint (HDJ)* and *Fragile connection (FC)*, since the “Pull-out” and the “Tensile timber breaking”, that are fragile collapse modes, occur before the ductile collapse modes of the connection, i.e. “T-stub in tension (mode 1-2)” and “T-stub in compression”. (Tab. V.6).

Table V.90 – HE100A joint [FS-HDJ-FC]: analytical evaluation vs numerical analysis.

	Collapse hierarchy	Analytical evaluation		Numerical evaluation	
		$OS_{el,ana}$	$\Omega_{,ana}$	$OS_{el,num}$	$\Omega_{,num}$
1)	Link	/	/	/	/
2)	Pull-out	1,00	0,76	/	/
3)	Stiffners	1,35	1,02	1,10	0,83
4)	Timber tensile break	1,53	1,16	/	/
5)	End-plate/Bolts (mode 1-2)	1,61	1,22	1,43	1,09
6)	End-plate (flange compression)	1,62	1,22		
7)	Timber beam bending	1,95	1,48	2,18	1,65
8)	Bolts (mode 3)	2,08	1,57	2,24	1,70

For completeness of results, with regards to the state of stress, examining the P_Y instant, the link reaches the yielding stress (355 MPa) while the end-plate (192 MPa), the bolts (401 MPa), the beam (11 MPa) and the stiffeners (251 MPa) are still in the elastic field; at the P_P instant, the cross-section of the link reaches the complete yielding, with a maximum value equal to 364 MPa and the stiffeners (277 MPa) reaches the yielding stress, while the end-plate (223 MPa), the bolts (482 MPa) and the beam 11,1 MPa) are in the elastic field; at the P_C instant, corresponding to the collapse of the joint with the buckling of the link flange, the link reaches a stress of 438 MPa, the stiffeners presents a maximum stress of 299 MPa, while the end-plate (260 MPa), the bolts (537 MPa) and the beam (11,9 MPa) are still in elastic field (Tab. V.4).

Figure V.16 shows the deformed configuration, respect to the unformulated configuration, in the 4 points: yielding, complete plasticization of the plastic hinge, displacement of 200 mm and collapse. The achievement of a displacement of 242 mm to the collapse manifests a high ductility of the system.

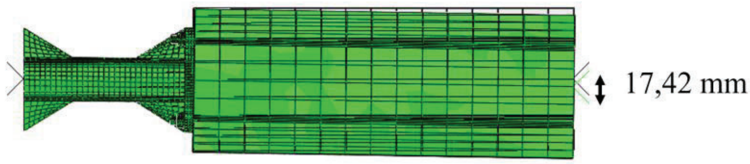

a)

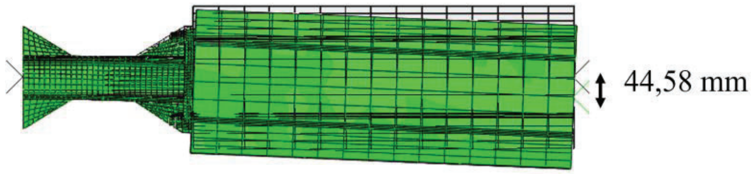

b)

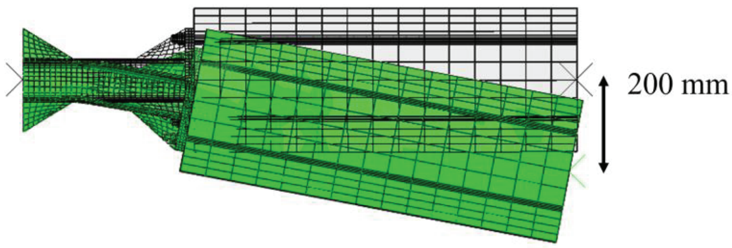

c)

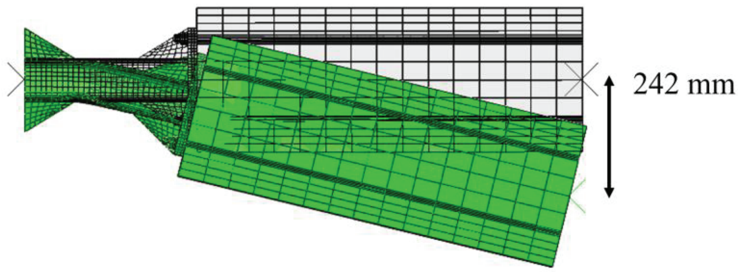

d)

Figure V.156 – HE100A joint [FS-HDJ-FC]: vertical deformed configuration in a) yield (P_Y), b) plastic (P_P), c) 200mm (P_{200}) and d) collapse (P_C) points.

Figure V.17 shows the AC YIELD diagram, which shows the evolution of the link yield and the extension of the plastic hinge through the normal stress distribution (σ). In particular, at the P_Y point, the first fiber of the link that catches the yield is in correspondence of the stiffener (Fig. V.17a,b), while the other elements of the connection (end-plate, bolts and stiffeners) and the timber beam are in the elastic field. At the P_P point (Fig. V.17c,d), when the yield has reached the full height of the cross section of the link (Hp= 96 mm), the yield extension is equal to the distance between the stiffeners (Lp= 140 mm). In the Figure V.17e,f is indicated the yielding condition and the stress distribution in P_{200} point while in Figure V.17g,h the buckling phenomena in the link web is perfectly clear.

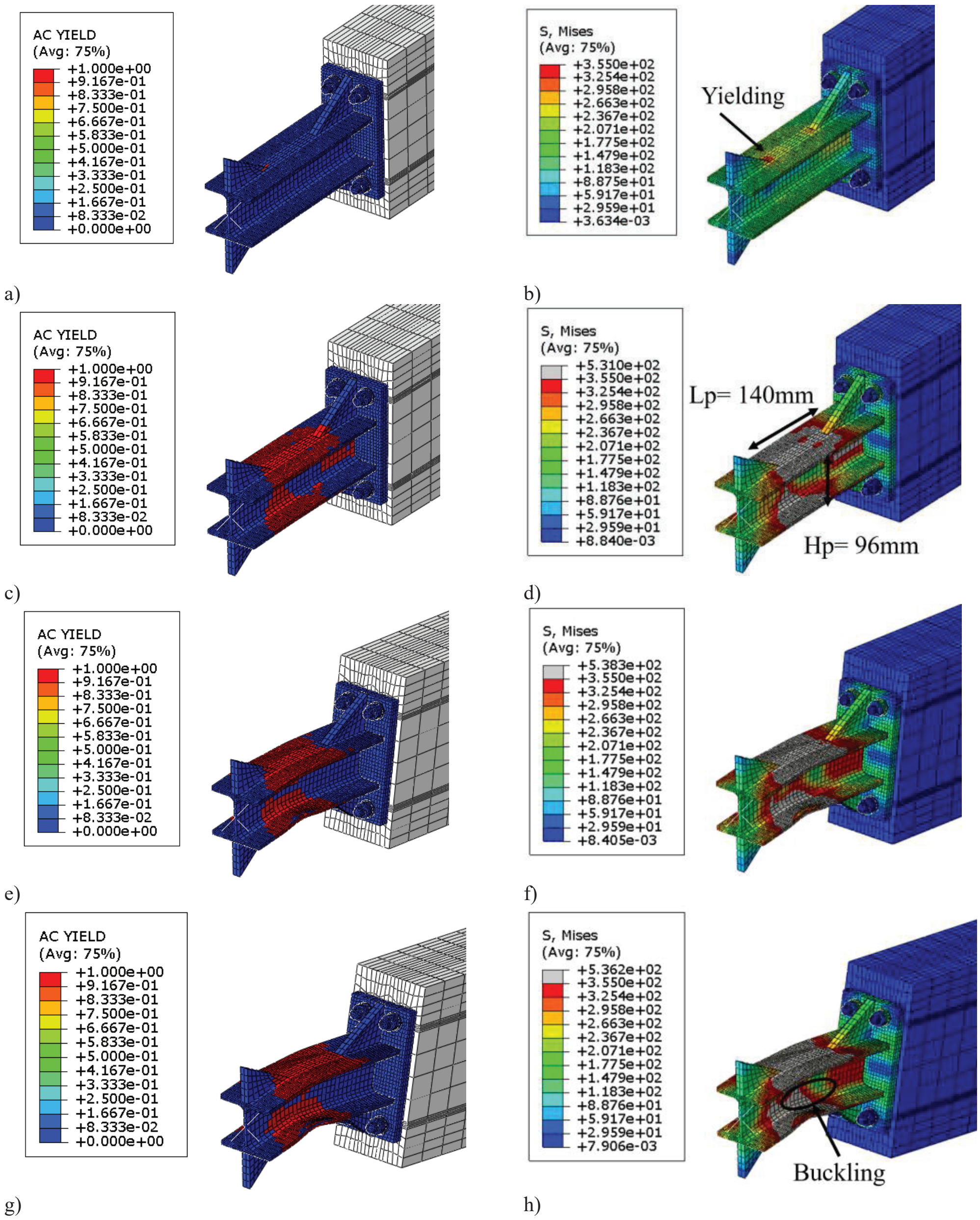

Figure V.157 – HE100A joint [FS-HDJ-FC]: yielding and stress distribution of the elements in in a) yield (P_Y), b) plastic (P_P), c) 200mm (P_{200}) and d) collapse (P_C) points. *Hp*: height of the plastic hinge; *Lp*: length of the plastic hinge.

At the P_P point, the following observations can be drawn. The capacity design procedure allowed the complete development of the plastic hinge (Lp= 140 mm) without any fragile collapse mode or the connection sub-component plasticization (Fig. V.18). As can be seen in the Figure V.18b, the presence of the stiffener in compression has led to the variation of the position of the centre of pressure between the upper end of the end-plate and the upper wing of the link.

The timber beam shows a rather uniform stress distribution, except for the areas around the holes and in correspondence with the compressed part, with low stress values (Fig. V.18c). Observing the stress distribution in the glued-bars in the timber beam, it is possible to notice that after about 250 mm from the nut there is a reduction of the stress values of 200% (from 482 MPa to 23 MPa). This length is, however, necessary to ensure an over-strength respect to the bending resistance of the link (Fig. V.18d). The stiffeners show a very variable stress distribution with a maximum value of 277MPa at the tip (Fig. V.18e).

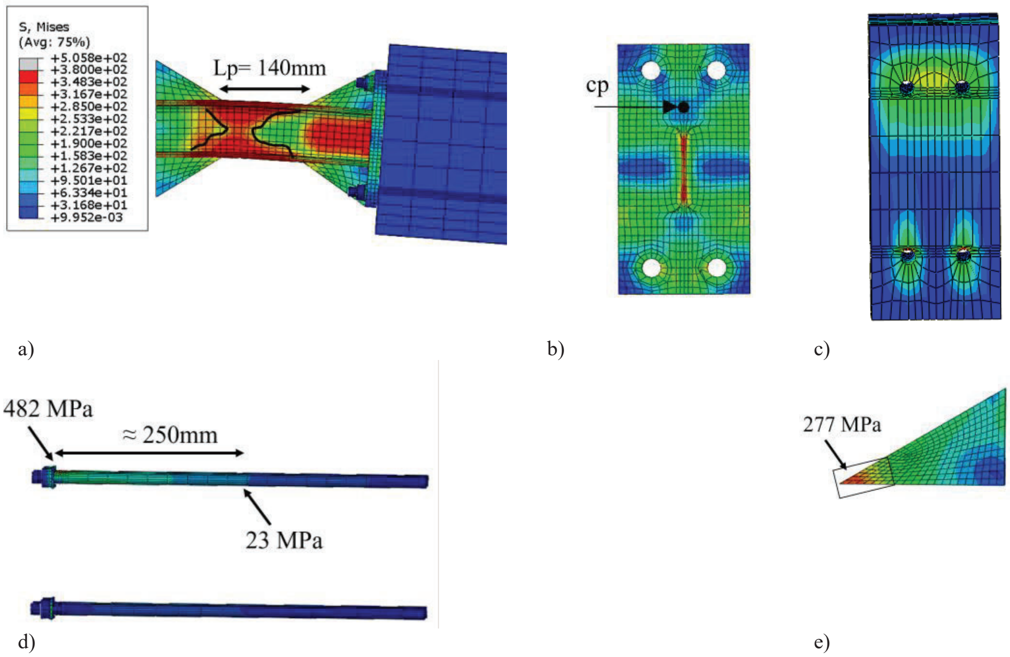

Figure V.158 – HE100A joint [FS-HDJ-FC]: stress distribution in a) link, b) end-plate, c) timber beam and d) bolts.

5.3.2 FS - HDJ WITH DUCTILE CONNECTION (DC)

The numerical analysis of the IPE100 Link (FU-HDJ-DC) model is carried out with the same set-up of the monotonic analysis on the *P10* specimen, using the structural calculation program ABAQUS. Geometrical features and materials are illustrated in the following table (Tab. V.7).

Table V.91 – IPE100 joint [FS-HDJ-DC]: structural features.

	Timber beam	**Thread Bolt**	**End plate**	**Stiffeners**	**IPE100**
Element	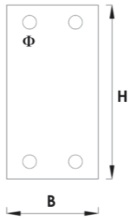		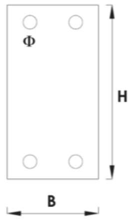	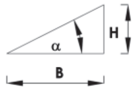	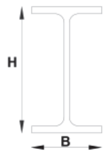
Geometry [mm]	θ= 18 H= 320 B= 140 L= 850	θ= 16 L= 540 Nut, Washer / Shank	θ= 18 H= 230 B=120 S= 15	H= 70 B=110 S= 15	L= 360 B= 55 H= 100
Material	**GL24h**	**10.9**	**S275**		**S355**
Density [N/mm^3]	3,80x e^{-6}		7,85 x e-5		
Elasticity [MPa]	E_{90}=390 E_0=11600		210000		
Plasticity [MPa] σ_{el}	24	900	275		355
σ_u	/	1000	430		510
ε_{el}		0	0		0
ε_u	/	0,178	0,376		0,261
Model	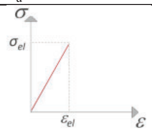		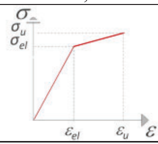		
Mesh			**Solid element**		
	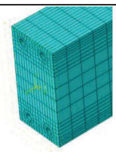	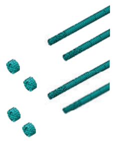			

The outputs are provided in terms of the maximum values of stresses (σ), DCR_{el} ($DCR_{el}=\sigma/\sigma_{el}$) and DCR_{ul} ($DCR_{ul}=\sigma/\sigma_{ul}$), for each component of the model (link, end-plate, threaded bolts, timber beam and stiffeners), the resistant bending moment (M), valuated in the "plastic hinge point" (PH), corresponding to the plastic hinge position in the link, and rotation (θ) in in x-z plane, valuated in the "load application point" (RP), the force (F) and the displacement (u) in z-direction, valuated in the "fixed point" (RF), corresponding to the fixed end-plate, for the global model. Outputs are detected at specific increments (In.) and times (t.), corresponding to the yielding of the steel link (P_Y), the complete plasticization of the link cross-section (P_P), the ultimate strength of the link (P_C), defined by the collapse of the model and the end of the numerical analysis, and the displacement value equal to 200 mm (P_{200}), corresponding to the maximum value of the vertical displacement reached by the transducer of the laboratory machine. Moreover, the F-u and the M-θ curves are shown. A special attention is also given to the collapse mode and hierarchy, in terms of the global behaviour and of the single component behaviour, to evaluate the accuracy of the numerical model respect to the analytical one, and the over-strength, *OS*, of each component respect to the yielding one (OS_{el}= $DCR_{el\text{-}link}/DCR_{el\text{-}component}$; OS_{ul}= $DCR_{ul\text{-}link}/DCR_{ul\text{-}component}$).

In the Figure V.19a,b presents the numerical F-u and the M-θ curves.

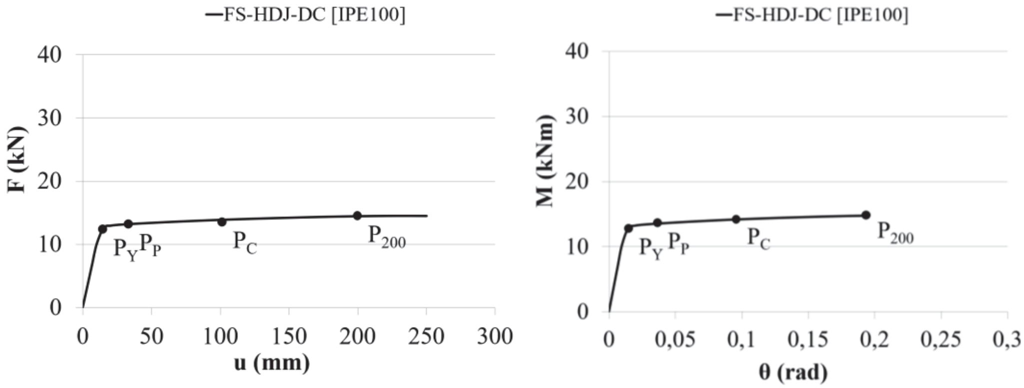

a) b)

Figure V.159 – IPE100 joint [FS-HDJ-DC]: numerical (a) F-u and (b) M-θ curves.

In Table V.8 and Tab. V.9 are depicted the stress values (σ), the DCR_{el} and the DCR_{ul}, for each connection element, in the P_Y, P_P, P_{200} and P_C instants. Moreover, the first element that reaches the elastic strength (σ_{el}) and the ultimate strength (σ_u) is gree-highlighted.

Table V.92 – IPE100 joint [FS-HDJ-DC]: yield (P_Y), plastic (P_P), 200mm (P_{200}) and collapse (P_C) stress value σ, bending moment M, rotation θ, force F and vertical displacement u.

Point	σ [MPa]					M	θ	F	u
	IPE100	End Plate	Thread Bolt	Timber beam	Stiffeners	[kNm]	[rad]	[kN]	[mm]
P_Y	355	163	241	5,9	201	11,24	0,009	11,61	13,38
P_P	364	211	287	7,1	278	12,89	0,039	13,11	27,82
P_C	402	222	308	7,5	289	14,28	0,11	14,01	105
P_{200}	426	228	321	7,7	300	15,01	0,19	14,45	200

Stress distribution

(P_Y) [In. 38; t. 4,10]

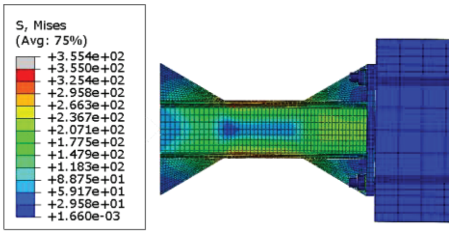

(P_P) [In. 42; t. 10,76]

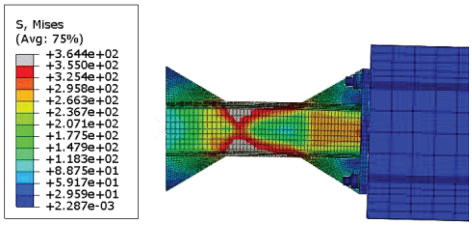

(Pc) [In. 53; t. 48,04]

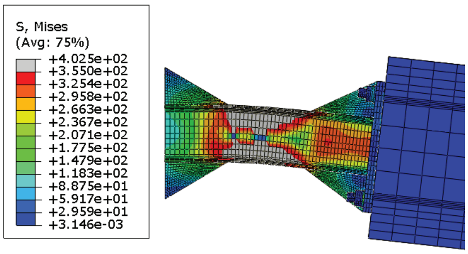

(P_{200}) [In. 57; t. 76,86]

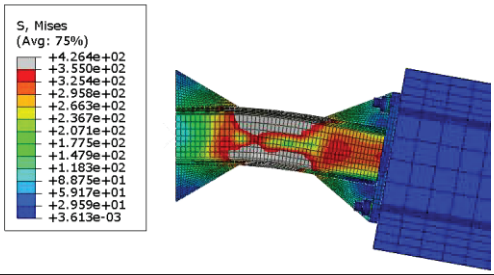

Table V.93 – IPE100 joint [FS-HDJ-DC]: yield (P_Y), plastic (P_P), 200mm (P_{200}) and collapse (P_C) stress σ, DCR_{el} (σ/σ_{el}) and DCR_{ul} (σ/σ_u).

	Link			End Plate			Thread Bolt			Timber beam		Stiffeners		
	σ	DCR		σ	DCR		σ	DCR		σ	DCR	σ	DCR	
	MPa	el	ul	MPa	el	ul	MPa	el	ul	MPa	el	MPa	el	ul
P_Y	355	100%	70%	163	59%	38%	241	27%	24%	5,9	25%	201	73%	47%
P_P	364	103%	71%	211	77%	49%	287	32%	29%	7,1	30%	278	101%	65%
P_C	402	113%	79%	222	81%	52%	308	34%	31%	7,5	31%	289	105%	67%
P_{200}	426	120%	84%	228	83%	53%	321	36%	32%	7,7	32%	300	109%	70%

Analysing the numerical results, the following observations can be drawn. At the instant P_Y, the first element to reach the yield is the link, with a DCR_{ul}= 70%. The second joint component most stressed is the stiffener, with a DCR_{el}= 73% and DCR_{ul}= 47%; the end-plate is the third joint component with a DCR_{el}= 59% respect to the yielding link and a DCR_{ul}= 38%; the bolts have a DCR_{el}= 27% and DCR_{ul}= 24% at the last, the timber beam with a DCR_{el}= 25%.

At the instant P_P, there is the complete hinge plasticization of the link with a DCR_{el}= 103% and a DCR_{ul}= 71%, and the stiffeners reach the yield, with a DCR_{el}= 101% and DCR_{ul}= 65%, while the end-plate (DCR_{el}= 77% and a DCR_{ul}= 49%) and the bolts (DCR_{el}= 32% and a DCR_{ul}= 29%) are in the elastic field and the timber beam presents a DCR_{el}= 30%.

At the instant P_C, corresponding to the collapse of the joint with the link's failure (DCR_{el}= 113% and a DCR_{ul}= 79%), the stiffeners have a DCR_{el}= 105% and a DCR_{ul}= 67%) while the end-plate (DCR_{el}= 81% and a DCR_{ul}= 52%) and the bolts (DCR_{el}= 34% and a DCR_{ul}= 31%) are in the elastic field, and the timber beam presents a DCR_{el}= 31%). In particular, the joint has reached the collapse due to the bulking of the link flange.

At the instant P_{200}, corresponding to the maximum value of the vertical displacement reached by the transducer, the link presents a DCR_{el}= 120% and a DCR_{ul}= 84%, the stiffeners have a DCR_{el}= 109% and a DCR_{ul}= 70%, while the end-plate (DCR_{el}= 83% and a DCR_{ul}= 53%) and the bolts (DCR_{el}= 36% and a DCR_{ul}= 32%) are in the elastic field and the timber beam has a DCR_{el}= 32% (Fig. V.20 and Fig. V.21).

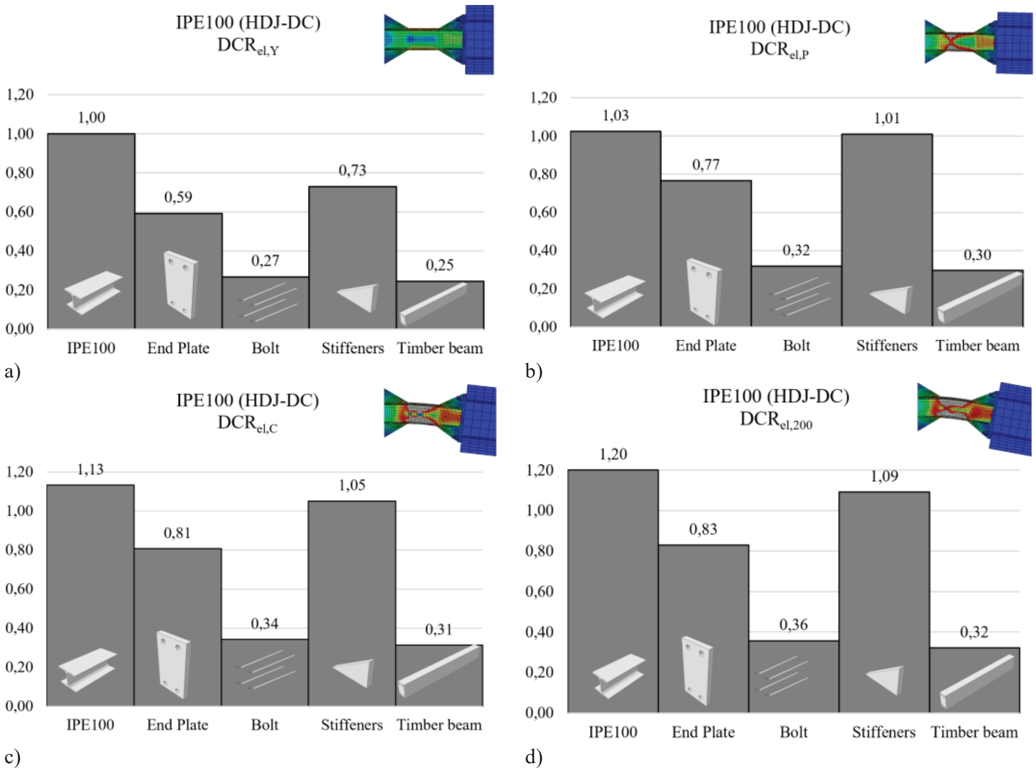

Figure V.160 – IPE100 joint [FS-HDJ-DC]: DCR_{el} in a) yield (P_Y), b) plastic (P_P), c) 200mm (P_{200}) and d) collapse (P_C) points.

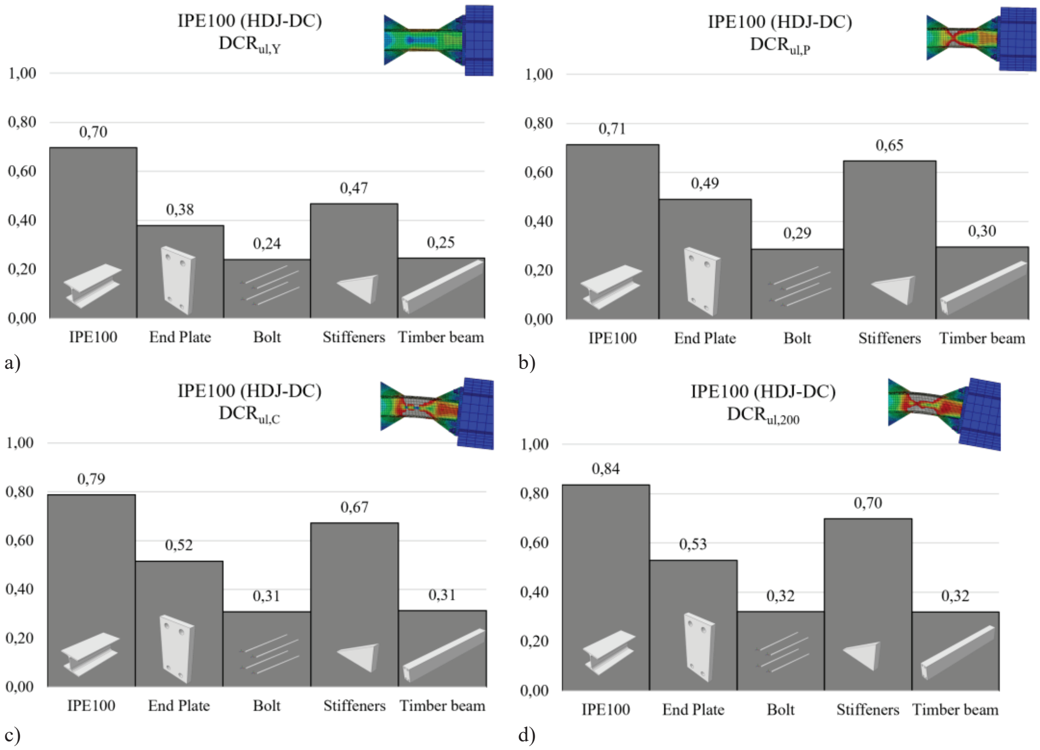

Figure V.161 – IPE100 joint [FS-HDJ-DC]: DCR$_{ul}$ in a) yield (P_Y), b) plastic (P_P), c) 200mm (P_{200}) and d) collapse (P_C) points.

At the end of P_Y, coinciding with the yielding of the link, the stiffeners (OS_{el}= 1,37), the end-plate (OS_{el}= 1,69), the bolts (OS_{el}= 3,73) and the timber beam (OS_{el}= 4,07) are over-resistant respect to the steel link, and the overstrength coefficient, OS_{el}, is indicated in the Table V.10 and Figure V.22a,. The $\Omega_{,el}$ coefficient, at the instant P_Y, is presented in the Table V.10 and in the Figure V.22b. In particular, the stiffeners have a $\Omega_{,el}$= 1,04, the end-plate a $\Omega_{,el}$= 1,28, the bolts a $\Omega_{,el}$= 2,83 and the timber beam a $\Omega_{,el}$= 3,08.

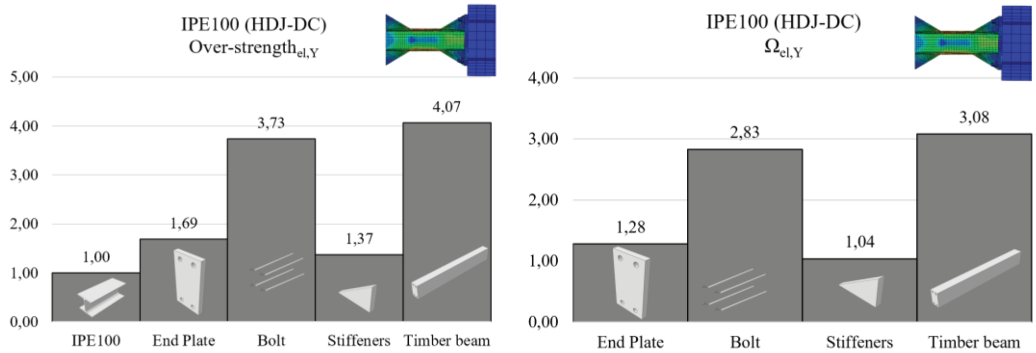

a) b)

Figure V.162 – IPE100 joint [FS-HDJ-DC]: a) over-strength (OS_{el}) and b) Ω-coefficient valuated in P_Y.

The collapse hierarchy of the elements connection, therefore, is: 1) Link; 2) Stiffeners; 3) End-plate; 4) Bolts; 5) Timber beam.

In particular, the numerical analysis has confirmed the analytical design and the type of joint, that is a *Full-strength connection (FS)* with a *High Ductility timber-steel link Joint (HDJ)* and *Ductile connection (DC)*, *)*, since the “Pull-out” and the “Tensile timber breaking”, that are fragile collapse modes, occur after the ductile collapse modes of the connection, i.e. “T-stub in tension (mode 1)” and “T-stub in compression” (Tab. V.10).

Table V.94 – IPE100 joint [FS-HDJ-DC]: analytical evaluation vs numerical analysis.

	Collapse hierarchy	Analytical evaluation		Numerical evaluation	
		$OS_{el,ana}$	$\Omega_{,ana}$	$OS_{el,num}$	$\Omega_{,num}$
1)	Link	/	/	/	/
2)	Stiffners	1,43	1,08	1,37	1,04
3)	End-plate yielding (mode 1)	2,12	1,61	1,69	1,28
4)	Pull-out	2,19	1,66	/	/
5)	End-plate (flange compression)	2,64	2,01	1,69	1,28
6)	End-plate/Bolts (mode 2)	2,82	2,14		
7)	Timber tensile break	3,33	2,52	/	/
8)	Bolts (mode 3)	3,62	2,75	3,73	2,83
9)	Timber beam bending	4,16	3,15	4,07	3,08

For completeness of results, with regards to the state of stress, examining the P_Y instant, the link reaches the yielding stress (355 MPa) while the end-plate (163 MPa), the bolts (241 MPa), the beam (5,9 MPa) and the stiffeners (201 MPa) are still in the elastic field; at the P_P instant, the cross-section of the link reaches the complete yielding, with a maximum value equal to 364 MPa and the stiffeners (278 MPa) reaches the yielding stress, while the end-plate (211 MPa), the bolts (287 MPa) and the beam 7,1 MPa) are in the elastic field; at the P_C instant, corresponding to the collapse of the joint with the buckling of the link flange, the link reaches a stress of 402 MPa, the stiffeners presents a maximum stress of 289 MPa, while the end-plate (222 MPa), the bolts (308 MPa) and the beam (7,5 MPa) are still in elastic field (Tab. V.8).

Figure V.23 shows the deformed configuration, respect to the unformulated configuration, in the 4 points: yielding, complete plasticization of the plastic hinge, displacement of 200 mm and collapse. The achievement of a displacement of 105 mm to the collapse manifests a high ductility of the system.

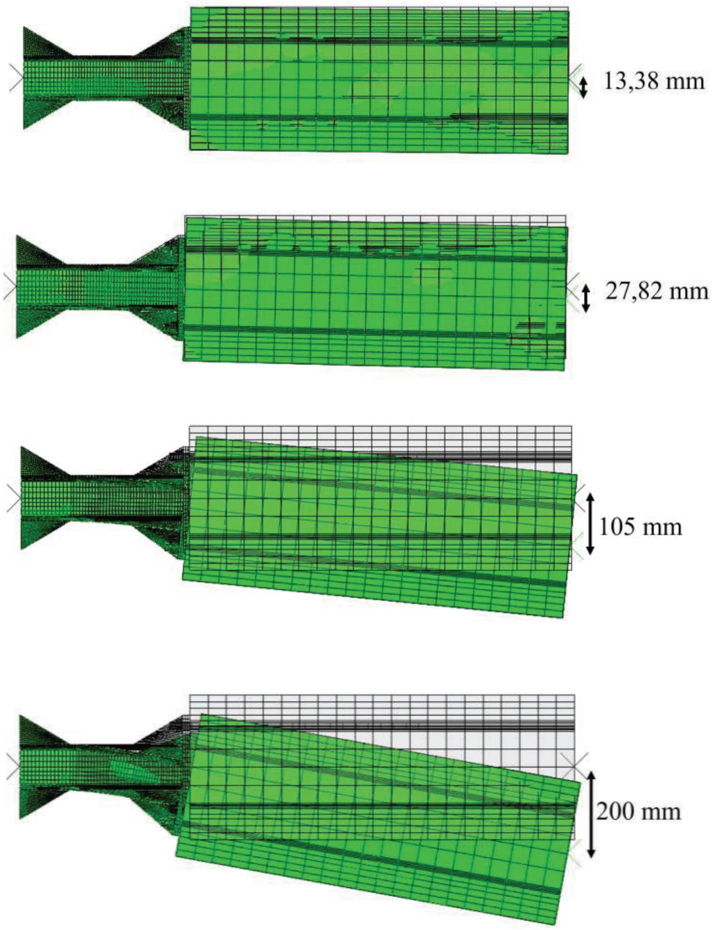

a)

b)

c)

d)

Figure V.163 – IPE100 joint [FS-HDJ-DC]: vertical deformed configuration in a) yield (P_Y), b) plastic (P_P), c) 200mm (P_{200}) and d) collapse (P_C) points.

Figure V.24 shows the AC YIELD diagram, which shows the evolution of the link yield and the extension of the plastic hinge through the normal stress distribution (σ). In particular, at the P_Y point, the first fiber of the link that catches the yield is in correspondence of the stiffener (Fig. V.24a,b), while the other elements of the connection (end-plate, bolts and stiffeners) and the timber beam are in the elastic field. At the P_P point (Fig. V.24c,d), when the yield has reached the full height of the cross section of the link (Hp= 100 mm), the yield extension is equal to the distance between the stiffeners (Lp= 140 mm). In Figure V.24e,f the buckling phenomena in the link flange is perfectly clear while in the Figure V.24g,h is indicated the yielding condition and the stress distribution in P_{200} point.

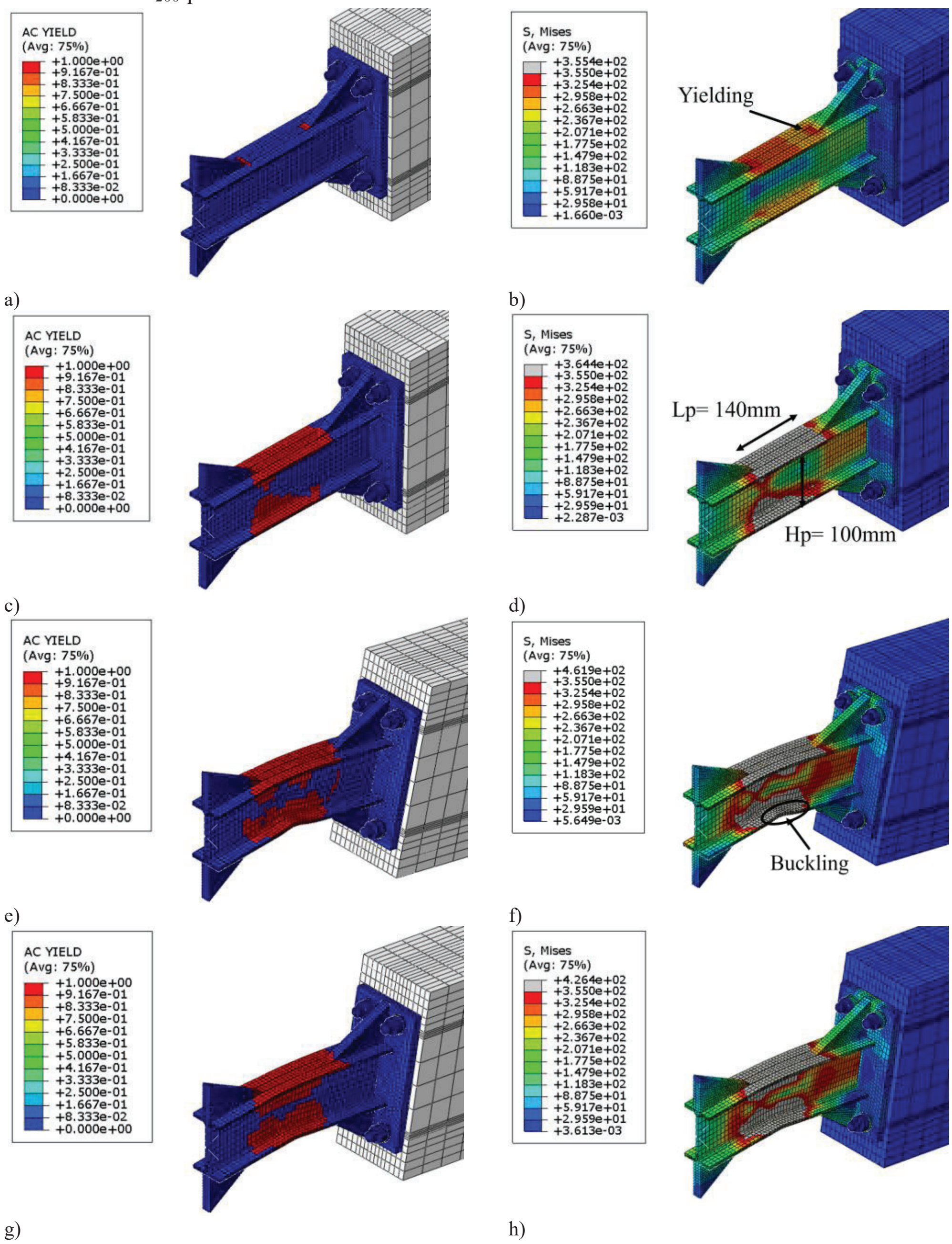

Figure V.164 – IPE100 joint [FS-HDJ-DC]: yielding and stress distribution of the elements in in a) yield (P_Y), b) plastic (P_P), c) 200mm (P_{200}) and d) collapse (P_C) points. *Hp*: height of the plastic hinge; *Lp*: length of the plastic hinge.

At the P_P point, the following observations can be drawn. The capacity design procedure allowed the complete development of the plastic hinge (Lp= 140 mm) without any fragile collapse modes or the connection sub-component plasticization (Fig. V.25). As can be seen from Figure V.25b, the presence of the stiffener in compression has led to the variation of the position of the centre of pressure between the upper end of the end-plate and the upper wing of the link.

The timber beam shows a rather uniform stress distribution, except for the areas around the holes and in correspondence with the compressed part, with low stress values (Fig. V.25c). Observing the stress distribution in the glued-bars in the timber beam, it is possible to notice that after about 250 mm from the nut there is a reduction of the stress values of 200% (from 287MPa to 8MPa). This length is, however, necessary to ensure an over-strength respect to the bending resistance of the link (Fig. V.25d). The stiffeners show a very variable stress distribution with a maximum value of 278MPa at the tip (Fig. V.25e).

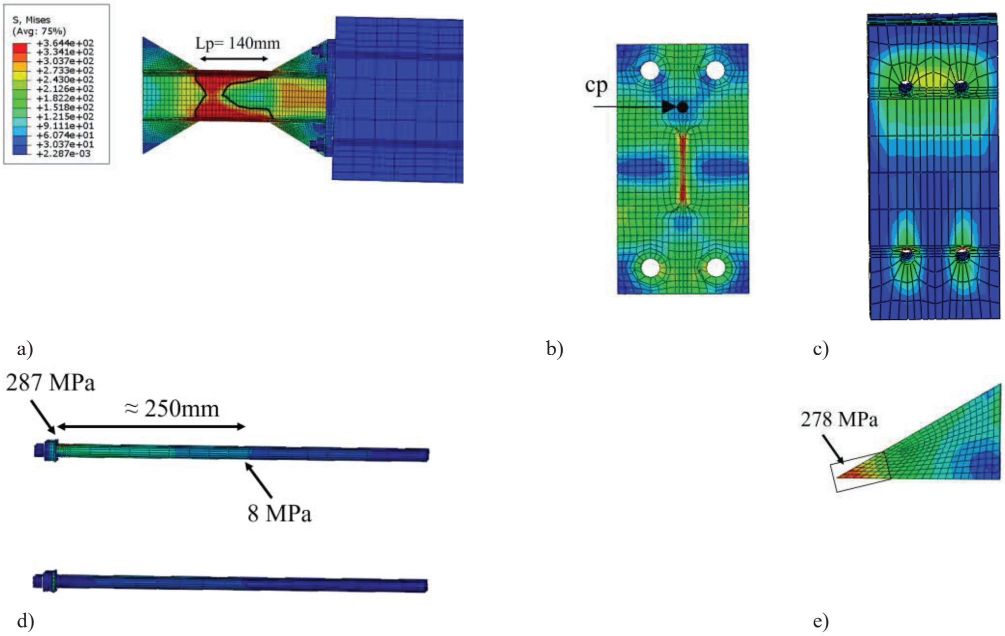

Figure V.165 – IPE100 joint [FS-HDJ-DC]: stress distribution in a) link, b) end-plate, c) timber beam and d) bolts.

5.4 Specimen features

5.4.1 Geometrical features

Based on the preliminary design of the joints, the study of the behavior of beam-to-column timber joint equipped with steel link for heavy timber Moment Resisting Frame (MRF) was tested at the University of Minho, in Guimaraes, Portugal, during an international Ph.D. research period, in a cooperation with Prof. Jorge Branco.

8 specimens, 4 *Full-Strength* - *High Ductile Joints* with *Fragile connection* (HE100A) and 4 *Full-Strength* - *High Ductile Joints* with *Ductile connection* (IPE100) were prepared for monotonic and cyclic tests in order to investigate the behavior of the connection, with special regard to the joint dissipation capacity and collapse mode. In particular, for each joint type, 2 specimens under monotonic loading and 2 specimens under cyclic loadings are tested (Tab. V.11).

Table V.95 – Types of joint for tests.

FS-HDJ-FC [HE100A]		**FS-HDJ-DC [IPE100]**	
Monotonic tests	**Cyclic tests**	**Monotonic tests**	**Cyclic tests**
S1-m	S1-c	S3-m	S3-c
S2-m	S2-c	S4-m	S4-c

Full-Strength - High Ductile Joints with Fragile connection (HE100A) [FS-HDJ-FC]

Each specimen (Fig. V.26a), 1250 mm long, is made by a laminated timber beams (GL24h), with a 140x320 mm rectangular cross section and 850 mm long (Fig. V.26b), equipped at one end with a steel link, HE100A profile 360 mm long (steel grade S355, Fig. V.26e) with two welded end-plates (120x230 mm, steel grade S275, Fig. V.26c), with 20 mm thickness, and four stiffeners (110x67 mm and 15 mm thickness, Fig. V.26d).

The link is connected at one side to the timber beam by means of 4 glued threaded bars (M16, 10.9 steel grade, 540 mm long) and at the other side rigidly connected to an end-plate (300x300 mm and 40 mm thickness) with 4 bolts (M16, 12.9 steel grade, 60 mm).

Further details of the specimen geometry are reported in Figure V.26.

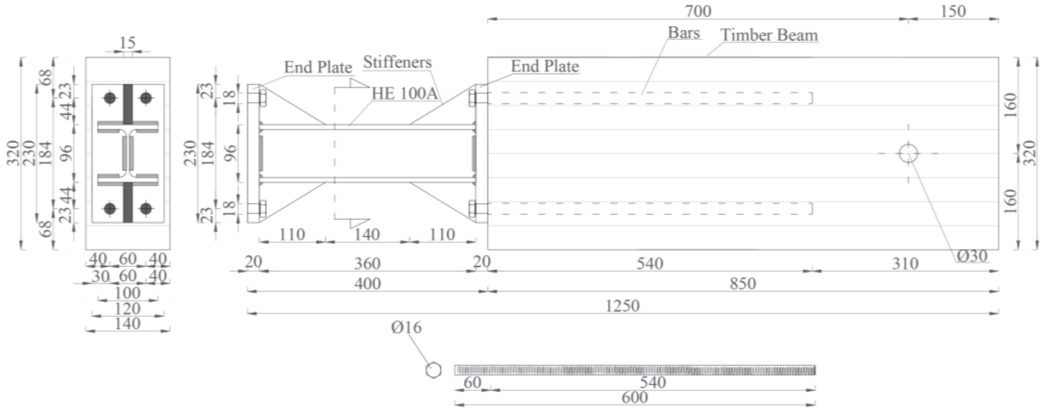

a)

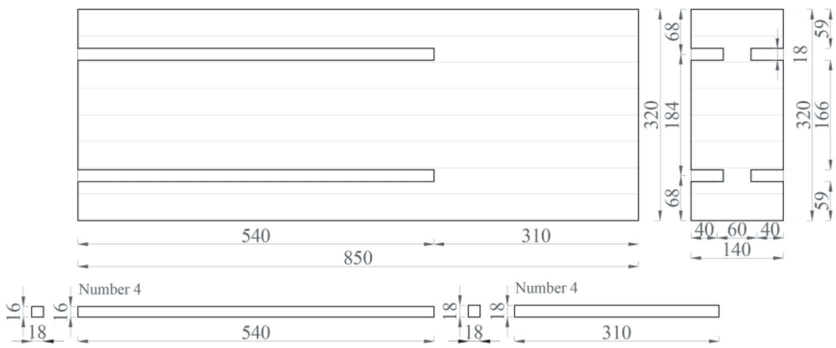

b)

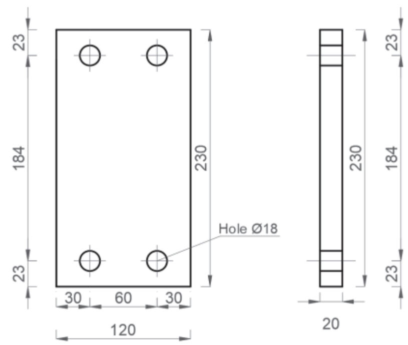

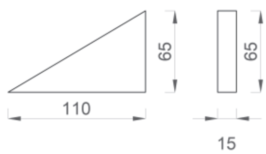

c) d)

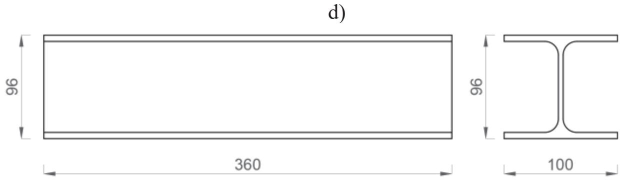

e)
Figure V.166 – HE100A joint [FS-HDJ-FC] geometrical features of the specimen [mm]: a) specimen assemblage; b) timber beam; c) end-plate; d) stiffeners; e) HE100A link.

FS - HDJ with Ductile connection (IPE100) [FS-HDJ-DC]

Each specimen(Fig. V.27a), 1250 mm long, is made by a laminated timber beams (GL24h), with a 140x320 mm rectangular cross section and 850 mm long (Fig. V.27b), equipped at one end with a steel link, IPE100 profile 360 mm long (steel grade S355, Fig. V.27e) with two welded end-plates (120x230 mm, steel grade S275, Fig. V.27c), with 15 mm thickness, and four stiffeners (110x67 mm and 15 mm thickness, Fig. V.27d).

The link is connected at one side to the timber beam by means of 4 glued threaded bars (M16, 10.9 steel grade, 540 mm long) and at the other side rigidly connected to an end-plate (300x300 mm and 40 mm thickness) with 4 bolts (M16, 12.9 steel grade, 60 mm).

Further details of the specimen geometry are reported in Figure V.27.

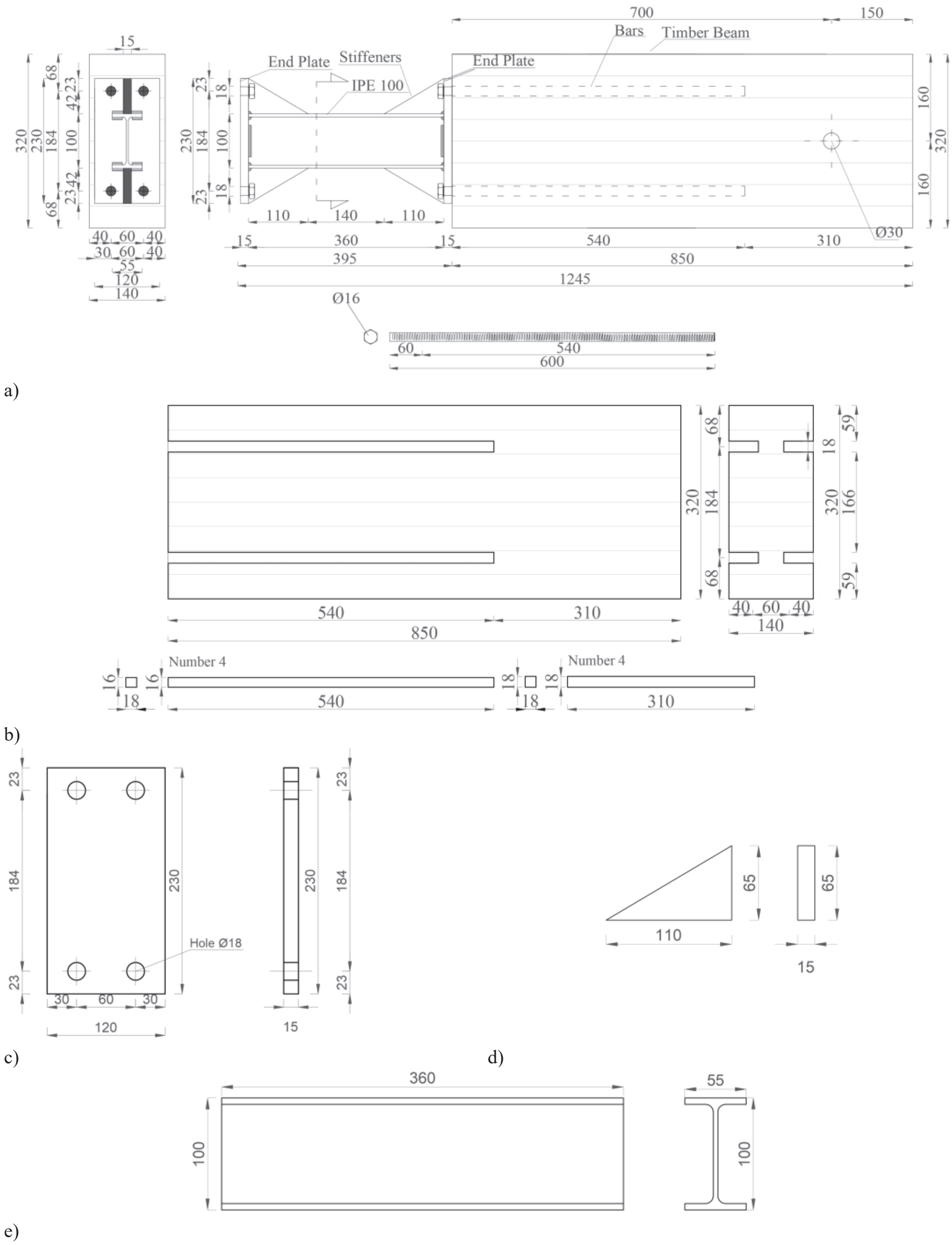

Figure V.167 – IPE100 joint [FS-HDJ-DC] geometrical features of the specimen [mm]: a) specimen assemblage; b) timber beam; c) end-plate; d) stiffeners; e) IPE100 link.

5.4.2 Manufacturing process and specimen assembly

In the specimens, four holes 18 mm diameter are performed in the end-plate, in order to allow full transfer of the shear and tension loads directly to the glued bars. The timber elements are financed by Portilame timber company and the manufacturing process, carried out at the timber company, is illustrated in Figure V.28.

Due to the high length of the bars, no holes are made on the timber beam. In particular, on the timber element (Fig. V.28a) 4 notches 16x18 mm and 540 mm long are performed in order to allow adequate anchorage of the bars.

To ensure that the steel bars are placed concentrically in the drilled holes, 2 mm thick wire is wrapped around the bars Fig. V.28b. A two-component epoxy resin (Xepox F-liquid, by Rothoblaas, Fig. V.28c) is poured into the notches (Fig. V.28d) and, after, the threaded steel bars are inserted (Fig. I.2e). At the end, the notches are closed by gluing additional timber elements (with structural timber glue), obtained by cutting the same element (Fig. V.28f). After gluing, the timber beam is left to dry for 4 days (Fig. V.28g).

g)
Figure V.168 – Manufacturing process: a) and b) notches in the timber element (18 mm diameter and 540 mm long); c) xepox F used for the glued bars; d) casting of the glue into the notches; e) inserting of the bars; f) gluing of the additional timber elements to close the notches; f) timber beam specimen assemblage.

5.4.3 Test set-up and procedure

For each type of joint, 2 types of test are carried out: 2 monotonic and 2 cyclic tests. The test set-up is designed so that bending and shear are both acting on the joint and used for both the monotonic and the cyclic tests. A cantilever configuration (Fig. V.32a) is adopted, where the steel end-plate of the joint is rigidly connected at one end to a steel end-plate (300x300 mm and 40 mm thickness, Fig. V.29a) with 4 bolts (M16, 12.9 steel grade, 60 mm, Fig. V.29b) which is connected directly at the reaction column of the laboratory with 6 bolts (M12, 12.9 steel grade, 60 mm) (Fig. V.29c).

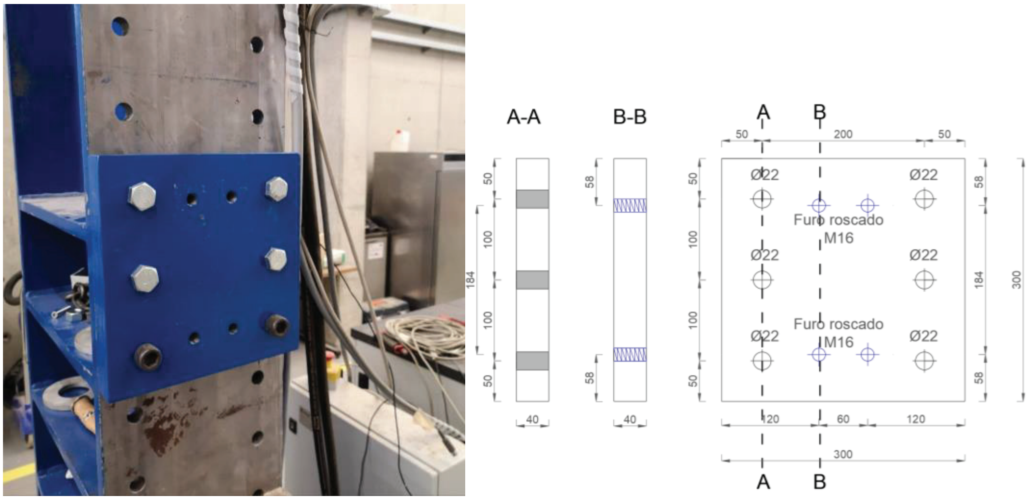

a)

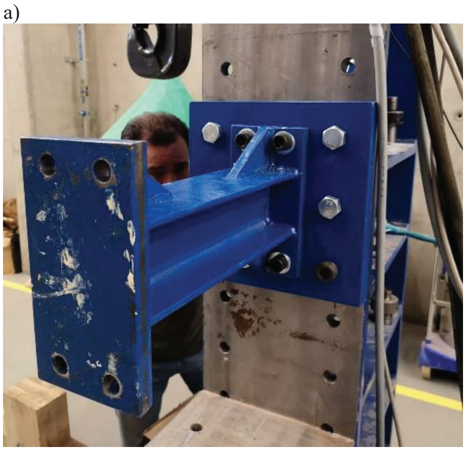

b)

c)

Figure V.169 – Specimen-laboratory machine components assemblage: a) fixed end-plate; b) steel fork [mm].

The load is applied by a hydraulic jack with a maximum displacement of 200 mm. The connection between the hydraulic jack and the timber beam was designed to act as a “perfect” hinge: a hole with 30 mm diameter (Fig. V.30a) is drilled and a steel fork is used to transfer the load to the beam (Fig. V.30b).

a)

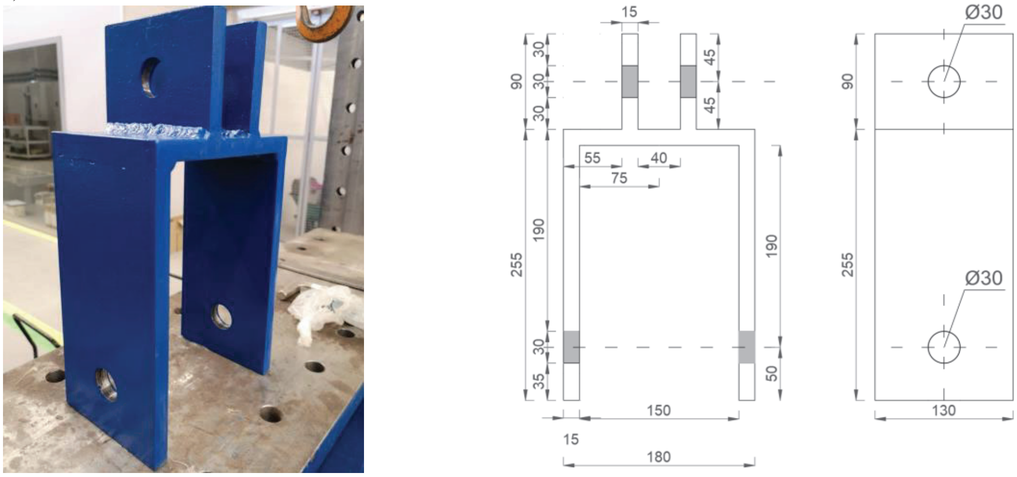

b)

Figure V.170 – a) fixed end-plate; b) steel fork [mm].

After rigidly fixing the link to the laboratory machinery, the timber beam is connected to the link, the nuts are tightened (Fig. V.31) and the fork is connected to both the actuator of laboratory machinery and the timber beam.

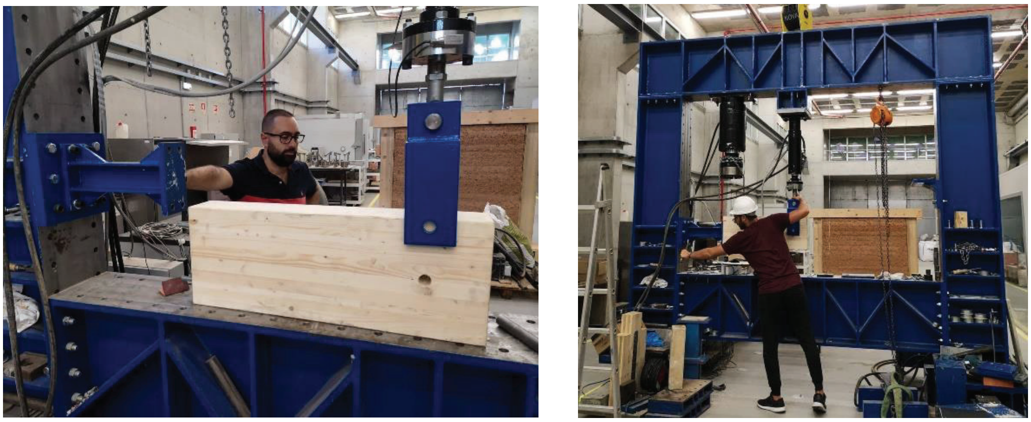

a)
Figure V.171 – a) timber beam-link assemblage; b) specimen in laboratory machine position [mm].

The laboratory machinery used features is presented in the Figure V.32.

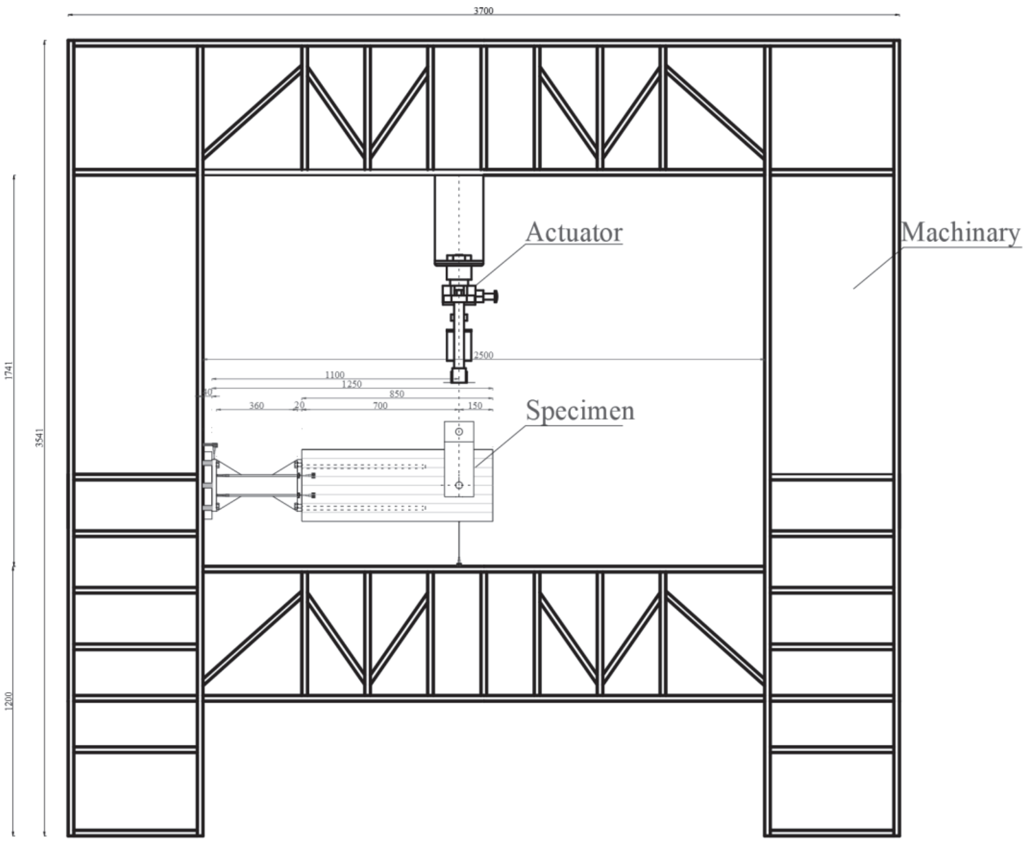

Figure V.172 – Laboratory machinery.

Global displacements of the entire test assembly and local rotations of individual connection components are measured using a series of linear variable differential transformers (LVDTs). Based on design equations, the approximate imposed displacements during testing are estimated to determine the range requirements of each instrument. Displacement transducers are mounted to steel and timber components using aluminium brackets held on by set screws.

Figure V.33 depicts the location of the displacement transducers. The applied force is measured by a load cell; the rotation between the timber beam and the steel end-plate is detected by 4 displacement transducers, 2 for each side (3-4 on side A and 9-10 on side B) measuring the relative displacement between the steel profile and the timber beam, the rotation between the fixed steel end-plate (FP) and the test machine is detected by 4 displacement transducers, 2 for each side (1-2 on side A and 7-8 on side B) measuring the relative displacement between them, while 1 displacement transducers (6) is placed under the hydraulic jack and 1 displacement transducer (5) is placed up the joint end plate connected to the fixed one to evaluate, respectively, the vertical displacement at the free-end of the cantilever scheme and the possible vertical displacement at the fixed end of the specimen.

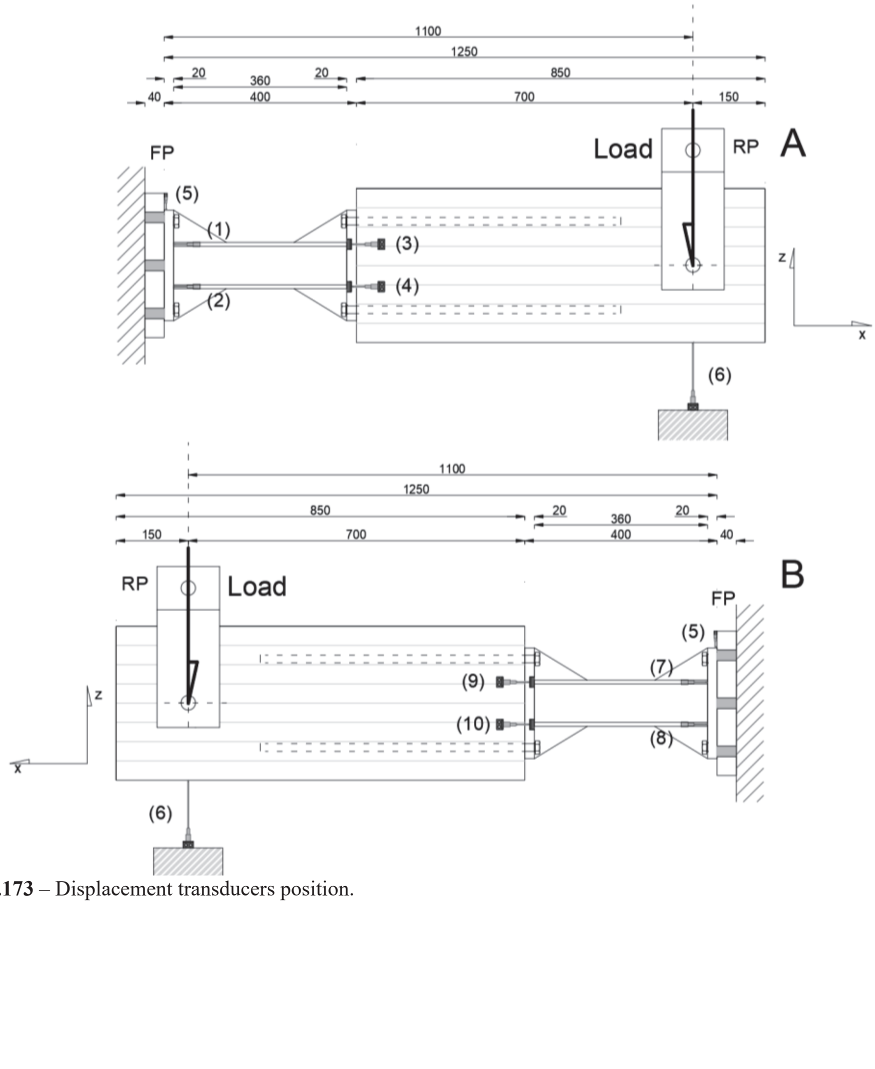

Figure V.173 – Displacement transducers position.

Details on the type and range of each instrument are presented in Table V.12. In the Figure V.34, photos of the displacement transducers used in the test are shown.

Table V.96 – Identification and position of the LVDT devices.

Side A	LVDT n.	Side B	LVDT n.
1	179679	**7**	197852
2	179682	**8**	179681
3	198379	**9**	152392
4	176621	**10**	179683
5	197869	**5**	197869
6	147586	**6**	147586


a)


b)


c)


d)

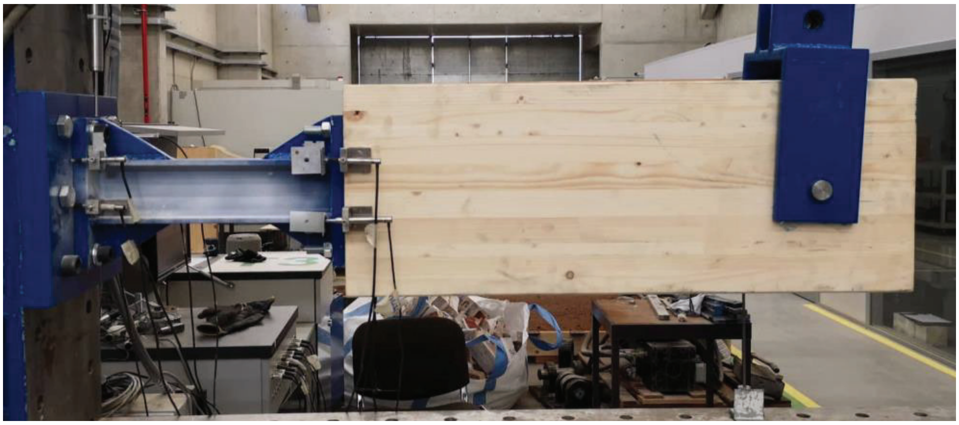

e)

Figure V.174 – LVDT devices position on the specimen: a) LVDTs 1, 2, 3 and 4; b) LVDTs 7, 8, 9 and 10; c) LVDT 6; d) LVDT 5; e) specimen position.

Displacement transducers are calibrated to convert voltage readings into direct displacement readings assuming a linear relationship between voltage and displacement. This is a valid assumption provided that the location of the core of the device is kept within the valid range relative to the location of the body. The change in voltage is recorded over a known displacement to determine the voltage-displacement relationship.

The LVDTs are calibrated using a large micrometre over a range of ±6 mm. The core of the device is set as close as possible to the zero locations, and then move 1 mm at a time over the aforementioned range.

In monotonic tests the loading is applied under displacement control at a constant rate of 0,1 mm/s so that the test end is achieved in about 30 minutes, in order to study the specimen response in elastic-plastic terms; therefore, generally a non-linear analysis must be carried out that takes into account the effects of:

- *Non-linearity of the material*, such as for example the formation of plastic hinges, the twisting of compressed elements, the yielding of traction elements;
- *Non-linearity of the geometry*, or second-order effects, if they have a non-negligible value.

In this case the only non-linearity of the material is considered.

For the cyclic test, the loading history in cyclic tests is shown in Fig. V.35. According to the procedure described in the European standard EN 12512 (CEN, 2005) for timber joints, the amplitude of the cycles is defined as a function of the yield displacement V_y, determined experimentally in the corresponding monotonic test. The rate of displacement increase is constant within each cycle, 0,2 mm/s during the entire process (which lasted approximately 3,5 hours).

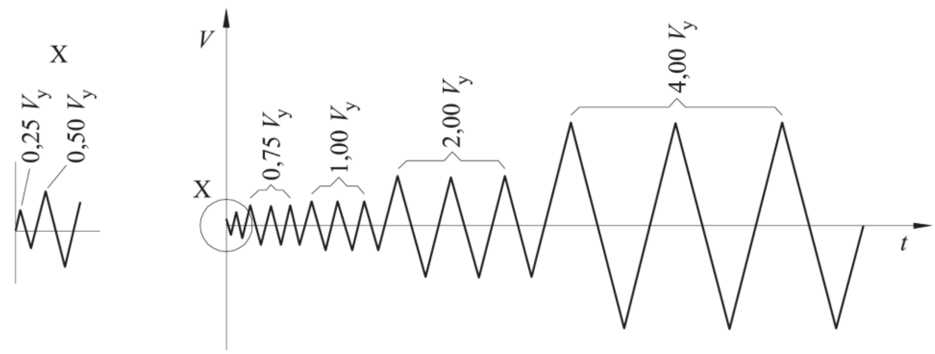

Figure V.175 – Cyclic test protocol according to EN 12512.

As regards the complete test procedure to determine the force-dispacement envelope curve, the complete load application procedure illustrated in Table V.13 must be used.

Table V.97 – Cyclic test protocol according to EN 12512, step by step.

Cycle 1°	- Application of a compressive load up to a displacement equal to 25% of that (d_y) corresponding to the estimated yield strength (F_y); - Application of a tensile load until zero displacement; - New application of the compression load up to a displacement equal to 25% of that (d_y) corresponding to the estimated yield strength (F_y); - Application of a tensile load until zero displacement.
Cycle 2°	The procedure of Cycle 1° is repeated until to a displacement equal to 50% of that (d_y) corresponding to the estimated yield strength (F_y).
Cycle 3°	The procedure of Cycle 2° is repeated for 3 times until to a displacement equal to 75% of that (d_y) corresponding to the estimated yield strength (F_y).
Cycle 4°	The procedure of Cycle 3° is repeated for 3 times until to a displacement equal to 100% of that (d_y) corresponding to the estimated yield strength (F_y).
Subsequent Cycles	The procedure of Cycle 4° is repeated for 3 times until to a displacement equal to 200-400-600-800% of that (d_y) corresponding to the estimated yield strength (F_y), until to the collapse.

The yield displacement of the specimen can be estimated graphically from the experimental data obtained from the monotonous tests, according to UNI EN 12512. In the force-displacement diagram, the value of the maximum force F_{max} is identified and $0,4F_{max}$ and $0,1F_{max}$ are obtained; from this point, the secant passing through the curve is traced and the angle respect to the horizontal line is identified α.

The β is then calculated:

$$\tan\beta = \frac{1}{6}\tan\alpha$$

Finally, the tangent to the curve with slope β is plotted, as shown in Figure V.36:

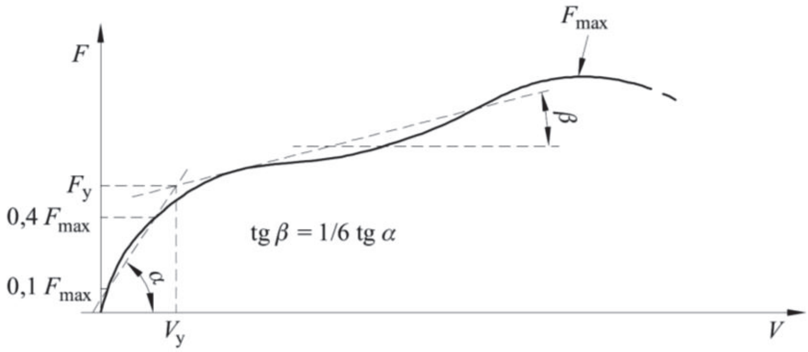

Figure V.176 – Definition of the yield value for a load-displacement curve (UNI EN 12512:2006).

From the observation of the analytical and numerical results, the ultimate vertical displacement of the load application point, corrisponding to the joint collapse, is 242 mm for HE100A joint and 120 mm for IPE100 joint. The lab machinary is characterized by a transducer that can reach a maximum vertical displacement of 200 mm, tha is not enough for the specimens collapse but it is sufficient to check the complete plasticization of the link.

5.4.4 Methodology for the outputs evaluation

The Figure V.37 shows an idealized deformation of the proposed connection in a full portal frame. Because the total inter-storey drift on the frame is equal to the rotation of the line extending from the column centerline to the middle of the beam, the total storey drift can be represented as the simplified frame shown in Figure Fig. V.37. In this frame, the total interstorey drift is effectively equal to the rotation of the line extending from the column centerline to the beam tip.

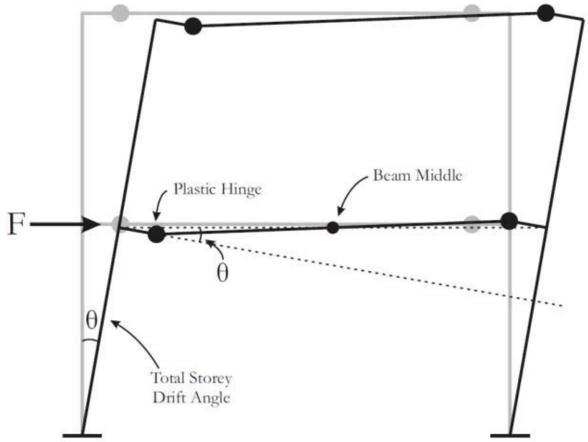

Figure V.177 – Idealized deformation of full frame.

The performance of the proposed joint is evaluated based on global joint response, local rotations of each individual link to beam connection, and strain profiles of various connection sub-components (bolts, end-plate and stiffeners).

The outputs are provided in terms of the maximum values of the the beam tip force (F) and the beam tip displacement (u) in z-direction, valuated in the "fixed point" (FP), and the resistant bending moment (M) and rotation (θ) in in x-z plane, valuated respect to the "plastic hinge point" (PH), for the global model, and the relative rotation between the end-plate and the timber beam, valuated in the "timber point" (TP) (Fig. V.38).

The beam tip force (F) is directly measured by a load cell attached to the actuator, and the beam tip displacement (u) is directly measured using displacement transducer n°6. The moment at the column face (M_{FP}) and the rotaion (θ_{FP}) are calculated using equations below respectively:

$$M_{FP} = F \cdot L_{FP}$$

$$\theta_{FP} = \frac{u_{FP}}{L_{FP}}$$

where L_{FP} is the distance from the point of load (RP) to the fixed point (FP): the length between the fixed end-plate and the load application point, u_{FP} is the vertical displacement evaluated in the RP point and F is lo corrispondence load.

The plastic rotation (θ_{PH}), respect to the PH point (in the link) is caluclated by subtracting the relative rotation between the timber beam and the end-plate (θ_{TP}), measured by the LVDs n°3,4,9,10, from the global rotation response (θ_{FP}), measured by the LVDs n°3,4,9,10, as shown below.

$$\theta_{PH} = \theta_{FP} - \theta_{TP}$$

where θ_{PH} is the rotation generated by the plastic hinge formation in the steel link and θ_{TP} is the rotation generated by the relative rotation between the timber beam and the end-plate, measured by the LVDs n°3,4,9,10.

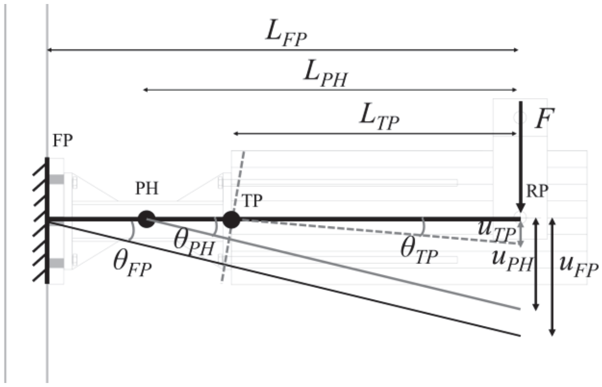

Figure V.178 – Identification of rotation and vertical displacement of the joint.

In particular, θ_{TP} is evaluated as (Fig. V.39):

$$\theta_{TP} = \frac{\delta_1 + \delta_2}{h}$$

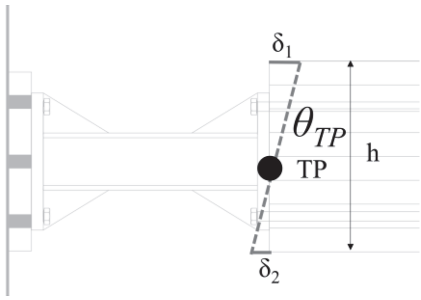

Figure V.179 – Identification of the relative rotation timber beam-link of the joint.

A positive movement refers to the actuator pushing outward, hence clock-wise rotations are considered positive.

Outputs are detected at specific increments (In.) and times (t.), corresponding to the occurrence of phenomena in the specimens (such as cracks, yielding, etc.), with particular attention to the yield point (*Yielding*) and to the end of the test point (*End fo test*). Moreover, the F-u and the M-θ curves are shown. A special attention is also given to the collapse mode and hierarchy identification, in terms of the global behaviour and of the relative rotation between end-plate and the timber beam, to evaluate the accuracy of numerical model.

Some errors are introduced into the test readings due to instrument calibration and support movement. Error in the calibration of the instruments is quantified prior to testing (during calibration) by accurately measuring the movement of the instrument and observing the reading output by the data acquisition system. Since the LVDTs are measuring small displacements (± 6,35 mm), the error is on the order of 1/10 of a millimeter. Such small error does not significantly impact the accuracy of the readings. No sudden changes in displacement are observed, indicating that there is no abrupt slip of connections, and movements varied based on force for the duration of the test. Since the error is found to be very small and the actual magnitude of the pin movement is not easily quantified, this effect is not accounted for in the rotation calculations.

The following section presents the findings of the experimental program. First, the test observations will be shown, followed by a discussion of the performance of each specimen, the behaviour of the timber-steel link joint, and a comparison of different test specimens. Experimental observations will be presented using a summary plot of major events, followed by photographs of such events. For components that show no obvious change in behaviour (remain elastic), photos are not presented, but the behaviour of such components is addressed in the discussion.

5.5 Pilot monotonic test

A pilot *S1-m* test is performed prior to the beginning of the experimental program. The main aims of this test are:

(i) Evaluating the joint behaviour with special attention to the timber beam-end plate relative rotation;
(ii) Evaluating the order of magnitude of the joint strength and compare it with the design load for the experimental setup and for the maximum load that it can bear;
(iii) Evaluating the joint displacement read by LVDTs top and bot (see the instruments' layout in Figure V.33), in order to verify the absence of fixed end-plate vertical translation during tests, i.e., the effectiveness of the experimental setup;
(iv) Assessing the effectiveness of the instrumentation layout adopted;
(v) Evaluating the effective strength of the glue.

The test result on the *S1-m* specimen are presented below step by step (P: point; u: displacement; F: force). In particular, based on the joint displacements read by instruments, the evolution of the reconstructed deformed shape of the specimen is shown in Table V.14.

In the *Point 1*, in corresponding of a force F= 21,61 kN and a displacement of u= 17,26 mm, a horizontal crack is formed on the A side of the timber beam (length: 200 mm; thickness: 0,5 mm), deep up to the bolt, in correspondence of the timber element added following the gluing of the bars. The relative rotation between the end-plate and the timber beam is $\theta_{TP} = 0$ rad.

In the *Point 2 (Yielding)*, in corresponding of a force F_y= 27,62 kN and a displacement of u_y= 26,75 mm, cracks appear in the paint of the steel link which has reached yielding. The crack thickness in the timber beam, on the A side, is increased, reaching a thickness of 0,7 mm. The relative rotation between the end-plate and the timber beam is θ_{TP} = 0 rad.

In the *Point 3*, in corresponding of a force F= 28,13 kN and a displacement of u= 53,89 mm, a horizontal crack is formed on the B side of the timber beam (length: 150 mm; thickness: 0,5 mm), deep up to the bolt, in correspondence of the timber element added following the gluing of the bars, and increase the plasticization of the link. The relative rotation between the end-plate and the timber beam is θ_{TP} = 0,0001 rad.

In the *Point 4 (End of the test)*, in corresponding of a force F= 29,87 kN and a displacement of u= 89,89 mm, the joint reaches the collapse due to the break of the threading of the bars without an increase of their length compared to the initial one (so that without plastic extension of the bars). This point corresponds to the collapse of the system. The relative rotation between the end-plate and the timber beam is θ_{TP} = 0,11 rad.

Table V.98 – S1-m specimen test results: identification of significative points.

Point 1

F=21,61 kN

u=17,26 mm

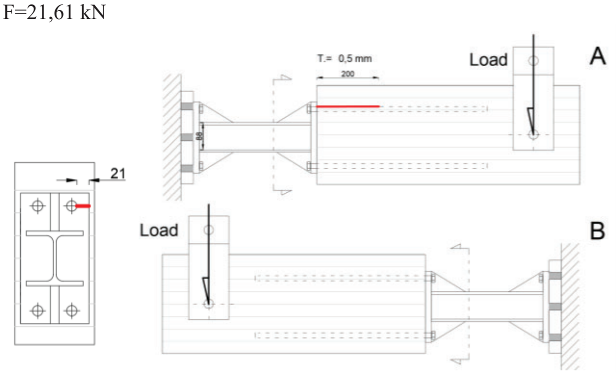

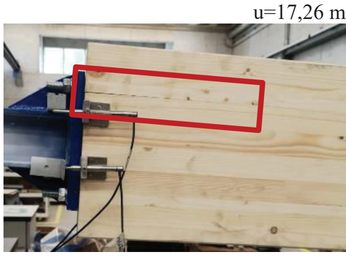

Point 2 (Yielding)

F=27,62 kN

u=26,75 mm

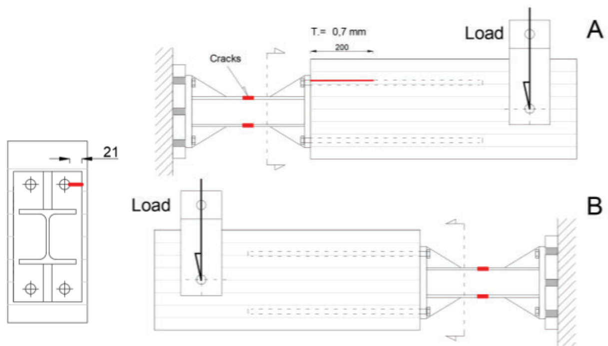

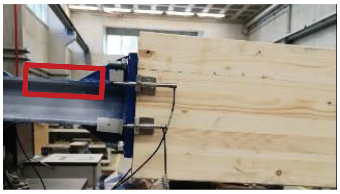

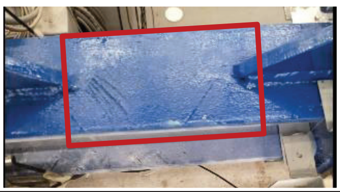

Point 3
F=28,13 kN

u=59,89 mm

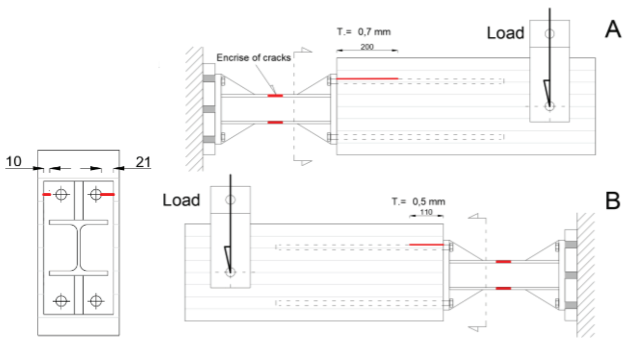

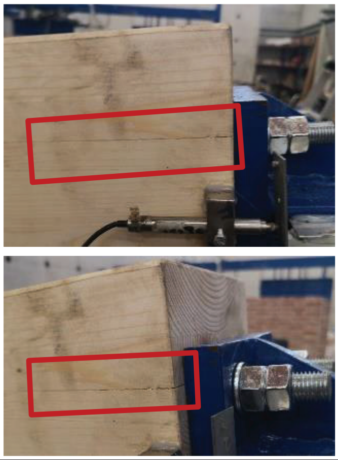

Point 4 (End of the test)
F=29,87 kN

u=89,89 mm

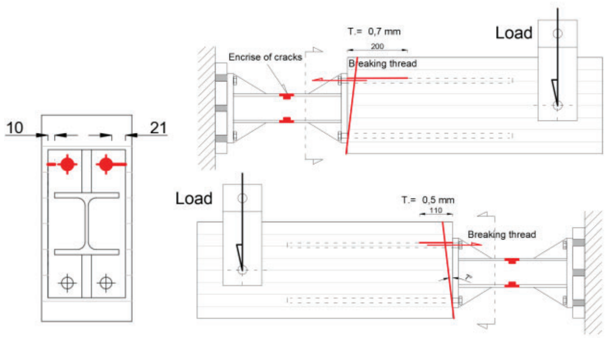

The comparison between the specimen before and after the test is shown in the Figure V.40a,b while the steel link and the bolts at the end of the test are shown in the Figure V.40c,d.

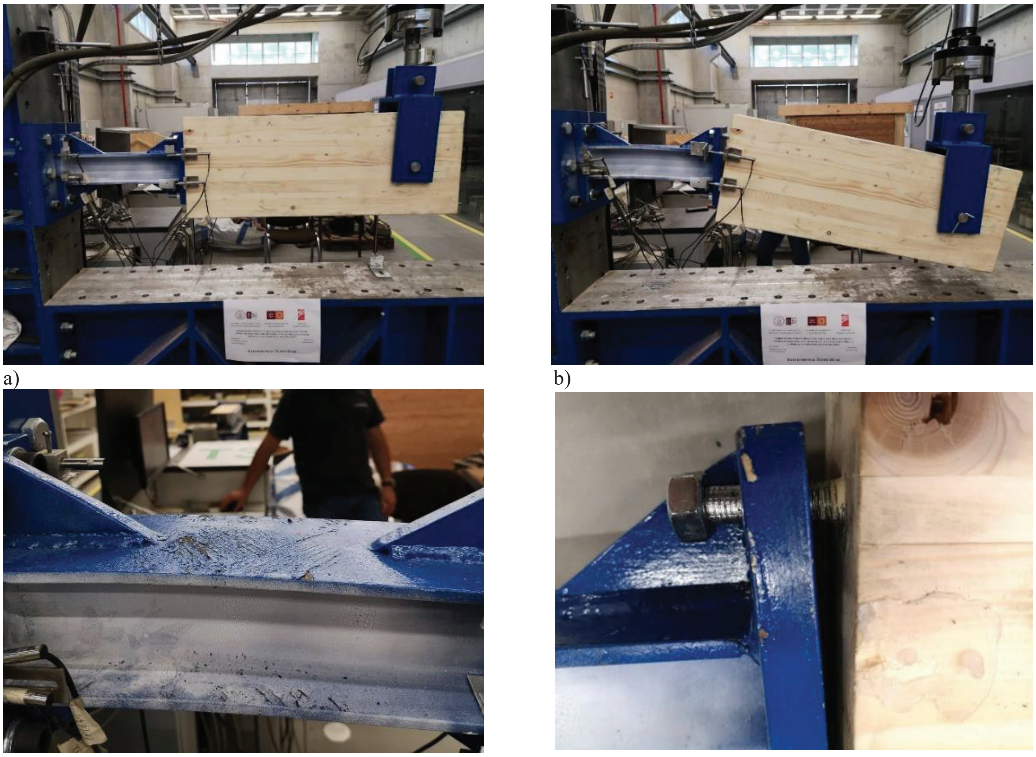

a) b) c) d)

Figure V.180 – a) system before the test; b) system after the test; c) link after the test; d) bolts after the test.

The F-u and M-θ curves are shown in Figure V.41. In particular, the F-u curve is a direct output of the test machine while the M-θ curve was analytically evaluated (see chapter 5.4.4).

The output are presented in terms of force (F [kN]) and vertical displacement (u [mm]), resistant bending moment (M [kNm]) and rotation of the free-end of the timber beam respect to the rotation plastic center in the steel link (θ [rad]). In particular, on the curves are reported the significative points presented in the Table V.15, in which, the test results are presented also in terms of numerical values.

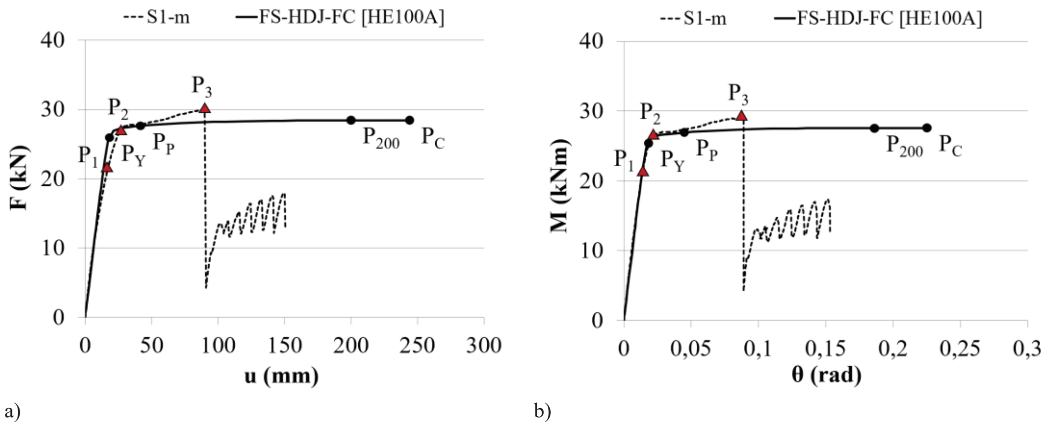

Figure V.181 –S1-m specimen test results: a) force-displacement and b) moment-rotation curves.

Table V.99 – Summary S1-m specimen test results: force (F), displacement (u), resistant bending moment (M) and rotation (θ) at yield (P_2) and end test (P_4) points.

Point	F [kN]	u [mm]	M [kNm]	θ [rad]
P_2 (Yielding)	27,62	26,75	26,14	0,035
P_4 (End test)	29,87	89,89	28,97	0,085

Analysing the test results on *S1-m* specimen, the following observations can be drawn:

- It is necessary to glue the additional timber elements more carefully to avoid the creaks at the interface;
- The specimen under loads shows a brittle failure due to the cracks in corresponding of the timber added glued parts;
- To avoid the break of the threading of the bars in tension, 2 nuts are used for each bar in the other tests.

The pilot test provides a positive feedback for what concerns all these issues.

However, as the experimental results have not to be used for comparison with other experimental tests in this experimental program, or with numerical and analytical design, the test is performed so that no significant or detailed information is available on the damage evolution of the specimen during the test, which is very brief (about 10/15 minutes).

5.6 Monotonic tests

5.6.1 S2-m Test

The test result on the *S2-m* (HE100A Link) specimen are presented below step by step (P: point; u: displacement; F: force). In particular, based on the joint displacements read by instruments, the evolution of the reconstructed deformed shape of the specimen is shown in Table V.16.

In the *Point 1 (Yielding)*, in corresponding of a force F_y= 27,11 kN and a displacement of u_y= 17,73 mm, cracks appear in the paint of the steel link which has reached yield point. The relative rotation between the end-plate and the timber beam is θ_{TP} = 0 rad.

In the *Point 2*, in corresponding of a force F= 29,98 kN and a displacement of u= 102 mm, a horizontal crack is formed on the B side of the timber beam (length: 150 mm; thickness: 0,3 mm), deep up to the bolt, in correspondence of the timber element added following the gluing of the bars and increase the plasticization of the link. The relative rotation between the end-plate and the timber beam is θ_{TP} = 0 rad.

In the *Point 3 (End test)*, in corresponding of a force F= 32,71 kN and a displacement of u= 184,97 mm, the test ended due to the maximum displacement allowed by the transducer. The relative rotation between the end-plate and the timber beam is θ_{TP} = 0,0041 rad.

Table V.100 – S2-m specimen test results: significative points.

Point 1 (Yielding)

F=27,11 kN

u=17,73 mm

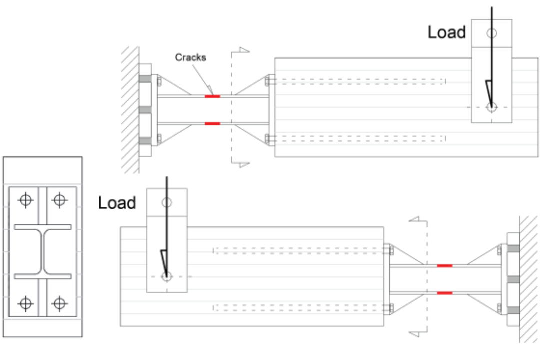

Point 2

F=29,98 kN

u=102 mm

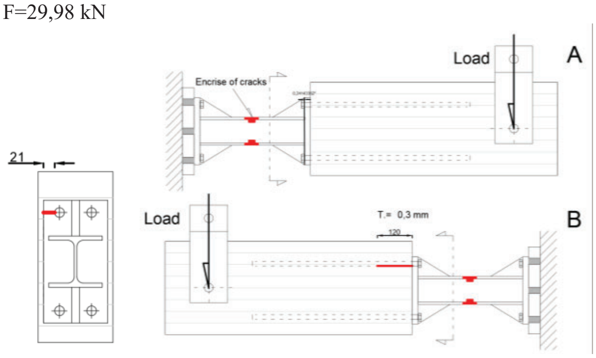

Point 3 (End of the test)

F=32,71 kN

u=184,97 mm

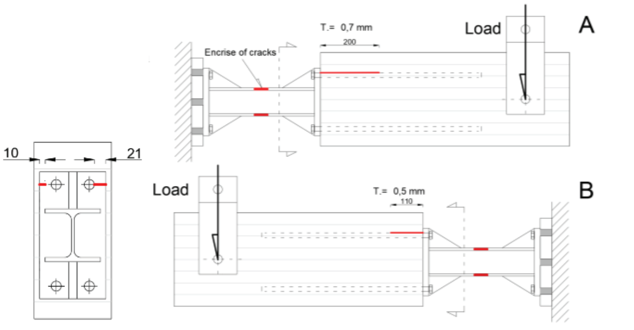

The comparison between the specimen before and after the test is shown in the Figure V.42a,b while the steel link and the bolts at the end of the test are shown in the Figure V:42c,d.

a)

b)

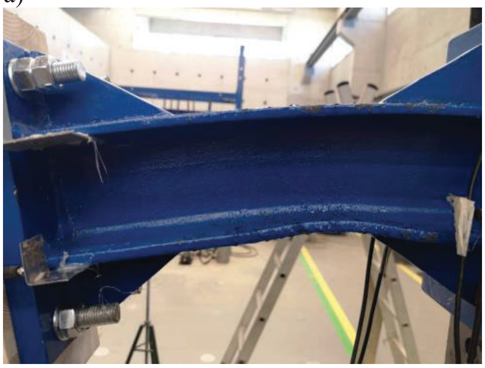

c)

d)

Figure V.182 – S2-m specimen: a) system before the test; b) system after the test; c) link after the test; d) bolts after the test.

The F-u and M-θ curves are shown in Figure V.43. In particular, the F-u curve is a direct output of the test machine while the M-θ curve was analytically evaluated (see chapter 5.4.4).

The output are presented in terms of force (F [kN]) and vertical displacement (u [mm]), resistant bending moment (M [kNm]) and rotation of the end of the timber beam respect to the rotation plastic center in the steel link (θ [rad]). In particular, on the curves are reported the significative points presented in the Table V.17, in which, the test results are presented also in terms of numerical values.

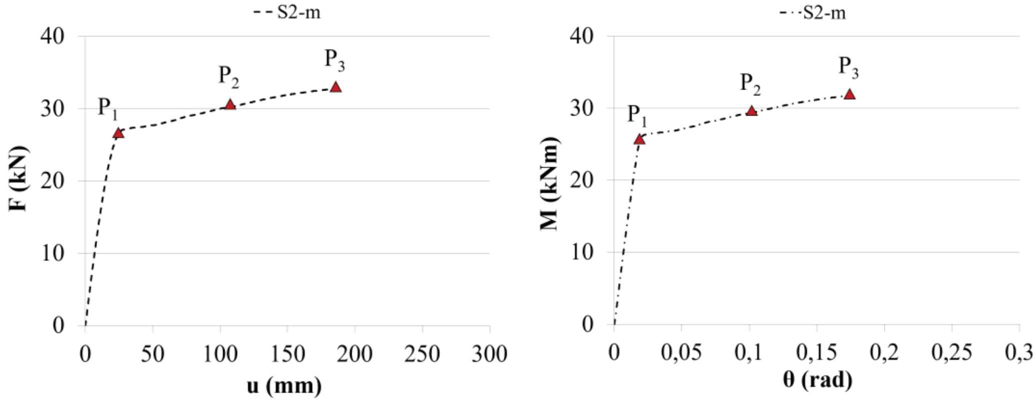

a) b)

Figure V.183 – S2-m specimen test results: a) force-displacement and b) moment-rotation curves.

Table V.101 – Summary of S2-m specimen test results: force (F), displacement (u), resistant bending moment (M) and rotation (θ) at yield (P_1) and end test (P_3) points.

Point	F [kN]	u [mm]	M [kNm]	θ [rad]
P_1 (Yielding)	27,11	17,73	25,77	0,021
P_3 (End test)	32,71	184,97	31,77	0,180

Analysing the test results on *S2-m* specimen, the following observations can be drawn:

- As shown in the pilot test, there is the formation of cracks at the added and glued timber parts which, however, do not have a structural importance and do not affect the relative rotation between the beam and the end-plate, that is very low.
- The joint shows great flexibility and ductility, as it is possibile to see by the F-u curve, without fragile collapse modes, as provided by the analytical and numerical evaluation;
- The glued joint resistes a tensile force F = 20% more than the expected resistance. This allows to affirm that the the safety coefficients for the “pull-out” and the “failure of the adhesive by debonding from steel or wood”, that are in the national and European standards, may be too high;
- The vertical displacement achieved, due to the transducer limit (200 mm), is approximately 82% of the displacement expected for the collapse joint, so that the specimen has not reached the collapse and it is not possible to check all the ductility capacity of the joint.

5.6.2 S3-m Test

The test result on the *S3-m* specimen (IPE100 link) are presented below step by step (P: point; u: displacement; F: force). In particular, based on the joint displacements read by instruments, the evolution of the reconstructed deformed shape of the specimen is shown in Table V.18.

In the *Point 1 (Yielding)*, in corresponding of a force F= 12,89 kN and a displacement of u= 14,96 mm, cracks appear in the paint of the steel link which has reached yield point. The relative rotation between the end-plate and the timber beam is θ_{TP} = 0 rad.

In the *Point 2*, in corresponding of a force F= 14,13 kN and a displacement of u= 50,02 mm, increase the plasticization of the link that reach the complete plasticization of the plastic hinge. The relative rotation between the end-plate and the timber beam is θ_{TP} = 0 rad.

In the *Point 3 (Buckling)*, in corresponding of a force F= 15,40 kN and a displacement of u= 97,32 mm, the link flange reaches the buckling. The relative rotation between the end-plate and the timber beam is θ_{TP} = 0,0022 rad.

In the *Point 4 (End test)*, in corresponding of a force F= 17,81 kN and a displacement of u= 184,97 mm, the test ended due to the maximum displacement allowed by the transducer. The relative rotation between the end-plate and the timber beam is θ_{TP} = 0,0022 rad.

Table V.102 – S3-m specimen test results: significative points.

Point 1 (yielding)

F=12,89 kN u=14,96 mm

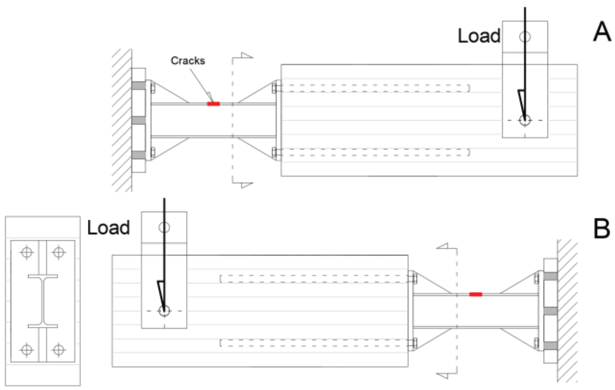

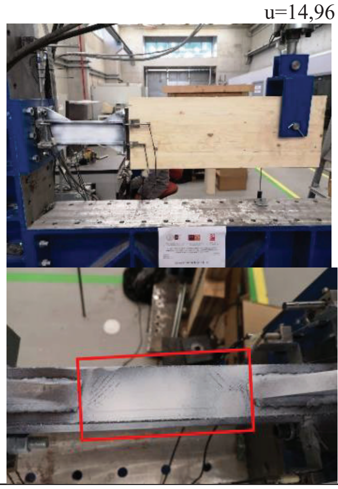

Point 2
F=14,13 kN

u=50,02 mm

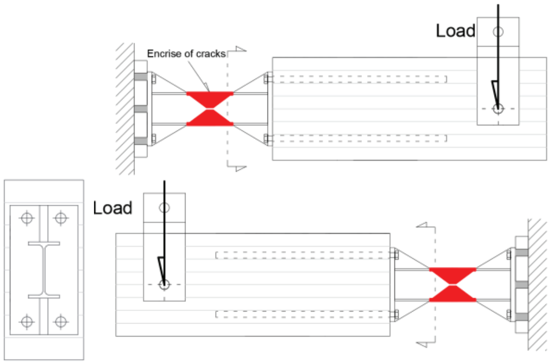

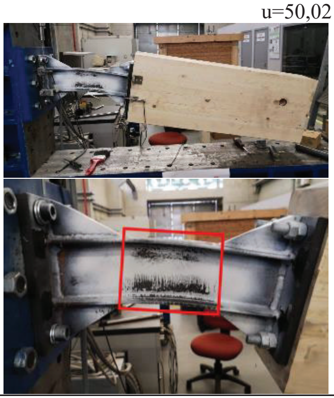

Point 3 (Buckling)
F=15,40 kN

u=97,32 mm

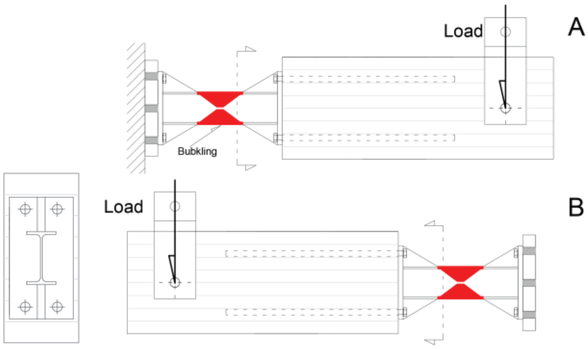

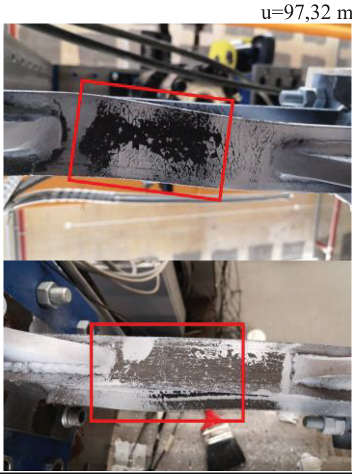

Point 4 (End of the test)
F=17,81 kN

u=184,97 mm

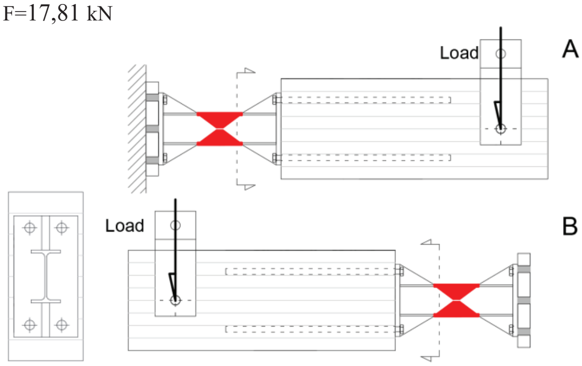

The comparison between the specimen before and after the test is shown in the Figure V.44a,b while the steel link and the bolts at the end of the test are shown in the Figure V.44c,d.

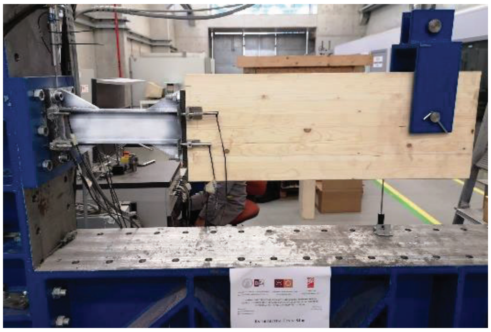

a)

b)

c)

d)

Figure V.184 – S3-m specimen: a) system before the test; b) system after the test; c) link after the test; d) bolts after the test.

The F-u and M-θ curves are shown in Figure V.45. In particular, the F-u curve is a direct output of the test machine while the M-θ curve was analytically evaluated (see chapter 5.4.4).

The output are presented in terms of force (F [kN]) and vertical displacement (u [mm]), resistant bending moment (M [kNm]) and rotation of the end of the timber beam respect to the rotation plastic center in the steel link (θ [rad]). In particular, on the curves are reported the significative points presented in the Table V.19, in which, the test results are presented also in terms of numerical values.

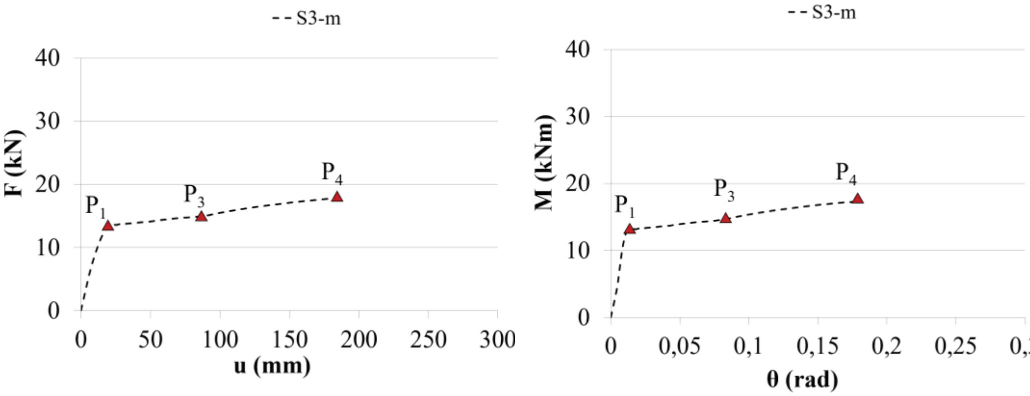

a) b)
Figure V.185 – S3-m specimen test results: a) force-displacement and b) moment-rotation curves.

Table V.103 – S3-m specimen test results: force (F), displacement (u), resistant bending moment (M) and rotation (θ) at yield (P_1), buckling (P_3) and end test (P_4) points.

Point	F [kN]	u [mm]	M [kNm]	θ [rad]
P_1 (Yielding)	12,89	14,96	12,04	0,013
P_3 (Buckling)	15,40	97,32	14,03	0,084
P_4 (End test)	17,81	184,97	17,27	0,176

Analysing the test results on *S2-m* specimen, the following observations can be drawn:

- The joint shows great flexibility and ductility, as it is possibile to see by the F-u curve, without fragile collapse modes, as provided by the analytical and numerical evaluation and, in corrisponding of P_3 istant, the buckling appears in the link flange.
- No cracks appear in the timbern beam;
- The vertical displacement achieves, due to the transducer limit (200 mm), is approximately 50% of the displacement expected for the collapse joint.

5.7 Cyclic tests

5.7.1 S2-c Test

Cyclic test is carried out according to the standard EN 12512 (CEN, 2005), which prescribes a loading history comprising of series of cycles at increasing amplitude, defined as a multiple of the yielding displacement u_y previously determined through the monotonic procedure (Fig. V.46).

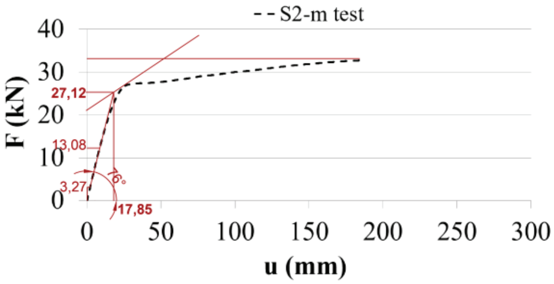

Figure V.186 – S2-c specimen: identification of yielding displacement from S2-m monotonic test for cyclic test protocol.

The test result on the *S2-c* specimen (HE100A joint) are presented in the Table V.21 step by step (P: point; C: cycle; F: force) and the test protocol is showed in the Figure V.47 and Table V.20.

$$u_y = 17,85 \text{ mm}$$

Table V.104 – S2-c specimen: imposed displacement values.

1x0,25u$_y$ [mm]	**1x0,5u$_y$ [mm]**	**3x0,75u$_y$ [mm]**	**3xu$_y$ [mm]**	**3x2u$_y$ [mm]**	**3x4u$_y$ [mm]**	**3x6u$_y$ [mm]**
4,4	8,9	13,3	17,8	35,7	71,4	107,1

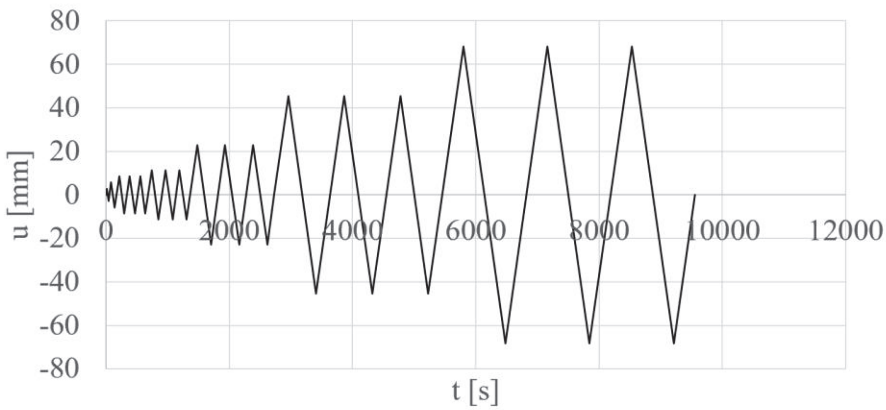

Figure V.187 – S2-c specimen: cyclic test protocol.

In the *Point 0*, in corresponding of a force F= 0 kN and a displacement of u= 0 mm, before the test, the specimen shows 2 visible cracks in the glue line of the additional element, on side B.

In the *Point 1 (Yielding)*, in corresponding of a force F_y= 27,72 kN and a displacement of u_y= 27,82 mm, cracks appear in the paint of the steel link which has reached yield point. The relative rotation between the end-plate and the timber beam is θ_{TP} = 0 rad.

In the *Point 2*, in corresponding of a force F= 33,12 kN and a displacement of u= 65,21 mm, the cracks thickness in the timber beam, on the B side, is increased. The relative rotation between the end-plate and the timber beam is θ_{TP} = 0,0019 rad.

In the *Point 3 (Ultimate cycle)*, in corresponding of a force F= 34,11 kN and a displacement of u= 89,95 mm, cracks appear in the paint of the stiffener which has reached yield point and the timber beam is θ_{TP} = 0,0034 rad.

Table V.105 –S2-c specimen test results: significative points.

Point 0
F=0 kN

u=0 mm

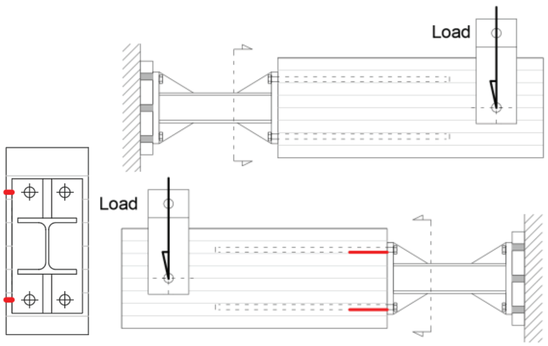

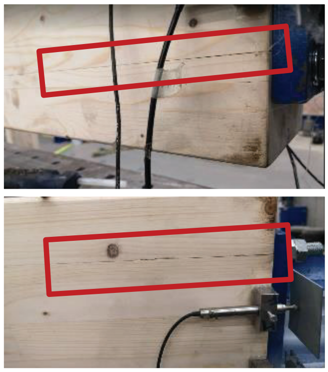

Point 1 (Yielding)
F=27,72 kN

u=27,82 mm

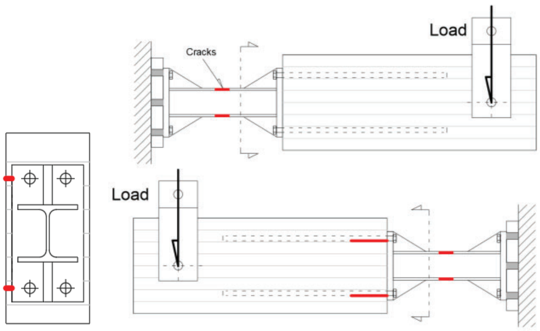

Point 2
F=33,12 kN

u=65,21 mm

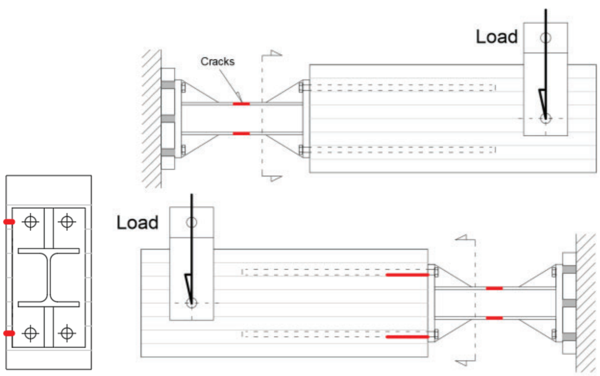

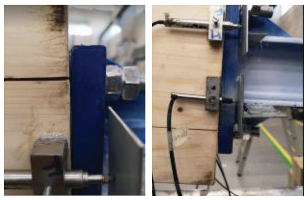

Point 3 (Ultimate cycle)

F=34,11 kN u=89,95 mm

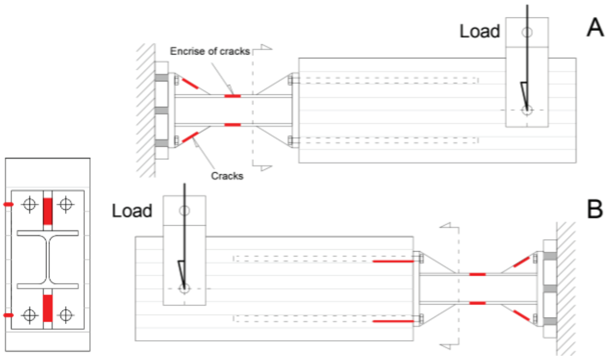

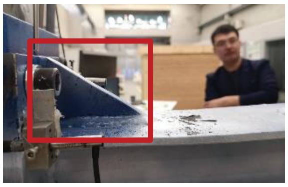

The comparison between the specimen before and after the test is shown in the Figure V.48a,b while the steel link and the bolts at the end of the test are shown in the Figure V:48c,d.

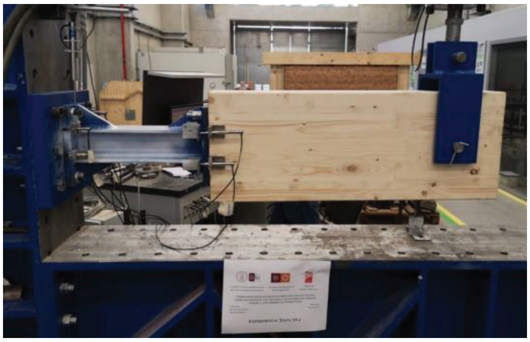

a)

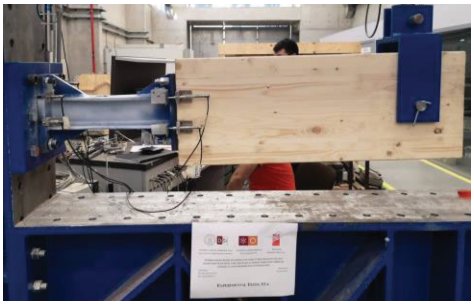

b)

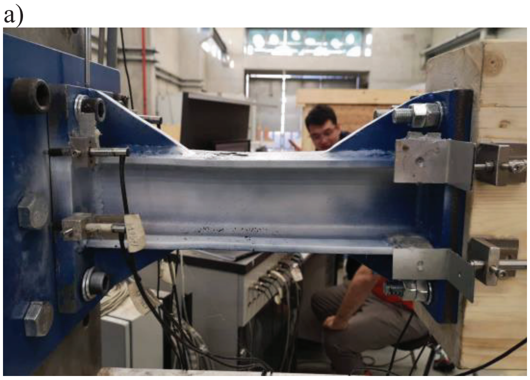

c)

d)

Figure V.188 – S2-c specimen: a) system before the test; b) system after the test; c) link after the test; d) bolts after the test.

The F-u and M-θ curves are shown in Figure V:49. In particular, the F-u curve is a direct output of the test machine while the M-θ curve was analytically evaluated (see chapter 5.4.4).

The output are presented in terms of force (F [kN]) and vertical displacement (u [mm]), resistant bending moment (M [kNm]) and rotation of the end of the timber beam respect to the rotation plastic center in the steel link (θ [rad]). In particular, on the curves are reported the significative points presented in the Table V.22, in which, the test results are presented also in terms of numerical values.

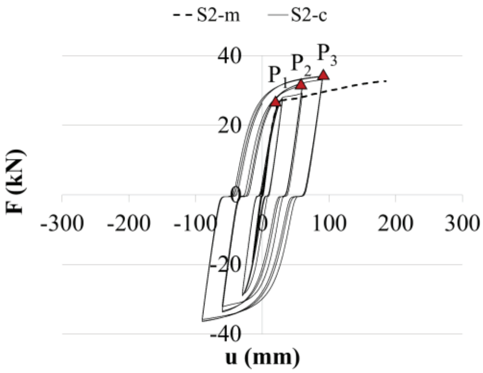

a)

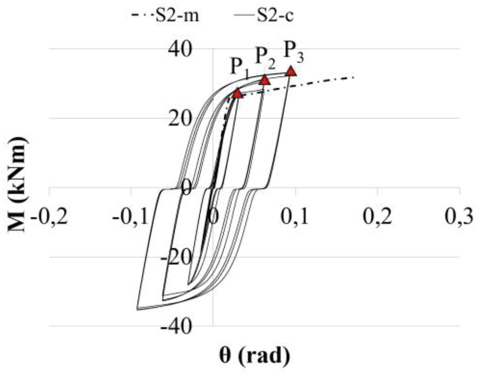

b)

Figure V.189 – S2-c specimen test results: a) force-displacement and b) moment-rotation curves.

Table V.106 – S2-c specimen test results: force (F), displacement (u), resistant bending moment (M) and rotation (θ) at yield (P_1) and end test (P_3) points.

Point	F [kN]	u [mm]	M [kNm]	θ [rad]
P_1 (Yielding)	27,72	27,82	26,01	0,025
P_3 (Ultimate cycle)	34,11	89,95	33,09	0,092

Analysing the test results on *S2-c* specimen, the following observations can be drawn:

- As shown in the pilot test, there is the formation of cracks at the added and glued timber parts which, however, do not have a structural importance and do not affect the relative rotation between the beam and the end-plate, that is very low.

- The joint shows great flexibility and ductility, as it is possibile to see by the F-u curve, without fragile collapse modes, as provided by the analytical and numerical evaluation;
- The glued joint resistes a tensile force F = 20% more than the expected resistance. This allows to affirm that the the safety coefficients for the “pull-out” and the “failure of the adhesive by debonding from steel or wood”, that are in the national and European standards, may be too high;
- The vertical displacement achieved, due to the transducer limit (200 mm), is approximately 82% of the displacement expected for the collapse joint, so that the specimen has not reached the collapse and it is not possible to check all the ductility capacity of the joint.

5.7.2 S3-c Test

Cyclic test is carried out according to the standard EN 12512 (CEN, 2005), which prescribes a loading history comprising of series of cycles at increasing amplitude, defined as a multiple of the yielding displacement u_y previously determined through the monotonic procedure (Fig. V.50).

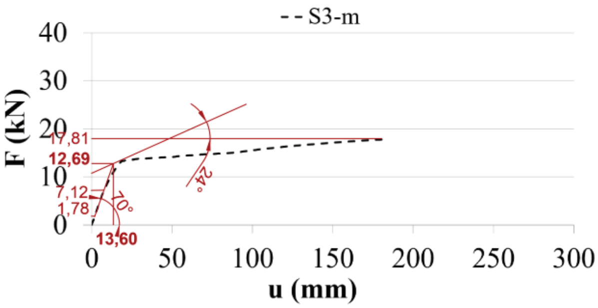

Figure V.190 – S3-c specimen: identification of yielding displacement from S2-m monotonic test for cyclic test protocol.

The test result on the *S3-c* specimen (IPE100 Link) are presented in the Table V.24 step by step (P: point; C: cycle; F: force) and the test protocol is showed in the Figure V.51 and Table V.23.

$$u_y = 13{,}60 \text{ mm}$$

Table V.107 – S3-c specimen: imposed displacement values.

1x0,25u_y [mm]	**1x0,5u_y [mm]**	**3x0,75u_y [mm]**	**3xu_y [mm]**	**3x2u_y [mm]**	**3x4u_y [mm]**	**3x6u_y [mm]**
3,4	6,8	10,2	13,6	27,2	54,4	81,6

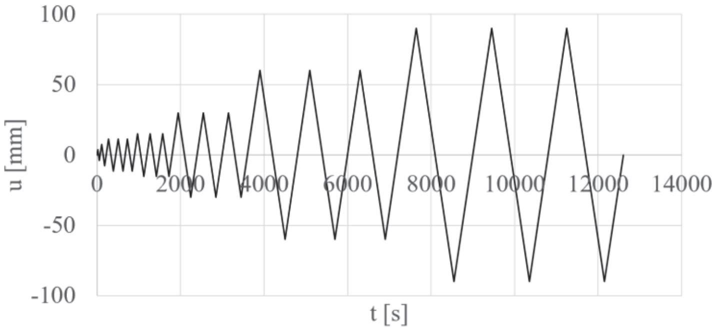

Figure V.191 – S3-c specimen: cyclic test protocol.

In this case, despite the total vertical displacement of the actuator reached during the last cycle $u_{up}+u_{down}$ = 163,2 mm, which is less than the maximum displacement allowed by the actuator, 200 mm, the test does not go further to avoid overheating of the lab machine.

In the *Point 1 (Yielding)*, in corresponding of a force F= 13,18 kN and a displacement of u= 12,94 mm, cracks appear in the paint of the steel link which has reached yield point. The relative rotation between the end-plate and the timber beam is θ_{TP} = 0 rad.

In the *Point 2*, in corresponding of a force F= 15,71 kN and a displacement of u= 65,21 mm, the cracks thickness in the timber beam, on the B side, is increased. The link that reach the complete plasticization of the plastic hinge. The relative rotation between the end-plate and the timber beam is θ_{TP} = 0 rad.

In the *Point 3 (Buckling)*, in corresponding of a force F= 16,83 kN and a displacement of u= 72,02 mm, the link flange reaches the buckling. The relative rotation between the end-plate and the timber beam is θ_{TP} = 0,0019 rad.

In the *Point 4 (Ultimate cycle)*, in corresponding of a force F= 11,93 kN and a displacement of u= 95,90 mm, cracks appear in the paint of the stiffener which has reached yield point and the timber beam is θ_{TP} = 0,101 rad.

Table V.108 – S3-c specimen test results: significative points.

Point 1 (Yielding) - Step 14/35

F=13,18 kN u=12,94 mm

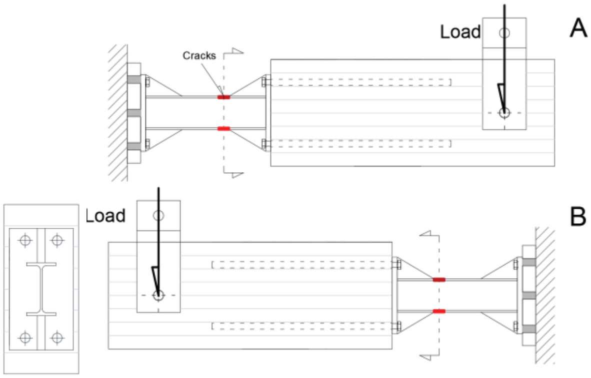

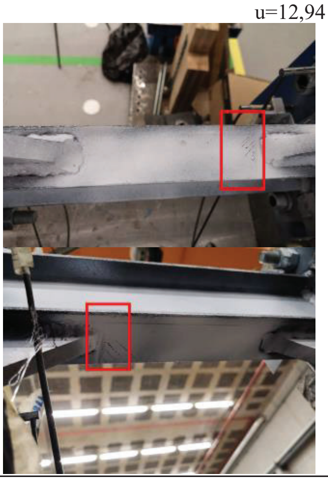

Point 2 - Step 22/35

F=15,71 kN u=65,21 mm

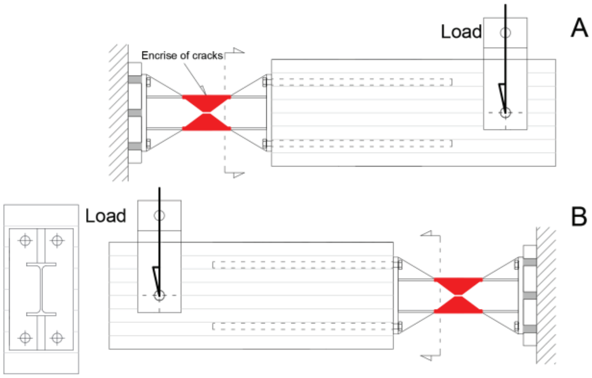

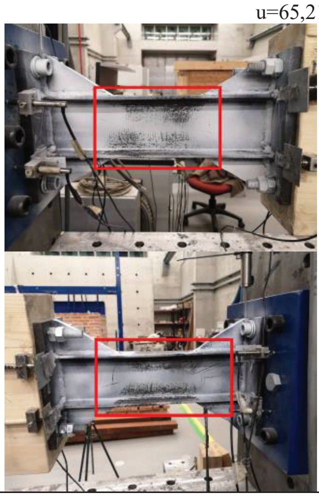

Point 3 (Buckling) - Step 35/35

F=16,83 kN

u=72,02 mm

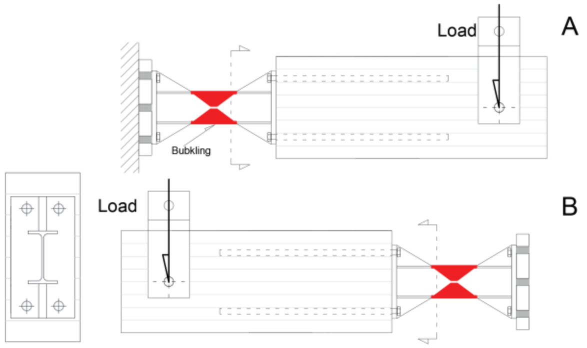

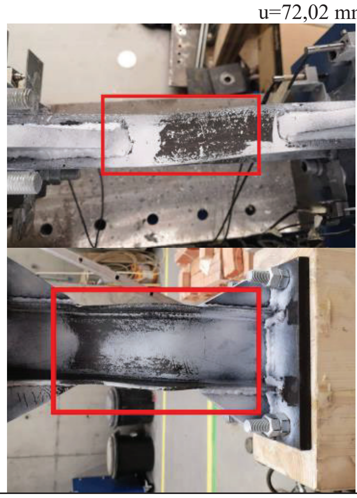

Point 4 (Ultimate cycle) - Step 35/35

F=11,93 kN

u=95,90 mm

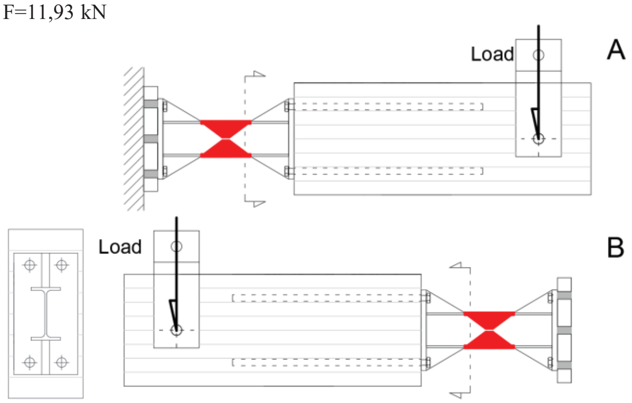

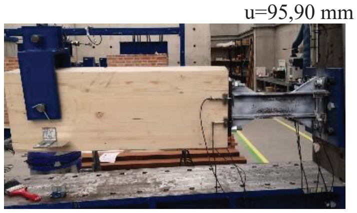

The comparison between the specimen before and after the test is shown in the Figure V.52a,b while the steel link and the bolts at the end of the test are shown in the Figure V.52c,d.

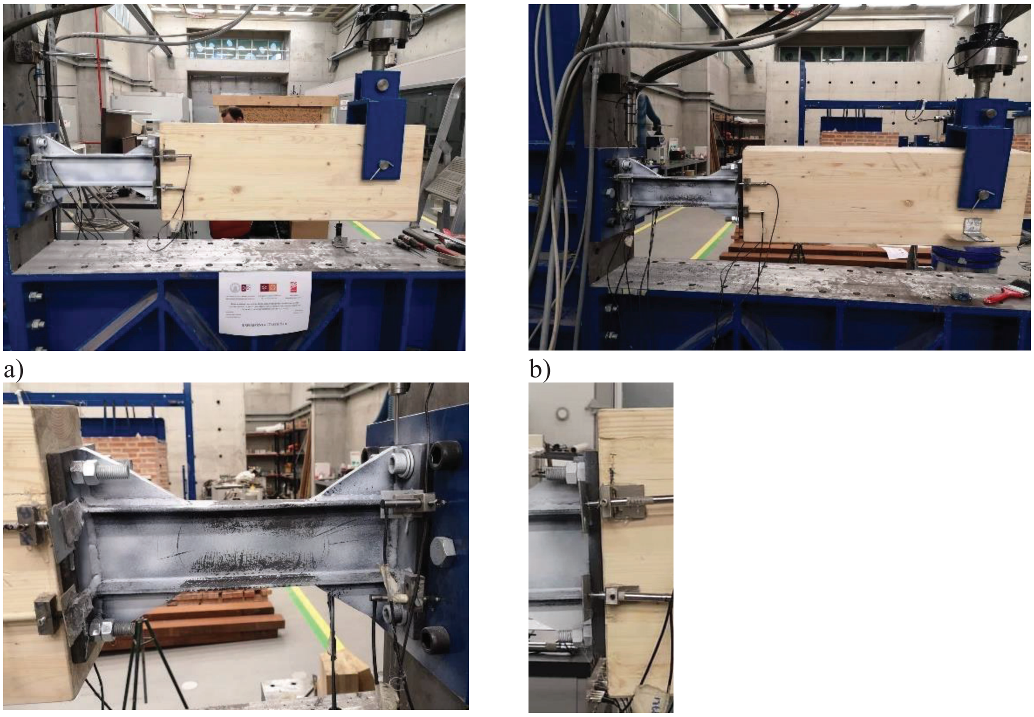

a) b) c) d)

Figure V.192 – S3-c specimen: a) system before the test; b) system after the test; c) link after the test; d) bolts after the test.

The F-u and M-θ curves are shown in Figure V.53. In particular, the F-u curve is a direct output of the test machine while the M-θ curve was analytically evaluated (see chapter 5.4.4).

The output are presented in terms of force (F [kN]) and vertical displacement (u [mm]), resistant bending moment (M [kNm]) and rotation of the end of the timber beam respect to the rotation plastic center in the steel link (θ [rad]). In particular, on the curves are reported the significative points presented in the Table V.25, in which, the test results are presented also in terms of numerical values.

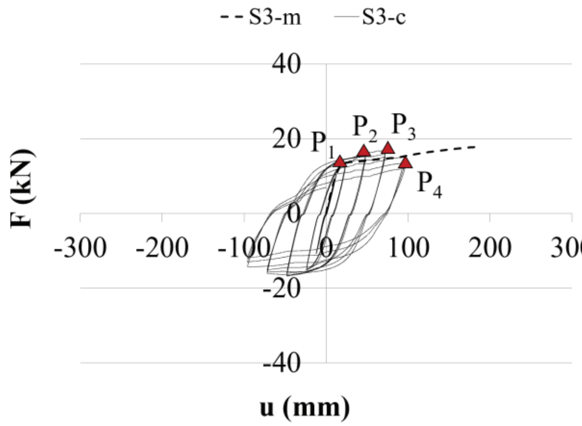

a)

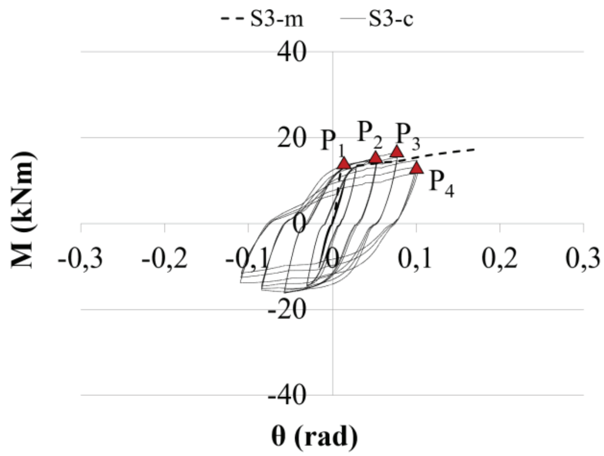

b)

Figure V.193 – S3-c specimen test results: a) force-displacement and b) moment-rotation curves.

Table V.109 – S3-c specimen test results: force (F), displacement (u), resistant bending moment (M) and rotation (θ) at yield (P_1), buckling (P_3) and end test (P_4) points.

Point	F [kN]	u [mm]	M [kNm]	θ [rad]
P_1 (Yielding)	13,18	12,94	14,01	0,011
P_3 (Buckling)	15,11	85,42	14,22	0,078
P_4 (Ultimate cycle)	11,93	95,90	11,66	0,101

Analysing the test results on *S3-c* specimen, the following observations can be drawn:

- The joint shows great flexibility and ductility, as it is possibile to see by the F-u curve, without fragile collapse modes, as provided by the analytical and numerical evaluation and, in corrisponding of P_3 istant, the buckling appears in the link flange;
- No cracks appear in the timbern beam;
- The vertical displacement achieves, due to the transducer limit (200 mm), is approximately 50% of the displacement expected for the collapse joint.

5.8 SUMMARY OF RESULTS

Analysing the experimental results, the following observations can be drawn. By comparing the experimental curves F-u and M-θ with the numerical ones, it is possible, first of all, to observe the correctness of the numerical model, perfectly calibrated.

In particular, as regard the monotonic tests, S2-m and S3-m, the yielding value (P_1) of force (F_y), displacement (u_y), bending moment (M_y) and rotation (θ_y) of both the specimens are perfectly coincident with those predicted by numerical analysis (P_Y). The models, therefore, show the same maximum elastic strength and stiffness of the tested specimens. The numerical models, however, have not been calibrated after the material tests on the steel link and the and-plate, for laboratory problem; for this reason, the post-elastic filed does not coincide. The comparison between the experimental and numerical F-u and M-θ curves are shown in Figure V.54.

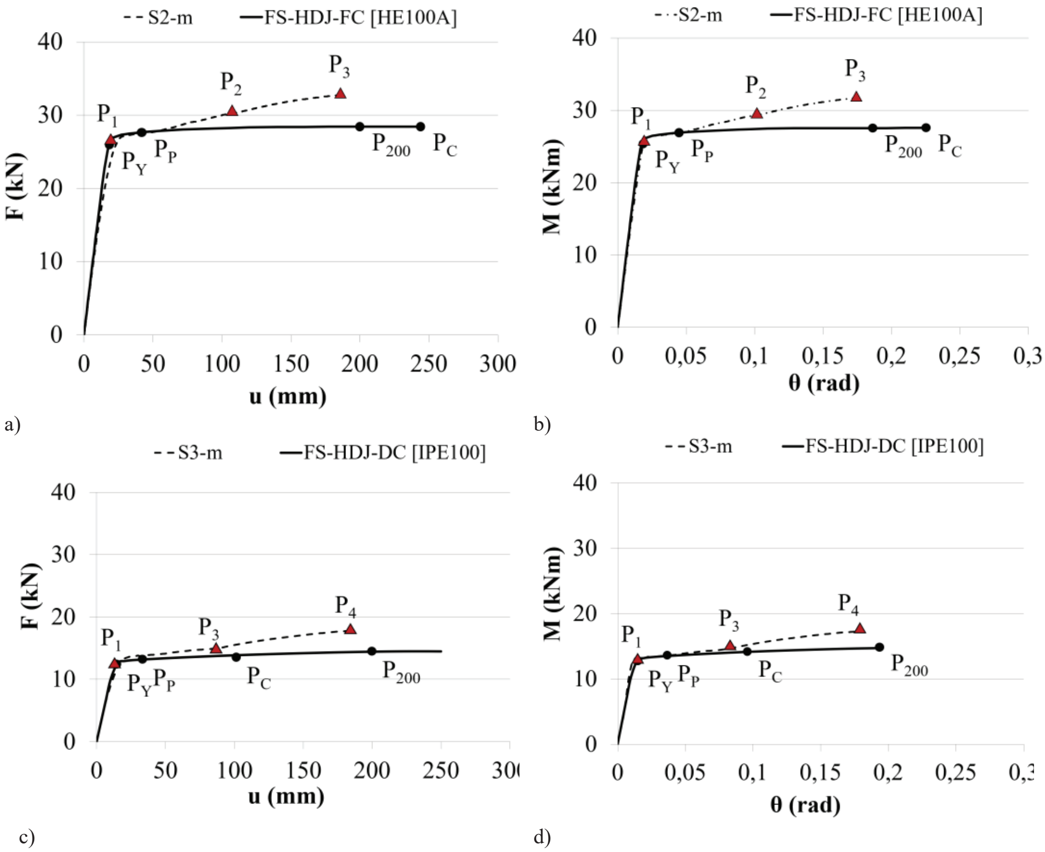

Figure V.194 – Comparison between numerical and experimental results: a) S2-m force-displacement and b) moment-rotation curves; c) S3-m force-displacement and d) moment-rotation curves.

The output are also presented in terms of numerical values of force (F [kN]), vertical displacement (u [mm]), resistant bending moment (M [kNm]) and rotation of the free end of the timber beam respect to the rotation plastic center in the steel link (θ [rad]) in the Table V.26 and Table V.27, both for S2-m and S3-m. In particular, the comparison between the numerical and the test results are presented. The proximity of the parameters values analysed is clearer by observing the histograms, which refer to the values of force, vertical displacement, moment and rotation evaluated in the significative points of yield (P_Y), collapse (P_C) and at 200 mm (P_{200}), for both S2-m and S3-m, compared to the numerical models results.

Below the comparison of the S2-m with its numerical model.

Table V.110 – S2-m joint: comparison between numerical, analytical and experimental results.

S2-m												
Point	**F [kN]**			**u [mm]**			**M [kNm]**			**θ [rad]**		
	Ana.	**Num.**	**Test**	**Ana.**	**Num.**	**Test**	**Ana.**	**Num.**	**Test**	**Ana.**	**Num.**	**Test**
P_Y	26,63	25,5	27,11	11,05	17,42	17,73	25,83	24,73	25,77	0,017	0,016	0,021
P_{200}	29,54	28,4	32,71	183	200	184,97	28,65	27,52	31,77	0,19	0,187	0,18
P_C	30,38	29,35	/	235	242	/	29,47	28,41	/	0,285	0,215	/

Force F [kN]

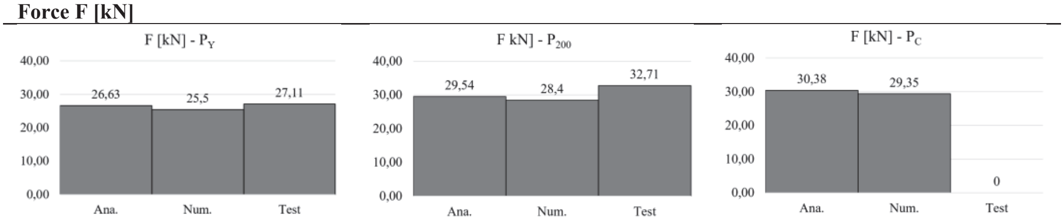

Vertical Displacement u [mm]

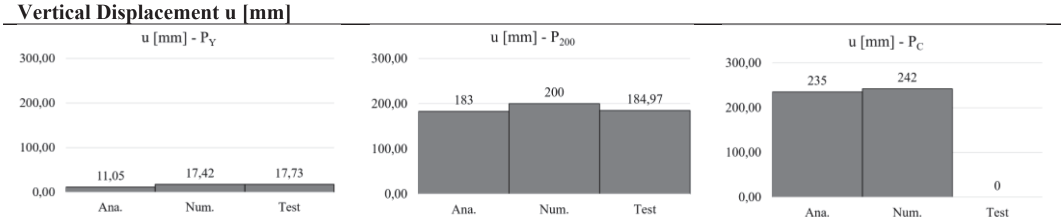

Bending moment M [kNm]

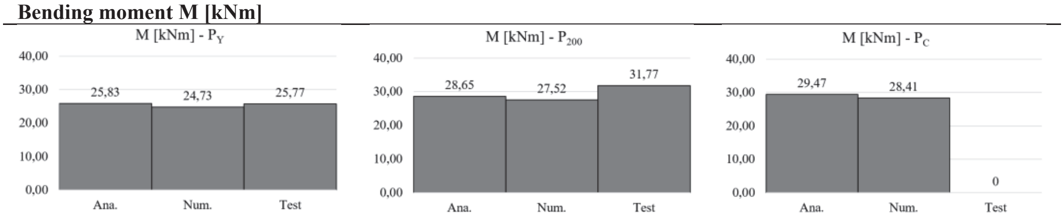

Rotation θ [rad]

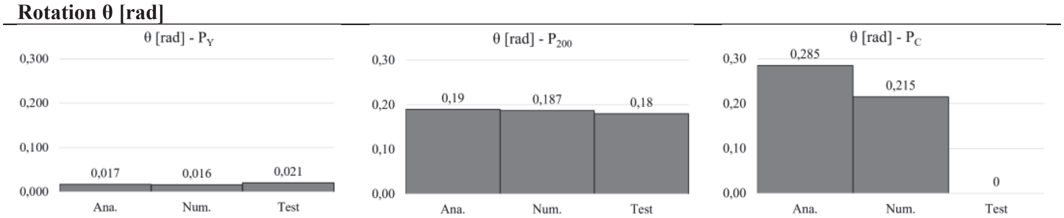

Below the comparison of the S3-m with its numerical model.

Table V.111 – S3-m joint: comparison between numerical, analytical and experimental results.

S3-m												
Point	**F [kN]**			**u [mm]**			**M [kNm]**			**θ [rad]**		
	Ana.	**Num.**	**Test**	**Ana.**	**Num.**	**Test**	**Ana.**	**Num.**	**Test**	**Ana.**	**Num.**	**Test**
P_Y	12,52	11,61	12,89	10,60	13,38	14,96	12,14	11,24	12,04	0,016	0,009	0,013
P_C	14,42	14,01	15,4	85,90	105	97,32	13,99	14,28	14,03	0,098	0,11	0,084
P_{200}	15,09	14,45	17,81	175,81	200	184,97	14,56	15,01	17,27	0,153	0,19	0,176

Force F [kN]

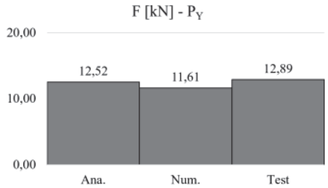

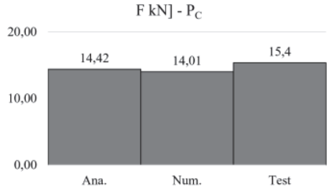

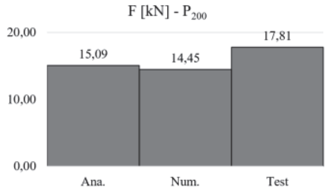

Vertical Displacement u [mm]

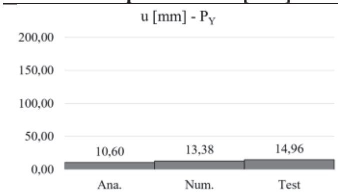

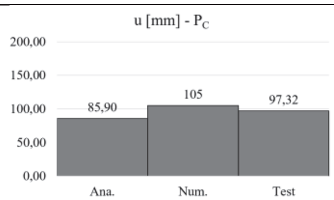

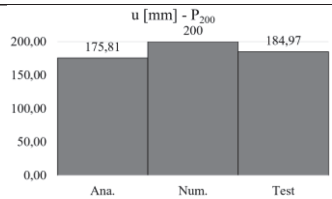

Bending moment M [kNm]

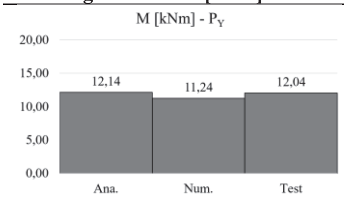

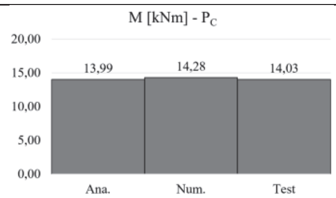

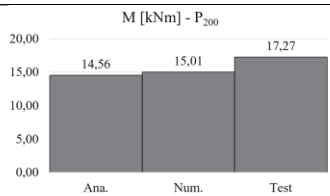

Rotation θ [rad]

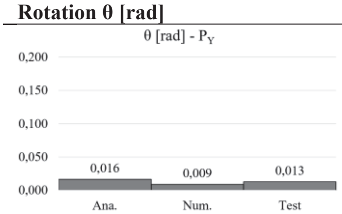

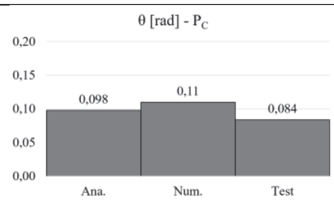

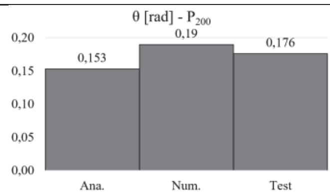

As for the collapse modes, it is not possible to evaluate, through experimental testing, the hierarchy of resistance of the connection "sub-components" but, by superimposing the images deriving from the numerical analysis with the photos taken at the end of the test (P_C), it is possible to observe a good coincidence between the results (Fig. V.55).

S2-m

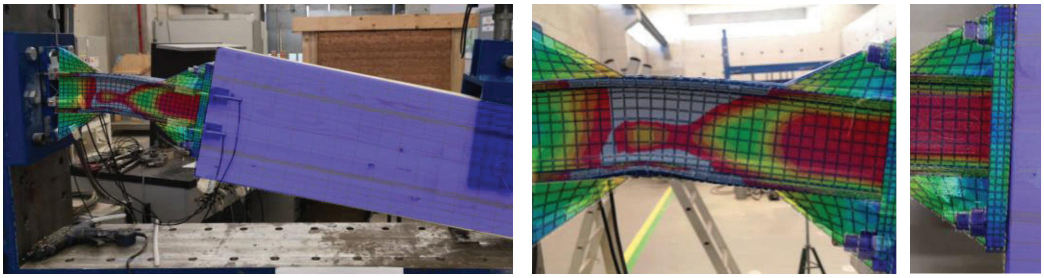

a) b) c)

S3-m

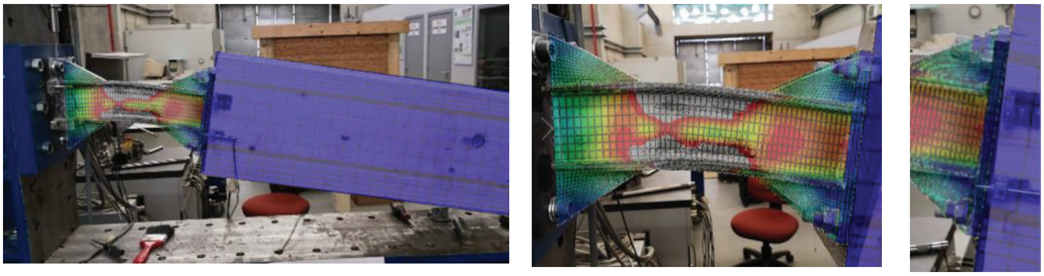

d) e) f)

Figure V.195 – S2-m and S3-m specimen comparison between numerical and experimental results: a) S2-m global joint, b) link and c) end-plate - timber beam connection; d) S3-m global joint, e) link and f) end-plate - timber beam connection.

Below the comparison of the S2-m and S3-m with their numerical models and monotonic tests (Fig. V.56).

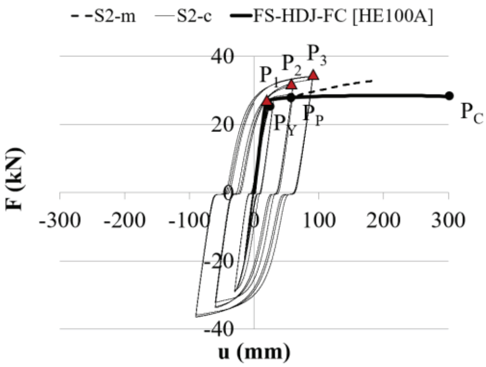

a)

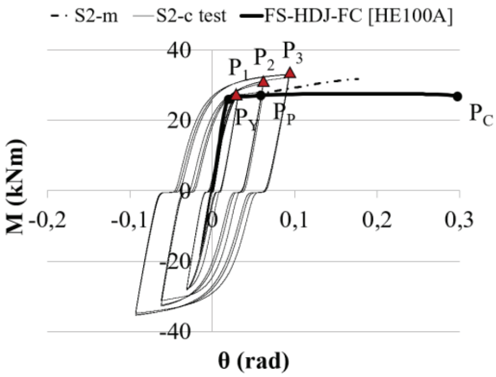

b)

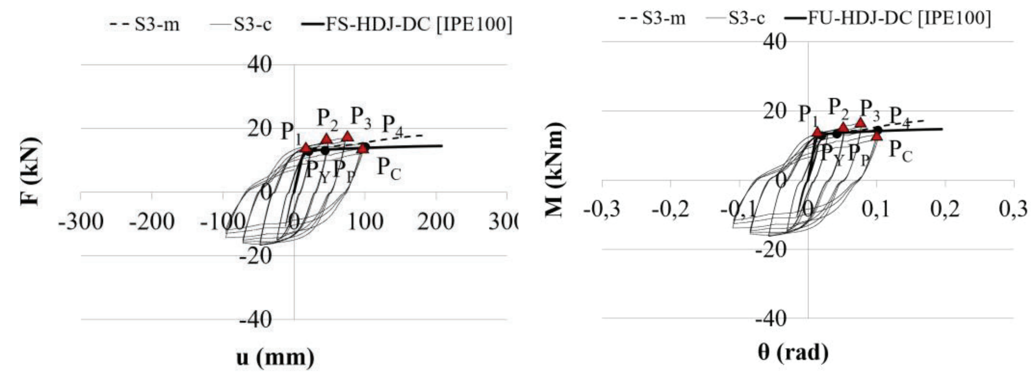

c) d)

Figure V.196 – Comparison between numerical, monotonic and cyclic tests results: a) S2-m force-displacement and b) moment-rotation curves; c) S3-m force-displacement and d) moment-rotation curves.

In conclusion, the experimental tests confirmed:

- The correctness of the numerical model;
- The validity of analytical formulations based on capacity design for "macro-components" and "sub-components";
- The ductility of the system is entirely delegated to the steel link which, being characterized by Class 1 steel profiles, has a high dissipative capacity. The joint, therefore, can be used for the design of structures in the high ductility class (HDC);
- The connection between the timber beam and the end-plate proved to be rigid.

CONCLUSIVE REMARKS

Timber is a structural material with numerous advantages that can be exploited for the design of structures in a seismic area, such as the low density and deformability that entail the reduction of seismic actions; on the other hand, it is a material with an elastic-fragile behaviour. Currently, in the seismic resistant timber structures design, the dissipative capacity is delegated to the connections with steel connectors, which can dissipate a part of the seismic energy through their plastic deformations. The connections, however, are themselves main structural elements, allowing the timber structural members assembly, typically prefabricated, and the transfer on internal forces between the members. To overcome this problem, therefore, the dissipative capacity should be delegated to specific devices, ad hoc designed. With these premises, the work focused on the study of seismic resistant heavy timber framed structures equipped with two different dissipative devices: *steel links* and *fluid viscous dampers* (FVD), which dissipate seismic energy respectively by plastic deformations and by viscous friction, while the remaining part of the structure, consisting of the timber members and the steel connections, is designed with opportune overstrength, so that to remain in the elastic field. This topic is noteworthy, it being as background for the development of the chapter on seismic-resistant timber structures of the technical standards for constructions in both Italian and European field. The study is object of the Reluis/DPC 2019-2021 WP3 project - Contributions to standards for timber structures - Task 1: Heavy timber frame structures (prof. B. Faggiano coordinator).

The study methodology is very extensive, including the following activities: conception of global structural type systems and structural details; definition of the design criteria for global and local systems; analysis of the seismic performance of the structures by means of non-linear, parametric numerical analysis, both static incremental and time-history dynamic analyses (using SAP2000 software); study of beam-to-column joints with dissipative steel links through both monotonic and cyclic numerical analysis on advanced FE models (using ABAQUS software), and through experimental tests on full-scale joint assemblies. In particular, the experimental campaign was carried out, in a research period of more than 3 months, at the Department of Civil Engineering of the University of Minho, in Guimaraes (Portugal), with the cooperation of Prof. Jorge Branco.

The results achieved are really interesting: for the design of seismic resistant heavy timber structures with rigid connections or bracings systems, with dissipative capacities, it is possible to use the design criteria based on the capacity design procedure, through the application of the component method, already widely used in the field of steel structures, extending it to the joints between the timber members and exemplifying the application to study cases. The structural performance of the global systems was assessed, through the performance parameters evaluation, such as stiffness, strength, ductility, dissipative capacity, and the behaviour factors were defined, with encouraging results that demonstrate the efficiency and convenience of the studied structural systems.

Based on the analytical and numerical results, for multi-story heavy timber buildings in seismic areas, the moment resisting frames and bracing systems with steel links appear to be very promising. In fact, by integrating this innovative system into timber structures, brittle wood failure modes can be avoided, and overall seismic performance can be improved. The dissipative joint behaviour, designed by the capacity design approach and studied by way of numerical analyses and experimental tests, confirmed the formation of the plastic hinge in the link and the collapse hierarchy of the connection sub-components, validating both the efficiency of the system, the used design method and showing a high dissipative capacity. In terms of the global behaviour, the steel links play a key role in the structural strength and stiffness since they are significantly influenced by their plastic strength, varying according to the structural type. One-storey structures are studied to understand if the q-factor, q_d, used for the same steel structural type could be applied also for the heavy timber structures with steel link. Ascertained this and observing that the q-factor is, in some cases, even greater than that for steel structures, the multi-storey structures are analysed. There was a proportional variation of the strength and the stiffness, with the low variation of q-factor. In terms of weight, all structural typologies show a mass reduction from 10%, for MRF structures, to 73% for structures with eccentric bracing (EBF). The mass reduction corresponds to low seismic design forces, smaller structural elements, lower foundation forces and consequent cost savings that can potentially offset the higher cost of timber as compared to steel or concrete. The expertise coming from steel constructions was a solid reference to approach this issue and to provide the bases for the seismic design of heavy timber structures.

The joint with steel link is conceived and designed to be easily replaced after earthquake, with minimal repair costs. In particular, the link is connected by bolts to a steel-box (Fig. 1a), consisting of two 15 mm steel end-plates welded to the ends of a steel profile (the same profile of the link) and closed by two 7 mm thickness steel T ribs; the steel-box is connected to the timber beam (Fig. 1b) and to the timber column (at the base) (Fig. 1c) by glued bolts. After earthquake, the bolts, which connect the link and the steel-box, can be removed and it is possible to replace the link.

In Figure 2 the 3D drawing of 2-storeys heavy timber frame structure with steel link is presented.

It is possible to insert inspection hatches inside the infill so that, after the earthquake, the link can be removed and replaced, without breaking down the infill or creating inconvenience to the functionality of the building.

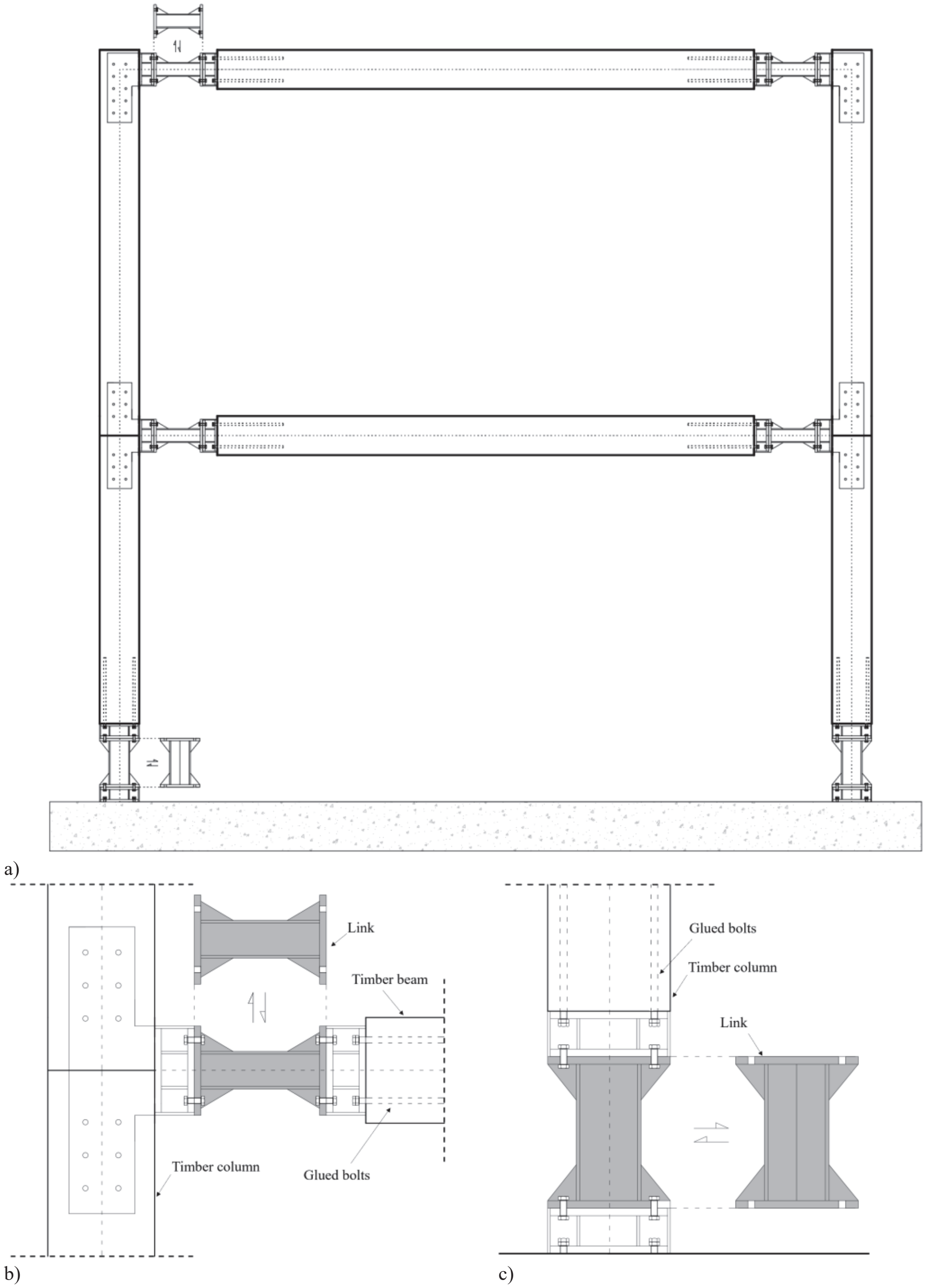

Figure .197 – Seismic resistant heavy timber frame structure with steel link: a) 2-storeys MRF structure; b) beam-to-column joint with link; c) column-to-foundation joint with link.

Below are presented a 3D of 2-storeys heavy timber frame structure with steel link (Fig. 2).

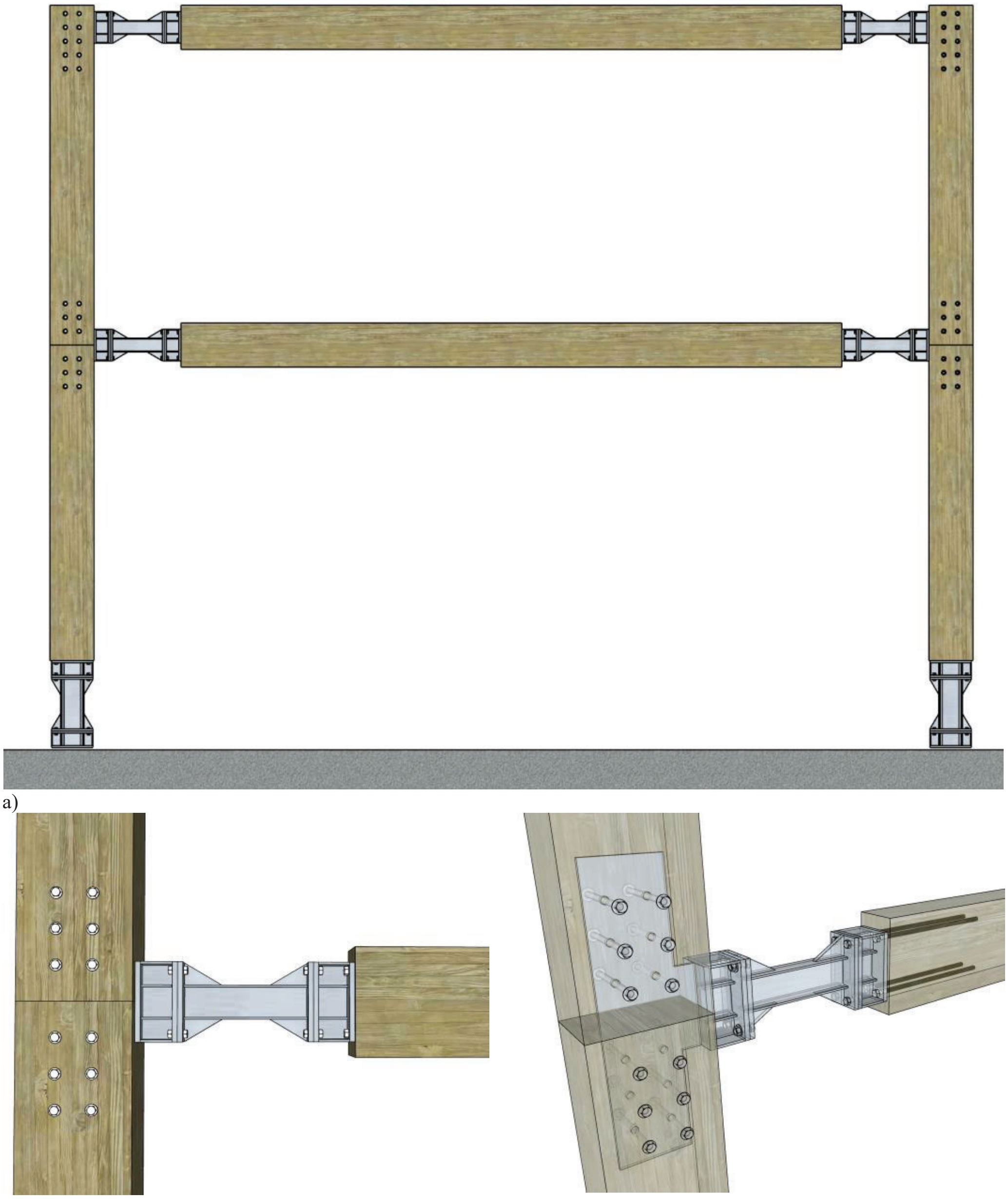

a)

b)

c)

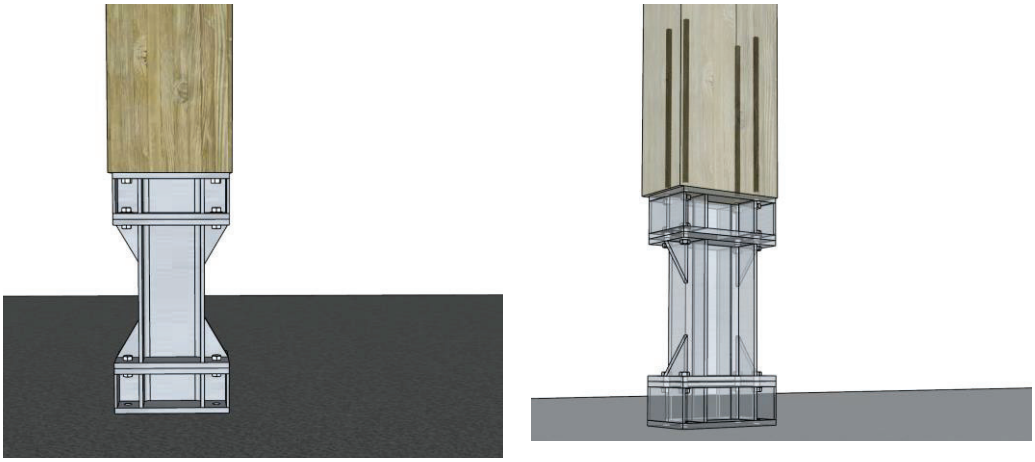

d) e)

Figure .198 – 3D of 2-storeys seismic resistant heavy timber frame structure with steel link: a) 2-storeys MRF structure; b) and c) beam-to-column joint with link; d) and e) column-to-foundation joint with link.

The results of the numerical investigation on the timber structures equipped by FVDs, however, show high reduction of the structural mass, up to 40-50%, compared to the non-dissipative ones, re-centering capability of the structure, which remains in the elastic field without damage, high dissipative capacity of the structure, which can absorb up to 95% of the seismic energy (Tab. 1), less expensive and complex connections. The reduction of production and maintenance costs follows. All these involve the enhancement of structural performance and sustainability under earthquakes.

Table .112 – Structural mass [kg] and DCR [%] for ξ=20%.

	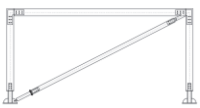		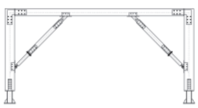	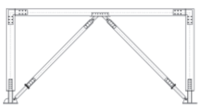
MRF	**MRF-D**	**MRF-H$_1$L$_1$**	**MRF-H$_2$L$_2$**	**MRF-H$_3$L$_3$**
M= 676 kg	M= 290 kg DCR= 90%	M= 489 kg DCR= 35%	M= 383 kg DCR= 89%	M= 375 kg DCR= 90%

Below are presented a 3D of 2-storeys heavy timber frame structure MRF-D and MRF-H$_2$L$_2$ with FVDs (Fig. 4).

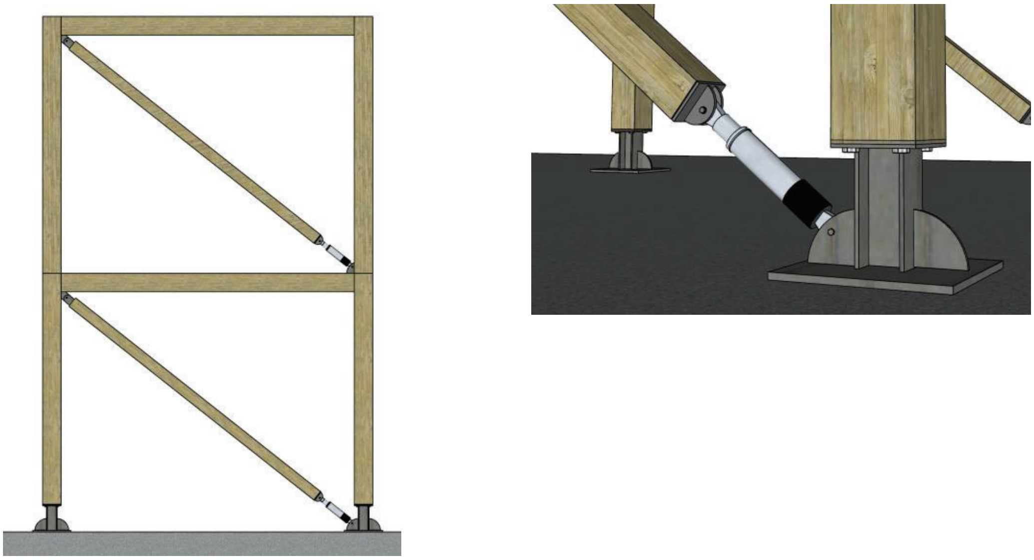

a) b)

Figure .199 – 3D of 2-storeys seismic resistant heavy timber frame structure with FVDs: a) and c) 2-storeys MRF-D structure; b) FVD in MRF-D structure.

It is possible, also in this case, to insert inspection hatches inside the infill in order to remove the FVD or for maintenance.

In conclusion, the proposed solutions allowed to obtain hybrid-structures timber-steel and structures with FVDs with a high dissipative capacity that, in some cases, are better than steel structures, with a consistent reduction of material but, for the purpose of design criteria calibration, huge both experimental and analytical campaigns of investigation on both timber structural systems, on their sub-assemblage and global components is required. In particular, it is necessary to define local requirements for dissipative zones and properties of materials; calibrate the behaviour factor, q_0, for the different ductility classes; specify the overstrength factors, γ_{Rd}; and therefore introduce the structural types of timber moment resisting frames and bracing frames with the respective design rules.

Studies will proceed in these articulated directions.

REFERENCES

JOURNALS, CONFERENCES AND TECHNICAL REPORTS

Abidelah A., Bouchaïr A., Kerdal D.E. (2012). Experimental and analytical behavior of bolted end-plate connections with or without stiffeners. In: *Journal of Constructional Steel Research*, 76:13.

Akan A. (2004). Some Observation on the seismic behaviour of traditional timber structures in Turkey. *Ph.D. thesis*, June 2004.

Andreolli M. (2001). Giunti semirigidi con barre incollate per strutture lignee. *Ph.D. thesis* in "Ingegneria dei Sistemi Strutturali Civili e Meccanici", Supervisor: Prof. Piazza M., Dott. Tomasi R.

ANSI/AISC 358-10 (2010). Prequalified Connections for Special and Intermediate Steel Moment Frames for Seismic Applications.

ANSI/AISC 358-16 (2016). Prequalified Connections for Special and Intermediate Steel Moment Frames for Seismic Applications.

Aytun A. (1981). Earthen buildings in seismic areas of Turkey. In: *Proceedings of the International Workshop on Earthen Buildings*, Vol. 2, Albuquerque, NM, 1976:352.1.

Bakel R.V., Rinaldin G., Leijten Ad. J.M., Fragiacomo M. (2016). Experimental tests and numerical modelling of timber joints with tube fasteners. In: *World Conference on Timber Engineering (WCTE2016)*, August 22-25, 2016, Vienna, Austria.

Bezabeh M.A., Tesfamariam S., Siegfried F.S. (2014). Equivalent viscous damping for CLT infilled steel moment frame structures. In: *World Conference of Timber Engineering (WCTE2014)*, August 10-14, 2014, Quebec City, Canada.

Bianco A. (2010). The baraccata house. Guide to desainig and restauration site (in Italian). Rome: GB EditoriA; 2010. p. 19, 29, 60.

Bijlaard F.S.K., Nethercot D.A., Stark J.W.B., Tschemmernegg F., Zoetemeijer P. (1989). Structural properties of semi-rigid joints in steel frames. In: *IABSE Periodica*, 2, 33.

Bouchair A., Racher P., Bocquet J. (2007). Analysis of Dowelled Timber Moment-Resisting Joints. In: *Materials and Structures*. 40, 1127-1141.

Buchanan A. and Fairweather R. (1993). Seismic Design of Glulam Structures. In: *Bulleton of the New Zealand National Society for Earthquake Engineering*. 26(4), 415-436.

Calderoni B., Bedon C., Ceraldi C., Faggiano B., Follesa M., Fragiacomo M., Gattesco N., Giubileo C., Gubana A., Iovane G., Lauriola M.P., Martinelli E., Pizzo B., Podestà S., Sandoli A. (2019). The instructions for the design, execution and control of timber construction (CNR-DT 206 R1/2018). In: *XVII Convegno ANIDIS*, Ascoli Piceno, 2019 September 15-19.

Casagrande D., Doudak G., Polastri A. (2019). A proposal for the capacity-design at wall- and building-level in light-frame and cross-laminated timber buildings. In: *Bulletin of Earthquake Engineering*, 17: 3139. doi: 10.1007/s10518-019-00578-4.

Ceccotti A., Follesa M., Lauriola M.P. (2005). Le strutture in legno in zona sismica. Clunt Editore, Torino, 456 p.

Ceccotti A., Follesa M., Lauriola M.P. (2007). Le strutture di legno in zona sismica. 2° edizione, ISBN: 9788879922418.

Christopoulos C., Filiatrault A., Uang C.M., Folz, B. (2002). Post-tensioned energy dissipating connections for moment-resisting steel frames. In: *Journal of Structural Engineering* 128:9, 1111-1120.

Cóias V. (2007). Structural rehabilitation of old buildings (in Portuguese). Lisbon: Argumentum, GECoPRA.

Cóias V. and Silva E. (2002). Using advanced composites to retrofit Lisbon's old seismic resistant timber framed buildings. C. Bertolini Cestari, J. Amorim Faria, A. Soikkeli, editors. In: *European Timber Buildings as an Expression of Technological and Technical Cultures*, Elsevier, p109-124.

Copani P. (2007). Timber-frame buildings in Scandinavia: high deformation prevent the system from collapse. In: *From Material to Structure - Mechanical Behaviour and Failures of the Timber Structures ICOMOS IWC - XVI International Symposium*. Florence, Venice and Vicenza 1116 November 2007. (Available at http://www.icomos.org/iiwc/2007.htm).

Curee (2008). Consortium of Universities for Research in Earthquake Engineering: Caltech Woodframe Project, last updated 2004. http://www.curee.org/projects/woodframe/.

D'Aniello M., Landolfo R., Piluso V., Rizzano G. (2012). Ultimate Behaviour of Steel Beams under NonUniform Bending. In: *Journal of Constructional Steel Research*, 78, 144–158.

D'Aniello M., Tartaglia R., Costanzo S., Landolfo R. (2017). Seismic design of extended stiffened end-plate joints in the framework of Eurocodes. In: *Journal of Constructional Steel Research*, Vol 128, pp 512-527.

Da Silva Simoes L. (2008). Towards a consistent design approach for steel joints under generalized loading. In: *Journal of Constructional Steel Research*, 64, 1059-1075, 2008.

Da Silva Simoes L. and Girao Coelho A. (2001). A ductility model for steel connections. In: *Journal of Constructional Steel Research*, 2001; 57:45–70.

Da Silva Simoes L. and Girao Coelho A.A. (2001). Ductility model for steel connections. In: *Journal of Constructional Steel Research*, 2001; 57:45–70.

Da Silva Simoes L., Santiago A., Vila Rea P. (2001). A component model for the behaviour of steel joints at elevated temperatures. In: *Journal of Constructional Steel Research*, 57 (2001) 1169–1195.

Del Savio A.A. (2008). A component method model for semi-rigid steel joints including bending moment-axial force interaction. *Ph.D. Degree Thesis*, Supervisors: Prof. Sebastião Arthur Lopes de Andrade, Prof. Pedro Colmar Gonçalves da Silva Vellasco, Prof. David Arthur Nethercot. Thesis presented to the Post-graduate Program in Structural Engineering, of Department of Civil Engineering, PUC-Rio, as partial fulfillment of the requirements for the Ph.D. Degree in Structural Engineering.

Del Savio A.A., Nethercot D.A., Vellasco P., Andrade S.A.L., Martha L.F. (2009). Generalised component-based model for beam-to-column connections including axial versus moment interaction. In: *Journal of Constructional Steel Research*, 65(8-9), pp. 1876-1895.

Della Corte G., De Matteis G., Landolfo R., Mazzolani F.M. (2002). Seismic analysis of MR steel frames based on refred hysteretic models of connections, In: Journal of Constructional Steel Research, vol. 58, no. 10, pp. 1331–1345, 2002.

Devereux C.P., Holden T.J., Buchanan A.H., Pampanin S. (2011). NMIT Arts & Media Building - Damage Mitigation Using Post-tensioned Timber Walls. In: *Proceedings of the Ninth Pacific Conference on Earthquake Engineering Building an Earthquake-Resilient Society*, 14-16 April, 2011, Auckland, New Zealand.

Dinehart D.W. and Shenton H.W. (1998). Comparison of the response of timber shear walls with and without passive dampers. In: *Proceeding of Structural Engineers World Congress*, San Francisco, CA, July, Paper T207-5.

Dinehart D.W., Shenton H.W., Elliott T.E. (1999). The dynamic response of wood-frame shear walls with viscoelastic dampers. In: *Earthquake Spectra* 15 (1), 67–86.

Dolan J.D. (1989). The dynamic response of timber shear walls. *Ph.D. Thesis*, University of British Columbia, Dept. of Civil Engineering, Vancouver, B.C., Canada.

Faella C., Piluso V., and Rizzano G. (2000). Structural Steel Semirigid Connections, CRC Press, Florida, FL, USA, 2000.

Faggiano B. and Iovane G. (2016). First considerations on the design approach and criteria for seismic resistant moment resisting and bracings timber frames. In: *World Conference on Timber Engineering (WCTE2016)*, 22-25 August, Vienna, Austria, CD-ROM. Full paper ID1094.

Faggiano B., De Cesbron E., De La Grennelais E., Landolfo R. (2003). Design criteria for RBS in MR frame retrofitting. In: *Proceedings of 4th International Conference Behaviour of steel structures in seismic areas*, edited by F.M. Mazzolani, (A.A. Balkema, Netherlands, 2003), pp. 683-690.

Faggiano B., Iovane G., Salzillo D., Mazzolani F.M., Landolfo R. (2019). Dissipative bracing systems for seismic upgrading of new and existing timber structures. In: *5th International Conference on Structural Health Assessment of Timber Structures (SHATIS 2019)*. ISBN: 978-989-54496-2-0.

Faggiano B., Iovane G., Tartaglia R., Ciccone G., Landolfo R., Mazzolani F.M., Andreolli M., Tomasi R., Piazza M. (2018). Numerical simulation of monotonic tests on beam-column timber joints equipped with steel links for heavy timber seismic resistant MRF. In: *International Conference of Numerical Analysis and Applied Mathematics (ICNAM2018)*.

Fajfar P. (1999). Capacity spectrum method based on inelastic demand spectra. In: *Earthquake Engineering & Structural Dynamics*. 28(9):979–993.

Fajfar P. and Krawinkler H. (2004). Performance-Based Seismic Design Concepts and Implementation. In: *Proceedings of the International Workshop Bled*, Slovenia, June 28 - July 1, 2004. PEER Report 2004/05, College of Engineering, University of California, Berkeley.

Federlegno Arredo (2018). Terzo rapporto case ed edifici in legno, 2018.

FEMA. 2000. Prestandard and Commentary for the Seismic Rehabilitation of Buildings, FEMA 356. Washington, DC: Federal Emergency Management Agency.

FEMA. 2010. Federal Emergency Management Agency. Last modified August 2010. http://www.photolibrary.fema.gov/photolibrary/index.jsp.

Filiatrault A. (1990). Analytical predictions of the seismic response of friction damped timber shear walls. In: *Earthquake Engineering & Structural Dynamics*. 19, 259–273.

Flanagan D.P. and Belytschko T. (1981). A Uniform Strain Hexahedron and Quadrilateral with Orthogonal Hourglass Control. In: *International Journal for Numerical Methods in Engineering*, vol. 17, pp. 679–706.

Follesa M., Fragiacomo M., Casagrande D., Tomasi R., Piazza M., Vassallo D., Canetti D. Rossi S. (2018). The New Provisions for the Seismic Design of Timber Buildings in Europe. In: *Engineering Structures* 168(2018) 736–747. doi:10.1016/j.engstruct.2018.04.090.

Fujita K., Hanazato T., Sakamoto I. (2004). Earthquake response monitoring and seismic performance of fivestoried timber pagoda. In: *World Conference on Earthquake Engineering (WCEE2004)*, Vancouver, B.C., Canada August 1-6, 2004 Paper No. 54.

Gohlich R. (2015). Development of an innovative hybrid timber-steel moment-resisting frame for seismic-resistant heavy timber structures. *Master's Thesis*: Department of Civil and Environmental Engineering, Carleton University, Ottawa, Canada; 2015.

Gohlich R. (2016). Development of an Innovative hybrid timber-steel moment-resisting Frame for seismic-resistant heavy timber structures. Carleton University. 2016.

Gohlich R. and Gilbert C.F. (2015). Nonlinear dynamic analysis of innovative high r-factor hybrid timber steel buildings. In: *The 11th Canadian Conference on Earthquake Engineering* (CCEE). Quebec City, Canada.

Gohlich R. and Gilbert C.F. (2016). Development of a heavy timber moment-resisting frame with ductile steel links. In: *World Conference on Timber Engineering (WCTE2016)*, August 22-25, 2016, Vienna, Austria.

Gohlich R., Gilbert C.F., Woods J.E. (2018). Experimental testing and numerical modelling of a heavy timber moment-resisting frame with ductile steel links. In: *Earthquake Engineering & Structural Dynamics*, 2018;47:1460–1477. DOI: 10.1002/eqe.3025.

Gonzalez B.G. (2016). Local ductility in timber beam to column connections. In: *World Conference on Timber Engineering (WCTE2016)*, August 22-25, 2016, Vienna, Austria.

Grippa M.R. (2009). Structural identification of ancient timber constructions by non-destructive techniques. *PhD Thesis*. University of Naples, Federico II.

Gross J.L., Engelhardt M.D., Uang C.M., Kasai K., Iwankiw N.R. (1999). Modification of Existing Welded Steel Moment Frame Connections for Seismic Resistance. In: *AISC Design Guide Series 12*, American Institute of Steel Construction, Chicago, Illinois.

Gülhan D. and Güney IÖ. (2000). The behavior of traditional building systems against earthquake and its comparison to reinforced concrete frame systems: experiences of Marmara earthquake damage assessment studies in Kocaeli and Sakarya. In: *Proceedings of Earthquake-safe: Lessons to be Learned from Traditional Construction*, Istanbul, Turkey, 2000. (Available at: http://www.icomos.org/iiwc/seismic/Gulhan.pdf).

Gulkan P. and Langenbach R. (2004). The earthquake resistance of traditional timber and masonry dwellings in Turkey. In: *World Conference on Earthquake Engineering (WCEE2004)*. Vancouver, 2004.

Gulkan P. and Sozen M.A. (1974). Inelastic response of reinforced concrete structures to earthquake motions. In: *ACI Journal*. 71, 601-610.

Güneyisi E.M., D'Aniello M., Landolfo R., Mermerdaş K. (2013). A novel formulation of the flexural overstrength factor for steel beams. In: *Journal of Constructional Steel Research*, 90, 60-71.

Güneyisi E.M., D'Aniello M., Landolfo R., Mermerdaş K. (2014). Prediction of the flexural overstrength factor for steel beams using artificial neural network. In: *Steel and Composite Structures*, an International Journal, 17(3), 215-236.

Henry R.S., Aaleti S., Sritharan A. (2012). Seismic analysis of a low-damage precast wall with end columns (PREWEC) including interaction with floor diaphragms. In: *Journal of the Structural Engineering Society of New Zealand*, 25(1) 2012:69-81.

Higgins C. (2001). Hysteretic dampers for wood frame shear walls. In: *Proceding of the 2001 Structures Congress and Exposition*, ASCE, edited by P. C. Chang, Washington, DC, May.

Humbert J., Lee S.J., Park J.S., Park M.J. (2014). Moment resistance of post-and-beam joints with concealed metallic connectors. In: *World Conference of Timber Engineering (WCTE2014)*, August 10-14, 2014, Quebec City, Canada.

Hwang S.J. (2002). Seismic Design of Structures with Viscous Dampers. In International Training Programs for Seismic Design of Building Structures. Hosted by *National Center for*

Research on Earthquake Engineering, Sponsored by Department of International Programs, National Science Council.

Ishigaki H., Sakamaki Y., Ishikawa Y., Hara T., Ohashi Y. (2008). A study on seismic performances of timber structures with moment resisting joint, In: *World Conference on Earthquake Engineering (WCEE2008)*, October 12-17, 2008, Beijing, China.

Jaspart J. P. (2000). General report: session on connections. In: *Journal of Constructional Steel Research*, vol. 55, no. 1–3, pp. 69–89, Elsevier.

Jaspart J.P. (1998). Contributions to recent advances in the field of steel joints. Column bases and further configurations for beam-to-column joints and beam splices. Professorship Thesis, Universitè de Liège, Belgium; 1998.

Jaspart J.P. (2002). Design of structural joints in building frames. In: *Progress in Structural Engineering and Materials*, 4 (2002) 18–34.

Johansen K. (1949). Theory of Timber Connections. Zurich: Ein Dienst der ETH-Bibliothek Ramistrasse, Switzerland.

Jorissen A. (1999). Double Shear Timber Connections with Dowel Type Fasteners. In: *HERON*. 44(3), 163-186.

Jorissen A. and Fragiacomo M. (2011). General notes on ductility in timber structures. In: *Engineering Structures*, 33 (2011) 2987-2997, The Netherlands, Italy.

Karacabeyli E. (2000). Performance of North American platform frame wood construction in earthquakes. In: *COST E5 Workshop on Seismic behaviour of Timber Structures*. September 28- 29 2000 Venice Italy.

Karacabeyli E. and Popovski M. (2003). Design for earthquake Resistance. In: *Timber Engineering*, edited by Thelandersson, S., and Larsen, H. J. 267-299. England: John Wiley & Sons Ltd.

Kasal B., Asce M., Guindos P., Polocoser T., Asce S. M., Heiduschke A., rushadze S., Pospisil S. (2014). Heavy laminated timber frames with rigid three-dimensional beam-to-column connections. In: *Journal of Performance of Constructed Facilities*, 28(6): A4014014.

Kasal B., Heiduschke A., Pospisil S., Urushadze S. (2010). Shake table tests of a three-story spatial timber frame with moment connections. In: *World Conference on Timber Engineering (WCTE2010)*. 2, 917-922. Riva del Garda (Trento), Italy.

Kitagawa Y. and Hiraishi H. (2004). Overview of the 1995 hyogo-ken nanbu earthquake and proposals for earthquake mitigation measures. In: *Journal of Japan Association for Earthquake Engineering*, 4(3): 1-28.

Kohara K., Inada M., Hoshiai K., Tabata M., Fukumoto M., Komoto K., Takimoto M. (2016). A study on portal frame structure with combined column for timber building. In: *World Conference on Timber Engineering (WCTE2016)*, August 22-25, 2016, Vienna, Austria.

Koj C. and Trautz M. (2016). Long-term behaviour of timber connections with selftapping screws in outdoor climate. In: *World Conference on Timber Engineering (WCTE2016)*, August 22-25, 2016, Vienna, Austria.

Komatsu K., Kitamori A., Mori T. (2014). Evaluation on dynamic performance of glulam frame structure composed of slotted bolted connection system. In: *World Conference of Timber Engineering (WCTE2014)*, August 10-14, 2014, Quebec City, Canada.

Kuhlmann U., Davison J.B., Kattner M. (1998). Structural systems and rotation capacity. In: *COST Conference*; Liege, Belgium, 1998. pp. 167–76.

Lachal A., Aribert J.M., Loho G. (2006). Analytical and experimental investigations of bolted haunched beam-to-column joints with a view of seismic design. In: *Advanced Steel Construction*, 2 (2006) 137-160.

Lam F., Gehloff M., Closen M. (2010). Moment-Resisting Bolted Timber Connections. In: *Structures and Buildings*, 163(SB4), 267-274.

Landolfo R., D'Aniello M., Tartaglia R., Costanzo S., Demonceau J.F., Jaspart J.P., Stratan A., Jaka D., Dubina D., Elghazouli A., Bompa D. (2018). Equaljoints PLUS Volume with pre-normative design recommendations for seismically qualified steel joints. Nº EQJ2-EN, 1st Edition, 2018, ECCS – *European Convention for Constructional Steelwork*. ISBN: 978-92-9147-144-7.

Langebach R. (2007). From "Opus Craticium" to the "Chicago frame": Earthquake-resistant traditional construction. In: *International Journal of Architectural Heritage*, 1, 29-59, 2007.

Langebach R., Kelley S., Sparks P., Rowell K., Hammer M., Julien O. (2010). Preserving Haiti's Gingerbread Houses. 2010 Earthquake Mission Report. In: *World Monuments Fund*. December 2010.

Langenbach R. (2003). Survivors amongst the rubble: traditional timber-laced masonry buildings that survived the great 1999 earthquakes in Turkey and the 2001 earthquake in India, while modern buildings fell. In: *Proceedings of the First International Congress on Construction History*, Instituto Juan de Herra, Escuela Técnica Superior de Arquitectura, Madrid, Vol. 2, 2003: 1257-1268.

Langenbach R. (2009). DON'T TEAR IT DOWN! Preserving the earthquake resistant vernacular architecture of Kashmir. New Delhi: UNESCO; 2009.

Lee C.H. (2002). Seismic Design of Rib-Reinforced Steel Moment Connections based on Equivalent Strut Model. In: *Journal of Structural Engineering*, ASCE, 128(9), 1121-1129.

Lee C.H. and Uang C.M. (1997). Analytical modeling of dual panel zone in haunch repaired. SAC, Technical report: Experimental investigations of beam-column subassemblies. In: *Journal of Structural Engineering*, ASCE, 1997, 123(1), pp.20-29.

Lee C.H., Jung J.H., Oh M.H., Koo E.S. (2005). Experimental Study of Cyclic Seismic Behavior of Steel Moment Connections Reinforced with Ribs. In: *Journal of Structural Engineering*, ASCE, 131(1), 108-118.

Leijten A.J.M. (2001). Requirements for moment connections in statically indeterminate timber structures. In: *Engineering Structures*, 33 (2011) 3027–3032.

Lemonis M. E. and Gantes C. J. (2009). Mechanical modeling of the nonlinear response of beam-to-column joints. In: *Journal of Constructional Steel Research*, vol. 65, no. 4, pp. 879–890, 2009.

Liu Y. and Xiong H. (2018). Lateral performance of a semi-rigid timber frame structure: theoretical analysis and experimental study. In: *Journal of Wood Science*, (2018) 64:591–600

Lueger O. (1894). Encyclopedia of total technology (in German).

Makarios T. and Demosthenous M. (2006). Seismic response of traditional buildings of Lefkas Island, Greece. In: *Engineering Structures*, 28, 264-278.

Malo K.A. and Stamatopoulos H. (2016). Connections with threaded rods in moment resisting frames. In: *World Conference on Timber Engineering (WCTE2016)*, August 22-25, 2016, Vienna, Austria.

Maquoi R. and Chabrolin B. (1998). Frame design including joint behaviour: final report. EUR, *Off. For Off. Publ. of the Europ. Communities*, Luxembourg.

Maris C., Vulcu C., Stratan A., Dubina D. (2015). Validation through numerical simulations of the design procedure for bolted beam-to-column connections with haunches. In: *Pollack Periodica*, 10(3), 95–107.

Mazzolani F.M. and Ballio G. (1979). Theory and design of steel structures. London New York, Chapman and Hall. Hoepli.

Mazzolani F.M. and Piluso V. (1992). Member behavioural classes of steel beams and beam-columns. In: *Proceeding of First State of the ArtWorkshop*, COST C1, Strasbourg, 517-29.

McLain T.E. (1998). Connectors and fasteners: Research needs and goals. In: *Wood Engineering in the 21st Century: Research Needs and Goals*, K. J. Fridley, ed, ASCE, Reston, Virginia, 56–69.

Minjuan H. and Liu H.F. (2014). Comparison of glulam post-to-beam connections reinforced by two different dowel-type fasteners. In: *Construction and Building Materials*, 99:99-108.

Minjuan H. and Liu H.F. (2016). Experimental investigation on lateral performance of pre-stressed tube bolted connection with high initial stiffness. In: *Advances in Structural Engineering*, 2016.

Montuori R. (2014). The Influence of Gravity Loads on the Seismic Design of RBS Connections. In: *The Open Construction and Building Technology Journal* (Betham Open, 2014), 8, pp. 248-261.

Montuori R. and Sagarese V. (2018). The use of steel rbs to increase ductility of wooden beams. In: *Engineering Structures*, Elsevier, 2018, 169, pp. 154-161.

Moroder D., Sarti F., Palermo A., Pampanin S., Buchanan A.H. (2014). Experimental investigation of wall-to-floor connections in post-tensioned timber buildings. In: *New Zealand Society for Earthquake Engineering (NZSEE)*, Annual Technical Conference, March 2014. Paper Number P25.

Najam F. (2018). Nonlinear Static Analysis Procedures for Seismic Performance Evaluation of Existing Buildings – Evolution and Issues. In: *International Congress and Exhibition "Sustainable Civil Infrastructures: Innovative Infrastructure Geotechnology*.

Nakatani M., Mori T., Kitamori A. (2012). Development of moment-resisting joint systems using lagscrewbolts. In: *World Conference on Timber Engineering (WCTE2012)*, Auckland; 2012; New Zealand, 1-4.

NBCC. 2005. National Building Code of Canada. Institute for Research in Construction, National Research Council of Canada, Ottawa, Ontario.

NIST (1998). Modification of existing Welded Steel Moment Frame Connections for Seismic Resistance. Draft Report, *National Institute for Standards and Testing*, Gaithersburg, MD.

Ogrizovic J., Wanninger F., Frangi A. (2017). Experimental and analytical analysis of moment-resisting connections with glued-in rods. In: *Engineering Structures*, 145 (2017) 322–332.

Ottenhaus L.M., Li M., Smith T., Quenneville P. (2018). mode cross-over and ductility of dowelled LVL and CLT connections under monotonic and cyclic loading. In: *Journal of Structural Engineering*, 144 (7), 04018074.

Palermo A. and Pampanin S. (2006). Experimental investigations on LVL seismic resistant wall and frame subassemblies. In: *First European Conference on Earthquake Engineering and Seismology* (a joint event of the 13th ECEE & 30th General Assembly of the ESC) Geneva, Switzerland, 3-8 September 2006. Paper Number: 983.

Palermo A., Sarti F., Baird A., Dekker D. (2012). From theory to practice: design, analysis and construction of dissipative timber rocking post-Tensioning wall system for Carterton Events Centre, New Zealand. In: *World Conference on Earthquake Engineering (WCTE2012)*. Lisbon, Portugal.

Pall A.S. and Pal R. (1991). Seismic response of a friction-base-isolated house in Montreal. In: *Proceeding of Sixth Canadian Conference on Earthquake Engineering*, Toronto, Canada, June, pp. 375–382.

Pampanin S, Fragiacomo M., Buchanan A.H., Deam B.L. (2006). Innovative Seismic Solutions for Multi-Storey LVL Timber Buildings. In: *World Conference on Timber Engineering (WCTE2006)*, August 6-10, Portland, U.S.A.

Pampanin S. (2005). Emerging Solutions for High Seismic Performance of Precast/Prestressed Concrete Buildings. In: *Journal of Advanced Concrete Technology*.

Pampanin S., Iqbal A., Buchanan A. (2016). Ductile connections for seismic design of timber structures. In: *World Conference on Timber Engineering (WCTE2016)*, August 22-25, 2016, Vienna, Austria.

Paulay T. and Priestley M.J.N. (1992). Seismic design of reinforced concrete and masonry buildings. In: *Wiley Online Library*, 1992.

Piazza M., Tomasi,R., Modena R. (2005). Strutture in legno. Hoepli Editor, Milano, Italy.

Polastri A. (2015). Caratterizzazione del comportamento di giunti semirigidi per strutture lignee in zona sismica. *PhD Thesis*, Supervisor: Piazza M., Smith I. Department of Civil Engineering, University of Trento.

Popovski M. and Karacabeyli E. (2004). Seismic Performance of Riveted Connections in Heavy Timber Construction. In: *World Conference on Earthquake Engineering (WCEE2004)*. (Paper No. 3356). Vancouver, B.C.

Popovski M. and Karacabeyli E. (2008). Force modification factors and capacity design procedures for braced timber frames. In: *World Conference on Earthquake Engineering (WCEE2008)*, October 12-17, 2008, Beijing, China.

Pozza L. (2013). Ductility and behaviour factor of wood structural systems. Theoretical and experimental development of a high ductility wood-concrete shear-wall system. *PhD Thesis*. University of Study of Padova. Director of PhD School: Lanzotti S., Supervisor: Scotta R., External Evaluator: Ceccotti Ario.

Reed J.W. and Kircher C. A. (1986). Base isolation of a five-story wood-frame building. In: *Proceeding of a Seminar and Workshop on Base Isolation and Passive Energy Dissipation*, (ATC-17), San Francisco, CA, March, pp. 133–142.

Ricles J.M., R. Sause, Garlock M., Zhao C., (2001). Post-Tensioned Seismic-Resistant Connections for Steel Frames. In: *ASCE Journal of Structural Engineering*, 127(2), 113-121.

Rossi S., Crocetti R., Honfi D., Hansson E.F. (2016). Load-bearing capacity of ductile multiple shear steel-to-timber connections. In: *World Conference on Timber Engineering (WCTE2016)*, August 22-25, 2016, Vienna, Austria.

Saiidi M. and Sozen M.A. (1981). Simple Nonlinear Seismic Analysis of R/C Structures. In: *Journal of the Structural Division*, Vol. 107, ST5, ASCE, 937-952.

Sakamoto I., Ohashi Y., Fuji, Y. (1990). Seismic behavior of base isolated two-storied wooden building. In: *Proceeding of the 1990 International Timber Engineering Conference*, Tokyo, Japan, 3, pp. 938–945.

Salem S. (2016). Experimental testing of steel-wood-steel glulam frame bolted connections. In: *World Conference on Timber Engineering (WCTE2016)*, August 22-25, 2016, Vienna, Austria.

Salem S. and Petrycki A. (2016). Experimental testing of wood-steel-wood moment resisting bolted connections. In: *World Conference on Timber Engineering (WCTE2016)*, August 22-25, 2016, Vienna, Austria.

Sarti F., Palermo A., Pampanin S. (2014). Quasi static cyclic tests of 2/3 scale post-tensioned timber wall and column-wall-column (CWC) systems. In: *New Zealand Society for Earthquake Engineering (NZSEE)*, Annual Technical Conference, March 2014. Paper Number O62.

Schick M. and Seim W. (2016). Local energy dissipators for skeleton structures – testing results and design considerations. In: *World Conference on Timber Engineering (WCTE2016)*, August 22-25, 2016, Vienna, Austria.

SCI/BCSA (2013). Joints in steel construction: moment-resisting joints to Eurocode 3. The Steel Construction Institute and The British Constructional Steelwork Association, London, UK. Publication Number: P398.

Seesl. 2006. Structural Engineering and Earthquake Simulation Laboratory: NEESWood Project. Last update September 2004. http://nees.buffalo.edu/projects/NEESWood/.

Seleemah A.A. and Constantinou M.C. (1997). Investigation of Seismic Response of Buildings with Linear and Nonlinear Fluid Viscous Dampers. Report No. NCEER-97-0004, National Center for Earthquake Engineering Research, Buffalo, New York.

Skinner R.I., Tyler R.G., Heine A.J., Robinson W.H. (1980). Hysteretic dampers for the protection of structures from earthquakes. In: *Bulletin of the New Zeland National Society for Earthquake Engineering*, 1980 - First published: 1974.

Smith T., Pampanin S., Carradine D. (2012). Dynamic Testing of Multi-storey Post-tensioned Glulam Building: Planning, Design and Numerical Analysis. In: *World Conference on Earthquake Engineering (WCEE2012),* Lisbon, Portugal. 24-28 September 2012. Volume 1 of 38. SBN: 978-1-63439-651-6.

Smith T., Pampanin S., Carradine D., Di Cesare A., Ponzo F.C., Auletta G., Nigro D., Simonetti M., Mossucca A. (2016). Dynamic Testing of Multi-storey Post-tensioned Glulam Building: Planning, Design and Numerical Analysis. In: *World Conference on Timber Engineering (WCTE2016),* Italy, New Zealand.

Soong T.T. and Constantinou M.C. (1994). Passive and Active Structural Vibration Control in Civil Engineering. Springer-Verlag, New York.

Steenhuis M., Gresnigt N., Weynand K. (1994). Pre-Design of Semi-Rigid Joints Ii Steel Frames. In: *Proceedings of the Second State of the Art Workshop on Semi-Rigid Behaviour of Civil Engineering Structural Connections*, COST C1, Prague, 1994, 131-140.

Stratan A., Maris C., Dubina D., Neagu C. (2016). Prequalification tests on bolted beam-to-column joints with haunches. In: *Proceedings of the 8th International Workshop Connections in Steel Structures VIII*, American Institute of Steel Construction, Boston, USA, 569–578.

Stratan A., Maris C., Dubina D., Neagu C. (2017). Experimental prequalification of bolted extended end plate beam to column connections with haunches. ce/papers, 1(2–3), 414–423.

Symans M.D. and Constantinou M.C. (1998). Passive fluid viscous damping systems for seismic energy dissipation. In: *Journal of Earthquake Technology*, ISET, Special issue on passive control of structures, 35 (4), 185–206.

Symans M.D., Cofer W.F., Fridley K.J., Du Y. (2002). Effects of supplemental energy dissipation systems on the seismic response of light-framed wood buildings. In: *Proceeding of Seventh National Conference on Earthquake Engineering*, Boston, MA, July.

Tamboli A.R. (1993). Handbook of Structural Steel Connection Design and Details. McGrawHills Press, NY, 1993.

Tampone G. (1996). The restoration of timber structures (in Italian). Milan, Libreria Tecnica Hoepli.

Tampone, G. (2001). Acquaintance of the ancient timber structures. Historical constructions. Possibilities of numerical and experimental techniques. Lourenco P.B. & Roca P. editors.

Tartaglia R. and D'Aniello M. (2017). Nonlinear performance of extended stiffened end-plate bolted beamto-column joints subjected to column removal. In: *The Open Civil Engineering Journal*, Vol 11, Issue Suppl-1, Pages 369-383.

Tartaglia R., D'Aniello M., Rassati G.A., Swanson J.A., Landolfo R. (2018). Full strength extended stiffened end-plate joints: AISC vs recent European design criteria. In: *Engineering Structures*, Volume 159, 15 March 2018, Pages 155–171.

Tlustochowicz G. and Serrano E. (2011). State-of-the-art Review on Timber Connections with Glued-in Steel Rods. In: *Materials and Structures*. 44, 997-1020.

Tobriner S. (1997). The baraccata house: an antiseismic system in the XVIII century Calabria (in Italian). In: *Costruire in laterizio*. 1997; 56: 110-115.

Tomasi R., Zandonini R., Piazza M., Andreolli M. (2008). Ductile End Connections for Glulam Beams. In: *Structural Engineering International* (Taylor & Francis, 2008), 18; pp. 290-296.

Touliatos P.G. (2000). Seismic disaster prevention in the history of structures in Greece. In: *Proceeding of Timebr building system*, COST E5, Workshop on Seismic behaviour of Timber Structures. September 28- 29 2000 Venice Italy.

Tsakanika-Theohari E. (2009). The constructional analysis of timber load bearing systems as a tool for interpreting Aegean Bronze Age architecture. In: *Proceedings of the Symposium Bronze Age Architectural Transitions in the Eastern Mediterranean: Diffusion and Diversity*, 07.-08. 05. 2008 in Munich (Weilheim 2009): 127-142, 2008.

Uang C.M. (1991). Establishing R (or Rw) and Cd Factors for Building Seismic Provisions. In: *Journal of structural Engineering*, vol. 117, pp. 19-28, 1991.

Uang C.M. and Bertero V. (1988). Use of energy as a design criterion in earthquake-resistant design. Report No. UCB/EERC-88/18. University of California, Berkeley.

Vasconcelos G., Lourenço P.B., Poletti E. (2013). An overview on the seismic behaviour of timber frame structures. In: *Proceedings of the 1st International Symposium on Historic Earthquake-Resistant Timber Frames in the Mediterranean Region*, H.Ea.R.T.2013, University of Calabria, ITALY.

Volkersen O. (1938). Die Nietkraftverteilung in zugbeanspruchten Nietverbindungen mit konstanten Laschenquerschnitten (in German), Luftfahrtvorschung, 15, 1938, 41–47.

Wald F., Sokol Z., Steenhouis M. and Jaspart, J.P. (2008). Component Method for Steel Column Bases. Heron 53 (2008) 3-20.

Wang K., Li Z., He M. (2016). Investigation into the hysteretic performance of selfcentering timber beam-to-column joints. In: *World Conference on Timber Engineering (WCTE2016),* August 22-25, 2016, Vienna, Austria.

Wang M., Song X., ASCE A.M., Gu X., Zhang Y. (2015). Rotational Behavior of Bolted Beam-to-Column Connections with Locally Cross-Laminated Glulam. In: *Journal of Structural Engineering,* 141: 04014121.

Whittaker A. and Constantinou M.C. (2000). Fluid Viscous Dampers for Building Construction. In: *First International Symposium on Passive Control*, pp 133-142, Tokyo Institute of Technology, Tokyo.

Yamaguchi N., Nakao M., Furuta T., Mikoshiba T. (2012). Development of Cylindrical Passive Damper using High Damping Rubber. In: *World Conference on Earthquake Engineering (WCEE2012)*: Lisbon Portugal, 24 - 28 September 2012.

Yeh M.C., Lin Y.L., Huang G.P. (2016). Moment-resisting performance of residential portal frame constructed with self-tapping-screws. In: *World Conference on Timber Engineering (WCTE2016),* August 22-25, 2016, Vienna, Austria.

Yu Q.S., Gilton C. Uang C. (2000). Cyclic response of RBS moment connections: Loading sequence and lateral bracing effects. Department of Structural Engineering, University of California, San Diego.

Zarnani P. and Quenneville P. (2014). Strength of Timber Connections Under Potential Failure Modes: An Improved Design Procedure. In: *Construction and Building Materials*, 60, 81-90.

Zarnani P., Valadbeigi A., Quenneville P. (2016). Resilient slip friction (RSF) joint: a novel connection system for seismic damage avoidance design of timber structures. In: *World Conference on Timber Engineering (WCTE2016),* August 22-25, 2016, Vienna, Austria.

Zayas V.A. and Low S.S. (1997). Seismic isolation of a four-story wood building. In: *Earthquake Performance and Safety of Timber Structures*, Forest Products Society, Proc. No. 7289, pp. 83–91.

Zoetemeijer P. (1974). A design method for the tension side of statically-loaded, bolted beam-to-column connections. Heron 1974;20(1):1–59.

Zoetemeijer P. (1981). Bolted Connections with Flush End Plates and Haunched Beams. Tests and Limit State Design Methods. Report 6-81-15, Delft University of Technology, Stevin Laboratory.

Zoetemeijer P. (1985). Summary of the Researches on Bolted Beam-to-Column Connections. In: Report 6-85-7, University of Technology, Delft 1985.

Zonta D., Piazza M., Zanon P., Loss C., Sartori T. (2008). Direct displacement based design of glulam timber frame buildings. In: *World Conference on Earthquake Engineering (WCEE2008)*, Beijing, China.

WEBLIOGRAPHY

http://www.frenchimmersion.wordpress.com/2012/10/15/house/colombage-house/

http://www.frenchimmersion.wordpress.com/2012/10/15/house/colombage-house/

http://www.old-fachwerk-house-in-wolfenbuttel--niedersachsen-germany http://www.old-fachwerk-house-in-wolfenbuttel--niedersachsen-germany

https://doi.org/10.1007/s10086-018-1727-7.

STANDARDS

EN 1995-1-1, 2004: Eurocode 5 - Design of timber structures - Part 1-1: General - Common rules and rules for buildings.

EN 1998-1-1, 2005: Eurocode 8 - Design of structures for earthquake resistance – Part 1: General rules, seismic actions and rules for buildings.

EN1993-1-8, Eurocode 3, Design of steel structures, Part 1-8, Design of joints, CEN, Brussels, 2006.

NTC2018: Technical Standards for Construction. D.M. 17.01.18 - “Norme tecniche per le costruzioni”.

CNR DT 206–R1 / 2018. Istruzioni per la Progettazione, l’Esecuzione ed il Controllo delle Strutture di Legno. CNR – Commissione di studio per la predisposizione e l’analisi di norme tecniche relative alle costruzioni.

STRUCTURAL PROGRAM

ABAQUS FEA 2019 - Abaqus/CAE, or “Complete Abaqus Environment”. Version 2019.

SAP2000. Version 22.0.0.

REXEL. Computer aided code-based real record selection for seismic analysis of structures. Iervolino I, Galasso C., Chioccarelli E. Version 2.31 beta.

GOOGLE SKETCHUP PRO. A 3D software design. Version 2020-Pro.

APPENDIX A

A.3.1 SEISMIC RESISTANT HEAVY TIMBER FRAME STRUCTURES WITH STEEL LINK

A.3.1.4 STRUCTURAL DESIGN

The linear-static analysis and, after, the linear-dynamic analysis are carried out and for the seismic design of the structural members the capacity design approach presented in chapter 2.2.3 is applied. The outputs of the analysis are presented in terms of structural sections, mass and vibration period (evaluated through modal analysis). In particular, for the 1-storey (1S) structures the analysis results are presented for 1A, 2A, and 3A plan layout, while for 2-storey (2S), 4-storey (4S) and 6-storey (6S) structures the analysis results are presented for only 2A plan layout. All the structures are designed under seismic acceleration, a_g, for seismic zones 1Z, 2Z and 3Z. 1S structures are designed both with $q=1$ and with q_d (behaviour factor of steel structures), while 2S, 3S, 4S and 6S structures are designed only with q_d. Moreover, for each structure, the value of the coefficient Ω used for the design of the non-dissipative elements is shown. In particular, Ω coefficient indicated is the smallest coefficient between that of the link in the column (Ω_c) and the link in the timber beam (Ω_b): $\Omega= \Omega_{min}= (\Omega_c; \Omega_b)$.

- ## 1S - 1A scheme

Table A.113 – Output results for timber structures – seismic zone 1: 1Z (1S-1A).

Type	q	Elements size						Fd [kN]	m [ton]	T* [s]	Ω
		Beam		Column		Diagonal					
		Timber	Link	Timber	Link	Timber	Link				
MRF	1	200x300	IPE200	340x400	HE160M	-	-	132,64	13,30	0,33	1,04
SLD	4	200x300	IPE200	320x380	HE140M	-	-	44,33	13,19	0,38	2,35
MRF	1	200x300	IPE200	320x380	HE140M	-	-	44,33	13,19	0,38	2,35
SLV	4	160x240	IPE240	260x280	HE100M	-	-	44,33	12,98	0,63	1,04
CBF	1	200x320	HE180A	260x280	-	160x160	40x40x4	130,19	12,95	0,09	1,44
V π	2	160x240	HE120B	140x140	-	140x140	30x30x2,5	72,40	12,78	0,11	1,15
CBF	1	200x320	-	260x280	-	160x160	40x40x4	130,19	12,95	0,09	1,44
V Λ	2	160x240	-	220x240	-	140x140	30x30x2,5	72,40	12,77	0,11	1,15
CBF	1	180x280	-	260x280	-	200x200	40x40x3	31,88	13,05	0,07	1,58
X	4	140x220	-	220x240	-	150x150	20x20x2	4,07	12,81	0,13	1,44
CBF	1	180x260	-	280x300	-	210x210	50x50x4	131,88	12,97	0,10	1,05
X D	4	140x240	-	220x240	-	160x160	25x25x3	44,07	12,76	0,16	1,09
EBF	1	240x340	IPE180	300x320	-	170x170	-	130,16	13,00	0,14	1,69
	4	120x180	IPE120	200x220	-	130x130	-	43,50	12,67	0,33	1,75

** evaluated through modal analysis*

Table A.114 – Output results for timber structures – seismic zone 2: 2Z (1S-1A).

Type	q	Elements size						Fd [kN]	m [ton]	T* [s]	Ω
		Beam		Column		Diagonal					
		Timber	Link	Timber	Link	Timber	Link				
MRF	1	240x280	IPE180	300x360	HE140M	-	-	94,74	13,14	0,39	1,11
SLD	4	200x280	IPE180	300x360	HE120M	-	-	31,66	13,09	0,45	2,68
MRF	1	140x240	IPE140	240x260	HE120B	-	-	31,66	12,90	0,70	1,04
SLV	4	200x280	IPE180	300x360	HE120M	-	-	31,66	13,09	0,45	2,68
CBF	1	180x280	HE160A	260x280	-	150x150	50x50x2	92,99	12,86	0,10	1,47
V π	2	140x220	HE120A	200x220	-	130x130	25x25x2	51,72	12,71	0,12	1,09
CBF	1	180x280	-	260x280	-	150x150	50x50x2	92,99	12,86	0,10	1,47
V Λ	2	140x220	-	200x220	-	130x130	25x25x2	51,72	12,70	0,12	1,09
CBF	1	180x280	-	240x260	-	180x180	40x40x2	94,20	12,95	0,08	1,51
X	4	140x220	-	200x220	-	140x140	100mm²	31,48	12,75	0,12	1,42
CBF	1	180x240	-	260x280	-	200x200	50x50x3	94,20	12,90	0,13	1,15
X D	4	140x220	-	220x240	-	150x150	25x25x2	31,48	12,73	0,17	1,10
EBF	1	220x300	IPE160	280x300	-	160x160	-	92,97	12,91	0,16	1,75
	4	120x180	IPE100	180x200	-	120x120	-	31,07	12,63	0,35	1,54

** evaluated through modal analysis*

Table A.115 – Output results for timber structures – seismic zone 3: 3Z (1S-1A).

Type	q	Elements size						Fd [kN]	m [ton]	T* [s]	Ω
		Beam		Column		Diagonal					
		Timber	Link	Timber	Link	Timber	Link				
MRF	1	200x260	IPE160	260x320	HE180A	-	-	56,85	12,94	0,47	1,19
SLD	4	180X260	IPE160	260X320	HE100M	-	-	19,00	12,94	0,57	2,84
MRF	1	140x220	IPE 140	220x240	HE100B	-	-	19,00	12,80	0,85	1,04
SLV	4	180X260	IPE160	260X320	HE100M	-	-	19,00	12,94	0,57	2,84
CBF	1	160x240	HE120B	220x240	-	140x140	25x25x3	55,80	12,77	0,11	1,76
V π	2	120x200	HE100A	180x200	-	120x120	20x20x2	31,03	12,64	0,13	1,41
CBF	1	160x240	-	220x240	-	40x140	25x25x3	55,80	12,77	0,11	1,76
V Λ	2	120x200	-	180x200	-	20x120	20x20x2	31,03	12,64	0,12	1,41
CBF	1	180x280	-	240x260	-	160x160	25x25x2	56,52	12,90	0,08	1,45
X	4	140x220	-	200x220	-	120x120	60mm²	18,89	12,70	0,14	1,53
CBF	1	180x240	-	240x260	-	170x170	30x30x3	56,52	12,82	0,14	1,06
X D	4	140x200	-	200x220	-	140x140	20x20x2	18,89	12,67	0,18	1,41
EBF	1	180x260	IPE140A	240x260	-	140x140	-	55,78	12,78	0,21	1,63
	4	120x180	PE100A	180x200	-	110x110	-	18,64	12,60	0,37	2,03

** evaluated through modal aalysis*

- ## 1S - 2A scheme

Table A.116 – Output results for timber structures – seismic zone 1: 1Z (1S-2A).

Type	q	Elements size						Fd [kN]	m [ton]	T* [s]	Ω
		Beam		Column		Diagonal					
		Timber	Link	Timber	Link	Timber	Link				
MRF	1	300x420	IPE270	420X500	HE220M	-	-	265,28	27,23	0,29	1,15
SLD	4	280x400	IPE220	340x460	HE180M	-	-	88,65	26,31	0,37	2,94
MRF	1	240x360	IPE180	300x380	HE140M	-	-	88,65	26,11	0,54	2,06
SLV	4	280x400	IPE220	340x460	HE180M	-	-	88,65	26,31	0,37	2,94
CBF	1	220x420	HE140M	280x300	-	190x190	60x60x5	260,38	26,39	0,10	1,33
V π	2	160x400	HE160B	240x260	-	160x160	50x50x3	144,80	25,35	0,12	1,29
CBF	1	220x420	-	280x300	-	190x190	60x60x5	260,38	26,37	0,10	1,33
V Λ	2	160x400	-	240x260	-	160x160	50x50x3	144,80	25,34	0,15	1,29
CBF	1	180x320	-	300x320	-	230x230	50x50x5	263,76	26,48	0,09	1,42
X	4	140x340	-	240x260	-	170x170	30x30x2,5	88,14	25,36	0,13	1,27
CBF	1	180x320	-	300x320	-	230x230	50x50x5	263,76	26,48	0,09	1,42
X D	4	140x340	-	240x260	-	170x170	30x30x2,5	88,14	25,36	0,13	1,27
EBF	1	280x440	IPE240A	340x360	-	200x200	-	260,31	25,65	0,15	1,85
	4	160x360	IPE160	220x260	-	160x160	-	86,99	25,65	0,22	1,69

** evaluated through modal analysis*

Table A.117 – Output results for timber structures – seismic zone 2: 2Z (1S-2A).

Type	q	Elements size						Fd [kN]	m [ton]	T* [s]	Ω
		Beam		Column		Diagonal					
		Timber	Link	Timber	Link	Timber	Link				
MRF	1	300x400	IPE270A	380X420	HE180M	-	-	189,49	26,78	0,36	1,23
SLD	4	260x380	IPE200	320x400	HE160M	-	-	63,32	26,12	0,45	2,81
MRF	1	220x360	IPE180	280x340	HE120M	-	-	63,32	25,96	0,62	2,12
SLV	4	260x380	IPE200	320x400	HE160M	-	-	63,32	26,12	0,45	2,81
CBF	1	200x380	HE120M	260x280	-	180x180	50x50x4	185,99	26,27	0,11	1,27
V π	2	140x360	HE140B	220x240	-	160x160	40x40x3	103,43	25,27	0,13	1,46
CBF	1	200x380	-	260x280	-	180x180	50x50x4	185,99	26,26	0,11	1,27
V Λ	2	140x360	-	220x240	-	160x160	40x40x3	103,43	25,26	0,13	1,46
CBF	1	180x280	-	280x300	-	210x210	50x50x3	188,40	26,35	0,10	1,27
X	4	140x340	-	220x240	-	160x160	25x25x2,5	62,96	25,30	0,13	1,46
CBF	1	180x280	-	280x300	-	210x210	50x50x3	188,40	26,35	0,10	1,27
X D	4	140x340	-	220x240	-	160x160	25x25x2,5	62,96	25,30	0,13	1,46
EBF	1	240x400	IPE200	300x320	-	180x180	-	185,94	25,65	0,17	1,83
	4	140x320	IPE140	200x220	-	140x140	-	62,14	25,65	0,27	1,75

** evaluated through modal analysis*

Table A.118 – Output results for timber structures – seismic zone 3: 3Z (1S-2A).

Type	q	Elements size						Fd [kN]	m [ton]	T* [s]	Ω
		Beam		Column		Diagonal					
		Timber	Link	Timber	Link	Timber	Link				
MRF	1	260X340	IPE220	320X400	HE160M	-	-	113,69	26,60	0,44	1,37
SLD	4	240x340	IPE180	300x360	HE140M	-	-	37,99	25,96	0,55	3,00
MRF	1	200x280	IPE160A	260x300	HE140A	-	-	37,99	25,80	0,84	1,35
SLV	4	240x340	IPE180	300x360	HE140M	-	-	37,99	25,96	0,55	3,00
CBF	1	180x300	HE100M	220x240	-	160x160	50x50x2,5	111,59	26,10	0,13	1,46
V π	2	140x300	HE120B	200x220	-	140x140	50x50x2,5	62,06	25,18	0,15	1,65
CBF	1	180x300	-	220x240	-	160x160	50x50x2,5	111,59	26,09	0,13	1,46
V Λ	2	140x300	-	200x220	-	140x140	30x30x2,5	62,06	25,17	0,15	1,65
CBF	1	160x280	-	260x280	-	190x190	40x40x2,5	113,04	26,22	0,10	1,37
X	4	140x340	-	220x240	-	160x160	20x20x2	37,78	25,26	0,13	1,55
CBF	1	160x280	-	260x280	-	190x190	40x40x2,5	113,04	26,22	0,10	1,37
X D	4	140x340	-	220x240	-	160x160	20x20x2	37,78	25,26	0,13	1,55
EBF	1	180x360	IPE180A	240x260	-	160x160	-	111,56	25,65	0,21	1,65
	4	120x260	IPE120A	180x200	-	130x130	-	37,28	25,65	0,37	1,63

** evaluated through modal analysis*

▪ 1S - 3A scheme

Table A.119 – Output results for timber structures – seismic zone 1: 1Z (1S-3A).

Type	q	Elements size						F_d [kN]	m [ton]	T* [s]	Ω
		Beam		Column		Diagonal					
		Timber	Link	Timber	Link	Timber	Link				
MRF	1	340x420	IPE300	480x580	HE240M	-	-	397,92	40,21	0,28	1,09
SLD	4	360x560	IPE270	420x520	HE180M	-	-	132,98	39,99	0,38	5,09
MRF	1	300x460	IPE220A	360x400	HE160M	-	-	132,98	39,62	0,52	2,69
SLV	4	360x560	IPE270	420x520	HE180M	-	-	132,98	39,99	0,38	5,09
CBF	1	240x460	HE180M	300x320	-	200x200	60x60x6,3	390,57	38,68	0,12	1,10
V π	2	200x400	HE180B	260x280	-	180x180	50x50x5	217,20	38,45	0,13	1,29
CBF	1	240x460	-	300x320	-	200x200	60x60x6,3	390,57	38,68	0,12	1,10
V Λ	2	200x400	-	260x280	-	180x180	50x50x5	217,20	38,45	0,13	1,29
CBF	1	200x300	-	320x340	-	260x260	60x60x6,3	395,63	38,79	0,09	1,44
X	4	140x340	-	260x280	-	200x200	40x40x3	132,21	38,46	0,13	1,43
CBF	1	240x340	-	340x360	-	280x280	90x90x6,3	395,63	38,73	0,12	1,05
X D	4	160x380	-	280x300	-	210x210	50x50x4	132,21	38,43	0,20	1,05
EBF	1	320x500	IPE270	380x400	-	230x230	-	390,47	38,84	0,15	1,65
	4	180x380	IPE180	240x260	-	170x170	-	130,49	38,32	0,24	1,68

** evaluated through modal analysis*

Table A.120 – Output results for timber structures – seismic zone 2: 2Z (1S-3A).

Type	q	Elements size						F_d [kN]	m [ton]	T* [s]	Ω
		Beam		Column		Diagonal					
		Timber	Link	Timber	Link	Timber	Link				
MRF	1	300X400	IPE270	420x520	HE220M	-	-	284,23	39,82	0,35	1,05
SLD	4	340x500	IPE240	400x500	HE160M	-	-	94,98	39,80	0,45	1,81
MRF	1	240x420	IPE 200	300x360	HE140M	-	-	94,98	39,39	0,61	2,06
SLV	4	340x500	IPE240	400x500	HE160M	-	-	94,98	39,80	0,45	1,81
CBF	1	220X420	HE160M	280X300	-	190X190	60x60x5	278,98	38,56	0,12	1,24
V π	2	180x380	HE140M	240x260	-	170x170	50x50x4	155,15	38,37	0,14	1,54
CBF	1	220X420	-	280X300	-	190X190	60x60x5	278,98	38,56	0,12	1,24
V Λ	2	180x380	-	240x260	-	170x170	50x50x4	155,15	38,37	0,14	1,54
CBF	1	180x300	-	300x320	-	230x230	60x60x4	282,60	38,63	0,11	1,37
X	4	140x340	-	240x260	-	180x180	30x30x3	94,44	38,37	0,14	1,42
CBF	1	220x320	-	320x340	-	260x260	70x70x6	282,60	38,61	0,17	1,06
X D	4	160x340	-	260x280	-	200x200	40x40x4	94,44	38,35	0,21	1,13
EBF	1	280x480	IPE240	340x360	-	210x210	-	278,90	38,66	0,17	1,76
	4	140x340	IPE160	220x240	-	160x160	-	93,20	38,21	0,29	1,73

** evaluated through modal analysis*

Table A.121 – Output results for timber structures – seismic zone 3: 3Z (1S-3A).

Type	q	Elements size						F_d [kN]	m [ton]	T* [s]	Ω
		Beam		Column		Diagonal					
		Timber	Link	Timber	Link	Timber	Link				
MRF	1	280x320	IPE220	360x440	HE180M	-	-	170,54	39,41	0,47	1,06
SLD	4	300x380	IPE220	360x400	HE140M	-	-	56,99	39,37	0,57	2,24
MRF	1	220x360	IPE 180	280x320	HE180AA	-	-	56,99	39,14	0,86	2,19
SLV	4	300x380	IPE220	360x400	HE140M	-	-	56,99	39,37	0,57	2,24
CBF	1	200X360	HE120M		-	170x170	60x60x3	167,39	38,42	0,14	1,32
V π	2	160x320	HE140B		-	150x150	50x50x2	93,09	38,24	0,17	1,47
CBF	1	200X360	-	260x280	-	170x170	60x60x3	167,39	38,42	0,14	1,32
V Λ	2	160x320	-	220x240	-	150x150	50x50x2	93,09	38,24	0,17	1,47
CBF	1	180x280	-	260x280	-	200x200	40x40x4	169,56	38,47	0,13	1,37
X	4	140x340	-	220x240	-	160x160	25x25x2	56,66	38,29	0,17	1,33
CBF	1	200x300	-	300x320	-	230x230	60x60x5	169,56	38,48	0,19	1,23
X D	4	140x340	-	240x260	-	170x170	30x30x3	56,66	38,25	0,25	1,06
EBF	1	240x400	IPE200	300x320	-	180x180	-	167,34	38,46	0,21	1,74
	4	140x300	IPE140A	200x220	-	140x140	-	55,92	38,14	0,34	1,63

** evaluated through modal analysis*

- **2S - 2A scheme**

Table A.122 – Output results for timber structures – seismic zone 1: 1Z (2S-2A).

Type	S	Elements size						F_d [kN]	m [ton]	T* [s]	Ω
		Beam		Column		Diagonal					
		Timber	Link	Timber	Link	Timber	Link				
MRF	1	380x500	IPE360	600x660	HE240M	-	-	153,23	55,17	0,52	1,76
SLD	2	340x440	IPE330	580x600	HE220M	-	-				
MRF	1	300x460	IPE300	380X420	HE180M	-	-	153,23	53,60	0,88	1,06
SLV	2	240x360	IPE240A	340X380	HE140M	-	-				
CBF	1	260x380	HE160M	320x340	-	190x190	60x60x5	304,22	51,23	0,18	1,13
V π	2	200x360	HE140M	280x300	-	170x170	50x50x4				
CBF	1	260x380	-	320x340	-	190x190	60x60x5	304,22	51,00	0,21	1,13
V Λ	2	200x360	-	280x300	-	170x170	50x50x4				
CBF	1	140x300	-	260x240	-	190x190	40x40x3	153,64	50,95	0,21	1,14
X	2	140x300	-	240x260	-	180x180	30x30x3				
CBF	1	160x380	-	280x300	-	220x220	50x50x5	152,89	51,20	0,29	1,05
X D	2	160x380	-	260x280	-	200x200	40x40x4				
EBF	1	200x400	IPE200	260x280	-	180x180	-	152,09	50,99	0,34	1,74
	2	160x380	IPE180A	220x240	-	160x160	-				

** evaluated through modal analysis*

Table A.123 – Output results for timber structures – seismic zone 2: 2Z (2S-2A).

Type	S	Elements size						F_d [kN]	m [ton]	T* [s]	Ω
		Beam		Column		Diagonal					
		Timber	Link	Timber	Link	Timber	Link				
MRF	1	360x480	IPE330	580x640	HE220M	-	-	109,45	54,79	0,61	2,18
SLD	2	320x420	IPE270	560x580	HE220M	-	-				
MRF	1	280x380	IPE270A	360x400	HE160M	-	-	109,45	53,27	1,07	1,08
SLV	2	220x340	IPE220A	320x360	HE120M	-	-				
CBF	1	240x360	HE140M	300x320	-	180x180	50x50x5	217,30	51,02	0,19	1,29
V π	2	180x340	HE120M	260x280	-	170x170	50x50x3				
CBF	1	240x360	-	300x320	-	180x180	50x50x5	217,30	50,81	0,22	1,29
V Λ	2	180x340	-	260x280	-	160x160	50x50x3				
CBF	1	140x300	-	240x260	-	180x180	40x40x2,5	109,74	50,83	0,22	1,38
X	2	140x300	-	240x260	-	170x170	25x25x3				
CBF	1	160x380	-	280x300	-	210x210	50x50x4	109,21	51,10	0,30	1,12
X D	2	160x380	-	260x280	-	190x190	40x40x3				
EBF	1	160x380	IPE180A	220x240	-	160x160	-	108,64	50,74	0,40	1,62
	2	140x340	IPE160A	220x240	-	150x150	-				

** evaluated through modal analysis*

Table A.124 – Output results for timber structures – seismic zone 3: 3Z (2S-2A).

Type	S	Elements size						F_d [kN]	m [ton]	T* [s]	Ω
		Beam		Column		Diagonal					
		Timber	Link	Timber	Link	Timber	Link				
MRF	1	340x420	IPE300	540x600	HE180M	-	-	65,67	54,12	0,78	2,53
SLD	2	300x360	IPE240	500x560	HE160M	-	-				
MRF	1	260x300	IPE200	320x360	HE140M	-	-	65,67	52,76	1,43	1,03
SLV	2	220x280	IPE180	280x320	HE120B	-	-				
CBF	1	200x320	HE120M	260x280	-	170x170	50x50x3	130,38	50,69	0,21	1,46
V π	2	160x300	HE100M	220x240	-	150x150	50x50x2				
CBF	1	200x320	-	260x280	-	170x170	50x50x3	130,38	50,51	0,24	1,46
V Λ	2	160x300	-	220x240	-	150x150	50x50x2				
CBF	1	140x300	-	220x240	-	160x160	25x25x2	65,85	50,60	0,27	1,36
X	2	140x300	-	220x240	-	150x150	20x20x2				
CBF	1	160x380	-		-	180x180	40x40x2,5	65,52	50,80	0,35	1,09
X D	2	160x380	-		-	160x160	30x30x2,5				
EBF	1	140x360	IPE160A	200x220	-	150x150	-	65,18	50,52	0,46	1,94
	2	140x320	IPE140A	200x220	-	140x140	-				

** evaluated through modal analysis*

- **4S - 2A scheme**

Table A.125 – Output results for timber structures – seismic zone 1: 1Z (4S-2A).

Type	S	Elements size						F_d [kN]	m [ton]	T* [s]	Ω
		Beam		Column		Diagonal					
		Timber	Link	Timber	Link	Timber	Link				
MRF SLD	1	500x700	IPE450	800x900	HE320M	-	-	306,46	117,17	0,74	1,78
	2	500x700	IPE450	760x860	HE300M	-	-				1,73
	3	500x700	IPE450	720x820	HE280M	-	-				1,89
	4	400x600	IPE400	680x780	HE260M	-	-				1,89
MRF SLV	1	380x500	IPE360	500x600	HE240M	-	-	306,46	111,46	1,23	1,07
	2	380x500	IPE360	440x540	HE220M	-	-				1,04
	3	380x500	IPE360	400x520	HE200M	-	-				1,13
	4	320x460	IPE330	400x460	HE180M	-	-				1,16
CBF V π	1	340x460	HE200M	400x420	-	230x230	90x90x6,3	608,45	103,65	0,34	1,09
	2	340x460	HE200M	400x420	-	220x220	100x100x5				1,12
	3	340x460	HE180M	400x420	-	210x210	80x80x5				1,12
	4	280x340	HE160M	340x360	-	180x180	60x60x4				1,19
CBF V Λ	1	340x460	-	400x420	-	230x230	90x90x6,3	608,45	103,28	0,35	1,09
	2	340x460	-	400x420	-	220x220	100x100x5				1,12
	3	340x460	-	400x420	-	210x210	80x80x5				1,12
	4	280x340	-	340x360	-	180x180	60x60x4				1,19
CBF X	1	160x300	-	320x340	-	250x250	80x80x4	307,28	102,54	0,38	1,60
	2	160x300	-	300x320	-	240x240	70x70x4				1,57
	3	160x300	-	300x320	-	230x230	70x70x3				1,62
	4	160x300	-	280x300	-	210x210	40x40x3				1,78
CBF X D	1	200x400	-	320x340	-	260x260	90x90x5	305,78	102,28	0,53	1,08
	2	200x400	-	320x340	-	250x250	80x80x5				1,08
	3	180x380	-	300x320	-	240x240	80x80x4				1,11
	4	180x380	-	280x300	-	210x210	60x60x3				1,09
EBF	1	280x440	IPE240	340x360	-	210x210	-	304,18	102,31	0,54	1,59
	2	280x440	IPE240	340x360	-	200x200	-				1,79
	3	240x420	IPE220	300x320	-	190x190	-				1,74
	4	240x420	IPE180	300x320	-	160x160	-				1,75

** evaluated through modal analysis*

Table A.126 – Output results for timber structures – seismic zone 2: 2Z (4S-2A).

Type	S	Elements size						F_d [kN]	m [ton]	T* [s]	Ω
		Beam		Column		Diagonal					
		Timber	Link	Timber	Link	Timber	Link				
MRF SLD	1	420x620	IPE400	760x860	HE300M	-	-	218,90	114,93	0,88	1,67
	2	420x620	IPE400	720x820	HE280M	-	-				1,51
	3	420x620	IPE400	680x780	HE260M	-	-				1,76
	4	360x560	IPE330	620x720	HE240M	-	-				2,22
MRF SLV	1	340x500	IPE360A	420x520	HE220M	-	-	218,90	109,69	1,45	1,16
	2	340x500	IPE360A	360x460	HE220B	-	-				1,05
	3	340x500	IPE330	360x460	HE220B	-	-				1,08
	4	260x380	IPE270A	300x400	HE140M	-	-				1,14
CBF V π	1	300x420	HE180M	360x380	-	210x210	70x70x6	434,61	102,82	0,37	1,11
	2	300x420	HE180M	360x380	-	200x200	60x60x6,3				1,12
	3	300x420	HE160M	360x380	-	190x190	60x60x5				1,16
	4	240x320	HE140M	300x320	-	170x170	60x60x3				1,32
CBF V Λ	1	300x420	-	360x380	-	210x210	70x70x6	434,61	102,50	0,40	1,11
	2	300x420	-	360x380	-	200x200	60x60x6,3				1,12
	3	300x420	-	360x380	-	190x190	60x60x5				1,16
	4	240x320	-	300x320	-	170x170	60x60x3				1,32
CBF X	1	160x300	-	300x320	-	230x230	70x70x3	219,49	102,08	0,42	1,51
	2	160x300	-	280x300	-	220x220	50x50x4				1,50
	3	160x300	-	280x300	-	210x210	50x50x3				1,57
	4	160x300	-	260x280	-	190x190	40x40x2				1,78
CBF X D	1	180x380	-	300x320	-	240x240	80x80x4	218,41	101,89	0,58	1,07
	2	180x380	-	300x320	-	230x230	70x70x4				1,06
	3	160x380	-	280x300	-	220x220	50x50x5				1,07
	4	160x380	-	260x280	-	190x190	50x50x2,5				1,03
EBF	1	240x420	IPE220	300x320	-	190x190	-	217,27	101,68	0,61	1,68
	2	240x420	IPE220A	300x320	-	180x180	-				1,61
	3	200x400	IPE200	260x280	-	170x170	-				1,85
	4	200x400	IPE160	260x280	-	150x150	-				1,81

** evaluated through modal analysis*

Table A.127 – Output results for timber structures – seismic zone 3: 3Z (4S-2A).

Type	S	Elements size						F_d [kN]	m [ton]	T* [s]	Ω
		Beam		Column		Diagonal					
		Timber	Link	Timber	Link	Timber	Link				
MRF SLD	1	360x540	IPE360	700x800	HE260M	-	-	131,34	111,68	1,11	2,85
	2	360x540	IPE360	640x740	HE240M	-	-				2,26
	3	360x540	IPE360	580x680	HE220M	-	-				2,28
	4	260x460	IPE270	520x620	HE200M	-	-				1,97
MRF SLV	1	300x400	IPE240	380x480	HE200M	-	-	131,34	107,66	1,99	1,03
	2	300x400	IPE240	320x420	HE220A	-	-				1,07
	3	300x400	IPE240	300x400	HE140M	-	-				1,08
	4	240x320	IPE220	260x360	HE120M	-	-				1,16
CBF V π	1	240x380	HE160M	300x320	-	190x190	70x70x4	260,76	101,83	0,43	1,31
	2	240x380	HE140M	300x320	-	180x180	60x60x4				1,29
	3	240x380	HE120M	300x320	-	170x170	60x60x3				1,26
	4	200x280	HE120M	260x280	-	150x150	40x40x3				1,43
CBF V Λ	1	240x380	-	300x320	-	190x190	70x70x4	260,76	101,59	0,45	1,31
	2	240x380	-	300x320	-	180x180	60x60x4				1,29
	3	240x380	-	300x320	-	170x170	60x60x3				1,26
	4	200x280	-	260x280	-	150x150	40x40x3				1,43
CBF X	1	160x300	-	260x280	-	200x200	60x60x2	131,69	101,44	0,49	1,45
	2	160x300	-	260x280	-	190x190	40x40x3				1,50
	3	160x300	-	240x260	-	180x180	40x40x2				1,43
	4	160x300	-	220x240	-	160x160	25x25x2				1,69
CBF X D	1	160x360	-	280x300	-	210x210	50x50x4	131,05	101,29	0,65	1,04
	2	160x360	-	260x280	-	200x200	60x60x3				1,12
	3	140x340	-	260x280	-	190x190	40x40x4				1,14
	4	140x340	-	240x260	-	170x170	30x30x3				1,12
EBF	1	180x380	IPE180	240x260	-	170x170	-	130,36	100,91	0,76	1,64
	2	180x380	IPE180	240x260	-	160x160	-				1,80
	3	160x340	IPE160	220x240	-	150x150	-				1,73
	4	160x340	IPE140A	220x240	-	140x140	-				1,72

** evaluated through modal analysis*

- **6S - 2A scheme**

Table A.128 – Output results for timber structures – seismic zone 1: 1Z (6S-2A).

Type	S	Elements size						F_d [kN]	m [ton]	T* [s]	Ω
		Beam		Column		Diagonal					
		Timber	Link	Timber	Link	Timber	Link				
MRF SLD	1	800x800	IPE600	1100x1200	HE600M	-	-	540,82	187,0	0,87	1,95
	2	800x800	IPE600	1060x1160	HE550M	-	-				1,45
	3	800x800	IPE600	1020x1120	HE500M	-	-				1,44
	4	800x800	IPE600	980x1080	HE450M	-	-				2,02
	5	600x700	IPE500	940x1040	HE400M	-	-				1,72
	6	500x600	IPE400	900x1000	HE360M	-	-				1,76
MRF SLV	1	500x600	IPE500A	600x760	HE300M	-	-	540,82	173,5	1,36	1,08
	2	600x640	IPE550A	540x700	HE240M	-	-				1,02
	3	600x640	IPE550	520x680	HE240M	-	-				1,14
	4	480x600	IPE500A	480x640	HE320A	-	-				1,12
	5	440x540	IPE400	460x620	HE220M	-	-				1,02
	6	360x460	IPE330	400x560	HE200M	-	-				1,08
CBF V π	1	420x560	HE240M	480x500	-	280x280	160x160x6	1073,73	159,01	0,52	1,09
	2	420x560	HE240M	480x500	-	270x270	100x100x10				1,10
	3	380x540	HE240M	480x500	-	260x260	160x160x5				1,07
	4	340x520	HE220M	420x440	-	250x250	90X90X8				1,08
	5	320x460	HE200M	420x440	-	220x220	100X100X5				1,08
	6	300x360	HE160M	360x380	-	190x190	60X60X5				1,14
CBF V Λ	1	420x560	-	480x500	-	280x280	160x160x6	1073,73	158,35	0,52	1,09
	2	420x560	-	480x500	-	270x270	100x100x10				1,10
	3	380x540	-	480x500	-	260x260	160x160x5				1,07
	4	340x520	-	420x440	-	250x250	90X90X8				1,08
	5	320x460	-	420x440	-	220x220	100X100X5				1,08
	6	300x360	-	360x380	-	190x190	60X60X5				1,14
CBF X	1	160x300	-	340x360	-	280x280	90X90X6,3	542,26	158,27	0,65	1,55
	2	160x300	-	340x360	-	280x280	90X90X6				1,58
	3	160x300	-	340x360	-	270x270	80X80X6				1,56
	4	160x300	-	320x340	-	260x260	80X80X5				1,65
	5	160x300	-	300x320	-	240x240	60X60X5				1,65
	6	160x300	-	280x300	-	220x220	40x40x4				1,87
CBF X D	1	240x400	-	360x380	-	300x300	100X100X8	539,61	155,93	0,80	1,06
	2	240x400	-	360x380	-	300x300	140x140x5				1,05
	3	240x360	-	360x380	-	290x290	90X90X8				1,11
	4	220x380	-	340x360	-	280x280	90X90X6,3				1,08
	5	200x360	-	320x340	-	250x250	100X100X4				1,06
	6	180x320	-	280x300	-	220x220	50X50X5				1,07
EBF	1	340x540	IPE300	440x460	-	260x260	-	536,79	157,06	0,76	1,54
	2	340x540	IPE300	440x460	-	250x250	-				1,64
	3	320x520	IPE300	420x440	-	240x240	-				1,80
	4	300x480	IPE270	420x440	-	230x230	-				1,69
	5	200x360	IPE240	400x420	-	210x210	-				1,73
	6	180x320	IPE180	360x380	-	170x170	-				1,69

** evaluated through modal analysis*

Table A.129 – Output results for timber structures – seismic zone 2: 2Z (6S-2A).

Type	S	Elements size						F_d [kN]	m [ton]	T* [s]	Ω
		Beam		Column		Diagonal					
		Timber	Link	Timber	Link	Timber	Link				
MRF SLD	1	600x700	IPE550	1060x1160	HE550M	-	-	386,30	176,81	1,00	1,98
	2	600x700	IPE550	1000x1100	HE500M	-	-				1,21
	3	600x700	IPE550	960x1060	HE450M	-	-				1,25
	4	600x700	IPE550	900x1000	HE400M	-	-				1,68
	5	500x500	IPE400A	860x960	HE360M	-	-				1,56
	6	400x400	IPE360	800x900	HE340M	-	-				1,90
MRF SLV	1	360x500	IPE450A	560x700	HE260M	-	-	386,30	165,88	1,56	1,06
	2	440x580	IPE550A	540x680	HE280B	-	-				1,08
	3	440x580	IPE550A	520x660	HE280B	-	-				1,11
	4	400x540	IPE450	480x620	HE200M	-	-				1,02
	5	360x480	IPE400A	460x580	HE180M	-	-				1,05
	6	300x360	IPE300	400x520	HE160M	-	-				1,17
CBF V π	1	360x520	HE220M	420x440	-	250x250	140x140x5	766,95	156,65	0,59	1,11
	2	360x500	HE220M	420x440	-	240x240	90x90x8				1,14
	3	340x500	HE220M	400x420	-	230x230	100X100X6,3				1,15
	4	300x480	HE200M	360x380	-	220x220	100X100X5				1,11
	5	300x400	HE180M	360x380	-	200x200	90X90X4				1,12
	6	260x340	HE140M	320x340	-	180x180	70X70X3				1,21
CBF V Λ	1	360x520	-	420x440	-	250x250	140x140x5	766,95	156,13	0,59	1,11
	2	360x500	-	420x440	-	240x240	90x90x8				1,14
	3	340x500	-	400x420	-	230x230	100X100X6,3				1,15
	4	300x480	-	360x380	-	220x220	100X100X5				1,11
	5	300x400	-	360x380	-	200x200	90X90X4				1,12
	6	260x340	-	320x340	-	180x180	70X70X3				1,21
CBF X	1	160x300	-	320x340	-	260x260	80X80X5	387,33	154,87	0,70	1,55
	2	160x300	-	320x340	-	250x250	90X90X4				1,53
	3	160x300	-	320x340	-	250x250	80X80X4				1,53
	4	160x300	-	300x320	-	240x240	70X70X4				1,64
	5	160x300	-	280x300	-	220x200	50X50X4				1,56
	6	160x300	-	260x280	-	200x200	50x50x2				1,90
CBF X D	1	220x380	-	340x360	-	280x280	90X90X6,3	385,44	154,61	0,87	1,06
	2	220x380	-	340x360	-	270x270	70X70X8				1,06
	3	220x340	-	320x340	-	260x260	80X80X6				1,05
	4	200x340	-	320x340	-	250x250	80X80X5				1,07
	5	200x280	-	300x320	-	230x230	60X60X5				1,06
	6	180x240	-	260x280	-	200x200	60X60X3				1,21
EBF	1	340x540	IPE300	400x420	-	230x230	-	383,42	155,52	0,81	1,66
	2	340x520	IPE300	400x420	-	220x220	-				1,76
	3	300x520	IPE300	360x380	-	220x220	-				1,67
	4	300x480	IPE270	360x380	-	200x200	-				1,83
	5	200x280	IPE220	320x340	-	190x190	-				1,84
	6	180x240	IPE180	260x280	-	160x160	-				1,93

** evaluated through modal analysis*

Table A.130 – Output results for timber structures – seismic zone 3: 3Z (6S-2A).

Type	S	Elements size						F_d [kN]	m [ton]	T* [s]	Ω
		Beam		Column		Diagonal					
		Timber	Link	Timber	Link	Timber	Link				
MRF SLD	1	460x500	IPE500	900x920	HE500M	-	-	231,78	164,22	1,23	2,53
	2	500x540	IPE500	860x880	HE450M	-	-				1,56
	3	500x540	IPE500	800x820	HE400M	-	-				1,62
	4	460x500	IPE500	760x780	HE360M	-	-				2,15
	5	400x440	IPE330A	700x720	HE320M	-	-				1,94
	6	300x360	IPE330A	660x680	HE320M	-	-				2,73
MRF SLV	1	300x440	IPE360A	500x640	HE220M	-	-	231,78	157,05	2,05	1,05
	2	360x500	IPE450A	460x580	HE240B	-	-				1,07
	3	360x500	IPE450A	440x540	HE240B	-	-				1,10
	4	360x440	IPE400A	400x500	HE220B	-	-				1,12
	5	300x420	IPE330A	360x460	HE220A	-	-				1,04
	6	240x320	IPE240	320x420	HE120M	-	-				1,08
CBF V π	1	280x460	HE180M	340x360	-	220x220	90x90x5	460,17	154,45	0,69	1,17
	2	280x440	HE180M	340x360	-	210x210	100x100x4				1,14
	3	280x440	HE180M	340x360	-	210x210	80X80X5				1,23
	4	260x400	HE160M	320x340	-	200x200	80X80X4				1,21
	5	240x360	HE140M	300x320	-	180x180	60X60X4				1,23
	6	220x300	HE120M	280x300	-	160x160	40x40x4				1,41
CBF V Λ	1	280x460	-	340x360	-	220x220	90x90x5	460,17	154,06	0,69	1,17
	2	280x440	-	340x360	-	210x210	100x100x4				1,14
	3	280x440	-	340x360	-	210x210	80X80X5				1,23
	4	260x400	-	320x340	-	200x200	80X80X4				1,21
	5	240x360	-	300x320	-	180x180	60X60X4				1,23
	6	220x300	-	280x300	-	160x160	40x40x4				1,41
CBF X	1	160x300	-	300x320	-	230x230	80X80X3	232,40	153,63	0,77	1,62
	2	160x300	-	300x320	-	230x230	60X60X4				1,64
	3	160x300	-	280x300	-	220x220	70X70X3				1,69
	4	160x300	-	280x300	-	210x210	60X60X3				1,77
	5	160x300	-	260x280	-	200x200	50x50x2,5				1,71
	6	160x300	-	240x260	-	170x170	25x25x3				2,00
CBF X D	1	200x340	-	320x340	-	250x250	60X60X6	231,26	153,32	0,97	1,08
	2	200x320	-	300x320	-	240x240	80X80X4				1,10
	3	200x300	-	300x320	-	230x230	60X60X5				1,08
	4	180x300	-	280x300	-	220x200	80X80X3				1,11
	5	180x260	-	280x300	-	210x210	60X60X3				1,12
	6	160x240	-	240x260	-	180x180	50x50x2				1,12
EBF	1	260x460	IPE240	320x340	-	200x200	-	230,05	153,64	0,91	1,60
	2	260x460	IPE240	320x340	-	190x190	-				1,71
	3	260x440	IPE240	320x340	-	190x190	-				1,86
	4	220x420	IPE220	280x300	-	180x180	-				1,77
	5	180x260	IPE180	260x280	-	160x160	-				1,75
	6	160x240	IPE140	220x240	-	140x140	-				1,65

** evaluated through modal analysis*

APPENDIX B

B.3.1. SEISMIC RESISTANT HEAVY TIMBER FRAME STRUCTURES WITH STEEL LINK

B.3.1.5 SEISMIC PERFORMANCE EVALUATION

B.3.1.5.6 Output

The seismic performance outputs of MRF-SLV, MRF-SLD, CBF V π, CBF V Λ, CBF X, CBF X D and EBF are presented.

1S - Number of storeys

For **MRF-SLV** and **MRF-SLD**:

1) For 1A, 2A and 3A, the comparison between the push-over curves (V-δ/h diagram), with the indication of the two reference ultimate displacements d_u (2,5% and 5%), with q=1 and q=4, for 1Z, 2Z and 3Z.
2) For 1A, 2A and 3A, the comparison between the push-over curves, with q=1, for 1Z, 2Z and 3Z, and between strength, stiffness and behaviour factor q (with its contributions related to overstrength, q_{Ω}, and ductility, q_{μ}), evaluated for the two reference ultimate displacements d_u (2,5% and 5%).
3) For 1A, 2A and 3A, the comparison between the push-over curves (V-Δ diagram), with q=4, for 1Z, 2Z and 3Z, and between strength, stiffness and behaviour factor q (with its contributions related to overstrength, q_{Ω}, and ductility, q_{μ}), evaluated for the two reference ultimate displacements d_u (2,5% and 5%).

4) For 1A, 2A and 3A, the comparison between the push-over curves (V-Δ diagram) of MRF-SLV and MRF-SLD, with the indication of the two reference ultimate displacements d_u (2,5% and 5%), with q=1 and q=4, for 1Z, 2Z and 3Z.

For **CBF V π** and **CBF V Λ**:

1) For 1A, 2A and 3A, the comparison between the push-over curves (V-δ/h diagram), with q=1, for 1Z, 2Z and 3Z, and between strength, stiffness and behaviour factor q (with its contributions related to overstrength, q_Ω, and ductility, q_μ), evaluated for the two reference ultimate displacements d_u (1,5% and 2%).
2) For 1A, 2A and 3A, the comparison between the push-over curves (V-δ/h diagram), with q=2, for 1Z, 2Z and 3Z, and between strength, stiffness and behaviour factor q (with its contributions related to overstrength, q_Ω, and ductility, q_μ), evaluated for the two reference ultimate displacements d_u (1,5% and 2%).

For **CBF X**, **CBF X D** and **EBF**:

1) For 1A, 2A and 3A, the comparison between the push-over curves (V-δ/h diagram), with q=1, for 1Z, 2Z and 3Z, and between strength, stiffness and behaviour factor q (with its contributions related to overstrength, q_Ω, and ductility, q_μ), evaluated for the two reference ultimate displacements d_u (1,5% and 2%).
2) For 1A, 2A and 3A, the comparison between the push-over curves (V-δ/h diagram), with q=4, for 1Z, 2Z and 3Z, and between strength, stiffness and behaviour factor q (with its contributions related to overstrength, q_Ω, and ductility, q_μ), evaluated for the two reference ultimate displacements d_u (1,5% and 2%).

Table B.131 – Analysis results: 1S, MRF-SLD with $q=1$ and $q_d=4$: a) 1A; 1Z, 2Z, 3Z; b) 2A; 1Z, 2Z, 3Z; c) 3A; 1Z, 2Z, 3Z.

Pushover curve

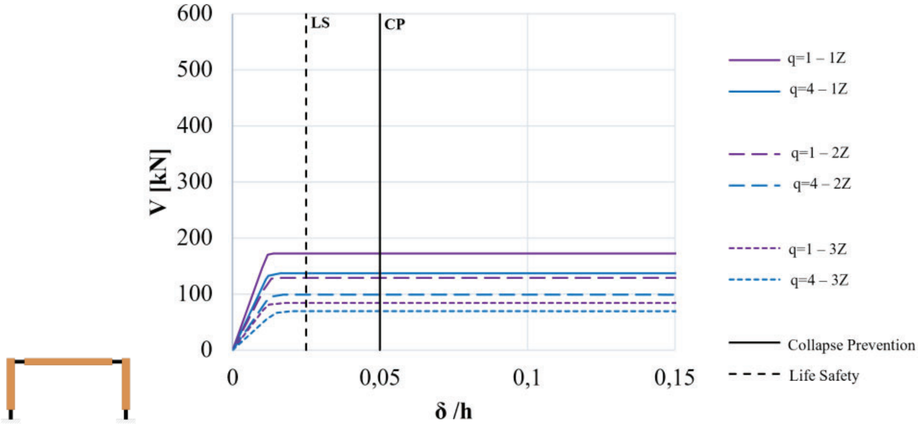

a)

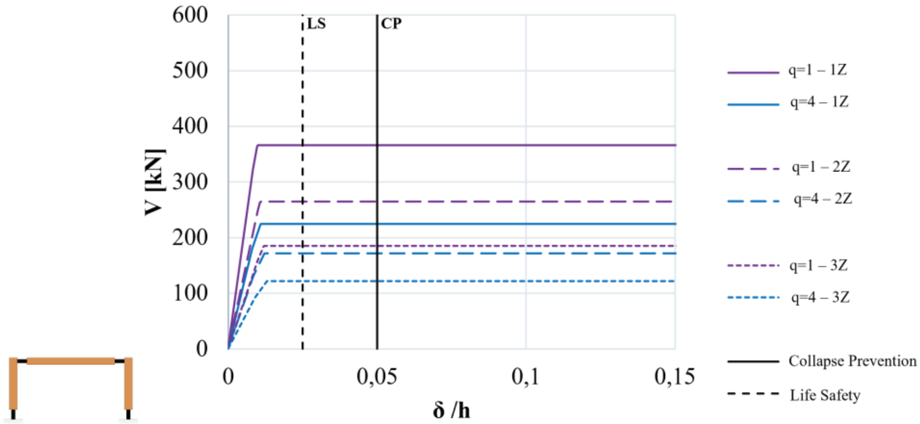

b)

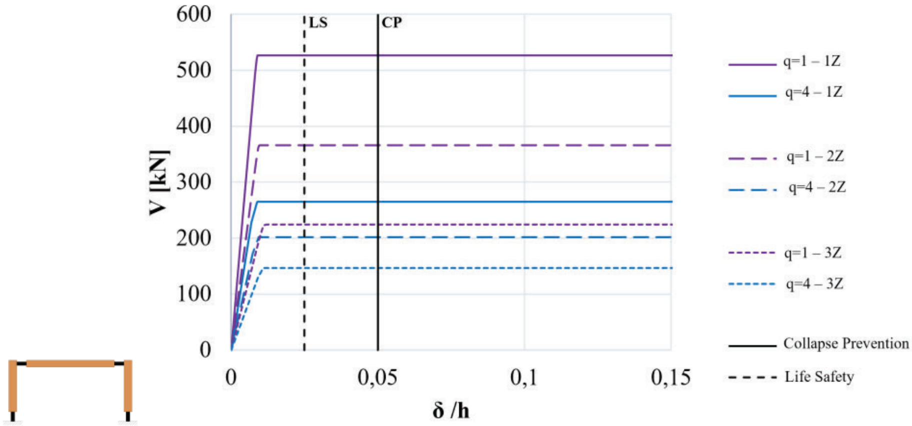

c)

Table B.132 – Analysis results: 1S, MRF-SLD with *q=1*; 1A, 2A, 3A; 1Z, 2Z, 3Z.

Pushover curve

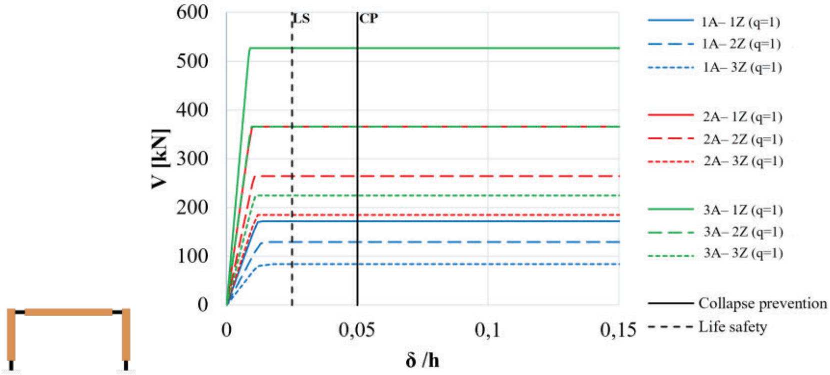

Strength [kN]

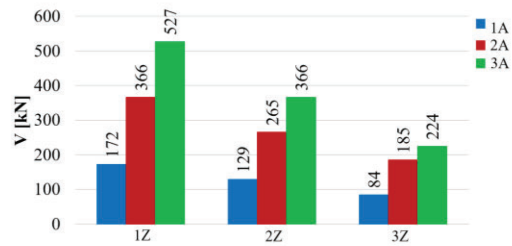

Stiffness [kN/cm]

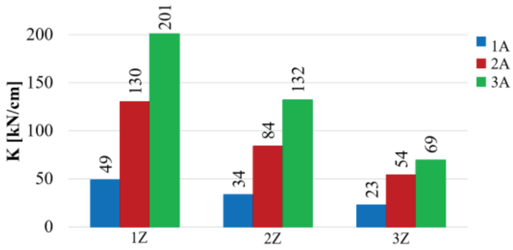

***q*_Ω (behaviour factor - overstrength)**

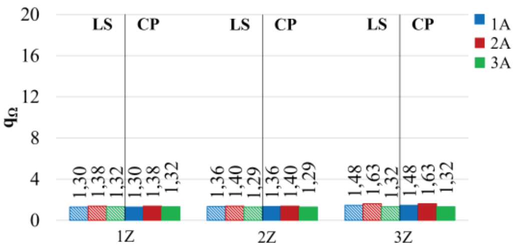

***q*_μ (behaviour factor - ductility)**

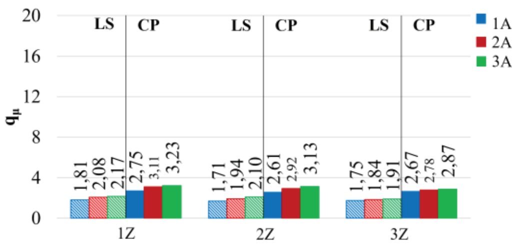

***q* (behaviour factor)**

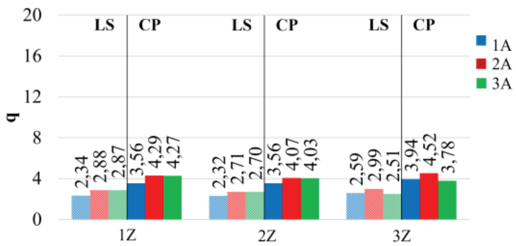

Table B.133 – Analysis results: 1S, MRF-SLD with q_d=4; 1A, 2A, 3A; 1Z, 2Z, 3Z.

Pushover curve

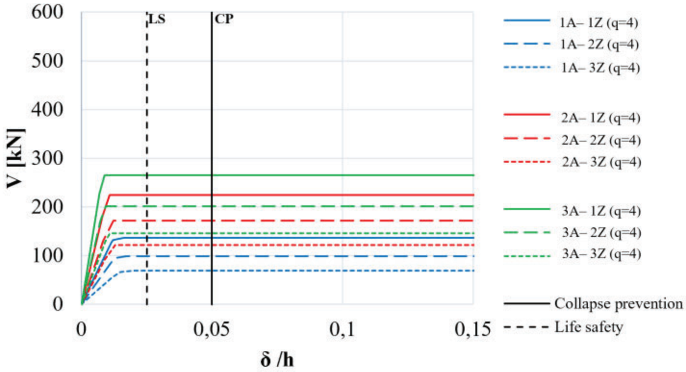

Strength [kN]

Stiffness [kN/cm]

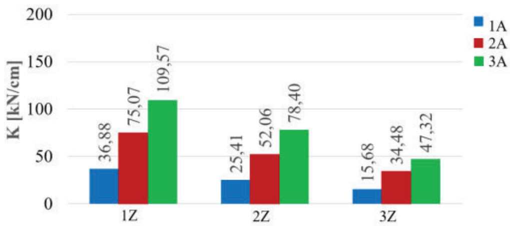

***q*$_\Omega$ (behaviour factor - overstrength)**

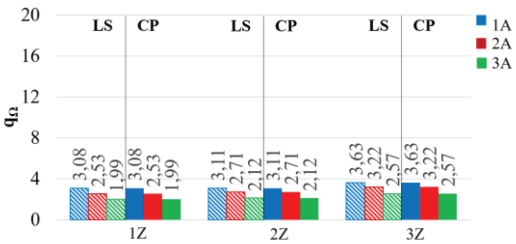

***q*$_\mu$ (behaviour factor - ductility)**

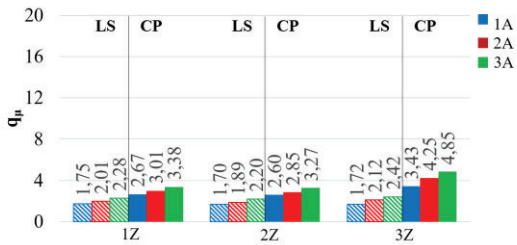

***q* (behaviour factor)**

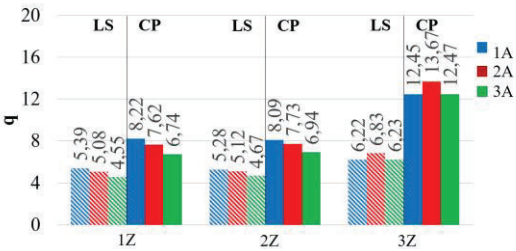

Table B.134 – Analysis results: 1S, MRF-SLV vs MRF-SLD with q_d=4: a) 1A; b) 2A; c) 3A.

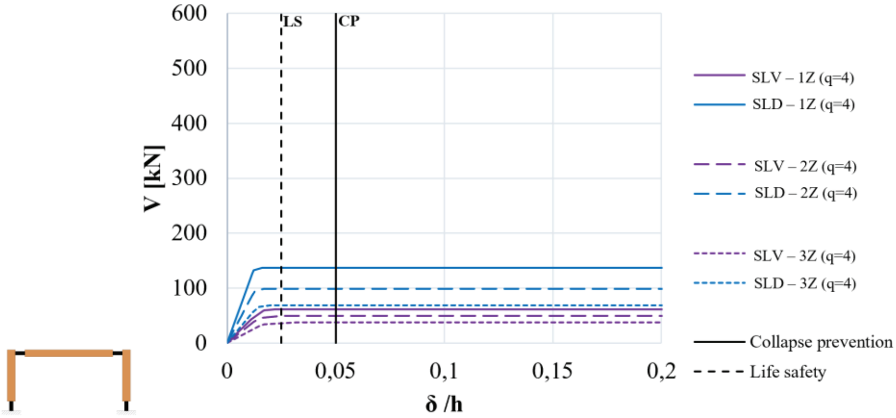

a)

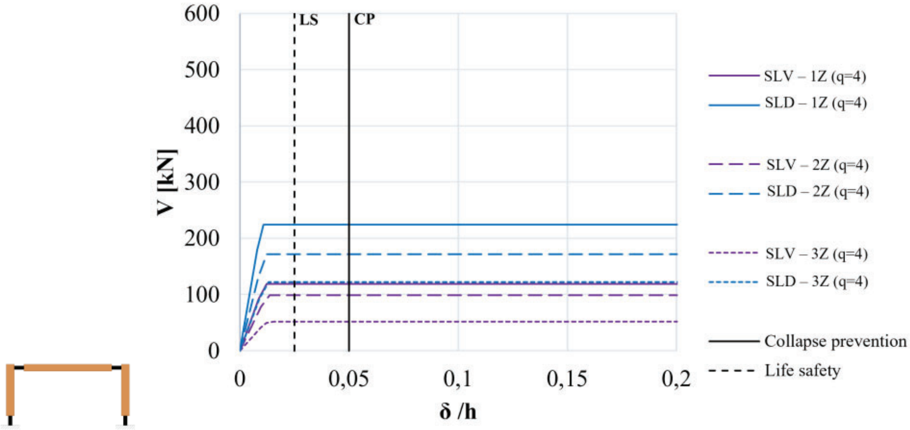

b)

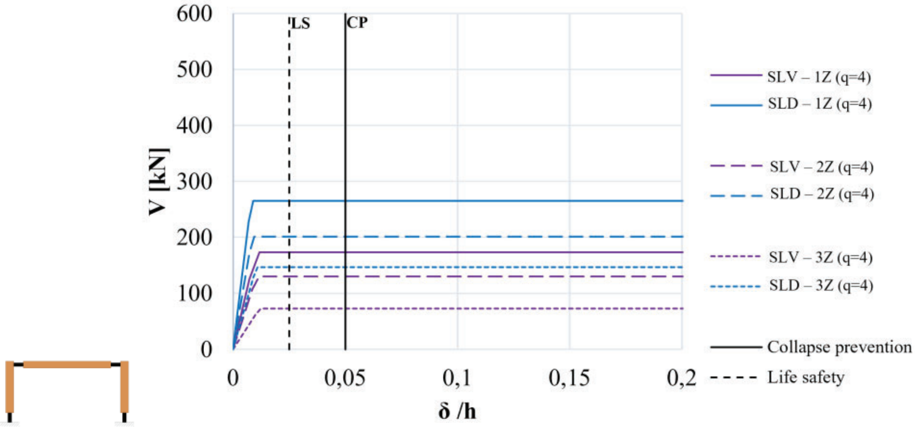

c)

Table B.135 – 1S, CBF V π with q_d=1; 1A, 2A, 3A; 1Z, 2Z, 3Z.

Pushover curve

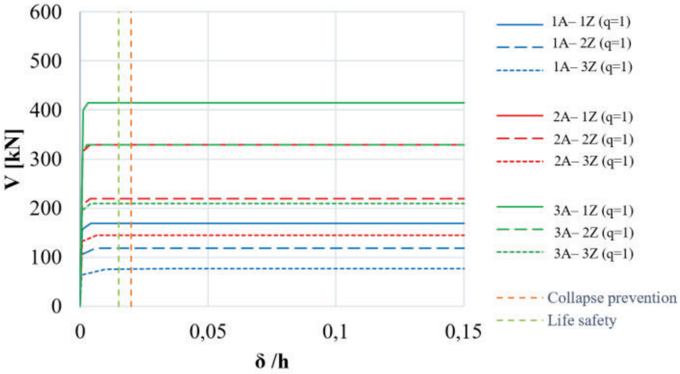

Strength [kN]

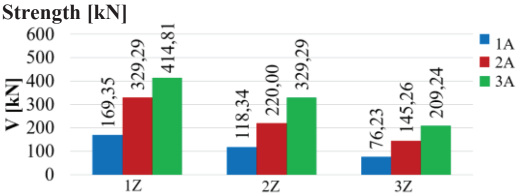

Stiffness [kN/cm]

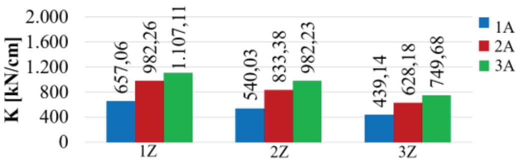

***q*$_{\Omega}$ (behaviour factor - overstrength)**

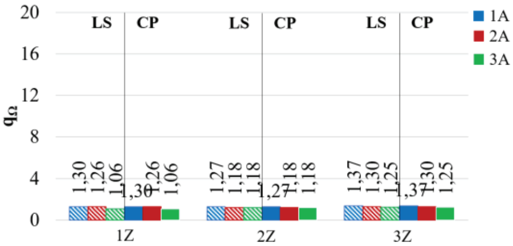

***q*$_{\mu}$ (behaviour factor - ductility)**

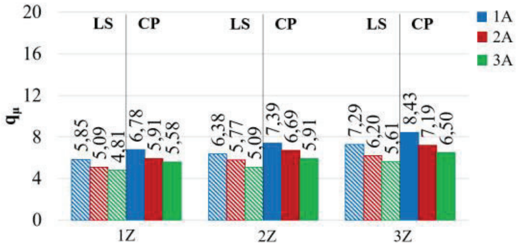

***q* (behaviour factor)**

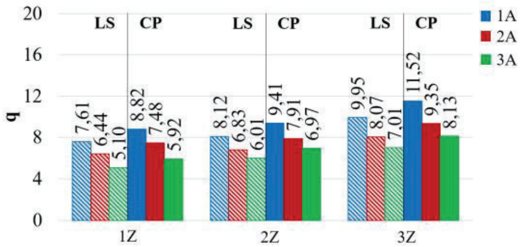

Table B.136 – 1S, CBF V π with q_d=2; 1A, 2A, 3A; 1Z, 2Z, 3Z.

Pushover curve

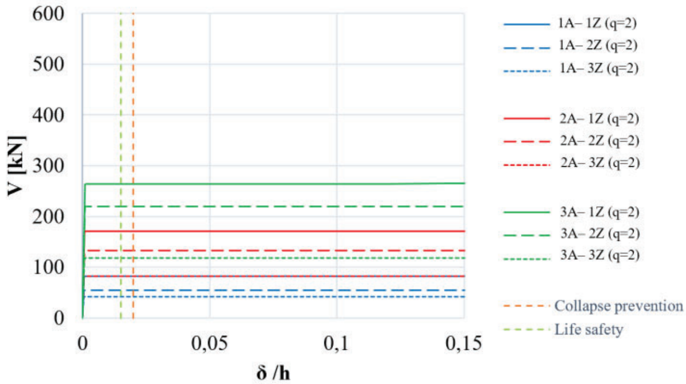

Strength [kN]

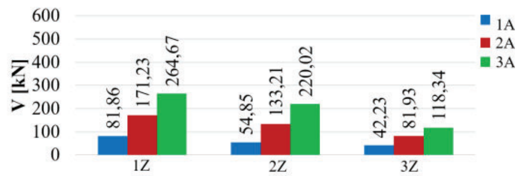

Stiffness [kN/cm]

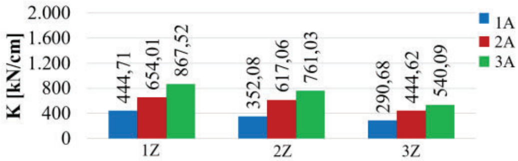

***q**$_\Omega$* **(behaviour factor - overstrength)**

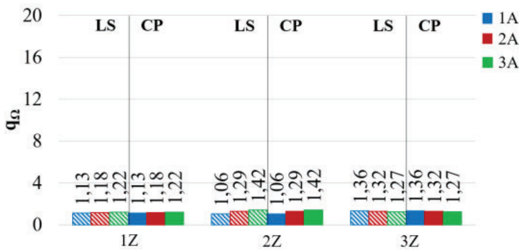

***q**$_\mu$* **(behaviour factor - ductility)**

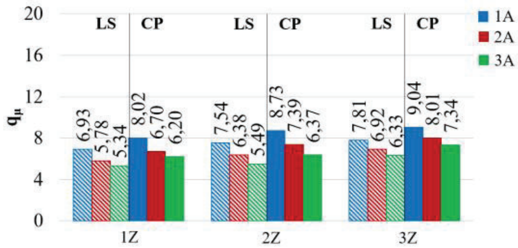

q **(behaviour factor)**

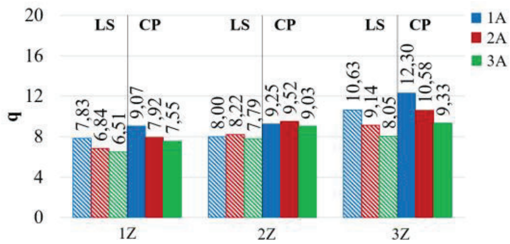

Table B.137 – 1S, CBF V Λ with q_d=1; 1A, 2A, 3A; 1Z, 2Z, 3Z.
Pushover curve

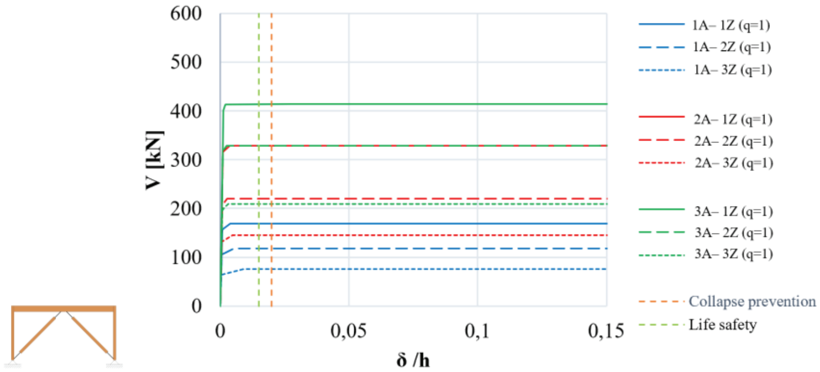

Strength [kN]

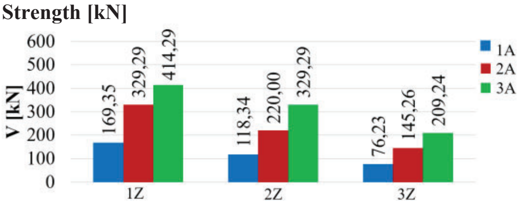

Stiffness [kN/cm]

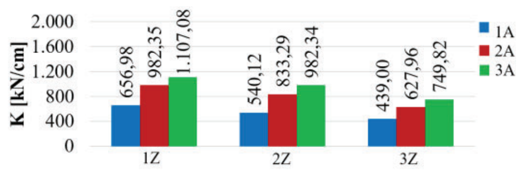

***q_Ω* (behaviour factor - overstrength)**

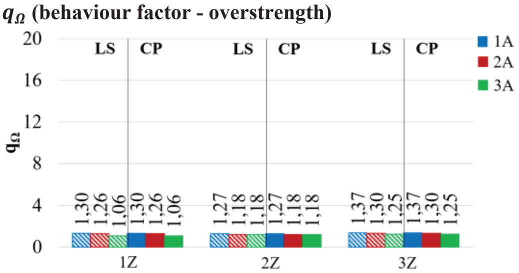

***q_μ* (behaviour factor - ductility)**

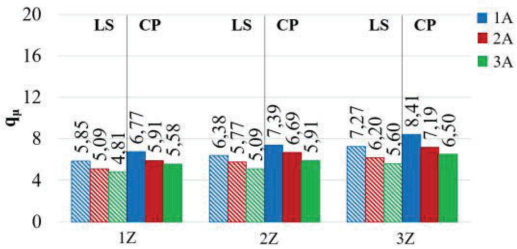

***q* (behaviour factor)**

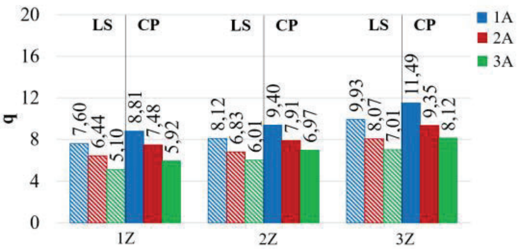

Table B.138 – 1S, CBF V Λ with q_d=2; 1A, 2A, 3A; 1Z, 2Z, 3Z.

Pushover curve

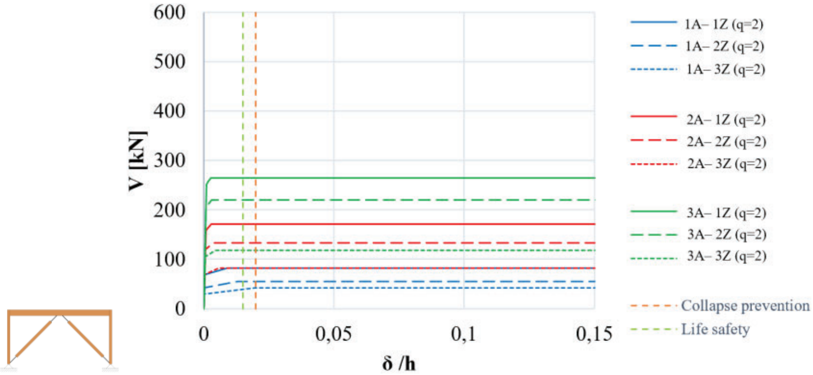

Strength [kN]

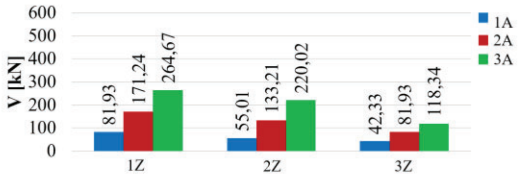

Stiffness [kN/cm]

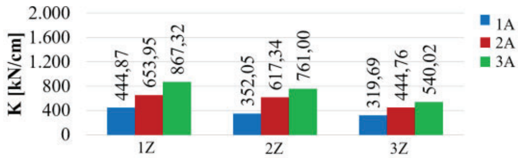

***q*$_\Omega$ (behaviour factor - overstrength)**

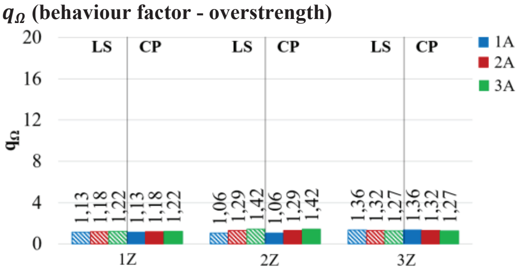

***q*$_\mu$ (behaviour factor - ductility)**

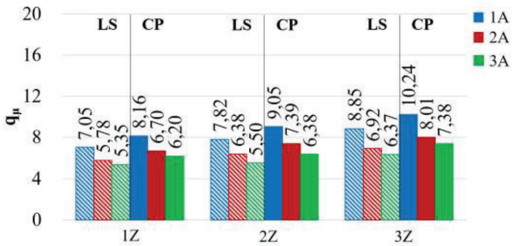

***q* (behaviour factor)**

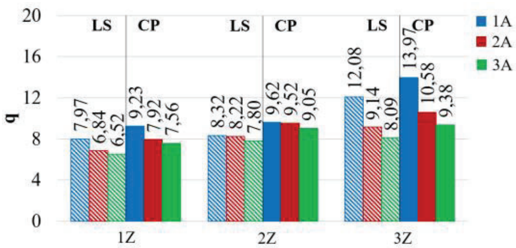

Table B.139 – 1S, CBF X with q_d=1; 1A, 2A, 3A; 1Z, 2Z, 3Z.
Pushover curve

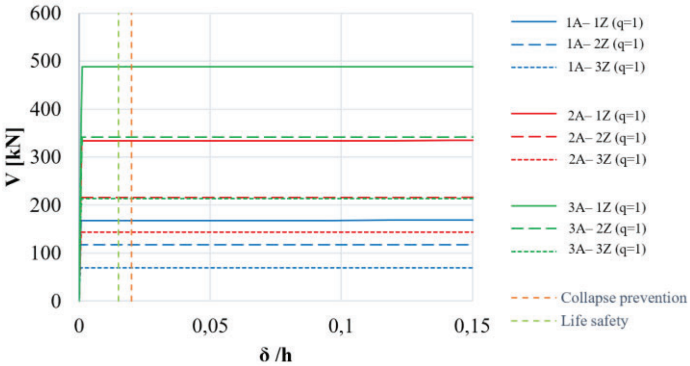

Strength [kN]

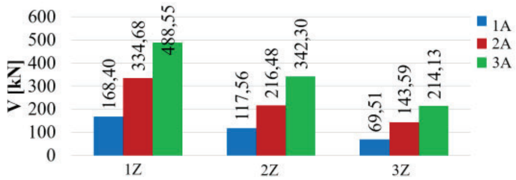

Stiffness [kN/cm]

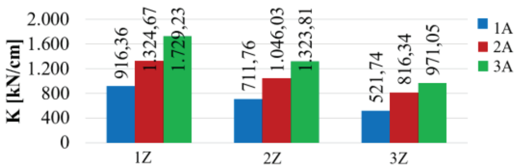

***q_Ω* (behaviour factor - overstrength)**

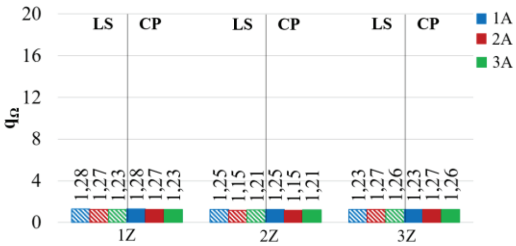

***q_μ* (behaviour factor - ductility)**

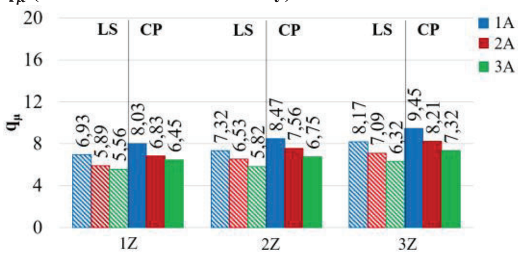

***q* (behaviour factor)**

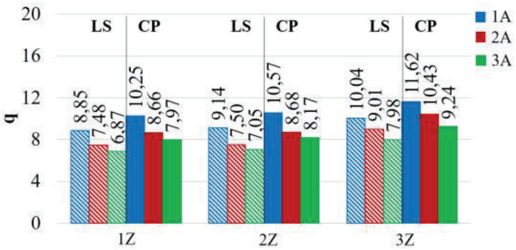

Table B.140 – 1S, CBF X with q_d=4; 1A, 2A, 3A; 1Z, 2Z, 3Z.

Pushover curve

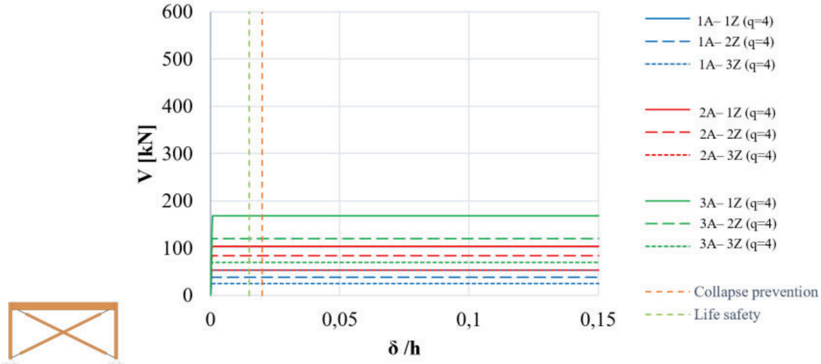

Strength [kN]

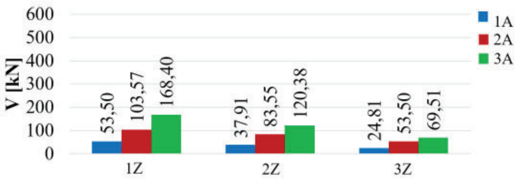

Stiffness [kN/cm]

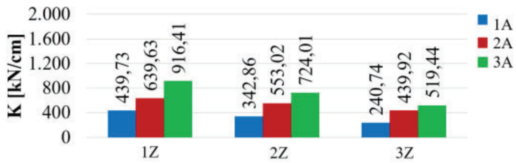

***q_Ω* (behaviour factor - overstrength)**

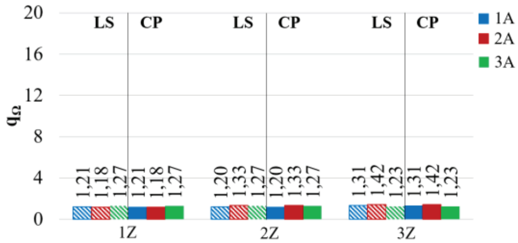

***q_μ* (behaviour factor - ductility)**

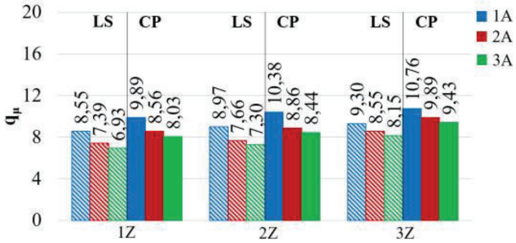

***q* (behaviour factor)**

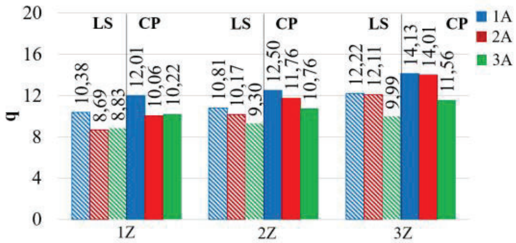

Table B.141 – 1S, CBF X D with q_d=1; 1A, 2A, 3A; 1Z, 2Z, 3Z.

Pushover curve

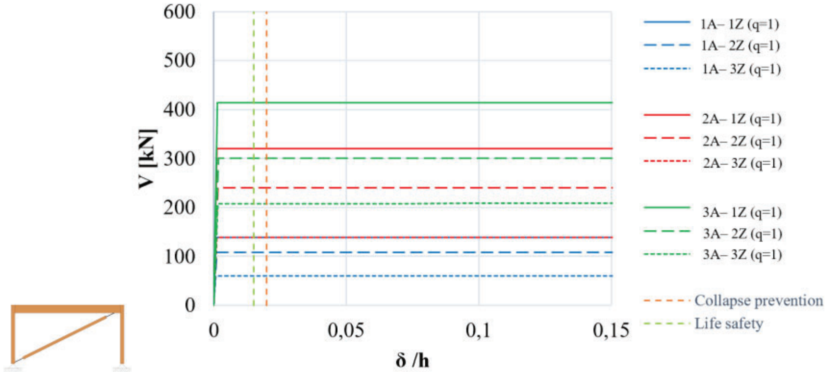

Strength [kN]

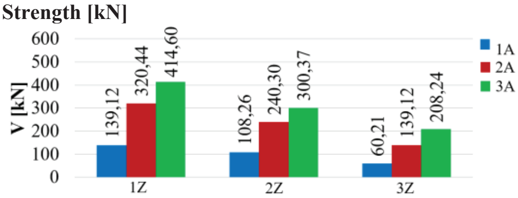

Stiffness [kN/cm]

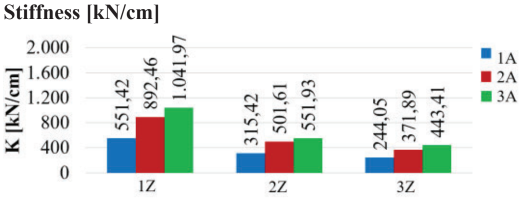

***qΩ* (behaviour factor - overstrength)**

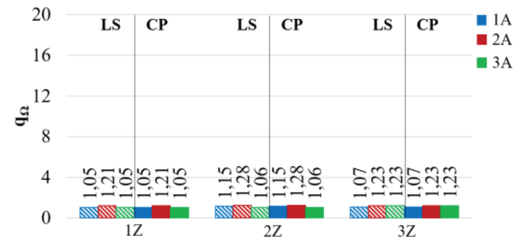

***qμ* (behaviour factor - ductility)**

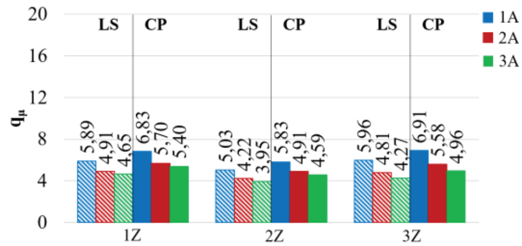

***q* (behaviour factor)**

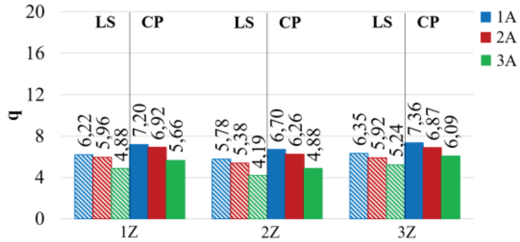

Table B.142 – 1S, CBF X D with q_d=4; 1A, 2A, 3A; 1Z, 2Z, 3Z.
Pushover curve

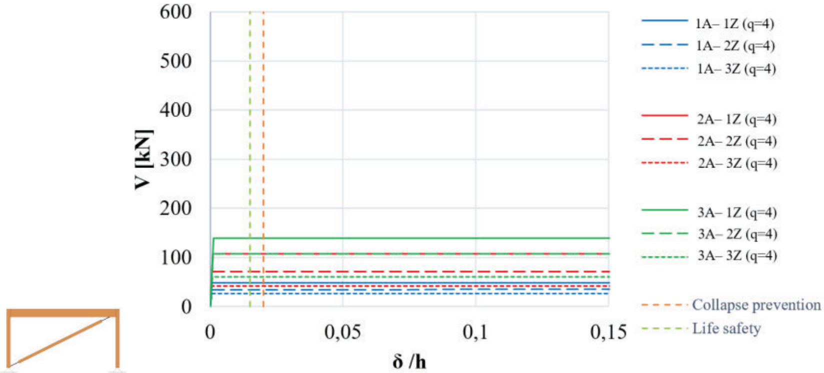

Strength [kN]

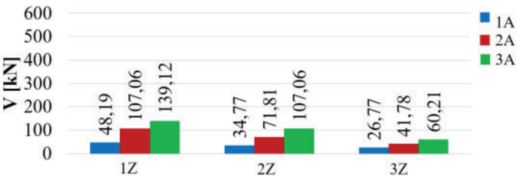

Stiffness [kN/cm]

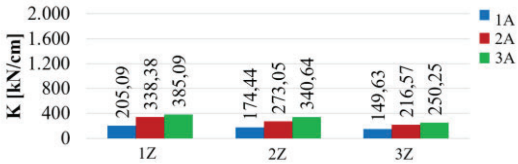

***q_Ω* (behaviour factor - overstrength)**

***q_μ* (behaviour factor - ductility)**

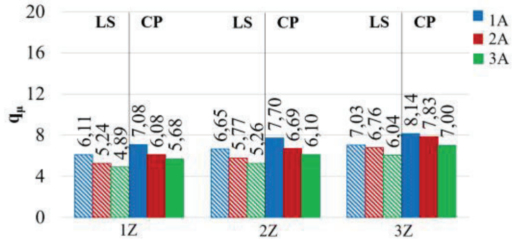

***q* (behaviour factor)**

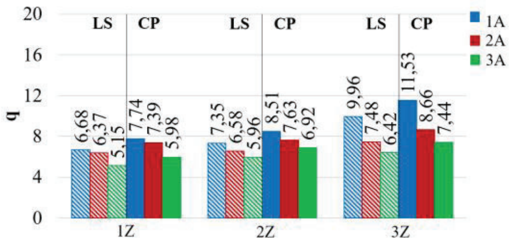

Table B.143 – 1S, EBF with q_d=1; 1A, 2A, 3A; 1Z, 2Z, 3Z.

Pushover curve

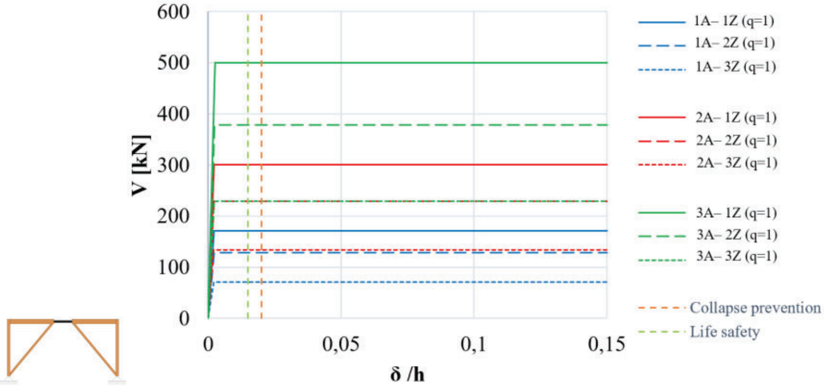

Strength [kN]

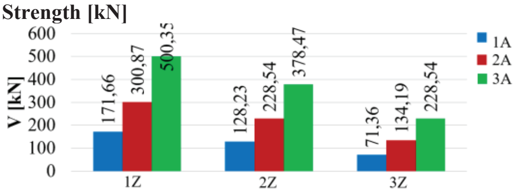

Stiffness [kN/cm]

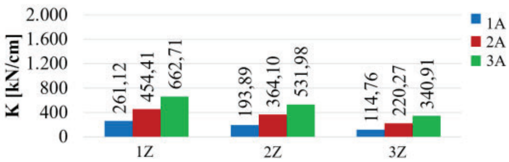

***q_Ω* (behaviour factor - overstrength)**

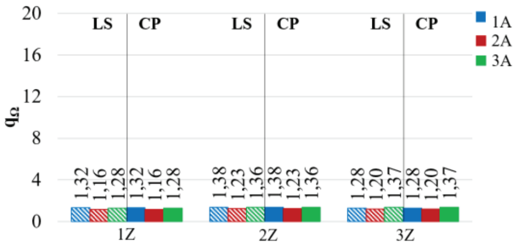

***q_μ* (behaviour factor - ductility)**

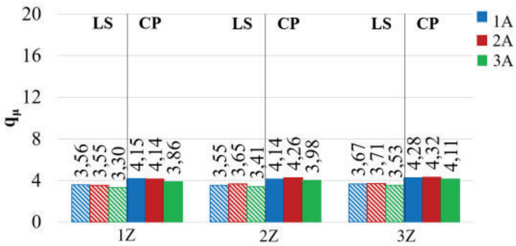

***q* (behaviour factor)**

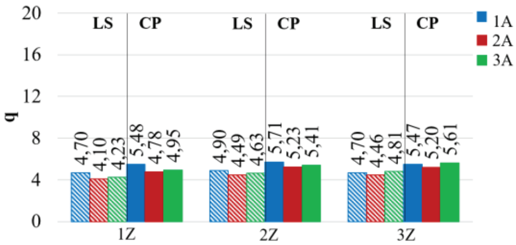

Table B.144 – 1S, EBF with q_d=4; 1A, 2A, 3A; 1Z, 2Z, 3Z.

Pushover curve

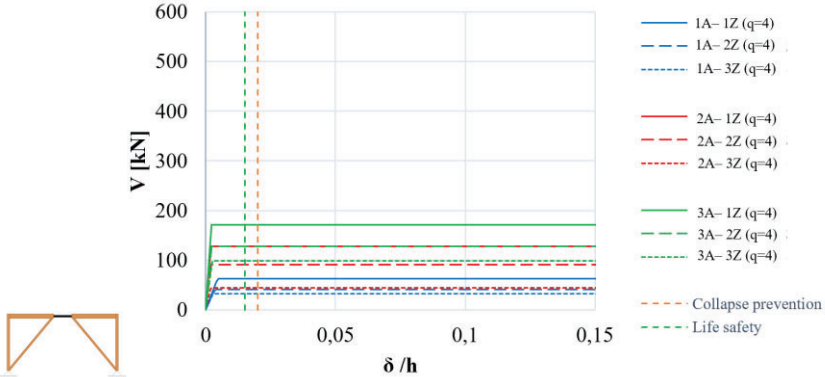

Strength [kN]

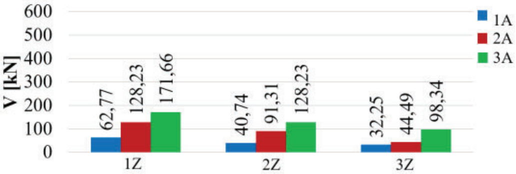

Stiffness [kN/cm]

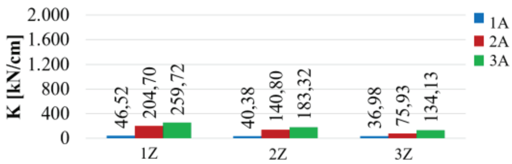

***q*$_\Omega$ (behaviour factor - overstrength)**

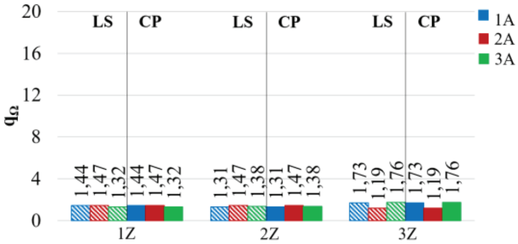

***q*$_\mu$ (behaviour factor - ductility)**

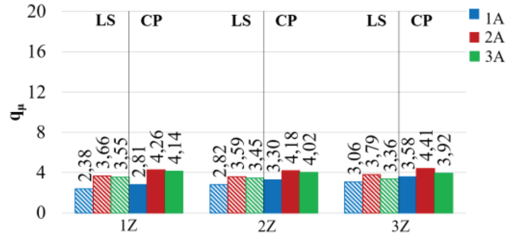

***q* (behaviour factor)**

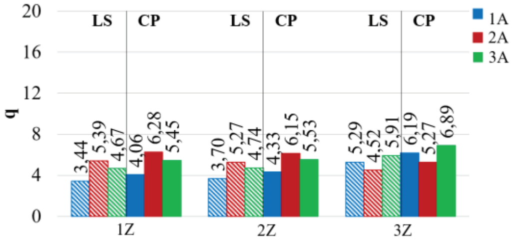

2S Number of storeys

For **MRF-SLV** and **MRF-SLD**:

For 2A, the comparison between the push-over curves (V-Δ diagram) of 2S and 1S elevation schemes, with q=4, for 1Z, 2Z and 3Z, and between strength, stiffness and behaviour factor q (with its contributions related to overstrength, q_{Ω}, and ductility, q_{μ}), evaluated for the two reference ultimate displacements d_u (2,5% and 5%).

For **CBF V π** and **CBF V Λ**:

For 2A, the comparison between the push-over curves (V-Δ diagram) of 2S and 1S elevation schemes, with q=2, for 1Z, 2Z and 3Z, and between strength, stiffness and behaviour factor q (with its contributions related to overstrength, q_{Ω}, and ductility, q_{μ}), evaluated for the two reference ultimate displacements d_u (1,5% and 2%).

For **CBF X**, **CBF X D** and **EBF**:

For 2A, the comparison between the push-over curves (V-Δ diagram) of 2S and 1S elevation schemes, with q=4, for 1Z, 2Z and 3Z, and between strength, stiffness and behaviour factor q (with its contributions related to overstrength, q_{Ω}, and ductility, q_{μ}), evaluated for the two reference ultimate displacements d_u (1,5% and 2%).

Table B.145 – Analysis results: 2S vs 1S, MRF-SLD with $q_d=4$: 2A; 1Z, 2Z, 3Z.

Pushover curve

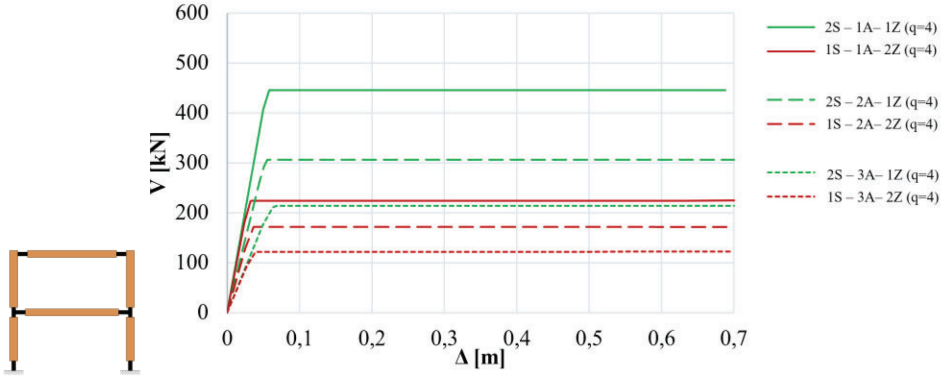

Strength [kN]

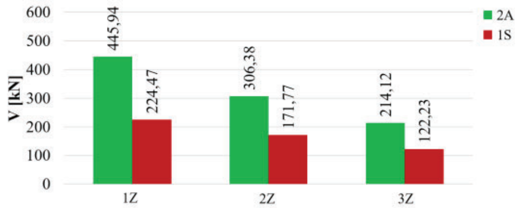

Stiffness [kN/cm]

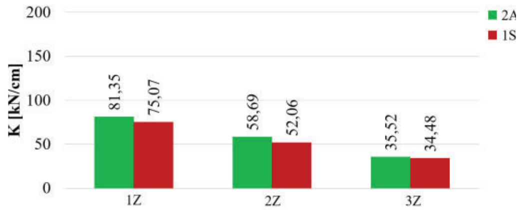

***q*$_{\Omega}$ (behaviour factor - overstrength)**

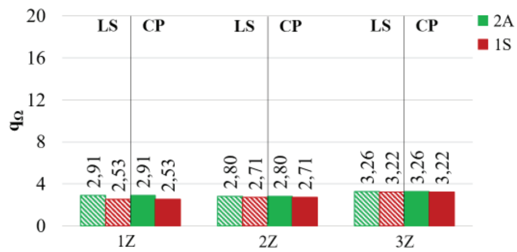

***q*$_{\mu}$ (behaviour factor - ductility)**

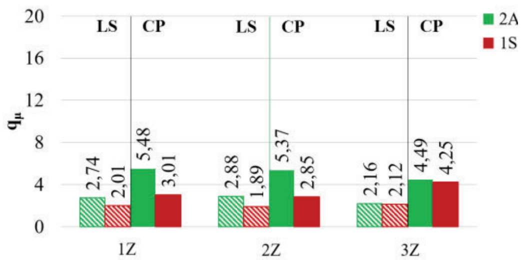

***q* (behaviour factor)**

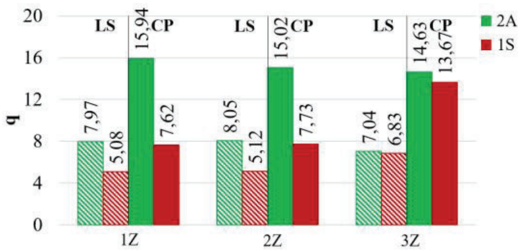

Table B.146 – Analysis results: 2S vs 1S, MRF-SLV with $q_d=4$: 2A; 1Z, 2Z, 3Z.

Pushover curve

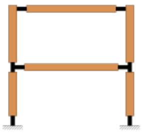

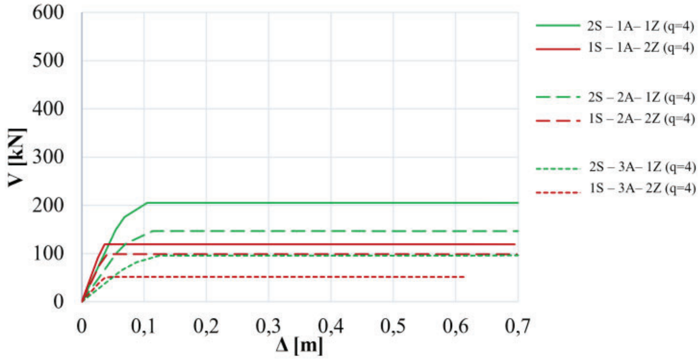

Strength [kN]

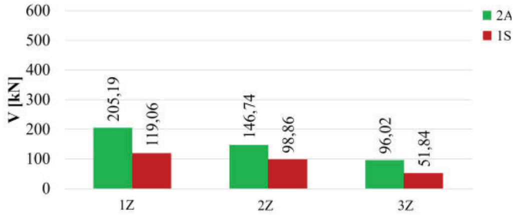

Stiffness [kN/cm]

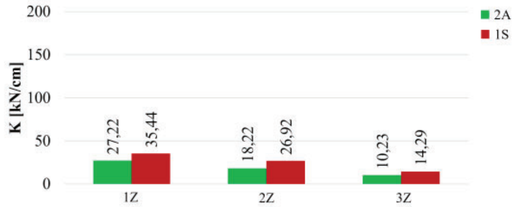

***q_Ω* (behaviour factor - overstrength)**

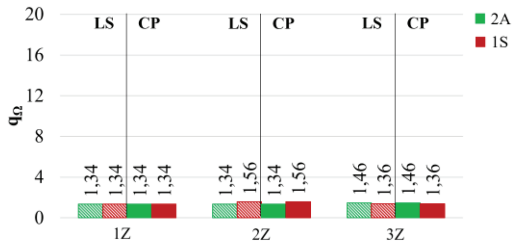

***q_μ* (behaviour factor - ductility)**

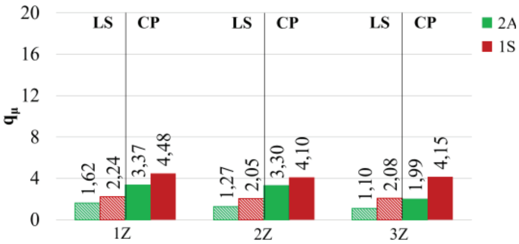

***q* (behaviour factor)**

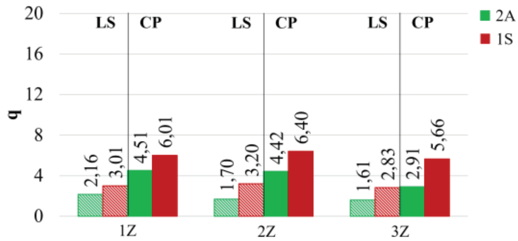

Table B.147 – 2S vs 1S, CBF V π with q_d=2: 2A; 1Z, 2Z, 3Z.

Pushover curve

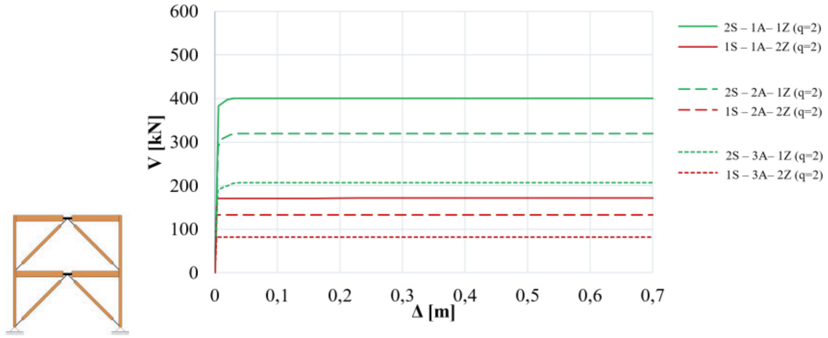

Strength [kN]

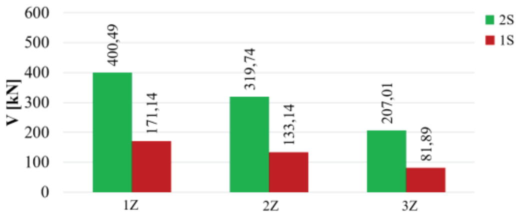

Stiffness [kN/cm]

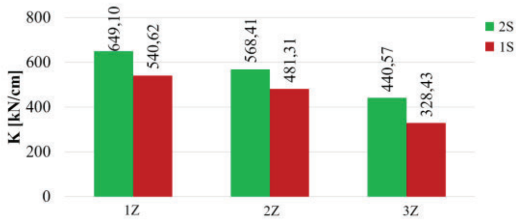

***q*$_Ω$ (behaviour factor - overstrength)**

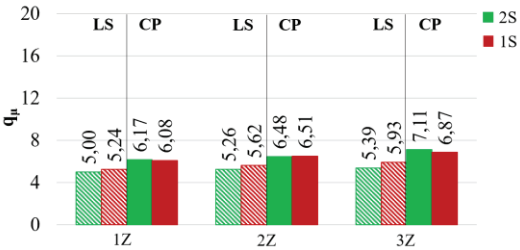

***q*$_μ$ (behaviour factor - ductility)**

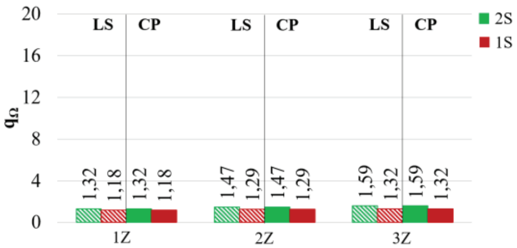

***q* (behaviour factor)**

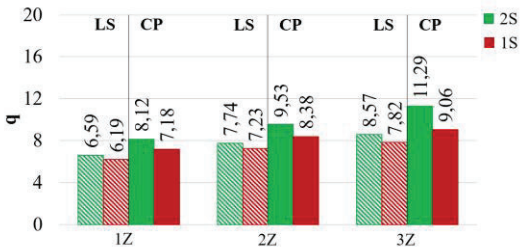

Table B.148 – 2S vs 1S, CBF V Λ with q_d=2: 2A; 1Z, 2Z, 3Z.
Pushover curve

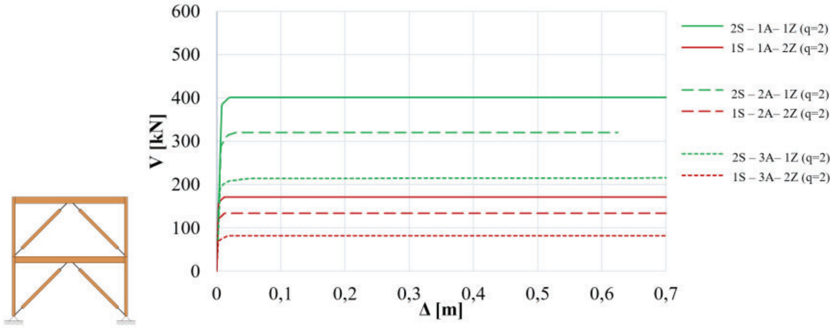

Strength [kN]

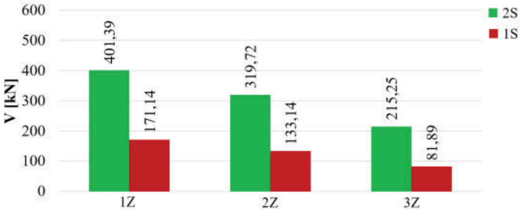

Stiffness [kN/cm]

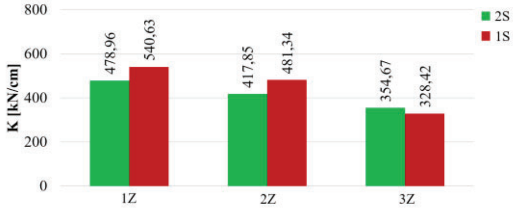

***q*$_\Omega$ (behaviour factor - overstrength)**

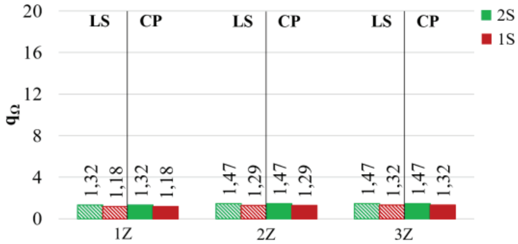

***q*$_\mu$ (behaviour factor - ductility)**

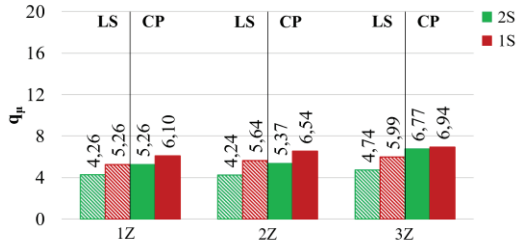

***q* (behaviour factor)**

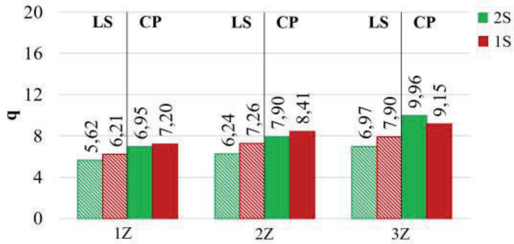

Table B.149 – 2S vs 1S, CBF X with q_d=4: 2A; 1Z, 2Z, 3Z.

Pushover curve

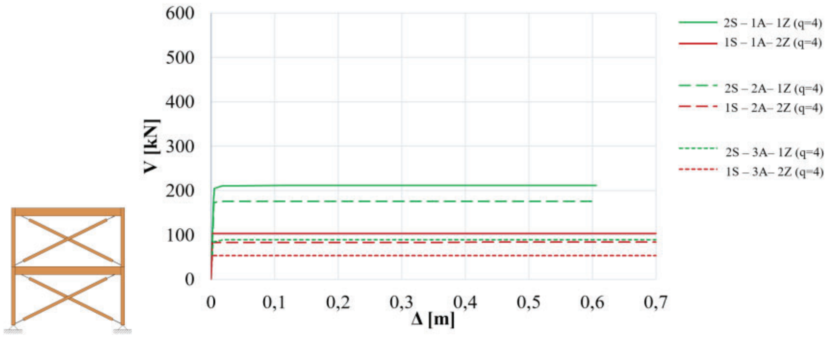

Strength [kN]

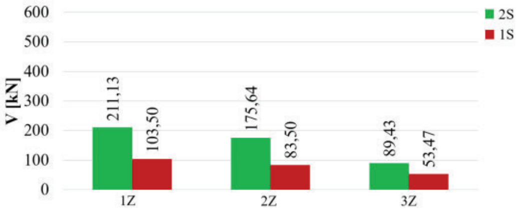

Stiffness [kN/cm]

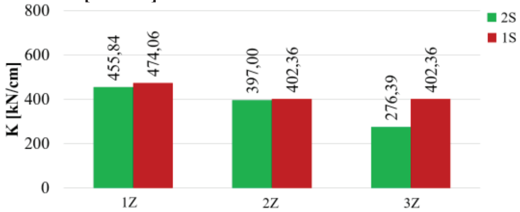

***q*$_\Omega$ (behaviour factor - overstrength)**

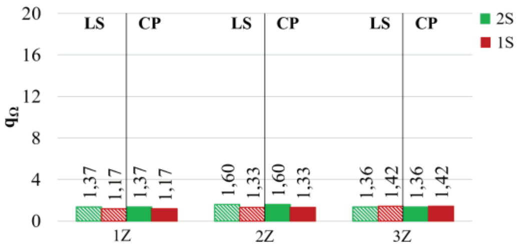

***q*$_\mu$ (behaviour factor - ductility)**

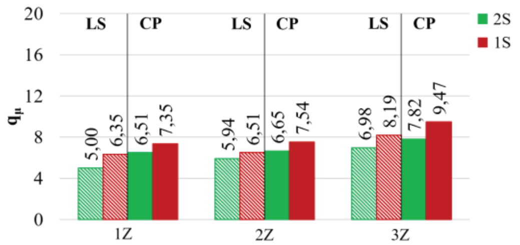

***q* (behaviour factor)**

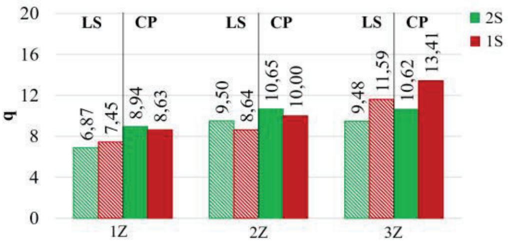

Table B.150 – 2S vs 1S, CBF X D with q_d=4: 2A; 1Z, 2Z, 3Z.

Pushover curve

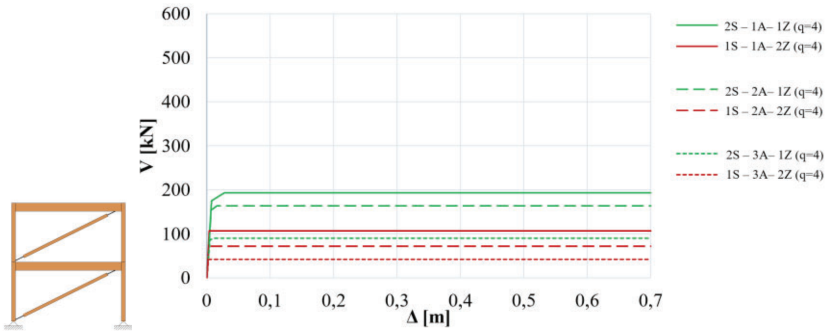

Strength [kN]

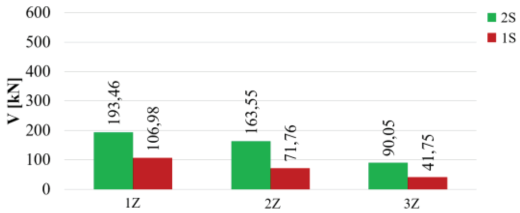

Stiffness [kN/cm]

***q*$_Ω$ (behaviour factor - overstrength)**

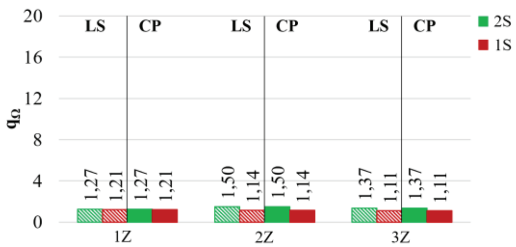

***q*$_μ$ (behaviour factor - ductility)**

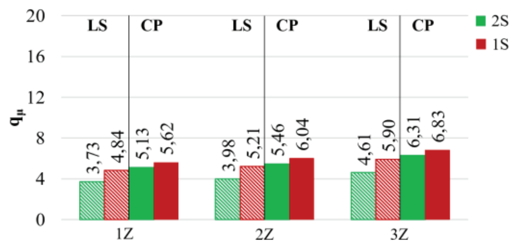

***q* (behaviour factor)**

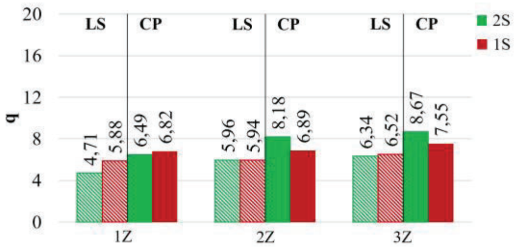

Table B.151 – 2S vs 1S, EBF with q_d=4: 2A; 1Z, 2Z, 3Z.

Pushover curve

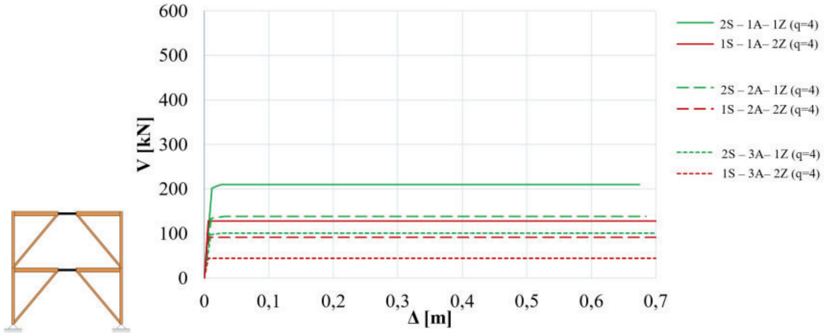

Strength [kN]

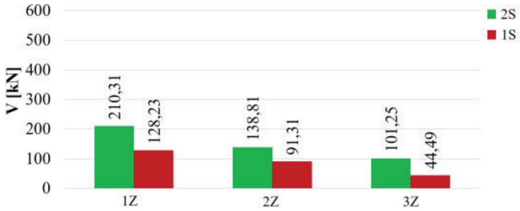

Stiffness [kN/cm]

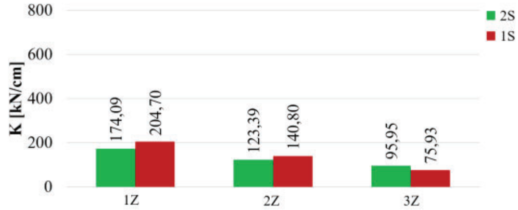

***q*$_\Omega$ (behaviour factor - overstrength)**

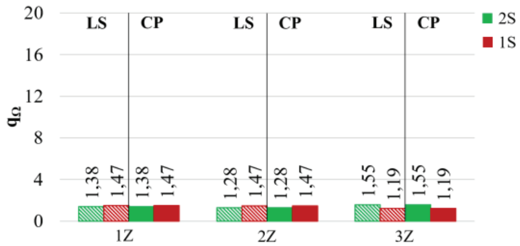

***q*$_\mu$ (behaviour factor - ductility)**

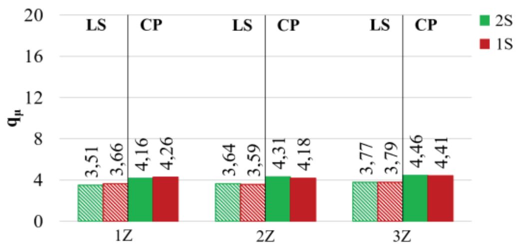

***q* (behaviour factor)**

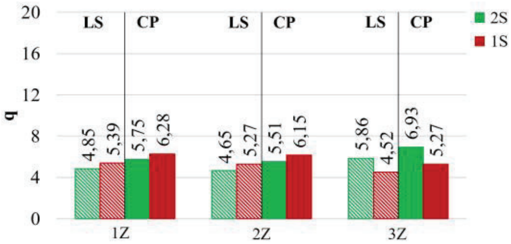

4S Number of storeys

For **MRF-SLV** and **MRF-SLD**:

For 4A, the comparison between the push-over curves (V-Δ diagram) of 2S and 1S elevation schemes, with q=4, for 1Z, 2Z and 3Z, and between strength, stiffness and behaviour factor *q* (with its contributions related to overstrength, q_{Ω}, and ductility, q_{μ}), evaluated for the two reference ultimate displacements d_u (2,5% and 5%).

For **CBF V π** and **CBF V Λ**:

For 4A, the comparison between the push-over curves (V-Δ diagram) of 2S and 1S elevation schemes, with q=2, for 1Z, 2Z and 3Z, and between strength, stiffness and behaviour factor *q* (with its contributions related to overstrength, q_{Ω}, and ductility, q_{μ}), evaluated for the two reference ultimate displacements d_u (1,5% and 2%).

For **CBF X**, **CBF X D** and **EBF**:

For 4A, the comparison between the push-over curves (V-Δ diagram) of 2S and 1S elevation schemes, with q=4, for 1Z, 2Z and 3Z, and between strength, stiffness and behaviour factor *q* (with its contributions related to overstrength, q_{Ω}, and ductility, q_{μ}), evaluated for the two reference ultimate displacements d_u (1,5% and 2%).

Table B.152 – Analysis results: 4S vs 1S, MRF-SLD with q_d=4: 2A; 1Z, 2Z, 3Z.

Pushover curve

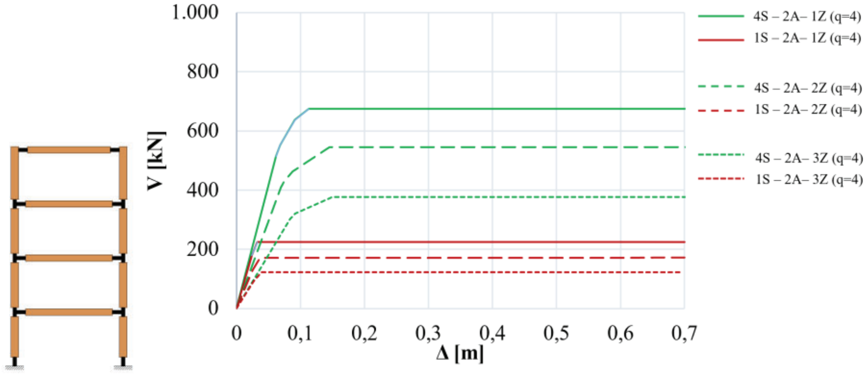

Strength [kN]

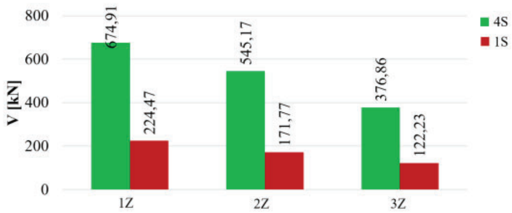

Stiffness [kN/cm]

***q*$_\Omega$ (behaviour factor - overstrength)**

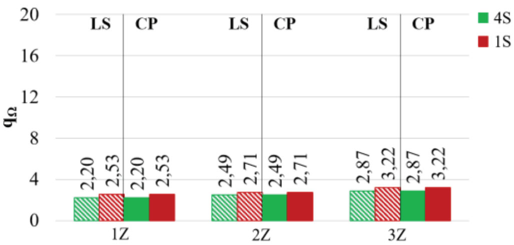

***q*$_\mu$ (behaviour factor - ductility)**

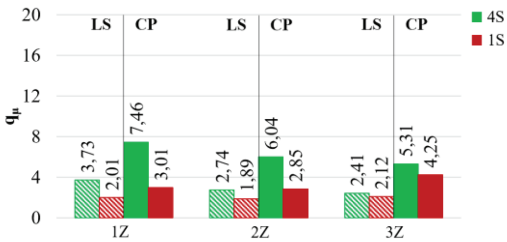

***q* (behaviour factor)**

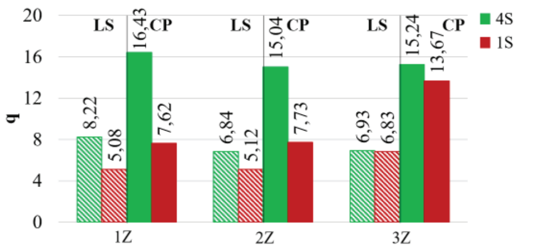

Table B.153 – Analysis results: 4S vs 1S, MRF-SLV with q_d=4: 2A; 1Z, 2Z, 3Z.

Pushover curve

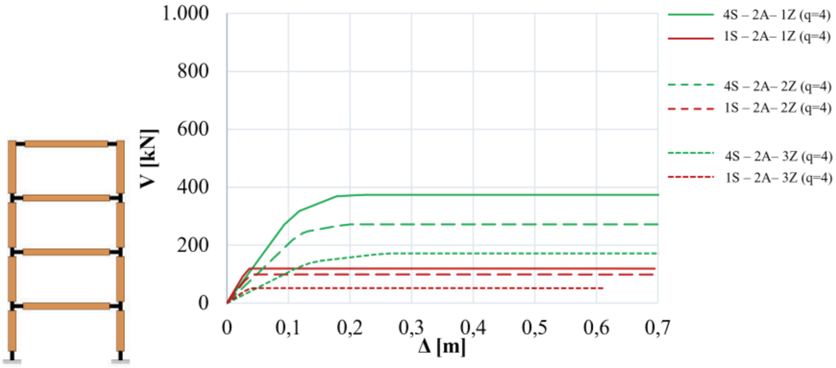

Strength [kN]

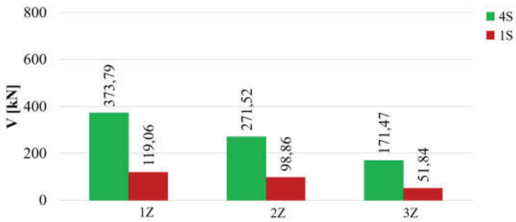

Stiffness [kN/cm]

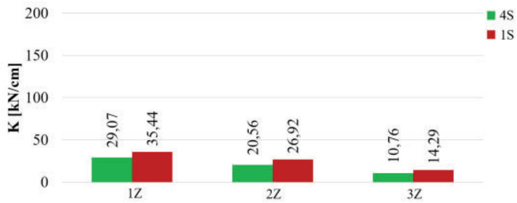

q_Ω (behaviour factor - overstrength)

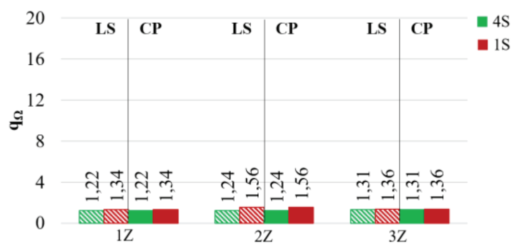

q_μ (behaviour factor - ductility)

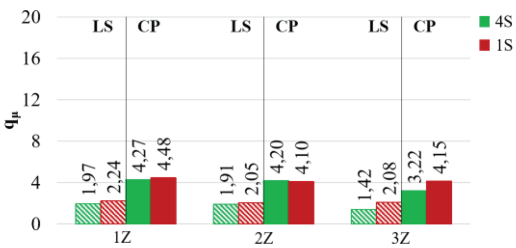

q (behaviour factor)

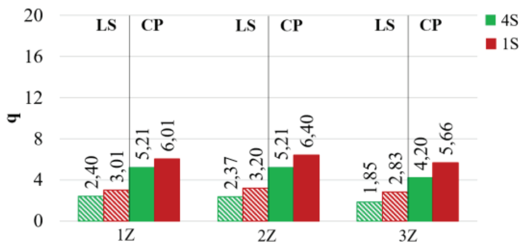

Table B.154 – 4S vs 1S, CBF V π with q_d=2: 2A; 1Z, 2Z, 3Z.

Pushover curve

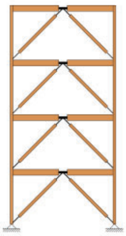

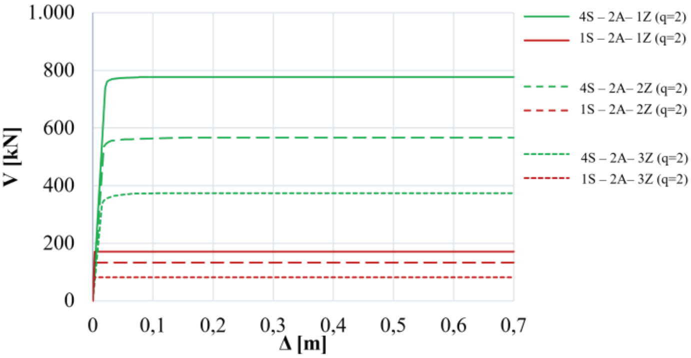

Strength [kN]

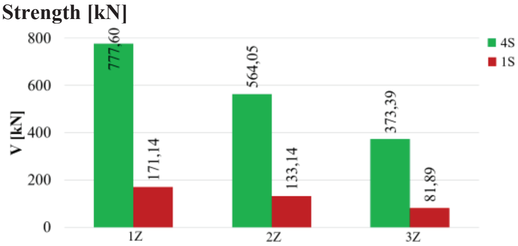

Stiffness [kN/cm]

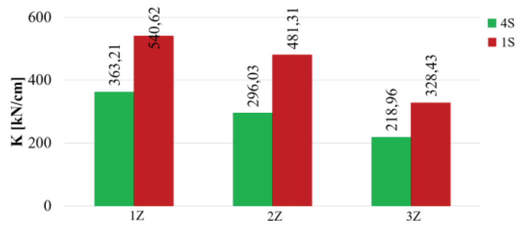

***q$_\Omega$* (behaviour factor - overstrength)**

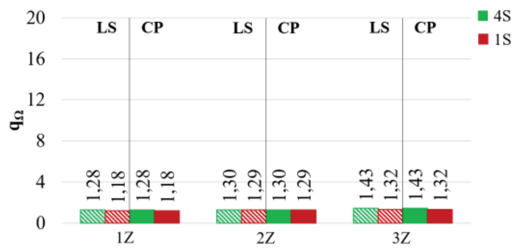

***q$_\mu$* (behaviour factor - ductility)**

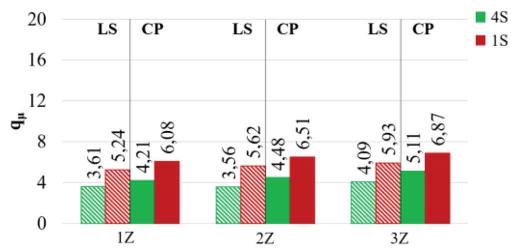

***q* (behaviour factor)**

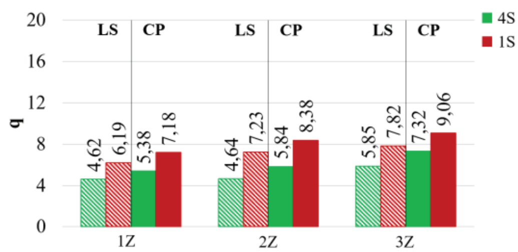

Table B.155 – 4S vs 1S, CBF V Λ with q_d=2: 2A; 1Z, 2Z, 3Z.

Pushover curve

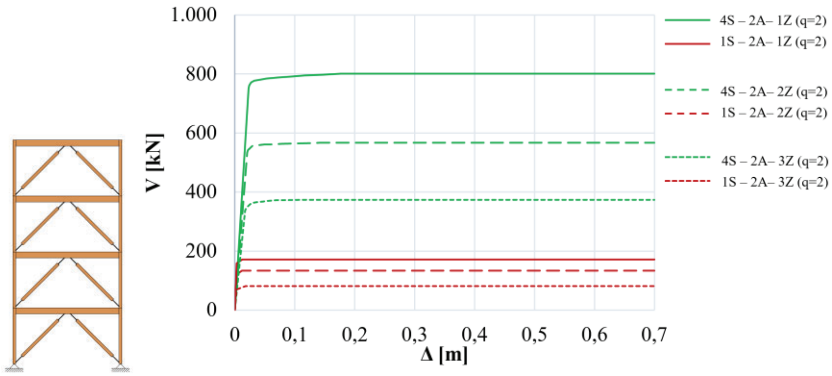

Strength [kN]

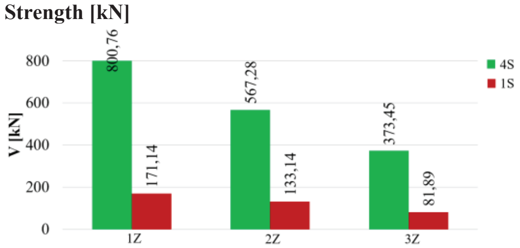

Stiffness [kN/cm]

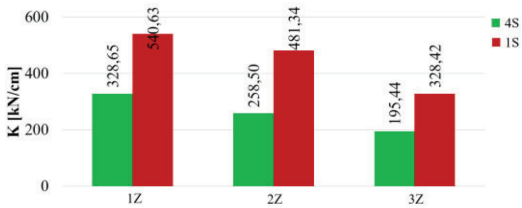

***q*$_\Omega$ (behaviour factor - overstrength)**

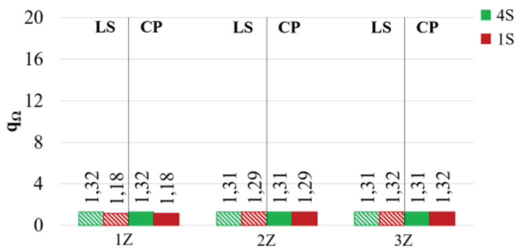

***q*$_\mu$ (behaviour factor - ductility)**

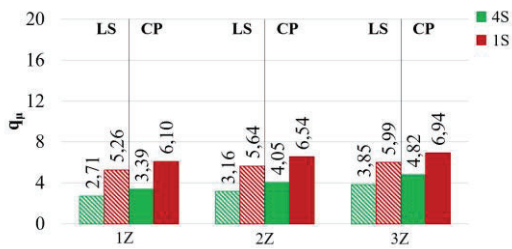

***q* (behaviour factor)**

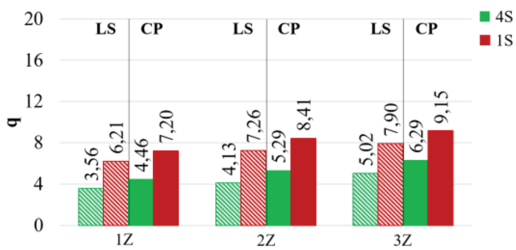

Table B.156 – 4S vs 1S, CBF X with q_d=4: 2A; 1Z, 2Z, 3Z.

Pushover curve

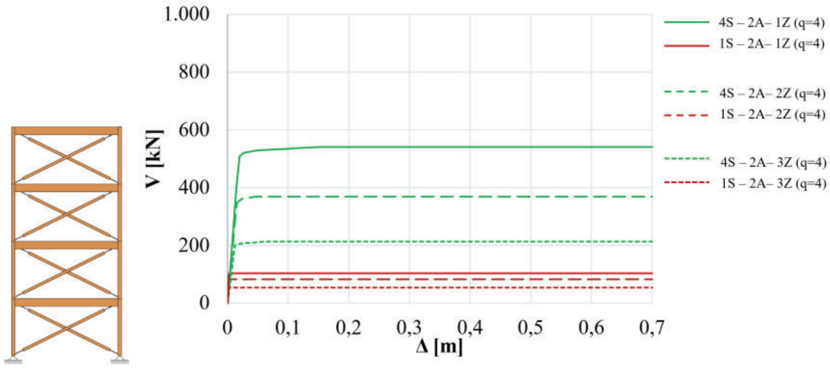

Strength [kN]

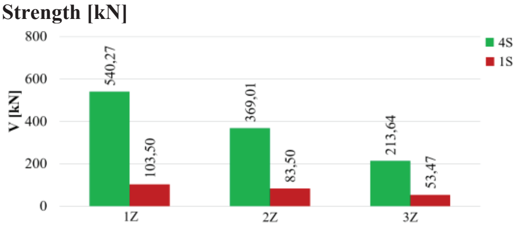

Stiffness [kN/cm]

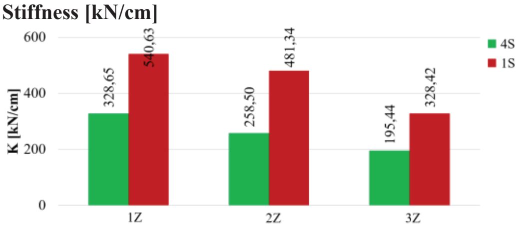

***q_Ω* (behaviour factor - overstrength)**

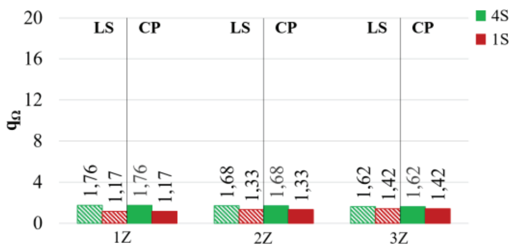

***q_μ* (behaviour factor - ductility)**

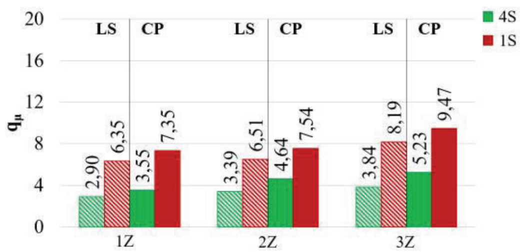

***q* (behaviour factor)**

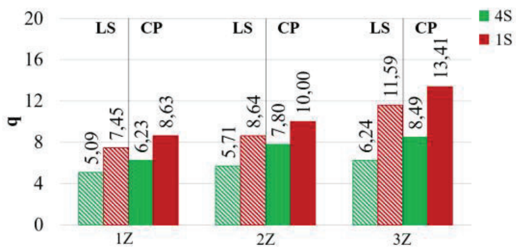

Table B.157 – 4S vs 1S, CBF X D with q_d=4: 2A; 1Z, 2Z, 3Z.

Pushover curve

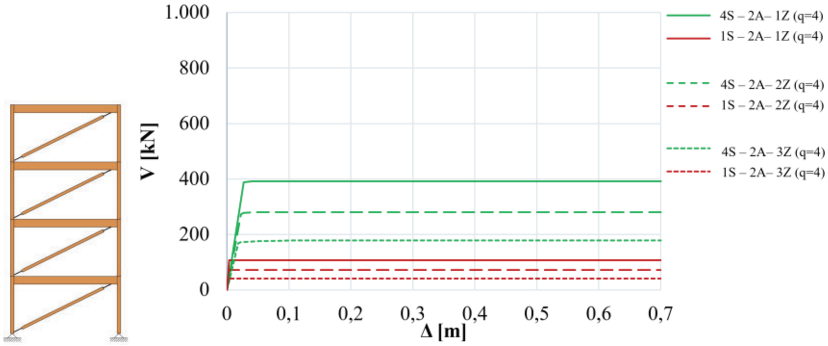

Strength [kN]

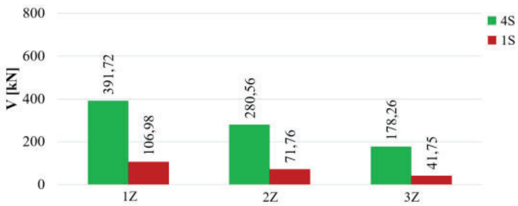

Stiffness [kN/cm]

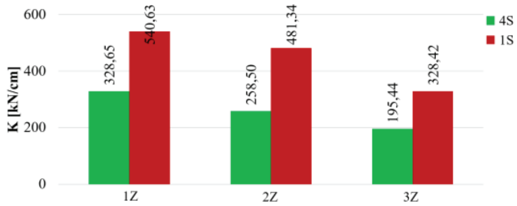

***q_Ω* (behaviour factor - overstrength)**

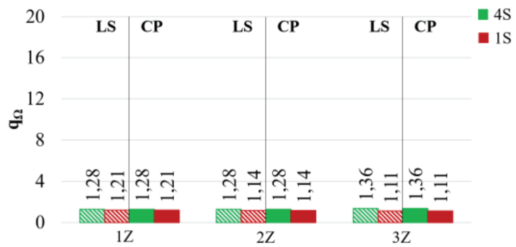

***q_μ* (behaviour factor - ductility)**

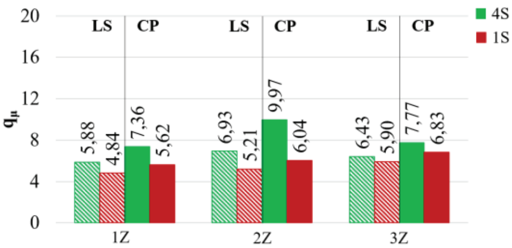

***q* (behaviour factor)**

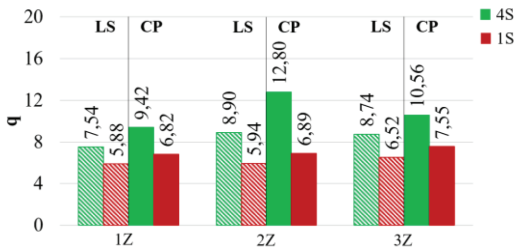

Table B.158 – 4S vs 1S, EBF with q_d=4: 2A; 1Z, 2Z, 3Z.

Pushover curve

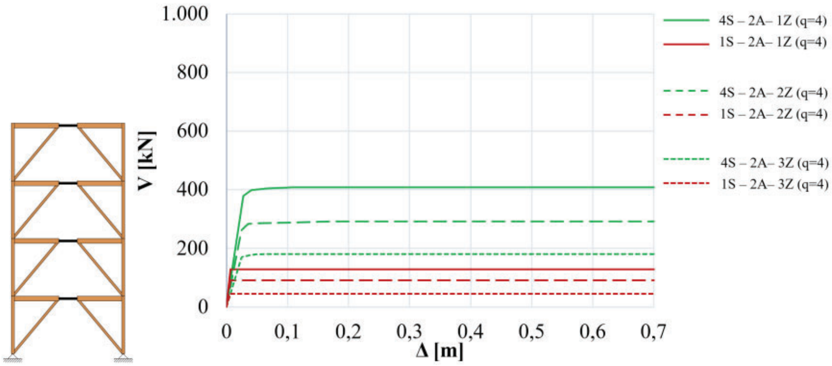

Strength [kN]

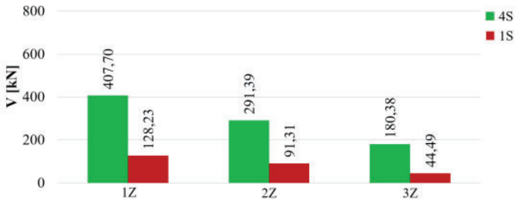

Stiffness [kN/cm]

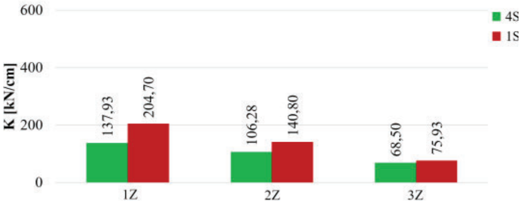

***qΩ* (behaviour factor - overstrength)**

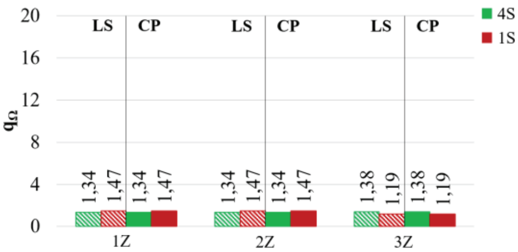

***qμ* (behaviour factor - ductility)**

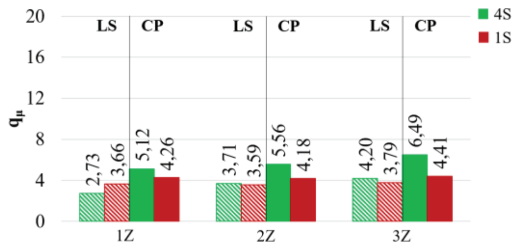

***q* (behaviour factor)**

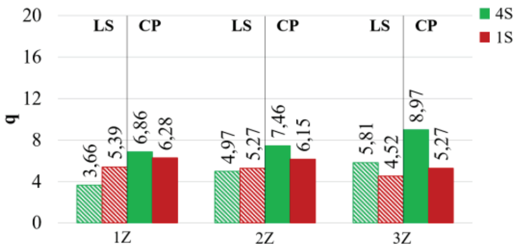

6S Number of storeys

For **MRF-SLV** and **MRF-SLD**:

For 6A, the comparison between the push-over curves (V-Δ diagram) of 2S and 1S elevation schemes, with q=4, for 1Z, 2Z and 3Z, and between strength, stiffness and behaviour factor q (with its contributions related to overstrength, q_{Ω}, and ductility, q_{μ}), evaluated for the two reference ultimate displacements d_u (2,5% and 5%).

For **CBF V π** and **CBF V Λ**:

For 6A, the comparison between the push-over curves (V- Δ diagram) of 2S and 1S elevation schemes, with q=2, for 1Z, 2Z and 3Z, and between strength, stiffness and behaviour factor q (with its contributions related to overstrength, q_{Ω}, and ductility, q_{μ}), evaluated for the two reference ultimate displacements d_u (1,5% and 2%).

For **CBF X**, **CBF X D** and **EBF**:

For 6A, the comparison between the push-over curves (V- Δ diagram) of 2S and 1S elevation schemes, with q=4, for 1Z, 2Z and 3Z, and between strength, stiffness and behaviour factor q (with its contributions related to overstrength, q_{Ω}, and ductility, q_{μ}), evaluated for the two reference ultimate displacements d_u (1,5% and 2%).

Table B.159 – Analysis results: 6S vs 1S, MRF-SLD with q_d=4: 2A; 1Z, 2Z, 3Z.

Pushover curve

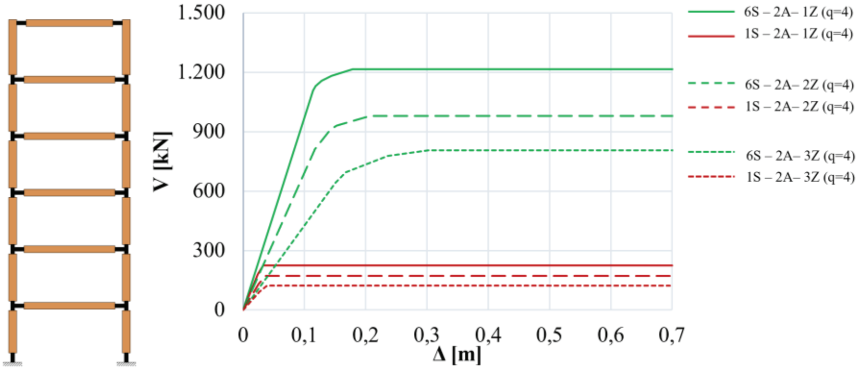

Strength [kN]

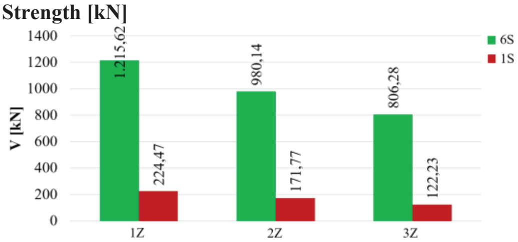

Stiffness [kN/cm]

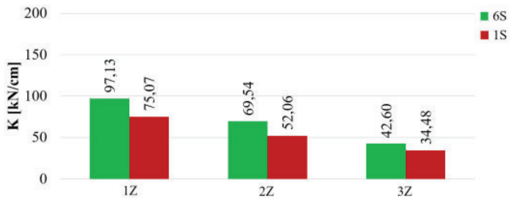

q_Ω (behaviour factor - overstrength)

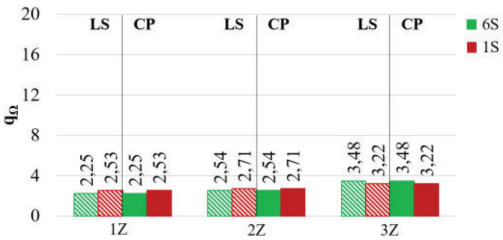

q_μ (behaviour factor - ductility)

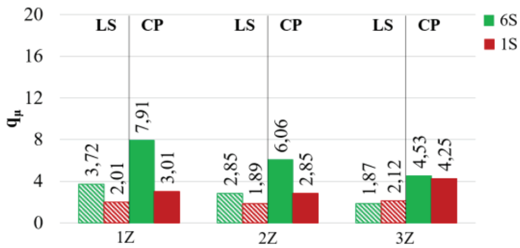

q (behaviour factor)

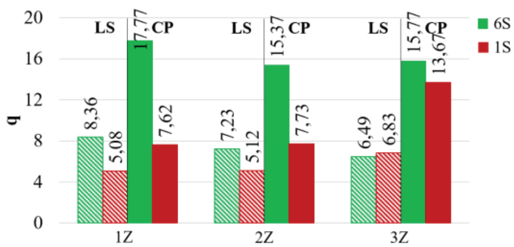

Table B.160 – Analysis results: 6S vs 1S, MRF-SLV with q_d=4: 2A; 1Z, 2Z, 3Z.

Pushover curve

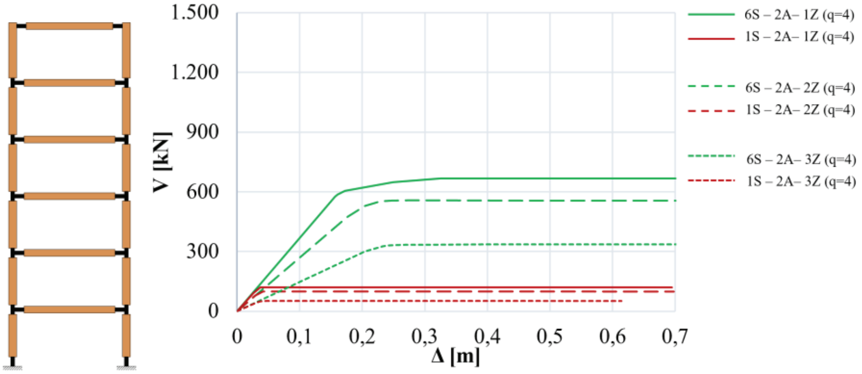

Strength [kN]

Stiffness [kN/cm]

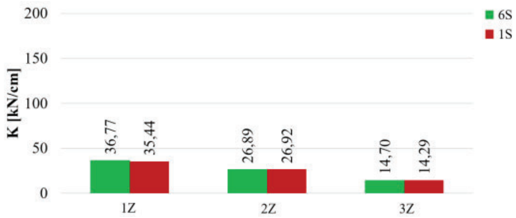

q_Ω **(behaviour factor - overstrength)**

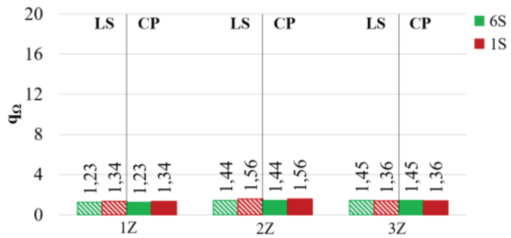

q_μ **(behaviour factor - ductility)**

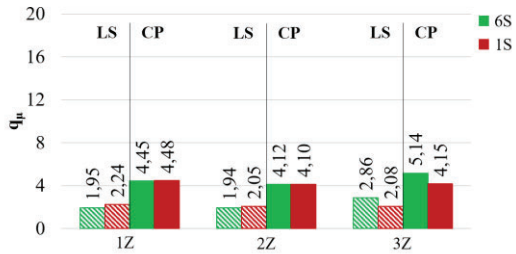

q **(behaviour factor)**

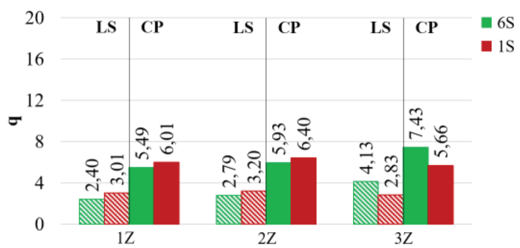

Table B.161 – 6S vs 1S, CBF V π with q_d=2: 2A; 1Z, 2Z, 3Z.

Pushover curve

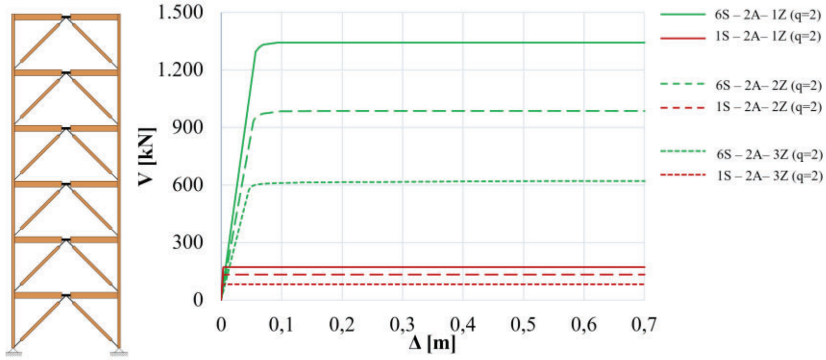

Strength [kN]

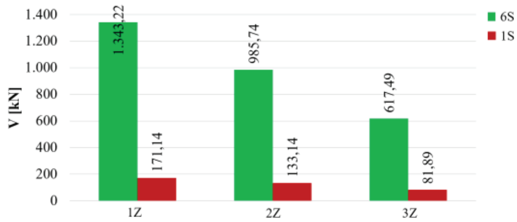

Stiffness [kN/cm]

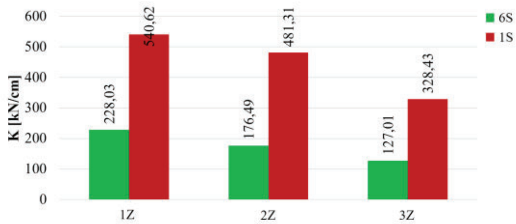

***q*$_\Omega$ (behaviour factor - overstrength)**

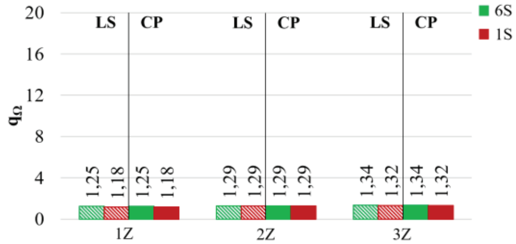

***q*$_\mu$ (behaviour factor - ductility)**

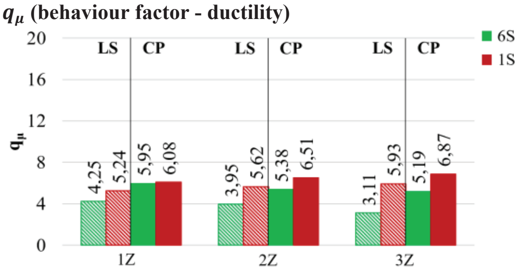

***q* (behaviour factor)**

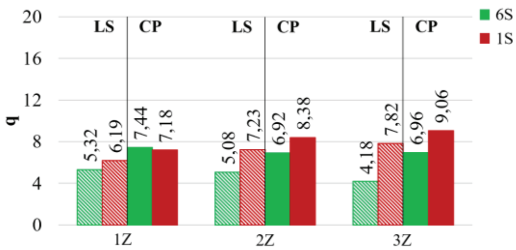

Table B.162 – 6S vs 1S, CBF V Λ with q_d=2: 2A; 1Z, 2Z, 3Z.

Pushover curve

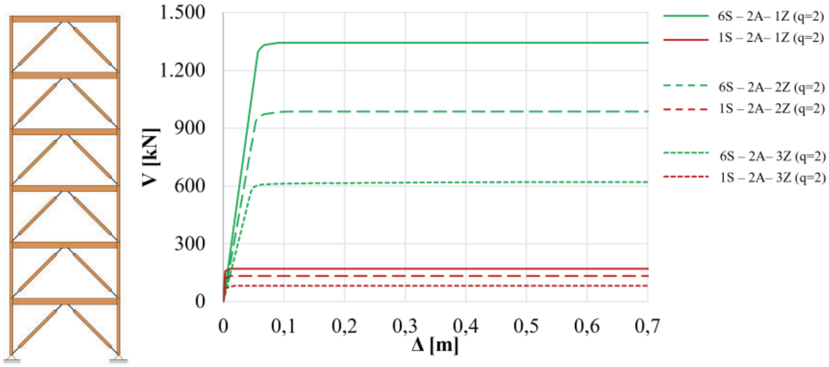

Strength [kN]

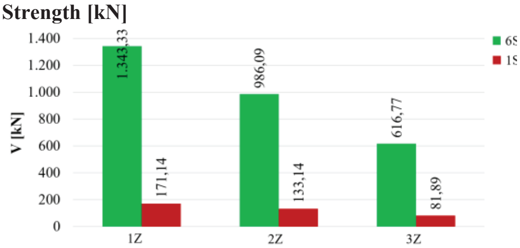

Stiffness [kN/cm]

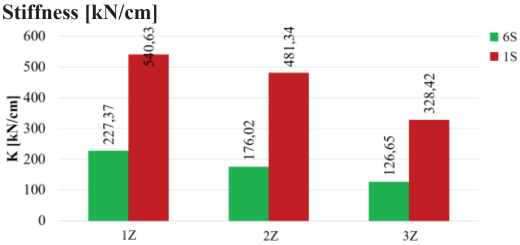

q_Ω (behaviour factor - overstrength)

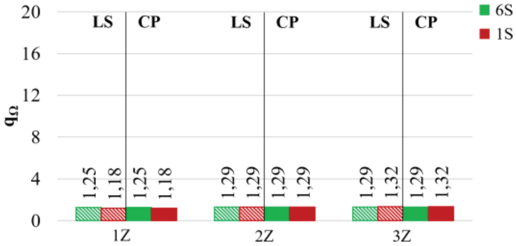

q_μ (behaviour factor - ductility)

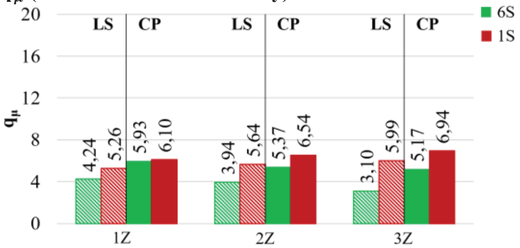

q (behaviour factor)

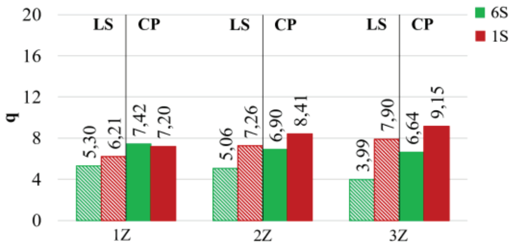

Table B.163 – 6S vs 1S, CBF X with q_d=4: 2A; 1Z, 2Z, 3Z.
Pushover curve

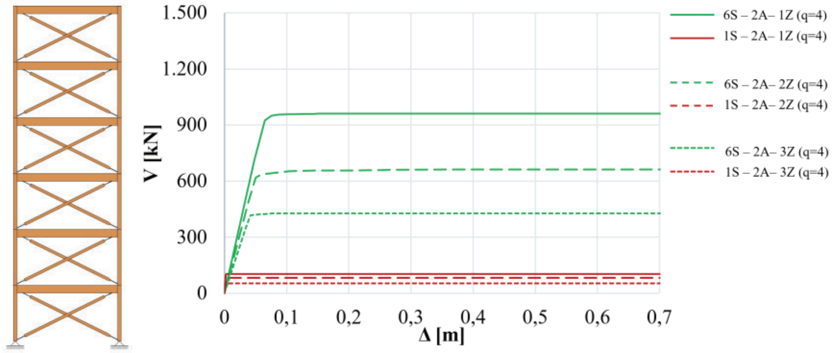

Strength [kN]

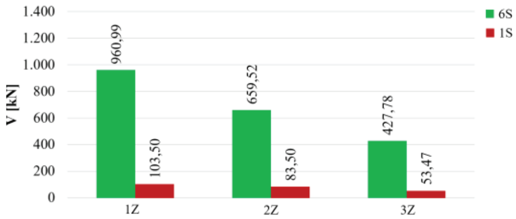

Stiffness [kN/cm]

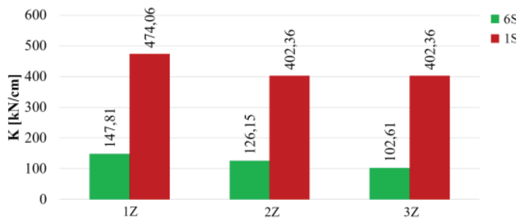

***q_Ω* (behaviour factor - overstrength)**

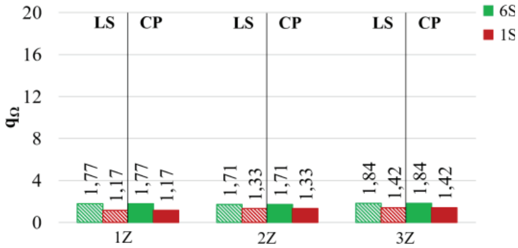

***q_μ* (behaviour factor - ductility)**

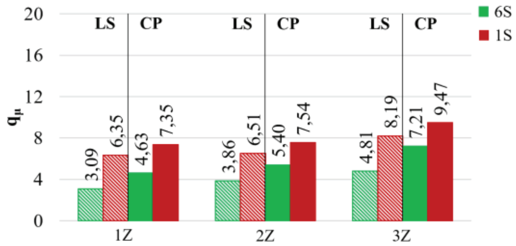

***q* (behaviour factor)**

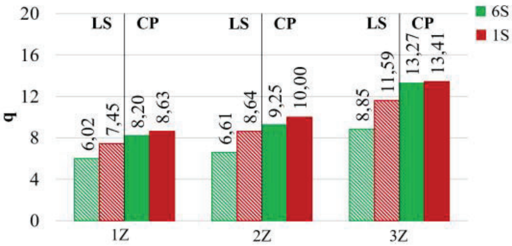

Table B.164 – 6S vs 1S, CBF X D with q_d=4: 2A; 1Z, 2Z, 3Z.

Pushover curve

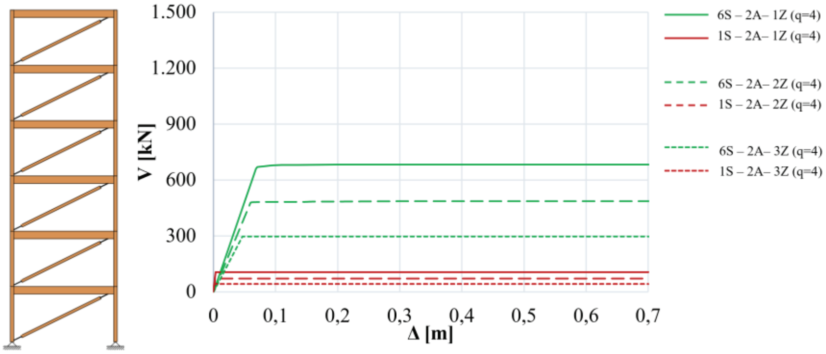

Strength [kN]

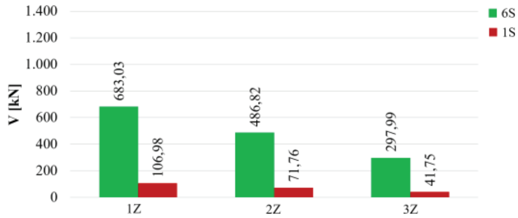

Stiffness [kN/cm]

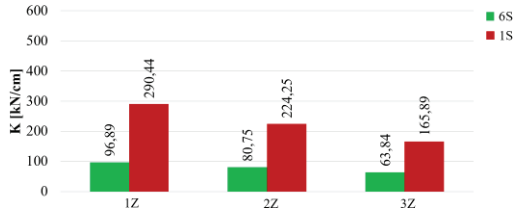

***q_Ω* (behaviour factor - overstrength)**

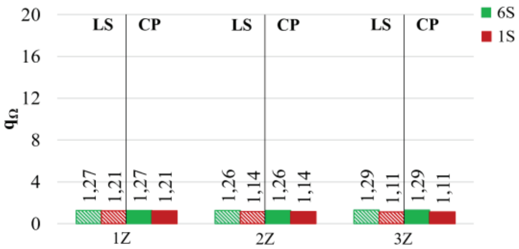

***q_μ* (behaviour factor - ductility)**

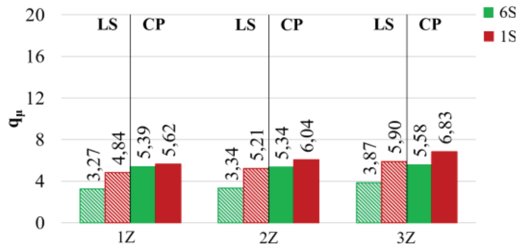

***q* (behaviour factor)**

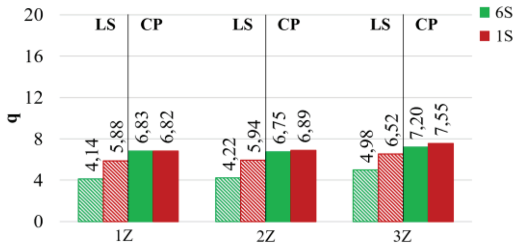

Table B.165 – 6S vs 1S, CBF EBF with q_d=4: 2A; 1Z, 2Z, 3Z.

Pushover curve

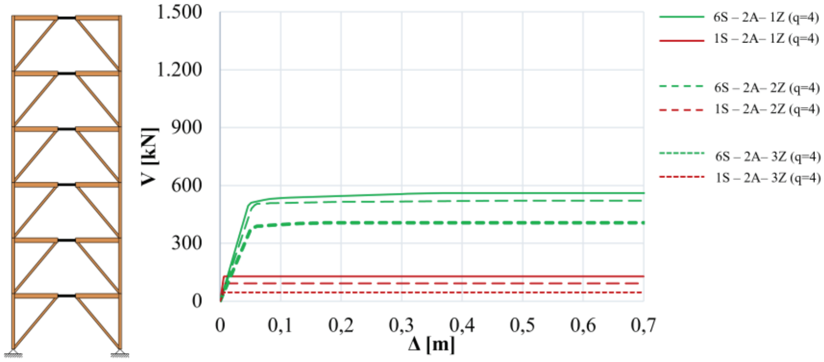

Strength [kN]

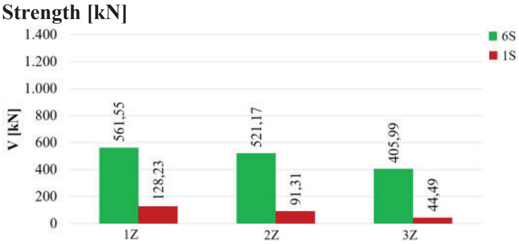

Stiffness [kN/cm]

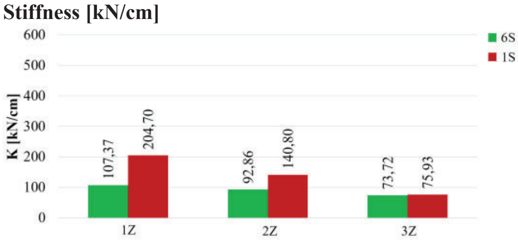

***q*$_\Omega$ (behaviour factor - overstrength)**

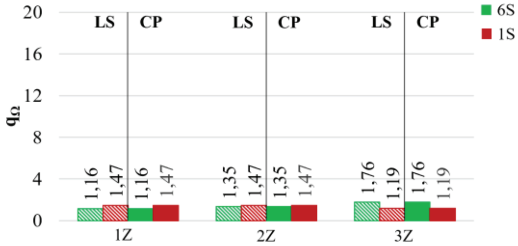

***q*$_\mu$ (behaviour factor - ductility)**

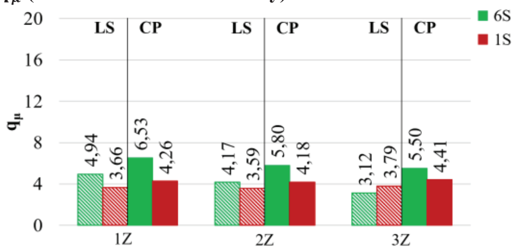

***q* (behaviour factor)**

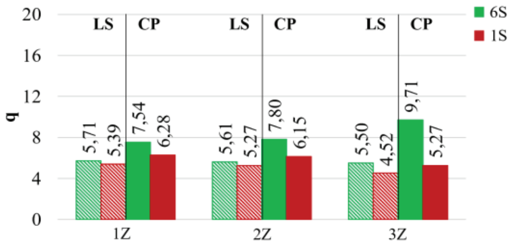

APPENDIX C

C.3.2 SEISMIC RESISTANT HEAVY TIMBER FRAME STRUCTURES WITH FVD DEVICES

C.3.2.7 STRUCTURAL DETAILS

The types of joints designed and the assembly between the structural parts are shown from the Figure C.1 to Figure C.4.

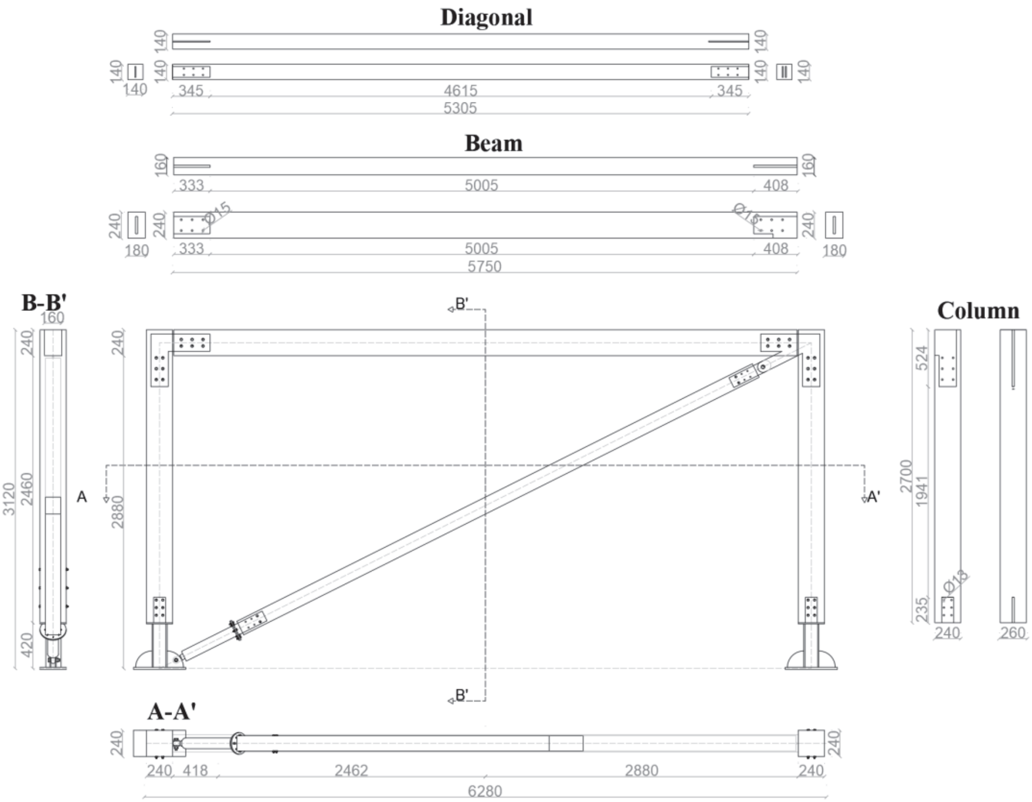
Diagonal
140
140
140
140
345
4615
345
140
140
140
5305
Beam
160
333
5005
408
160
240
180
240
Ø15
333
5005
Ø15
408
240
180
5750
B-B'
160
240
2460
3120
420
A
B'
240
2880
A'
B'
Column
524
2700
1941
Ø18
235
240
260
A-A'
240
240
418
2462
2880
240
240
6280

a)

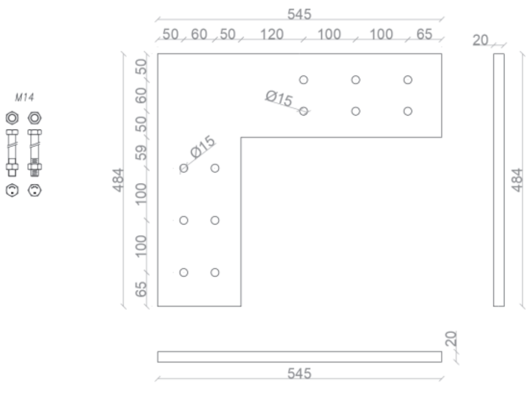
M14
545
50
60
50
120
100
100
65
20
50
60
50
59
100
100
65
484
Ø15
Ø15
484
20
545

b)

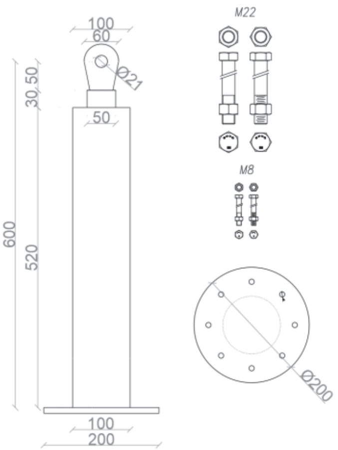
100
60
Ø21
30
50
50
600
520
100
200
M22
M8
Ø200

c)

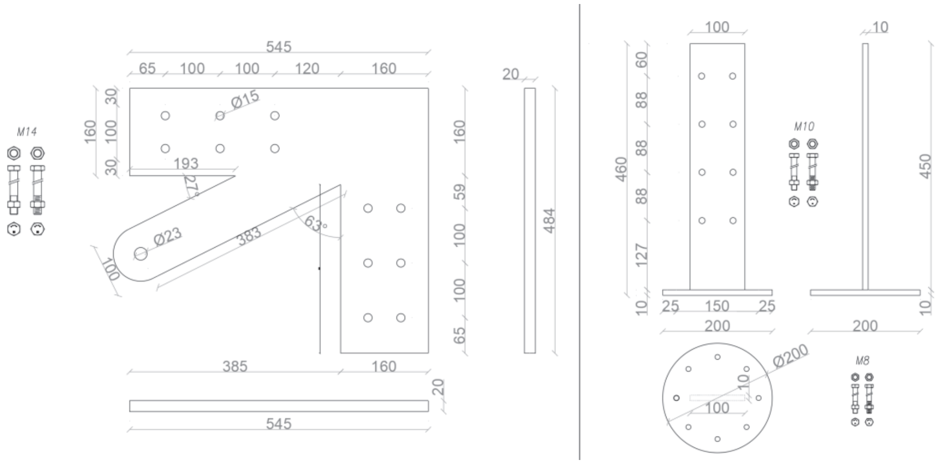

d)

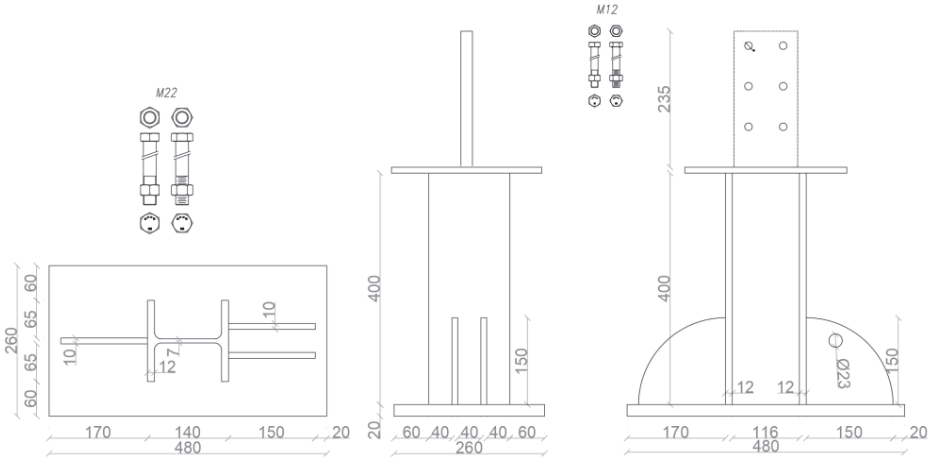

e)

Figure C.200 – MRF-D: a) Structural scheme; b) Beam-column node; c) FVD device; d) Beam-diagonal-column and FVD-diagonal nodes; e) Column-HE140-FVD-fondation node [mm].

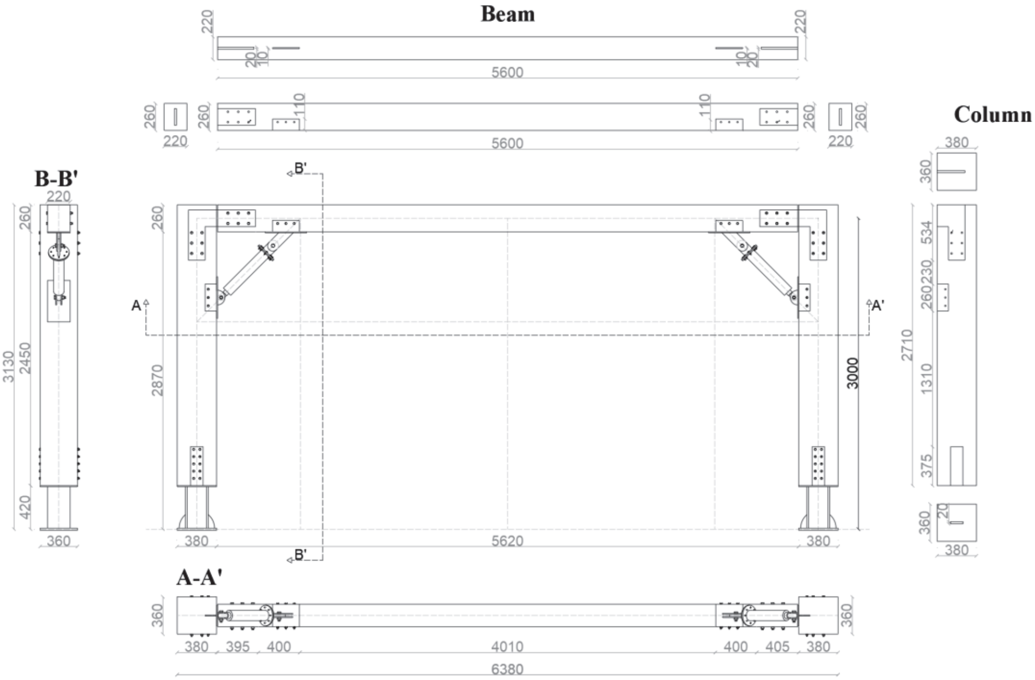
Beam
Column
B-B'
A-A'
A
A'
B'
5600
6380
5620
3000

a)

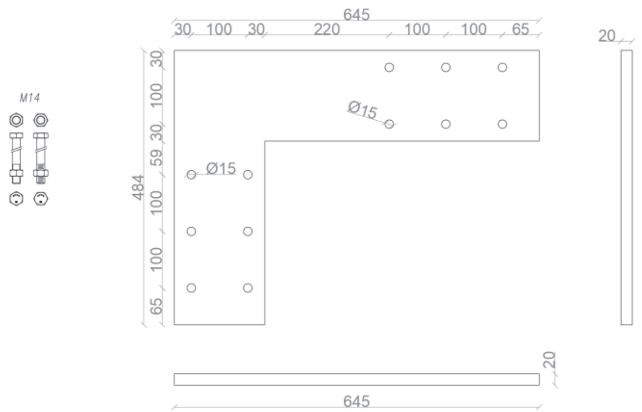
M14
645
Ø15
484

b)

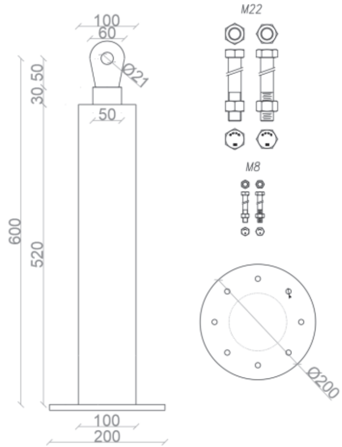
M22
M8
Ø21
600
520
Ø200

c)

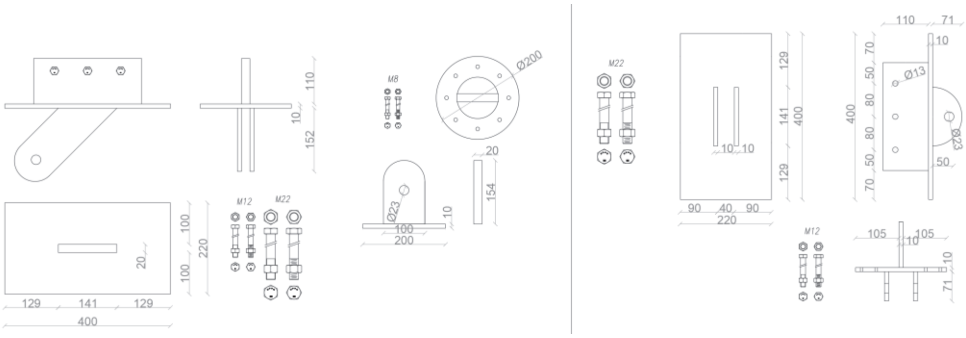

d)

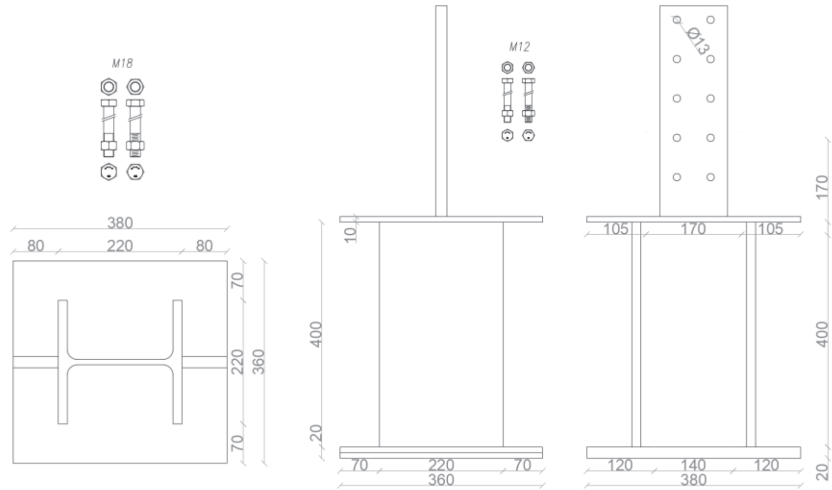

e)

Figure C.201 – MRF-H_1L_1: a) Structural scheme; b) Beam-column node; c) FVD device; d) Beam-FVD and FVD-column nodes; e) Column-HE220-fondation node [mm].

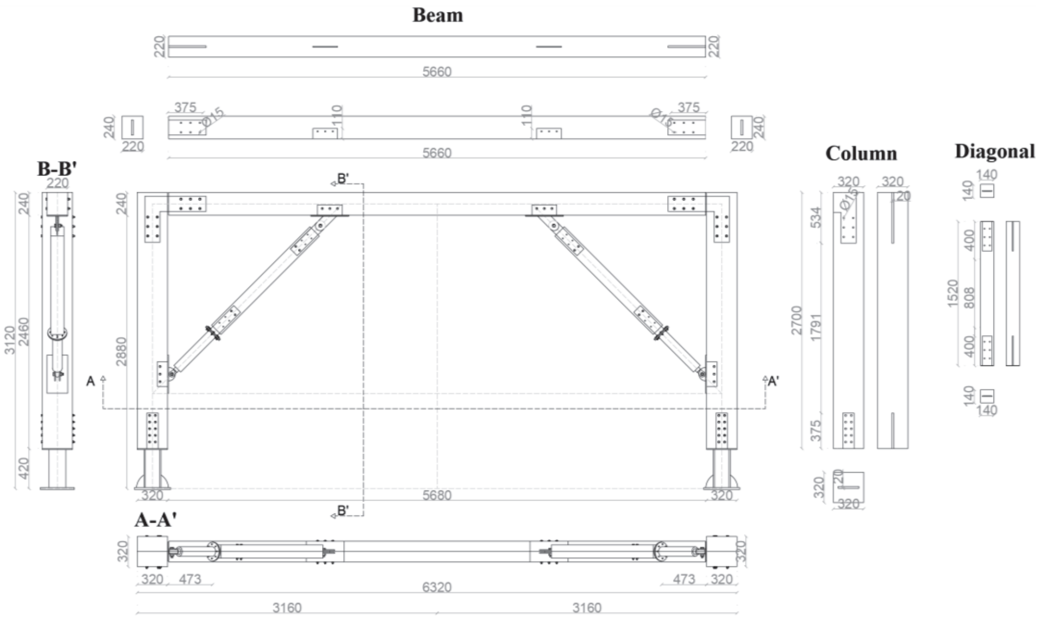
Beam
Column
Diagonal
B-B'
A-A'
A
A'
B'
5660
5680
6320
3160
3160

a)

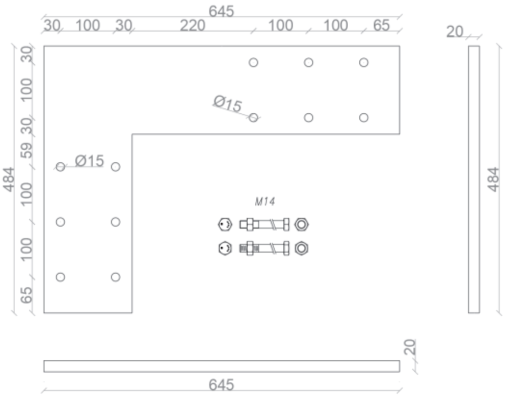
645
Ø15
M14
484
20

b)

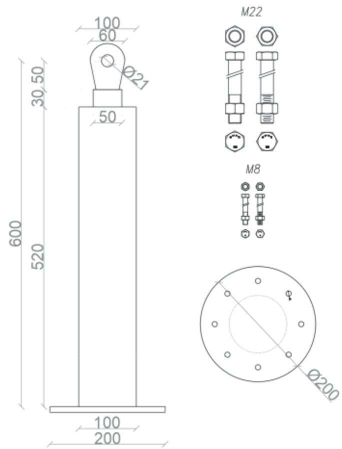
M22
M8
Ø21
Ø200
600
520
200

c)

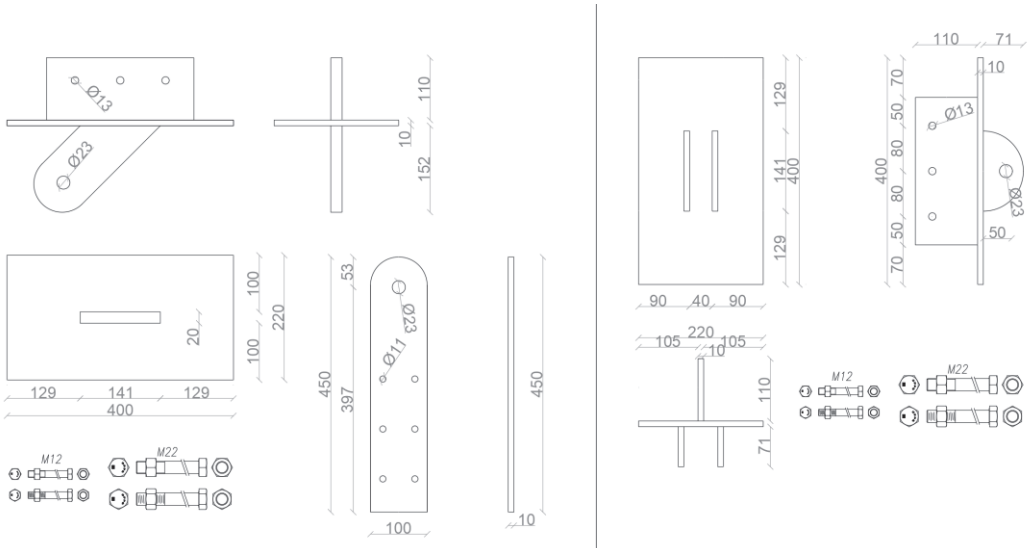

d)

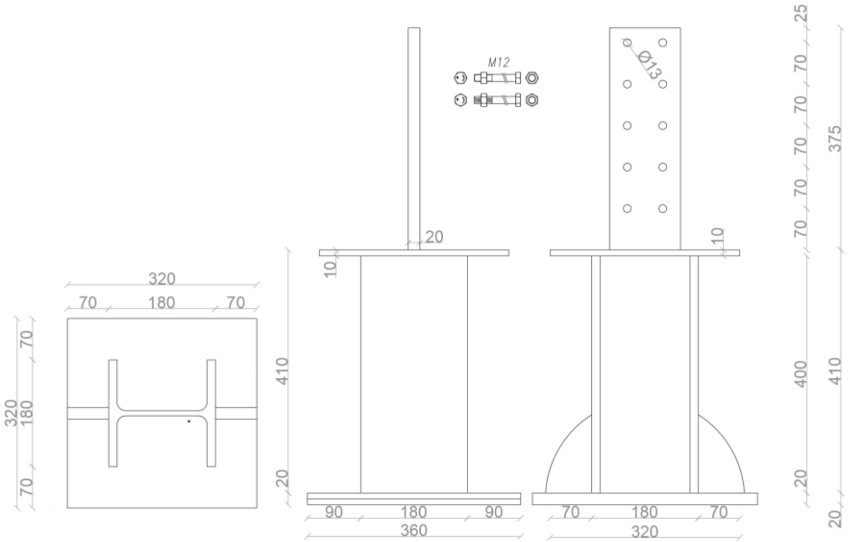

e)

Figure C.202 – MRF-H_2L_2: a) Structural scheme; b) Beam-column node; c) FVD device; d) Beam-diagonal and FVD-column nodes; e) Column-HE180-fondation node [mm].

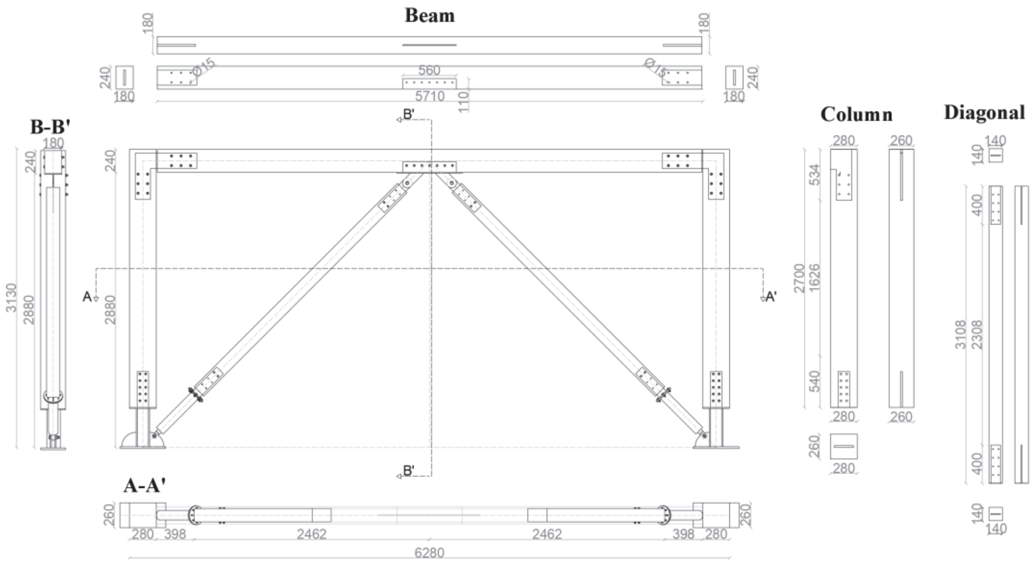
Beam
180
180
240
Ø15
560
Ø15
240
180
5710
110
180
B-B'
B'
180
240
240
3130
2880
A
2880
A'
B'
A-A'
260
280
398
2462
2462
398
280
260
6280
Column
280
260
534
2700
1626
540
280
260
260
280
Diagonal
140
140
400
3108
2308
400
140
140

a)

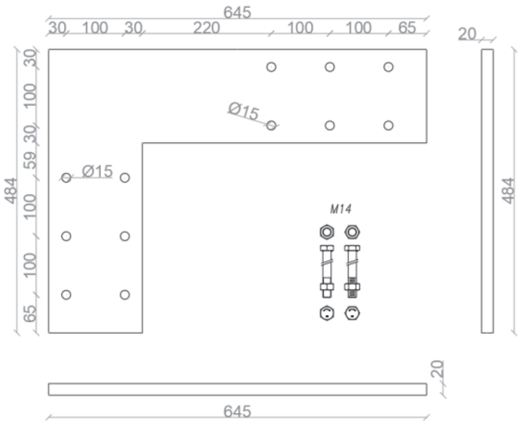
645
30
100
30
220
100
100
65
20
30
100
30
59
484
100
100
65
Ø15
Ø15
M14
484
20
645

b)

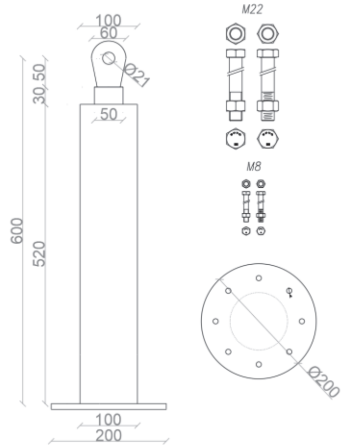
100
60
Ø21
30
50
50
600
520
100
200
M22
M8
Ø200

c)

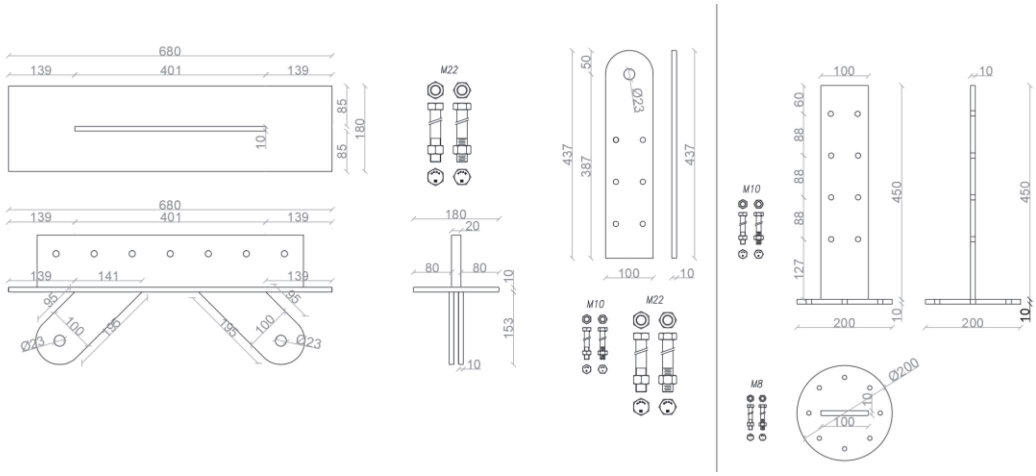

d)

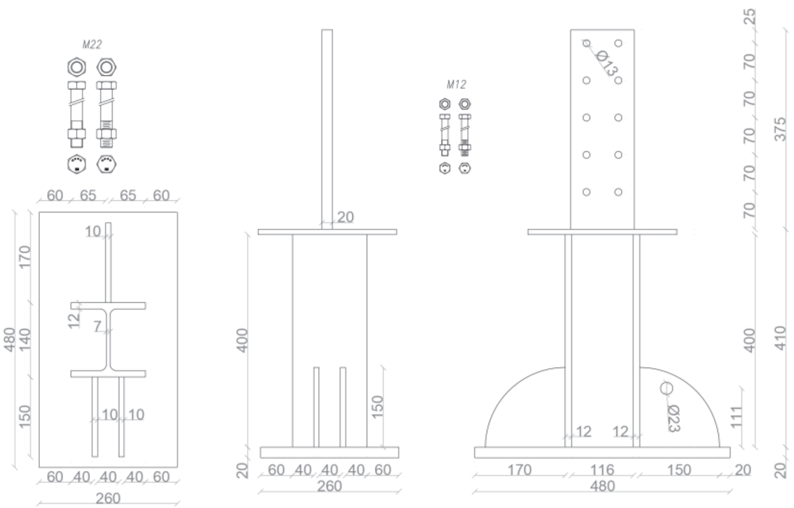

e)
Figure C.203 – MRF-H_3L_3: a) Structural scheme; b) Beam-column node; c) FVD device; d) Beam-diagonals and FVD-diagonal nodes; e) Column-HE140-FVD-fondation node [mm].